Use of Ethanol from Sweet Sorghum for Diesel Applications and the Generation of Energy from the Waste Products

Francis Omotola OLANREWAJU

Submitted in accordance with the requirements for the degree of Doctor of Philosophy

The University of Leeds

School of Chemical and Process Engineering

September 2021

Dedication

…dedicated in humble reverence to the Resurrection and the Life (Jesus Christ).

The candidate confirms that the work submitted is his own, except where work which has formed part of jointly authored publications has been included. The contribution of the candidate and the other authors to this work has been explicitly indicated below. The candidate confirms that appropriate credit has been given within the thesis where reference has been made to the work of others.

List of publications

- **Francis Omotola Olanrewaju**, Gordon E. Andrews, Hu Li, Herodotos N. Phylaktou. Bioenergy potential in Nigeria. Proceedings of the 14th International Congress on Chemical and Process Engineering, 26th – 29th May 2019, Bologna, Italy, DOI: https://doi.org/10.3303/CET1974011

Candidate as the first author of the paper procured the data during the field work that was carried out, analysed the data and wrote the paper under the supervision of Dr. Hu Li, Prof. Gordon E. Andrews, and Dr. Herodotos N. Phylaktou.

(Based on Chapter 2 of thesis)

- **Francis Omotola Olanrewaju**, Gordon E. Andrews, Hu Li, Herodotos N. Phylaktou. Improved model for the analysis of the Heat Release Rate (HRR) in Compression Ignition (CI) engines. *Journal of the Energy Institute,* 93**,** 1901-1913. DOI: https://doi.org/10.1016/j.joei.2020.04.005

Candidate as the first author of the paper carried out the experimental work on the Engine Test Bed to generate the basic model input data. Candidate developed, solved, validated the Leeds HRR model, analysed the model results and wrote the paper under the supervision of Dr. Hu Li, Prof. Gordon E. Andrews, and Dr. Herodotos N. Phylaktou.

(Introduction in Chapter 3, Methodology in Chapter 4, Results in Chapter 6; Section 6.4)

- **Francis Omotola Olanrewaju**, Yanlong Wu, Gordon E. Andrews, Hu Li, Herodotos N. Phylaktou. An improved Heat Release Rate (HRR) model for the analysis of combustion behaviour of diesel, GTL and HVO diesel. Proceedings of Powertrains, Fuels and Lubricants Virtual Conference,

22nd – 23rd September 2020, SAE Technical Paper 2020-01-2060, 2020. DOI: https://doi.org/10.4271/2020-01-2060

Candidate as the first author of the paper validated and applied the Leeds HRR model to alternative diesel fuels (GTL and HVO diesels) based on the experiment that was done by Yanlong Wu on the Engine Test Bed using pure ULSD, GTL, and HVO diesels. Candidate analysed the model results and wrote the paper under the supervision of Dr. Hu Li, Prof. Gordon E. Andrews, and Dr. Herodotos N. Phylaktou.

(Introduction in Chapter 3, Methodology in Chapter 4, Results in Chapter 6; Section 6.5)

- **Francis Omotola Olanrewaju**, Hu Li, Gordon E. Andrews, Herodotos N. Phylaktou. Effect of diesel-ethanol fuel blends on engine performance and combustion behaviour of Compression Ignition (CI) engines. Proceedings of the 2021 Powertrain Systems for Net-Zero Transport, 7th-8th December 2021, IMechE, London. CRC Press, Taylor and Francis Group. DOI: 10.1201/9781003219217-7

Candidate as the first author of the paper carried out the experimental work on the modern Yanmar diesel Gen-set engine. Candidate analysed the experimental data and wrote the paper under the supervision of Dr. Hu Li, Prof. Gordon E. Andrews, and Dr. Herodotos N. Phylaktou.

(Introduction in Chapter 3, Methodology in Chapter 4, Results in Chapter 7; Sections 7.1 to 7.7)

- **Francis Omotola Olanrewaju**, Hu Li, Zahida Aslam, James Hammerton, Jon C. Lovett. Analysis of the Effect of Syngas Substitution of Diesel on the Heat Release Rate and Combustion Behaviour of Diesel-Syngas Dual

Fuel Engine. *Fuel,* 312 (2022)**,** 1901-1913. DOI: https://doi.org/10.1016/j.fuel.2021.122842

Candidate as the first author of the paper developed and validated the HRR model for diesel-syngas dual-fuel RCCI diesel engines based on the experiment that was done by Zahida Aslam on the diesel-syngas dual-fuel RCCI Gen-set engine. Candidate analysed the model results and wrote the paper under the supervision of Dr. Hu Li. This is one of the outputs of a short-term contract with the project: Creating Resilient Sustainable Microgrids through Hybrid Renewable Energy Systems, another evidence of original and publishable research on the HRR.

(Methodology based on the concepts of the previously developed Leeds HRR model; Chapter 4 of thesis)

Acknowledgements

I would like to appreciate Dr. Hu Li, Professor Gordon E. Andrews, and Dr. Herodotos N. Phylaktou for guiding me through this work. The consistent supervision that was provided during the work was very helpful. I sincerely appreciate the encouragements given to me during the trying and uncertain times of the project.

I would like to thank the Petroleum Technology Development Fund (PTDF), Nigeria for the scholarship award to pursue my PhD. I appreciate the National Agency for Science and Engineering Infrastructure (NASENI), Nigeria for supporting me through the research.

I am grateful to Scott Prichard for the timely interventions and assistance during the engine tests. Thanks to Dr. Adrian Cunliffe and Karine Alves Thorne, for assisting with the analytical tests. Thanks also to Ed Woodhouse, Diane Cochrane, Simon Lloyd, Gurdev Bhogal, and Lucy Leonard for assistance offered during the preparation of samples for the analytical tests.

I wish to thank my colleagues: Yanlong Wu, James Hammertan (for trainings on the engines), Bintu G. Mustafa and Miss H. Mat Kiah (for trainings on the Cone), Zahida Anslam and Nina Oritz for helpful conversations during the project.

I am grateful to Professor Benjamin O. Aderemi, Professor Mukhtar Abdulkadir, and Professor Paul Okonkwo (my academic mentors).

I heartily express my thanks to my lovely Oluwakemi Esther (my supportive wife and human angel) and cheerful children (Fiyinfoluwa, Folafoluwa, and Fopefoluwa). Thanks to my dear mum, Mrs. Beatrice A. Osatuyi, my mother-in-law, Mrs. Mary Aduke Adeyele, extended families and friends. I appreciate my brethren in Christ for prayers and encouragements during my research.

Abstract

The efficient use of biofuels derived from sweet sorghum in transportation and power generation in Nigeria was investigated in this research. The work was divided into four components (resources assessment, diesel-ethanol (DE) blends stability test, diesel engine combustion test, and biomass gasification). An improved Heat Release Rate (HRR) model was developed to analyse the combustion behaviour of diesel engines. Two novel techniques were used to estimate combustion parameters in the HRR analysis that was done.

The resources assessment showed that Nigeria has a biomass potential of 200 billion kg/year while the bioethanol potential in the country is 10.1 billion litres. This shows that Nigeria has the potential to produce bioethanol for domestic use and for export.

The DE blends stability test showed that the range of concentrations for which pure ethanol is insoluble in diesel (the blend wall for diesel-ethanol (DE) blends) at 20 ^{o}C is 25-70% of ethanol. Pure ethanol has unlimited solubility in diesel at 38 ^{o}C. The investigated DE blends reduced the engine-out NOx by up to 40%. Also, 15% ethanol in diesel will reduce CO_2 emissions by 9%. However, the DE blends led to an increase in the emission levels of unburned hydrocarbons (THC), CO, and nanoparticles. The diesel emission aftertreatment devices (DOC and DPF) effectively reduced the tailpipe THC, CO, and particulate emissions.

It was confirmed from the HRR analysis that the excess air ratio (λ) has significant effect on the accuracy of the HRR model of diesel engines. Accurate predictions of the fuel consumption were obtained for different engine configurations and

fuels (pure diesel, alternative diesels, DE blends) when the specific heats ratio, γ was expressed as a function of temperature and λ in the HRR model.

Finally, the biomass gasification test showed that the stalk residue of sweet sorghum can be partially oxidised to generate syngas for electricity. The estimated optimum Ø, Cold Gas Efficiency (CGE), and Hot Gas Efficiency (HGE) for the gasification of the stalk residue of sweet sorghum are 2.1, 76.6% and 81% respectively. The current work shows that the investigated biofuels (bioethanol and syngas) from sweet sorghum stalk residue can be used in transportation and power generation for reduced CO_2 emissions.

Table of contents

List of figures

List of tables

Abbreviations and symbols

Abbreviations:

AFR	Air Fuel Ratio	
AN	Agriculture Nigeria	
ASC	Ammonia Slip Catalyst	
BDC	Bottom Dead Centre	
BMEP	Brake Mean Effective Pressure	Pa
BP	British Petroleum	
BSFC	Brake Specific Fuel Consumption	kg_{fuel}/kWh
BSHC	Brake Specific Heat Consumption	
BTE	Brake Thermal Efficiency	
CAD	Crank Angle Degree	
CCI	Cetane Index	
CDM	Clean Development Mechanism	
CFPP	Cold Filter Plugging Point	
CGE	Cold Gas Efficiency	%
CGT	Char Gasification Temperature	^oC
CI	Compression Ignition	
CN	Cetane Number	
COME	Castor Oil Methyl Ester	

CR	Compression Ratio	
CSF	Catalytic Soot Filter	
Cv	Calorific Value	MJ/kg
DBE	Diesel-biodiesel-ethanol	
DE	Diesel-ethanol	
DEE	Diethyl Ether	
DMS	Dynamic Mobility Spectrometer	
DOC	Diesel Oxidation Catalyst	
DOHC	Dual Overhead Camshaft	
DPF	Diesel Particulate Filter	
DPT	Differential Pressure and Temperature	
DSG	Dynamometer Services Group	
ECU	Engine Control Unit	
EGR	Exhaust Gas Recirculation	
EI	Emission Index	
EoC	End of Combustion	
ET	Engineering Toolbox	
ETB	Engine Test Bed	
ETCS	Engine Test Control System	
EVC	Exhaust Valve Closing	
FAO	Food and Agriculture Organization	
FBN	Fuel Bound Nitrogen	

FC	Fixed Carbon	
FDAE	Federal Department of Agricultural Extension	
FGN	Federal Government of Nigeria	
FID	Flame Ionization Detector	
FR	Forest Research	
FRN	Federal Republic of Nigeria	
FRS	Forest Resources Study	
FTIR	Fourier Transform Infrared	
GCV	Gross Calorific Value	
GDI	Gasoline Direct Injection	
GHG	Green House Gases	
GS	Global Security	
GTL	Gas-to-Liquid	
HC	Hydrocarbon	
HCCI	Homogeneous Charge Compression Ignition	
HGE	Hot Gases Efficiency	%
HHV	Higher Heating Value	MJ/kg
HRR	Heat Release Rate	J/CAD
HVO	Hydrotreated Vegetable Oil	
ICE	Internal Combustion Engine	
ID	Ignition Delay	millisecond
IDI	Indirect Injection	

IEA	International Energy Agency	
IMEP	Indicated Mean Effective Pressure	Pa
ISFC	Indicated Specific Fuel Consumption	kg_{fuel}/kWh
ITE	Indicated Thermal Efficiency	
IVC	Intake Valve Closing	
LHV	Lower Heating Value	MJ/kg
MEXA	Motor Exhaust Analyser	
MFB	Mass Fraction Burned	
MFIS	Multiple Fuel Injection Strategy	
MFM	Mass Flow Meters	
MFT	Maximum Flue Temperature	^oC
MLR	Mass Loss Rate	g/s
MSW	Municipal Solid Waste	
Mtoe	Million tonnes of oil equivalent	
NAERLS	National Agricultural Extension and Research Liaison Services	
NBS	National Bureau of Standards	
NDIR	Non-Dispersive Infrared	
NMHC	Non-Methane Hydrocarbons	
NOx	Oxides of nitrogen	
NPK	Nitrogen-Phosphorus-Potassium	
PEO	Polyethylene Oxide	

PFI	Port Fuel Injection	
PHRR	Peak Heat Release Rate	J/CAD
P'HRR	Primary Heat Release Rate	kW/m^2
PHSC-AS	Perturbed Hard Sphere Chain Association	
PKME	Palm Kernel Methyl Ester	
PM	Particulate Matter	
PMD	Paramagnetic Detector	
PN	Particulate Number	
PPE	Personal Protective Equipment	
RA	Risk Assessment	
RCCI	Reactivity Controlled Compression Ignition	
RME	Rape Methyl Ester	
RPR	Residue-to-product	
SCR	Selective Catalytic Reduction	
SFIS	Single Fuel Injection Strategy	
SHRR	Secondary Heat Release Rate	kW/m^2
SI	Spark Ignition	
SoC	Start of Combustion	
SOF	Soluble Organic Fraction	
SOHC	Single Overhead Camshaft	
SoI	Start of Injection	
SS	Sweet sorghum	

TDC	Top Dead Centre	
THC	Total Hydrocarbons	
TGA	Thermogravimetric Analyser	
THRR_mlr	Total Heat Release Rate (based on the mass loss rate)	kW/m^2
THR	Total Heat Release	MJ/m^2
TWC	Three-way-catalyst	
ULSD	Ultra Low Sulphur Diesel	
UN	United Nations	
USGS	US Geological Survey	
UVO	Used Vegetable Oil	
VAT	Value-Added Tax	
WB	World Bank	
WE	Wood Energy	
WEC	World Energy Council	
WLTP	Worldwide Harmonised Light Vehicles Test Procedure	
WPR	World Population Review	
WSD	Wear Scar Diameter	

Symbols:

a	Percentage of carbon in fuel	
A	Constant in Antoine's equation	

A'	Percentage (by mass) of ash in biomass on dry basis	
$A_1 - A_5$	Parameters in the AFR equation	
A_n	Nozzle minimum area	m^2
Af_g	Optimum gasification air flux	$g/(m^2s)$
Af_s	Stoichiometric air flux	$g/(m^2s)$
AFR_g	Optimum gasification AFR	
AFR_s	Stoichiometric AFR of Sweet sorghum stalks	
b	Percentage of H in fuel	
B	Constant in Antoine's equation	
c	Percentage of O in fuel	
C	Constant in Antoine's equation	
C'	Percentage (by mass) of carbon in biomass on dry basis	
C_A	Area coefficient	
C_D	Discharge coefficient	
C_{pj}	Concentration of pollutant j	ppm/vol %
d	Percentage of N in fuel	
d_h	Hydraulic diameter of exit duct	m
D	Diameter of syngas pipe	m
Dp	Particle diameter	nm

E'	Net heat of combustion per unit volume of oxygen consumed referred to 25 ^{o}C when CO_2 was formed	MJ/m^3 O_2
E''	Net heat of combustion per unit volume of oxygen consumed referred to 25 ^{o}C when CO was burned	MJ/m^3 O_2
g	Acceleration due to gravity	m/s^2
h	Height between the gasifier air inlet and flue gas outlet	m
H	Percentage (by mass) of hydrogen in biomass on dry basis	
Hv	Latent heat of vaporisation	kJ/kg
j	Pollutant species	
K	Equilibrium constant of water gas shift reaction	
K_1, k_1, k_2	Constants in γ functions from literature	
l	Vertical height of exit duct	m
L	Length of syngas pipe	m
M	Molar mass	kg/kgmol
m_f	Mass of fuel injected	kg
M_t	Engine brake torque	Nm
MW_e	Molar weight of exhaust gas	kg/kgmol
MW_p	Molar weight of pollutant	kg/kgmol

N	Speed of engine	rev/s
N'	Percentage (by mass) of nitrogen in biomass on dry basis	
O'	Percentage (by mass) of oxygen in biomass on dry basis	
O_{2_con}	Mole fraction of oxygen depleted in the first stage of the gasification	
p	Pressure	Pa
P	Brake power	W
p_a	Atmospheric pressure mmHg	
p_g	Saturated water vapour pressure at ambient temperature (20 ^{o}C)	mmHg
p_v	Partial pressure of water vapour in atmosphere	
P_{ch}	Sugden's parachor	
P_{fp}	Power to overcome friction and pumping losses	kW
Q	Volumetric flow rate of syngas	m^3/s
S	Depth of penetration	m
S'	Percentage (by mass) of sulphur in biomass on dry basis	
T_1	Average chimney temperature at the optimum Ø during the first stage of the	

	combustion (maximum temperature of the chimney at the optimum Ø)	K
T_2	Average chimney temperature at the optimum gasification Ø (during gasification)	K
T_{50}	Temperature of fuel @ 50% distilled point	K
t_d	Ignition delay time	millisecond
T_g	Temperature of gases in the cylinder at fuel injection	K
T_{ref}	Reference temperature	K
v_a	Natural draft intake air velocity	m/s
$\dot{V}_A$	Volumetric flow rate of air into the controlled atmosphere air box	m^3/s
V_{fc}	Volume of fuel consumed	m^3
V_H	Engine total displacement	m^3
x_1, x_2	Mole fractions of pure components	
x	H/C mole ratio	
$x_{CO_2}^{A^0}$	Initial concentration (in mole fraction) of carbon dioxide in the analyser (dry basis)	
$x_{CO_2}^{A}$	Concentration of carbon dioxide (in mole fraction) in the oxygen analyser (dry basis)	
x_{CO}^{A}	Concentration of CO (in mole fraction) in the oxygen analyser (dry basis)	

$x_{O_2}^{o}$	Initial concentration of oxygen (in mole fraction) in the inlet air (wet basis)	
$x_{O_2}^{A^0}$	Initial concentration of oxygen (in mole fraction) in the analyser (dry basis)	
$x_{O_2}^{A}$	Concentration of oxygen (in mole fraction) in the oxygen analyser (dry basis)	

Greek symbols:

γ	Specific heats ratio	
γ_0	Constant in γ function from literature	
γ_b	Specific heats ratio for burned mixtures	
γ_{mod}	Modified γ	
γ_u	Specific heats ratio for unburned mixtures	
ΔH_{298}^{o}	Heat of reaction at 298 K	KJ/mol
Δp	Pressure drop	Pa
$\Delta\theta$	Nozzle open period	CAD
ε	Parameter in the AFR equation	
ϵ	Darcy-Weisbach friction coefficient	
λ	Excess air ratio	
μ	Viscosity of the syngas	Pa.s
π	Constant	
ϕ	Equivalence ratio	
φ	Relative humidity	

ρ_o	Density of the intake air (air outside the gasifier) at ambient temperature (20 ^oC)	kg/m^3
ρ_{a1}	Density of air at T_1	kg/m^3
ρ_{a2}	Density of air at T_2	kg/m^3
ρ_f	Density of fuel	kg/m^3
ρ_g	Density of gas	kg/m^3
ρ_l	Density of liquid	kg/m^3
ρ_r	Density of the air in the gasifier	kg/m^3
ρ_v	Saturated vapour density	kg/m^3
σ	Surface tension	mN/m
σ_1, σ_2	Surface tension of pure components	mN/m
σ_m	Surface tension of mixture	mN/m
θ	Crank angle	CAD
ξ	Minor loss coefficients	
$\omega_1, \omega_2, \omega_3$	Constants in the derived exponential model of experimental γ data	

Chapter 1 Introduction

The combustion of conventional diesel in Internal Combustion Engines (ICEs) results in the emission of the environmentally harmful compounds: nitrogen oxides (NOx), carbon monoxide (CO), total hydrocarbons (THC), and soot (particulate emissions). Stringent emission standards have necessitated cleaner combustion and increased fuel efficiency from ICEs. This work investigates the stability of ethanol in diesel, the use of ethanol in diesel engines to reduce NOx and other harmful emissions from diesel engines as well as the gasification of the waste biomass from sweet sorghum and other agricultural wastes in Nigeria for heat and power.

Sweet sorghum is an attractive ethanol feedstock because ethanol can be produced from the juice of the crop by fermentation. Agriculture Nigeria (AN) reported that Nigeria has the third largest sweet sorghum bioresource in the world (AN, 2012). The country has the largest worldwide production of cassava. Both of these bioresources can be used to produce ethanol as an engine fuel. In addition, both of these bioresources have a large biowaste in the plant stems. For sweet sorghum, it is 1.25 kg of biowaste for one kg of sweet sorghum produced; for cassava it is 2 kg (Simonyan and Fasina, 2013). This waste can be gasified to produce heat or electricity. This research project looks at both ethanol for transport/electricity production and biomass waste gasification for power generation.

Ethanol use in Spark Ignition (SI) engines is well known and vehicles to burn ethanol up to 85% (fuel-flexible vehicles) are available. However, ethanol in gasoline is exclusively a transport fuel, whereas ethanol in diesel can be used in

power generation or transport. Also, Nigeria relies more on diesel for truck transport and this work investigated the use of ethanol in diesel engines. Ethanol can be used in diesel engines with a co-solvent and this work investigates ethanol used in diesels for electric power generation and truck transport using binary fuel blends of diesel and ethanol (diesohol).

This work looks at engine performance, emissions (including particle size and the use of a particle trap in combustion) as well as the Heat Release Rate (HRR) behaviour of diesel engines. In addition, the gasification of solid waste for electricity in a dual-fuel Reactivity Controlled Compression Ignition (RCCI) diesel engine was investigated using a two-stage gasification system for the gasification of solid biomass. Gaseous and particulate emissions were also be determined.

Bioenergy is a route to reduced CO_2 emission in Nigeria plus a route to improve energy supply for rural farmers. Nigeria is ranked 110 on the World Energy Council (WEC) Energy Trilema Index of 2017 with a ‘CDC’ score in energy security, energy equity, and environmental sustainability respectively (WEC, 2017). Nigeria’s rank and score on the Energy Trilema Index as shown in Figure 1.1 is quite very low relative to the highest rating (AAA) on the index. Energy security, affordability, and environmental sustainability in Nigeria will be greatly enhanced if the nation harnesses its abundant biomass resources for bioenergy production. This will, in turn, drastically improve Nigeria’s rating on the WEC Energy Trilema Index. Therefore, this research will help to achieve energy security, energy equity and environmental sustainability in Nigeria and in other developing countries by maximising the use of biofuels in transportation, power, and heat generation in Nigeria.

	2015	2016	2017	Trend	Score
Overall rank and balance score	**101**	**104**	**110**	▶	**CDC**
Energy performance					
Energy security	5	8	67	▶	C
Energy equity	107	108	113	▶	D
Environmental sustainability	102	101	98	▶	C
Contextual performance	117	117	114	▶	

Figure 1.1 Nigeria's Trilema Index ranking balance score (WEC, 2017)

1.1 Project outline

This research focusses on sweet sorghum biomass from Nigeria. The project was divided into four components, all of which were centred on sweet sorghum biomass as follows:

i. Resources assessment (availability and yield)

ii. Alcohol fuel blend stability test

iii. Ethanol for transportation (diesel engine combustion test)

iv. Energy recovery from sweet sorghum stalk/residue (two-stage gasification, Cone calorimeter experiments)

Figure 1.2 depicts the components of the project.

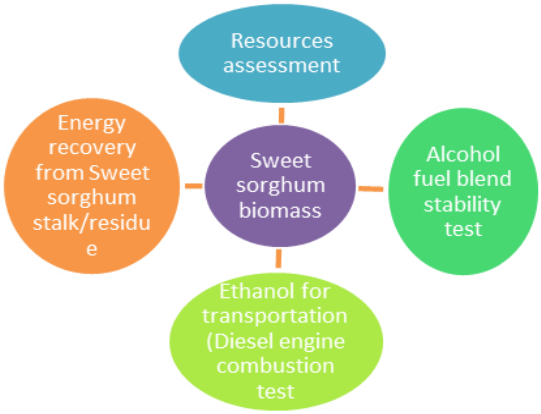

Figure 1.2 Research components

The first stage of this work involved the assessment of the biomass and bioenergy potential in Nigeria. The first stage of the work also established the bioethanol potential of sweet sorghum and the availability of the stalk residue of the crop in Nigeria. The results of the resources assessment that was conducted established the basis for the investigation of the use of ethanol from sweet sorghum for diesel applications and the recovery of energy from the stalk residue of the crop. Therefore, the resources assessment aspect of the work is presented in Chapter 2 of the thesis. The second stage involved the investigation of the stability of alcohol fuel blends. The third stage of the work was centred on a 96 kW, Euro V, IVECO Fiat Powertrain diesel engine on the Engine Test Bed (ETB) as well as the modern 5.7 kW Yanmar diesel Gen-set in the School of Chemical and Process Engineering (SCaPE). Data was collected in this research by direct measurements from the ETB. The parameters that were measured were torque, exhaust composition (NOx, CO_2, CO, O_2, unburnt hydrocarbon (THC) and particulate matter), engine fuel consumption rate, brake power, temperatures, and pressure traces (P-CAD data). This aspect of the work could not be completed on the IVECO engine due to the breakdown of the engine and the impact of the COVID-19 pandemic. The diesel engine combustion test was completed on the smaller diesel Gen-set engine which had a modern combustion chamber design. The data that was obtained from the two diesel engines (IVECO diesel and Yanmar diesel Gen-set engines) were analysed using software tools and compared to the results of previous researchers. The second major stage of the experimental work involved the use of the Cone calorimeter to test the fire behaviour of the stalk residue of sweet sorghum.

Sweet sorghum crop established the link between the two rigs that were used in the current investigation (the diesel Engine Test Bed and the Cone calorimeter).

The diesel engine combustion tests were carried out to investigate the potential of bio-ethanol (which can be produced from the juice in the stalk of sweet sorghum) to reduce the emissions from diesel engines. On the other hand, the Cone calorimeter tests were conducted to investigate the syngas potential of the stalk residue of sweet sorghum for electricity generation in dual-fuel, RCCI diesel engines.

1.2 Research questions

Nigeria is richly endowed with biomass resources. However, the nation has not started harnessing its biomass resources fully for biofuel or bioenergy production. This is partly because there are no recent and reliable estimates of the nation's biomass potential to show how enormous the biomass resources are in the country. There is a need also in Nigeria to minimise environmentally harmful emissions from diesel engines. Diesel engines are widely used in Nigeria in trucks for the transportation of goods and in power generating sets.

This research was aimed at proffering answers to the following research questions:

1. What are the current biomass and bioenergy potentials in Nigeria?
2. What is the current bioethanol potential of sweet sorghum in Nigeria?
3. What is the miscibility and storage stability limit of diesohol?
4. What is the blending ratio for stable diesel-ethanol (DE) blend fuels?
5. What are the effects of diesel-ethanol blend fuels on the performance and the combustion characteristics of diesel engines (emissions and HRR)?
6. What is the bioenergy potential of sweet sorghum waste (stalk residue)?

1.3 Aim and objectives

The aim of this research work was to assess the bioresources potential in Nigeria and harness the nation's bioenergy potential in transportation, and power generation with emphasis on sweet sorghum.

The objectives of the research were set as follows to address the research questions listed above:

1. To assess the bioenergy and bioethanol potentials in Nigeria.
2. To investigate the stability of binary (diesel-ethanol) fuel blends.
3. To investigate the use of ethanol blend fuels in diesel engines for emission reduction and increase in engine efficiency.
4. To investigate the HRR behaviour of diesel engines for different engine configurations and fuels/fuel blends.
5. To investigate the energy potential of sweet sorghum crop residue for electricity.

Chapter 2 Resources Assessment

2.1 Introduction

Biomass is an organic material that is derived from plant or animal sources. Nigeria is naturally endowed with large quantities of biomass. Biomass exists in different forms such as agricultural crops and residue, energy crops, forestry resources, algae, municipal and industrial wastes. This Chapter presents the biomass and bioenergy potentials in Nigeria. The bioethanol potential in Nigeria was also estimated.

2.2 Energy consumption and supply in Nigeria

Nigeria is a country in West Africa with a population of about 182,202,000 in 2015 and a yearly population growth rate of 2.55% as shown in Table 1 (FAO, 2016). The country has a land area of 92,377,000 ha from which 70,800,000 ha is used for agricultural purposes.

Table 2.1 Nigeria's statistics and population

Physical areas:	**Year**	**Value**	**Unit**
Area of the country	2013	92,377,000 (923,770)	ha (km^2)
Agricultural land (permanent meadows and pasture + cultivated land)	2013	70,800,000 (708,000)	ha (km^2)
➢ As % of the total area of the country	2013	77	%
➢ Permanent meadows and pasture	2013	30,300,000 (303,000)	ha (km^2)

➢ Cultivated area (arable land + area under permanent crops)	2013	40,500,000 (405,000)	ha (km^2)
• As % of the total area of the country	2013	44	%
• Arable land (temp. crops + temp. fallow + temp. meadows)	2013	34,000,000 (340,000)	ha (km^2)
• Area under permanent crops	2013	6,500,000 (65,000)	ha (km^2)
Population:			
Total population	2015	182,202,000	Inhabitants
• % rural	2015	52	%
Population density	2015	197	inhabitants/km^2

The industrial and economic growth of any nation requires steady power supply. Unfortunately, electricity is not easily or readily available in Nigeria. The low per capita consumption of electricity in Nigeria (100 kW as against about 10,000 kW for developed nations) results from low generation of electricity as well as the challenges of the national grid (FGN, 2006). Owing to the frequent power outages in Nigeria, industries, households and commercial firms have resorted to private diesel- and petrol-fuelled generators. This development has resulted in the death of over 10,000 Nigerians between 2008 and 2014 from the inhalation of poisonous CO gas that is emitted from the generators (Anyagafu, 2014). Heft-Neal et al. (2018) on the other hand, reported that exposure to particulate matter with diameter less than 2.5 μm ($PM_{2.5}$) in concentrations above the minimum

exposure levels led to 449,000 infant deaths in 2015 in sub-Saharan Africa. This incidence underscores the dire need for the incorporation of clean combustion technologies in combustion engines. Table 2.2 compares the energy consumption of Nigeria to that of Africa and the world.

Table 2.2 Energy consumption in Nigeria, Africa, and the world as of 2015

	Population (Inhabitants)	**Population density (Inhabitants/km^2)**	**Energy consumption (Mtoe)**	**Consumption per capita (GJ)**
Nigeria	182,202,000[a]	197[a]	120.60[e]	27.71
Africa	1,150,000,000[b]	39[c]	435[f]	15.84
World	7,260,000,000[b]	56.70[d]	13,147[f]	75.82

[a]FAO (2016); [b]Roser and Ortiz-Ospina (2017); [c]WPR (2017); [d]WB (2016); [e]IEA (2015); [f]BP (2017)

Table 2.2 shows that the population of the world as of 2015 was 7.26 billion while the population of Africa was 1.15 billion. Nigeria's population as of 2015 was 15.83% of Africa's population and 2.51% of the population of the world. The average population density of the world was 56.70 inhabitants/km^2 while that of Africa was 39 inhabitants/km^2 as of 2015. Nigeria, on the other hand, as the most populous nation in Africa had an average population density of 197 inhabitants/km^2. As of 2015, the energy consumption of the world and Africa were 13,147 Million tonnes of oil equivalent (Mtoe) and 435 Mtoe respectively. Nigeria's energy consumption as of 2015 was 120.60 Mtoe (27.7% of the continent's consumption). The annual energy consumption per capita of Africa and Nigeria (as of 2015) were 15.84 GJ and 27.71 GJ respectively. As the

population of the country and the population of the world grow annually, the consumption of energy and the demand for energy inadvertently increase. This underscores the need for the development and utilisation of sustainable (renewable) energy to meet the projected energy demands and avert global energy crisis.

The total production and importation of energy in Nigeria as of 2015 was 265 Mtoe while the overall consumption was 121 Mtoe as shown in Table 2.3, based on data from the International Energy Agency (IEA) (IEA, 2015). Table 2.3 shows that about 85% of total energy consumption in Nigeria comes from wood fuel and charcoal (traditional biomass). This is because the rural dwellers and the urban poor in Nigeria (the majority of the population) depend on traditional biomass for heating and cooking. According to Sambo (2006) wood fuel and charcoal are utilised by 80% of Nigerian households that live in the rural and urban areas for heating and cooking. The consumption of wood and charcoal for household cooking in Nigeria in 2014 was 46 and 3.2 million tonnes respectively (UN, 2017). This shows that wood fuel accounts for 94% of domestic traditional biomass consumption in Nigerian households. The relatively low consumption of charcoal in Nigerian households compared to wood is strictly related with the local process adopted for charcoal production. The local production method does not favour large scale production of charcoal, which is derived from wood, but is of a higher Calorific value (Cv) and a low yield relative to the original wood.

Table 2.3 Energy consumption by different sectors in Nigeria (IEA, 2015)

Sector	**Oil products**		**Coal**		**Natural gas**		**Biofuels/waste**		**Electricity**	
	Mtoe	**%**	**Mtoe**	**%**	**Mtoe**	**%**	**Mtoe**	**%**	**Mtoe**	**%**
Industry	0.40	5.26	0.00	0.00	2.60	34.21	4.20	55.60	0.40	5.26
Transport	8.40	100	0.00	0.00	0.00	0.00	0.00	0.00	0.00	0.00

Household/Others	2.70	2.62	0.00	0.00	0.00	0.00	98.70	95.64	1.80	1.74
Non-energy use	0.00	0.00	0.00	0.00	1.40	100	0.00	0.00	0.00	0.00

Table 2.3 also shows that 96% of biomass energy is utilised by the household sector in Nigeria. Saeed et al. (2015) reported that the household sector in Pakistan used 86% of the country's total biomass energy. Households in Nigeria use a relatively large share of the nation's total biomass energy compared to households in Pakistan. Both countries have a large rural population with no access to electricity but have agricultural waste that can be used to generate electricity instead of being burnt in the fields. The policy of the Federal Government of Nigeria (FGN) on the exploitation of forest resources requires that for every forest tree that is cut down, two trees must be planted, the Cut-one-plant-two policy (Ogunesan, 2017).

Table 2.3 shows that 8.40 Mtoe of total oil products (73% of oil products in 2015) was used in the transport sector in Nigeria. Also, 2.70 Mtoe (23.48%) was used in diesel generators for electricity in small and large-scale businesses, organizations, and households.

Figure 2.1 depicts the rising trend of bioenergy consumption in Nigerian households. Data on Nigeria's biofuel consumption from 1973 to 2015 were obtained from the IEA (2015) and plotted to depict the rising trend in the nation's household and non-industrial biofuels consumption. Nigeria's domestic utilisation of biofuels rose from 31.70 Mtoes in 1973 to 98.70 Mtoes in 2015.

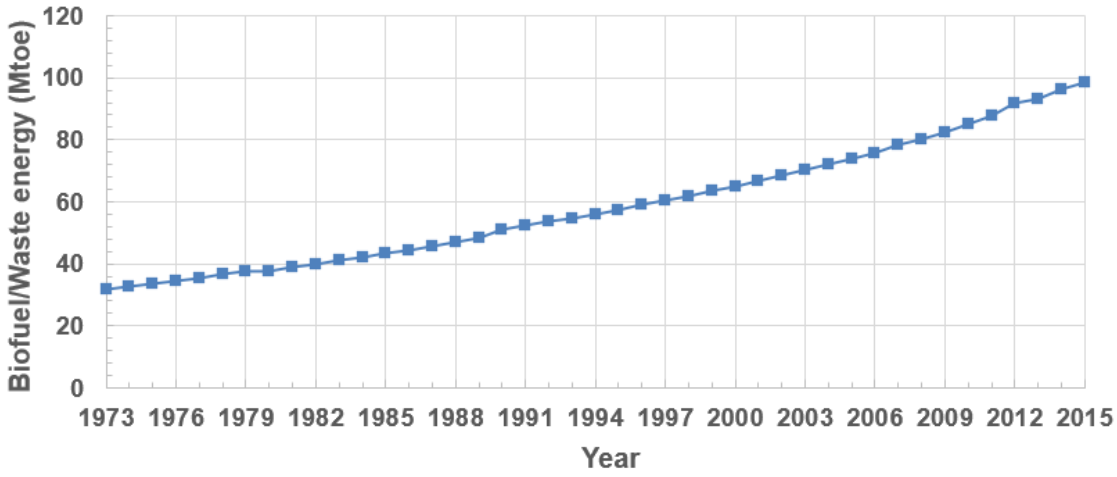

Figure 2.1 Nigeria's increasing biofuels consumption in households and non-industrial sectors (IEA, 2015)

2.3 Biomass resources in Nigeria

The climate of Nigeria determines the distribution of the biomass in the country. Nigeria is divided into seven major ecological zones as shown in Figure 2.2 (GS, 2013). These include: Sahel (marginal) savanna, Sudan (short grass) savanna, Guinea (woodland and tall grass) savanna, Rain forest, Freshwater swamp, Mangrove swamp, and Montane vegetation. The biomass resources in Nigeria are broadly classified into two categories, viz: agricultural resources and forestry resources. The southern part of Nigeria has more of woody biomass (forest vegetation) while the northern part of Nigeria has less woody biomass than the southern part.

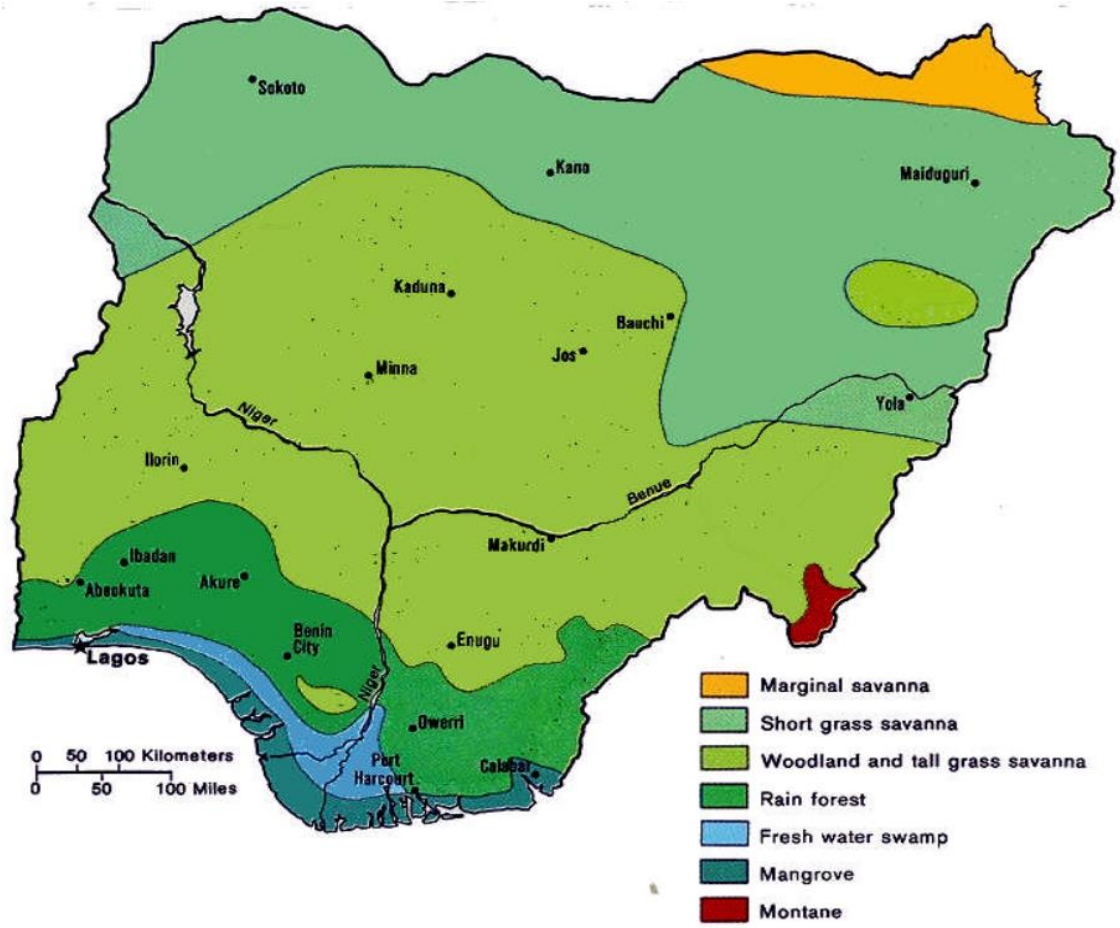

Figure 2.2 Climatic zones of Nigeria (GS, 2013)

The biomass and bioenergy potentials in Nigeria were quantitatively investigated by Jekayinfa and Scholz (2009) and Simonyan and Fasina (2013). Simonyan and Fasina (2013) reported a biomass potential and a bioenergy potential of 168.5 million tonnes and 48 Mtoe respectively for Nigeria based on the production data of 2010. Jekayinfa and Scholz (2009) estimated a biomass potential of 58 million tonnes and a bioenergy potential of 20.8 Mtoe for the country for 2004. The estimates of Jekayinfa and Scholz (2009) were specifically based on the production of major agricultural crops. The previous estimates of the biomass and the bioenergy potentials in Nigeria were not based on recent production/biomass data. Therefore, there is a need to estimate the biomass and bioenergy potentials in Nigeria using recent biomass and crop production data. Recent biomass data

were utilised in the current work to estimate the biomass potential in Nigeria. This enhanced the accuracy of the bioethanol potential that was subsequently estimated for the country.

2.3.1 Agricultural resources

The agricultural resources in Nigeria include agricultural crops and residues as well as energy crops. The quantities of agricultural crop residues are usually estimated from the crop production figures by multiplying the production figures by the corresponding residue-to-product ratio (RPR). The energy crops in Nigeria are crops that are produced or planted for energy and not for food. Examples of energy crops in Nigeria include jatropha, eucalyptus, and poplar. The production of some major agricultural crops that are cultivated in Nigeria is presented in Figure 2.3 for the years 2004 to 2014 (based on the data obtained from the National Agricultural Extension and Research Liaison Services (NAERLS), and the Federal Department of Agricultural Extension (FDAE), Nigeria (NAERLS and FDAE (2014)). Table 2.4 shows the crop production figures for the year 2014.

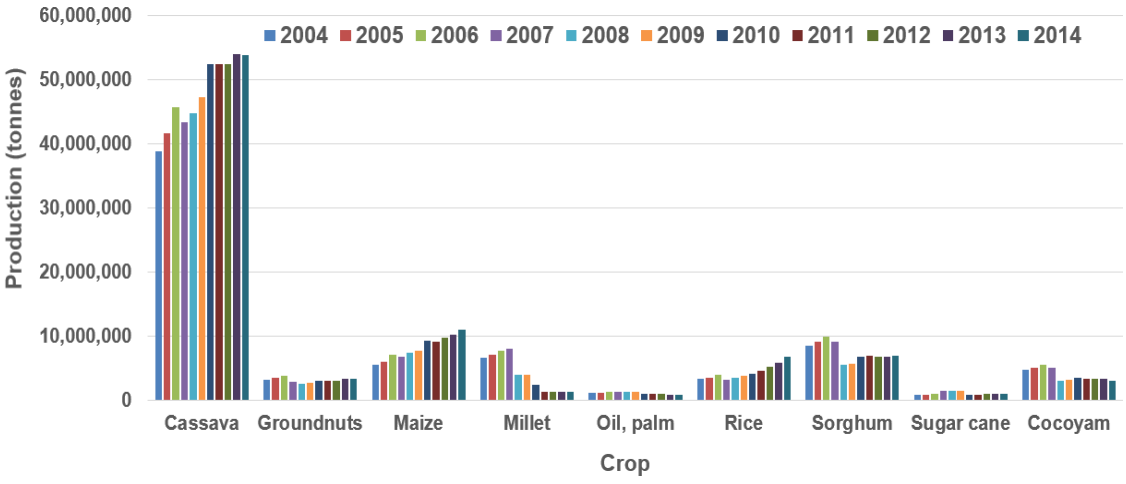

Figure 2.3 Crops cultivated in Nigeria (2004-2014)

Table 2.4 Crops cultivated in Nigeria (2014)

Crop	Element	2014
Sugar cane*	Area harvested (x1000ha)	64.97
	Yield (tonne/ha)	16.27
	Production (tonnes)	1,057,324
Cassava	Area harvested (x1000ha)	7,147.68
	Yield (tonne/ha)	7.52
	Production (tonnes)	53,782,800
Sorghum	Area harvested (x1000ha)	5,437.66
	Yield (tonne/ha)	1.28
	Production (tonnes)	6,941,100
Maize	Area harvested (x1000ha)	5,780.76
	Yield (tonne/ha)	1.90
	Production (tonnes)	10,990,500
Oil, palm*	Area harvested (x1000ha)	
	Yield (tonne/ha)	
	Production (tonnes)	910,000
Soybeans	Area harvested (x1000ha)	719.37
	Yield (tonne/ha)	0.94
	Production (tonnes)	678,900
Millet	Area harvested (x1000ha)	1,575.78

	Yield (tonne/ha)	0.88
	Production (tonnes)	1,385,100
Groundnut	Area harvested (x1000ha)	2,752.9
	Yield (tonne/ha)	1.24
	Production (tonnes)	3,410,000
Rice	Area harvested (x1000ha)	3,095.9
	Yield (tonne/ha)	2.18
	Production (tonnes)	6,734,100
Cowpea	Area harvested (x1000ha)	3,612.22
	Yield (tonne/ha)	0.58
	Production (tonnes)	2,093,200

* FAO, 2014

The production figures for sorghum declined from 9,866,000 tonnes in 2006 to 6,941,100 tonnes in 2014 (Figure 2.3). Sorghum is mainly cultivated in Northern Nigeria. The observed decline in the production of the crop was due to the insurgency that affected the regions where the crop is grown from 2009 to 2014. However, peace is being restored in Northern Nigeria and the production of sorghum is expected to soar again.

The land use in Nigeria is depicted in Figure 2.4 (FAO, 2014). Figure 2.4 shows that Nigeria still has vast lands that are left uncultivated in the arable land sector.

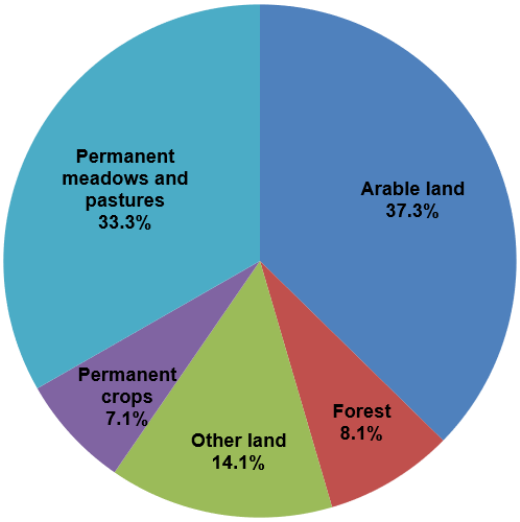

Figure 2.4 Land use in Nigeria (FAO, 2014)

Nigeria has great potentials to increase its bioenergy resources. The cultivated land in Nigeria is 44% of the total area (FAO, 2016). This leaves about 30,000,000 ha of agricultural land uncultivated. If 50% (15,000,000 ha) of the uncultivated land is available for energy crop production, the production of the crops can be increased by 37%.

2.3.2 Forestry resources

The forestry resources in Nigeria are categorised into forestry biomass and forestry residues.

2.3.2.1 Forestry biomass

Nigeria's forest reserve is estimated to be 10 million hectares which is about 11.3% of the total land area of the country (Beak, 1998). Tables 2.5 and 2.6 show the forest resources and forest products that are available in Nigeria as of 2010.

Table 2.5 Forest resources in Nigeria in 2010 (Beak, 1998)

Forest types	Area in forest reserves (ha)	Portion of total forested area in reserves (%)	Area in free forest areas (ha)	Total areas of forest types in FRS* study area (ha)	Portion of total forested area in FRS study area (%)
Savanna woodland	1,424,029	52.00	6,922,663	9,736,158	58.00
Lowland rainforest	832,237	30.40	1,580,928	2,881,755	17.20
Freshwater swamp forest	226,242	8.30	1,430,436	1,656,499	9.90
Mangrove forest	48,859	1.80	945,592	997,451	5.90
Montane forest	18,271	0.70	466,036	685,150	4.10
Riparian forest	46,583	1.70	431,537	509,415	3.00
Plantations (agriculture)	0	0	0	164,100	1.00
Plantation (forest)	144,666	5.30	704	145,379	0.90
Total	**2,740,887**		**11,777,896**		

*Forest Resources Study

Table 2.6 Production of forest products in Nigeria in 2010 (FAO, 2012)

Forest product	Quantity	
	m^3	tonnes
Chemical wood pulp	-	14,000
Industrial round wood	2,279,000	-
Wood fuel	63,214,728	17,384,050[a]
Wood charcoal	17,909,495[b]	3,940,089
Paper board	-	18,000
Particle board	40,000	-
Plywood	56,000	-
Printing/writing paper	-	1,000
Pulp wood/round/split	39,000	-
Recovered paper	-	8,000
Sawn logs + Veneer logs	7,100,000	-
Sawn wood	2,000,000	-
Veneer sheets	1,000	-
Wrapping + packaging + board	-	18,000

[a]Based on wood density of 275 kg/m^3; [b]Based on charcoal density of 220 kg/m^3 (WE, 2006)

2.3.2.2 Forest residues

Forest residues are logging residues (tops, branches) and process residues (off-cuts, sawdust) from wood industries. Forest residues are mainly produced in the southern part of Nigeria where the climate favours forest vegetation.

2.3.3 Urban wastes and other wastes

These are the wastes that are generated from the activities of man. They are broadly classified into municipal solid wastes, animal wastes and human wastes. The organic component of these wastes can be digested anaerobically to produce biogas.

2.4 Potential yield of biomass and bioenergy in Nigeria

The government of Nigeria has initiated several biofuels projects in recognition of the bioenergy potential in the country. These biomass projects and their status were reported by Ohimain (2010). Lands have been procured for the construction of the plants as well as the cultivation of the commercial crops that will provide the required quantity of feedstock based on the targeted plant capacity. The uncultivated arable lands in Nigeria can also be used to cultivate identified commercial crops such as sweet sorghum strictly for biofuel production. This will further boost the nation's bioenergy potential and biomass resources in general. This implies that Nigeria has biomass and bioenergy potentials that are beyond the figures that have been estimated in this work.

2.5 Nigeria's bioenergy potential

2.5.1 Crop residues

There are no official estimates for the residues that result from agricultural crops. The estimates are usually based on crop production figures such as those shown in Table 2.4. The quantity of residues for selected annual crops (Table 2.7) were

arrived at by using the averages of the latest available production figures for the crops (2004-2014) and their RPR. On this basis, the calculated crop residue that was available for energy in 2014 was 153.75 million tonnes of residues. The estimated available crop residues in this work is 8.13 million tonnes greater than the estimate of Simonyan and Fasina (2013). The authors' estimate of 145.62 million tonnes of crop residues was based on the production figures of 2010. Therefore, the updated crop residues estimate in the current work is more accurate than the estimate of the authors. Table 2.7 presents the estimated energy potentials of the crop residues. The estimated crop residues energy potential in the current work is 48.58 Mtoe (2,033.85 PJ). The current estimate is 1.79 Mtoe above the estimate of previous authors as of 2010. If 30% biomass to energy conversion efficiency is applied, the effective bioenergy that is obtainable from crop residues in Nigeria is 14.57 Mtoe (~2% above the estimate of previous authors). This also shows that Nigeria's bioenergy potential increases by the year.

Table 2.7 Energy potential estimate for agricultural crops in Nigeria (2014)

Crop	Production ($x10^3$ tonne)	Residue type	RPR[a*]	Moisture content (%)*	Total residue ($x10^6$ tonnes)	% available	Weight available ($x10^6$ tonnes)	LHV[b*] (MJ/kg)	Residue energy potential (PJ[c])	Residue energy (Mtoe)
Rice	4354	Straw	1.757	12.71	7.65	100	7.65	16.02	122.55	2.93
		Husk	0.2	2.37	0.87	100	0.87	19.33	16.83	0.4
Maize	8181	Stalk	2	15	16.36	70	11.45	19.66	225.17	5.38
		Cob	0.273	7.53	2.23	100	2.23	16.28	36.36	0.87
		Husk	0.2	11.11	1.64	60	0.98	15.56	15.28	0.36
Cassava	47886	Stalks	2	15	95.77	20	19.15	17.5	335.20	8.01
		Peelings	3	50	143.66	60	86.19	10.61	914.53	21.84
Groundnut	3128	Shells	0.477	8.2	1.49	100	1.49	15.66	23.37	0.56
		Straw	2.3	15	7.19	50	3.60	17.58	63.24	1.51
Soybean	580	Straw	2.5	15	1.45	100	1.45	12.38	17.95	0.43
		Pods	1	15	0.58	100	0.58	12.38	7.18	0.17
Sugarcane	1076	Bagasse	0.29	50	0.31	80	0.25	18.1	4.52	0.11
		Tops/leaves	0.3	10	0.32	100	0.32	15.81	5.10	0.12
Cotton	263	Stalk	3.743	12	0.98	100	0.98	18.61	8.32	0.44

Millet	4110	Straw	1.75	15	7.19	80	5.75	12.38	71.23	1.70
Sorghum	7460	Straw	1.25	15	9.33	80	7.46	12.38	92.35	2.21
Cowpea	2294	Shell	2.9		6.65	50	3.33	19.44	64.66	1.54
Total							**153.76**		**2033.85**	**48.58**

*Simonyan and Fasina (2013); [a]Residue-to-product ratio; [b]Lower Heating Value; [c]petajoule

The estimated quantity and residue energy for perennial crops in Nigeria were computed as shown in Table 2.8 by using the residues percentages reported by Koopmans and Koppeyan (1997), the wood densities reported by Alakangas (2005) and the LHV for wood residues (WE, 2006). Also, the RPR data for perennial crops of Chong and Idrus (1988) were used. The summary of the available quantity and residue energy for the perennial crops are presented in Figures 2.5 and 2.6 respectively. Figures 2.5 and 2.6 show that Nigeria has a perennial crop biomass capacity of about 2,346 million tonnes of residues from which 0.69 Mtoe (28.88 PJ) of energy can be generated.

Table 2.8 Residues estimate for plantation crops (2014)

Crop type	Production (tonnes)	Residue type	RPR	Total residue (tonnes)	Fraction available	Total amount available (Mtonnes)	LHV[b] (MJ/kg)	Energy potential (PJ)	Residue energy (Mtoe)
Oil palm	910,000	Fibre	0.66[a]	600,600	0.8	480.48	11.34	5.45	0.13
		Empty bunches	1.1[a]	1,001,000	1.0	1001	8.16	8.17	0.20
		Palm kernel	0.29[a]	68,150	0.75	51.11	18.83	0.96	0.02
Cocoa	248,000	Pods	0.56[b]	138,880	0.9	125	15.12	1.89	0.05
Coconut	267,520	Husk	0.97[a]	259,494.4	0.9	233.5	18.63	4.35	0.10
		Shell	0.49[a]	131,084.8	0.75	98.31	18.09	1.78	0.04
Natural rubber	151,104	Leaves	3.37	509,220.48	0.7	356.45	17.63	6.28	0.15
Total				**2,708,429.68**		**2.35**		**28.88**	**0.69**

[a]Chong and Idrus (1988); [b]Simonyan and Fasina (2013)

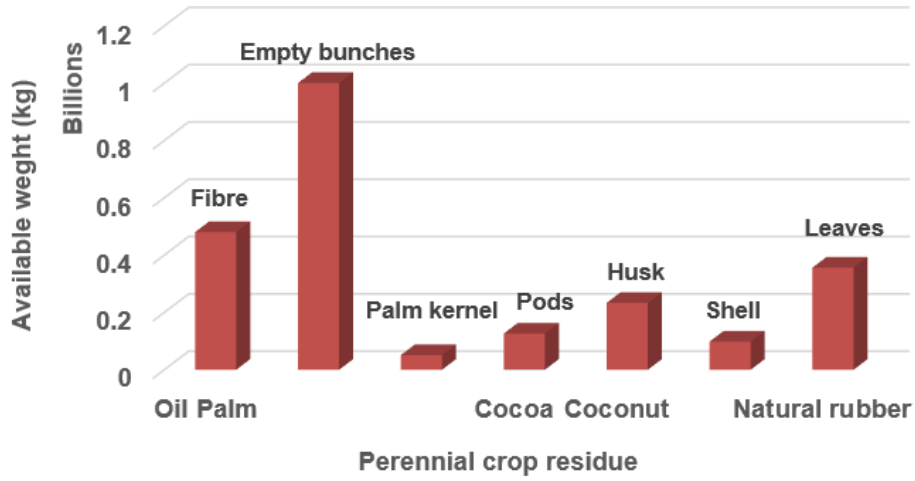

Figure 2.5 Residue weight estimates for perennial crops in Nigeria

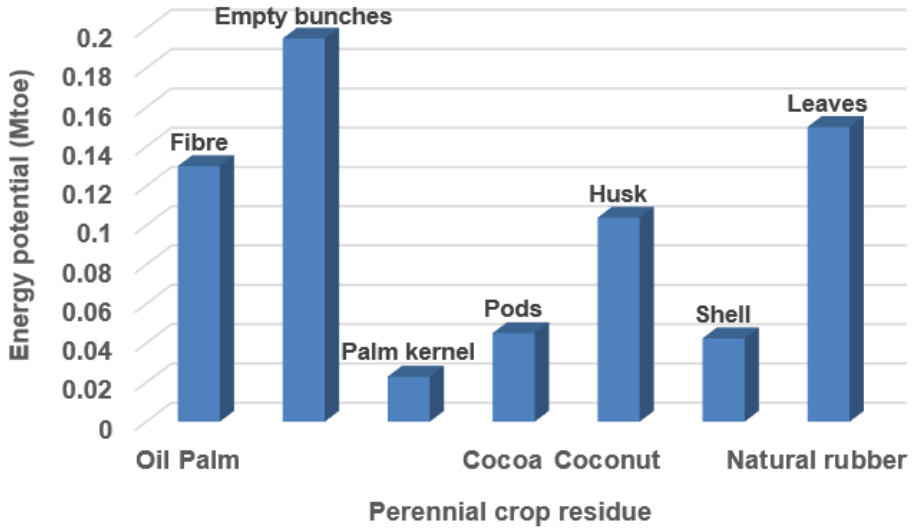

Figure 2.6 Residue potential energy for perennial crops in Nigeria

2.5.2 Forest residues

Table 2.9 summarises the forest residues that are available in Nigeria. The energy potentials for the residues were estimated as shown in the table based on the data that was obtained from FAO (2012). The estimated energy potential of Nigeria's forest residue as shown in Table 2.9 is about 8.68 Mtoe (363 PJ) which is obtainable from a biomass weight of about 19 million tonnes of forest residues.

Table 2.9 Forest and wood processing residues in Nigeria (2010)

Type of residue	Residues	% of residues[a]	Total residues (m^3)	Density[b] (kg/m^3)	Total residues (tonnes)	LHV[b] (MJ/kg)	Residue energy (PJ)	Residue energy (Mtoe)
Logging	Solid wood	40	911,600	395	360,082	19.31	7.00	0.17
	Dust	20	455,800	250	113,950	19.10	2.18	0.05
Sawmilling	Sawdust	12	273,480	300	82,044	19.10	1.57	0.04
	Solid wood	38	866,020	395	342,077.90	19.31	6.61	0.16
Plywood	Solid	45	25,200	395	9,954	19.31	0.19	0.005
	Dust	5	2,800	250	700	19.10	0.01	0.0002
Particle board	Dust	10	4,000	250	1,000	19.10	0.02	0.0005
Wood fuel			65,753,628	275[c]	1,808.2	19.10	345.37	8.25
Total					18,992,055.60		362.95	8.68

[a]Koopmans and Koppeyan (1997) [b]Alakangas (2005) [c]WE (2006)

2.5.3 Municipal Solid Waste (MSW)

The estimated yearly Municipal Solid Waste (MSW) potential in Nigeria is 17 million tonnes with an organic content of 7.5 million tonnes (Table 2.10). Simonyan and Fasina (2013) estimated 3.17 million tonnes of MSW for the urban population of Nigeria in 2010. The estimate was based on the per capita waste generation of Ibadan (a city in Nigeria) as reported by Eisa and Visvanathan (2002). The authors estimated a total recoverable MSW of 1.90 million tonnes of waste based on 60% waste recovery from which 4.45×10^{-6} Mtoe (186.33 GJ) could be generated. However, the estimate in this work is based on MSW data that was obtained for the entire country. The estimated recoverable organic waste from the annual MSW produced in Nigeria is 4.51 million tonnes based on 60% recovery. The energy potential of the recoverable organic waste is 0.51 Mtoe (21.36 PJ). The MSW estimate of Simonyan and Fasina (2013) was 1.9 million tonnes which is 58% lower than the current estimate.

Table 2.10 Bioenergy potential from Municipal Solid Waste (MSW) in Nigeria

Region	**Annual waste (tonnes)***	**Annual organic waste (tonnes)***
Northeast	1511712	1018007.52
Northwest	2898948	630398.32
Northcentral	1675272	939813.64
Southeast	894955	560860.44
Southwest	6644132	1693144.64
South-south	1482080	1388796.32
Other cities	1958016	1281029.28
Total	**17065115**	**7512050.16**

Estimation of energy from organic waste: Waste recovery (%): 60 Available organic waste (million tonnes): **4.507** Biogas yield from waste (m^3/kg): 0.212** LHV of biogas (MJ/m^3): 22.35[a] Total biogas from organic waste (x10^6 m^3): **955.48** **Total energy from organic waste (PJ): 21.36** **Total energy from organic waste (Mtoe): 0.51**		

*Suberu et al. (2013); **Neilfa et al. (2014); [a]Astals and Mata (2011)

2.5.4 Animal waste

A total of 17.69 million tonnes of dry animal dung/year was estimated for 2013 from which the calculated yield of biogas was 4.76 billion m^3/year (Table 2.11). Figures 2.7 and 2.8 present the estimated biomass and bioenergy potentials of animal wastes in Nigeria. The estimated volume of biogas in this work is equivalent to 2.54 Mtoe (106.39 PJ). Simonyan and Fasina (2013) estimated 15.76 million tonnes of dry matter and 4.19 billion m^3 of biogas for Nigeria as of 2010. Ben-Iwo et al. (2016) reported an annual biogas yield of 2.48 billion m^3 based on 0.03 m^3 gas yield per kg of fresh animal waste. Compared to the estimate in this work, these authors have under-estimated the biogas yield that

is obtainable from animal wastes in Nigeria. The estimates in this work are more reliable than previous estimates because they are based on recent animal population data. The dry matter and potential biogas estimates in this work are higher than those of the authors (approximately 12% and 14% higher respectively) because over the years, the population figures of animals in Nigeria have increased.

Table 2.11 Animal wastes production and potential for biogas yield in Nigeria (2013)

Type	Population*	Dry matter production (kg/head/day)[a]	Amount of dry matter produced per year (Mtonnes)	Fraction recoverable	Amount of dry matter available per year (Mtonnes)	Biogas yield	
						m^3/kg dry matter[b]	Billion m^3
Cattle	19,374,029	2.860	20.22	0.3	6.07	0.20	1.21
Goat	70,699,218	0.552	14.24	0.4	5.70	0.25	1.42
Pig	6,795,101	0.661	1.64	1.0	1.64	0.56	0.92
Sheep	40,318,809	0.329	4.84	0.3	1.45	0.25	0.36
Chicken	170,352,000	0.043	2.67	1.0	2.67	0.28	0.75
Duck	9,553,911[a]	0.051	0.18	0.9	0.16	0.56	0.09
Total					**17.69**		**4.76**
LHV of biogas**:	22.35 MJ/m^3						
Total energy:	**2.54 Mtoe (106.39 PJ)**						

*FAO (2015); **Astals and Mata (2011); [a]NASS (2012); [b]Jain (1993)

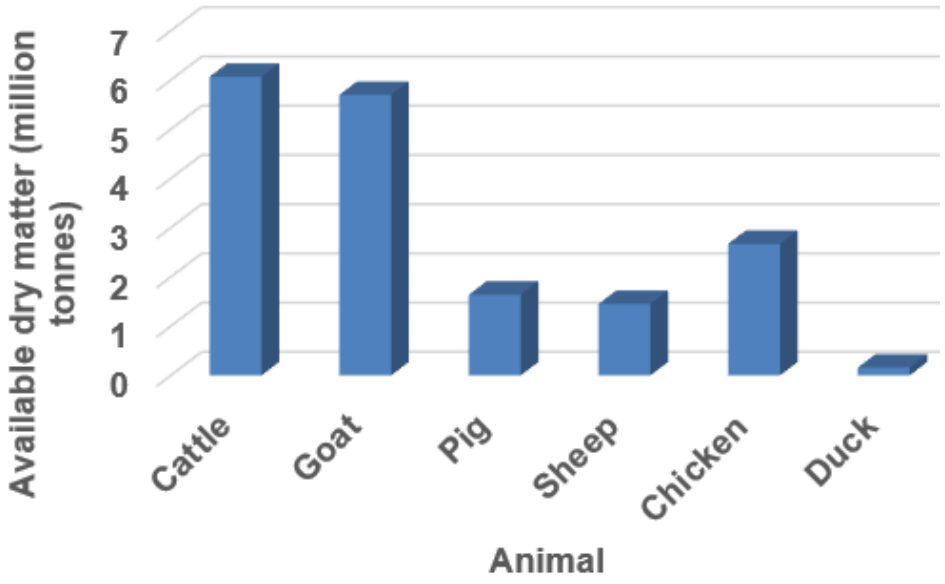

Figure 2.7 Biomass potential of animal wastes in Nigeria

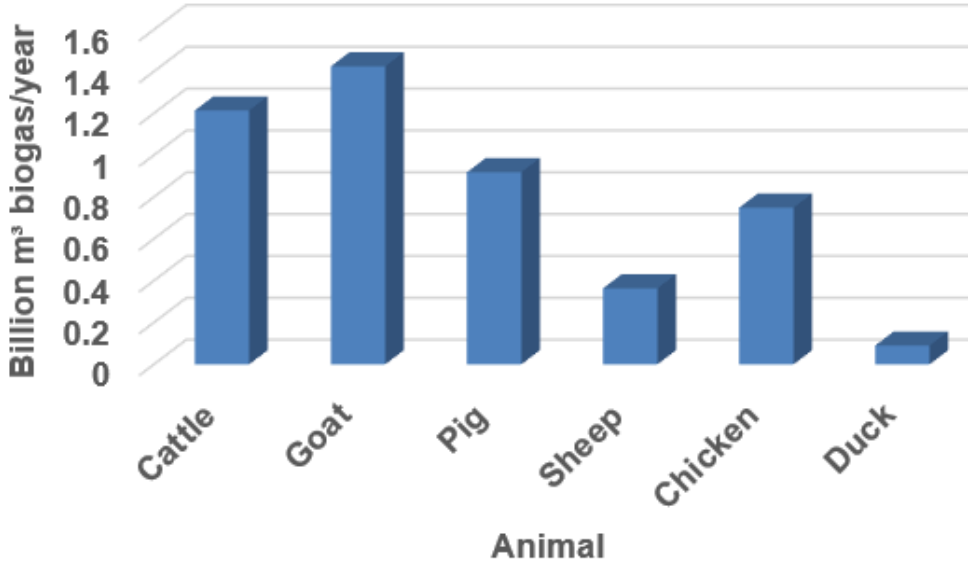

Figure 2.8 Bioenergy potential of animal wastes in Nigeria

2.5.5 Human waste

Given the densely populated nature of Nigeria, the country generates a large amount of human wastes. Based on the figure of Jossy (1994); a dry matter of 0.09 kg per head per day for urban population, Nigeria produced an annual dry matter of 2.87 million tonnes of waste in 2015. The overall estimate of biogas that could be produced from this dry matter was 1.29 billion m^3 (28.83 PJ). The

potential yield of biogas from Nigeria's urban population, as estimated in this work, is 1.29 billion m^3 which value is ~10% higher than the estimate of Simonyan and Fasina (2013).

2.6 Summary of Nigeria's biomass and bioenergy potentials

Table 2.12 presents the summary of the estimated biomass and bioenergy potentials in Nigeria in the current work. The estimated overall biomass and bioenergy potentials in Nigeria for 2015 were 200 billion kg/year and 2.58 billion GJ (61.67 Mtoe) respectively. The estimate is 51% of the nation's total energy consumption in 2015.

Table 2.12 Summary of Nigeria's biomass and bioenergy potentials

Biomass resource	**Biomass quantity (billion kg biomass/year)**	**Estimated energy potential (PJ/year)**
Crop residues	153.76	2,033.85
Perennial/Plantation crop residues	2.35	28.88
Forest residues	19	362.95
Municipal solid wastes	4.51	21.36
Animal wastes	17.69	106.39
Human wastes	2.87	28.83
Overall total	**200.18**	**2,582.26 (61.67 Mtoe)**

2.7 Biofuels policy and incentives in Nigeria

In recognition of the need to join in the global fight against climate change and to achieve the objectives of the Clean Development Mechanism (CDM) of Nigeria, the Government of the Federal Republic of Nigeria (FRN) came up with the nation's biofuels policy in 2007. The policy seeks to synergise the Oil and Gas industry in Nigeria with the agricultural sector through biofuels production and the blending of biofuels with conventional fuels.

The policy of the Government of the Federal Republic of Nigeria on biofuels aims at achieving 10% blend of fuel ethanol with gasoline (E10) and 20% biodiesel blend (B20) (FRN, 2007). The transport sector in Nigeria consumes the largest share of the nation's petroleum products. In 2015, 8.4 Mtoe was consumed by transportation in Nigeria (IEA, 2015). Nigeria's consumption of petrol was estimated to be 11.7 billion litres in 2007 and projected to increase to 18 billion litres by 2020. The nation's consumption of diesel on the other hand was 1.9 billion litres as of 2007 with a projection of 3.6 billion litres by 2020. Based on the statistics above, it was estimated that the nation's demand for fuel ethanol as of 2007 was 1.3 billion litres. The demand was projected to increase to 2 billion litres by 2020 (FRN, 2007).

Nigeria's biofuels policy also incorporates several incentives to encourage large scale cultivation of potential biofuel feedstock crops (commercial crops such as sweet sorghum, cassava, sugar cane and oil palm) as well as the establishment of biofuels plants in the country. This is so that the nation can achieve self-sufficiency in the production of biofuels to meet her demands. The incentives that Nigeria's biofuels policy bestows on registered biofuels businesses in Nigeria include (FRN, 2007): Tax holiday of at least ten years, exemption from taxation, withholding tax and tax on capital gains, exemption from import (customs) duties

and Value-Added Tax (VAT). Furthermore, the biofuels investments in the country enjoy preferential access to long term loans for investments in the biofuels industry.

The first phase of the implementation of the policy involves the importation of fuel ethanol to meet the nation's demand for the biofuel. The importation will continue until the nation is able to produce bioethanol locally to fully meet its demand for the biofuel. Ben-Iwo et al. (2016) presented the figures shown in Table 2.13 for the production of ethanol in Nigeria.

Table 2.13 Ethanol producing firms in Nigeria (Ben-Iwo et al., 2016)

Name of company	**Plant location**	**Feedstock**	**Installed capacity (million litre/year)**
Alconi/Nosak	Lagos	Crude ethanol (imported)	43.80
UNIKEM	Lagos	Crude ethanol (imported)	65.70
Intercontinental Distilleries	Ota-Idiroko	Crude ethanol (imported)	9.10
Dura clean (formerly NIYAMCO)	Bacita	Molasses/Cassava	4.40
Allied Atlantic Distilleries Ltd. (AADL)	Sango-Ota	Cassava	10.90
Total			**133.90**

As at the time that field work (resources assessment) was conducted in Nigeria in December 2017, two new ethanol plants were already completed but were yet to commence full production. These plants are SONA Group ethanol plant, Sango-Ota (with a capacity of 43.8 million litres/year) and UNICANE, Lokoja, Kogi State.

2.7.1 Sweet sorghum

Sweet sorghum is reputed to be the fifth most important grain in the world. According to Agriculture Nigeria (AN), the United States (US) is the largest producer of the grain, followed by India and Nigeria (AN, 2012). Sweet sorghum, unlike the other bioresources, is cultivated for food, feed, and fuel (biofuel) (Figure 2.9).

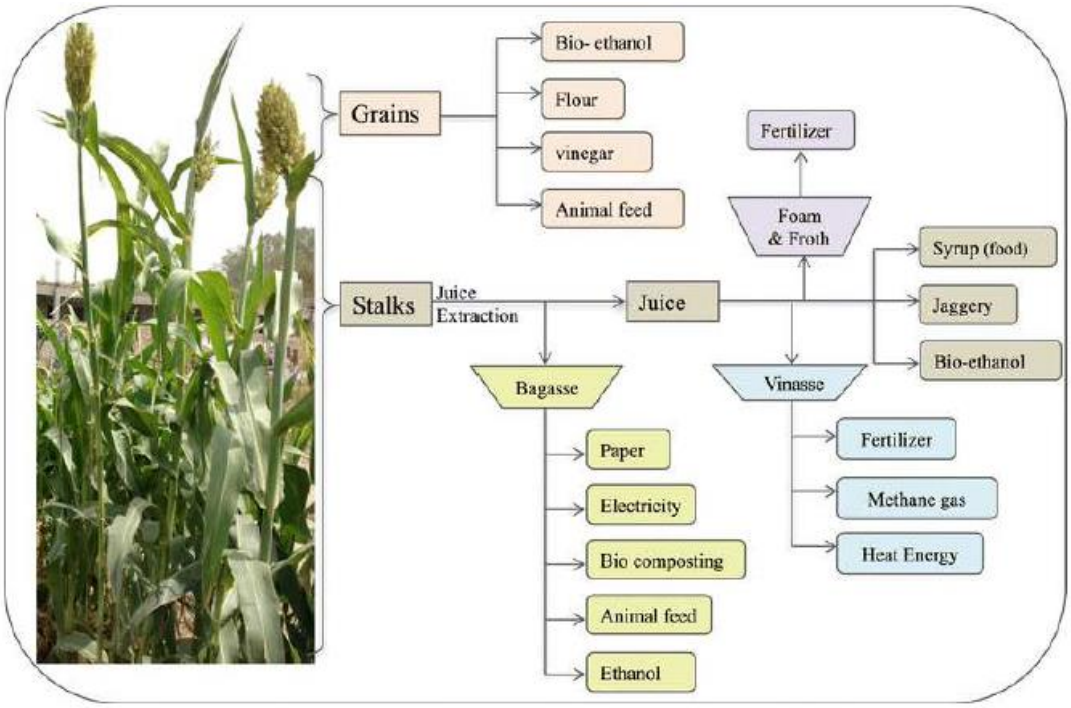

Figure 2.9 Sweet sorghum; a multipurpose crop (Mathur et al., 2017)

Sweet sorghum is exceptionally an attractive source of bioethanol because of the ease of obtaining the biofuel from it compared to the other feedstocks such as maize, cassava or forest residues.

2.7.2 Bioethanol production processes

Biofuels are generally categorised into first, second, third and fourth generation biofuels based on the processes that are involved in their production. These processes are depicted in Figures 2.10 and 2.11.

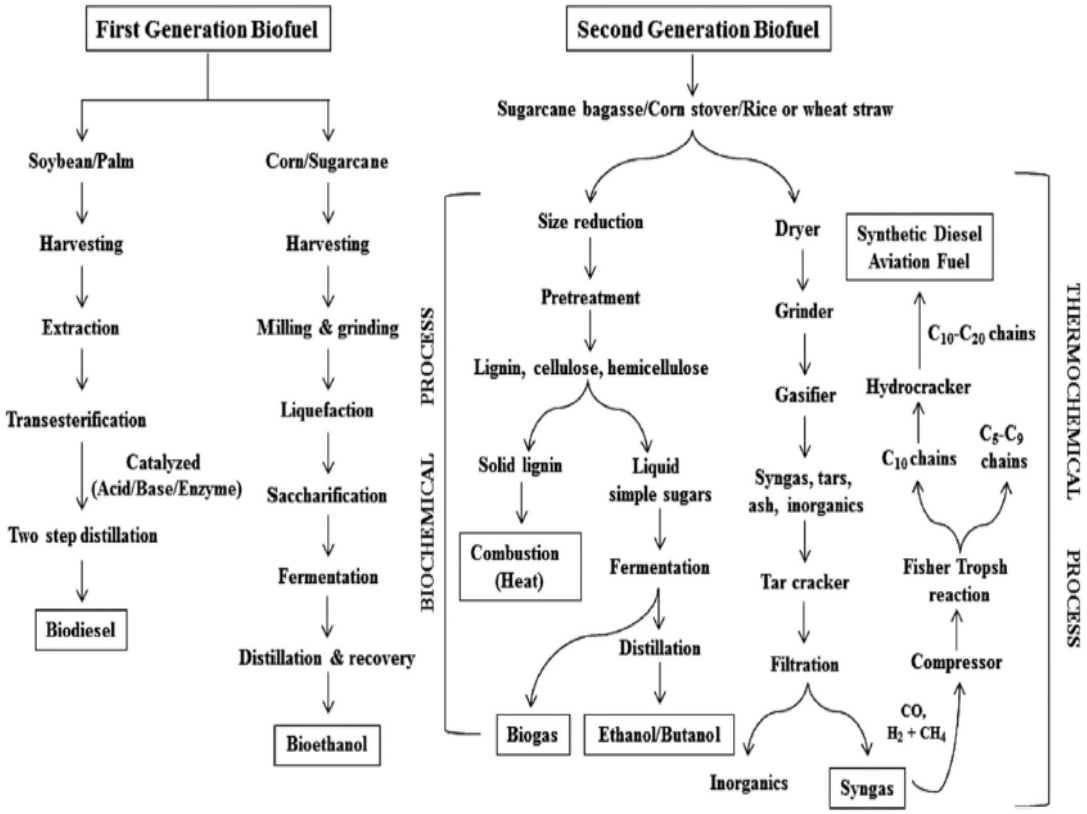

Figure 2.10 Production of first and second generation biofuels (Dutta et al., 2014)

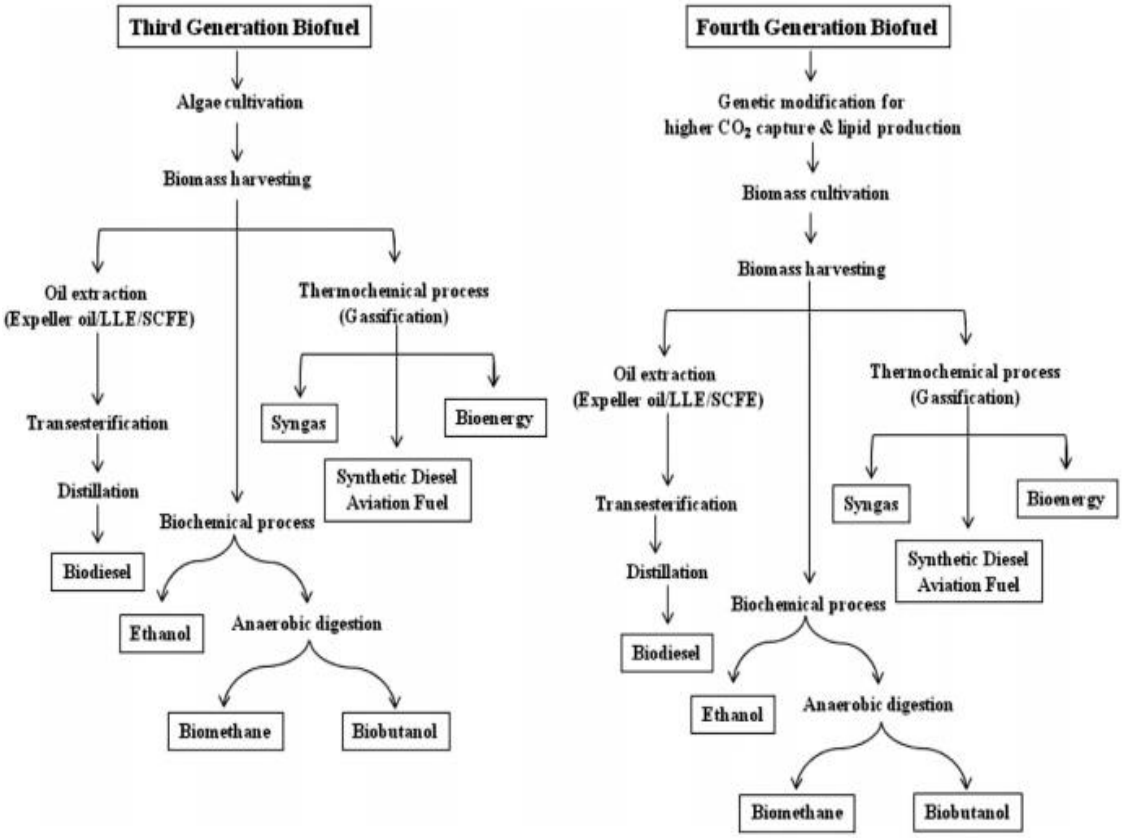

Figure 2.11 Production of third and fourth generation biofuels (Dutta et al., 2014)

The processes to produce second, third, and fourth generation biofuels are quite complex and costly as is evident in Figures 2.10 and 2.11. Bioethanol can be produced from the juice that is extracted from the stalk of sweet sorghum or sugarcane by the simple and less expensive process of fermentation using yeast. However, sugarcane is already a feedstock for the sugar industry in Nigeria. As such, using sugarcane juice to produce bioethanol can cause feedstock shortage for the sugar industry and ultimately lead to food crisis. According to Srinivasa Rao et al. (2009), sweet sorghum juice is preferred to sugarcane juice for the production of ethanol because sweet sorghum juice contains more reducing sugars than the juice of sugarcane. Furthermore, according to Obada (2011) the combustion of ethanol that is produced from sweet sorghum is cleaner than the

combustion of the biofuel that is obtained from sugarcane because the biofuel from sweet sorghum contains less sulphur.

The estimates of the yield of bioethanol from sweet sorghum as reported by previous authors are shown in Table 2.14. The parameters that were used for the conversion of the units in Table 2.14 are presented in Table 2.15.

Table 2.14 Estimates of sorghum-based bioethanol yields from previous authors

Author	**Estimate**	**Cycle /year**	**Yield**		**[a]SS feedstock**
			litre/ha -year	**tonne ethanol/tonne crop**	
Ben-Iwo et al. (2016)	1,319.82 gallon/ha	2	6,000	2.552	Sugar (juice)
K. Rutto et al. (2013)	1,544 litre/ha-year	1	1,544	0.985	Sugar (juice)
Obada (2011)	2,760 litre/ha-year	1	2,760	1.761	Sugar (juice)
	5,500 litre/ha-year (average yield)	2	5,500	3.508	Sugar (juice)
Srinivasa Rao et al. (2009)	4,000 litre/ha-year	2	4,000	2.552	Sugar (juice)
FAO (2008)	494 litre/ha-year	1	494	0.315	Grain

[a]Sweet sorghum

Table 2.15 Parameters used for the unit conversions in Table 2.14

Parameter	Value
Ethanol density @ 15 ^{o}C Barabás and Todoruţ (2009), kg/m^3	794.85
Sorghum harvested area (2014), ha	5,437,200
Sorghum production, tonne grain	6,741,100
Crop yield, tonne/ha	1.24

The estimates of sorghum-based bioethanol yield given in Table 2.14 were based on one-point source (ethanol from sweet sorghum juice or from the grain). Also, the authors did not consider the availability of the grain (as in the case of FAO (2008)) or the availability of the stalk residue from which the juice is extracted. Estimates of the yield of ethanol that are more accurate than the figures in Table 2.14 can be made by considering the combined yield from sweet sorghum juice-based and grain-based ethanol as well as the availability of the stalk and the grain of the crop.

The figures in Table 2.14 show that, based on a single cycle per year, the potential average yield of bioethanol from sweet sorghum sugar is 2,152 litre/ha while for two cycles, the average yield is 5,167 litre/year. The reason for the observed wide variations in the yield figures reported by the authors in Table 2.14 is the dependence of sugar/juice-based ethanol yield on the variety (cultivar) of sweet sorghum. The yield of bioethanol from the grain of sweet sorghum as seen in the Table 2.14 is very low compared to the potential yield figures of the biofuel from the juice of the crop (about 23% of the average yield of juice-based ethanol for one cycle). This is another reason for the global interest in sweet sorghum juice as an attractive feedstock for the commercial production of bioethanol. The low yield of ethanol from sweet sorghum grain is attributed to the resistance of

the starch of the grain of sweet sorghum cultivars to digestion during saccharification (K. Rutto et al., 2013). Therefore, the grain of sweet sorghum is not often used as feedstock for the commercial production of bioethanol.

The cost of cultivation of various potential ethanol feedstock crops as well as the cost of producing bioethanol from the crops are compared in Table 2.16 (Obada, 2011) and Table 2.17 (Srinivasa Rao et al., 2009) respectively.

Table 2.16 Comparison of sweet sorghum and sugarcane as bioethanol feedstocks

Parameter	**Sweet sorghum**	**Sugarcane**
Harvesting cycle	4 months	9-16months
Cycle(s) per year	2-3	1
Water requirement	60-70%	100%
Fertilizer requirement	40%	100%
Stalk production (MT/ha/cycle)	45-75 per cycle 80-110 per 2 cycles	65-80
Fermentable sugars (concentration in stalk %w/w)	9.00-12.00	10.00-14.00
Fermentable sugars (Yield MT/ha/cycle)	3.60-6.20 per cycle 7.20-12.40 per 2 cycles	6.00-10.50
Ethanol yield (Litres/ha/cycle)	2,020-3,500 per cycle 4,000-7,000 per 2 cycles	3,400-6,000

Bagasse yield (MT/ha/cycle @ 50% moisture)	10-14 per cycle 20-28 per 2 cycles (25% on stalk weight)	19-24 (30% on cane weight)

Table 2.17 Crop cultivation and ethanol production cost for potential ethanol feedstock crops

Crop	Cost of cultivation (USD/ha)	Crop duration (months)	Fertilizer requirement (N- P-K* kg/ha)	Water requirement (m^3)	Ethanol yield (litre/ha)	Average stalk yield (t/ha)	Per day ethanol productivity (kg/ha)	Cost of ethanol production (USD/litre)
Sweet sorghum	217/crop	4	80-50-40	4,000/crop	4,000/year for 2 crops	50	416.67	0.32
Maize	300/crop	4-4.50	120-60-50	4,500/crop	4,000/year for 2 crops	50	416.67	0.46
Sugarcane	1,079/crop	12-16	250 to 400-125-125	3,6000/crop	6,500/crop	75	205.47	
Sugarcane molasses					850/year			0.37

*N-P-K: Nitrogen-Phosphorus-Potassium

The figures given in the Tables 2.16 and 2.17 confirm that it is more economically feasible to produce fuel ethanol from sweet sorghum than from any of the other crops that have been considered. The cost of producing fuel ethanol from sweet sorghum (USD 0.32/litre) is the lowest (Table 2.17). Also, the cost of cultivating sugarcane (1,079 USD per ha per crop) is about five times the cultivation cost of sweet sorghum (217 USD per ha per crop).

2.7.3 Bioethanol potential of sweet sorghum in Nigeria

Bioethanol can be produced economically from two parts of sweet sorghum: the grain and the juice from the stalk. Production of bioethanol from sweet sorghum grain involves the enzymatic digestion of the starch of the grain into sugar followed by the fermentation of the resulting sugar by yeast. This is being done in countries where the grain is fully or partially available for biofuel production. Production of bioethanol from the juice that is extracted from the stalk of sweet sorghum, on the other hand, is by direct fermentation of the sugar in the juice by yeast – the easiest and cheapest production process. It is reported that 26% of the grain from sweet sorghum (the crop produce) is used for bioethanol production (Shoemaker and Bransby, 2010). In countries where sweet sorghum is not grown for food such as the US, the entire grain (crop produce) is available for biofuel production.

The third column of Table 2.18 presents the global and national estimates of the conversion efficiency of producing bioethanol from various crops and grains (FAO, 2008). The fifth column was added to the table to show the maximum possible bioethanol yield from the crops based on 2014 crop production data.

Table 2.18 Yield of bioethanol from different crops/grains

Crop	**Production (tonnes)**	**Conversion yield (litre/tonne)**	**Conversion efficiency (tonne/tonne)[a]**	**Bioethanol yield (billion litre)**
Sugarcane	1,057,324	70	0.06	0.07
Sorghum	6,941,100	380	0.30	2.64
Cassava	54,831,600	180	0.14	9.87
Maize	10,790,600	400	0.32	4.32
Rice	6,734,000	430	0.34	2.90
Total:				**19.80**

[a]FAO (2008)

The figures for the yield of bioethanol in Table 2.18 are realisable in countries where the crops are cultivated solely for biofuels production. In Nigeria, all the crops in Table 2.18 are food crops and diverting the produce into fuel ethanol production will trigger off food crisis. However, the extracted juice from sweet sorghum is advantageous as a feedstock for bioethanol because it is neither used for food like sugarcane nor is it a feedstock for the sugar industry.

Table 2.19 presents the possible (estimated) yield of bioethanol from sweet sorghum based on the crop production data of 2014 and 26% availability of the grain for biofuel production in Nigeria. The bagasse has not been considered because it is used as feed for livestock in Nigeria and being cellulosic, it will be expensive to produce ethanol from it.

Table 2.19 Possible yield of bioethanol from sweet sorghum in Nigeria

Item	**Value**
Sorghum production (2014), tonnes	6,941,100
Harvested area (2014), ha	5,437,660
Estimate of bioethanol from Sweet sorghum grain:	
Grain (product) availability, %	26
Conversion yield of grain to bioethanol (FAO (2008)), litres/ha	494
Bioethanol yield from Sweet sorghum grain, billion litres: 0.26 x 494 x 5,437,660	0.70
Estimate of bioethanol from Sweet sorghum sugar:	
Residue type	Stalk
Residue availability, %	80
Average yield of bioethanol from SS juice (1 cycle), litre/ha	2,152
Bioethanol produced from extracted juice, billion litres 0.80 x 2,152 x 5,437,660	9.40
Total possible yield of fuel ethanol from sweet sorghum, billion litres/year (Effective yield: 10.10 x 10^9/5,437,660 = **1,857.42 litres/ha**)	**10.10**

Ratio of potential yield of sweet sorghum-based ethanol to projected demand (for 2020): 10.10/2	**5.05**

Table 2.19 shows that Nigeria's estimated potential annual yield of bioethanol from sweet sorghum is 10.10 billion litres which is 47% of the country's projected total demand for gasoline and diesel (21.6 billion litres) in 2020. The nation's bioethanol potential is about 8.10 billion litres more than the projection for 2020. Therefore, Nigeria has high prospects of becoming an exporter of bioethanol.

2.8 Conclusion

The foregoing analysis has shown that Nigeria's biomass resources are 200 billion kg/year and have the potential to generate 62 Mtoe (2.58 billion GJ) of energy annually. The bioenergy potential of Nigeria's forest residue was estimated to be 363 PJ (8.7 Mtoe or 101 TWh). This estimate is similar to the energy consumed by transport in 2015 and four times greater than the nation's electricity consumption in 2015. If properly harnessed, Nigeria's biomass resources can generate sufficient bioenergy to reduce the pump price of petroleum products in the country as well as stabilise the power sector. The analysis that was carried out in this work showed that Nigeria has the potential to produce sufficient bioethanol to cater for domestic demand and for export. The nation's estimated potential annual yield of bioethanol from sweet sorghum is 10.10 billion litres which is about 8.10 billion litres more than the projection for 2020. Therefore, Nigeria has high prospects of becoming an exporter of bioethanol. Life-cycle energy consumption and carbon footprint analyses could not be carried out on ethanol production process in Nigeria because of unavailability of data. Nigeria's production of sweet sorghum can be drastically increased by cultivating the crop in the vast uncultivated arable lands in the

country. This will boost the country's sweet sorghum potential. Bioethanol can be produced from the different inedible feedstocks highlighted above and then blended to boost the biofuel potential of the country.

Chapter 3 Literature review for diesel-ethanol (DE) blends stability, diesel engine combustion, and biomass gasification tests

3.1 Introduction

This Chapter reviews the previous works that were carried out on fuel blends as well as the effect of blend fuels on the performance and emissions from Spark Ignition (SI) and diesel engines. The previous works on the Heat Release Rate (HRR) models of Internal Combustion Engines (ICEs) were also reviewed. The chapter ends with a review of literature on the gasification of biomass.

3.2 Fuel blends

3.2.1 Liquid-liquid solutions

Liquid-liquid solutions are homogeneous mixtures of two or more liquids. Liquid-liquid solutions can be binary (two liquids) or ternary (three liquids). The liquid that is present in the higher/highest proportion is called the solvent while the other component(s) is/are usually referred to as the solute(s). The major factors that influence the solubility of one liquid in another are temperature, polarity, concentration, and purity. At higher temperatures, more of the solute tends to dissolve in the solvent just as in the case of liquid-solid systems. Generally, polar compounds dissolve and blend well in polar solvents (due to inter-molecular hydrogen bonding) while non-polar compounds dissolve in non-polar solvents. Ethanol is perfectly soluble in water because both liquids are polar compounds. Water and gasoline are immiscible, they form two phases because water is polar whereas gasoline is non-polar. On the other hand, gasoline blends well with fossil diesel because both liquids (hydrocarbons) are non-polar.

Lee (2018) investigated the effect of temperature, concentration, and pressure on the degree of hydrogen bonding for each molecule in aqueous polyethylene oxide (PEO) solution by Perturbed Hard Sphere Chain Association (PHSC-AS) models. The author reported that, as the concentration of water (the solvent) increased, the degree of hydrogen bonding reduced gradually for water-water association whereas it increased drastically for the cross-association between water and PEO. However, the degree of hydrogen bonding decreased as the temperature increased for both water-water and water-PEO associations. The effect of temperature on the hydrogen bond structure of anhydrous methanol (a low molecular weight alcohol) was investigated by Wallen et al. (1996). The authors reported that the extent of hydrogen bonding in liquid methanol decreased as the temperature was increased. The results of the investigations of Lee (2018) and Wallen et al. (1996) confirm that the strength of inter-molecular hydrogen bonding decreases for both self-association (same molecules) and cross-association (different molecules) with increase temperature.

Apart from temperature, concentration, purity and polarity, the solubility of a liquid in another liquid is also depended on the length of the molecules of the liquids in question. Butanol is known to have unlimited solubility in fossil diesel (a mixture of hydrocarbons with long carbon chains) unlike ethanol. This suggests that the alcohols that have relatively long carbon chains (high molecular weights) will be perfectly miscible with fossil diesel.

3.2.2 Diesel-ethanol (DE) fuel blends

Diesel engines (invented by Rudolf Diesel in 1893) can be made to run on biofuel and alternative fuels without modifying the engines by blending biodiesel or ethanol with fossil diesel in the engines. The use of vegetable oil in diesel engine dates to 1900 when Rudolf was reported to have used peanut oil to run the engine

(Shahid and Jamal, 2008). However, the use of biodiesel or vegetable oils in Compression Ignition (CI) engines is limited by the high viscosity and density of the fuels relative to standard diesel. High density and viscosity values of vegetable oils and biodiesel can affect fuel atomisation leading to poor combustion characteristics when they are used as fuels in diesels or blended with fossil diesel in CI engines.

Ethanol found wide use as a fuel in engines after 1970 though its use as fuel was initially suggested in the USA in 1930 (Shrivastava et al., 2014). Ethanol has been successfully blended with gasoline in Spark Ignition (SI) engines. The blending of ethanol with fossil diesel has been a topic of investigation as far back as the 1980s (Pidol et al., 2012). According to Hulwan and Joshi (2011), the major incentive of blending ethanol with fossil diesel has been the high oxygen content of ethanol (about 34% by weight) which has the potential to reduce emissions from diesel engines. However, ethanol also has some limitations that make it either impossible to use 100% ethanol or difficult to use its blends with fossil diesel (diesohol) in CI engines. The Cetane Number (CN) of ethanol is very low, it cannot auto-ignite and as such, diesel engines cannot run on 100% ethanol. Ethanol also has lower heating value and viscosity (lubricity) than biodiesel and fossil diesel. Hence, if ethanol is used as a binary blend in diesel to produce diesohol, the heating value, lubricity and auto-ignition property of the final fuel blend (diesohol) will be drastically reduced at high concentrations of the alcohol leading to poor engine performance. Another disadvantage of ethanol is that, unlike biodiesel, it has limited solubility in fossil diesel and can cause phase-separation if blend ratios above 5% are used at low temperatures (Lapuerta et al., 2009) or if ratios above 20% are used at room temperature.

The challenges of DE fuel blends highlighted above have necessitated the use of biodiesel in diesohol to achieve optimum blends that will give good engine performance. However, to incorporate biodiesel in diesohol, it is imperative that the limits of solubility of ethanol in fossil diesel be established. It is therefore, important to ascertain the precise range of solubility of ethanol in fossil diesel. The solubility limits of pure ethanol in fossil diesel at room temperature will establish the DE concentration range within which co-solvents or additives will be required to enhance the solubility and stability of ethanol in fossil diesel. Furthermore, little work has been carried out in terms of investigating the actual time at which phase separation occurs for different DE fuel blends, the variation of the height of the interphase (volume of the diesel phase) with time in unstable DE blends, as well as the temperature-dependence of unstable DE blends. Therefore, there is a need to investigate the transient behaviour of DE blend fuels.

3.2.3 Advantages of blending diesohol with biodiesel

The advantages of blending diesohol with biodiesel are:

i. Ethanol has limited solubility as well as low-temperature instability in diesel. Biodiesel acts as a surface-active agent (amphiphile) when it is blended with diesohol thereby increasing the amount of ethanol that can dissolve in diesel. The stability of the final blend at low temperatures is also drastically improved by biodiesel (Kwanchareon et al., 2007).

ii. Diesel-ethanol blends have low flash points which pose great risks in the storage and handling of the blends. The use of biodiesel in the blends increases the flash point of the ternary blend fuel thereby making it safe to store (Shahir et al., 2014).

iii. The low density and viscosity of ethanol reduces the viscosity and consequently, the lubricity of diesohol which will cause wear of engine parts if the

low-viscosity fuel is used in diesels. Addition of biodiesel to diesohols increases the lubricity of the final fuel to levels within the range of the recommended standard (Fungtammasan, 2010).

iv. The low heating value of ethanol reduces the heating value of diesohol. Biodiesel has high heating values and as such, it increases the Calorific value (Cv) of diesohol when it is blended with diesohol (Zöldy, 2011).

v. Ethanol also has very low CN which reduces the CN (auto-ignition property) of diesohol. Biodiesel increases the CN of diesohol when it is added to the blend because it has a relatively high CN (Zöldy, 2011).

3.2.4 Previous work on fuel blends

Researchers in the past have investigated the stability of binary and ternary fuel blends. Notable among the researchers were Kwanchareon et al. (2007), Rahimi et al. (2009), Guarieiro et al. (2009), Lapuerta et al. (2007), and Lapuerta et al. (2009).

Kwanchareon et al. (2007) investigated the stability of ternary blends at ambient temperature using 95%, 99.5% and 99.9% pure ethanol. The authors found that blends of 95% pure ethanol were not soluble in diesel. This was because the large amount of water, a polar liquid, in the 95% pure ethanol enhanced the polarity of ethanol and the cross-association between water and ethanol via hydrogen bonding thereby making it highly immiscible with diesel (a non-polar liquid). The authors added biodiesel (which is completely soluble in both 95% ethanol and fossil diesel) to the diesel-95% pure ethanol blend and discovered that the solubility of the mixture did not improve. It was therefore concluded by the authors that hydrous ethanol was not suitable for the preparation of diesohol

or ternary diesel-biodiesel-ethanol (DBE) blends. Kwanchareon et al. (2007) presented the phase diagram for the DBE (95%) blends as shown in Figure 3.1.

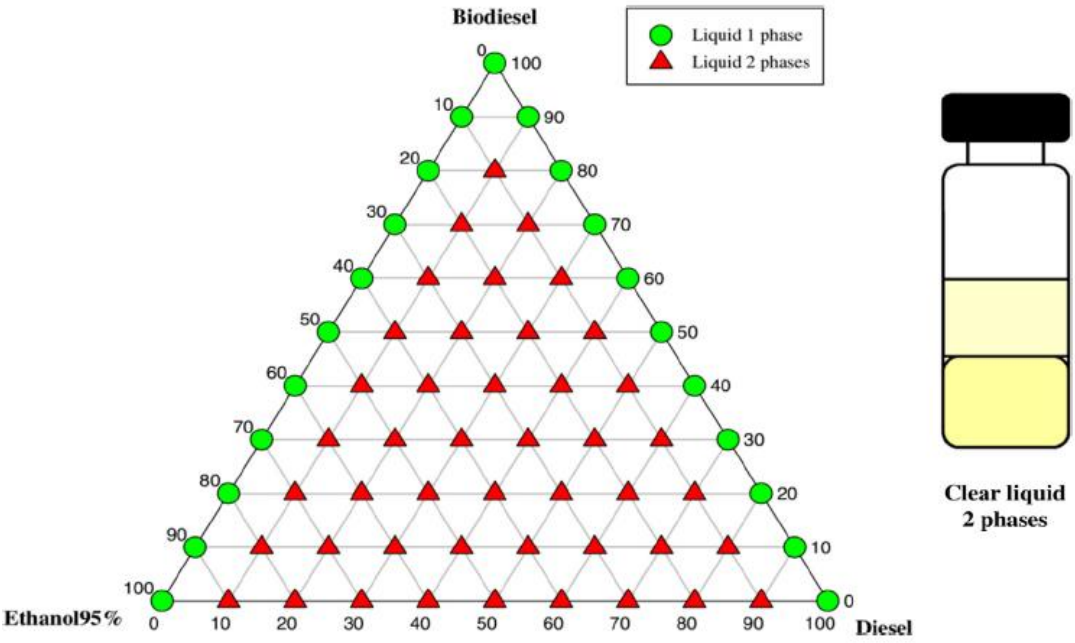

Figure 3.1 Diesel-biodiesel-ethanol 95% (DBE) ternary blends at room temperature (Kwanchareon et al., 2007)

The authors reported that 99.5% ethanol gave unlimited solubility in the DBE ternary blends at room temperature. This was because biodiesel acted as an amphiphile enhancing the solubility and stability of DBE blends when anhydrous ethanol was used by forming micelles which had polar heads and non-polar tails. The polar head of the biodiesel molecule attached to ethanol while the non-polar tail attached to diesel (the continuous phase) in the blend giving rise to a stable, single-phase emulsion or mixture. The ternary blends of 99.9% ethanol were found to have the same results as the blends of 99.5% ethanol.

Kwanchareon et al. (2007) also investigated the phase stability of the blends at different temperatures. They found that at 10 ^{o}C, 20-80% by volume ethanol and diesel fuel blends were clear liquids in two crystalline phases. On the other hand, blends of 70-100% biodiesel that were void of ethanol turned into gel (owing to

the fatty acid content of biodiesel). The authors also reported that, at 20 ^{o}C, all the blends were one phase liquid except diesohol that had 30-70% ethanol as depicted in Figure 3.2. According to the authors, the binary blends containing 30-70% ethanol became unstable after 90 days. The authors, however, did not state the precise time of phase separation for each of the unstable blends. The transient behaviour of the blend fuels containing 10% to 90% pure ethanol at room temperature is therefore, open for investigation. According to the authors, at 20 ^{o}C, ethanol was fully soluble in diesel fuel when the concentration of diesel was less than 30% or greater than 70%. Furthermore, at higher ambient temperatures (30-40^{o}C), the authors found that ethanol was soluble in diesel at all concentrations and the ternary DBE system remained a stable, single phase liquid.

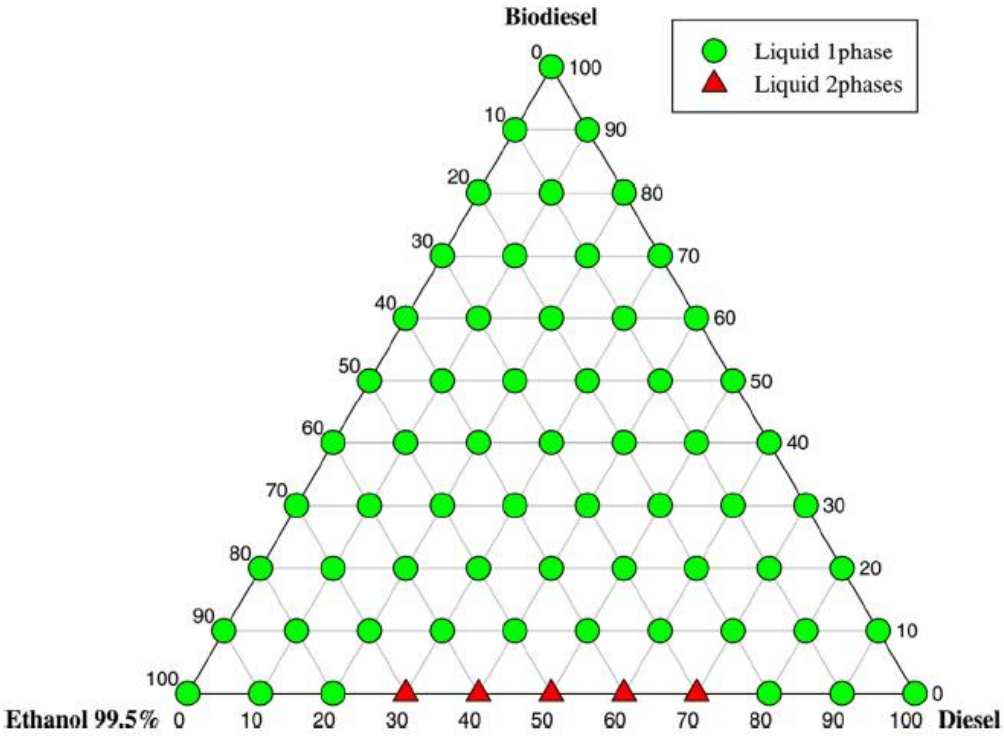

Figure 3.2 Diesel-biodiesel-ethanol 99.5% (DBE) ternary blends at 20 ^{o}C (Kwanchareon et al., 2007)

Rahimi et al. (2009) reported that the temperature of phase separation of 4-5% bioethanol (DE4 or DE5) in standard diesel fuel (Ultra Low Sulphur Diesel, ULSD) was the same as the cloud point of pure diesel fuel provided that anhydrous ethanol was used. According to the authors, the cloud point of diesohol increased by 25 ^{o}C when ethanol was blended with zero aromatic diesel. The authors found that increasing the percentage of ethanol in the diesohol beyond 12% or decreasing the temperature of DE12 below ambient led to phase separation. However, when 8% biodiesel was added to the blend, the authors reported that phase separation did not occur.

Guarieiro et al. (2009) investigated the phase stability of diesohol and DBE systems at ambient temperature. The authors used different concentrations of hydrous and anhydrous ethanol in their study. The authors also reported the insolubility of 95% pure ethanol in diesel fuel. They repeated the test with 10% anhydrous ethanol (99.5%) and observed that the blend remained stable beyond ninety days. The authors reported that, when the proportion of ethanol (99.5%) was increased to 15% (DE15), phase separation occurred the same day. However, Kwanchareon et al. (2007) reported that DE20 was stable after ninety days at 20 ^{o}C. The contradicting reports from different authors on the stability of DE blends underscores the need for further investigation of the stability of the blends.

Guarieiro et al. (2009) also tested blends of diesel fuel and anhydrous ethanol, using soybean biodiesel (SB), castor biodiesel (AB), residual biodiesel (RB), soybean oil (SO) and castor oil (AO) as co-solvents in the ternary blends. The authors found the following blends to be stable after 90 days:

1. Diesel/ethanol: 90/10% (D90E10)
2. Diesel/ethanol/SB: 80/15/5% (D80E15SB5)

3. Diesel/ethanol/AB: 80/15/5% (D80E15AB5)
4. Diesel/ethanol/RB: 80/15/5% (D80E15RB5)
5. Diesel/ethanol/SO: 90/7/3% (D90E7SO3)
6. Diesel/ethanol/AO: 90/7/3% (D90E7AO3)

The stability of blends 2, 3, and 4 above (ethanol concentration >10%) in the presence of biodiesel confirms the potential of biodiesel to enhance the solubility of ethanol in diesel.

Lapuerta et al. (2007) investigated the combined effects of different conditions of temperature (-5 ^{o}C to 15 ^{o}C), water percentage (0 to 2.5 w/w) and additive on the stability of DE blends. The range of concentration of ethanol that was considered by the authors was 5% to 20% by volume. The time of phase separation and the volume of the separated phase were investigated by the authors under low temperature conditions. The authors identified three stages in the separation of unstable DE blends. These stages are: initial turbidity, appearance of interphase, and displacement of the interphase before equilibrium. According to the authors, the separated phase consisted solely of ethanol. The results of the current work, however, contradicts what was reported by the authors because the separated phase in this work was not colourless (off-road diesel was used in the current work). It should be expected then, that both diesel and ethanol molecules would be transported across the interphase during the phase separation.

Lapuerta et al. (2009) studied the stability of ternary DBE blends. The authors reported three types of blend instability in their work (two liquid phases, formation of gel in the interphase and formation of gel in the lower part of the blend glass). According to the authors, at high concentrations of ethanol (75%), gel formation occurred at the bottom of the glass vessel. Though the authors attributed the

formation of the gelatinous phase to the presence of biodiesel, gel formation was observed in the current work in DE70.

The forgoing discussion as well as the summary of the previous related work on fuel blends presented in Table 3.1 show that there is a need to conduct an in-depth investigation of the transient behaviour of diesohol fuel blends.

Table 3.1 Previous related works on fuel blends

	Braun and Stephenson (1982)	**Salih (1990)**	**Kwanchareon et al. (2007)**	**Rahimi et al. (2009)**	**Raslavicius and Žilvinas (2010)**	**Sukjit et al. (2014)**
Blend type	Ternary; D-B-E (Diesel:degummed soybean oil:ethanol)	Ternary (Diesohol, naphtha as co-solvent)	Ternary (Diesel:biodiesel: ethanol)	Binary (diesohol) and ternary; D-B-E (diesel:biodiesel:ethanol)	Ternary (Diesel:biodiesel: ethanol)	Ternary (Diesel:biodiesel: ethanol)
Blend property/ratios investigated	D40%B40%E20% and D30%B30%E40%	7.5% naphtha based on diesohol volume	Different ratios for 95%, 99.5%, 99.9% pure ethanol	DE4, DE5, DE12 and D80%B8%E12%	D70%B25%E5% and D80%B15%E5%	D75%R15%E10% (ULSD-RME-ethanol) and D80%C10%E10% (ULSD-COME-ethanol)

Test temperature (°C)		Ambient	20 °C, 30 °C and 40 °C	Ambient and below		
Blend stability			Blends from 95% pure ethanol not stable even in presence of co-solvent	No phase separation for D80%B8%E12%.	Stable	Stable
Engine type	6-cylinder, energy cell, indirect injection, diesel engine	Petter (DI) diesel engine			D144, 4-cycled, air-cooled 37 kW diesel engine	Air-cooled, single cylinder, research DI engine
Findings	No irregularities in injector spray pattern	30% reduction in engine	99.5% and 99.9% pure ethanol had	Temperature of phase separation of DE4 and DE5 same as cloud	D70B25E5 gave no reduction in	1. longer ignition delay when ethanol

		NOx, 3% increase in thermal efficiency, 30-40% higher SOF, 40-50% lower particulate emissions than diesel fuel	unlimited solubility in diesel from 30^{o}C to 40^{o}C. At 20^{o}C, ethanol is soluble if diesel in ternary blend is less than 30% or greater than 70%	point of standard diesel (for anhydrous ethanol), phase separation occurred for ethanol percentages above DE12 or when temperature is decreased below ambient for DE12	engine power, 2% increase in fuel economy (compared to pure B30), 40% decrease in PM, 25% decrease in HC and 6% decrease in CO compared to fossil diesel when the vehicle operated at maximum power,	blended fuels were used than when ultra-low sulphur diesel was used. 2. Higher indicated specific fuel consumption of the blend fuels than of ULSD. 3. Increase in THC and NOx but decrease in CO for

					increased NOx emission from engine compared to diesel fuel.	blend fuels. COME blend had longer ignition delay and lower CO and soot than RME blend.
Recommended blend				D80%B8%E12%	D80%B15%E5%	D80%C10%E10% (ULSD-COME-ethanol)

3.3 Diesel-ethanol (DE) blends as fuel for diesel engines

Biofuels are fuels that are obtained from biomass such as corn, sorghum, sugarcane, vegetable oils (rape seed oil, castor oil). Examples of biofuels are bioethanol, biodiesel and biogas which is obtained from the anaerobic digestion of organic wastes such as animal dung. Biofuels are used as transportation fuels. Biofuels are usually blended with conventional (fossil) fuels such as gasoline or diesel and at specific ratios in gasoline and diesel engines. Biofuels in general are known to undergo cleaner combustion than conventional diesel or gasoline. The blending of biofuels with conventional fuels enhances clean combustion by reducing the emission levels of ICEs. Typical blend ratios of ethanol are E5, E10 (gasoline with 5% or 10% ethanol), E85 (gasoline with 85% ethanol), B7 (diesel with 7% biodiesel).

Bioethanol (also simply called ethanol) can be obtained by direct fermentation of the sugar of sweet sorghum or sugarcane. It is also produced by enzymatic digestion of the starch of corn, grain sorghum, wheat or rice followed by the fermentation of the resulting sugar. Pure (100%) ethanol cannot be used as fuel in diesel engines because of the low CN of ethanol. Therefore, ethanol is blended with diesel in combustion engines in ratios that can auto-ignite. Additives (cetane enhancers) will also be required if it is desired to use high percentages of ethanol (>75%) in diesels.

Biodiesel is obtained by the transesterification of vegetable oils such as rape seed oil and castor oil. Typical examples of biodiesels are Rape Methyl Ester (RME) and Castor Oil Methyl Ester (COME). Biodiesel is usually blended with petroleum diesel in diesel engines. Several researchers (Andrews (2015), Li et al. (2014), Agarwal (2007)) have shown that Used Vegetable Oil (UVO) can also be utilised

directly in diesel engines. 100% biodiesel can be used in diesel engines because biodiesel has good auto-ignition properties and similar cetane values.

3.3.1 Internal Combustion Engines (ICEs)

Internal Combustion Engines (ICEs) include reciprocating engines such as piston engines. There are two types of piston engines: the Spark Ignition (SI) engines and the Compression Ignition (CI) or diesel engines. This work focuses on diesel engines. Large amount of work has been carried out on gasoline blends and SI engines. Therefore, the works done by previous researchers on SI engines will be reviewed so that the similarities and differences between the SI and diesel engine researches as well as the combustion in the two engines can be appreciated. The operation of the two engines is based on piston strokes which convert the chemical energy of fuels to torque. The torque is transmitted to the final drive in a vehicle for propulsion. Piston stroke is the movement of the piston of an ICE from the Bottom Dead Centre (BDC) to the Top Dead Centre (TDC) or vice versa. A piston engine can be categorised as a two-stroke (two-cycle) engine or a four-stroke (four-cycle) engine. In a four-stroke engine, the piston strokes are the intake, the compression, the power, and the exhaust strokes. The crank shaft undergoes two complete revolutions to complete the four strokes of a four-cycle engine.

3.3.1.1 Spark Ignition (SI) engines

The Spark Ignition (SI) engine is also called gasoline engine. The first stroke of an SI engine is the intake stroke during which stroke the piston moves downwards in the cylinder and the intake valve opens. Air-fuel mixture passes through the intake port into the cylinder of the engine as the piston moves downwards. The intake valve closes as the piston passes through the BDC thereby sealing up the top of the cylinder.

The compression stroke begins after the piston passes the BDC. During the compression stroke, the piston moves upward, and the intake and exhaust valves are closed. The upward movement of the piston compresses the air-fuel mixture into a smaller volume between the top of the piston and the cylinder head. The space that is occupied by the compressed charge is called the combustion chamber. The amount by which the charge is compressed is called the Compression Ratio (CR). According to Andrews (2018a), modern SI engines have compression ratios between 10.5 and 12.

The power stroke occurs at the end of the compression stroke as the piston approaches the TDC. An electric spark is released from the spark plug into the combustion chamber. The compressed air-fuel mixture is ignited by the heat from the spark. The high temperature that results from the rapid combustion of the compressed charge generates a high pressure in the combustion chamber which pushes the piston downwards. The connecting rod of the piston transmits the force to the crankshaft which rotates to move the drive wheels.

The power stroke is followed by the exhaust stroke. During the power stroke, as the piston nears the BDC, the exhaust valves open. The piston begins another upward movement after it passes through the BDC at the end of the power stroke. This upward movement of the piston in the cylinder pushes the combustion gases out of the cylinder through the exhaust port. The intake valve opens when the piston approaches the TDC. The upward motion of the piston in the exhaust stroke is reversed when the piston passes through the TDC and the intake valve opens (Figure 3.3). The sequence is repeated (from the intake stroke to the exhaust stroke). Figure 3.4 illustrates the ideal air standard cycle of an SI engine (Stone, 1992).

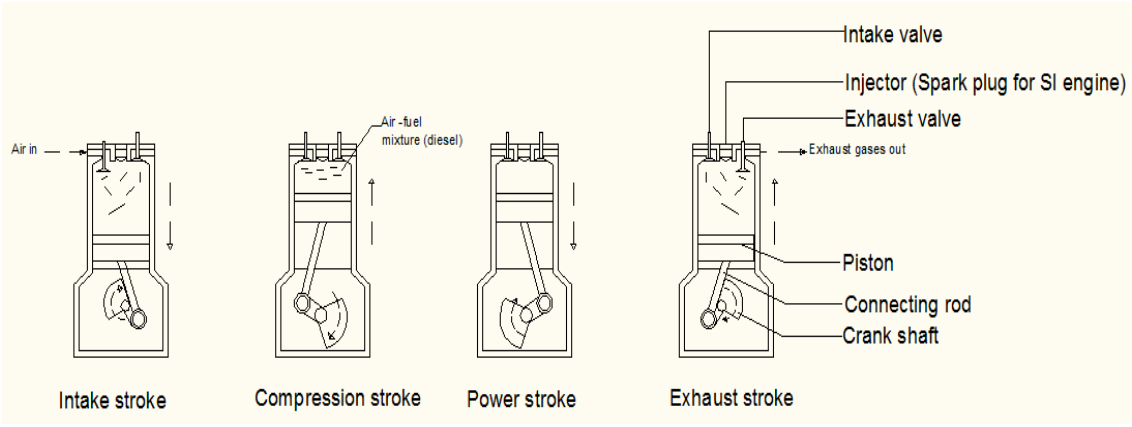

Figure 3.3 Piston strokes in a four-cycle engine

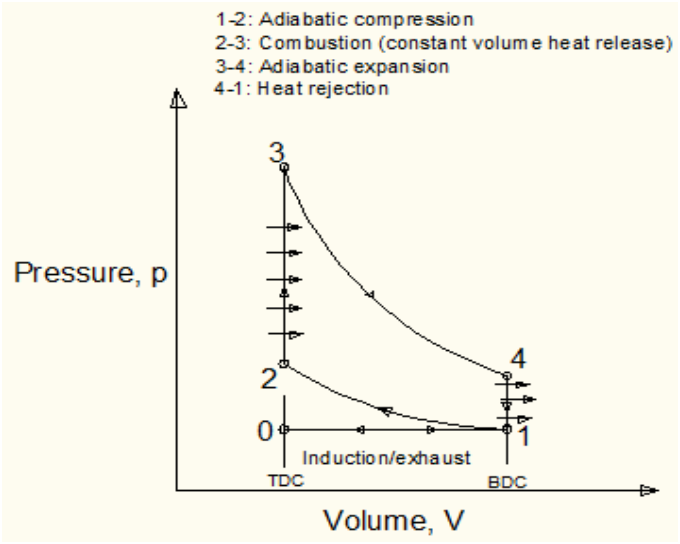

Figure 3.4 Spark Ignition (SI) engine ideal air standard cycle

3.3.1.2 Compression Ignition (CI) engines

Diesel engines are typical examples of Compression Ignition (CI) engines. The diesel engine takes in only air during the intake stroke unlike an SI engine. Also, the air inflow in a diesel engine is not controlled by a throttle valve. The intake stroke in a diesel engine is also followed by the compression stroke during which the piston moves upward and compresses the air that was drawn into the cylinder during the intake stroke. The compression of air in the cylinder of diesel engines increases the temperature of the air. The compression stroke is followed by the power stroke during which diesel (a high CN fuel) is injected into the compressed,

hot air in the cylinder. The hot air then ignites the fuel. The sudden expansion of the combustion gases in the cylinder pushes the piston down. The pressure on the piston is transmitted to the crank shaft and this results in rotation. The last stroke in CI engines is the exhaust stroke. The exhaust stroke is the same in both SI and CI engines (Figure 3.2). The upward moving piston pushes the combustion gases out of the cylinder through the exhaust valve.

The stoichiometric air/fuel ratio for both petrol and diesel fuels is about 14.6 while the compression ratios in diesels range from 16-21 (Andrews, 2018a). Figure 3.5 illustrates the ideal air constant pressure cycle of diesel engines .

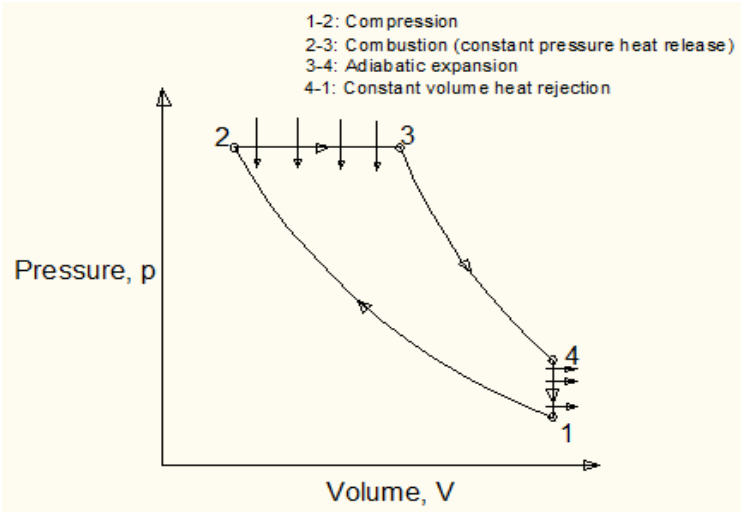

Figure 3.5 Diesel engine ideal air constant pressure cycle

3.3.2 Fuel requirements for diesel engines

The fuel properties of interest in engine research are fuel density, viscosity, Cetane Number, lubricity, flash point, surface tension, and Cold Filter Plugging Point (CFPP), sulphur content, carbon residue, ash content, water content, copper strip corrosion, oxidation stability, Lower Heating Value (LHV), and distillation. These properties are determined by using the recommended standard methods in EN 590. EN 590 standard specifies the quality of European diesel

fuels. Table 3.2 presents the standard properties of diesel fuel in EN 590:1993 (Regulations, 2015).

Table 3.2 Recommended properties of diesel

Property	**Minimum**	**Maximum**	**Standard test method**
Cetane Number	49	-	ISO 5165
Cetane index	46	-	ISO 4264
Density @ 15 ^{o}C (kg/m^{3})	820	860	ISO 3675/ASTM D4052
Sulphur (% wt.)	-	0.20	EN 24260/ISO 8754
Flash point (^{o}C)	55	-	ISO 2719
Carbon residue (10% btms[a]) (% wt.)	-	0.30[b]	ISO 10370
Ash (% wt.)	-	0.01	EN 26245
Water content (mg/kg)	-	200	ASTM D1744
Copper strip corrosion, 3h @50 ^{o}C	-	Class 1	ISO 2160
Oxidation stability (g/ m^{3})	-	25	ASTM D2247
Viscosity @ 40 ^{o}C (mm^{2}/s)	2.00	4.50	ISO 3104
LHV (MJ/kg)[c]		42.5	
Heat of evaporation (MJ/kg)[c]		544-795	
Distillation (vol.% recovered) (^{o}C)			
10% point	report		

50% point	report		
65% point	250	-	
85% point	-	350	
95% point	-	370	

[a]Value differs when additives (ignition improvers) are present in the fuel, [b]AVL (2015)

Typical properties of biofuels (biodiesel and bioethanol) are given in Table 3.3 (Barabás and Todoruţ, 2009).

Table 3.3 Properties of biofuels

Property	**Biodiesel (RME)**	**Bioethanol**
Chemical formula*	$C_{18.96}H_{35.29}O_2$	C_2H_5OH
Density @ 15 ^oC (kg/m^3)	887.40	794.85
Viscosity @ 40 ^oC (mm^2/s)	5.54	1.07
Cetane Number	51	8
Flash point (^oC)	>140	13
Surface tension (mN/m)	-	-
Sulphur (mg/kg)	9.5	1.62
Lubricity, corrected WSD[a] 1.4 @ 60 ^oC (µm)	218	-
LHV (MJ/kg)		26.9[b]
Heat of evaporation (kJ/kg)		840[b]

*Sukjit et al. (2014), [a]Wear Scar Diameter, [b]Rakopoulos et al. (2011)

3.3.2.1 Density

Fuel density is a function of temperature, composition, and pressure. Fuel atomisation and fuel jet penetration in diesels are affected by the density of the

fuel and the injection pressure. Fuel jet penetration can be estimated from Equations 3.1 and 3.2 (Heywood, 1988).

$$m_f = C_D A_n \sqrt{2\rho_f \Delta p}\,\frac{\Delta\theta}{360N} \qquad 3.1$$

$$S = 3.07\left(\frac{\Delta p}{\rho_g}\right)^{1/4}(t d_n)^{1/2}\left(\frac{294}{T_g}\right)^{1/4} \qquad 3.2$$

m_f is the mass of fuel injected in kg, C_D is the discharge coefficient, A_n is the nozzle minimum area in m^2, ρ_f is the density of the fuel in kg/m^3, Δp is the pressure drop in pascal, $\Delta\theta$ is the nozzle open period in Crank Angle Degrees (CAD), N is the speed of the engine in revolutions per seconds, S is the depth of penetration (m), ρ_g is density of gas, t is time after the start of injection in seconds, d_n is nozzle diameter in m, ρ_g is gas density in kg/m^3, and T_g is the temperature of the gas in the cylinder at fuel injection in K. The minimum area of the nozzle is the product of the area of the nozzle (calculated from d_n) and the area coefficient, C_A. The values of C_A range from 0.85 to 0.97 while C_D ranges from 0.62 to 0.84 (Desantes et al., 2003).

Fuel atomisation also affects combustion characteristics. The density of biodiesel is above the maximum limit of standard diesel while pure ethanol has a density below the minimum standard (Tables 3.2 and 3.3). Fuels that are denser than standard diesel lead to poor atomisation. The denser the fuel, the less the fuel mass that is injected by the injector, and consequently, the lower the power output from the engine. Dense fuels like biodiesel also have poor flow characteristics at low temperatures as the fuels tend to solidify.

The dependence of the densities of blend fuels on the concentration of ethanol is depicted in Figure 3.6 as reported by Barabás and Todoruţ (2009).

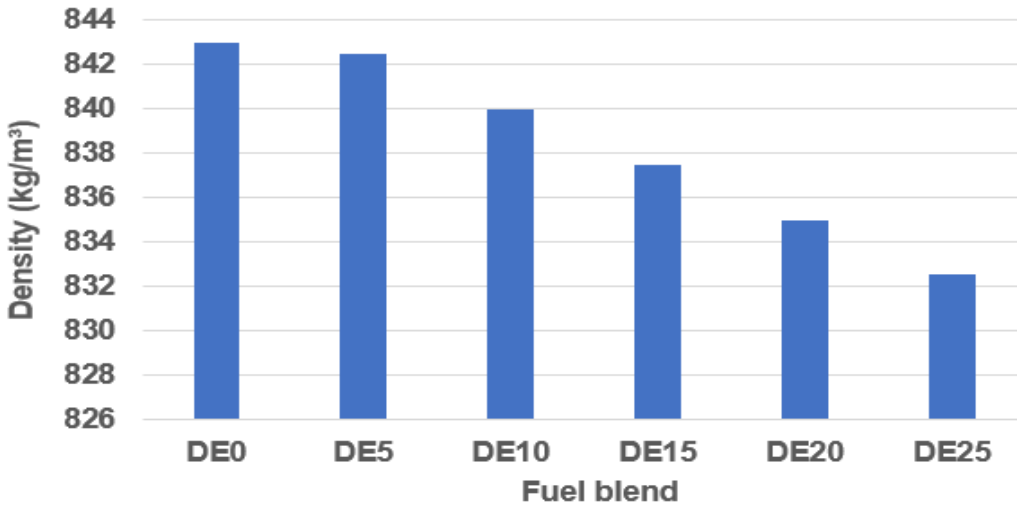

Figure 3.6 Dependence of densities of blend fuels on the concentration of ethanol (Barabás and Todoruţ, 2009)

Fuel injection in diesel engines occur at elevated temperatures and pressures. This necessitates the correction of the density of the fuel to the injection pressure and temperature. Schaschke et al. (2013) investigated the effects of fuel injection pressure and temperatures on the density of diesel fuels. The authors proposed the mathematical expression given in Equation 3.3 for the correction of the density, ρ of standard diesel to the injection pressure, p at 50 ^{o}C.

$$\rho = 829 + 0.59p - 0.0007p^2 \qquad 3.3$$

3.3.2.2 Viscosity

The viscosity of fuels also affects fuel atomisation, jet penetration and ultimately the combustion characteristics of the fuel and engine performance. The viscosity of fuels affects the ability of the fuel to lubricate and cool the metallic components of the engine for the prevention of wear and overheating. The viscosity of biodiesel is higher than the standard maximum limit while the viscosity of ethanol is lower than the standard minimum limit (Table 3.2 and Table 3.3). 100% biodiesel fuel will have poor flow within narrow constrictions such as injector

nozzles and the clearance between the piston and cylinder especially in wintry temperatures. This can cause wear of engine parts and overheating due to poor lubrication. Ethanol, on the other hand, is lighter than standard diesel, and as such, it is highly volatile. The low viscosity of pure ethanol makes it a poor lubricant. The use of high ethanol fuel blends, therefore, will have damaging effects on combustion engines.

The dependence of the kinematic viscosities of blend fuels on the concentration of ethanol is depicted in Figure 3.7 as reported by Barabás and Todoruţ (2009).

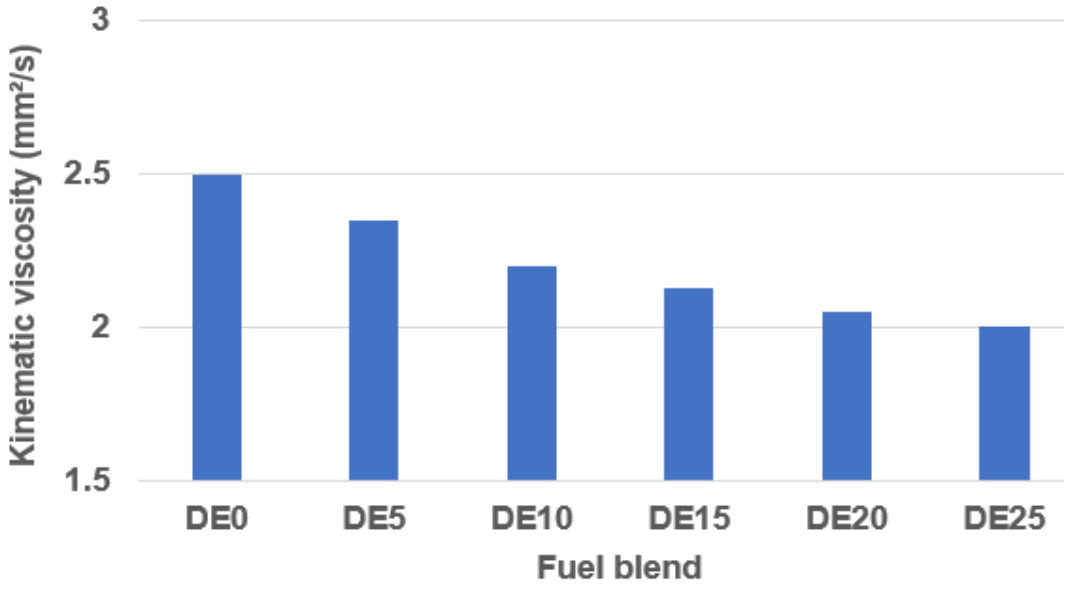

Figure 3.7 Dependence of kinematic viscosity of blend fuels on the concentration of ethanol (Barabás and Todoruţ, 2009)

3.3.2.3 Lubricity

The lubricity of a fuel is its potential to minimise friction between surfaces that are in contact and moving relative to each other under load. Good fuel lubricity is required to prevent damages to engine parts such as the fuel pump and the injectors. Poor lubrication causes engine wear and overheating. Biodiesel has good lubricity while bioethanol has poor lubricity.

3.3.2.4 Cetane Number (CN)

The Cetane Number (CN) is a measure of how easily a fuel auto-ignites. The CN of biodiesel is 1.04 times higher than that of standard diesel while pure ethanol has the lowest CN (CN of 8) as shown in Table 3.2 and Table 3.3. Ethanol can only be used in diesels as a blend because of its poor auto-ignition property. Furthermore, too high a concentration of ethanol in fuel blends undermines the CN of the blend leading to long ignition delays, high emission levels of unburned hydrocarbons (THC) and poor engine performance. According to Li et al. (2004), every 10 vol% increase in the concentration of ethanol in diesohol reduces the CN of the final blend fuel by 7.1. Lapuerta et al. (2009), reported an increase in THC of 20 ppm above reference diesel when DE17 was used at 1,853 rpm and 6.34 Brake Mean Effective Pressure (BMEP). However, when the engine was operated at the same conditions with DE7.7, THC emission was the same as that of reference diesel (17.5 ppm; which is 20 ppm lower than the THC emission with DE17). Rakopoulos et al. (2008), on the other hand, reported an increase in THC emission of 21.74% above baseline diesel with DE5 when the engine was operated at 1,200 rpm and 3.56 BMEP. However, when DE10 was used, THC emission was 30.43% above base diesel. The authors reported that the THC emission increased as the percentage of ethanol in the blends increased at all the loads that were considered.

The auto-ignition property of a fuel can be estimated from Equation 3.4 as CN (Ryan et al., 1994) or as Cetane Index, CCI from Equation 3.5 of the National Bureau of Standards (NBS, 1987).

$$CN = 55.51 \times (t_d - 1.23)^{-0.79} \quad 3.4$$

t_d in Equation 3.5 is the Ignition Delay (ID) time (millisecond).

$$CCI = 455 - 1641\rho + 775\rho^2 - 0.554T_{50} + 97.8(logT_{50})^2 \quad 3.5$$

ρ, in Equation 3.4 is the density of the fuel in kg/dm^3, while T_{50} is the temperature of the fuel at 50% distilled point.

Equation 3.4 depicts the relationship between the CN and the ID. It can be seen from the equation that a decrease in the CN of a fuel will result in an increase the ID. The CN decreases as the concentration of ethanol in a blend fuel increases. Therefore, as the ethanol content of a blend fuel increases, the ID will increase due to a decrease in the CN of the blend.

3.3.2.5 Flash point

The flash point of a fuel defines the lowest temperature, corrected to atmospheric pressure, at which the vapour above the fuel ignites in the presence of an ignition source (Barabás and Todoruţ, 2009). Biodiesel has the highest flash point of the three fuels in Tables 3.2 and 3.3 while bioethanol has the lowest flash point. The flash point of a fuel determines the safety measures that must be taken in the storage and transportation of the fuel. Ethanol has a very low flash point. As such, adequate safety measures must be put in place in the storage and transportation of pure ethanol and ethanol blend fuels.

3.3.2.6 Surface tension

Surface tension results at the liquid-air interphase when cohesion (the attraction between the molecules of the liquid) is greater than adhesion (the attraction between liquid-air molecules) (USGS, 2015). The surface tension of a liquid is a function of the density of the liquid, saturated vapour pressure, temperature, and solute concentration. The surface tension, σ of a pure liquid can be estimated from Sugden parachor (Sinnott, 2003) given in Equation 3.6.

$$\sigma = [P_{ch}(\rho_l - \rho_V)/M]^4 x 10^{-12} \quad 3.6$$

σ = surface tension in mN/m, P_{ch} = Sugden's parachor, ρ_l= density of liquid in kg/m^3, ρ_V= saturated vapour density, M = molecular mass.

The surface tension of a mixture, on the other hand is estimated from Equation 3.7 (Sinnott, 2003). Equation 3.7 can be used to estimate the surface tension of a binary fuel blend.

$$\sigma_m = \sigma_1 x_1 + \sigma_2 x_2 \quad 3.7$$

σ_m= surface tension of mixture, σ_1 and σ_2 = surface tensions of the constituent liquids, x_1 and x_2 are mole fractions of the components of the blend.

The temperature at which σ is estimated using Equations 3.6 and 3.7 is always stated because of the dependency of the parameters in the equations on temperature. Equations 3.6 and 3.7 also depict vividly the dependency of σ on density, vapour pressure and solute concentration.

Fuels that have high surface tension values do not atomise easily; the spray will consist of relatively large fuel droplets. This leads to incomplete combustion and poor combustion characteristics.

The dependence of surface tension on the composition of a fuel or fuel blend as well as on the concentration of ethanol in the blend is presented graphically in Figure 3.8 (Li et al., 2004).

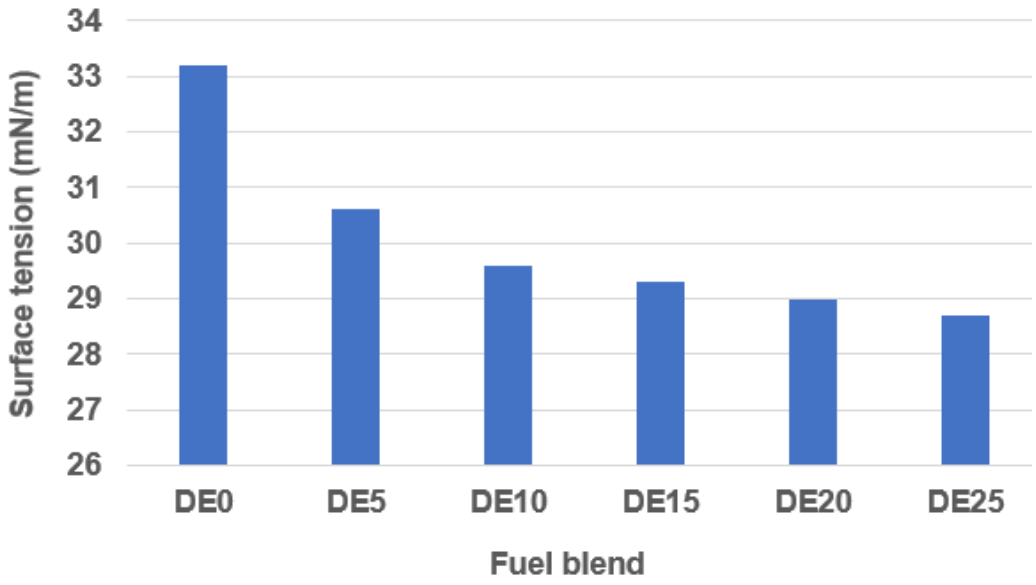

Figure 3.8 Dependence of the surface tension of diesel-ethanol (DE) fuel blends on the concentration of ethanol (Li et al., 2004)

It can be discerned from the measured values of the kinematic viscosities and the surface tensions shown in Figures 3.7 and 3.8 that the kinematic viscosities and surface tensions of diesel-ethanol blend fuels are exponential functions of the concentration of ethanol in the blends.

3.3.2.7 Cold Filter Plugging Point (CFPP)

The Cold Filter Plugging Point (CFPP) of a fuel is the lowest temperature below which the fuel will not flow freely in engine fuel systems. Biodiesel (RME) has a CFPP of -20 ^{o}C. If an RME–fuelled engine is subjected to climatic temperatures below -20 ^{o}C, the flow of the fuel in the engine becomes problematic because RME becomes gelatinous at such low temperatures.

3.3.2.8 Blend properties

The objective of blending fossil diesel with biofuels is to achieve a fuel blend whose fuel properties are similar to the recommended standard properties of diesel. The optimum blend therefore, is the blend that has similar properties to standard diesel and yet, gives similar performance with better economy,

availability, and lower engine-out emissions than fossil diesel. The properties of a blend fuel are mainly determined by the blend components, concentration of each component, and temperature. Typical measured properties of selected fuel blends are shown in Table 3.4 as reported by Barabás and Todoruţ (2009). The values of the density in Table 3.4 were measured at 15 ^{o}C while viscosity values were measured at 40 ^{o}C by the authors. Table 3.4 depicts the measured flash point and surface tension of binary DE blends (Li et al., 2004). The blends used by Li et al. (2004) contained 1.5% by volume of solubiliser. In Table 3.4, DE and DB represent binary diesel-ethanol and diesel-biodiesel blends respectively while DBE represents ternary diesel-biodiesel-ethanol blends. The number following each letter represents the percentage (by volume) of the component in the blend.

Table 3.4 Blend properties (Barabás and Todoruţ (2009), Li et al. (2004))

Blend fuel (ratio in vol%)	**Density (kg/m^3)**	**Kinematic viscosity (mm^2/s)**	**Flash point (^{o}C)**	**Surface tension (mN/m)**
D100 (100% Diesel)	843	2.50	77.50	33.20
DE5 (Diesel:Ethanol 95:5)	842.50	2.35	19	30.80
DE10 (Diesel:Ethanol 90:10)	840	2.20	17	29.60
DE15 (Diesel:Ethanol 85:15)	837.50	2.13	16	29.30
DE20 (Diesel:Ethanol 80:20)	835	2.05	15	29
DE25 (Diesel:Ethanol 75:25)	832.50	2.00	14	28.70
DB5 (Diesel: Biodiesel 95:5)	847	2.70		
DB10 (Diesel: Biodiesel 90:10)	849	2.80		
DB20 (Diesel: Biodiesel 80:20)	852.50	3.05		
DB25 (Diesel: Biodiesel 75:5)	855	3.18		
D90B5E5 (Diesel:Biodiesel:Ethanol 90:5:5)	841.25	2.45	18	31

D85B5E10(Diesel:Biodiesel:Ethanol 85:5:10)	843	2.20	15	28.50
D85B10E5(Diesel:Biodiesel:Ethanol 85:10:5)	845	2.40	14	34.50
D80B15E5(Diesel:Biodiesel:Ethanol 80:15:5)	847.50	2.50	17	34.50
D80B10E10(Diesel:Biodiesel:Ethanol 80:10:10)	843	2.25	15	29
D75B20E5(Diesel:Biodiesel:Ethanol 75:20:5)	850	2.65	17	32.50
D75B15E10(Diesel:Biodiesel:Ethanol 75:15:10)	845	2.30	15.50	30.75

Key: D: Diesel, B: Biodiesel, E: Ethanol

3.3.2.9 Potential challenges of using ethanol as blend component in diesel

The potential key challenges of using ethanol as a blend component in diesel are miscibility (instability of blend), safety (handling of blend), low CN, poor lubricity, high affinity for water, corrosion and low energy density.

Ethanol is not perfectly soluble in diesel in all proportions. The stability of diesel-ethanol (DE) blends is highly depended on temperature, concentration, and the purity of ethanol. At very low temperatures such as during winter, DE blends that are stable at room temperature (20 ^{o}C) undergo phase separation.

Safety issues must be duly considered when using ethanol as a blend component. Ethanol is highly volatile and highly inflammable. Ethanol also has a very low flash point (13 ^{o}C as shown in Table 3.3). Furthermore, the presence of ethanol in a binary or ternary fuel blend drastically reduces the flash point of the blend to values close to the flash point of ethanol as shown in Table 3.4. The

vapour of ethanol forms an explosive mixture with ambient air. Ethanol also has a corrosive effect on the skin and on most rubber. Fluorocarbon rubber has been recommended in lieu of rubber (Naegeli et al., 1997). Safety precautions must be adhered to in the storage and handling of ethanol and its blends. Ethanol blends must be stored in air-tight containers (stainless steel or glass) and kept away from sources of heat or ignition.

The low CN of ethanol (Table 3.3) undermines the auto-ignition property of DE fuel blends thereby, increasing the ID in diesel engines. Increase in the ID leads to incomplete combustion which can increase the THC emission levels (Section 3.3.2.4). The higher the concentration of ethanol in the blend, the longer the ID. High concentrations of ethanol in a fuel blend will necessitate the use of cetane improvers in the blend which implies additional costs.

The viscosity of ethanol is very low relative to standard diesel. Consequently, the potential of ethanol to lubricate moving engine surfaces is very low. The poor lubricity of ethanol also undermines the lubricity of the fuel blend. The tendency of damages occurring in engine components because of wear and overheating is increased when ethanol is used in diesel in relatively high proportions.

Ethanol has a high affinity for water (being a polar solvent just like water). Ethanol is known to absorb water even from the atmosphere because of its hygroscopicity. Prolonged contact of the fuel blend with air in fuel tanks will cause ethanol in the fuel blend to dissolve moisture from air and phase separate. This challenge further compounds the storage and handling issues of ethanol. Furthermore, the affinity of ethanol for water makes it corrosive to copper, brass and aluminium materials. Fuel delivery systems should not be made from the materials above (Coelho et al., 1996).

Another potential challenge of using ethanol as a blend component in diesel is that ethanol has a lower energy density/Lower Heating Value (LHV) than diesel. The heat of combustion of diesel is 45 MJ/kg while that of ethanol is 27 MJ/kg (Kwanchareon et al., 2007). The low heating value of ethanol reduces the power output of the engine for the same injected mass of diesel. The actual energy density of the fuel blend is then less than that of diesel. Therefore, to achieve the same engine power, the injector must inject more blend fuel mass than diesel mass at every injection to compensate for the relatively low heating value of ethanol.

3.3.3 Emissions Index (EI)

Emissions from transport engines are usually measured from engine test beds or real driving cycles in units of pollutant concentration (volume % or ppm). It is, however, desired to convert raw emission measurements into standard units for comparison with legislated limits. Emission Index (EI) is an intermediate unit of pollutant emissions from which emission measurements can be converted into other standard units such as mass of pollutant per kilometre driven on a test cycle or mass of pollutant per kilowatt hour.

Emissions Index (EI) is the ratio of the mass of pollutant emitted to the mass of fuel that is burnt (Andrews, 2018a). EI is given by Equation 3.8.

$$EI\left(g_{pollutant}/kg_{fuel}\right) = mass_{pollutant}/mass_{fuel} \qquad 3.8$$

The legislated units of emission for passenger cars and Heavy Duty Diesels as well as the various expressions for EI in terms of pollutant concentration are given in Equations 3.9 to 3.13 (Andrews, 2018a).

The legislated emissions unit for passenger cars is the ratio of the mass of the pollutant (in g) and the total kilometer driven on the test cycle (Equation 3.9).

$$EI\ (g_{pollutant}/km) = EI(g/kg_{fuel}) \times fuel\ consumption(kg_{fuel}/km) \quad 3.9$$

The legislated emissions unit for heavy duty diesels (diesel engines in buses and trucks) is expressed in g/kWh (Equation 3.10). It is the ratio of the mass of the pollutant (in g) and the energy produced.

$$EI(g/kWh) = EI(g/kg_{fuel}) \times BSFC(kg_{fuel}/kWh) \quad 3.10$$

$BSFC$ in Equation 3.10 is the Brake Specific Fuel Consumption.

The EI is estimated directly from the measured pollutant concentration from Equation 3.11.

$$EI_j(g_{pollutant}/kg_{fuel}) = C_{pj} \times MW_p/MW_e \times (1 + AFR) \quad 3.11$$

In Equation 3.11, j represents the pollutant such as CO, or NO_2, C_{pj} is the concentration of pollutant (v/v), MW_p is the molecular weight of pollutant, MW_e is the molecular weight of exhaust gas, AFR is the air-fuel ratio (the ratio of the mass of air to the mass of fuel in the combustion mixture). MW_e is assumed equal to the molecular weight of air, (28.84 kg air/kgmol). This assumption is accurate to <1% for lean mixtures.

Equation 3.12 is used in lieu of Equation 3.11 if C_{pj} is in volume %.

$$EI_j(g_{pollutant}/kg_{fuel}) = C_{pj} \times MW_p/MW_e \times (1 + AFR) \times 10 \quad 3.12$$

Raw emissions data are also taken in ppm (volume). Equation 3.13 is used to evaluate EI if C_{pj} is in ppm.

$$EI_j(g_{pollutant}/kg_{fuel}) = C_{pj} \times MW_p/MW_e \times (1 + AFR) \times 10^{-3} \quad 3.13$$

The AFR in Equations 3.11 to 3.13 can be estimated from the method of Chan and Zhu (1996). The stoichiometric AFR (AFR_s) and the actual AFR (AFR_a) are

estimated from Equations 3.14 to 3.22 for a fuel $C_aH_bO_cN_d$ (Chan and Zhu, 1996), where a, b, c, d are the percentages of carbon, hydrogen, oxygen, and nitrogen respectively in the fuel.

$$AFR_s = 28.85/\varepsilon(12.011\alpha + 1.008\beta + 15.999\gamma + 14.007\delta) \quad 3.14$$

$$\varepsilon = 0.21/(\alpha + 0.25\beta - 0.5\gamma) \quad 3.15$$

$$AFR_a = \frac{138.324}{12.011\alpha+1.008\beta+15.999\gamma+14.007\delta} \times \frac{\alpha A_1-\gamma+\frac{\beta K[CO_2]}{2A_2}-\frac{\alpha A_3 A_4}{2A_2}}{2.0038+A_5-\frac{A_5 K[CO_2]}{A_2}+\frac{0.0019 A_3 A_4}{2A_2}-0.0019A_1} \quad 3.16$$

The parameters in Equation 3.16 are defined as follows:

$$A_1 = [CO] + 2[CO_2] + 2[O_2] + [NO] + 2[NO_2]/([CO] + [CO_2] + [HC]) \quad 3.17$$

$$A_2 = K[CO_2] + [CO] \quad 3.18$$

$$A_3 = K[CO_2]/[CO]\{[CO] + [CO_2] + [HC]\} \quad 3.19$$

$$A_4 = x[HC][CO] \quad 3.20$$

$$A_5 = 4.7755\,\varphi p_g/(p_a - p_v) \quad 3.21$$

φ = relative humidity

p_g = saturated water vapour pressure at ambient temperature (20 ^{o}C) in mmHg

p_a= atmospheric pressure in mmHg

p_v= partial pressure of water vapour in the atmosphere (also expressed as the product of p_g and φ.

K is the equilibrium constant. The values that are commonly used for K are 3.5 and 3.8 which values correspond to equilibrium temperatures of 1,738 K and 1,814 K respectively (Chan and Zhu, 1996).

x is the H/C mole ratio of the fuel (b/a).

p_g in Equation 3.21 can be estimated from Equation 3.22.

$$\log_{10} p_{\mathrm{g}} = \mathrm{A} - \mathrm{B}/(\mathrm{C} + \mathrm{T}) \qquad 3.22$$

The values of the constants $A, B,$ and C in Equation 3.22 (for temperatures between 1 and 99 ^{o}C) are 8.07131, 1,730.63, and 233.426 respectively (Sinnott, 2005).

The engine parameters that are used in the evaluation of pollutants EI such as the Brake Mean Effective Pressure, BMEP (bar), the brake power, P (W), the Brake Specific Fuel Consumption, BSFC (kg/kWh), and the Brake Thermal Efficiency, BTE can be estimated from Equations 3.23 to 3.26 respectively (Rakopoulos et al., 2008).

$$BMEP = (4\pi M_t/V_H) \times 10^{-5} \qquad 3.23$$

M_t in Equation 3.23 is the engine brake torque in Nm while V_H is the engine total displacement volume in m^3.

$$P = M_t(2\pi N/60) \qquad 3.24$$

N in Equation 3.25 is the engine speed in rpm.

$$BSFC = \left(V_{fc}\rho_f/P\right) \times 3.6 \times 10^6 \qquad 3.25$$

V_{fc} is the volume of fuel consumed in m^3/s while ρ_f is the density of the fuel in kg/m^3.

$$BTE = P/\left(V_{fc}\rho_f Cv\right) \qquad 3.26$$

Cv in Equation 3.26 represents the Calorific value (Cv) of the fuel in J/kg.

Another crucial parameter in engine research is lambda, λ, the excess air ratio (Equation 3.27). λ expresses the leanness of a combustion mixture.

$$\lambda = (AFR)_a/(AFR)_s \quad 3.27$$

The combustion mixture is lean when $\lambda > 1$. The mixture is rich when $\lambda < 1$ and it is said to be stoichiometric when $\lambda = 1$.

A similar parameter to λ is the equivalence ratio, $\emptyset$ which is given by Equation 3.28.

$$\emptyset = 1/\lambda \quad 3.28$$

The combustion mixture is lean when $\emptyset < 1$. The mixture is rich when $\emptyset > 1$ and it is said to be stoichiometric when $\emptyset = 1$.

3.3.4 Emissions from Internal Combustion Engines (ICEs)

The legislated pollutants of transport engines include carbon monoxide (CO), total hydrocarbons (THC or HC), NOx (oxides of nitrogen) and particulates. These pollutants are strictly regulated because of their harmful effects on the environment and on human health. Exposure to CO causes the gas to combine irreversibly with haemoglobin thereby reducing the oxygen uptake of the human blood which is fatal. Unburned hydrocarbons such as benzene are carcinogenic when inhaled. Excessive exposure to nanoparticles can cause inflammation of the lungs. Though CO and HC are not primary Greenhouse Gases (GHGs), they react with NOx in the presence of sunlight to form ozone (a powerful GHG) (Andrews, 2018a).

NO_2 emission is a problem in non-stoichiometric (lean combustion) Gasoline Direct Injection (GDI) engines. Lean-burn GDI SI engines also have high PN

emissions. The NOx emission from SI engines occurs mainly during cold start because SI engines are now fitted with three-way-catalysts (TWC) (Gidney and Gorsmann, 2018). The catalysts control CO, HC, and NOx emissions after cold start when the engine is heated up. HC emissions also occur at cold start in SI engines. However, when the catalyst is heated to its light off temperature, HC emissions reduce drastically.

Diesel engines have higher thermal efficiencies than gasoline engines. The diesel engine is reported to be about 30% more efficient than the gasoline engine (Andrews, 2015). Combustion in diesel engines occurs by auto-ignition unlike in SI engines which utilise spark ignition. High pressures are also required in diesel engines for the charge (air/fuel mixture) to auto-ignite in the combustion chamber. Therefore, the CR in diesels is higher than the CR in SI engines. The range of CR in diesels is 16-21/1 while in SI engines, the CR is 10.5-12/1 (Andrews, 2018a). Another major difference between diesel engines and SI engines is that, diesel engines utilise turbocharging and intercooling to further increase the inlet air pressure and the power of the engine. SI engines use inlet air throttle valve to control the inlet air mass flow and power. High CR and turbocharging make diesel engines stronger and more expensive to manufacture than SI engines. The two types of engines utilise reciprocating pistons and both have a stoichiometric mass air/fuel ratio of 14.6 (Andrews, 2018a).

Unlike SI engines, diesel engines have low CO and HC emissions, the major emission challenge in diesels being NOx and PM. HC and CO in diesels are usually low due to lean combustion conditions (the excess oxygen from air oxidises the CO and the unburnt HC). Biofuels (biodiesel and bioethanol) have been reported to have benefits in terms of the reduction of harmful emissions from diesel engines when they are blended with diesel in CI engines. The

potential of biofuels to reduce harmful emissions can be attributed to the presence of oxygen in their molecules.

The percentage contributions of road transport to the total emissions of 2015 are shown in Table 3.5 (Wakeling and Passant, 2017).

Table 3.5 Contributions of road transport to 2015 total emissions (Wakeling and Passant, 2017)

Emission	**Contribution of road transport (%)**
CO	32.60
Volatile Organic Compounds (VOC)	3.10
NOx (as NO_2)	34..00
PM_{10}	14.20
$PM_{2.5}$	13.30

PM_{10} and $PM_{2.5}$ in Table 3.5 represent the masses of particulate matter less than 10 μm and 2.5 μm respectively.

The high contribution of transport engines to the overall emission of pollutant gases (Table 3.5) is the reason for the stringent regulation of the emissions as shown in Table 3.6 and Table 3.7 (Gidney and Gorsmann, 2018).

Table 3.6 European emission limits for Spark Ignition (SI) engines (Gidney and Gorsmann, 2018)

	Euro 4	**Euro 5**	**Euro 6b**	**Euro 6c**
Year of Implementation	2005	2009	2014	2017
Distance (‘000 km)	100	160	160	160
THC (mg/km)	100	100	100	100
NMHC* (mg/km)	-	68	68	68
CO (mg/km)	1000	1000	1000	1000

NOx (mg/km)	80	60	60	60
PM (DI, mg/km)	-	5	4.5	4.5
PN (#/km)	-	-	6×10^{12}	6×10^{11}

*Non-Methane Hydrocarbons

Table 3.7 European emission limits for diesel engines (Gidney and Gorsmann, 2018)

	Euro 4	**Euro 5**	**Euro 6**
Year of Implementation	2005	2009	2014
Distance (‘000 km)	100	160	160
NOx (mg/km)	250	180	80
HC + NOx (mg/km)	300	230	170
CO (mg/km)	500	500	500
PM (DI, mg/km)	25	4.50	4.50
PN (#/km)	-	6×10^{11}	6×10^{11}

3.3.4.1 Total hydrocarbon (THC) emission in Spark Ignition (SI) engines

Non-direct injected SI engines or port fuel injected SI engines utilise Port Fuel Injection (PFI) into the inlet air before the intake valve. The injected fuel in PFI SI engines is completely vaporised. Poor vaporisation of fuel occurs in Gasoline Direct Injection (GDI) SI engines and the fuel droplets that are not vaporised dissolve in the lube oil film on the cylinder walls. At the end of combustion, they boil out, thereby, increasing the THC emission in SI engines. According to Andrews (2018a), the major source of HC in SI engine emission is the space between the top of the piston, along the side of the piston, and the first piston seal ring (crevice volume).

3.3.4.2 Carbon monoxide (CO) emission in Spark Ignition engines

Carbon monoxide (CO) in SI engines is generated in three ways. These include: CO from combustion at equilibrium, CO from inefficient combustion, and CO from excessive EGR (Gidney and Gorsmann, 2018). Rich combustion mixtures give rise to high equilibrium CO whereas lean mixtures have relatively low equilibrium CO. PFI SI engines do not have unmixedness problem because the fuel is completely vaporised. However, GDI SI engines have local rich and local lean zones which affect the CO emission from the engines.

Inefficient combustion occurs when fuel combustion does not reach equilibrium. Incomplete oxidation of fuel results in CO emission. According to Andrews (2018a), incomplete oxidation is due to:

i) Insufficient residence time for the combustion to attain equilibrium.
ii) Improper mixing of fuel and air during cold start leading to rich regions wherein oxygen is not sufficient to fully oxidise the fuel.
iii) Heat extraction: cooling or quenching of the flame before equilibrium is attained

Generally, GDI SI engines have higher CO emission than PFI SI engines.

3.3.4.3 Nitrogen oxides (NOx) emissions in Spark Ignition (SI) and diesel engines

There are three sources of NOx in SI and diesel engines. These include: thermal (Zeldovich) NOx, prompt NOx (NOx from N_2O) and NOx from Fuel Bound Nitrogen (FBN) (Heywood (1988), Andrews (2018a)). Thermal NOx results from the reaction between oxygen and nitrogen in air at temperatures above 1,800 K. Thermal NOx is the major source of NOx in ICEs. Prompt NOx is generated rapidly from the reaction between hydrocarbon (HC) intermediaries. Prompt NOx

is mainly generated from rich mixtures which are encountered in diesels due to poor mixing (though the combustion in diesels is generally lean). NOx from FBN results if the fuel contains nitrogen compounds.

Naturally, lean combustion should give low NOx. However, because fuel is introduced into the cylinder in diesels by direct injection at the TDC, local rich regions arise which give rise to high flame temperatures. Local rich regions and high combustion temperatures favour the production of NOx. The use of Diesel Oxidation Catalyst (DOC) has also increased NO_2 in diesels while reducing NO. NOx can be controlled in diesels by using emission aftertreatment systems. A typical diesel emission aftertreatment is shown in Figure 3.9 (Joshi et al., 2018). Figure 3.9 depicts the reactions that occur in the different catalytic sections of the aftertreatment system. The catalytic sections in the system include the Diesel Oxidation Catalyst (DOC) section, the Catalytic Soot Filter (CSF) (Gasoline Particulate Filter (GPF) in SI engines), the Selective Catalytic Reduction (SCR) section, and the Ammonia Slip Catalyst (ASC) section.

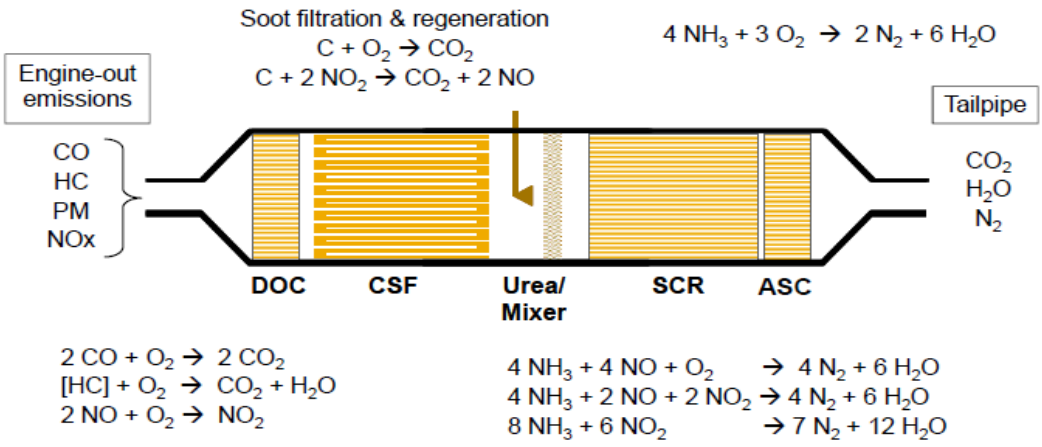

Figure 3.9 Diesel emission aftertreatment system (Joshi et al., 2018)

The SCR, in more recent configurations of the aftertreatment system, is placed just after the DOC so that the incoming hot exhaust gases quickly heat up the

SCR catalyst to its light off temperature. The new configuration enhances the efficiency of the system towards meeting stringent emission standards such as the Worldwide Harmonised Light Vehicles Test Procedure (WLTP).

NOx can be controlled in both SI and diesel engines by Exhaust Gas Recirculation (EGR) and by the injection of water. The inert gases of water and EGR reduce NOx by lowering the temperature of the flame. Water, however, has an advantage over EGR; it increases the power of the engine via the increased expansion that occurs in the cylinder due to the formation of steam (Andrews, 2018a). EGR also has the disadvantage of reducing fuel economy and increasing the emission of soot and CO from the engine especially at high EGR rates. Soot formation reaches its peak at 2,000 K whereas thermal NOx is negligible at temperatures below 1,900 K. The average operation temperature of diesel is < 1,800 K. This implies that it is possible to obtain low soot and NOx emissions from diesels (Andrews, 2018a).

NOx is controlled in-cylinder by controlling peak temperatures and the ID to enhance the premixing of fuel and air so that local rich regions are not formed in the cylinder.

3.3.4.4 Particulate Matter (PM)

Particulate Matter (PM) are materials that collect on a filter paper after the exhaust temperature is brought to about 50 ^{o}C by dilution (Andrews, 2018a). The causes of particulate matter in ICEs are poor fuel-air mixing, excessive EGR, excessive oil consumption, poor atomisation which results in large oil droplets, wetting of cylinder walls by fuel and low flame temperatures (Gidney and Gorsmann, 2018). Particulate matter is currently regulated in terms of the mass of particulates (PM) and the Particulate Number (PN).

Particulate Matter (PM) emissions from diesels are similar to those of PFI SI engines because modern diesels have particulate filters fitted to their exhaust. The typical composition of PM from diesel is shown in Figure 3.10 (Kittelson, 1998). Figure 3.10 shows that the PM from diesels (unlike the particulates from SI engines) have a complex composition.

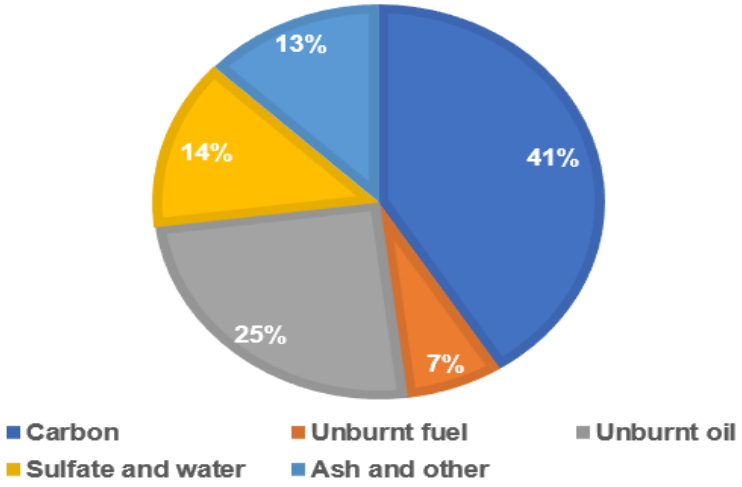

Figure 3.10 Composition of Particulate Matter (PM) from diesel (Kittelson, 1998)

THC, CO, NOx, and PM are simultaneously controlled by using combined three-way catalyst (TWC) and Diesel Particulate Filters (DPF). TWC usually consists of Diesel Oxidation Catalysts (DOC) for the oxidation of THC and CO and a Selective Catalytic Reduction (SCR) system for the reduction of NOx.

3.3.4.5 Formation of particulates in diesel engines

Diesel particulates consists mainly of soot - a carbonaceous material that is produced during combustion (Heywood, 1988). Soot is classified into extractable or soluble organic fraction (SOF) and dry-soot fraction. According to Heywood (1988), lubricating oil accounted for 2 to 25% by weight of the total particulate and 16-80% of the SOF in a radioactive tracer studies that was carried out on a light-duty Indirect Injection (IDI) diesel. The contribution from lubricating oil was

entirely in the SOF. The highest percentages of oil in the SOF were measured at the highest engine speed. Dry soot, on the other hand, was reported to have much lower H/C ratio than the SOF.

The formation of particulates in diesel engines is known to occur in two major stages: particle formation (nucleation) and particle growth. The nucleation stage involves the formation of the first particles by the condensation of unsaturated hydrocarbons (acetylene and Polycyclic Aromatic Hydrocarbons, PAH). The particle diameter, Dp of these first particles is <2 nm (Heywood, 1988). The particle growth stage is further divided into surface growth (the attachment of gas-phase species on to the nuclei to form spherules) and agglomeration. There are three types of agglomeration in diesels (Heywood, 1988):

i. Collision of two spherules to form spheroids (Dp≈10 nm) prior to the solidification of spherules.
ii. Collision of solidified spherules to form clusters at diminished surface growth rates.
iii. Collision of solidified spherules to form chainlike structures when surface growth has ended (aggregation).

Diesel particulates are known to exhibit multiple modes (nucleation mode and accumulation mode). The nucleation mode occurs in the particle diameter, Dp range of 3-30 nm. The accumulation mode occurs within 30-500 nm Dp (Kittelson, 1998). Diesel particulate distributions that have two (2) accumulation modes within the accumulation mode Dp range have been reported in literature (Wu et al., 2017). However, a few authors have reported diesel particulate distributions that have the second accumulation mode in the 500-1,000 nm Dp range (Mueller et al. (2015), Nestor (2001)).

3.3.5 Ethanol as blend fuel in Spark Ignition engines

Ethanol has unlimited solubility in gasoline (unlike its solubility in diesel). This is because the carbon chain in gasoline is relatively short (C_5 to C_{12}) compared to the carbon chains in the components of diesel (C_8 to C_{21}). Diesel contains much heavier hydrocarbon molecules than gasoline. The use of gasoline-ethanol oxygenated fuel blends in SI engines is well established. In the US for instance, gasoline-ethanol blends (gasohol) are extensively used in passenger cars. The oxygen content of ethanol enhances the oxidation of CO and HCs in the exhaust of SI engines. This leads to a drastic reduction in CO and HC emissions in SI engines that utilise oxygenated blend fuels. Modern gasoline engines incorporate the three-way catalyst (TWC) for effective control of CO, HC and NOx emissions. NOx in SI engines that utilise gasohol is controlled by TWC. The conversion efficiency of the catalyst is highly depended on the excess air ratio, λ or the equivalence ratio, $\emptyset$.

3.3.5.1 Previous works on emissions from SI engines

Researchers in the past have worked extensively on emissions from gasoline engines. Table 3.8 summarises some of the previous research on the control of emissions from gasoline engines. Table 3.8 shows that a lot of work has been carried out on emissions from the use of gasoline-ethanol blend fuels (gasohol) in SI engines as well as the application of emission aftertreatment systems to control the emissions. The reports of the authors are consistent unlike in the case of diesel engines as shown in the subsequent sections.

Table 3.8 Previous works on Spark Ignition (SI) engines

	Salih (1990)	**Hsieh et al. (2002)**	**Pikonas et al. (2003)**	**Wu et al. (2004)**	**Jia et al. (2005)**	**Reksowardojo et al. (2017)**
Investigation	Effect of ethanol on fuel economy and exhaust emissions	Engine performance and pollutant emission of an SI engine using gasohol (1,000-4,000 rpm; 0-100% throttle valve opening)	Influence of gasohol on SI engine performance and emission (1,500-6,500 rpm)	Influence of air-fuel ratio on engine performance and pollutant emission using gasohol (3,000, 4,000 rpm; 0-100% throttle opening; open-loop control)	Influence of gasohol on emission characteristics of motorcycle engine	Effect of gasohol blend on performance and emissions of motorcycle engine (without and with catalyst)
Engine type	1987 FORD Valencia, compact 4-	New Sentra GA16DE, 1600 cc, multi-point	Toyota Corolla (1994): 4E-FE D.O.H.C 16V	4-cylinder, 8-valve commercial New	HONDA CG125, monocylinder,	Single cylinder, 4-stroke, water-

	cylinder 1117 cc gasoline engine	injection D.O.H.C[a] commercial gasoline engine.		Sentra GA16DE, 1600 cc, multi-point injection, D.O.H.C engine.	4-stroke air-cooled engine	cooled SOHC engine.
Fuel type	Unleaded gasoline (E0), gasohol (E5, E10, E15, E20, E25)	Unleaded gasoline (E0), E5, E10, E20, E30.	Pure gasoline (E0), E10	Unleaded gasoline (E0), E5, E10, E20, E30.	Unleaded gasoline (E0), E10	Unleaded gasoline (E0), E5, E10, E20
Catalytic converter	No	No	No	No	No	TWC
Findings/results	i. Slight increase in power output with gasoline-	i. Torque output of E5-E30 slightly higher than that of base fuel for	i. 5% increase in engine power over gasoline.	i. For all throttle valve openings, λ slightly <1 gave	i. 30.8% and 31.7% dramatic decrease in CO and HC	i. Original ECU[d] without and with catalyst had slight increase in

	ethanol blends. ii. CO decreased relative to fossil gasoline for leaner mixtures (λ >1). CO of unleaded gasoline 1.5 times higher than E10 @ λ =1; 2,000rpm.	low throttle valve opening (20%) @ 2,000 rpm and at engine speeds > 3,000 rpm. ii. No difference between BSFC of E0 and gasohol blends because of leaning effect of gasohol blends.	ii. 2-3% increase in SFC[b] with E10. iii. 10-30% decrease in CO @ high power. iv. 5-10% increase in CO_2. v. HC decreased @ low and medium loads but increases	maximum torque output. At engine speeds considered, torque increased with increasing valve opening. ii. Slight increase in torque with ethanol fuel blends in small throttle opening (20 and 40%) at	respectively with E10. ii. Insignificant (5.9%) decrease in NOx over gasoline. iii. CO decreased by 14.8 and 16.9% at idle and 50 km/h drive modes respectively with E10; insignificant effect at	SFC of 2.68%, 2.86% 5.31% and 1.33%, 2.44%, 5.26% respectively for E5, E10, and E20. ii. Modified ECU without and with catalyst had more pronounced increase in SFC as ethanol concentration

	iii. 10-25% increase in ethanol led to 30-40% increase in HC at 1,500 rpm. No appreciable increase in HC with ethanol blend fuels at 2,500 rpm. Lowest HC emission occurred between 0.8-1.10 λ.	iii. Engine operated in leaner conditions; $\lambda \approx 1$ as ethanol content increases iv. @ 3,000 rpm, CO decreased as λ approached 1; combustion becomes	above gasoline @ very high loads (>6000 rpm).	both engine speeds. Highest torque @ λ =0.95, 4,000 rpm and for E30. iii. BSHC[c] lowest at $\lambda \approx$ 1. iv. CO reduced drastically as λ approached 1. Lowest CO with E10 @ $\lambda \approx$ 1.04. v. CO_2 highest when	intermediate drive speeds (15, 32 and 35 km/h). iv. More ethylene, acetaldehyde and ethanol in exhaust when E10 was used.	increased; increases of 2.15%, 5.67%, 10.26% and 3.15%, 5.59%, 10.06% respectively for the blends. iii. CO_2 increased as % of ethanol and driving speed increased while the opposite trend was

	iv. Less NOx from ethanol blends than unleaded gasoline at all speeds and applied loads. Blends with high % ethanol gave lower NOx at all conditions especially medium and low speeds.	more complete. v. CO_2 showed opposite trend to CO. vi. HC decreased as λ approached 1. vii. NOx increased λ approached 1; flame temperature increased		λ slightly above 1. When λ far from 1 (above and below) CO_2 decreases. Maximum CO_2 @ λ =1.01 for all fuels. Increasing ethanol decreased CO_2 emission. vi. Lowest HC observed between		observed for CO. iv. HC decreased as concentration of ethanol and speed increased. v. NOx increased with increase in driving speed and % of ethanol in blend. vi. Generally, lower CO,

	NOx increased to a point as λ increased, thereafter a decline in NOx occurred. v. Gasohols caused 30-50 ^{o}C decrease in temperature of exhaust gas. vi. Thermal efficiency of	due to more complete combustion. Insignificant influence of ethanol on NOx @ λ <1. At 3,000 rpm: i. @ throttle valve > 60%, torque increased 2-4% as ethanol content increased.		stoichiometric and slightly lean combustion. HC reduced by 5-30% as ethanol content increased for all valve openings. vii. Optimal condition to control HC given as λ $\approx$1.02 with E10.		HC and NOx when TWC was used than without TWC.

	the engine increased as λ increased; E25 had 3-5% thermal efficiency above unleaded gasoline. vii. Specific fuel consumption (SFC) for ethanol blend fuels was higher than the SFC for	ii. CO decreased as ethanol concentration increased; 10-90% reduction in CO possible depending on engine operating condition. CO_2 increased by 5-25% as ethanol content				

	gasoline by at least 13%. viii. At idle conditions, HC of gasohol rose as % of ethanol increased while NOx decreased as % of ethanol in the blend fuel increased.	increased (depending on operating condition). iii. HC decreased 20 to 80% over base fuel as ethanol content increased. iv. NOx dependent on engine operating conditions				

	CO of gasohol lower than that of gasoline at idle condition.	and not on ethanol content.				

[a]Dual Overhead Camshaft, [b]Specific Fuel Consumption, [c]Brake Specific Heat Consumption, [d]Engine Control Unit

3.3.6 Ethanol as blend fuel in diesel engines

One of the practical ways by which low temperature combustion can be achieved in diesels to control NOx is the use of diesel-ethanol (DE) fuel blends (diesohol). The use of gasoline-ethanol fuel blends (gasohol) in SI engines is well established already unlike the use of diesohol in CI engines. This is due to the inherent challenges in using DE blend fuels (Section 3.3.2.9). The current work investigates the effects of different DE fuel blends on the performance and emissions of diesel engines. Ethanol was used as the biofuel component of the blend in lieu of biodiesel. This is because it is relatively easy to produce ethanol from sweet sorghum and other biomass feedstocks, such as cassava, in Nigeria compared to the production of biodiesel by transesterification.

It has been demonstrated that high efficiency and low nitrogen oxides (NOx) and soot emissions can be achieved via low temperature dual-fuel combustion strategy (Reitz and Duraisamy (2015), Sukjit et al. (2014), Lapuerta et al. (2009), Li et al. (2004)). There is a need to further investigate the use of fuel blends (diesel-ethanol) to achieve much lower reduction of emissions from diesel engines. The summary of the work done by previous researchers on diesel engine emissions is presented in Table 3.9. Salih (1990) reported 30% reduction in NOx when diesohol was used with 7.5% naphtha on a Petter DI diesel engine. Raslavicius and Žilvinas (2010) on the other hand reported an increase in NOx (Table 3.9) from the test that they conducted on a D144 air-cooled diesel engine using ternary diesel-biodiesel-ethanol blends. Rakopoulos et al. (2008) and Lapuerta et al. (2009) reported an increase in THC emissions as the concentration of ethanol in blend fuels increased. However, Andrews and Salih (1990) reported a decrease in THC with increase in the concentration of ethanol in the blend. Kass et al. (2001) investigated the emissions from a 5.9 litre

Cummins B series diesel engine that was run on DE fuel blends. The authors reported that the levels of NOx and aldehydes were not significantly affected by the diesohol fuel blends. According to the authors, the levels of CO and THC increased above the baseline while the PM emission decreased below the baseline. Furthermore, Kass et al. (2001) reported that the raw engine-out ethanol was <20 ppm for the tested DE fuel blends (DE10 and DE15). The contradicting reports of previous researchers underscore the need for more investigations on the effects of alcohol blend fuels on NOx.

Table 3.9 Previous related works on diesel emissions

	Andrews and Salih (1990)	**Salih (1990)**	**Li et al. (2004)**	**Rakopoulos et al. (2008)**	**Lapuerta et al. (2009)**	**Sukjit et al. (2014)**
Investigation	Diesel particulate and NOx emissions	Effects of fuel blends on engine performance and emissions at different loads.	Effect of diesel-ethanol blend fuels on performance, emission of diesel engines; 25, 50, 75, 90 100% loads; 1,760 and 2,200 rpm.	Effects of diesel-ethanol fuel blends on the performance and exhaust emissions of heavy-duty DI diesel engine (1,200, 1,500 rpm; 20, 40, 60% load).	Effects of ethanol on diesel engine emissions (speed range 1,853-2,126 rpm; 8-110 Nm torques)	Fuel blend properties, emissions and particle size distribution.
Engine type	Petter (DI) diesel engine	Petter (DI) diesel engine	Water-cooled, single cylinder	Fully-instrumented,	4-cylinder, 4-stroke,	Single cylinder research

			(DI) diesel engine	4-stroke, 6-cylinder, OM366LA turbocharged, after-cooled, heavy duty DI Mercedes-Benz 177kW engine.	turbocharged, intercooled, common-rail, 2.2L, 82 kW Nissan diesel engine.	engine, pump-line-nozzle DI system, air-cooled and naturally aspirated.
Fuel type	Binary (diesel-ethanol: DE0, DE5, DE10, DE15, DE20)	Binary (diesel-ethanol); ternary (ethanol-naphtha*-diesel).	Binary (diesel-ethanol: DE0, DE5, DE10, E15, DE20 with 1.5% emulsifier)	Binary (diesel-ethanol: DE0, DE5, DE10 with Betz GE emulsifier)	Binary (diesel-ethanol: DE0, DE7.7, DE17 with 0.62% O_2Diesel additive); ternary (diesel-biodiesel-	Ternary (diesel-biodiesel-ethanol)

					ethanol: D62.3B30E7.7). B: Soybean biodiesel	
Catalytic converter/Emission aftertreatment	No	No	No	No	No	No
Ignition delay	Unquantified	Quantified	Unquantified	Unquantified	Unquantified	Unquantified
Findings/results	i. Ethanol caused maximum decrease of 15% in HC for same power. ii. NOx also reduced, but less relative	i. 30% reduction in NOx emissions ii. Slight increase in unburned hydrocarbon	i. BSFC decreased at maximum load at 2200 rpm; but increased slightly after 75% load at 1760 rpm. BSFC	i. Soot increased at same engine speed as load increased, but @ higher speeds and	i. Higher BSFC with ethanol blends compared to base diesel. ii. BTE similar for all fuels at low-loads. At 1,853 rpm and 110	i. Castor oil methyl ester (COME) enhanced lubricity of ethanol-diesel blends more than rapeseed oil

	decrease at high powers. iii. 30-40% decrease in PM with DE30. Also decreased soluble organic fraction (SOF) with ethanol blend. iv. 50-70% decrease in particulate carbon with	(UHC) at low loads iii. 3% increase in thermal efficiency at advanced timing of 24 BTDC iv. 30-40% higher SOF with ethanol blended fuels v. 40-50% lower PM at full and part loads.	increased as ethanol content in blend increased (dramatic increase for DE20). ii. BTE increased with DE blends for all conditions except DE15 at 25% load, 2200 rpm. Also, BTE increased as	higher loads, it decreased. ii. Blend fuels emitted significantly lower soot than base fuel; soot decreased as concentration of ethanol increased. iii. NOx of blends slightly lower than that of base	Nm, ED7.7 had slightly higher BTE. iii. HC of DE7.7 similar to diesel. HC increased as % ethanol increased especially @ 2,126 rpm; 8 Nm, high HC resulting from higher heat of vaporisation of ethanol.	methyl ester (RME). ii. Hydroxylated biodiesel (COME) reduced soot emissions better than ester functional group of RME. iii. Higher proportion of premixed combustion than base

	DE20 (depending on engine load).		% ethanol in blends increased at same operating conditions. iii. Smoke opacity increased @ low and medium loads for DE15, DE20; it increased for DE5, DE10 @2200 rpm. Opacity was	diesel. Ignition delay was longer for blend fuels. Generally, NOx decreased for all fuels as engine speed increased at the same load, however, increasing the load at	v. NOx slightly lower than baseline diesel @1,410; 1,526; 1,743 rpm and the corresponding torques (26, 46, 77 Nm). iv. Smoke opacity reduced as % ethanol increased. The reduction became	diesel due to longer ignition delay of ethanol blend fuels. iv. Increase in total HC emissions with blend fuels. v. Reduction in CO. vi. NOx increased when

			very low from 25-90% load for all fuels but was high at 100% load. It decreased for blend fuels at maximum load and 1760 rpm. iv. CO increased at rated speed (2200 rpm), low and medium loads with DE10,	same rpm resulted in higher NOx emission. iv. CO also decreased as speed and load increased for all fuels. CO decreased as % ethanol in fuel increased; lowest NOx	pronounced at high loads. v. Smoke opacity of D62.3B30E7.7 less than DE7.7 despite same concentration of ethanol. vii. At low load, reduction in PM was not significant, but at high loads, reduction was significant with	biodiesel was used.

			DE15 (DE5, DE20 deemed not suitable for diesels). v. At high to full loads and rated speed, CO decreased appreciably as load increased for the blend fuels. CO decreased by 49 and 29%	for all fuels was obtained @ higher speed and 40% load. v. HC increased as % ethanol increased. vi. BSFC higher than baseline for all blend fuels; it also increased as %	the blends. DBE had highest reduction in PM. viii. VOF/HC increased with blend fuels as % ethanol increased. ix. Particle size distribution of DE7.7 similar to diesel. Number concentration	

			at maximum load for DE10 and DE15 respectively. Generally, CO reduced by 16.7 and 5.8% for DE10 and DE15 respectively. vi. At rated speed, DE10, DE15 reduced NOx by 50% and 32-35% at	ethanol increased. vii. BTE of blends was slightly higher than diesel baseline. At the same rpm, BTE of all fuels increased as load increased.	of particles (PNC) of DBE lower than that of diesel fuel. x. Mean diameter, dm of particles decreased as % ethanol increased. DE7.7 and DBE had similar dm while DE17 had much lower	

			low and medium loads respectively, with slight NOx reduction at 75% load. @ full load, blends had higher NOx than base diesel. Generally, NOx reduced by 2.2 and 4.2% for DE10 and		(biodiesel has negligible effect on dm). xi. DE7.7 had similar PNC to base diesel, DBE and DE17 had lower PNC than base. xii. DE blends gave higher opacity reduction than DBE; oxygen of ethanol is more efficient	

			DE15 respectively. vii. Drastic increase in HC @ various engine conditions with ethanol blend fuels. DE10 had greater HC than DE15 @ tested conditions except 10% load @ 2200 rpm.		than equivalent oxygen of biodiesel; opacity reduction depended on functional group providing the oxygen. xiii. Above 20% ethanol, PM reductions ceased; high HC prevents	

			Generally, HC increased by up to 40% with blended fuels compared to diesel. viii. Blend fuels had opposite effects on CO and NOx emissions.		PM reductions of oxygenated fuels. xiv. Oxygen of ethanol favours higher increases in VOF than that of biodiesel. xv. Fuel oxygen of ethanol enhances	

					higher reductions in dm than that of biodiesel. xvi. High fuel oxygen content generally enhances the reduction of total PNC emission.	

*7.50% naphtha (based on volume of ethanol-diesel blend)

Table 3.9 shows that little work has been carried out by previous researchers on the effect of the concentration of ethanol in diesohol on the Ignition Delay (ID) in diesel engines. A quantitative investigation of the effects of the concentration of ethanol on the ID at 1,500 rpm and varying engine loads was carried out by Salih (1990). According to the author, the ID increased with increase in the excess air ratio (λ). The ID also increased as the concentration of ethanol increased at constant λ. DE15 had the highest ID at the given values of λ (Table 3.10).

Table 3.10 Effect of the concentration of on the Ignition Delay (ID) in a Petter Direct Injection (DI) diesel engine (1,500 and 25% load) (Salih, 1990)

Blend	**Ignition Delay, CAD bTDC**		
	λ =1.6	**λ =1.8**	**λ =2.2**
DE0	17.00	17.25	19.10
DE5	18.80	19.00	19.20
DE10	19.10	19.70	20.20
DE15	21.00	21.60	22.20
DE20	20.90	21.10	22.00

3.4 Heat Release Rate (HRR) analysis of Internal Combustion Engines (ICEs)

Heat Release Rate (HRR) analysis of Internal Combustion Engines (ICEs) is necessary in engine research to analyse of the performance of the engines for pure diesel and renewable/blend fuels engine operation. HRR analysis is also necessary to determine the combustion phasing: Start of Combustion (SoC), End of Combustion (EoC), Peak Heat Release Rate (PHRR), and to enhance the thermal efficiency of the engine. As indispensable as the HRR analysis is in

engine research, the HRR of an ICE cannot be measured real-time, it can only be modelled mathematically. As such, accuracy is of the essence in the development of HRR models for ICEs. The HRR model of ICEs is derived from the First Law of thermodynamics (Heywood, 1988). The ratio of specific heats, gamma (γ) is the most important thermodynamic property in the modelling of the HRR of an ICE (Ceviz and Kaymaz, 2005). γ has the greatest impact on the accuracy of the HRR model of ICEs. The existing models of γ were largely expressed in terms of the temperature of the gases in the cylinder even though γ is known to be strongly depended on the excess air ratio (λ) of the engine. The EGR rate also has some effect on γ. The existing HRR models were developed for ICEs that were operated at near–stoichiometric conditions ($\lambda \approx 1$). However, Compression Ignition (CI) engines operate within a wide range of λ. Therefore, it is necessary to develop an improved model for the determination of the HRR of CI engines. In the current work, a modified function, $\gamma_{mod}(T, \lambda)$ based on the γ function of Ceviz and Kaymaz (2005) was used to model the HRR of a modern, Multiple Fuel Injection Strategy (MFIS), CI engine for values of $\lambda > 1$. The effect of the EGR rate on γ was also studied in this work using the improved HRR model. The HRR model of Ceviz and Kaymaz (2005) and the improved HRR model in this work (Leeds HRR model) were both based on $\gamma(T, \lambda)$. However, the basic difference between the two models is that, the model of Ceviz and Kaymaz (2005) is based on $\gamma(T, \lambda)$ for both burned and unburned fuel mixtures while the Leeds HRR model is based on $\gamma(T, \lambda)$ for only burned mixtures (CI engines are lean combustion engines therefore, the injected fuel mass is relatively low and the fraction of unburned fuel in the exhaust gases is negligible). Secondly, the model of Ceviz and Kaymaz (2005) is applicable to SI engines operating at near-

stoichiometric conditions while the Leeds HRR model is for CI engines at non-stoichiometric conditions.

3.4.1 Effect of fuel injection strategy on the HRR profile of ICEs

Fuel injection in CI engines occurs either by Single Fuel Injection Strategy (SFIS) or Multiple Fuel Injection Strategy (MFIS). Fuel injection occurs at a specific crank angle in a SFIS engine. Consequently, the HRR profile of the engine has only one peak as depicted by the lower curve of Figure 3.11 (Vipavanich et al., 2018). On the other hand, in an MFIS CI engine, fuel injection occurs at more than one crank angle. Therefore, in contrast to a SFIS engine, multiple peaks are observed in the HRR profile of an MFIS engine as shown in Figure 3.12 (Mathivanan et al., 2016).

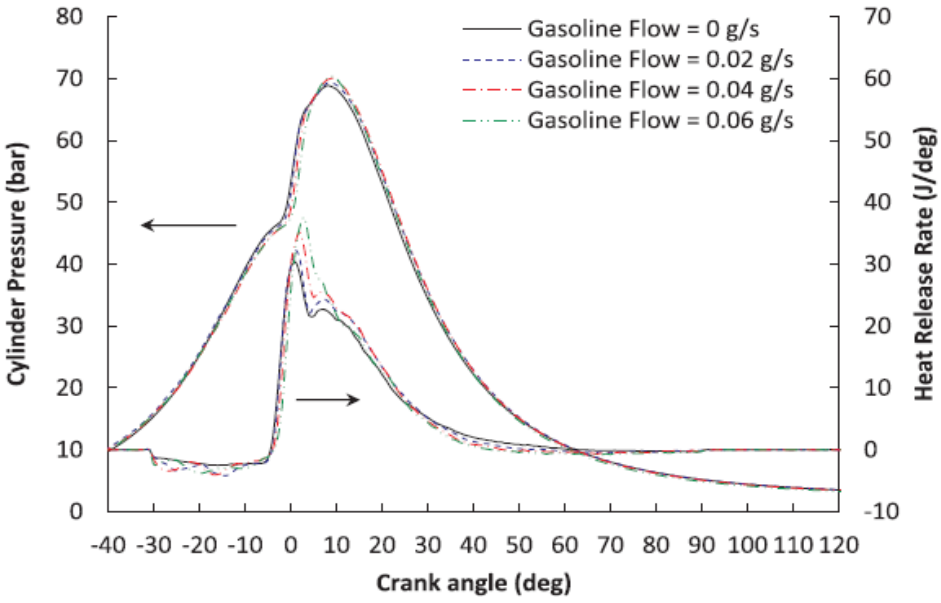

Figure 3.11 Heat Release Rate (HRR) profile for a Single Fuel Injection Strategy (SFIS) engine (lower curve) (Vipavanich et al., 2018)

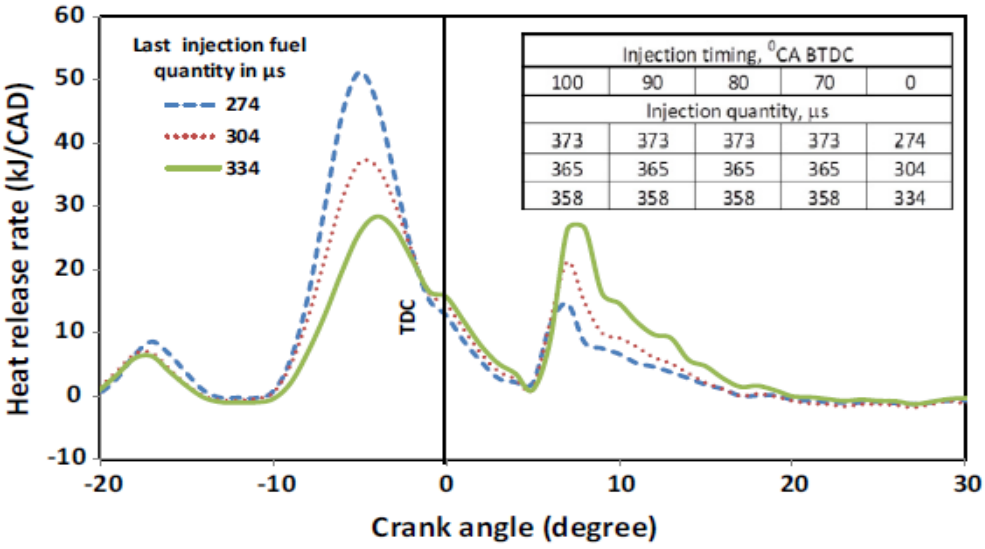

Figure 3.12 Heat Release Rate (HRR) profile for a Multiple Fuel Injection Strategy (MFIS) engine (Mathivanan et al., 2016)

Figure 3.12 depicts the HRR profile of a MFIS engine which shows five (5) different injections events for each of three different scenarios. The figure compares the effect of injecting different fuel masses (in µg) per injection on the HRR profile. The last injection occurred at the Top Dead Center (TDC). The last injected fuel masses for the three scenarios were 274, 304, and 334 µg respectively. The HRR peaks that occurred at 8^{o} after the TDC for the three scenarios were as a result of the evaporation, ignition and combustion of the last injection fuel masses. Figure 3.12 shows that the height of the HRR peak in a MFIS diesel engine is proportional to the quantity of the fuel that was injected in the preceding injection event.

Fuel injection in a MFIS engine involves three types of injection events: pilot injection (for the control of noise and emissions), main injection and post injection. Post injection is further divided into close-post injection (for emissions control) and late-post injection (for the regeneration of aftertreatment devices) (Smith, 2012). Pilot and post injection fuel masses are much less than the mass of fuel

that is injected during the main injection event. (MFIS is used in modern CI engines to control Peak Pressure (PP), PHRR, noise, emissions as well as for the regeneration of aftertreatment devices).

3.4.2 Previous specific heats ratio (γ) and Heat Release Rate (HRR) models

The HRR models in literature differ in terms of the γ functions and the heat transfer coefficient models that were used in the HRR models by the authors. Various γ models have been proposed in literature (Gatowski et al. (1984), Brunt and Emtage (1997), Egnell (1998), Blair (1990), Heywood (1988)). Gatowski et al. (1984) used a linear function of the mean charge temperature to model the specific heats ratio (γ). The γ model of the authors was solely a function of temperature (Equation 3.29).

$$\gamma = \gamma_0 - \frac{K_1(T - T_{ref})}{1000} \qquad 3.29$$

The reference value in Equation 3.29, γ_0 = 1.38, the constant K_1 = 0.08 and the reference temperature, T_{ref} = 300 K.

Brunt and Emtage (1997) evaluated the HRR of a Spark Ignition (SI) engine by using a second-order function that was derived from a multidimensional model (Equation 3.30). The γ function in their HRR model was evaluated as the mean function of γ functions within a narrow range of λ (0.83< λ<1.25). The γ model was based on the temperature of the gases in the cylinder, T in Kelvin.

$$\gamma = 1.338 - 6.0 \times 10^{-5} T + 1.0 \times 10^{-8} T^2 \qquad 3.30$$

Egnell (1998) proposed an exponential γ function given in Equation 3.31. The exponential model in Equation 3.31 is explicitly a function of temperature though

the authors chose the values of the constants in the equation based on the combined effects of temperature and the composition of the gas.

$$\gamma = \gamma_0 - k_1 \exp(-k_2/T) \quad 3.31$$

The reference value in Equation 3.31, γ_0 = 1.38, while the constants k_1 and k_2 have values 0.2 and 900 respectively.

Blair (1990) proposed a γ model which is specifically for exhaust gas at stoichiometric condition, equivalence ratio, $\phi = 1$ ($\lambda = 1$). The model of Blair (1990) is also solely depended on temperature as shown in Equation 3.32.

$$\gamma = 1.4221 - 1.8752e-4T + 6.9668e-8T^2 - 9.099e-12T^3 \quad 3.32$$

Ceviz and Kaymaz (2005) derived γ functions for unburned and burned mixtures in terms of in-cylinder temperature and λ (Equation 3.33 and Equation 3.34 respectively). The ranges of temperature for the unburned and burned mixtures respectively were 300 K to 1,500 K and 300 K to 2,500 K.

$$\gamma_u = a_1 + a_2T + a_3T^2 + a_4T^3 + a_5T^4 + a_6T^5 + a_7/\lambda \quad 3.33$$

$$\gamma_b = b_1 + b_2T + b_3/\lambda + b_4T^2 + b_5/\lambda^2 + b_6T/\lambda + b_7T^3 + b_8/\lambda^3 + b_9T/\lambda^2 + b_{10}T^2/\lambda \quad 3.34$$

The final derived equation of γ was expressed as given in Equation 3.35.

$$\gamma = MFB\gamma_b + (1 - MFB)\gamma_u \quad 3.35$$

MFB in Equation 3.35 represents the Mass Fraction Burned.

The coefficients in Equations 3.33 and 3.34 were given by the authors as shown in Table 3.11.

Table 3.11 Coefficients for use in the gamma functions of Ceviz and Kaymaz (2005)

Coefficients (γ_u)	Values	Coefficients (γ_b)	Values
a_1	1.4642	b_1	1.4981
a_2	1.5067 x 10^{-4}	b_2	-1.1303 x 10^{-4}
a_3	-7.3485 x 10^{-8}	b_3	-2.6689 x 10^{-1}
a_4	1.5573 x 10^{-10}	b_4	4.0364 x 10^{-8}
a_5	-7.6951 x 10^{-14}	b_5	2.7343 x10^{-1}
a_6	1.1954 x 10^{-17}	b_6	5.7462 x 10^{-5}
a_7	-6.3115 x 10^{-2}	b_7	-7.2026 x 10^{-12}
		b_8	-8.2188 x 10^{-2}
		b_9	-1.3029 x 10^{-5}
		b_{10}	2.3573 x 10^{-8}

Ceviz and Kaymaz (2005) used a FIAT, 1.801 dm^3 (0.0018 m^3), four stroke SI engine to investigate the accuracy of their γ and HRR model. The engine was operated at ¾ throttle valve opening position and 2,500 rpm at λ values of 0.996, 1.089, 1.216, and 1.341. According to the authors, the proposed γ model was accurate for SI engines when λ was approximately 1.1.

The derived γ model of Ceviz and Kaymaz (2005) cannot be used as it is for the analysis of the HRR of a CI engine. The authors validated the model using an SI engine operating at near-stoichiometric conditions and a specified speed (2,500 rpm). Modern diesel engines operate by the auto-ignition of compressed, lean

air-fuel mixtures. Consequently, the unburned mass fraction in diesels is negligible. Burned mixtures refer to the working fluid or products of combustion in the combustion chamber during the expansion process (after the SoC) when temperatures are high (>1,700 K). Unburned mixtures refer to the working fluid during the compression stroke prior to combustion and at T<1,700 K. In both cases the fuel is assumed to be in the vapour phase (Heywood, 1988). Unburned mixtures are mostly applicable to SI and Homogeneous Charge Compression Ignition (HCCI) diesel engines for which fuel injection occurs during the intake stroke. The current work was carried out on a Multiple Fuel Injection Strategy (MFIS) CI engine (a lean combustion engine); the injected fuel mass per power stroke was injected in phases during the power stroke. The injection of fuel occurred near the TDC. The auto-ignition and combustion of the injected fuel also commenced near the TDC. The duration that the air-fuel mixture was unburned in the engine prior to the Start of Combustion (SoC) was relatively short compared to SI engines or HCCI-mode diesel engines. Therefore, burned mixture properties were assumed for the power stroke of the engine in the current work. Furthermore, CI (diesel) engines operate within a relatively wide range of λ. For these reasons, the derived equation of Ceviz and Kaymaz (2005) was modified in the current work by equating MFB to 1 so that $\gamma_{mod}(T,\lambda) = \gamma_b$ (Equation 3.34).

Ebrahimi (2011) investigated the effects of assumed specific heats ratio (1.25, 1.3, and 1.35) on the HRR in a stoichiometric SI engine that was run on natural gas and gasoline fuels at 3,300 rpm. The author reported that a low value of specific heats ratio resulted in an increase in the magnitude and shape of the HRR and the CHR curves. Vipavanich et al. (2018) investigated the HRR of a gasoline-diesel dual fuel engine using the net HRR model given in Equation 3.36.

$$\frac{dQ}{d\theta} = \frac{\gamma}{\gamma-1} p \frac{dV}{d\theta} + \frac{1}{\gamma-1} V \frac{dp}{d\theta} \quad 3.36$$

θ is degree crank angle (CAD), $\frac{dQ}{d\theta}$ is the HRR (J/CAD), p and V are the instantaneous cylinder pressure and volume respectively. The HRR model expressed in Equation 3.36 is simplistic (cylinder wall and blow-by heat losses were not accounted for in the model). The authors did not give the details of the γ model that was used in their investigation. Yedithasatyam and Reddy (2015) investigated the combustion behaviour of Palm Kernel Methyl Ester (PKME) with secondary co-injection of saturated Diethyl Ether (DEE)-water solution. A 3.7 kW, 4 stroke, single cylinder, Kirloskar AV-1 CI engine was used in the investigation. The details of the γ model that was used in the HRR analysis were not given. The authors reported that the PHRR for all the percentages of DEE-water injection improved with increase in load for the same SoI timing.

Heywood (1988) investigated the dependence of γ on temperature, λ and the EGR rate (residual gas composition) for a gasoline-air mixture. The results were presented as a graph of γ against temperature for various values of λ and EGR (Figure 3.13). However, the γ profiles presented need to be fitted into a mathematical expression so that they can be readily utilised in mathematical modelling. The maximum temperature in the data that is depicted in Figure 3.13 is 1,000 K. The combustion temperatures that are obtainable in CI engines are known to be much higher than 1,000 K. As such, the fitted data of Heywood (1988) were extrapolated to values beyond 1,000 K in the current work.

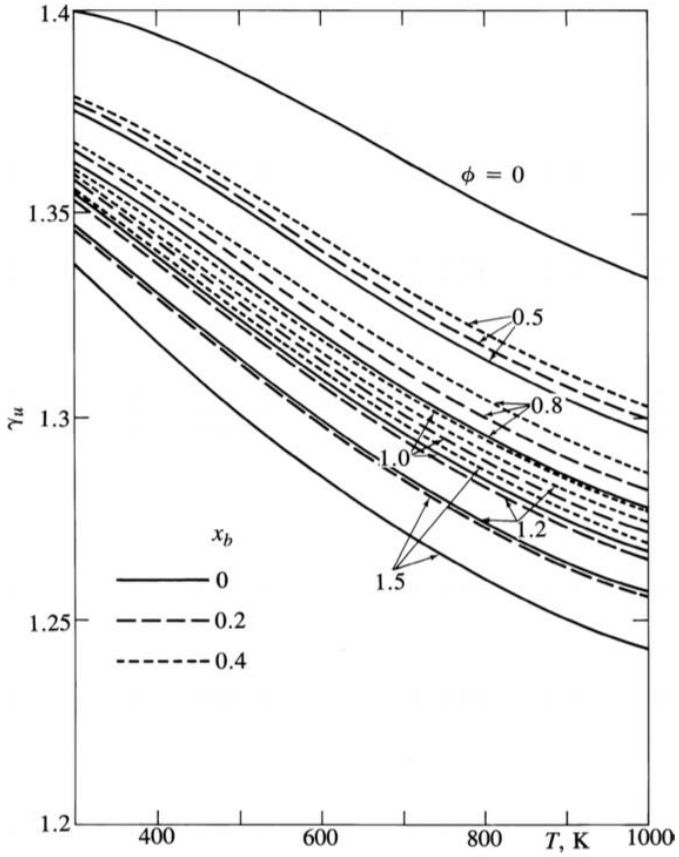

Figure 3.13 Dependence of the specific heats ratio of unburned gasoline, air, burned gas mixtures on the temperature, equivalence ratio, and unburned gas fraction (Heywood, 1988)

The EGR operating limits in stoichiometric SI engines is 20 to 35%. This is because the lowest possible NOx emission occurs within the EGR rates of 20 to 40% as depicted in Figure 3.14 (Heywood, 1988) for an SI engine at 1,400 rpm and 324 kPa Indicated Mean Effective Pressure (IMEP). Also, moderate-burn and fast-burn SI engine operations have the same NOx emission values within the given EGR operating range. The effect of EGR rate on the HRR model of diesel engines was investigated in the current work within the stated EGR operating range (20 to 40%).

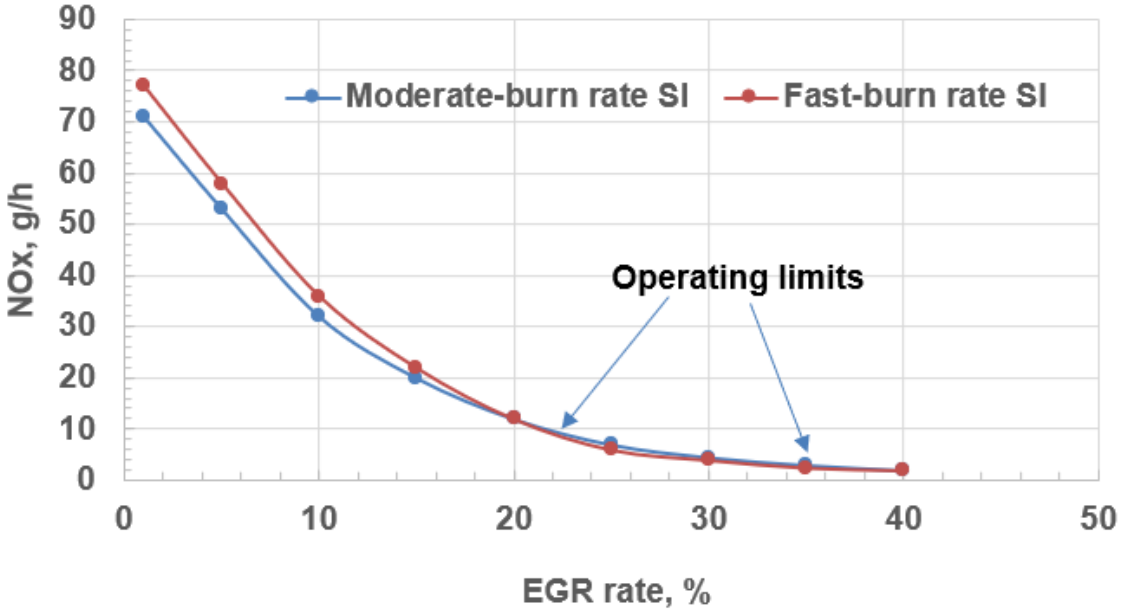

Figure 3.14 Exhaust Gas Recirculation (EGR) operating limits in stoichiometric Spark Ignition (SI) engine (1,400 rpm and 324 kPa) (Heywood, 1988)

The foregoing discussion shows that no work has been done in the past to investigate the accuracy of existing γ functions for the modelling of the HRR of Multiple Fuel Injection Strategy (MFIS), diesel engines operated at non–stoichiometric conditions. Also, no work has been done in the past to validate the HRR model and investigate the HRR of alternative diesel fuels (GTL and HVO diesels) and DE fuel blends in MFIS or SFIS, diesel engines. Therefore, there is a need to investigate the suitability of the existing γ functions for use in the HRR model of diesel engines. There is also a need to develop an improved HRR model for the analysis of the combustion behaviour of different diesel fuels and fuel blends in different diesel engine configurations.

3.4.3 Alternative diesels

Gas-to-Liquid (GTL) diesel and Hydrotreated Vegetable Oil (HVO) diesel are alternative diesel fuels that can be used directly in existing diesel engines without modifying the existing infrastructure (design of the engines). The existing infrastructure also includes storage facilities, refueling stations, pipelines and tankers. Binary blends of the alternative diesel fuels (GTL and HVO diesels) and standard diesel (Ultra Low Sulphur Diesel, ULSD) can also be used as fuel in existing diesel engines. GTL diesel is produced from the Fischer-Tropsch process (Speight, 2020) by the conversion of methane-rich gases into longer-chain hydrocarbons (liquid synthetic fuels/second generation biofuel – Figure 2.10) while HVO diesel is derived from waste cooking oil or animal fats (Neste, 2020).

Table 3.12 shows that the thermo-physical properties of GTL and HVO diesels are similar (Smith (2012), Hohenberg (1979), Regulations (2015), Sajjad et al. (2014)).

Table 3.12 Comparison of properties of ULSD, GTL, and HVO diesels

Property	**ULSD**	**GTL**	**HVO**
Kinematic viscosity @ 40 ^{o}C, mm^2/s	~2.7	~3.5	2.8
Density @ 40 ^{o}C, kg/m^3	~830	762	762
Cetane Number (CN)	>51	79	78.8
NCV, MJ/kg	44	44	44
Sulphur, mg/kg	<10	0.05	<1

3.5 Conversion of biomass to energy

There are basically two processes by which solid biomass can be converted to energy. These are biochemical and thermochemical processes.

3.5.1 Biochemical conversion of biomass to energy

The biochemical conversion processes include fermentation and anaerobic digestion. Both processes are carried out in the absence of air. Fermentation is the production of ethanol from sugar (glucose) by the action of yeast. It is therefore, also called bioethanol because it is mainly produced from organic feedstock. Anaerobic digestion involves the use of bacteria to produce biogas (mixture of methane and CO_2) from biomass such as animal dung.

3.5.2 Thermochemical conversion of biomass to energy

Thermochemical processes involve the oxidation of biomass to release energy (McKendry, 2002) or the subjection of biomass to heat in the absence of oxygen (pyrolysis). The processes that involve oxidation are combustion and gasification.

Combustion involves the complete burning of biomass in air. The energy content of the biomass is completely converted to hot gases for heating or power generation.

Gasification is the conversion of solid biomass or coal into syngas (a combustible gaseous product) by the use of a gasifying agent in sub-stoichiometric conditions (Formica et al., 2016). The Cv of the syngas is low (4-6 MJ/m^3) if the gasifying agent is air but a higher Cv is obtained if oxygen is utilised (McKendry, 2002). Other products of gasification are char, ash, and condensables (tars).

Pyrolysis is a thermochemical biomass conversion process that involves the heating of biomass in the absence of air. The products of pyrolysis are liquid (bio-

oil), charcoal (solid) and gases. The bio–oil can be used to run engines and turbines.

3.6 Biomass gasifiers

A biomass gasifier is utilised to generate syngas from biomass feedstock. The generated syngas can be used to generate steam for heating or to turn a turbine for electricity generation. The syngas can also be piped directly into a diesel-syngas dual-fuel CI engine for the generation of electricity. Biomass gasification systems have the potential to combine high efficiency with cost competitiveness to generate 20 to 100 MW of electricity. Small, modular biomass conversion systems that can generate 100 kW to 5 MW are also being developed (Spellman, 2012).

Biomass gasifiers are broadly classified into two: fluidised bed and fixed bed gasifiers. The fixed bed gasifiers are further classified into updraught and downdraught gasifiers.

3.6.1 Fluidised bed gasifiers

Fluidised bed gasifiers operate by suspending the biomass feed during the gasification (bubbling fluidised bed) or by the entrainment of the feed during the gasification (circulating fluidised bed). The biomass feed is suspended or entrained by forcing the oxidant (air) through the biomass particles (Spellman, 2012).

3.6.2 Updraught gasifiers

Updraught gasifiers are also referred to as counter current-flow gasifiers. The biomass feed is introduced at the top. A grate supports the reacting bed at the bottom of the reactor. In updraught gasification, the oxidant (air) is introduced at the bottom of the grate (with or without steam). As the oxidant flows up through

the bed of biomass and char, complete combustion of char occurs at the bottom of the bed. The resulting hot gases (H_2O and CO_2) pass through the biomass above ~1,000 ^oC. As the gases flow through the biomass above, they are reduced to H_2 and CO while the temperature drops to 750 ^oC. The resulting gases pyrolyse the dried biomass above and finally, dry the incoming wet biomass feed. The syngas exits the gasifier at ~500 ^oC (Bridgewater and Evans (1993); Reed and Siddhartha (2001); Stultz and Kitto (1993)).

The updraught gasification process is simple and relatively low-cost. It is suitable for the gasification of biomass that is high in moisture and inorganic content such as municipal solid waste. However, updraught gasifiers produce syngas that has 10 to 20% tar by weight. This necessitates extensive syngas clean-up upstream of the engine or turbine (Spellman, 2012).

3.6.3 Downdraught gasifiers

Downdraught gasifiers are also known as cocurrent-flow gasifiers because the biomass, oxidant, and product gases flow in the same direction. The mechanical structure of the gasifier is similar to that of the updraught gasifier. Tar entrainment does not occur in downdraught gasifiers as most of the tar is burned. Pyrolysis gas and vapour are generated in the reaction zone of the gasifier. The combustion of the pyrolysis gas produces 5 to 15% char and hot combustion gases. The gases flow downwards and are reduced as they react with char at 800 to 1,200 ^oC to produce more H_2 and CO. The syngas exits the gasifier at ~800 ^oC while the unconverted char and ash pass through the grate to the base (Paisley et al. (2000), Reed and Siddhartha (2001), Stultz and Kitto (1993)).

The advantages of downdraught gasifiers are that the process is low-cost, tar cleanup is not required, and minerals are contained in the ash thereby eliminating

the need for a cyclone. The major disadvantages of the process are that the biomass feed must be dried to moisture contents below 20% and about 4 to 7% of the carbon is unconverted (Spellman, 2012). The downdraught biomass gasification process is most suitable for electricity generation from diesel-syngas dual-fuel Gen-sets.

Knowledge of the optimum gasification equivalence ratio and air flux are required for the design of biomass gasification systems. The current work involves the utilisation of the Cone calorimeter method to determine the optimum gasification equivalence ratio and air flux for the gasification of sweet sorghum stalk residue.

3.7 Cone calorimeter

The Cone calorimeter is an equipment for measuring the rate of heat release of materials on the basis of oxygen concentration (Twilley and Babrauskas, 2001). The services that are required to use the equipment include ventilation, electrical power, water supply, 99% pure methane for the calibration burner, and oxygen-free nitrogen. The Cone calorimeter is always calibrated before it is used to investigate the oxidation behaviour of fuels. The pieces of equipment that are required to calibrate the Cone calorimeter are the reference heat flux meter, micro-balance, laboratory weights, specimen holder equipment, and vacuum cleaner.

The gasification of solid biomass in biomass gasifiers usually occurs in two stages with respect to the release of heat from the biomass during the process. As such, two Heat Release Rates (HRR) are of interest during biomass gasification: the Primary Heat Release Rate (P'HRR) and the Secondary Heat Release Rate (SHRR). The objective of the gasification of biomass for syngas generation is to minimise the heat that is released in the first stage of the oxidation thereby

increasing the yield of combustible species in the flue gas (the products of incomplete combustion: CO, H_2, and unburned hydrocarbons). In the case of complete combustion, the heat release occurs in one stage. The Cone calorimeter can be operated to mimic a two-stage gasifier by incorporating the controlled atmosphere air box (restricted ventilation box). This allows for the metering of the intake air flow such as to achieve rich combustion in the first stage of the gasification.

3.8 Composition and properties of syngas from different biomass feed and gasifiers

The composition and the properties of syngas are depended on the type of biomass feedstock as well as the type of gasifier. Table 3.13 summarises the composition and the properties of syngas from different biomass feedstock and biomass gasifiers.

Table 3.13 Composition of syngas from selected biomass feedstock

Feed, GCV, MJ/kg	**Soft wood chips 19.6**	**Oak Dry 20.5**	**Sorghum Dry 14.3 17.4 daf**	**Wood**	**Wood**	**Wood**	**Biomass 15.5**	**Dairy Biomass 21.5 daf**	**Pine Wood**
Gasifier	Air	Air	Air	Air Fixed bed Updraught	Air Fixed bed downdraught	Air Fluidised Bed	Air Fixed bed updraught	Fixed Bed Updraught Ø = 3 Air/steam Steam/fuel 0.8	Air Fixed bed Updraught Ø = 2.8 No steam
CO, %	16.0	18	14.6	24	21	14	27	11.5	14
H_2, %	7.7 8.7dry	16	12.9 14.2 dry	11	17	9	17.3	25	8 10.4 (dry)
CO_2, %	15.3	13	15.2	9	13	20	9.0	26	12
CH_4, %	7.6	1.5	5.4	3	1	7	4.0	1.5	8 (THC)
H_2O, %	11.0	-	9.4	-	-	-	4.1	-	23
N_2, %	41.5	48	42.3	53	48	50	38.6	36	35
MW	-	24.8	25.4				24.05		~55
LHV MJ/m^3	5.59	4.8	5.35 6.52 dry	5.5	5.7	5.4		4.9	
LHV, MJ/kg_{gas}	4.72	4.35	4.72 6.16 dry				5.38		

LHV, MJ/kg_{fuel}	14.2	13.0	14.1 wet 18.5 dry				15.04		15.0
Efficiency, %	72	63.6	99 wet 106 dry				97	62	78
Reference	Lepszy and Chmielniak (2010)	Pinta and Vergnet (1994)	Baldacci et al. (1994)	Gordillo et al. (2009)	Gordillo et al. (2009)	Gordillo et al. (2009)	Porta et al. (2006)	Gordillo et al. (2009)	Andrews et al. (2019)

Key: MW= Molecular Weight; LHV = Lower Heating Value; daf = dry ash free; THC total hydrocarbons (methane was zero)

Efficiency = kW gas energy output/kW biomass energy input

3.9 Conclusion

The foregoing discussion shows that the stalk residue of sweet sorghum is a potential source of syngas (apart from being a potential source bioethanol as analysed in Chapter 2). The production of biofuels from the stalk residue of sweet sorghum can be maximised in Nigeria by producing bioethanol (for transportation) from the glucose-rich juice of the stalks and syngas (for power generation) from the stalk residues. The biofuels potential of the crop can be further boosted by cultivating the crop as an energy crop in the currently uncultivated arable lands in Nigeria. The co-production of syngas from sweet sorghum stalk residues and the residues of other agricultural crops (which are currently burned in the open fields in Nigeria preparatory to the next planting season) will enhance the recovery of energy from the residues.

Downdraught gasifier design was chosen/proposed for the gasification of sweet sorghum stalk residue in the current work because downdraught gasifiers are most suitable for the production of syngas for electricity generation from dual-fuel diesel engines. The advantages of the downdraught gasifier over the other gasifiers (fluidised bed and updraught gasifiers) are that tar cleanup and a cyclone separation are not required for downdraught gasifiers.

Chapter 4 Materials and Methodologies

4.1 Introduction

This Chapter presents the materials and the procedures for the experimental aspects of the current work (diesel-ethanol (DE) fuel blends stability test, IVECO diesel engine combustion test, diesel Gen-set combustion test, and biomass gasification test). Section 4.2 presents the materials and the procedure for the DE fuel blends stability test. The DE fuel blends stability test was conducted to ascertain the limits of the solubility of ethanol in fossil diesel. Knowledge of the limits of the solubility of ethanol in diesel was necessary for the diesel engine combustion test because only stable binary blends of diesel and ethanol (diesohol) were desired for the diesel engine combustion tests. Sections 4.3 and 4.4 present the materials, equipment description, and methodologies for the IVECO diesel engine combustion test and the diesel Gen-set combustion test respectively. Finally, Section 4.5 presents the materials and procedure for the biomass gasification (Cone calorimeter) tests.

4.2 Diesel-ethanol (DE) fuel blends stability test

The test was carried out in two stages. The aim of the first stage of the test was to ascertain the maximum amount of anhydrous ethanol that would dissolve in fossil diesel to form a stable blend at room temperature (20 ^{o}C). The second stage of the test was the temperature-sensitivity test. The aim of the temperature-sensitivity test was to determine the temperature of homogenisation of the DE blends that phase-separated at room temperature. The DE fuel blends that were prepared and tested were binary blends of diesel and anhydrous ethanol that contained 10, 20, 25, 30, 40, 50, 60, 70, 75, 80, and 90% by volume of anhydrous ethanol in fossil diesel (DE10, DE20, DE25, DE30, DE40, DE50, DE60, DE70,

DE75, DE80, and DE90 respectively). The total volume of each of the DE blends was 20 ml.

4.2.1 Materials

The following materials were used to carry out the diesel-ethanol (diesohol) fuel blends stability test: diesel (off-road diesel), pure (anhydrous) ethanol, anhydrous normal butanol (n-butanol), scale, semi micro balance, glass pipettes (2 ml, 5 ml, and 10 ml), pipette pumps, 20 ml calibrated glass test tubes (with stoppers), two (2) test tube racks, glass beakers, 2.5 litre plastic bottle (container for waste fuel), hexane solvent for rinsing, sample bottles (6 sealed, calibrated centrifuge test tubes), plastic tray, temperature-controlled water bath, red spirit filled (alcohol) glass thermometer, FTir-Thermo iS10 (the equipment was used for the qualitative analysis of the unstable DE blends).

4.2.2 Fuel blending procedure

Table 4.1 shows the volumes of diesel and ethanol in each of the DE blends.

Table 4.1 Volumes of pure diesel and ethanol in the binary diesel-ethanol (DE) blends

Binary DE blend	**Volume, ml**	
	Pure diesel	**Pure ethanol**
DE10	18	2
DE20	16	4
DE25	15	5
DE30	14	6
DE40	12	8
DE50	10	10
DE60	8	12
DE70	6	14
DE75	5	15

DE80	4	16
DE90	2	18

The DE blends were produced by splash-blending. Splash blending is the process by which homogeneous liquid mixtures (blends) are produced by shaking two or more liquid components intensely in a sealed container. Intense shaking can be achieved manually or by a magnetic stirrer (depending on the nature of the liquids). 90% binary diesel-n-butanol blend (DnB90) was prepared by splash-blending 2 ml of pure diesel and 18 ml of pure n-butanol (to ascertain the unlimited solubility of pure n-butanol in diesel).

The DE blends were prepared as follows:

1. The appropriate Personal Protective Equipment, PPE (lab coat, gloves, eye protection, face mask) for the test were worn.

2. The sample bottles were labelled and the fuel samples/liquids (diesel, anhydrous ethanol, anhydrous n-butanol, hexane) were put into the sample bottles and transferred in the plastic tray (300 mm x 200 mm x 200 mm (height) spill bund) from the flammable cupboard to the lab (Lab G03g).

3. Eleven (11) calibrated glass test tubes were labelled according to the eleven blends depicted in Table 4.1. The twelfth glass test tube was labelled DnB90.

4. The weight of the glass beaker and the weight of the calibrated glass test tubes (with the stoppers in place) were measured and recorded using the scale.

5. The densities of the fuels were used to convert the volumes of the liquids (in ml) in each of the blends to mass (in grams). The estimated masses were used to check for accuracy when the fuels were pipetted into the test tubes by comparing the estimated mass of tube plus fuel to the measured mass.

6. 18 ml of pure diesel was drawn from the diesel sample bottle using the calibrated glass pipettes and pipette pump. The sample bottle was sealed immediately after the desired volume of diesel was drawn. The measured volume of diesel was pipetted into the first test tube (labelled DE10). The mouth-suction method was not used during the preparation of the blends for safety reasons. Thereafter, the test tube was sealed. (Anhydrous ethanol was introduced into the test tubes after diesel because of the volatility and hygroscopicity of pure ethanol)

7. The test tube was weighed to confirm that the calculated mass of the fuel in the tube was approximately the same as the measured mass. Thereafter, the test tube was placed in the test tube rack.

8. Steps 6 and 7 were repeated to introduce the appropriate volumes of pure diesel into the remaining test tubes (labelled DE20 to DE90).

9. Waste/remnant diesel in the pipette was dispensed into the waste bottle.

10. The glass pipettes were thoroughly rinsed with hexane and left to dry. The rinsing was done by drawing hexane into the pipettes up to the maximum mark and then, gradually dispensing the hexane into the waste fuel container. The rinsing was repeated thrice.

12. Thereafter, Steps 6-8 were repeated for each of the DE blend test tubes to add the appropriate volumes of anhydrous ethanol to the volumes of the pure diesel in the test tubes.

13. Each test tube was stoppered immediately after the measured volume of pure ethanol was dispensed in it. The total blend volume in the tube was checked after the tube was sealed to ensure that it was 20 ml. Thereafter, the tube was shaken intensely (manually) for about 2 minutes to splash-blend the fuels. At the end of

the splash-blending, the blend preparation time was noted, and the test tube was placed in the test tube rack.

14. Steps 6-13 were repeated to prepare the DnB90 blend.

15. The two test tube racks containing the eleven DE fuel blends and the binary DnB90 blend were placed in the fume cupboard and left unshaken throughout the period of observation.

16. The glass pipettes were thoroughly rinsed with hexane and left to dry in the fume cupboard. The left-over fuel samples were discarded into the waste bottle and the used sample bottles were discarded into the waste bin.

The blends were observed for 3 months during which the changes in the physical state of the blends were recorded.

4.2.3 Precautions

The following precautions were taken during the test (based on the Risk Assessment (RA) that was submitted on RIVO for the test):

1. The recommended PPE were worn prior to the test.
2. The fuel samples and blend fuels were stored away from sources of spark, electrostatic discharge or ignition.
3. Plastic spill bund was used to transfer the sample bottles from the flammable store to the Lab.
4. The test tube racks containing the sealed blend test tubes were placed in the fume cupboard throughout the period of observation.

4.2.4 Unstable DE fuel blends temperature-sensitivity test procedure

At the end of the room-temperature blend stability test, the unstable DE fuel blends were placed in a separate test tube rack preparatory to the DE blend

temperature-sensitivity test. The glass thermometer was fixed in one of the vacant holes of the test tube rack. The experimental set up for the temperature sensitivity test that was conducted on the unstable blends and the placement of the unstable DE blends within the temperature-controlled water bath are shown in Figures 4.1 and 4.2.

Figure 4.1 Experimental set up for the temperature sensitivity test of the unstable diesel-ethanol (DE) fuel blends

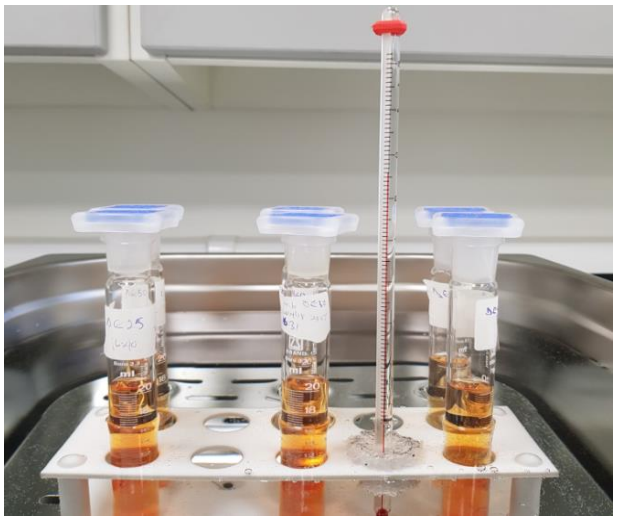

Figure 4.2 Placement of the unstable diesel-ethanol (DE) fuel blends within the temperature-controlled water bath

The thermometer within the bath measured the actual temperature of the water in the bath (bath temperature).

The following steps were followed to carry out the temperature-sensitivity test:

1. The water bath was plugged to the mains and switched on.
2. The position of the interphase (the height of the diesel phase) in each of the unstable blends was noted.
3. Thereafter, the cover of the water bath was removed and the test tube rack containing the unstable DE blends and the thermometer was placed in the water bath (the thermometer was placed in the test tube rack to measure the actual temperature of the water in the water bath).
4. Water (at room temperature) was carefully poured into the water bath until the level of the water in the bath was a few centimetres above the level of the blends in the test tubes. The water level in the bath was maintained above the level of the blends throughout the test.
5. The temperature of the bath was set to 21 ^{o}C. The temperature of the water in the water bath (actual bath temperature) was read from the thermometer after the temperature on the display stabilised at approximately 21 ^{o}C.
6. The temperature of the bath was incremented initially by 1 ^{o}C at an interval of 2 hours to determine the actual test start time.
7. The temperature and time at which the first change in the status of the DE blends occurred were noted.
8. The actual test start time was taken as the time that the water bath was set to the temperature at which the first change in the status of the DE blends was observed.

9. The temperature of the bath was incremented by 2 ^{o}C after the actual test start time was determined. The temperature increment was stepped up to 2 ^{o}C to reduce the time lapse between changes in blend status.
10. The changing positions of the interphase of the blends were observed and recorded at intervals of 3 hours.
11. Whenever the positions of the interphase in the blends became static (unchanging), the temperature of the bath was increased by 2 ^{o}C.
12. The time and the temperature at which each of the investigated DE blends became homogeneous (time and temperature for the disappearance of the interphase) were noted.
13. The test was ended when the interphase in the unstable blends disappeared and each of the blends became a clear, homogeneous single phase.

At the end of the tests, the investigated fuel blends were discarded into the waste fuel container and the calibrated test tubes were thoroughly rinsed with hexane. The rinsed test tubes were left unsealed to dry in the fume cupboard. The temperature of the water bath was turned down to the temperature of the lab. Thereafter, the water bath was turned off and unplugged from the mains.

4.3 IVECO diesel engine combustion test

The aim of the diesel engine combustion test was to investigate the effects of DE fuel blends on the performance, emissions, and HRR of diesel engines. The strategies that were proposed in literature for the introduction of ethanol in diesel engines include fumigation (Port Fuel Injection (PFI) of ethanol), in-line mixing (for unstable DE blends), and use of stable DE fuel blends (direct injection of splash-blended ethanol and diesel) (Likos et al., 1982). The direct injection of splash-blended DE fuel blends is a less costly strategy compared to fumigation

and in-line mixing of the two fuels. Fumigation involves the injection of ethanol (the low reactivity fuel) via the air intake port to form a background premixed charge in the cylinder prior to the direct injection of diesel (the high reactivity fuel) near the TDC. The dual-fuel engine is operated in Reactivity Controlled Compression Ignition (RCCI) mode when ethanol is introduced by fumigation. Direct injection of stable DE fuel blends (splash-blended DE fuel) is the simplest strategy to introduce ethanol into diesel engines as the approach does not require a major retrofit on existing engines unlike the other strategies.

Ethanol was introduced into the engine in the current work by splash-blending the alcohol with fossil diesel. The parameters that were measured for the tested modes were the exhaust composition (THC, NOx, NO, CO_2, CO, O_2, particulate distribution), the pressure traces (P-CAD), the engine fuel consumption rate, the AFR, and temperatures. The composition of the exhaust gas was measured upstream and downstream of the DPF.

4.3.1 Materials and Methodology

Analytical tests (Thermogravimetric analysis and elemental analysis) were conducted on the ULSD using the Mettler Toledo Thermogravimetric Analyser (TGA) and the Thermo Scientific Elemental Analyser 2000).

The materials and instrumentation which were used for the IVECO diesel engine combustion test were the Engine Test Bed (ETB), dynamometer, UPE cooling, Engine Test Control System (ETCS), HORIBA Motor Exhaust Analyser (MEXA-7100D), AVL FlexIFEM Indi 601 (2-channel), Dynamic Mobility Spectrometer (DMS500), red (off-road) diesel. The diesel-ethanol (DE) fuel blends aspect of the IVECO diesel engine combustion test was carried out on the Gen-set because the IVECO engine developed mechanical faults towards the end of the baseline

tests. As at the time of compiling this thesis, the fault had not been rectified due to the nature of the fault and the impact of the pandemic.

A brief description of the pieces of equipment above is given in the sections that follow.

4.3.1.1 Engine Test Bed (ETB)

The Engine Test Bed (ETB) consists of the Euro V emission compliant IVECO, four-cylinder, 128 hp (96 kW) diesel engine mounted on steel framework, the auxiliary systems and instrumentation. Table 4.2 gives the description of the engine.

Table 4.2 Engine description

Feature	**Specification**
Type	4-stroke, 4-cylinder CI engine
Make	IVECO
Rated power, kW	96
Bore/Stroke, mm	95.8/104
Compression ratio	18:1
Injection strategy	Multiple
Swept volume per cylinder, cc	749
Total/effective volume per cylinder, cc	794
Dynamometer	100 kW AC Dynamometer
Injection pressure, MPa	160

The ETB consists of the following auxiliary systems (DSG, 2014):

1. Fuel delivery system
2. Exhaust extraction
3. Cooling and combustion air flow

4. Engine coolant temperature and oil temperature control system
5. Throttle position control system
6. Engine electrical system
7. Engine starting system

Figure 4.3 depicts the schematic view of the ETB.

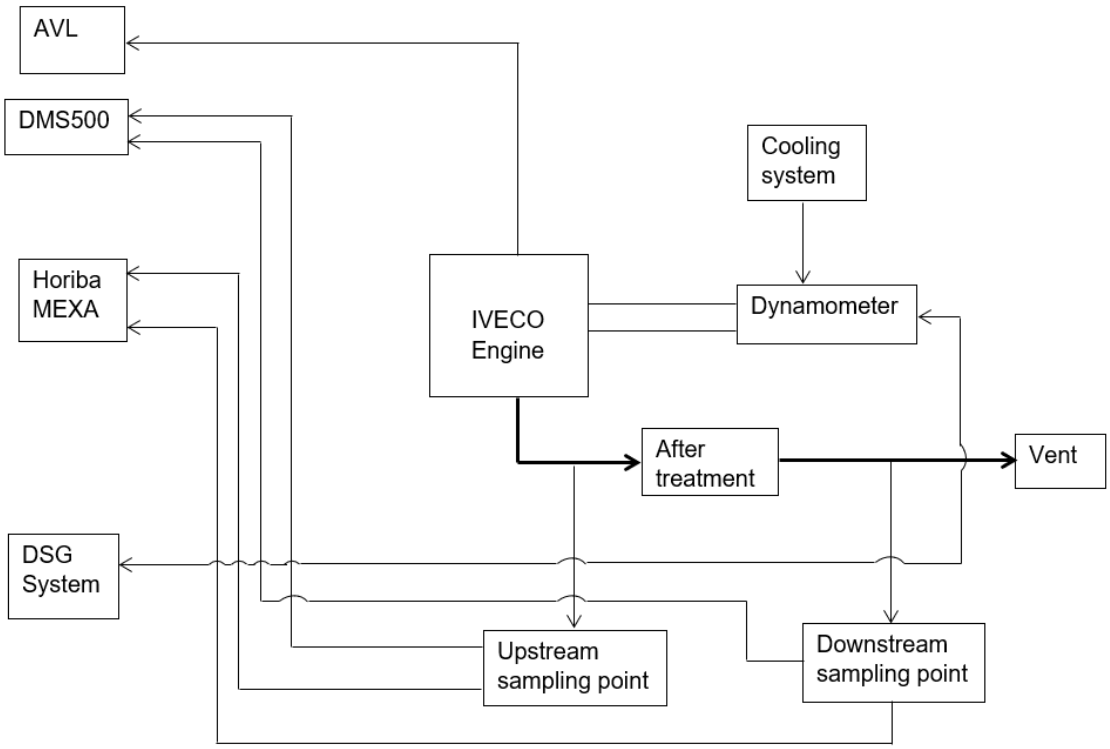

Figure 4.3 Schematic view of the Engine Test Bed (ETB)

4.3.1.2 Dynamometer

The specification, power rating, and minimum water flow rate of the AC dynamometer are 5000/EN60034, 100 kW, and 12 litres/min respectively. The dynamometer measures the speed and the torque of the engine. Equation 4.1 expresses the power of the engine in terms of the speed and the torque (DSG, 2014).

$$Power\ (kW) = Speed\ (rpm) \times Torque(Nm)/9549.3 \qquad 4.1$$

4.3.1.3 UPE cooling

The UPE cooling is the cooling system of the dynamometer. It uses water to cool the dynamometer whenever the engine is in operation.

4.3.1.4 AVL flexifem Indi 601

The AVL flexifem Indi 601 has 2 channels, a charge input range of 0-14,400 pC, and a voltage input range of -10 to +10 V (AVL, 2011). The equipment measured the pressure in one of the four cylinders of the engine during the test. The AVL flexifem Indi 601 measured the in-cylinder pressure in real-time by amplifying the analogue signal from the piezoelectric pressure sensor in the cylinder of the engine. The piezoelectric pressure sensor worked on the principle of electrical charge output of piezoelectric material (a material derived from a natural crystal) under mechanical load. They represent an active measuring element with the output charge being proportional to the pressure applied. The charge amplifier then converts the charge into voltage. The amplified signal was, thereafter, converted into digital data by the in-built analogue-digital converter of the device. The digital data was then streamed through the Gigabit Ethernet connector to the laptop (IndiCom software). The piezoelectric sensor has a sensitivity of 19 pC/bar, a sampling rate of 1 MHz, and a thermo-shock-error of $\pm$ 0.3 bar (AVL, 2011).

4.3.1.5 DSG signal relay box

The 16-channel DSG signal relay box encloses the cold ends of the thermocouples that measure the temperatures at specific points within the engine. Analogue temperatures were taken in by the device during the test and converted into voltage signals for output by the computerised system. 3 mm thick, sealed, mineral-insulated k-type thermocouples with stainless steel sheath were used to measure engine temperatures.

4.3.1.6 Fuel meter (BC 3034)

The fuel meter measures the flow rate of the fuel correct to one decimal place. The fuel consumption was logged during the test by the DaTAQ Pro software in litre per hour (l/h). The fuel meter utilises a volumetric, oscillating piston with microprocessor-controlled pulse emitter to measure the fuel flow rate (AIC, 2012).

4.3.1.7 Engine Test Control System (ETCS)

The Engine Test Control System (ETCS) consists of the DaTAQ Pro software (an advanced data acquisition and control software) and the DaTAQ Pro computer hardware (the DSG Tower). The DSG Tower is the engine controller. The speed and torque of the IVECO diesel engine were varied during the test by dialling the Dynamometer and the Throttle Encoders on the DSG Tower.

4.3.1.8 HORIBA Motor Exhaust Analyser (MEXA-7100D)

The HORIBA MEXA-7100D gas analyser measures the NOx, NO, CO_2, CO, O_2, and THC in the sampled exhaust gas. The HORIBA MEXA-7100D has its secondary unit which consists of the HORIBA OVN flame ionization unit and the chemiluminescent analyser. The flame ionization unit and the chemiluminescent analyser measure the total unburned hydrocarbons and the NOx in the sampled exhaust. The actual measurement of the emission levels by the HORIBA MEXA-7100D is described below (Hammerton, 2018).

The HORIBA has two CO detectors (a high band and a low band) and a CO_2 detector all of which work using Non-Dispersive Infrared (NDIR) detector. O_2 was measured using paramagnetism. Table 4.3 depicts the instruments used in the MEXA-7100D to analyse the sampled exhaust gas.

Table 4.3 Instruments used in the MEXA-7100D

S/n	Instrument	Gas analysed
1	Non-Dispersive Infrared (NDIR) detector	CO, CO_2
2	Paramagnetic detector (PMD)	O_2
3	Chemiluminescent analyser	NOx and NO
4	Flame ionization detector	THC

NOx and THC were measured during the test by the HORIBA MEXA in the secondary unit next to the stack. NOx and NO were calculated by chemiluminesence. Ozone reacted with NO to form NO_2 and oxygen, releasing a photon in the process which was measured. NO was evaluated separately. NOx was evaluated by converting NO_2 to NO and CO via the reaction of NO_2 with carbon over a carbon catalyst. Total NOx was determined by chemiluminesence. (NO_2 was evaluated as the difference between NOx and NO).

THC was calculated by Flame Ionization Detection (FID). The H_2 and He (40% H_2 and 60% He) from the hydrogen-helium bottle reacted with pure air to produce a clean flame. As the exhaust sample passed through the flame, the hydrocarbons broke down into ions before they formed CO_2 and H_2O. The flame had a ring around it which detected the current that was caused by the hydrocarbons burning. The detector was calibrated using propane.

The HORIBA MEXA-7100D calculates the air-fuel ratio (AFR) by the Brettschneider Spindt method . The method uses the elemental analysis of the fuel with the composition of the exhaust gas to compute the amount of air.

4.3.1.9 Differential Mobility Spectrometer (DMS500)

The Differential Mobility Spectrometer (DMS500) fast particle analyser consists of the DMS500 Main Control Unit, a computer, a vacuum scroll pump, and a heated line. These are used to determine the Particle Number (PN) and size distribution of the sampled exhaust stream from the diesel engine. The equipment classifies the exhaust particles with particle diameter (Dp) ranging from 5-1,000 nm (Cambustion, 2011). The classification is based on the charge on the emitted particles and their aerodynamic drag.

The exhaust sample stream enters the DMS500 through an electrically conductive silicone tube. The cyclone separator in the DMS500 separates the particles that are larger than 1,000 nm. A high voltage rod, coaxial with the classifier column and along the path of flow of the charged particles repels the particles on to grounded electrometer rings. The electrometer has twenty two (22) rings. The points at which the particles drop on the electrometer depend on their charge and aerodynamic drag. PN spectra are generated by the equipment based on the charge that is lost by the particles to the electrometer.

4.3.2 IVECO diesel engine combustion test matrix.

Table 4.4 shows the tested engine modes. Three different engine speeds were investigated. The engine was operated at four different torques for each of the tested speeds. The combustion test began with the diesel baseline test.

Table 4.4 IVECO diesel engine combustion test matrix

S/n	Engine speed, rpm	Torque, Nm
1	1,500	30
2		75
3		150
4		220

5	1,600	30
6		75
7		150
8		220
9	3,000 (rated speed)	30
10		75
11		150
12		220

The test modes in Table 4.4 were chosen based on the ISO 8178 specifications for emission test cycles that are relevant to dynamometer tests (off-road and constant speed test cycles). The constant speed emission test cycle (the modes at the rated speed) are relevant to diesel Gen-sets which are used to generate electricity as single units or in micro-grids. Generally, the selected test modes were chosen so that the combustion behaviour of the engine could be investigated for operation at low load (30 and 75 Nm), medium load (150 Nm), and high load (220 Nm) conditions.

4.3.3 Calibrating the HORIBA

The HORIBA MEXA-7100D was calibrated prior to the commencement of the engine combustion test. The HORIBA MEXA-7100D was calibrated as follows:

1. The HORIBA was warmed up.
2. Thereafter, the valves on the wall were turned on and the gas cylinders in the Control room (two CO mix cylinders, O_2, compressed air, H_2/He, N_2, and propane cylinders) were also turned on by turning the regulators anticlockwise.

3. The calibration of THC and NOx was enabled on the HORIBA MEXA-7100D by turning the Flame and the OZU (ozonated unit) on.
4. Finally, Calibrate was selected from the screen to commence the calibration. The two CO cylinders were turned off at the end of calibration.

4.3.4 IVECO engine start procedure

The safety checks and the operating instructions that were observed prior to engine start-up are highlighted below.

4.3.4.1 Safety checks

1. The engine oil, water and dynamometer cooling water levels were checked.
2. The ETB was checked to ensure that there was no leakage of fuel, oil or water from the engine or the dynamometer.
3. The fuel level was checked to confirm that there was sufficient fuel (pure diesel) in the tank for the intended test.
4. The test bed was checked to ensure that there were no loose wiring or thermocouples and to ensure that guards were securely in position.
5. The Exhaust extraction system was checked to ensure that it was switched “on” at the control cabinet and fully operational. Also, the exhaust ducting of the engine was put in the “Fully Open” position.
6. The heated lines of the HORIBA MEXA-7100D and the DMS500 were checked to ensure that they were well connected to the desired exhaust sampling point.

4.3.4.2 Initial operating instructions

1. The battery and ignition of the engine were switched on by using the appropriate keys from the control room.

2. The dynamometer water cooling system was switched on from the wall isolator. The on/off red Isolator switch and the on/off Toggle switch on the UPE cooling cabinet were also switched on. The flow of water was observed through the visual indicator on the dynamometer.
3. The Emergency Stop push-buttons were checked to ensure that they were in their deactivated (out) position.
4. The UNICO dynamometer drive control cabinet isolator was turned on.
5. The computer was switched on and the Power pushbutton on the DSG control tower was pressed.
6. DaTAQProV26 was launched on the left-hand screen.
7. Select Test and Start Test were clicked. The date of the test (YYMMDD) was entered in the Datalog File ID window that popped up.
8. The DSG tower green Reset push-button was pressed and held for 2 seconds (“Resetting” appeared in the Reset box).
9. The Reset push-button was pressed again immediately and held for 8 seconds until the Reset box became green and displayed “Reset”.
10. The Emergency stop push-button reset (red button) on the UNICO drive control cabinet was pressed.

4.3.4.3 Engine start procedure

1. The Motor on/off and Drive Reset icons on the Right-hand screen were activated. The Oil Pressure, Alternator, and Ignition lights (Red, Amber and Green lights respectively) on the IVECO engine came on after the icons were activated.
2. Speed was chosen for Dyno Mode and Direct for Engine (Throttle Mode).

3. A Speed of 1,000 rpm was dialled using the Dynamometer Encoder on the DSG tower (the idle speed of the Engine was 760 rpm). The Engine was motored by the Dyno at the dialled speed.
4. Fast Encoder was deselected on the Left-hand screen.
5. The ignition icon was triggered to fully activate the engine.
6. The required speed was dialled manually while throttling was done via the DSG tower Encoders to set the desired torque.
7. The engine was allowed to run for 30 minutes to warm up as well as flush out residual fuels from the previous tests.
8. The AVL computer was powered on and the AVL Indicom application was launched.
9. The engine was allowed to stabilise for 5 minutes after dialling to the first test condition (1,500 rpm; 30 Nm). Thereafter, gaseous and particulate emissions data were logged on the DaTAQ Pro computer and the DMS500 computer respectively. The pressure trace for the test mode was also captured on the AVL laptop. Engine parameters (fuel consumption, temperatures, speed, torque) were also logged using the DaTAQ Pro software.
10. While still on the same test mode, the HORIBA MEXA-7100D was toggled from NOx mode to NO. The engine was maintained on the same mode for another 5 minutes to log the emissions data for NO.
11. The engine was changed to the next condition/test mode and Steps 9 and 10 were repeated.

At the end of each day's test, the engine was shut down according to the engine stop procedure highlighted in the next section (4.3.4.4).

4.3.4.4 Engine stop procedure

1. The speed of the engine was reduced to 1,000 rpm.
2. The Engine was run at the reduced speed for 15 minutes.
3. Ignition was deactivated to drive the Engine by the Dyno.
4. The Motor on/off icon was also deactivated.
5. Stop Test was double clicked and “Yes” was pressed from the red Stop Test selected box.
6. Accept was pressed from the Shutdown Condition box.
7. Thereafter, Exit System was pressed.
8. The UNICO Dynamometer drive control cabinet isolator was switched off.
9. The Dynamometer water cooling system was allowed to cool for 15 minutes and thereafter, it was switched off.
10. The battery and ignition were switched off and the keys were returned to the locked key cabinet in the Control room G03b.
11. The DMS500 system was shut down.

The mode of the HORIBA was changed from Stand-by to Pause from the TCS setting of the Utility menu. The gas cylinders in the Control room were closed by turning them clockwise. The valves were also turned off.

At the end of the baseline tests for the upstream DPF positions, the engine was shut down according to the engine shut down procedure given in Section 4.3.4.4. The heated lines for the HORIBA MEXA-7100D and the DMS500 were then disconnected from the upstream DPF sampling points and connected to the downstream DPF sampling points. The combustion test was then repeated to log the emissions data (gaseous and particulate) for the post-DPF exhaust sampling positions.

4.4 Development of the HRR of diesel engines from the first law of thermodynamics

Figure 4.4 was used to develop the Leeds HRR model. Figure 4.4 depicts the energy conversions, transfer, and losses that occurred in the cylinder of the diesel engine during the power stroke. A fraction of the heat that was released (dQ) from the combustion of the injected fuel in the cylinder was lost through the walls of the cylinder (dQ_w), through the gap between the piston and the cylinder liner by the blow-by gases (dQ_b), and as heat retained to increase the internal energy of the gas in the cylinder. The remaining heat was converted to pV (piston) work (pdV). The heat that was lost via the blow-by gases, dQ_b was expressed as the product of the enthalpy of the blow-by gases, h_{bb} and the mass, dm_{bb}.

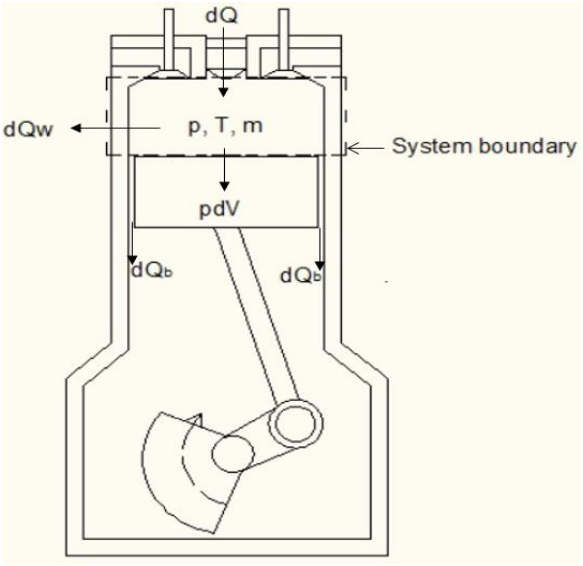

Figure 4.4 Power stroke of a diesel engine

4.4.1 Model assumptions

The following assumptions were made to develop the Leeds HRR model:

1. Single zone combustion (combustion parameters were uniform in the cylinder).
2. A zero-dimensional (transient) HRR model.

3. Ideal gas behaviour.

4. The injected fuel mass per power stroke was equal for all the four cylinders.

5. Evaporation of the injected fuel mass was followed by combustion (AVL, 2015).

6. Complete combustion of the evaporated fuel mass per injection

7. The unburned fuel mass was negligible owing to lean combustion and auto-ignition of compressed charge in diesels (Olanrewaju et al., 2020a).

4.4.2 Leeds HRR model formulation

The first law of thermodynamics was expressed as given in Equation 4.2 for the period between Intake Valve Closing (IVC) and Exhaust Valve Closing (EVC) of engine. The mass in the system boundary (Figure 4.4) was assumed constant during this period.

$$\frac{dU}{d\theta} = \frac{dQ}{d\theta} - \frac{dW}{d\theta} - \frac{dQ_W}{d\theta} - h_{bb}\frac{dm_{bb}}{d\theta} - q_e\frac{dm_f}{d\theta} \qquad 4.2$$

$\frac{dU}{d\theta}$ = rate of change of the internal energy of cylinder content, J/CAD

$\frac{dQ}{d\theta}$ = rate of release of heat energy from the injected fuel, J/CAD

$\frac{dW}{d\theta}$ = pV work due to piston motion, J/CAD

$\frac{dQ_W}{d\theta}$ = heat losses through the walls, J/CAD

$\frac{dm_{bb}}{d\theta}$ = blow-by mass flow, kg/CAD

h_{bb} = enthalpy of blow-by gases, J/kg

$\frac{dm_f}{d\theta}$ = rate of evaporation of injected fuel, kg/CAD

q_e = heat of evaporation of fuel, J/kg

θ = crank angle degree, CAD

The pressure-volume work and the change in the internal energy were rewritten as in Equations 4.3 and 4.4 respectively.

$$dW = pdV \quad 4.3$$

$$dU = mc_v dT \quad 4.4$$

$m =$ amount of gas in the cylinder in kmol

$c_v =$ specific heat capacity at constant volume, kJ/kmol K and T = temperature in K

The ideal gas law was expressed as given in Equation 4.5:

$$dT = d(pV)/mR \quad 4.5$$

$R =$ universal gas constant, kJ/kmol K

Equation 4.5 was used to express the relationship between R, gamma and c_v.

$$R/c_v = \gamma - 1 \quad 4.6$$

The final HRR model; Leeds HRR model, (Equation 4.7) was obtained by substituting Equations 4.3 to 4.6 into Equation 4.2 and rearranging.

$$\frac{dQ}{d\theta} = \frac{\gamma}{\gamma-1} p \frac{dV}{d\theta} + \frac{1}{\gamma-1} V \frac{dp}{d\theta} + \frac{dQ_W}{d\theta} + h_{bb} \frac{dm_{bb}}{d\theta} + q_e \frac{dm_f}{d\theta} \quad 4.7$$

The Leeds HRR model utilised $\gamma_{mod}(T, \lambda)$ (Equation 3.34). The in-cylinder λ was used in Equation 3.34 to estimate γ_{mod}. The values of the in-cylinder λ for the tested engine modes were obtained by dividing the in-cylinder AFRs by the stoichiometric AFR (the in-cylinder AFR for each of the tested engine modes was evaluated as the ratio of the trapped air mass to the injected fuel mass).

The heat flow to the walls, Q_W was calculated from Equation 4.8.

$$Q_w = hA_s\left(T - T_{ref}\right) \quad 4.8$$

$Q_w =$ wall losses, J/s

$h =$ heat transfer coefficient, W/m^2 K

A_s = total surface area of heat loss (cylinder liner area, piston surface and cylinder head above piston), m^2

The cylinder temperature on the other hand, was estimated from the ideal gas law (Equation 4.9)

$$T = pV/mR \quad 4.9$$

m = amount of gas in the cylinder, kmol

The observed steady state temperature of the coolant/lubricant oil was used as the reference temperature in Equation 4.8. The lubricant oil absorbed the heat that was transferred across the walls of the cylinder of the engine. The temperature of the lubricant was among the data that was logged during the experiment.

The blow-by rate, $\frac{dm_{bb}}{dt}$ in Equation 4.7 was estimated as a function of pressure from Equations 4.10 and 4.11 (AVL, 2015):

$$\frac{dm_{bb}}{dt} = A_{eff} p \left(\sqrt{2/(RT)}\right) (2/(\gamma+1))^{1/\gamma-1} \sqrt{\gamma/(\gamma+1)} \quad 4.10$$

$$A_{eff} = D\pi\delta \quad 4.11$$

$\frac{dm_{bb}}{dt}$ = mass flow rate, kg/s

A_{eff} = effective flow area, m^2

p = cylinder pressure, Pa

T = cylinder temperature, K

γ = ratio of specific heats

D = cylinder bore, m

δ = blow-by gap (the clearance between the piston rings and the cylinder liner/wall), m. The value of δ was specified as 0.00001 m (AVL, 2015).

The differential, $\frac{dm_{bb}}{dt}$ was converted to $\frac{dm_{bb}}{d\theta}$ by multiplying the equation (Equation 4.10) by the appropriate conversion factor (a function of the speed of the engine) for each of the tested modes.

The fuel evaporation rate ($\frac{dm_f}{d\theta}$) in Equation 4.7 was estimated by using a novel approximation approach. The approach that was used to estimate the rate of evaporation of the fuel in this work was based on the knowledge that each of the prominent peaks in the HRR profile of the multiple fuel injection strategy CI engine resulted from the auto-ignition and combustion of the fuel mass that was injected immediately before the peak in the preceding main injection event. Prior to auto-ignition, the injected fuel mass absorbed heat from the hot gases in the cylinder to evaporate. The HRR profile was initially modelled from the basic input data (the pressure trace) without the evaporation term of Equation 4.7. The crank angle timing for each of the main injection events was meticulously determined from the HRR profiles between the estimated SoC and EoC. The heat that was released between the injection events was then determined cumulatively. The corresponding injected fuel masses were determined by dividing the estimated heat release per injection event by the Calorific value (Cv) of the fuel. Thereafter, the heat that was absorbed by the injected fuel from the gases in the combustion chamber to evaporate was determined by multiplying the estimated fuel masses by the heat of evaporation of the fuel. The estimated heat of evaporation for each of the injection events was incorporated into the model in Excel specifically at the crank angle of the prominent peak that was sequel to the injection (fuel injection did not occur at all the crank angles of the power stroke).

4.4.3 Exponential fit of experimental specific heats data

The experimental data of Heywood (1988) (Figure 3.12) were fitted into an exponential function (Equation 4.12) using Mathcad14 software.

$$\gamma = \omega_1 \times exp(\omega_2 \times T) + \omega_3 \quad 4.12$$

Table 4.5 presents the estimated values of the constants ω_1, ω_2 and ω_3 in Equation 4.12 for various values of the equivalence ratio, ∅ as well as the EGR rate.

Equation 4.12 was used to model the HRR of the engine at ∅ = 1 and at EGR rates of 0, 0.2 and 0.4 in order to investigate and ascertain the effect of the EGR rate on the HRR of the engine.

Table 4.5 Constants to be used in the derived (fitted) model of γ

Equivalence ratio, ∅	EGR	ω_1	ω_2	ω_3
0.5	0.4	0.429	-0.000306	0.988
0.8	0.2	0.412	-0.000378	0.997
0.8	0.4	0.358	-0.000443	1.050
1	0	0.241	-0.000921	1.170
1	0.2	0.223	-0.001050	1.200
1	0.4	0.384	-0.000419	1.020

4.5 Diesel Gen-set combustion test

The diesel engine combustion test which could not be completed on the IVECO engine (due to the break-down of the engine and the impact of the pandemic) was completed on the modern diesel Gen-set engine. The work featured the use of bioethanol in the Yanmar diesel Gen-set rather than in a gasoline Gen-set because diesel engines are more prominently utilised than gasoline Gen-set engines for power generation in Nigeria in households, small and medium scale businesses as well as in industries and corporate (Government and Private)

organizations. The baseline and DE fuel blends combustion tests were completed on the diesel Gen-set.

4.5.1 Materials and Methodology for the Gen-set combustion test

The materials and instrumentation that were used for the test were off-road (red) diesel, anhydrous ethanol, hexane solvent, diesel container (5 litres), 2 litre graduated plastic container (with spout for easy pouring of liquid), five 2.5 litre mixing bottles, 300 ml glass beaker, three 50 ml centrifuge bottles, Yanmar 5.7 kW Gen-set, scale (ADAM CPW plus-35), Hillstone load bank (HAC240-10, 240 V maximum, 11 kW maximum load), Gasmet FTIR (DX-4000) analyser, National Instrument (NI) data logger (NI-CRIO9066 controller with NI-9211, 8-channel thermocouple reader), AVL flexifem Indi 601 (2-channel), AVL GH14D pressure sensor, desktop computer and data acquisition software (LabView CRIO program V2-v1).

The air intake, exhaust manifold, lube oil, and exhaust gas temperatures were measured by thermocouples. The thermocouples were connected to the 8-channel thermocouple reader of the NI-CRIO9066 controller which read and transmitted the measured temperatures to the PC via the ethernet connector.

Table 4.6 presents the details of the diesel Gen-set engine.

Table 4.6 Specifications of the diesel Gen-set engine

Parameter	**Specification**
Make	Yanmar
Type	4-stroke, single cylinder
Rated power (kW)	5.7
Speed (rpm)	3,000
Bore (mm)	86

Stroke (mm)	75
Piston design	Re-entrant bowl
Compression ratio	20.9:1
Displacement (cm^3)	435.66
Total cylinder volume (cm^3)	457.55
Injection pressure (MPa)	~20
Injection timing (bTDC)	13º

Figure 4.5 shows the schematic view of the diesel Gen-set combustion test set up.

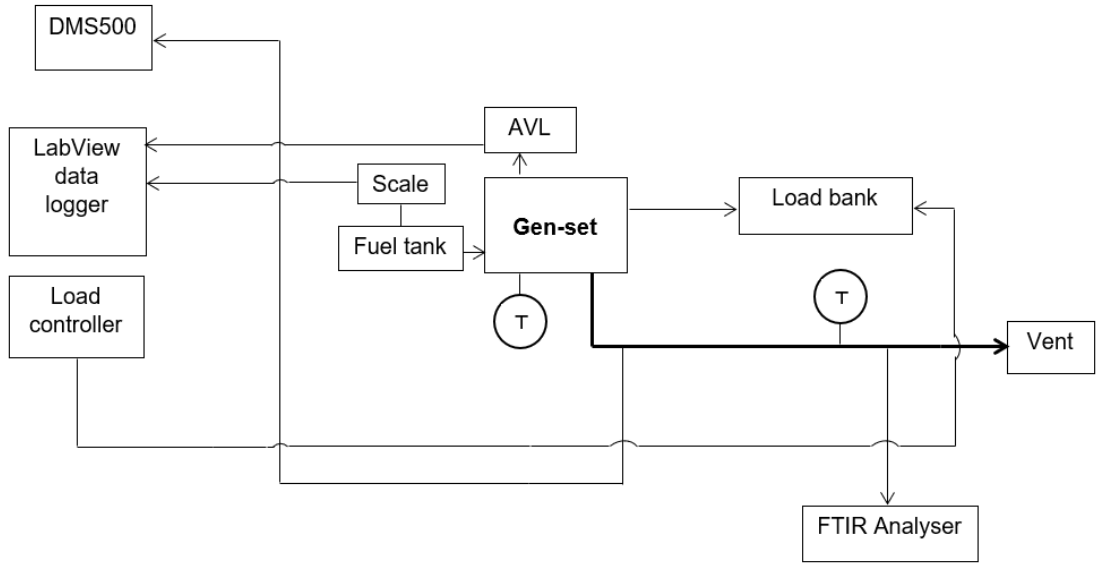

Figure 4.5 Experimental set up for the diesel Gen-set combustion test

4.5.2 Methodology

4.5.2.1 Preparation of the tested DE fuel blends

2 litres of the tested DE fuel blends (DE0 (baseline diesel), DE5, DE10, DE15) were prepared in the Engine room by splash-blending the appropriate volumes of Ultra Low Sulphur Diesel (ULSD) and absolute ethanol as shown in Table 4.7.

Table 4.7 Preparation of diesel-ethanol (DE) fuel blends for the Gen-set combustion test

Binary DE blend	Volume, ml	
	Pure diesel (ULSD)	Pure ethanol
DE0 (pure diesel)	2,000	0
DE5	1,900	100
DE10	1,800	200
DE20	1,700	300

4.5.2.2 Diesel Gen-set combustion test procedure

Table 4.8 presents the test matrix for the Gen-set combustion test. Each of the investigated DE fuel blends was tested at three different kilowatt electric (kW_e) loads (idle, 2, and 3 kW_e). The Gen-set had a power loss of about 25% by the alternator. Therefore, the 2 and 3 kW_e power conditions were equivalent to engine-out power conditions of 2.7 and 4 kW respectively.

Table 4.8 Diesel Gen-set engine combustion test matrix

S/n	Binary DE blend	Load (kW_e)	Engine-out power (kW)
1	DE0 (pure diesel)	0	0
2		2	2.7
3		3	4
4	DE5	0	0
5		2	2.7
6		3	4
7	DE10	0	0
8		2	2.7
9		3	4
10	DE15	0	0

11		2	2.7
12		3	4

Safety checks were carried out prior to the commencement of the test. The Exhaust extraction system was checked to ensure that it was switched on at the control cabinet and fully operational. Also, the exhaust ducting of the Gen-set engine was put in the “Fully Open” position. The heated lines of the FTIR analyser and the DMS500 were properly connected to the desired exhaust sampling points.

4.5.2.3 Gen-set engine start and test procedure

The following steps were followed to carry out the diesel Gen-set combustion tests:

1. The Hillstone load bank, the FTIR analyser, the DMS500, the AVL flexifem Indi 601, and the scale were powered on.
2. The DMS500 computer was powered on. The Cambustion software was launched and “On” was selected to warm the DMS500.
3. The LabView computer was powered on and the CRIO software was launched.
4. The FTIR analyser was zeroed using nitrogen gas and calibrated. Thereafter, it was set on continuous measurement mode.
5. The fuel canister for pure diesel was connected to the engine
6. The Gen-set was switched on and allowed to run for 60 seconds to allow for proper circulation of the pure diesel and the flushing of the left-over fuel from the previous test.
7. The Gen-set was allowed to run on idle until the Lube oil temperature became steady at 50 ^{o}C.

8. The engine parameters (temperatures and fuel consumption) were logged for 10 minutes on LabView after the engine became stable. The pressure-crank angle (P-CAD) data were also logged on LabView while the engine parameters were logged.
9. The engine-out particulate emission for the idle mode was logged on the DMS computer for 5 minutes and saved.
10. Steps 7 to 9 were repeated for the 2 and 3 kW_e load conditions.
11. The Gen-set was turned off after the diesel baseline test was completed to change the fuel canister to the next fuel blend.
12. Steps 6 to 11 were repeated until all the DE fuel blends were tested.

4.5.2.4 Gen-set engine stop procedure

At the end of the tests, the engine stop procedure highlighted below was followed to shut down the Gen-set:

1. The ignition was turned off.
2. Logging of data was stopped on all the computers (LabView, DMS500, and FTIR).
3. Nitrogen gas was passed through the FTIR analyser to purge the system.
4. The spectral files were analysed on the FTIR laptop.
5. The logged engine parameters and P-CAD data were downloaded from the LabView software and saved. The LabView software was closed, and the computer was shut down.
6. The Cambustion software was closed, and the DMS500 computer was shut down.
7. The DMS500, the FTIR analyser, the scale, and the AVL flexifem Indi 601 were powered off.
8. The ventilation system of the Engine room was turned off.

4.6 Biomass gasification test

The aim of the biomass gasification test was to determine the optimum gasification equivalence ratio, Ø for the gasification of agricultural biomass residues with focus on sweet sorghum stalk residue. The residue-to-product ratio of the crop was reported to be 1.25 (Simonyan and Fasina, 2013). As such, the bioenergy potential of the crop residue could be harnessed for heating (during the cold season in Nigeria) or for power generation by passing the product of the gasification of the biomass (syngas) into a fuel-flexible, diesel-syngas, dual-fuel RCCI engine.

The different methods that are available for the biomass gasification aspect of the current work are building a full gasifier, the bottled method, and the Cone calorimeter method. The Cone calorimeter method was chosen for the gasification work because the equipment is well suited for the investigation of the fire behaviour of fuels (both solid and liquid fuels). The Cone calorimeter also has its gas analysers (FTIR and oxygen analysers) for the speciation of the sampled raw gas from the burning fuel. The first option (building a full gasifier) is not feasible for the current work due to the limited time for the research. It is also more costly than the Cone calorimeter option. The bottled option involves the use of equilibrium calculation software to simulate the syngas that (possibly) can be generated from the biomass based on the carbon, hydrogen, nitrogen, sulphur, and oxygen content of the biomass. Thereafter, the syngas is physically simulated from different bottles of CO, H_2, CH_4, and N_2. The bottled method does not approximate the reality as closely as the Cone calorimeter method because actual gasification/burning of the biomass fuel does not occur as in the case of the Cone calorimeter option.

4.6.1 Materials and Methodology for the biomass gasification tests

4.6.1.1 Materials

The materials that were used for the gasification tests were air-dried sweet sorghum stalk residue, grain sorghum stalk residue, corn stalk residue, steel rule, saw, scale, semi micro balance, standard weight (100 g), Mettler Toledo TGA, Thermo Scientific Elemental Analyser 2000, Parr 6200 bomb calorimeter, the fire rig, heavy-duty aluminium foil, latex hand gloves, cryogenic gloves, safety gloves, and boots. The fire rig that was used for the gasification tests consisted of the Cone calorimeter, Agitent Data logger, Gasmet FTIR gas analyser (CR2000), portable oxygen analyser, and DMS500 (Figure 4.7). The Gasmet FTIR analyser was calibrated for 60 species.

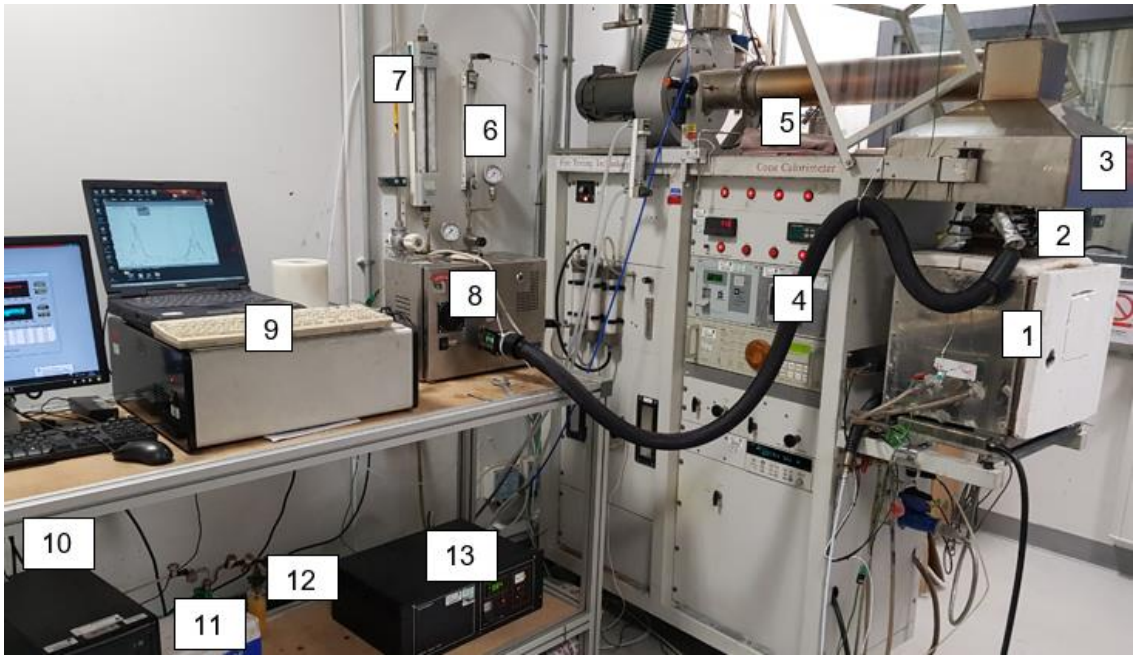

1. Restricted ventilation box
2. Chimney stack
3. Secondary air entrainment duct
4. Heated line
5. Sampling point for DMS500
6. Flow meter (nitrogen)
7. Flow meter (air)
8. FTIR pump
9. Gasmet FTIR
10. Computer (ConCalc5 programme)
11. Condenser
12. Silica gel
13. O_2 analyser

Figure 4.6 The Cone calorimeter and the associated gas analysers

4.6.1.2 Methodology

Analytical test:

Proximate analysis, elemental analysis, and bomb calorimetry were carried out on the biomass samples (sweet sorghum stalk residue, grain sorghum stalk residue, and corn stalk residue) using the Mettler Toledo TGA, Thermo Scientific Elemental Analyser 2000, and Parr 6200 bomb calorimeter respectively.

The Higher Heating Values (HHV) of the biomass residues were also predicted from the unified correlation of Channiwala and Parikh (2002) (Equation 4.13). The predicted HHV (or Gross Calorific Values, GCV) of the biomass residues (in MJ/kg biomass) were compared with the values that were determined by bomb calorimetry.

$$HHV = 0.3491C' + 1.1783H' + 0.1005S' - 0.1034O' - 0.0151N' - 0.0211A' \quad 4.13$$

C', H', S', O', N', and A' in Equation 4.13 are the percentages by mass on a dry basis of carbon, hydrogen, sulphur, oxygen, nitrogen, and ash respectively in the biomass.

Sample preparation:

The procedures that were followed to prepare the sweet sorghum stalk residues for the test are highlighted below:

1. The sweet sorghum stalks were cut and placed side-by-side to form a 100 mm x 100 mm sample. The thickness of the stalks was ~20 mm.
2. The samples were weighed on the scale and the mass of the test sample was noted.
3. The stalks were carefully wrapped in the aluminium foil such that only the top surface of the stalks was exposed. This was to minimise heat loss from the sides and bottom of the test sample during the test.

4. The completed sample was placed on top of the ceramic fibre blanket.
5. Thereafter, the blanket (together with the sample) was placed into the sample holder and covered to prevent contamination.

The biomass samples were tested at the conditions of air flow/air flux shown in Table 4.9.

Table 4.9 Sweet sorghum stalk residue gasification air flow conditions

S/n	Air flow rate, lpm	Air flux, g/(m^2.s)
1	4.4	9.0
2	5.5	11.2
3	6.3	12.9
4	7.0	14.3
5	7.6	15.5
6	8.0	16.3
7	9.4	19.2

Daily Start-up procedure:

The following daily start-up procedure were observed for the Cone calorimeter:

1. The filters and drying agents were checked. The Silica gel (drying agent) was replaced when it turned from orange to clear-white. The filters were also checked. The filters were replaced when they became dirty. Dirty filters were discarded in the regular trash.

2. Liquid N_2 was decanted into the liquid N_2 flask from the liquid N_2 dewar (the safety googles and cryogenic hand gloves were always worn whenever liquid N_2 was handled).

3. The condenser unit was also set up by putting liquid ice into the condenser box.

4. The Cone systems were switched on by following the steps below:

   i. The Cold trap was closed.

   ii. Compressed air was turned on and maintained at 2 bar.

   iii. The ventilation shutters were opened using the black rod at the side of the Cone calorimeter. The combustion fan was put on and the rate on the digital meter was set to 0.2 m^3/s.

   iv. At this stage, Power, Laser, and Analyser functions were ON.

   v. Agitent Data Logger, Cold trap, Hartmann and Braun analyser were turned on.

   vi. The Computer was turned on and the Cone software (ConCalc5) was launched. The Excel Add-in programme was also launched.

   vii. The temperature of the Cold trap was checked from the status window in the program to ensure that it was below 0 ^oC. (The cold trap was drained whenever its temperature stabilised at a positive value)

   viii. The Load cell was switched on after the ceramic fibre plate was put in place.

5. The FTIR, the O_2 analyser, and the DMS500 were powered on by following the steps below:

   i. The O_2 analyser (downstream of the FTIR) was connected to the outlet of the FTIR analyser.

   ii. The FTIR laptop was connected to the FTIR analyser and powered on. The FTIR pump and FTIR analyser were connected to the heated lines and electricity. Thereafter they were powered on.

   iii. The Calcmet program was launched on the laptop.

iv. Liquid nitrogen was poured into the FTIR cell.

v. The O_2 analyser was turned on.

vi. The DMS500 was powered on and warmed up.

Daily calibration procedure:

The daily calibration of the Cone calorimeter was done according to the steps below (the calibration of the heat flux was done on a monthly basis).

First of all, the C-factor was checked in Configurations to ensure that it was set at 0.0429. Thereafter, the Calibrations tab was selected on ConeCalc5 and the instructions displayed on the screen were followed. Each item of the Cone calorimeter was calibrated sequentially as follows:

1. Mass Flow Meters (MFMs) were zeroed (the instructions on the screen were followed).
2. DPT and Flow were also zeroed by following the steps below:
    i. The room exhaust system and the Cone Exhaust fan (upper left-hand switch on Cone) were put off. The room exhaust system was put off by setting the rate on the Ventilation panel to 0.0 m^3/s and closing the ventilation shutters.
    ii. The “Zero” screen on the Calibration bar was opened and the Zero button was clicked.
    iii. Thereafter, the ventilation shutters were opened and the room exhaust system was turned on. The ventilation rate was set back to 0.2 m^3/s on the ventilation panel.
3. The gas analysers on the Cone calorimeter were calibrated. This step involved two stages: Zeroing and Spanning.

a. Zeroing:

- The nitrogen isolation valve (the red handle) was closed, the pressure regulator was kept almost at full decreased pressure and the rotameter flow control was closed.
- The Combination line bottom diverter valve was set to air while the top diverter valve was set to the cone line.
- The O_2 pump was switched off while the dial on the Cone was set to Nitrogen.
- The nitrogen supply line was set to 1 barg (1 bar gauge).
- The nitrogen isolation valve was opened, the line was initially set to 0.3 barg.
- The flow meter on the Cone was used to adjust the rate to 200 cc/min while the value of pressure was adjusted to 0.3 barg.
- The digital display on the Cone servomex analyser was observed while the displayed oxygen value stabilised.
- The Zero screw on the machine was adjusted until $\pm$ “0.0” blinked on the readout.
- “Zero” was then pressed on the Computer.
- The Hartmann and Braun analyser was zeroed by pressing “cal” until the display showed a flashing “ZERO”.
- Whenever the display was not zero, the “Enter” button was pressed and the up-down arrows were used to adjust the value to zero. Enter was pressed again to confirm that “ZERO” was displayed.
- Thereafter, “Channel” was pressed and the step above was repeated for the four channels.
- pDAQ was accessed on Excel and 1 minute record for the zero baseline was taken.

- The arrow key was pressed to scroll from “ZERO” to “SPCC” to span the Hartmann and Braun (H&B) analyser.
- The four channels were allowed to stabilise at the prescribed values: Channel 1 (714), Channel 2 (208), Channel 3 (3.94), Channel 4: (13.25).
- pDAQ was accessed again and 1 minute record for the span baseline was taken.
- The arrow key was used to return to “ZERO” on the blinking “SPCC” and thereafter, “Meas” was pressed.

b. Spanning:

i. The nitrogen supply valve was turned off. The diverter on the Cone was switched to “Air” and the pump on the Cone was turned on.

ii. The valve was turned to “Air” and the flow rate was adjusted to 200 cc/min.

iii. The value of oxygen on the display was allowed to stabilise.

iv. The “Span” screw on the Cone was adjusted until the readout blinked between 20.9 and 21.0.

v. “Span” and “OK” were then clicked on the ConCalc5 software.

4. Smoke

Smoke calibration was carried out in two stages as follows:

i. Zeroing: The sample holder on the laser was blocked with a slip of paper, and then, “Zero” was clicked on the screen.

ii. Balancing: the paper was removed and the sample holder door was closed. “Balance” was selected on the screen, and thereafter, “OK”.

5. Mass

   i. The shutters of the conical heaters were closed and the ceramic plate was removed. Thereafter, “Tare” was pressed on the Cone calorimeter.

   ii. The values were observed on the display as well as on the ConCalc5 software until they were fairly stable (~0) and then zeroing was done.

   iii. Thereafter, the 100 g standard weight was placed on the Load cell to span the mass balance.

   iv. The samples were removed from the sample holder and the empty sample holder was placed on the Load cell.

   v. Steps i and ii above were repeated to zero the Load cell on the empty sample holder.

   vi. The sample holder was removed and the biomass samples were placed back in it.

   vii. The sample holder (with the samples in it) was placed on the Load cell again to confirm that the mass displayed was approximately equal to the recorded mass of the biomass sample.

   viii. The sample holder was removed from the Load cell and the ceramic plate was placed on the Load cell.

6. Heat flux calibration

Heat flux calibration of the Cone calorimeter was done on a monthly basis. The ceramic plate was in place throughout the calibration to insulate the load plate from the heat. The steps below were followed to calibrate the heat flux:

   i. On the main calibration screen, heat flux calibration was clicked.

   ii. The valve of the water inlet to the Load cell was closed.

iii. The valve below the controlled atmosphere air box was opened by turning it towards the Cone. This ensured that the cooling water circulated in the Cone during the heat flux calibration.

iv. The water tap was slightly opened for moderate flow of water.

v. The heat flux meter was inserted ensuring that the gap between the base of the heating element and the heat flux meter was 25 mm.

vi. The shutter was closed and the temperature was set to 100 ^{o}C on the Cone.

vii. The shutter was opened when the set temperature was attained to expose the heat flux meter to the radiant heat.

viii. The corresponding heat flux reading to the set temperature was taken from the computer.

ix. The shutter was closed again. A new temperature set point was made and steps vi to ix were repeated. The temperature of the Cone was increased at an interval of 100 ^{o}C to obtain eight heat flux readings.

x. At the end of the heat flux calibration, the temperature was turned down to zero.

xi. The heat flux meter was removed. The water tap was closed. The valve below the restricted ventilation box was closed while the valve that controlled the flow of water to the Load cell was opened.

The heat flux that was chosen for the gasification of the tested stalk residues was 25 kW/m^2. The chosen heat flux corresponds to a Cone temperature of 590 ^{o}C.

7. Zeroing of the FTIR and O_2 analyser downstream of the FTIR analyser.

i. The top diverter was switched to the FTIR line and directed towards the zero gas inlet.

ii. The dial of the FTIR pump was set to zero gas.

iii. The nitrogen supply line was set to 1 barg (the pressure in the nitrogen line was kept at 0.3 barg).

iv. The control valve was used to set the flow of gaseous N_2 from the flow meter to a value between 2-4 litre/min.

v. The values of % O_2 were allowed to stabilise on the O_2 analyser which was downstream of the FTIR. Thereafter, a screwdriver was used to set the “Zero” until it blinked $\pm$”0.0”. The zero baseline for the O_2 analyser was recorded on pDAQ for 1 minute.

vi. 3 minutes sampling time was selected on the Calcmet programme. “Autosave” was clicked under Options and the file name to save the test as was entered.

vii. “Zero” was clicked on the “Measure” tab of the Laptop Calcmet program to zero the FTIR and obtain zero calibration (background reading).

viii. Thereafter, the program was run for 3 minutes sample, to obtain a zero line that was fairly straight about zero. (Whenever the zero line was observed to deviate conspicuously from zero, the liquid nitrogen in the FTIR analyser was topped up and the detection cell temperature was checked to ensure that it was -196.0 ^oC on the hardware.

ix. The sampling interval for the FTIR analyser was set to 1 second (for the test) and the N_2 gas valve was closed.

x. The dial of FTIR pump was set towards the sample gas.

xi. The FTIR pump was then switched on to span the O_2 analyser.

xii. The values of % oxygen were allowed to stabilise for about 5 minutes on the O_2 analyser. The dial was set to between 20.9 and 21.0 when stability was attained and recording was done for 1 minute on pDAQ.

Running the test:

The steps below were followed to run the gasification tests after the calibration of the Cone calorimeter and the analysers.

1. The air flow to the restricted ventilation box was set on the air flow meter to the first condition. The tap was opened for moderate circulation of water through the Load cell.
2. The DMS500 was set to sample mode so that data logging commenced on the DMS500.
3. The temperature of the Cone was set to the 590 ^oC on the temperature control
4. Thereafter, 60 seconds baseline reading was started on ConCalc5, at the same time, logging on the Calcmet program and pDAQ was started.
5. After the baseline reading was taken, the ceramic plate was removed and replaced with the prepared sample in the sample holder (protective hand gloves were worn).
6. The door of the box was closed, the shutters were opened to expose the surface of the sample to the heat. At the same time, the Start button was clicked on the ConCalc5 programme.
7. The sample was observed within the box, as soon as it auto-ignited, key “I” was pressed on the keyboard to record the time of ignition.

8. key “F” was pressed when the flame went out to record the flame-out time.
9. The shutters were shut when no visible smoke was observed from the sample holder and data logging was stopped on all the computers.

Shut down procedure:

The prescribed shut down procedure of the Cone calorimeter was followed to shut down the Cone at the end of every gasification test.

1. The Analyser, Power supply and Laser were not shut down (so that the electronics were kept stable and long warm-up periods on subsequent days were averted).
2. The heater was turned off by lowering the temperature to 0 ^{o}C on the temperature control.
3. The FTIR pump was turned off.
4. The FTIR pump valve was set to zero gas to flush the FTIR and O_2 analysers with N_2 gas.
5. All gas supplies were turned off after flushing the FTIR and O_2 analysers, the pressure gauges were observed to ensure that they were off.
6. The Load cell and Cold Trap were turned off on the Cone.
7. The logged data were saved and copied out from the computers.
8. The pump was turned off on the Cone.
9. The valve of the cold trap was opened.
10. The Cone software was then shut down and the computers were turned off.
11. The floor was swept to get rid of ash/debris from the gasification test.
12. The combustion fan was switched off and the ventilation shutters were closed.

The daily start-up, calibration, test, and shut down procedures highlighted above were followed to carry out the gasification test at the other air flow conditions (Table 4.9).

4.6.2 Estimation of the Heat Release Rate (HRR) of biomass gasification

Heat Release Rate (HRR) estimation was carried out for the first (rich combustion) and the second stages of the gasification of the biomass samples. The HRR for the first stage of the gasification (the Primary Heat Release Rate, P'HRR in kW) was determined from the logged data by oxygen consumption calorimetry. The HRR equation of Parker (1982) (Equation 4.14) was utilised to estimate the P'HRR because the equation accounted for the CO that was produced during the rich/incomplete combustion of the biomass samples.

$$P'HHR = E' x_{O_2}^{o} \dot{V}_A \left[O_{2_{con}} - \left(\frac{E'' - E'}{E'} \right) \left(\frac{1 - O_{2_{con}}}{2} \right) \frac{x_{CO}^{A}}{x_{O_2}^{A}} \right] \quad 4.14$$

The parameters in Equation 4.14 were defined as follows:

$x_{O_2}^{o}$ = the initial concentration in mole fraction of the oxygen in the inlet air (wet basis)

$\dot{V}_A$ = the volumetric flow rate of air into the controlled atmosphere air box (m^3/s)

O_{2_con} = the fraction of oxygen that was consumed in the first stage of the gasification

E' = the net heat of combustion per unit volume of oxygen consumed referred to 25 ^oC when CO_2 was formed (E' = 17.2 MJ/m^3 (13.1 MJ/kg oxygen)

E'' = the net heat of combustion per unit volume of oxygen consumed referred to 25 ^oC when CO was burned (E'' =23.1 MJ/m^3 (17.6 MJ/kg oxygen))

x_{CO}^{A} and $x_{O_2}^{A}$ = the concentrations of CO and oxygen respectively in the oxygen analyser (dry basis)

The fraction of oxygen that was depleted (O_{2_con}) was estimated from Equation 4.15.

$$O_{2\_con} = \frac{x_{O_2}^{A^0} - \frac{x_{O_2}^{A}\left(1 - x_{CO_2}^{A^0}\right)}{\left(1 - x_{CO_2}^{A} - x_{CO}^{A}\right)}}{x_{O_2}^{A^0}\left[1 - \frac{x_{O_2}^{A}}{\left(1 - x_{CO_2}^{A} - x_{CO}^{A}\right)}\right]} \qquad 4.15$$

$x_{O_2}^{A^0}$ and $x_{CO_2}^{A^0}$ = the initial concentrations of oxygen and carbon dioxide, respectively in the analyser

$x_{CO_2}^{A}$ = the concentration of carbon dioxide in the analyser.

The Secondary Heat Release Rate (S'HRR) was based on the measured Mass Loss Rate (MLR). The S'HRR was estimated as the difference between the Total Heat Release Rate (THRR) and the P'HRR (Irshad, 2017). The THRR was obtained by multiplying the MLR by the Higher Heating Value (HHV) of the biomass.

4.6.3 Estimation of the Cold Gas Efficiency (CGE) and Hot Gas Efficiency (HGE)

The cold gas efficiency (CGE) is the ratio of the Calorific value (Cv) of the produced gases in MJ/kg biomass to the Cv of the biomass fuel in MJ/kg biomass (Equation 4.16) (Cohce et al., 2011). The sensible heat of the non-combustible product gases is not considered in the equation for the CGE. On the other hand, the Hot Gas Efficiency (HGE) is calculated from the heating value of the combustible gases as well as the heat that is released from the produced gases as a result of the cooling process – the physical/sensible heat (Kirsanovs and Zandeckis, 2015). The HGE is estimated by adding the sensible heat term to the

numerator of Equation 4.16 (as shown in Equation 4.17). The CGE is of interest if the gas produced is intended for use in diesel engines for electricity generation (Dogru et al., 2002).

$$CGE = \frac{(HHV\ of\ the\ product\ gases)\left(\frac{MJ}{kg\ biomass}\right)}{HHV\ of\ the\ biomass\ fuel\left(\frac{MJ}{kg\ biomass}\right)} \quad 4.16$$

$$HGE = \frac{(HHV\ of\ the\ product\ gases + sensible\ heat\ of\ the\ gases)\left(\frac{MJ}{kg\ biomass}\right)}{HHV\ of\ the\ biomass\ fuel\left(\frac{MJ}{kg\ biomass}\right)} \quad 4.17$$

The HHV for each of the product gases was obtained by multiplying the HHV of the gaseous component (MJ/kg species) by the EI of the species (kg species/kg biomass). The reference temperature that was used in Equation 4.16 was the room temperature (20 ^{o}C). Hydrogen was not detected by the FTIR (hydrogen does not absorb infrared radiation). Therefore, the concentration of hydrogen was estimated from the equilibrium constant (K) of the water gas shift reaction given in Equations 4.18 and 4.19 (Choi and Stenger, 2003).

$$CO + H_2O \rightleftharpoons CO_2 + H_2 \qquad \Delta H^o_{298} = -41.1\ \frac{kJ}{mol} \quad 4.18$$

$$K = \frac{[CO_2][H_2]}{[CO][H_2O]} \quad 4.19$$

$[CO_2]$, $[H_2]$, $[CO]$, and $[H_2O]$ in Equation 4.19 represent the equilibrium concentrations of carbon dioxide, hydrogen, carbon monoxide, and water vapour, respectively.

The value that was used for K in Equation 4.19 was 3.5, corresponding to an equilibrium temperature of 1,738 K (Chan and Zhu, 1996).

Kirsanovs and Zandeckis (2015) reported CGE and HGE values of 75.1% and 83.2% respectively for torrefied biomass (wood chips) while Dogru et al. (2002) reported CGE and HGE values of 75% and 81% respectively (for sewage sludge).

4.7 Estimation of the air intake area of the gasifier

The open areas of air intake at the start of combustion (near-stoichiometric combustion period) and during the gasification (rich combustion) for the proposed gasifier design in the current work were estimated from Equations 4.20 (ET, 2003) and 4.21. The expression for the natural draft intake air velocity, v_a (Equation 4.20) was used to estimate the velocity of the air flowing into the gasifier.

$$v_a = \left[2gh(\rho_o - \rho_r)/\left((\epsilon l \rho_r / d_h) + \Sigma\xi\rho_r\right)\right]^{1/2} \quad 4.20$$

g = acceleration due to gravity (9.8m/s^2)

h = Height between the air inlet and flue gas (syngas) outlet, m

ρ_o = density of the intake air (air outside the gasifier) at ambient temperature (20 ^{o}C), kg/m^3

ρ_r = density of the air in the gasifier, kg/m^3

ϵ = Darcy-Weisbach friction coefficient (0.019)

l = vertical height of exit duct

d_h = hydraulic diameter of exit duct

$\Sigma\xi$ = summation of minor loss coefficients (assumed to be equal to 1)

The other parameters that were used for the estimation of v_a, and the initial and final open areas for the intake air were:

AFR_s, the stoichiometric AFR of sweet sorghum stalks

AFR_g, the optimum gasification AFR

Af_g, the optimum gasification air flux

T_1, the average chimney temperature at the optimum Ø during the first stage of the combustion (the maximum temperature of the chimney at the optimum Ø), K

T_2, the average chimney temperature at the optimum gasification Ø (during gasification), K

ρ_{a1} = density of air at T_1, kg/m^3

ρ_{a2} = density of air at T_2, kg/m^3

Near-stoichiometric conditions were assumed within the restricted ventilation system of the Cone calorimeter at the start of the combustion (when the concentration of oxygen within the box was relatively high). Therefore, the stoichiometric air flux, Af_s was estimated from Equation 4.21.

$$Af_s = Af_g \times \left(AFR_s/AFR_g\right) \quad 4.21$$

Poiseuille equation (Equation 4.22) was utilised to determine the pressure drop (Δp) between the syngas outlet pipe and the throttle box as well as the diameter of the syngas outlet pipe of the gasifier (Ostadfar, 2016).

$$\Delta p = 128\mu LQ/(\pi D^4) \quad 4.22$$

μ is the viscosity of the syngas (Pa.s) corrected to the temperature of the gasifier, L is length of pipe (m), Q is volumetric flow rate of gas (m^3/s), D is the diameter of the syngas pipe (in m).

4.8 Conclusion

The direct injection of splash-blended, stable diesel-ethanol (DE) fuel blends approach was chosen in the current work to investigate the effect of the blending of ethanol with fossil diesel on the performance and emission of diesel engines. The other strategies for introducing ethanol into diesel engines (fumigation (Port Fuel Injection (PFI) of ethanol) and in-line mixing (for unstable DE blends)) require major modification of existing engines. Therefore, the use of splash-

blended, stable DE blends is a simpler and less expensive strategy than the other approaches.

The Cone calorimeter method was chosen for the biomass gasification aspect of the current work because it is the most feasible option for the gasification tests. The Cone calorimeter has its gas analysers (FTIR and oxygen analysers) for the speciation of the raw gas from the burning fuel. The option of building a full gasifier is costly and also time-consuming. As such, it is not suitable for the current research. The bottled option involves software simulation of the possible syngas from the biomass and the physical simulation of the syngas from different bottles containing the components of the syngas. Therefore, it does not accurately mimic the gasification process because actual burning (rich combustion) of the biomass does not occur. The limitations of building a full gasifier and the bottled option made the Cone calorimeter method the most appropriate approach for the biomass gasification aspect of the current work.

Chapter 5 Investigation of the miscibility and stability of diesel-ethanol (DE) blends at different temperatures

5.1 Introduction

This Chapter presents the results of the diesel-ethanol (DE) fuel blends stability test that was carried out. Section 5.2 presents the results of the room temperature stability test that was carried out on the DE blends. Section 5.3 on the other hand, presents the results of the temperature sensitivity test that was carried out on the DE blends that phase-separated.

5.2 Stability of diesel-ethanol (DE) fuel blends at room temperature (20 ºC)

The experimental set up for the room temperature DE fuel blends stability test is depicted in Figure 5.1 which shows ten of the tested diesel-ethanol (diesohol) blends (a total of twelve blends were investigated as stated in Chapter 4; Section 4.1).

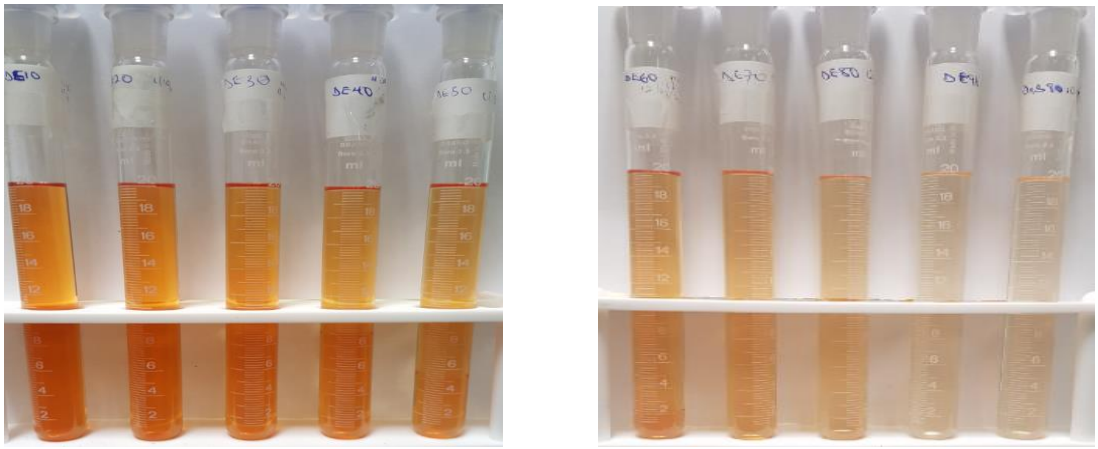

(a) (b)

Figure 5.1 Experimental set up for the room temperature diesel-ethanol (DE) stability test: a) Blends DE10-DE50 (from left to right) b) Blends DE60-DE90, and DnB90

The test tube was sketched to depict the height of the tube H (20 cm), and the partition between the two phases for the unstable blends (Figure 5.2).

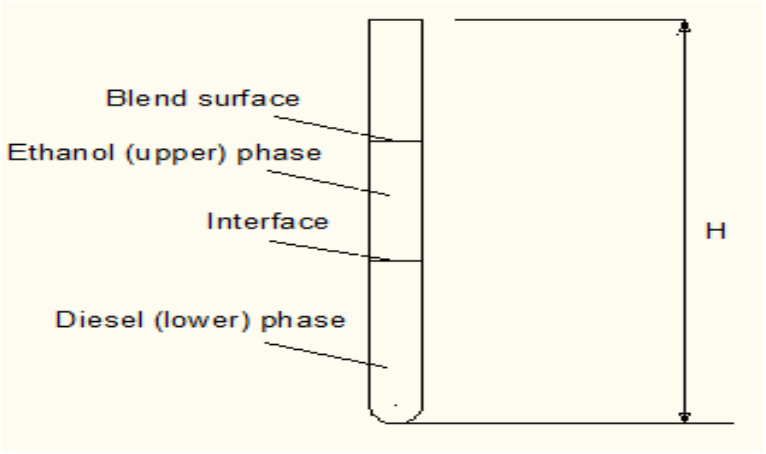

Figure 5.2 Schematic diagram of test tube

Figure 5.3 shows the status of the blends about ten days after blend preparation. Five of the twelve binary blends (DE30, DE40, DE50, DE60, and DE70) phase-separated after the splash-blending while the remaining seven (DE10-DE25, DE75-DE90, and DnB90) were stable throughout the period of observation (90 days). DE25 phase-separated after 90 days. As such, it was added to the five blends that phase-separated initially during the temperature sensitivity test. The equilibrium volume of the lower (diesel) phase in DE25 after it became unstable was 84% of the total blend volume. The current work confirms that the blend wall for binary diesel-ethanol fuel blends is 25-70% ethanol in diesel.

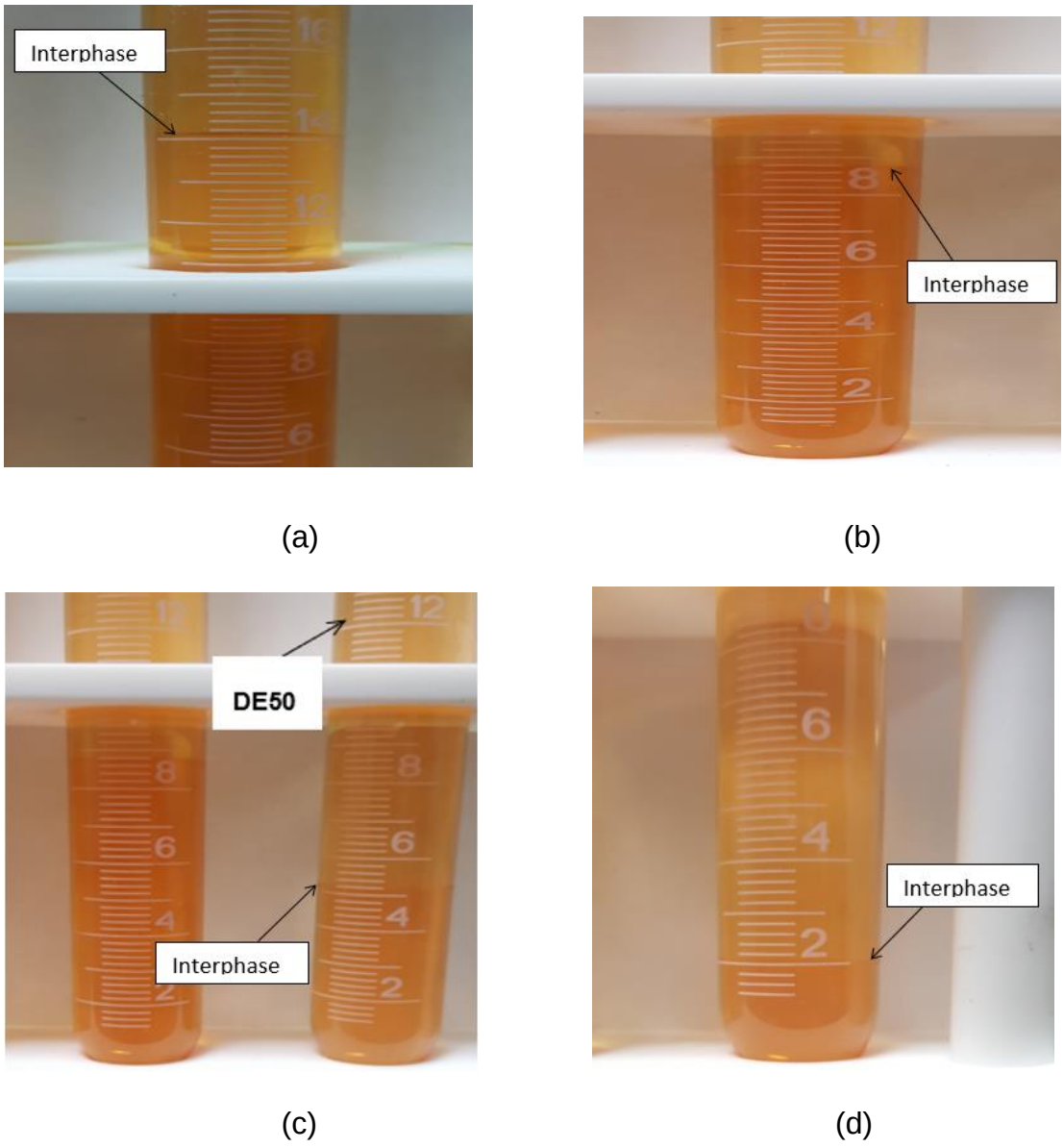

Figure 5.3 Positions of the interphase within the unstable diesel-ethanol (DE) blends ten days after blend preparation: a) Interphase of DE30 @ 14.2 ml b) Interphase of DE40 @ 8.8 ml c) Interphase of DE50 @ 5.2 ml d) Interphase of DE60 @ 2 ml

Two types of blend instability were observed during the room temperature DE blend stability test: the formation of two liquid phases (DE30, DE40, DE50 and DE60) and the formation of a gelatinous phase at the bottom of the test tube (DE70). Lapuerta et al. (2007) also reported the same types of DE fuel blends instability. The details about the time and the mechanism of separation of the unstable DE blends are given in the next section (Section 5.2.1).

Table A.1 (APPENDIX A) shows the detailed record of the status of the blends during the period of observation (90 days).

5.2.1 The Unstable Blends

The blends that separated into two clear phases during the 90 days period of observation were DE30, DE40, DE50 and DE60. Immediately after the blends were prepared, they became turbid (single phase). DE30 separated into two turbid phases 44 minutes after it was prepared with the interphase at the 18 ml mark of the test tube. The two phases became clear 1 hour 33 minutes after blend preparation. The volume of the lower phase (diesel phase) continued to decrease until it became steady at the 14.1 ml mark after fourteen days.

The single turbid phase of DE40 separated into two turbid phases 30 minutes after the blend was prepared with the interphase at the 8 ml mark. The turbidity cleared off 1 hour 19 minutes after the blend was prepared. However, unlike DE30, the diesel phase of DE40 rose to 8.4 ml after about 5 hours and finally became steady at the 8.8 ml mark after nine days.

The single turbid phase of DE50 separated into two turbid phases 8 minutes after the blend was prepared with the interphase at the 4 ml mark. The turbid phases became clear after 57 minutes. The interphase of the blend also rose to the 4.6 ml mark after 4 hours 33 minutes and finally became steady at the 5.2 ml mark after ten days.

DE60 was a single turbid phase which later separated into two turbid phases 37 minutes after it was prepared. The phases became clear after 3 hours. The interphase (visible physical partition between the diesel phase and the ethanol phase) was then at the 1.4 ml mark but after nine days, the interphase rose to the 2 ml mark as shown in Figure 5.3 (d). On the other hand, DE70 was stable

for six days. Thereafter, tiny gelatinous precipitates were observed at the lower part of the glass test tube close to the wall. The suspended precipitates later coalesced (on the 7th day) to form a gel (about 0.01ml) at the bottom of the tube. Lapuerta et al. (2009) reported that, at 5 ^{o}C, the formation of the gelatinous phase occurred in the DE blends that had high concentration of ethanol (>75%) as well as in the ternary (diesel-ethanol-biodiesel) blends that had very high concentration of ethanol (>75%) and <10% biodiesel. The authors attributed the formation of the gelatinous phase largely to the presence of biodiesel. Contrary to what was reported in literature, in the current work, the formation of the gelatinous phase occurred only in DE70 (that is, ethanol concentration of 70%).

Figure 5.4 depicts the actual volumes of pure diesel and pure ethanol as well as the blend volumes at the end of the stability test. Each of the tested DE blends is represented by a pair of bars. The first bar of each pair (yellow and blue) shows the volumes of diesel and ethanol added to produce the blend. It also shows the position of the theoretical interface (the expected position of the interface if the two liquids were perfectly immiscible).

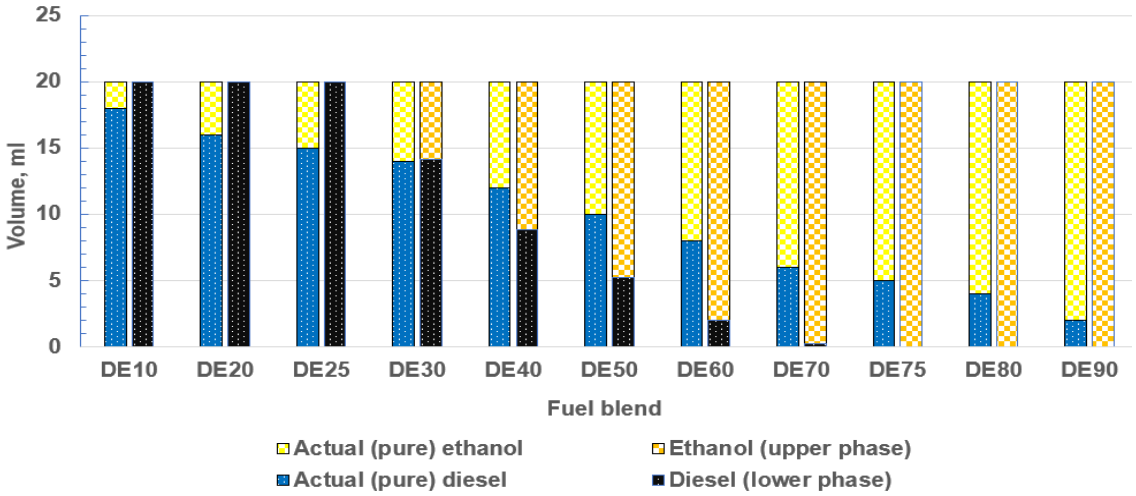

Figure 5.4 Status of the diesel-ethanol (DE) blends at the end of the room temperature stability test

The blue portion of the bars by the left in each pair represents the volume of pure diesel added while the yellow portion represents the volume of pure ethanol added. The second bar in each pair represents the actual state of the tested DE blends at the end of the test. The black coloration represents the observed volume of the diesel phase (or lower phase if separated) in the blends while the orange portion represents the observed volume of the ethanol phase (or upper phase if separated). Off-road diesel (red diesel) was used to prepare the blends. The colour of the diesel phase became lighter in the unstable blends after phase separation. The upper phase also acquired some orange coloration, though lighter than the lower phase. The bars with uniform coloration represent the stable blends (completely miscible) in Figure 5.4. The added volume of diesel in the homogeneous (stable) blends to the left of Figure 5.4 (DE10-DE25) was much higher than that of anhydrous ethanol (diesel was the solvent while ethanol was the solute in DE10-DE25; Section 3.2.1). However, the added volume of ethanol in the stable blends to the right of the figure (DE75-DE90) was much higher than that of diesel (ethanol was the solvent while diesel was the solute in DE75-DE90). Therefore, the second bars for DE10-DE25 and DE75-DE90 were represented by a single colour (black and orange respectively) to differentiate the homogeneous (stable) DE blends from the unstable ones. Figure 5.4 clearly shows the difference between the volume of diesel added in the blends and the volume of the diesel phase in the unstable blends.

The percentage volumes of the diesel phase for the unstable blends were plotted as a function of time in Figure 5.5. The volumes of the diesel phase of the DE blends in Figure 5.4 were expressed as percentages of the total blend volume in Figure 5.5. It shows that the unstable blends attained equilibrium after about 220 hours.

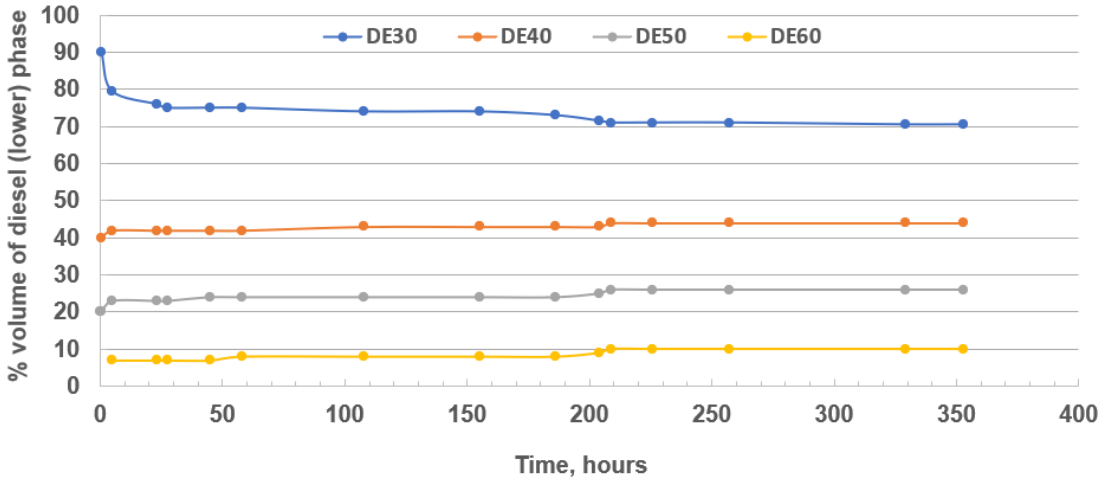

Figure 5.5 Percentage volume of diesel phase in the unstable diesel-ethanol (DE) blends versus time

It was observed that DE40-DE70 had negative diesel phase volume changes (Figures 5.4 and 5.5). The volume of the diesel phase in each of the blends (DE40-DE70) was lower than the volume of the pure diesel that was used to prepare the blend from the start to the end of the stability test. On the other hand, DE30 had a positive change in volume because the volume of the lower phase was 18 ml after the blend was prepared (4 ml greater than the volume of the pure diesel that was used to prepare the blend). At equilibrium, the volume of the diesel phase in DE30 dropped to 14.1 ml.

Figure 5.5 depicts the transient behaviour of the unstable blends. The initial actual volumes of the diesel phase (the volumes of the diesel phase after splash-blending) in the unstable blends (DE30, DE40, DE50, and DE60) were 18 ml, 8 ml, 4 ml, and 1.4 ml respectively. As shown in Figure 5.5, 14 days after the blend was prepared, the volume of the diesel phase in DE30 stabilised by decreasing to 14.1 ml (70.50% of total blend volume). On the other hand, the volumes of the lower phase in DE40, DE50, and DE60 became steady by increasing to 8.8 ml, 5.2 ml, and 2 ml respectively. These equilibrium volumes correspond to 44%,

26%, and 10% of the total blend volume for DE40, DE50, and DE60 respectively (Figure 5.5). 0.01 ml of gelatinous phase (0.05% of total blend volume as depicted in Figure 5.4) was formed at the bottom of the test tube in DE70.

As highlighted in Chapter 3 (Section 3.2.1), polar substances dissolve in polar solvents while non-polar substances dissolve in non-polar solvents. However, as explained in the previous paragraphs, only five out of the investigated eleven DE blends (DE30-DE60) were unstable. Ethanol is a polar liquid, however it exhibits limited solubility in diesel (a non-polar liquid). Normal butanol (a relatively long alcohol molecule compared to ethanol) is also polar, but it is perfectly soluble in diesel. Therefore, the observed limited solubility of ethanol in diesel can be attributed to the difference in the polarity and the difference in the length of the molecules of diesel and ethanol. The polarity of the -OH group of ethanol molecules caused inter-molecular association (hydrogen bonding) between the molecules of ethanol (self-association). As the concentration of ethanol increased in the DE blends beyond 25% at room temperature (Figure 5.4), the hydrogen bonding between the molecules of ethanol was enhanced leading to the separation of the ethanol phase. At the very high concentrations of ethanol (>70%) (in which case, ethanol becomes the solvent) the association of the molecules of ethanol caused the polarity of the ethanol in the blend to cancel out thereby reducing the degree of hydrogen bonding between the molecules of ethanol. Consequently, as the polarity of the ethanol phase diminished, the solubility of diesel in the ethanol phase was enhanced leading to the observed formation of the homogeneous/stable DE blends at concentrations of ethanol >70%. Therefore, similar to the water-PEO solution described in Section 3.2.1, at the high concentrations of ethanol (>70%), self-association of ethanol molecules

decreased drastically while cross-association between the molecules of ethanol and diesel was enhanced.

It was also observed in the current work that the volume of the diesel phase began to decrease below the added volume of pure diesel when the concentration of ethanol in the blend was 40% (Figure 5.4 and Table A.2). This implies that DE40 is a critical binary DE blend. At the critical concentration of ethanol, the volume of the diesel phase reduced below the volume of the added diesel because more volume of diesel from the lower phase dissolved in the upper phase than the volume of ethanol that dissolved in the lower phase. The volume of the diesel phase continued to decrease below the volume of the added diesel as the concentration of ethanol in the DE blends increased until the blends became stable again at concentrations of ethanol >70%. Therefore, it can be inferred that 40% ethanol in fossil diesel is the concentration of ethanol at which the polarity of the ethanol phase in the unstable DE blends begins to diminish.

In terms of the difference in the length of the molecules (structure of molecules), the molecules of ethanol are much shorter than those of diesel. Therefore, there was limited association between the molecules of the two liquids which contributed to the observed limited solubility of ethanol in diesel. Normal butanol (n-butanol) has four carbon atoms in its molecule which makes its molecule relatively long compared to ethanol. Therefore, n-butanol has unlimited solubility in fossil diesel.

Apart from establishing the limits of solubility of ethanol in diesel, the blend wall of ethanol in diesel (25-70% by volume of ethanol) also establishes the maximum possible concentrations of ethanol in the diesel and ethanol phases of the unstable blends at equilibrium. Each of the separated phases were clear (stable) at equilibrium. Therefore, it can be inferred that, at 20 ^{o}C, the concentration of

ethanol in the diesel phase of the unstable DE blends at equilibrium is < 25% whereas in the upper phase, it is > 70%.

Tables A.2 and A.3 (Appendix A) present the data which were depicted graphically in Figures 5.4 and 5.5.

5.2.2 The Stable Blends

DE10, DE20, DE25, DE75, DE80, DE90, (Figure 5.4) and the n-butanol blend, DnB90 were stable throughout the period of observation of the blends. Each of the stable DE blends was a clear, single phase solution from the time it was splash-blended to the end of the experiment.

Kwanchareon et al. (2007) reported that DE blends that have 30-70% absolute (anhydrous) ethanol were stable for 90 days at 20 ^{o}C. However, the results of the current work shows that binary fuel blends of 30-60% ethanol in fossil diesel were never stable at room temperature as the blends became turbid immediately after they were prepared by splash-blending. The blends also separated into two clear phases on the same day that they were prepared. DE70 became unstable after a week. The observed difference in the behaviour of the blends in the current work and the works of previous authors could be attributed to the diesel that was used as well as the geometry and volume of the sample tubes (glass cells). Fossil diesel from different locations differ in composition because diesel is a complex mixture of hydrocarbons of different chain lengths and structures.

5.2.3 Turbidity and displacement of the interphase in the unstable blends

The observed turbidity and displacement of the interphase (change in the volume of the diesel phase over time) in the unstable blends could be attributed to mass transfer mechanisms. The blends became turbid immediately after the tubes

were shaken due to convective mass transfer as the immiscible volumes of the liquids separated out gradually to form the upper (lighter) phase and the lower (heavier) phase. As the two phases became clearer, the interphase became more conspicuous, and the mass transfer mechanism changed gradually from bulk transfer of fluid to molecular mass transfer mechanism.

Net molecular mass transfer across the interphase resulted in the displacement of the established interphase as the volumes of the two phases changed. The total volume of each of the blends was fixed at 20 ml. Therefore, the observed change in the volume of the phases could only be accommodated by the displacement of the interphase. The interphase of DE30 stabilised at 14.1 ml from the initial 18 ml position. The volume of the upper phase increased from 2 ml to 5.9 ml while that of the heavier (diesel) phase decreased from 18 ml to 14.1 ml. However, DE30 was prepared by adding 6 ml of pure ethanol to 14 ml of red diesel. Therefore, it was concluded that there was a transfer of a certain volume of ethanol across the interphase into the diesel phase while some components of diesel also diffused across the boundary (interphase) into the ethanol phase (the upper layer). The upper (lighter) phase of the unstable blends contained more of ethanol - the less dense liquid, while the lower phase contained more of diesel. The high concentration of diesel in the lower phase relative to the upper phase made the lower phase denser than the upper phase. The volumes of the two phases became stable in the unstable DE blends when there was no more molecular transfer across the interphase (when the rates of molecular mass transfer into both phases became equal).

Fourier Transform Infra-Red (FTIR) spectroscopy was conducted on samples of the upper and lower phases of DE50. The resulting spectra were compared to the spectrum of pure ethanol as shown in Figure 5.6. The black spectrum in

Figure 5.6 represents pure ethanol, the red spectrum represents the upper phase of DE50, while the blue spectrum represents the lower phase. The spectra in Figure 5.6 qualitatively confirm that the upper phases of the unstable DE blends were not pure ethanol, rather they were mixtures of ethanol and diesel with relatively high proportions of ethanol compared to the lower phase. The -OH peaks in the spectra did not overlap with that of pure ethanol. The upper phase of DE50 (the red curve) gave a stronger peak for ethanol (a stronger -OH peak) than the lower phase. This confirms qualitatively that the upper phases of the unstable blends contained more volume of ethanol than the lower phases.

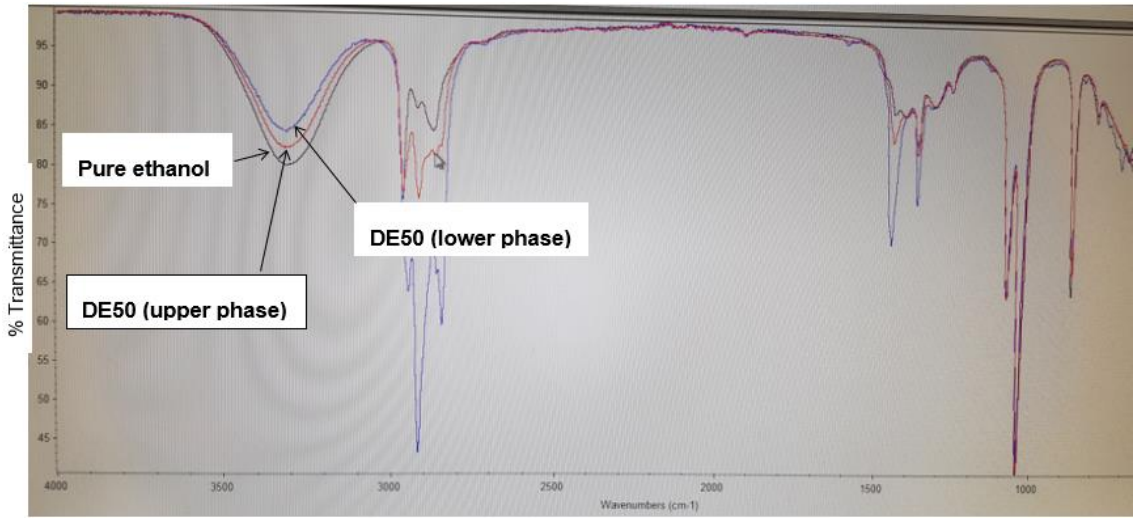

Figure 5.6 FTIR spectroscopy results for pure ethanol, upper and lower phases of DE50

5.3 Temperature sensitivity of the unstable diesel-ethanol (DE) fuel blends.

The DE blends temperature sensitivity test was carried out to determine the temperatures at which the unstable DE blends became stable. As described in Chapter 4 (Section 4.2.4), the temperature of the water bath was initially incremented by 1 ^{o}C to determine the actual test start time (the time that corresponds to the temperature at which the first change in the status of the

unstable DE bends was observed). The temperature increment was stepped up to 2 ^{o}C when the volumes of the diesel phase of the blends were observed to be unchanging after the first change in the blend status. The volumes of the diesel phase of the blends were observed at an interval of three (3) hours and changes in the volume were recorded. The temperature of the bath was stepped up whenever the volumes of the diesel phase in the blends became fairly stable. Therefore, the temperature of the bath was not stepped up at uniform intervals of time. The stepping up of the bath temperature continued until the unstable DE blends became stable.

Figure 5.7 shows the results of the temperature sensitivity test that was carried out on the unstable blends. The curves for the DE blends in Figure 5.7 show how the volumes of the diesel phase in the unstable DE blends decreased with increase in time and bath temperature (the transient behaviour of the volumes of the diesel phase with respect to the bath temperature). The end of each curve indicates the temperature and time of stabilisation of the corresponding DE blend. The temperatures at which the interphase was observed to disappear in the unstable DE blends (temperatures of blend stabilisation) were read from the points of termination of the curves of the blends in Figure 5.7 and tabulated as shown in Table 5.1. The gelatinous phase in DE70 disappeared after 69.5 hours while the temperature of the bath was steady at 25 ^{o}C.

It can be inferred that the unstable DE blends became homogeneous at temperatures above room temperature because the degree of hydrogen bonding between the molecules of ethanol decreased as the temperature of the unstable DE blends increased. As explained in Section 3.2.1, the degree of hydrogen bonding between the molecules of anhydrous methanol decreased as the temperature increased. Methanol and ethanol are quite similar in terms of their

molecular structure because ethanol has two carbon atoms while methanol has one.

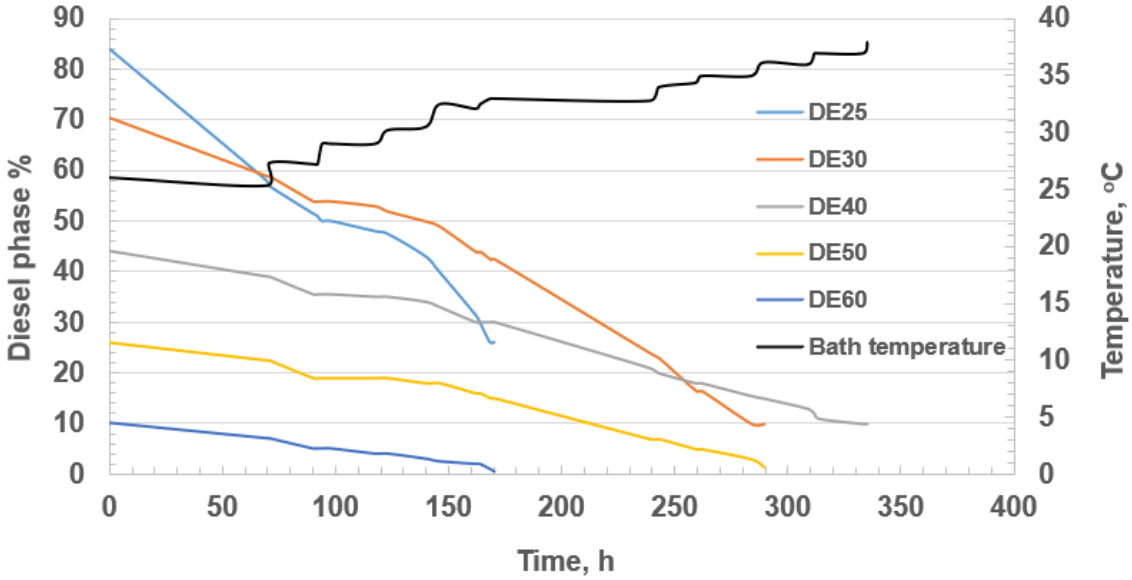

Figure 5.7 Temperature dependence of the volume of the separated phases of the unstable diesel-ethanol (DE) blends

Table 5.1 Stabilisation temperatures of the unstable diesel-ethanol blends

Fuel blend	Time to stabilise, h	Temperature of stabilisation, ºC
DE25	170.5	33
DE30	289.5	36.2
DE40	335.5	38
DE50	289.5	36.2
DE60	170.5	33
DE70	69.5	25

The temperatures at which the unstable blends became homogeneous and the duration for each of the blends to become a clear, single phase were plotted

against the concentration of ethanol as shown in Figure 5.8. Table 5.1 and Figure 5.8 show that 40% ethanol in diesel (DE40) is the critical concentration of ethanol that partitions the unstable DE blends. The current work has shown that the unstable DE blends with ethanol concentrations < 40% as well as the blends with ethanol concentrations > 40% have lower stabilisation temperatures and times compared to DE40 (Figure 5.8). DE40 was observed to be the turning point for the unstable DE blends because it had the highest stabilisation temperature and time (38 ^{o}C and 335.5 hours respectively). DE40 was also found to be the critical unstable DE fuel blend (Section 5.2.1).

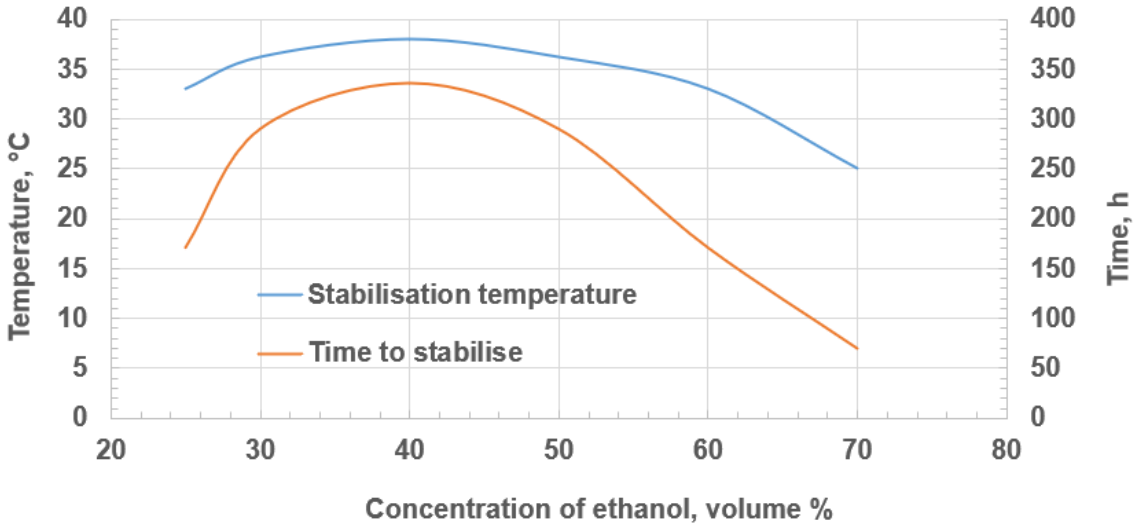

Figure 5.8 Graph of temperature and time of stabilisation of the unstable diesel-ethanol (DE) blends versus blend concentration of ethanol (volume %)

Table A.4 (Appendix A) presents the details of the temperature sensitivity test that was carried out on the unstable DE fuel blends.

5.4 Conclusion

The miscibility and storage stability of diesel-ethanol (DE) fuel blends at 20 ^{o}C was investigated in this aspect of the current work. The temperature sensitivity of the unstable DE blends was investigated using a water bath with temperature

control. It was ascertained that the blend wall for diesel-ethanol fuel blends (range of concentrations for which pure ethanol is insoluble in fossil diesel) at room temperature (20 ^{o}C) is 25-70% by volume. This range defines the compositions of diesohol for which co-solvent will be required to enhance the solubility of anhydrous ethanol in fossil diesel at 20 ^{o}C. The blends that contained 30-60% of pure ethanol were insoluble in fossil diesel throughout the period of observation of the DE blends. 70% pure ethanol in diesel (DE70) became unstable after a week at which time tiny gelatinous precipitates were observed close to the wall and bottom of the test tube. The precipitates finally settled at the bottom of the tube as a gel. DE25 on the other hand, phase-separated after the 90 days of observation of the blends. At the end of the room temperature DE blends stability test, the equilibrium volumes of the lower (diesel) phase in the unstable blends, DE25, DE30, DE40, DE50, and DE60 were 84%, 70.50%, 44%, 26% and 10% of the total blend volume respectively. It was confirmed from the temperature sensitivity test that was carried out on the unstable DE blends that the temperatures and the corresponding times of stabilisation for DE25, DE30, DE40, DE50, DE60, and DE70 are 33, 36.2, 38, 36.2, 33, and 25 ^{o}C and 170.5, 289.5, 335.5, 289.5, 170.5 and 69.5 hours respectively. DE40 has the highest stabilisation temperature of the six DE blends that phase-separated.

Chapter 6 Development and validation of the Leeds HRR model

6.1 Introduction

This Chapter presents and discusses the results of the IVECO diesel engine combustion test. The performance of the engine was investigated at twelve (12) engine modes consisting of three (3) conditions of speed (1,500; 1,600 and 3,000 rpm) and four (4) conditions of torque (30, 75, 150, and 220 Nm) for each of the tested conditions of speed. The 30 and 75 Nm conditions of torque correspond to 10% and 25% loads (low loads/power). The 150 Nm torque condition corresponds to 50% load (intermediate engine load). The 220 Nm condition corresponds to 75% load (the high power condition). The engine performance results are presented and discussed in Section 6.2 in terms of the Specific Fuel Consumption (SFC), thermal efficiency, mechanical efficiency, and combustion stability at the tested modes. The emissions results for the tested conditions are presented and discussed in Section 6.3 in terms of gaseous and particulate emissions at the two exhaust sampling points (upstream and downstream of the Diesel Particulate Filter (DPF)). The emission results were presented graphically by plotting the concentrations of the emitted species against the torque in Nm and power in kW per litre of displaced volume to allow for ease of comparison to other engines. The results of the Heat Release Rate (HRR) analysis of the engine for the tested conditions of power are presented and discussed Section 6.4. The initial objective was to compare the baseline results to the results for diesel-ethanol (DE) fuel blends. This objective was not achieved for the Euro V IVECO diesel engine due to the mechanical fault that the engine developed towards the end of the baseline tests as well as the impact of the pandemic (COVID-19). Lastly, the results for the application of the Leeds HRR model to alternative diesel

fuels (Gas-to-Liquid (GTL) diesel and Hydrotreated Vegetable Oil (HVO) diesel) are given in Section 6.5.

6.1.1 Estimated brake power, Brake Mean Effective Pressure (BMEP) and excess air ratios (λ)

The rated power and displacement of the engine that was used for the current work were 96 kW and 3 litres respectively. Table 6.1 shows the values of the brake power, brake power per displaced volume, Brake Mean Effective Pressure (BMEP) of the engine, and the in-cylinder excess air ratio (λ) at the tested conditions.

Table 6.1 Values of brake power and excess air ratio

Speed, rpm	Torque, Nm	Brake power, kW	Power/displaced volume, kW/l	BMEP, bar	Fuel consumption, l/h	λ
1,500	30	4.92	1.64	1.30	1.61	8.40
	75	12.06	4.02	3.19	3.46	4.04
	150	23.66	7.89	6.26	6.44	2.14
	220	34.72	11.57	9.19	9.30	1.46
1,600	30	5.13	1.71	1.27	1.84	8.35
	75	12.76	4.25	3.17	3.60	3.97
	150	25.36	8.45	6.29	6.78	2.10
	220	37.28	12.43	9.25	9.90	1.45
3,000	30	9.70	3.23	1.28	4.81	5.49
	75	23.90	7.97	3.16	8.06	3.56
	150	47.40	15.8	6.27	13.96	2.16

	220	69.8	23.27	9.24	19.15	1.53

Table 6.1 shows that λ decreased (the combustion became richer) as the brake power of the engine increased at each of the tested engine speeds. The observed decrease in the value of λ as the power of the engine increased was due to the increase in the fuel consumption of the engine when the load on the engine was increased.

6.2 Engine performance

6.2.1 Specific Fuel Consumption (SFC)

The Brake Specific Fuel Consumption (BSFC) and the Indicated Specific Fuel Consumption (ISFC) of the engine were evaluated at the tested modes and plotted against the Brake Mean Effective Pressure (BMEP) and the Indicated Mean Effective Pressure (IMEP) as depicted in Figures 6.1 and 6.2.

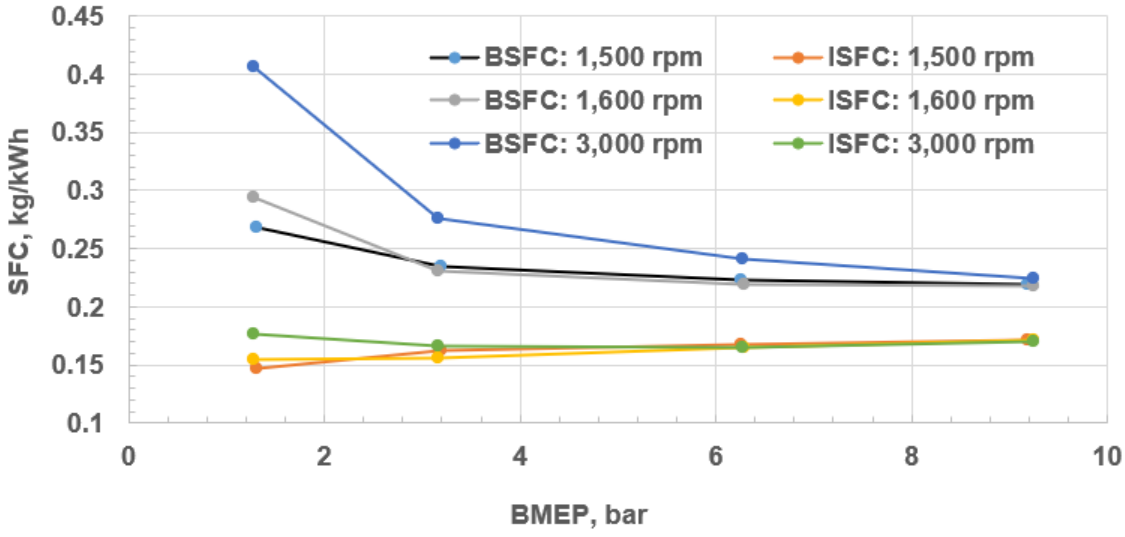

Figure 6.1 Plot of the Specific Fuel Consumption (SFC) of the engine against the Brake Mean Effective Pressure (BMEP)

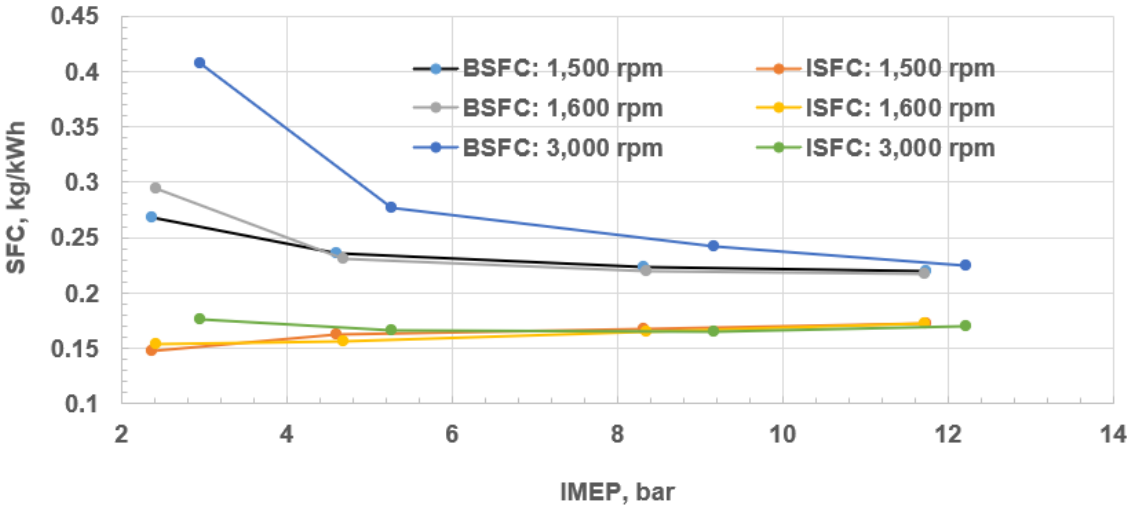

Figure 6.2 Plot of the Specific Fuel Consumption (SFC) of the engine against the Indicated Mean Effective Pressure (IMEP)

Figures 6.1 and 6.2 show that for each of the tested speeds, the BSFC of the engine decreased as the BMEP and the IMEP increased. However, the opposite trend was observed for the ISFC. Generally, the ISFC of the engine increased as the BMEP and the IMEP increased. As shown in Figures 6.1 and 6.2, at the rated speed (3,000 rpm) and high load condition (220 Nm), the BSFC of the engine was 225 g/kWh. Li et al. (2004), Lapuerta et al. (2009), and Rakopoulos et al. (2008) also reported BSFC of 225 g/kWh at the maximum load for baseline diesel in their investigations.

6.2.2 Engine efficiency

The variation of the Brake Thermal Efficiency (BTE), Indicated Thermal Efficiency (ITE), and the mechanical efficiency of the engine with the BMEP were presented graphically as shown in Figures 6.3, 6.4, and 6.5 for the three conditions of speed that were investigated.

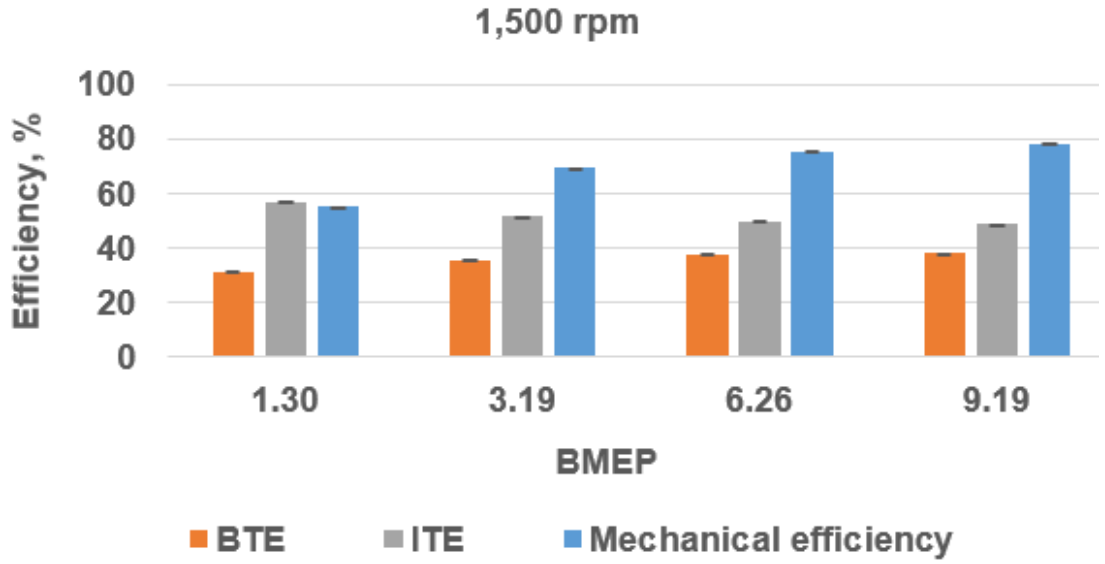

Figure 6.3 Variation of engine efficiency with BMEP (1,500 rpm)

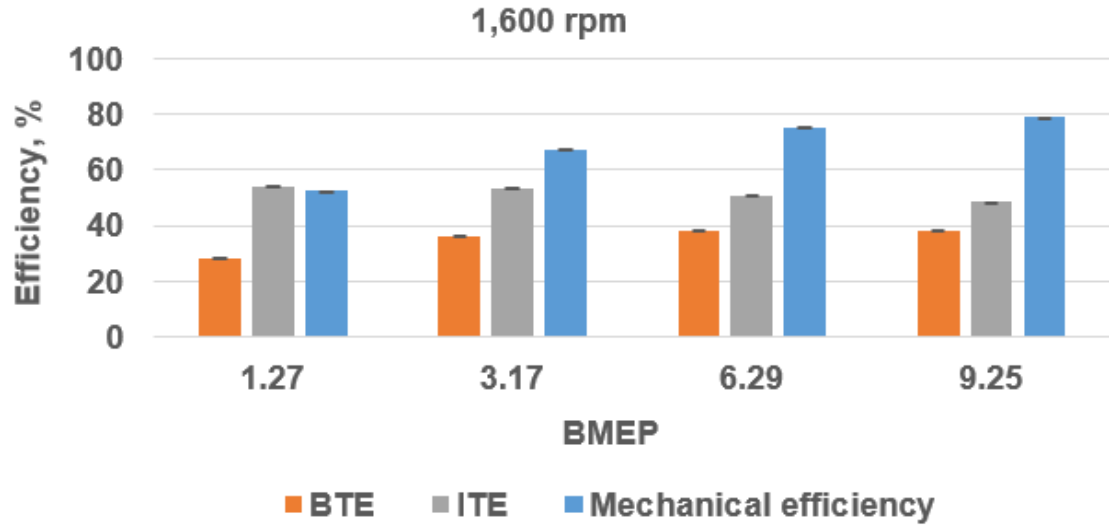

Figure 6.4 Variation of engine efficiency with BMEP (1,600 rpm)

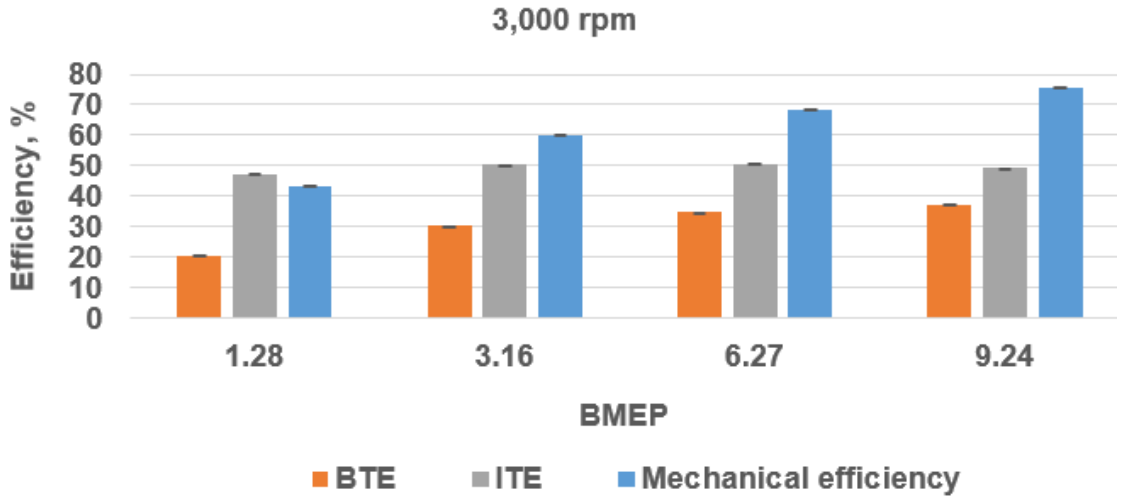

Figure 6.5 Variation of engine efficiency with BMEP (3,000 rpm)

Figure 6.3 shows that at the intermediate speed and load (1,500 rpm; 150 Nm), the BTE of the IVECO engine was 37.5%. Sukjit et al. (2014) reported the same BTE of 37.5% for the single cylinder, research diesel engine which was operated in a similar mode (1,500 rpm; 40% load) in their investigation. Furthermore, at the rated speed and high load condition, the BTE of the engine was 37% (Figure 6.5). Li et al. (2004) and Rakopoulos et al. (2008) also reported a BTE of 37% for baseline diesel at the high load condition in their investigations. Generally, it was observed that the efficiencies of the engine (BTE, ITE, and mechanical efficiency) increased as the BMEP increased (Figures 6.3 to 6.5). The engine attained the highest mechanical efficiency of 79% (typical of modern diesels) at the 1,600 rpm condition of speed. Figures 6.3 to 6.5 also show that the mechanical efficiencies of the engine decreased at the rated/maximum engine speed (3,000 rpm). This was due to the expansion of the piston rings against the cylinder liners that occurred as the speed of the engine was increased. This expansion increased the friction between the piston ring and the cylinder liners. Consequently, the frictional losses of the engine were relatively high when the engine was run at the

rated speed. Figure 6.6 also shows the observed decrease in the mechanical efficiency when the engine was run at the highest speed.

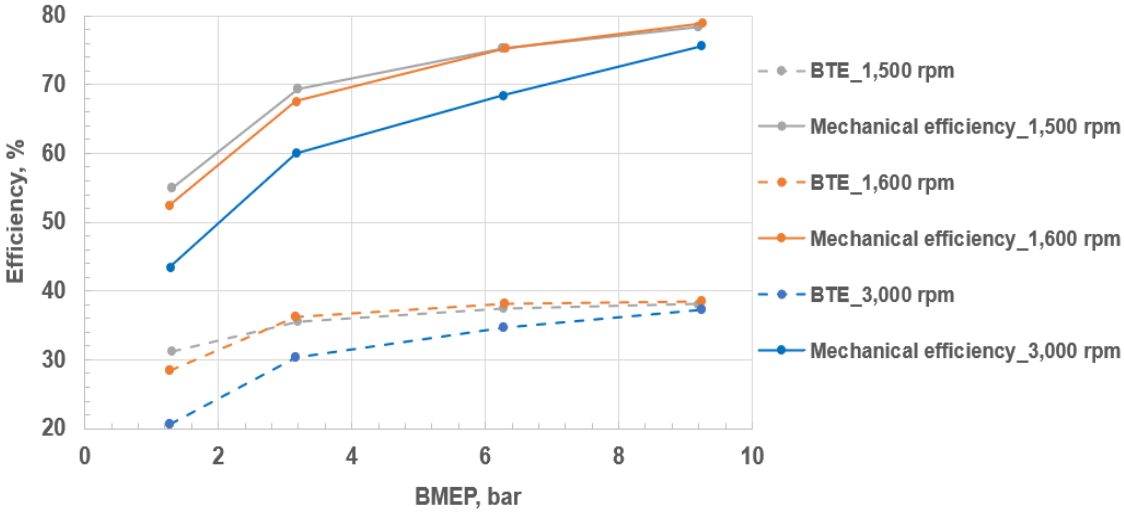

Figure 6.6 Plot of engine efficiency against the BMEP for the tested engine modes

6.2.3 Combustion stability

The Indicated Mean Effective Pressure (IMEP) data were used to investigate the combustion stability of the engine for baseline diesel (off-road diesel) at the tested modes. Figure 6.7 shows that the stability of the engine increased as the load on the engine increased for each of the tested engine speeds. Generally, the combustion stability values of the engine were below 2%. This showed that the engine had a good combustion stability when it was run on baseline diesel.

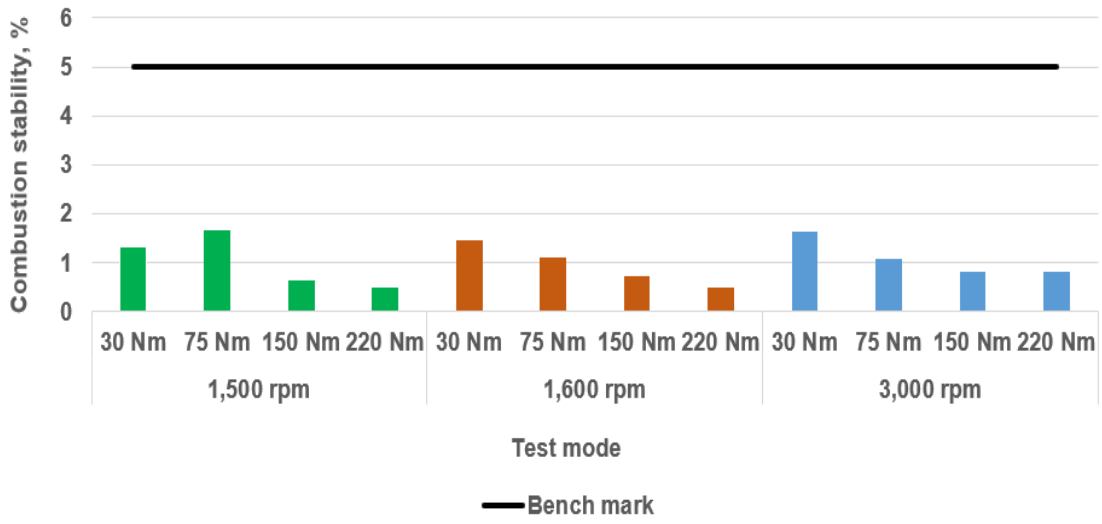

Figure 6.7 Combustion stability of the engine by IMEP

6.3 Baseline diesel emissions

The exhaust gases from the engine were sampled from two positions along the exhaust line. The two sampling points for the analysis of gaseous and particulate emissions were designated as Sampling points A and Sampling points B as depicted pictorially in Figure 6.8. The first sampling point was upstream of the DPF (sampling of engine-out exhaust) while the second sampling point was downstream of the DPF. This sampling strategy made it possible to investigate the efficiency of the after-treatment system of the engine (the DPF and DOC).

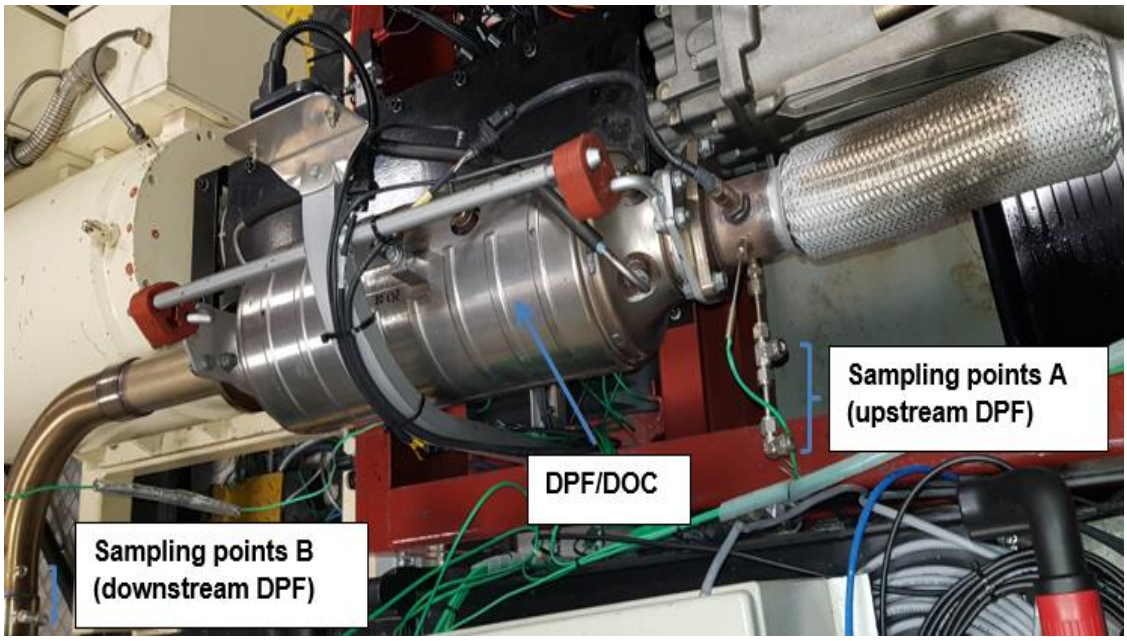

Figure 6.8 Engine exhaust sampling points (upstream and downstream of the DPF)

6.3.1 Gaseous emissions

6.3.1.1 NOx emission

Figures 6.9 to 6.16 depict the engine-out NOx emissions (NO and NO_2) for the two sampling positions shown in Figure 6.8 (upstream and downstream of the DPF). The percentage post-catalyst reductions in NO for the tested modes were expressed graphically as shown in Figure 6.17.

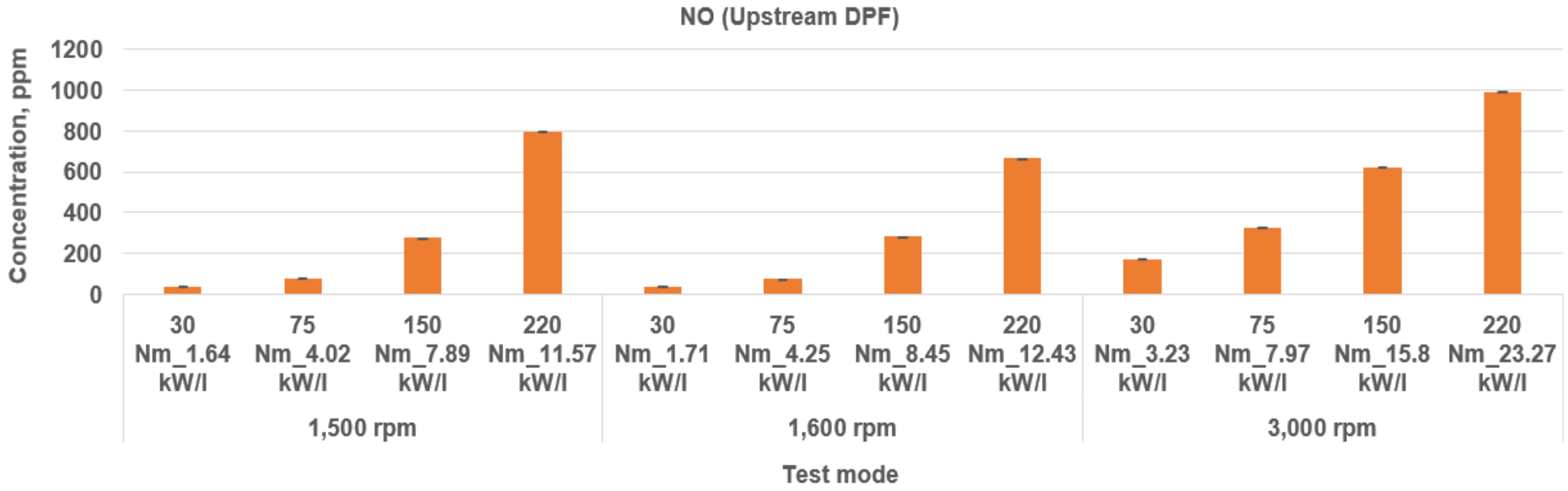

Figure 6.9 NO emissions at the tested engine modes (upstream DPF)

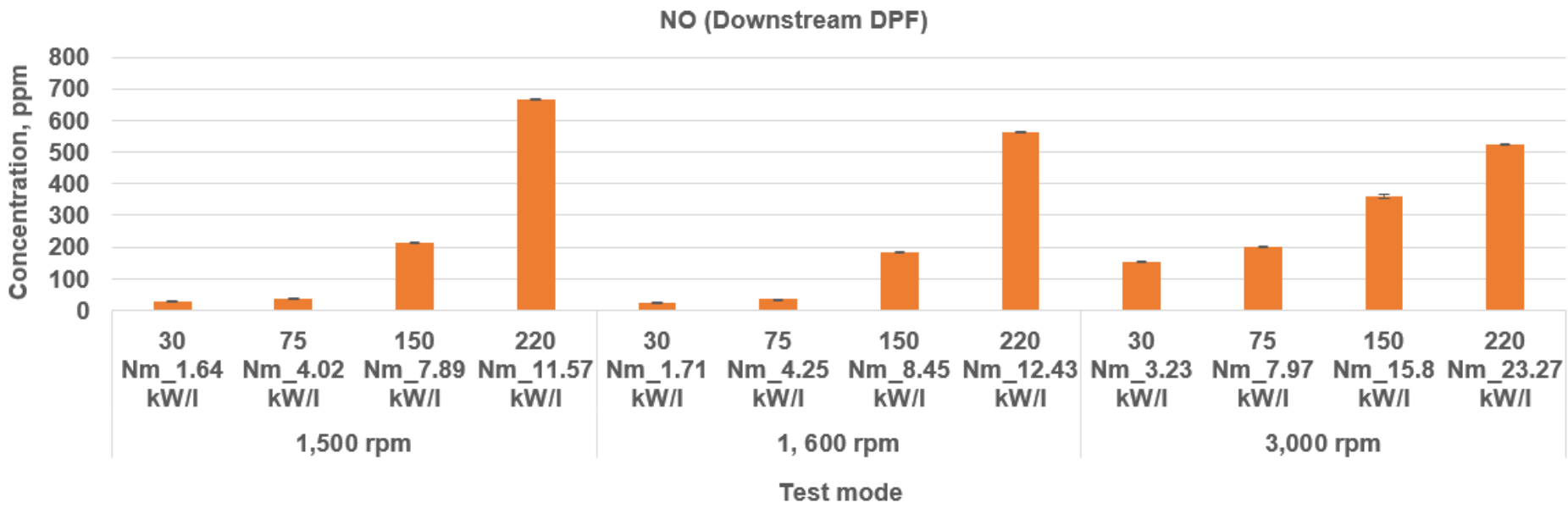

Figure 6.10 NO emissions at the tested engine modes (downstream DPF)

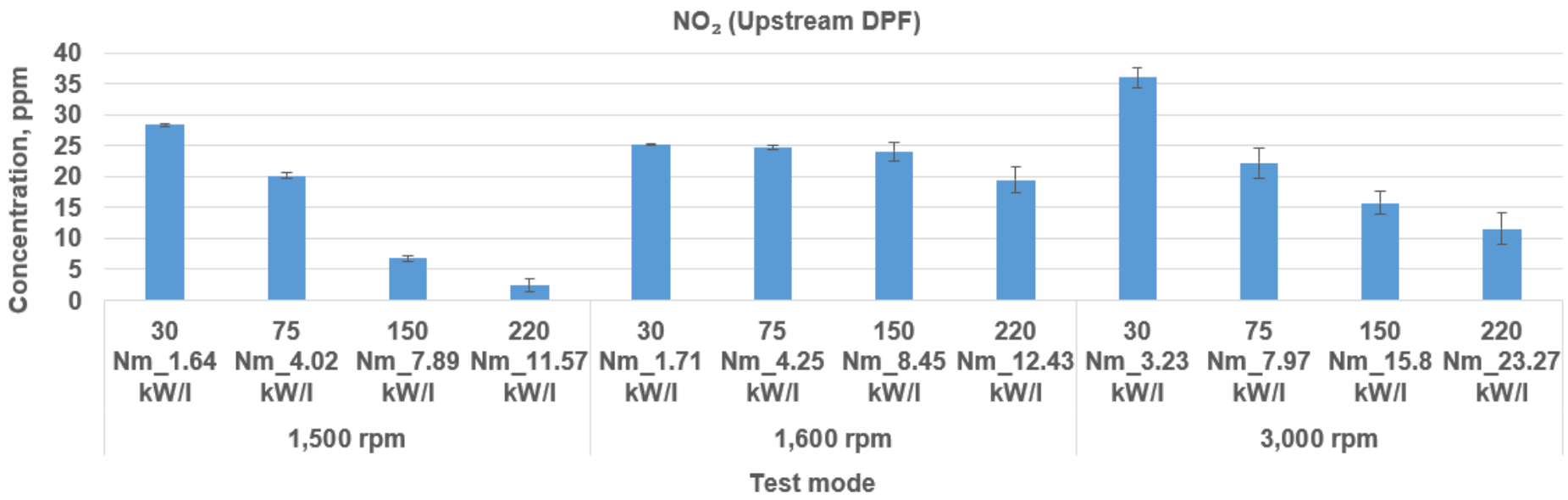

Figure 6.11 NO_2 emissions at the tested engine modes (upstream DPF)

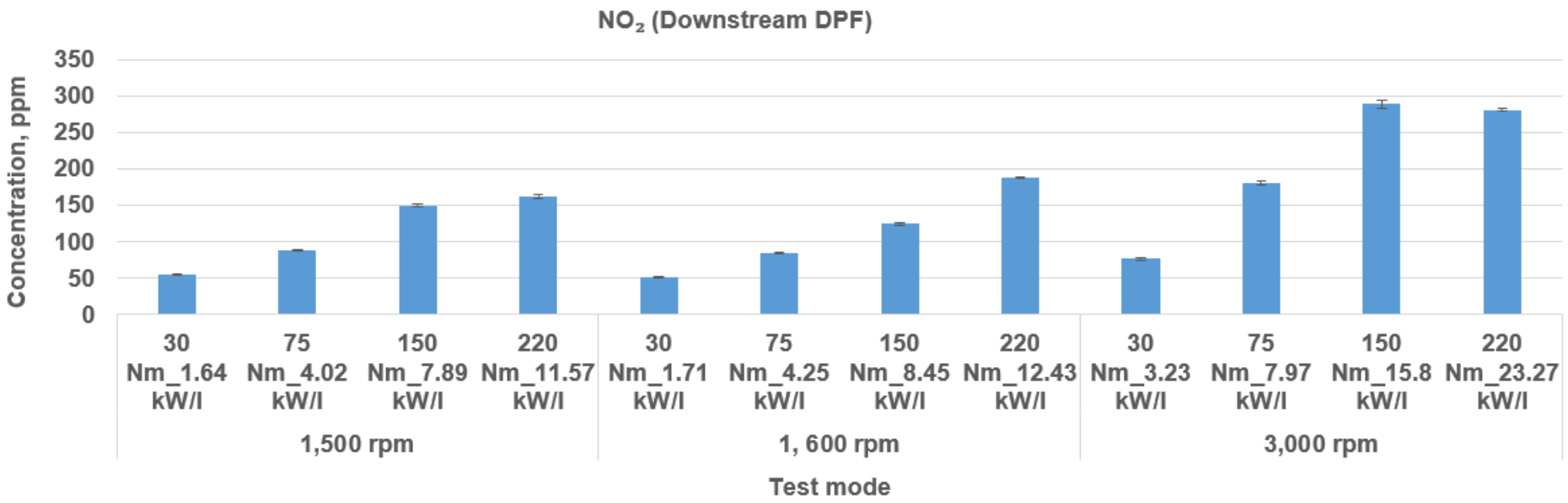

Figure 6.12 NO_2 emissions at the tested engine modes (downstream DPF)

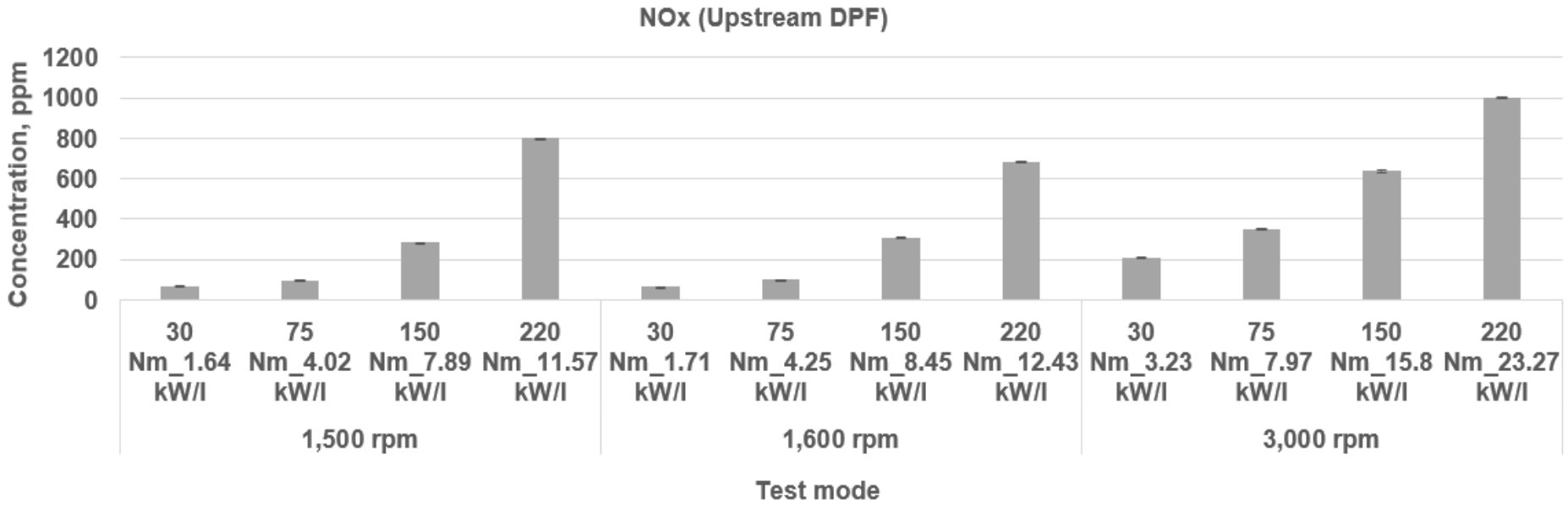

Figure 6.13 NOx emissions at the tested engine modes (upstream DPF)

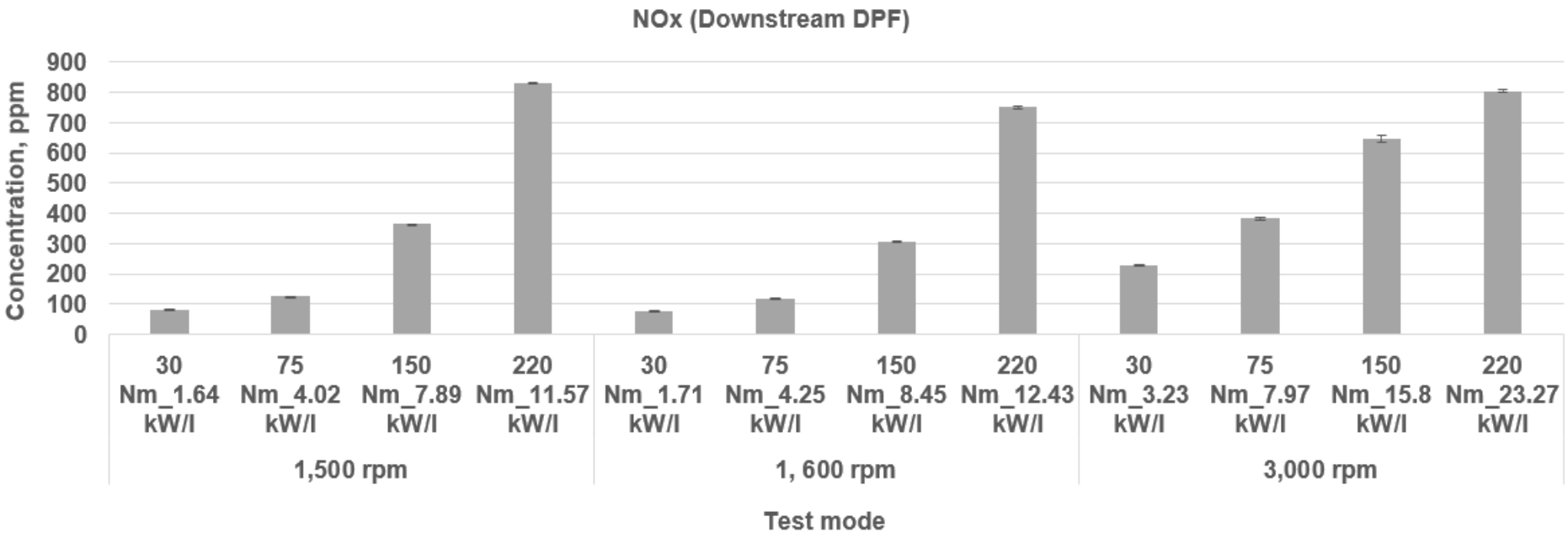

Figure 6.14 NOx emissions at the tested engine modes (downstream DPF)

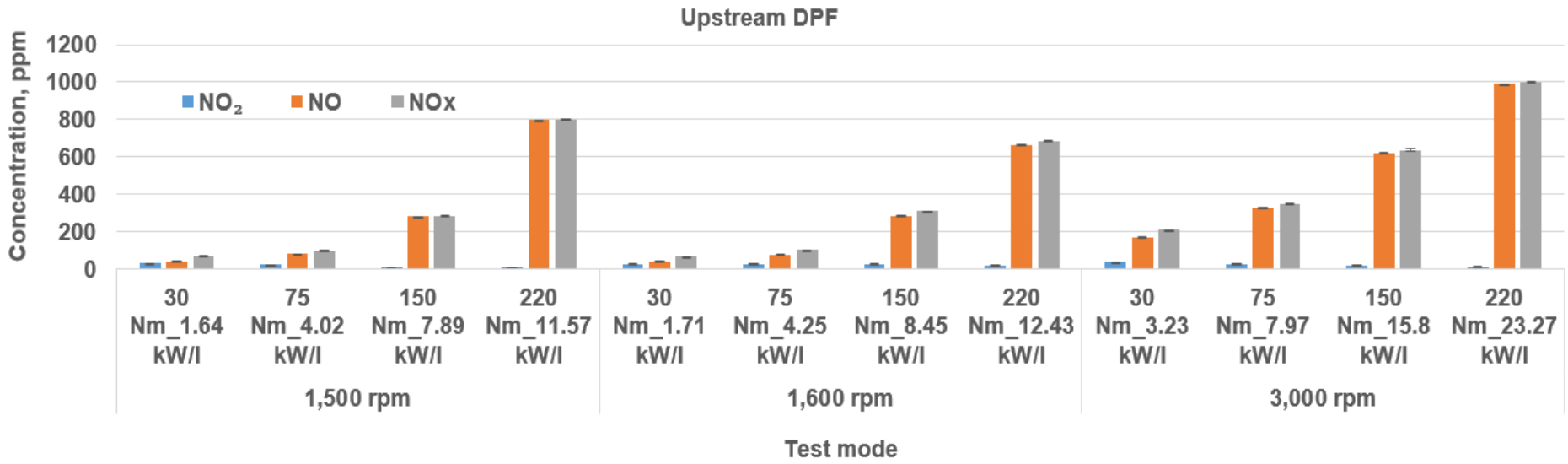

Figure 6.15 Summary of NOx emissions at the tested engine modes (upstream DPF)

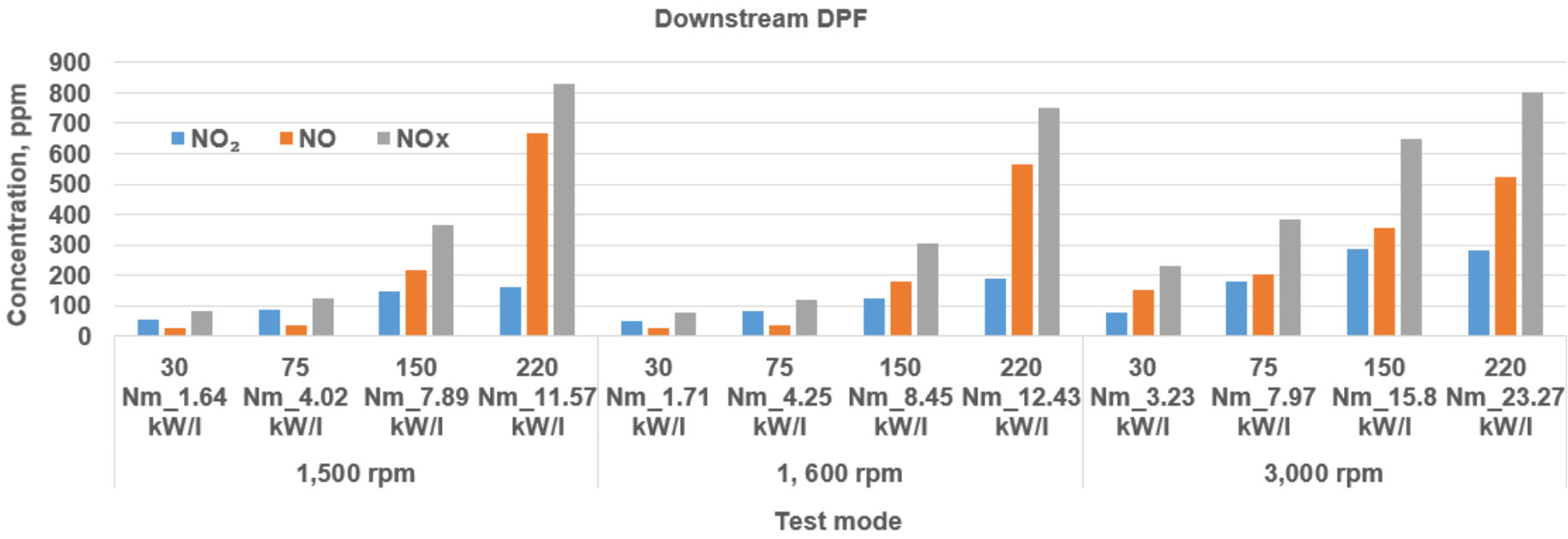

Figure 6.16 Summary of NOx emissions at the tested engine modes (downstream DPF)

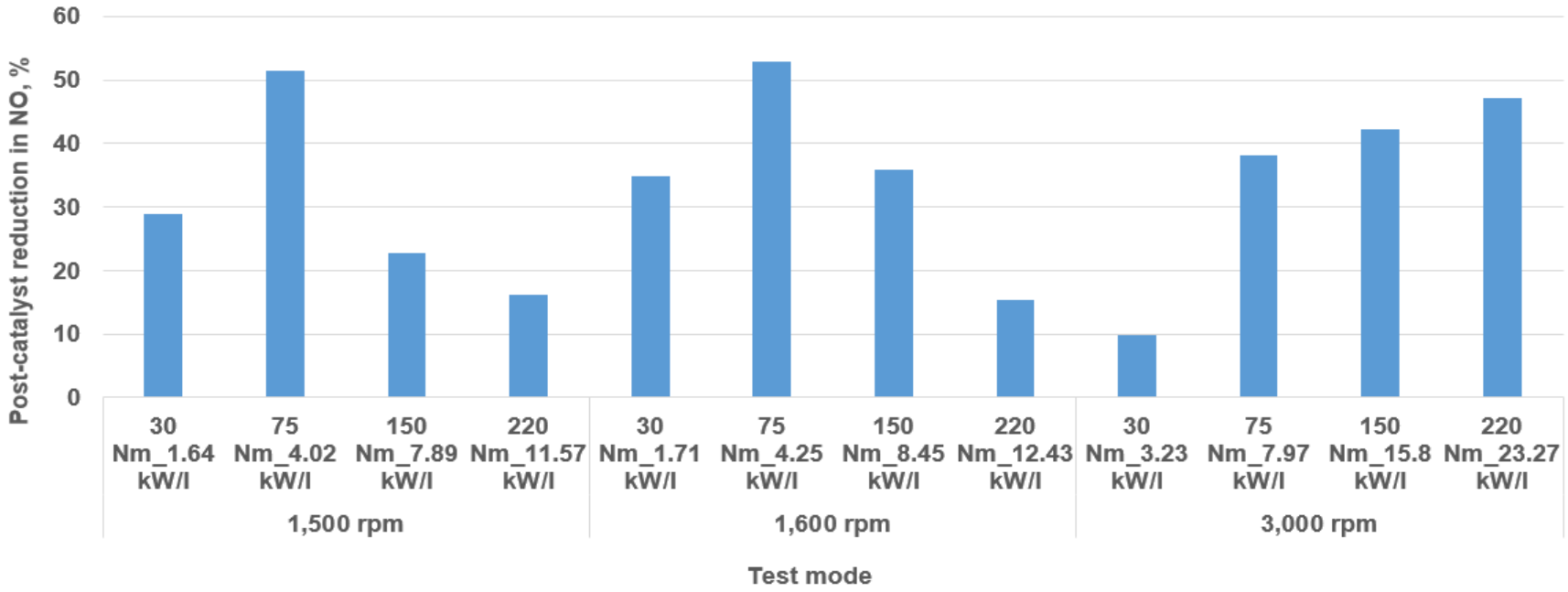

Figure 6.17 Evaluated post-catalyst reduction in NO for the tested modes

The emission results for NO and NOx (upstream and downstream of the DPF) as well as the results for NO_2 (downstream of the DPF) show that the emission levels increased as the power of the engine increased for each of the tested speeds (Figures 6.9 to 6.10 and Figures 6.12 to 6.14). This was due to the increase in the combustion temperature as the power of the engine increased. High combustion temperatures favour NO and NOx production in ICEs. Table 6.2 shows how the measured exhaust manifold temperatures increased as the torque of the engine was increased.

Table 6.2 Measured exhaust manifold temperatures

Speed, rpm	**Torque, Nm**	**Power/displaced volume, kW/l**	**Exhaust manifold temperature, ^oC**
1,500	30	1.64	215
	75	4.02	320
	150	7.89	469.3
	220	11.57	564
1,600	30	1.71	227.3
	75	4.25	333.5
	150	8.45	475.4
	220	12.43	549
3,000	30	3.23	274
	75	7.97	352.3
	150	15.8	448.4

	220	23.27	510.8

The opposite trend was observed for NO_2 emissions upstream of the DPF. Figure 6.11 shows that the engine-out NO_2 emissions decreased for each of the tested speed conditions as the torque of the engine increased. This was due to the observed increase in the temperature of the flame as the torque was increased. Engine-out NO_2 emission levels decrease as the engine warms up. The observed post-DPF increase in the levels of NO_2 for the tested speeds as the torque increased (Figure 6.12) was due to the conversion of NO to NO_2 by the catalyst. The conversion of NO to NO_2 by the catalyst was enhanced as the temperature of the flame increased at the relatively high conditions of power. The summary of the NOx emission levels presented in Figures 6.15 and 6.16 show that the emission aftertreatment device led to 47% and 20% reductions in the levels of NO and NOx respectively for the 3,000 rpm; 220 Nm test mode. The observed maximum concentration for NOx in the current work was 1,000.5 ppm at the highest power condition (3,000 rpm; 220 Nm). The observed maximum concentration for NOx in this work compares well to the reported typical 500 to 1,000 ppm emission range for NOx in ICEs (Heywood, 1988).

Ethanol-blended fuels (DE fuel blends) are known to reduce the temperature of the flame when they are utilised in ICEs due to the relatively high heat of vaporisation of ethanol. Therefore, if the current engine was run on DE fuel blends, the same trends shown in Figures 6.9 and 6.13 would be observed for NO and NOx except that the levels of the pollutants would be relatively low compared to the baseline results.

6.3.1.2 THC emissions

Figures 6.18 and 6.19 show the Total hydrocarbon (THC) emissions for the tested conditions (upstream and downstream of the DPF respectively). Figure 6.18 shows that at all the tested conditions of speed, the engine-out THC concentrations reduced as the torque of the engine increased. The observed reduction in the engine-out THC levels with increase in torque (power) was due to the increase in the temperature of the flame that occurred when the power of the engine was increased (Table 6.2).

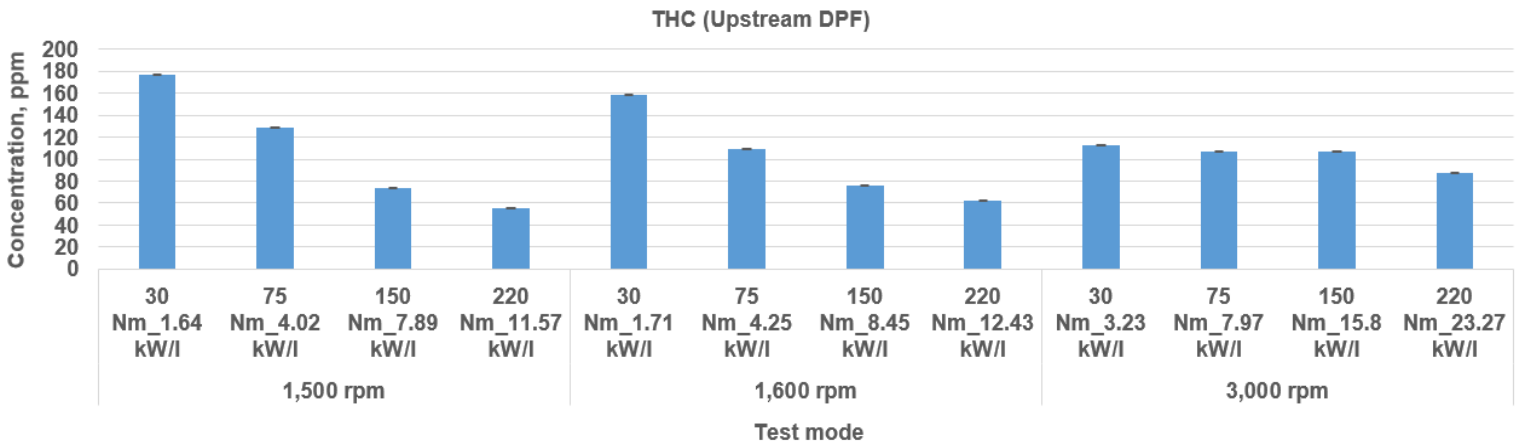

Figure 6.18 Total hydrocarbons (THC) emissions at the tested engine modes (upstream DPF)

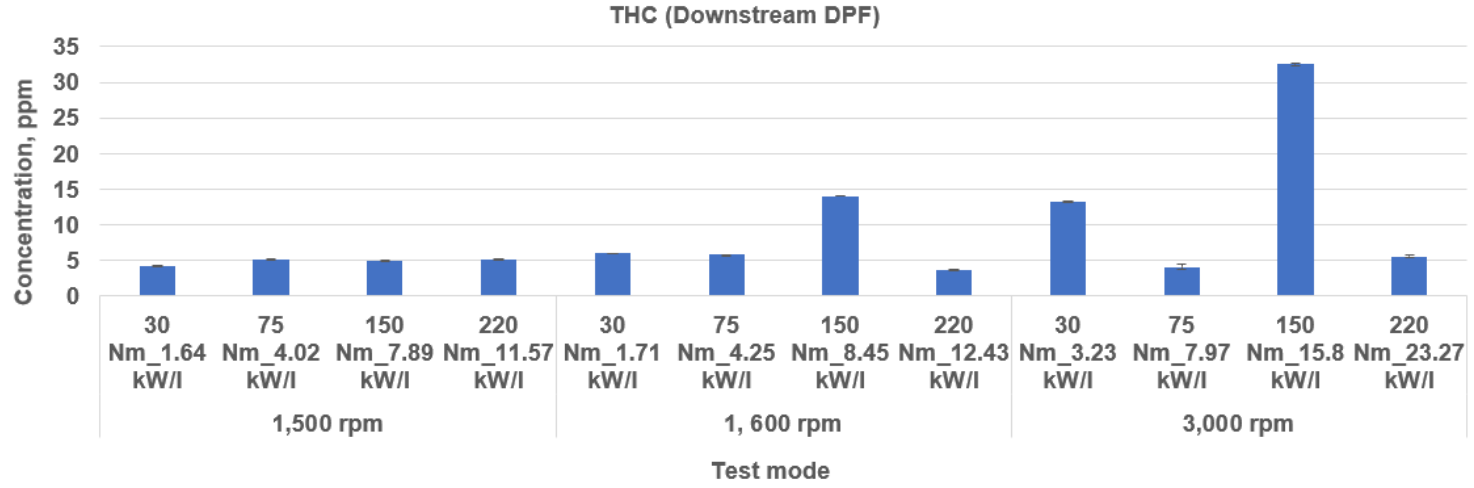

Figure 6.19 Total hydrocarbons (THC) emissions at the tested engine modes (downstream DPF)

The evaporation of the injected fuel mass was enhanced by the relatively high flame temperatures that resulted when the engine was operated at the relatively high torque conditions for each of the tested speeds. This in turn enhanced the combustion of the injected fuel thereby leading to the observed decrease in the emission levels for THC with increase in torque. The THC concentration was highest when the engine was run at 1,500 rpm; 30 Nm mode (177 ppm). This was due to the relatively low flame temperature (215 ^{o}C) at the 1,500 rpm; 30 Nm mode compared to the flame temperature at the highest condition of torque for the same engine speed (564 ^{o}C). The THC emission for CI engines was reported to be of the order of 600 ppm (Heywood, 1988). The observed maximum engine-out THC concentration in this work is 71% less than the typical THC concentration reported in literature. The engine-out THC concentrations in this work (Figure 6.18) were generally low due to lean combustion as well as the Multiple Fuel Injection Strategy (MFIS) of the diesel engine that was used.

Figure 6.19 shows the efficiency of the DOC at reducing the concentration of THC in the exhaust of the engine. As observed in Figure 6.19, the THC concentration in the exhaust that was sampled post-catalyst was about 5 ppm except for the 1,600 rpm; 150 Nm, 3,000 rpm; 30 Nm and 3,000 rpm; 150 Nm test modes. The observed peaks at these three test modes were due to cold start, during which time the catalyst had not heated up to its light off temperature.

6.3.1.3 CO emissions

Figures 6.20 and 6.21 present the CO emissions for the tested conditions (upstream and downstream DPF).

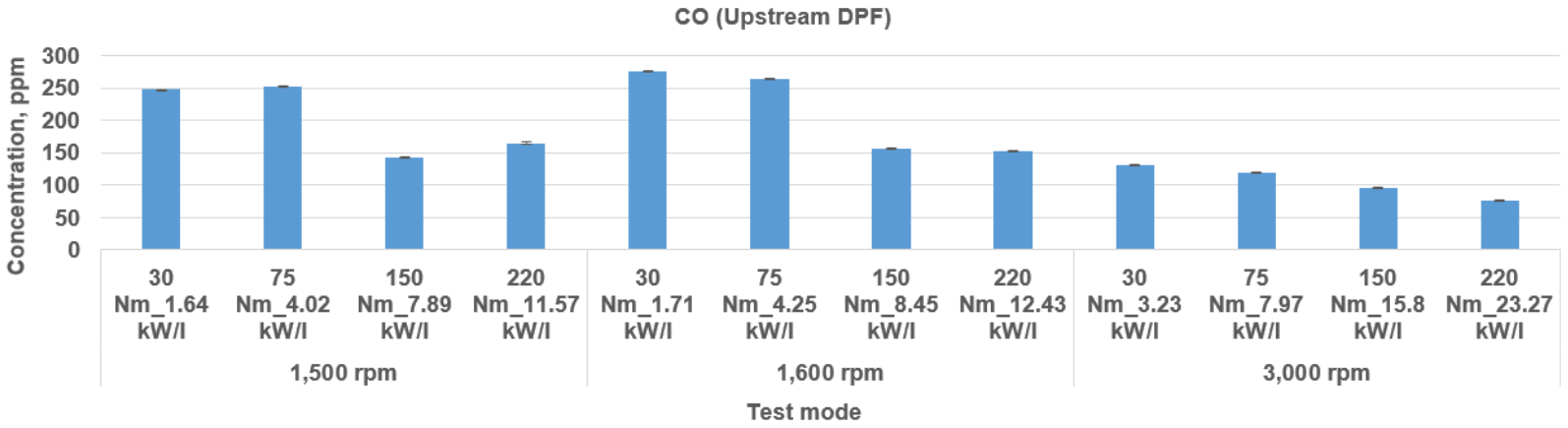

Figure 6.20 CO emissions at the tested engine modes (upstream DPF)

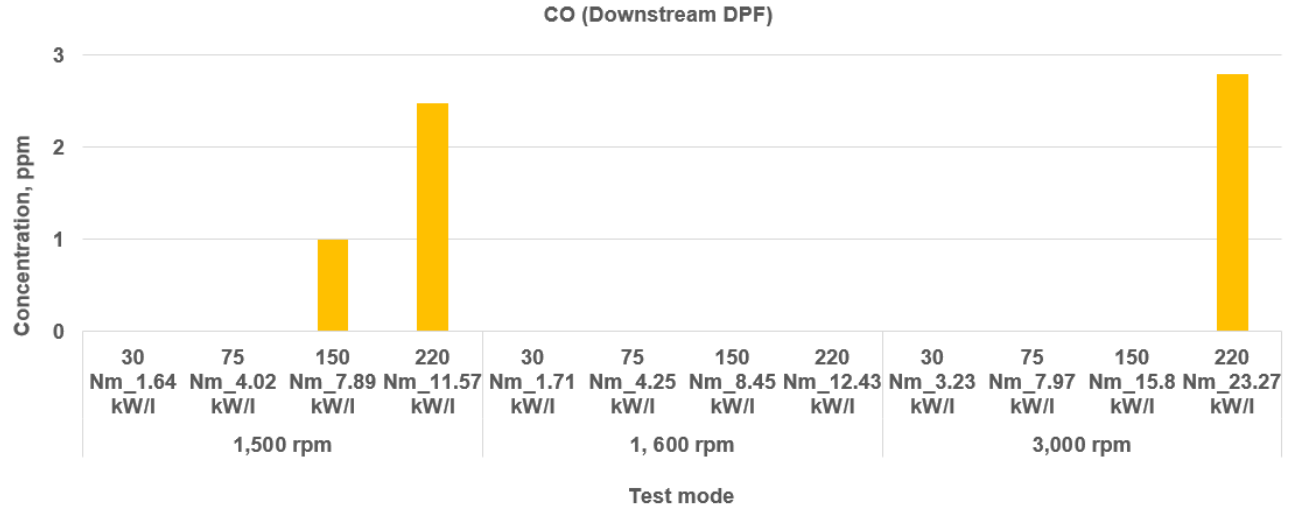

Figure 6.21 CO emissions at the tested engine modes (downstream DPF)

Generally, for each of the tested speeds, the concentration of CO decreased as the torque of the engine increased (Figure 6.20). The temperature of the exhaust gas increased as the torque of the engine increased (Table 6.2). It is known that high combustion temperatures favour the oxidation of CO to CO_2. Therefore, as the torque of the engine was increased, the flame temperature increased and the oxidation of CO to CO_2 was enhanced leading to relatively low CO levels at the high torque conditions.

CO emissions from CI engines are generally low due to lean combustion. The typical concentration of CO for ICEs is 200 g/kg fuel (Heywood, 1988). The observed maximum concentration of CO in this work (Figure 6.20) was 11 g/kg fuel (275 ppm). The CO levels in the exhaust that was sampled downstream of the catalyst (Figure 6.21) showed that the DOC of the engine virtually eliminated the tailpipe CO emissions of the engine. The detected concentrations of CO were less than 3 ppm.

The emission levels of the pollutant gases in g/kWh were also compared graphically for the upstream and the downstream sampling positions as depicted in Figures 6.22 to 6.24. The observed maximum engine-out NOx in this work was 7.7 g/kWh at the rated speed and high load condition (Figure 6.24 (a)). The observed maximum engine-out NOx for baseline diesel in this work is 23% less than the NOx emission level (10 g/kWh) that was reported in literature (Rakopoulos et al. (2008), Li et al. (2004)).

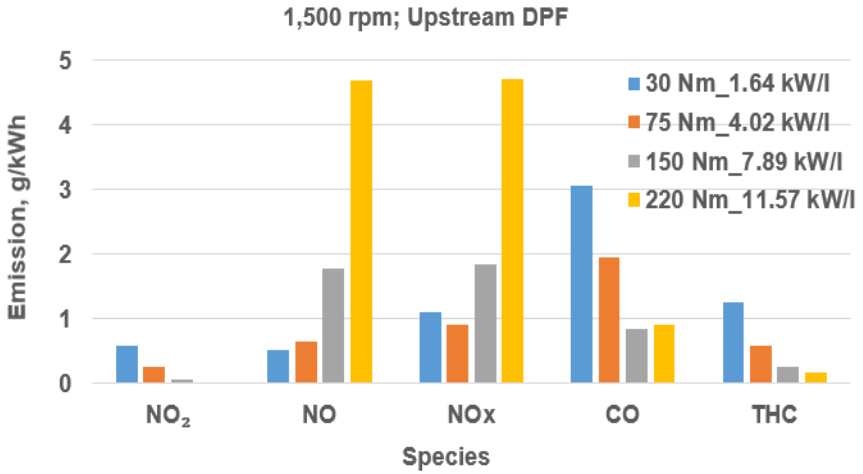

(a)

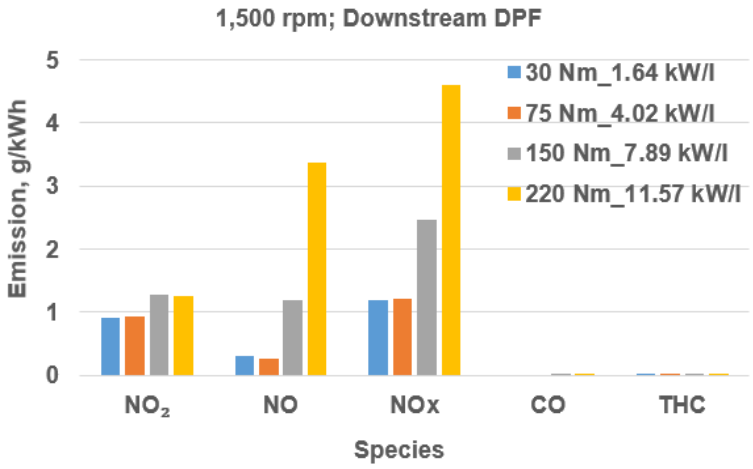

(b)

Figure 6.22 Comparison of emission levels of pollutant gases for 1,500 rpm modes: a) Upstream DPF b) Downstream DPF

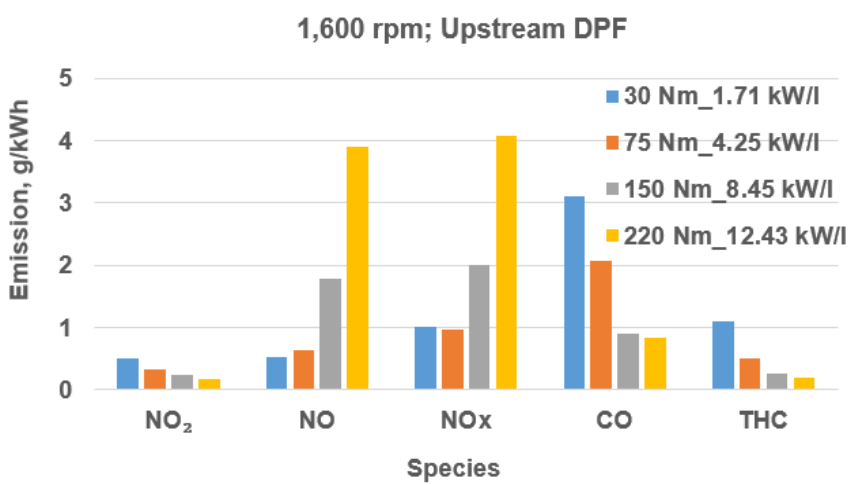

(a)

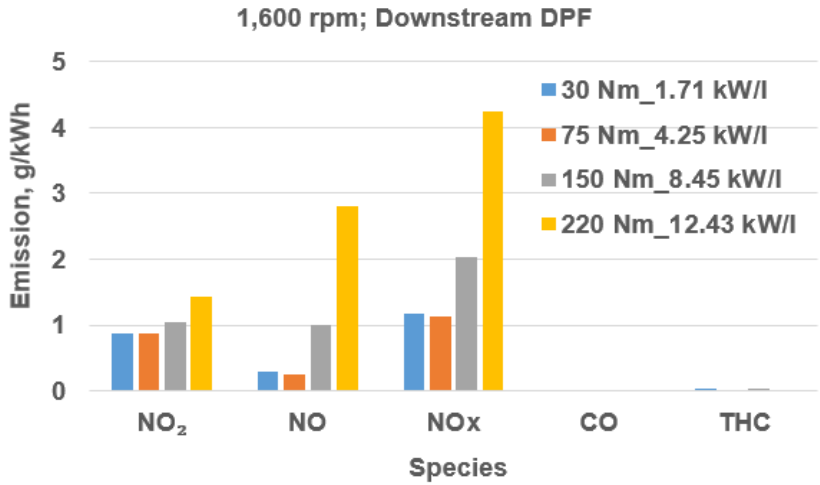

(b)

Figure 6.23 Comparison of emission levels of pollutant gases for 1,600 rpm modes a) Upstream DPF b) Downstream DPF

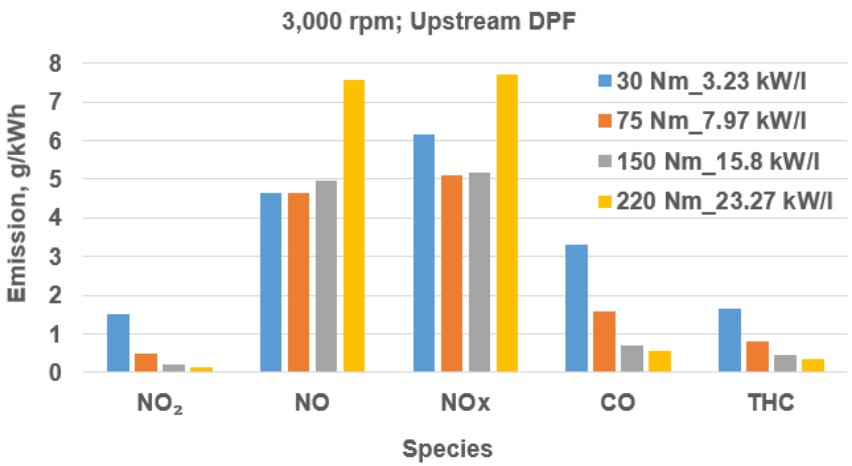

(a)

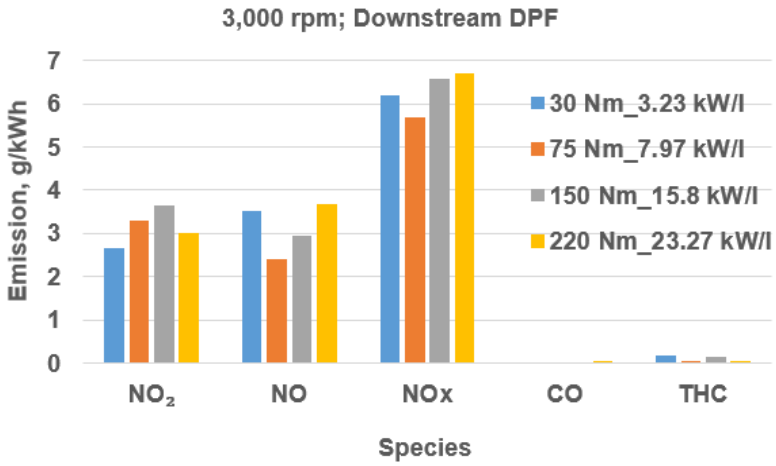

(b)

Figure 6.24 Comparison of emission levels of pollutant gases for 3,000 rpm modes a) Upstream DPF b) Downstream DPF

The maximum baseline engine-out NOx in this work is lower than the NOx levels reported in literature because of the MFIS of the IVECO engine. The MFIS of the engine enhanced efficient air-fuel mixing, thereby minimising the formation of local rich zones within the combustion chamber of the engine. Local fuel rich zones lead to high combustion temperatures which in turn leads to high levels of engine-out NOx.

The maximum engine-out CO emissions range from 3.05-3.32 g/kWh for the lowest speed, lowest load (1,500 rpm; 30 Nm) and the rated speed, lowest load (3,000 rpm; 30 Nm) engine modes (Figures 6.22 to 6.24). Li et al. (2004) reported a baseline CO emission level of 5.32 g/kWh for the investigation that they conducted at 2,200 rpm and maximum load. The highest engine-out baseline CO level in this work is 38% less than the value reported in literature. At 1,500 rpm; 40% load (similar to the 1,500 rpm; 150 Nm mode in this work), Sukjit et al. (2014) reported a baseline CO emission level of 1.8 g/kWh. The baseline CO emission level of the IVECO engine for the 1,500 rpm; 50% load condition is 0.85 g/kWh (53% lower than the baseline CO level reported by Sukjit et al. (2014)). The baseline engine-out CO emission level in this work is lower than the reported values in literature also because of the MFIS of the IVECO engine. The engine-out baseline THC emission level in this work at the rated speed and high load condition was 0.35 g/kWh as shown in Figure 6.24 (a). This is lower than the value reported by Li et al. (2004) (0.95 g/kWh) at 100% load and rated speed due to the enhanced combustion of the injected fuel in the modern IVECO engine. The MFIS of the engine enhanced the combustion of the injected fuel thereby leading to relatively low baseline THC emissions from the IVECO engine compared to the baseline THC levels reported in literature.

Figures 6.22 (b), 6. 23 (b), and 6.24 (b) graphically depict the significant reduction in the levels of CO and THC emissions by the catalyst.

6.3.2 Particulate emissions

The particulate emission results were analysed in terms of Particle Number (PN) and Particle Matter (PM). This section presents the effect of changing the torque (load) of the engine at constant engine speed on the particulate emissions. The effect of changing the speed of the engine at constant torque on the engine-out particulate emissions (PN) were also investigated. The particulate yield results for the tested engine modes were estimated from the logged PN data.

6.3.2.1 Effects of changing the load of the engine at constant speed on particulate emissions

Figures 6.25 to 6.45 present the particulate emission results for the 1,500 rpm, 1,600 rpm and 3,000 rpm test modes. Figures 6.25 to 6.27 show the effect of varying the load on the engine at constant speed on the particulate emission from the engine (engine-out particulate emission). The nucleation mode on the bimodal Particle Number (PN) concentration profile in diesel engines usually occurs in the nanoparticles diameter range (Dp<50 nm) while the accumulation/agglomeration mode usually occurs in the ultrafine particles diameter range (Dp<100 nm) (Kittelson, 1998). However, as shown in Figures 6.25 to 6.45, a second accumulation mode was observed in the PN and PM distributions of the engine. The second accumulation mode usually occurs at Dp<500 nm but in the current work, it occurred between 500 and 1,000 nm for the tested conditions (Section 6.3.2.3 explains the observed occurrence of the second accumulation mode between 500 and 1,000 nm Dp).

Figures 6.25 to 6.27 show that, at the low load conditions (30 Nm and 75 Nm) for each of the tested speeds, the peak PN occurred in the agglomeration mode.

However, at the relatively high load conditions (150 Nm and 220 Nm), the peak PN occurred in the nucleation mode (the number of nucleation mode particles was larger than that of agglomeration mode). The peak PN occurred in the agglomeration mode at the low load conditions due to the relatively low flame temperatures that resulted when the engine was run at the low load conditions. The relatively low combustion temperatures at the low load conditions enhanced particle growth (the attachment of condensed gas-phase species onto the nucleation mode particles/spherules as well as the collision of spherules to form spheroids). Therefore, the PN concentrations of the agglomeration mode particles were greater than those of the nucleation mode particles at the low load conditions. This inadvertently led to the occurrence of the peak PN in the agglomeration mode when the engine was run at the low load conditions (Figures 6.25 to 6.27).

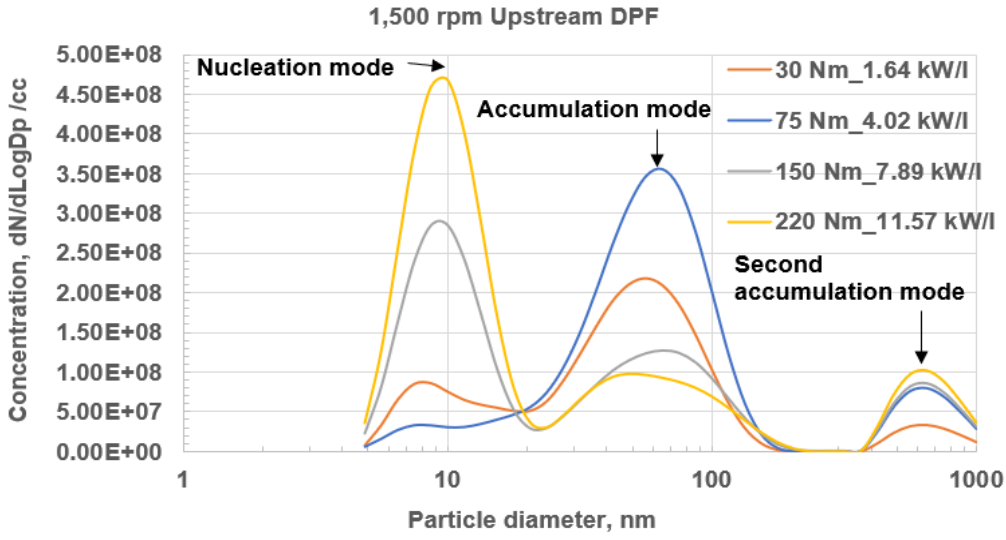

Figure 6.25 Baseline engine-out particulate emissions (PN) for 1,500 rpm modes

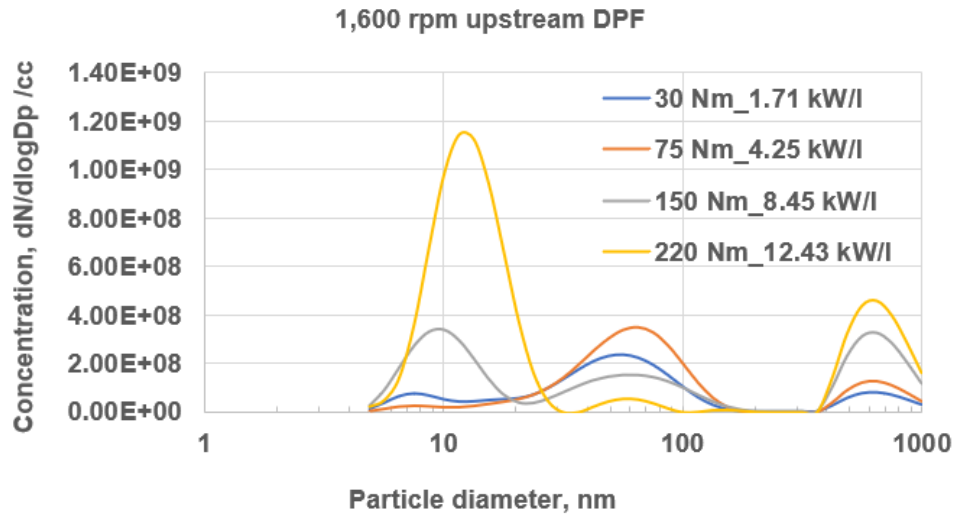

Figure 6.26 Baseline engine-out particulate emissions (PN) for 1,600 rpm modes

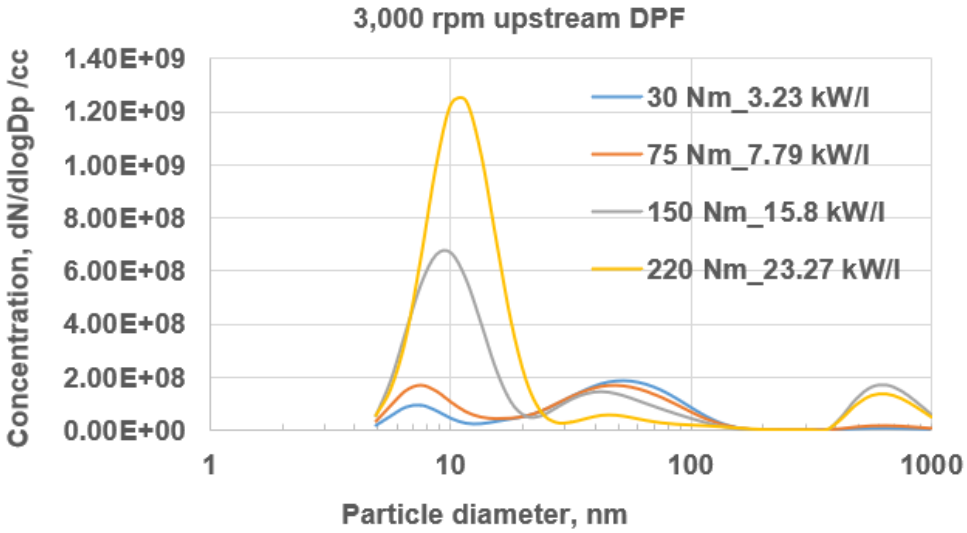

Figure 6.27 Baseline engine-out particulate emissions (PN) for 3,000 rpm modes

Figures 6.28 to 6.45 depict the particulate emission profiles upstream and downstream of the DPF. Figure 6.28 shows the 99.9% efficiency of the DPF of the engine. Figures 6.33, 6.39, and 6.45 present the PM profiles. Figures 6.32, 6.38, and 6.44 also show that at the medium and high load conditions for each of the tested speeds, the number of nanoparticles (nucleation mode particles) in the engine-out exhaust was more than the number of the agglomeration mode particles. Heywood (1988) reported that, at temperatures > 500 ^{o}C, the emitted

particles were predominantly clusters of small spheres (spherules) of carbon with individual spherule Dp in the range of 15 to 30 nm. However, at temperatures below 500 ^{o}C, condensed heavy molecular weight organic compounds were adsorbed on the spherules. It would be expected then that, at temperatures > 500 ^{o}C, the diesel engine-out exhaust would predominantly consist of nucleation mode particles (that is, the peak PN would occur in the nucleation mode) while at temperatures < 500 ^{o}C, the peak number concentration of agglomeration mode particles would be greater than that of the nucleation mode. In the current work, at temperatures > 448 ^{o}C, corresponding to the higher torque conditions: 150 Nm and 220 Nm (Table 6.2), it was observed that the peak PN occurred in the nucleation mode. However, at temperatures < 448 ^{o}C, the peak PN occurred in the agglomeration mode (Figures 6.32, 6.38, and 6.44). This compares well with what was reported in literature.

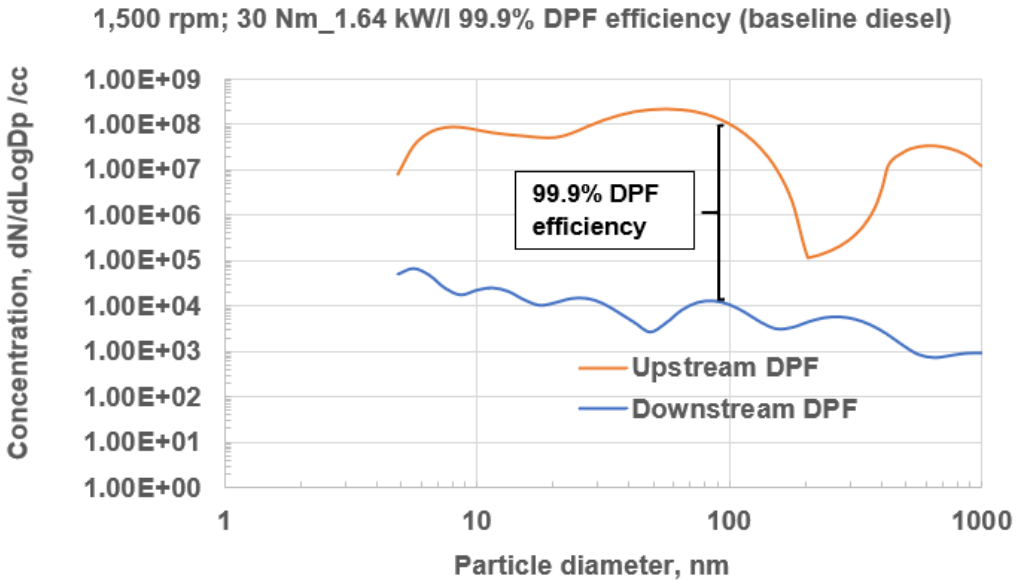

Figure 6.28 Particulate number profiles (1,500 rpm; 30 Nm_1.64 kW/l)

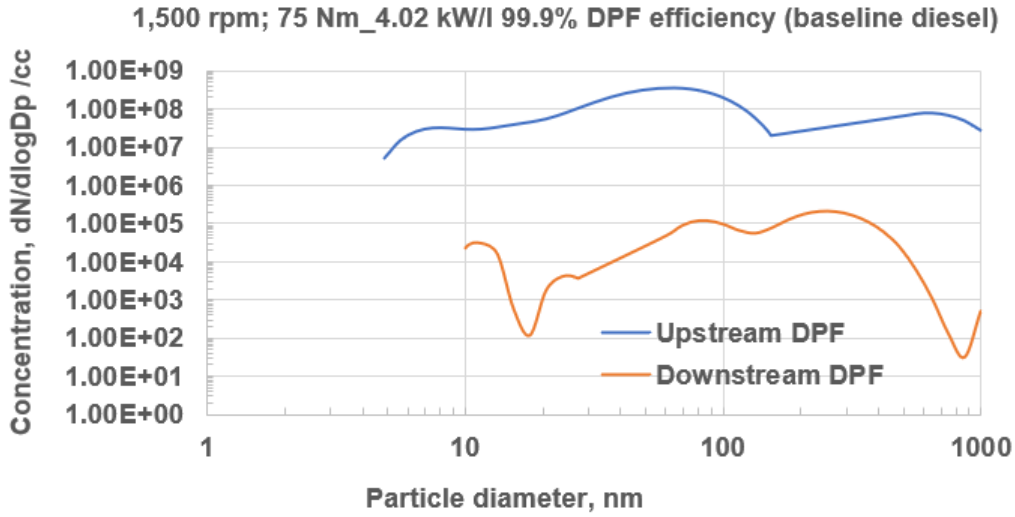

Figure 6.29 Particulate number profiles (1,500 rpm; 75 Nm_4.02 kW/l)

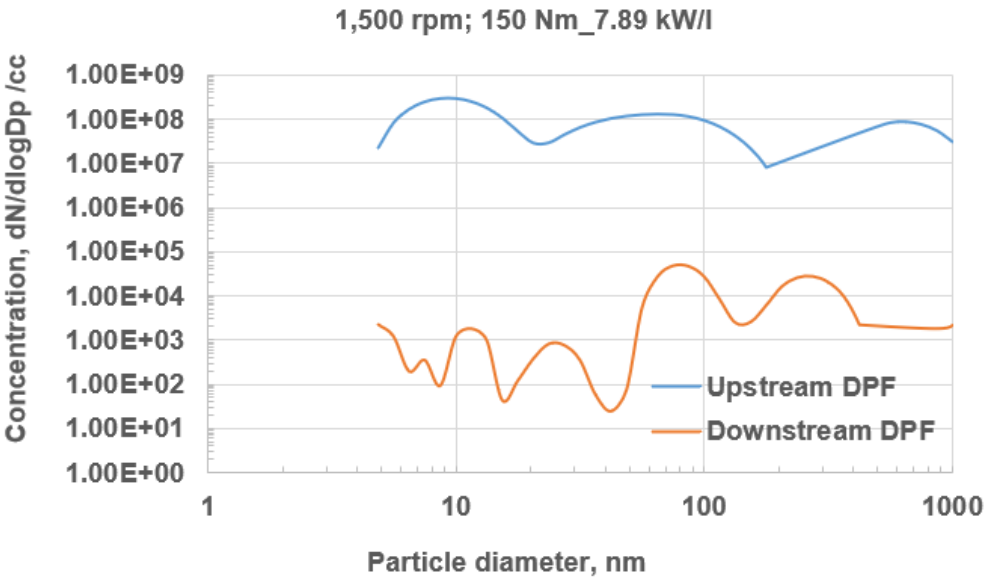

Figure 6.30 Particulate number profiles (1,500 rpm; 150 Nm_7.89 kW/l

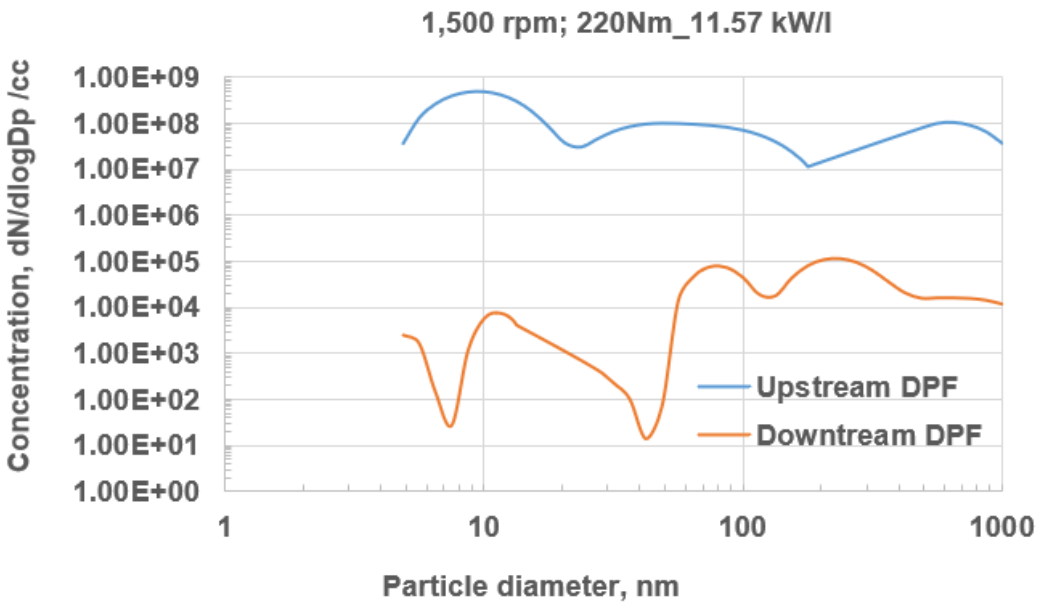

Figure 6.31 Particulate number profiles (1,500 rpm; 220 Nm_11.57 kW/l)

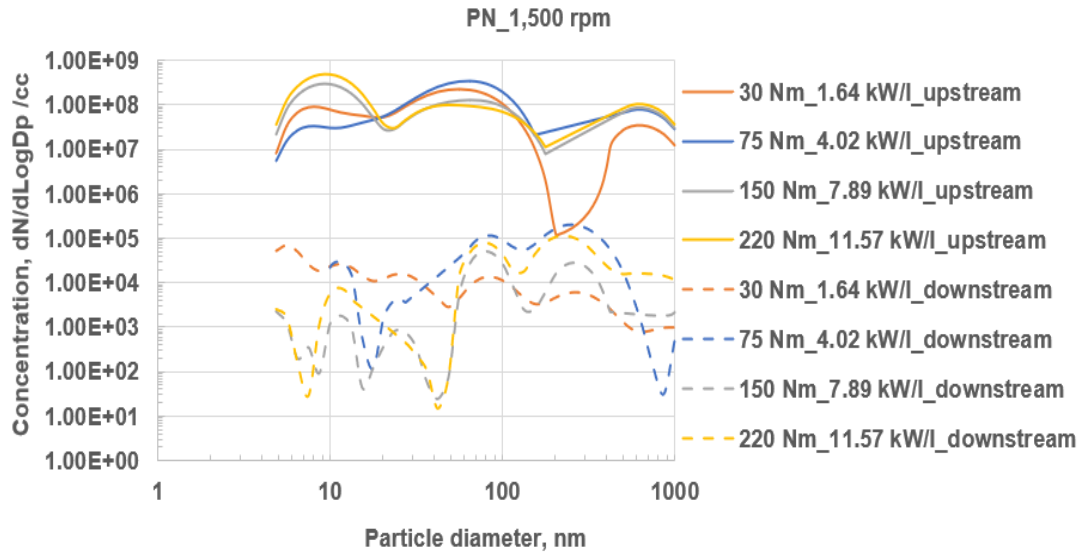

Figure 6.32 Comparison of PN emissions (1,500 rpm modes)

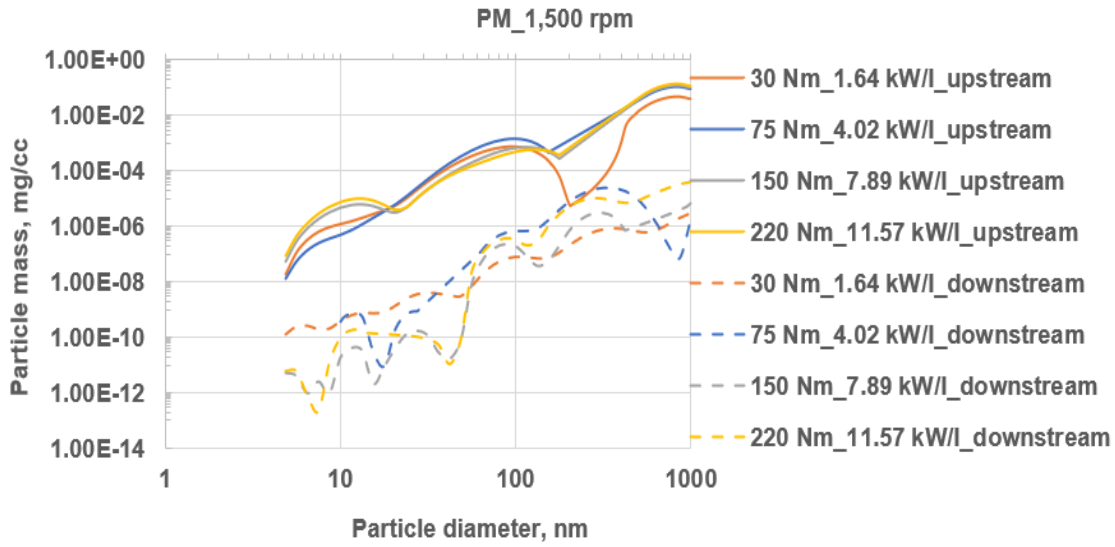

Figure 6.33 Comparison of PM emissions (1,500 rpm modes)

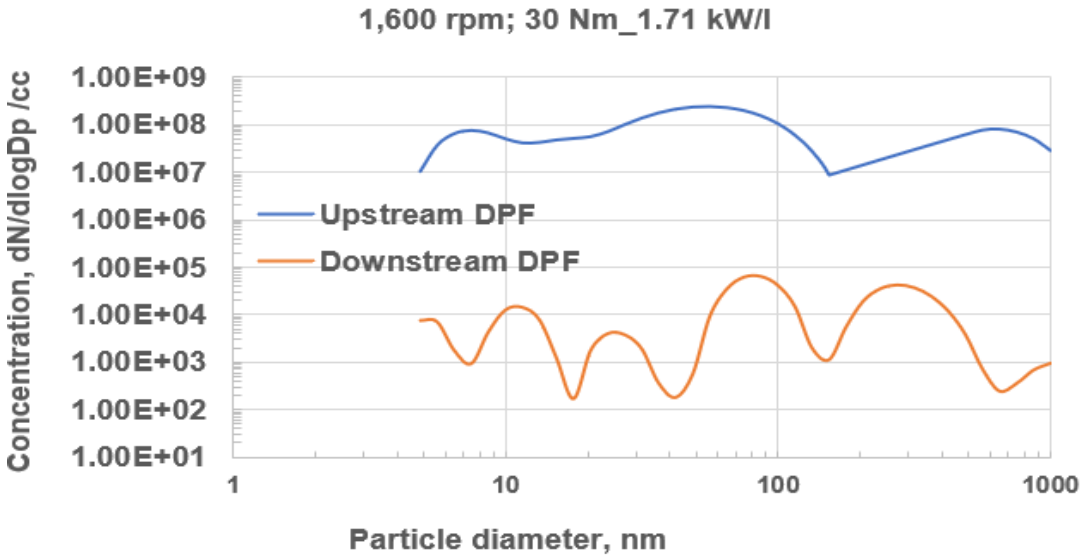

Figure 6.34 Particulate number profiles (1,600 rpm; 30 Nm_1.71 kW/l)

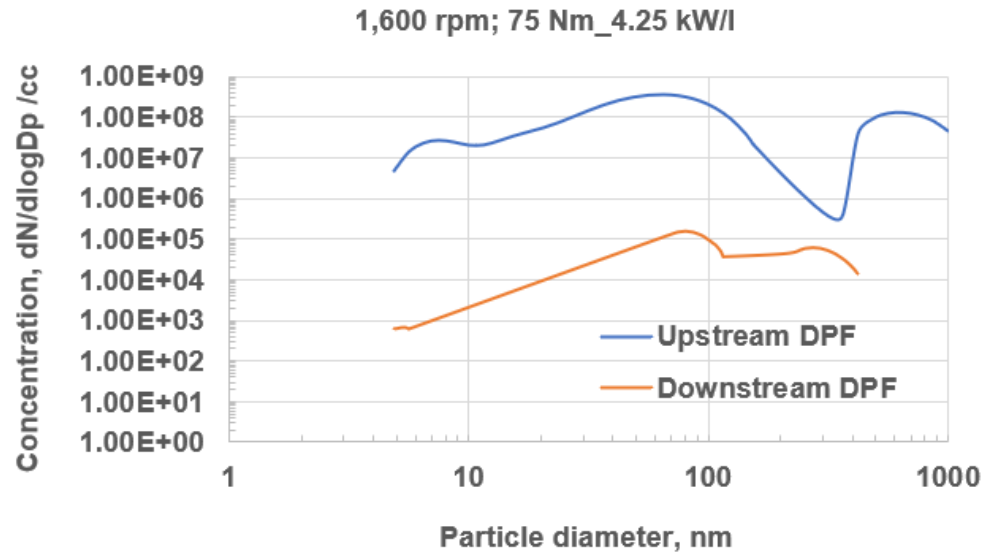

Figure 6.35 Particulate number profiles (1,600 rpm; 75 Nm_4.25 kW/l)

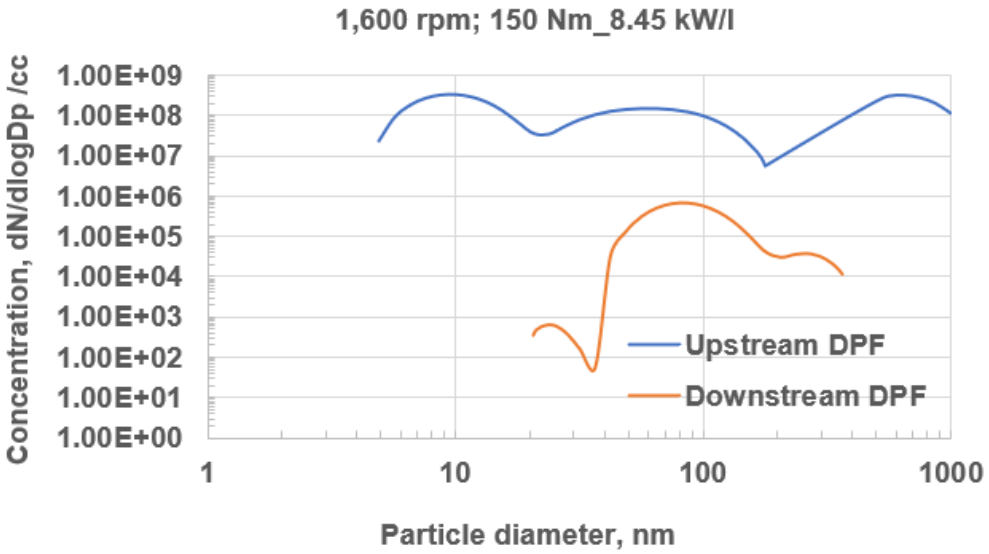

Figure 6.36 Particulate number profiles (1,600 rpm; 150 Nm_8.45 kW/l)

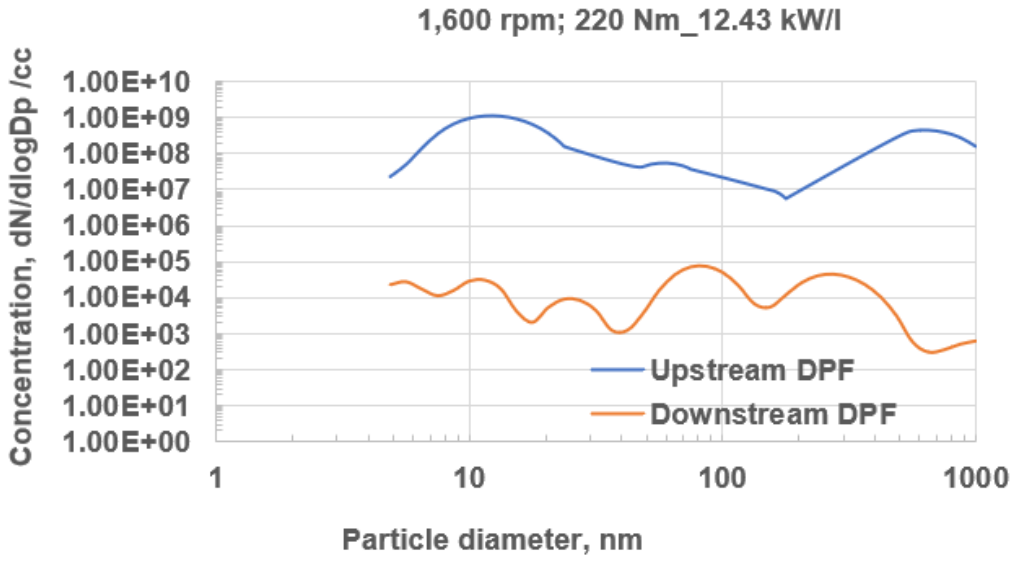

Figure 6.37 Particulate number profiles (1,600 rpm; 220 Nm_12.43 kW/l)

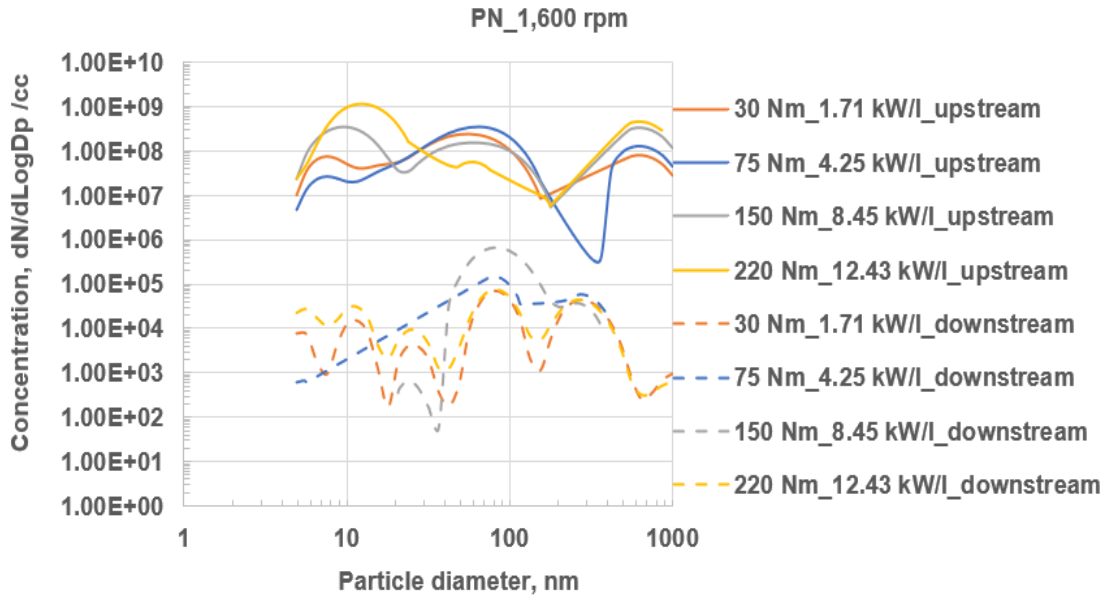

Figure 6.38 Comparison of PN emissions (1,600 rpm modes)

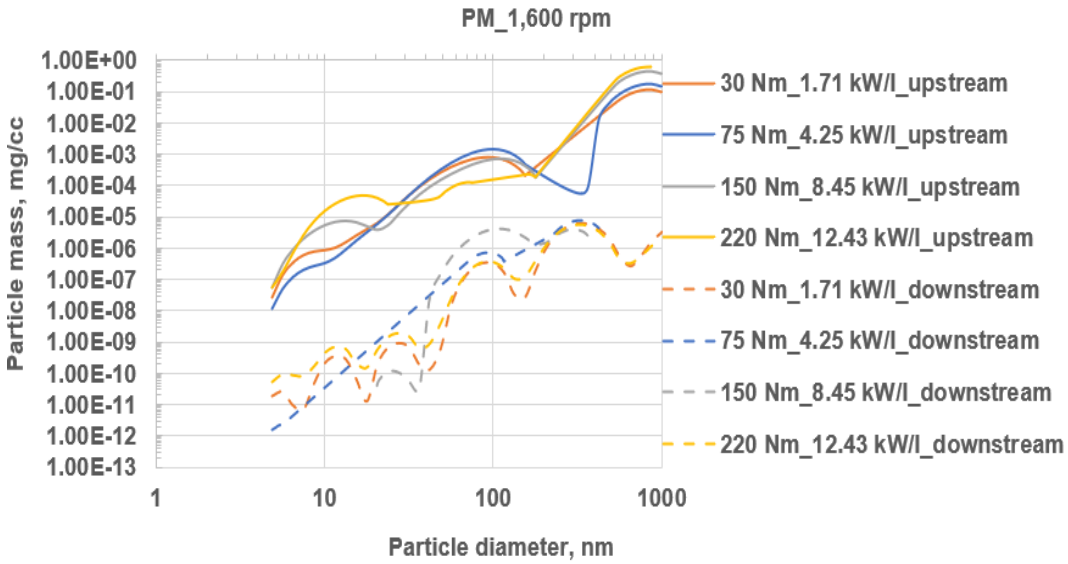

Figure 6.39 Comparison of PM emissions (1,600 rpm modes)

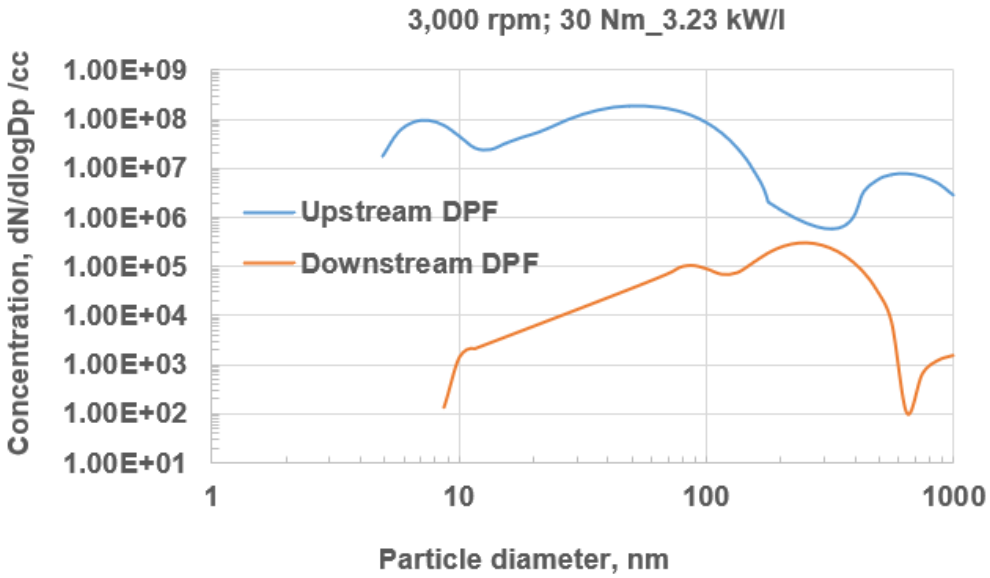

Figure 6.40 Particulate number profiles (3,000 rpm; 30 Nm_3.23 kW/l)

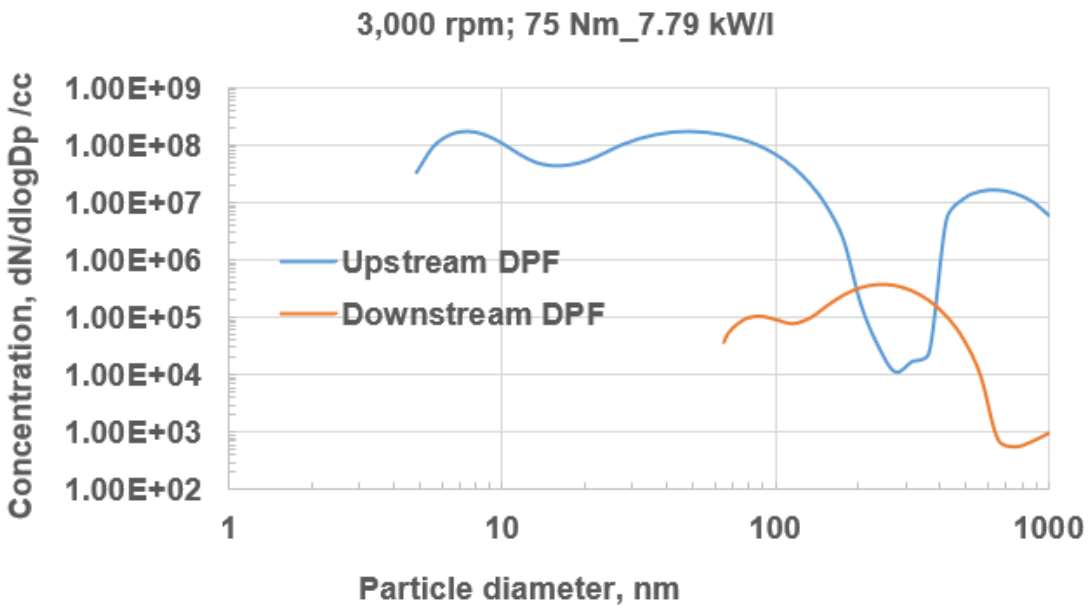

Figure 6.41 Particulate number profiles (3,000 rpm; 75 Nm_7.79 kW/l)

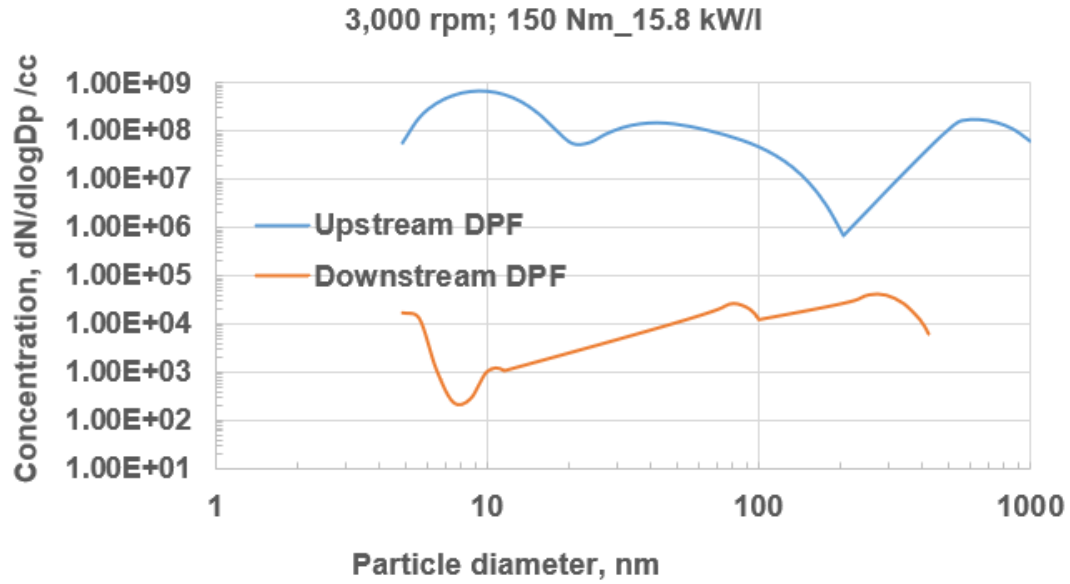

Figure 6.42 Particulate number profiles (3,000 rpm; 150 Nm_15.8 kW/l)

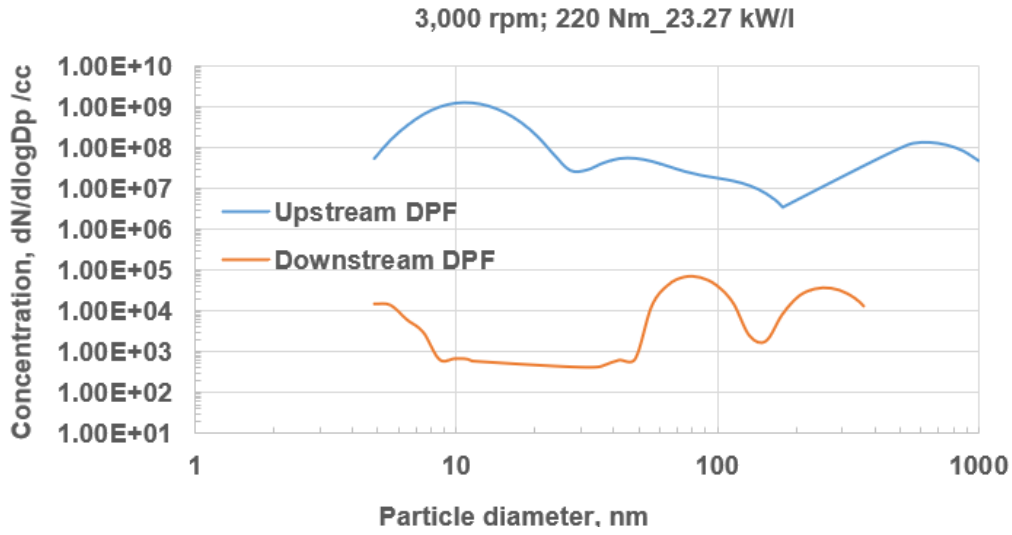

Figure 6.43 Particulate number profiles (3,000 rpm; 220 Nm_23.27 kW/l)

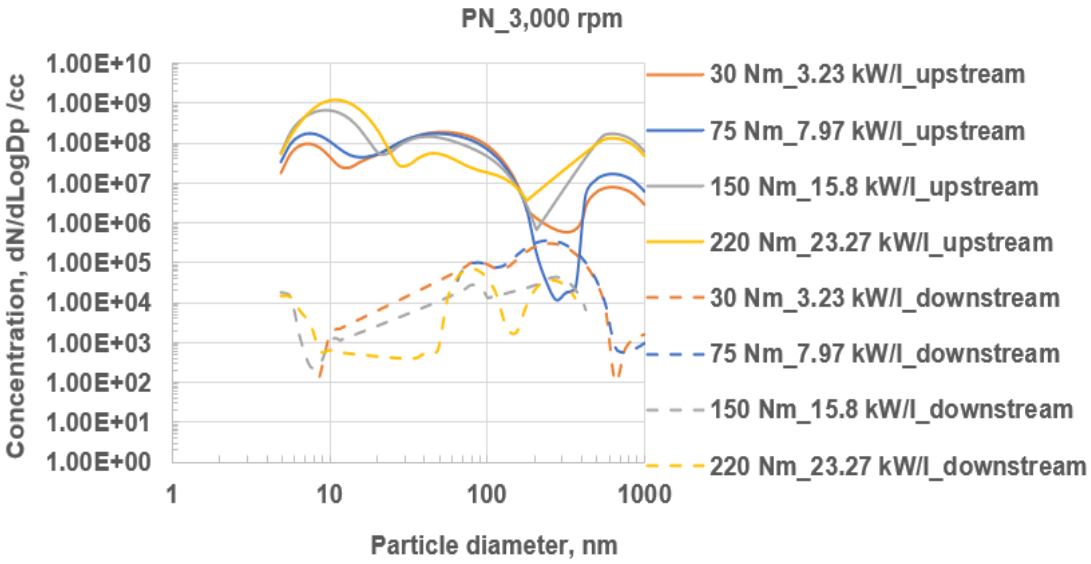

Figure 6.44 Comparison of PN emissions (3,000 rpm modes)

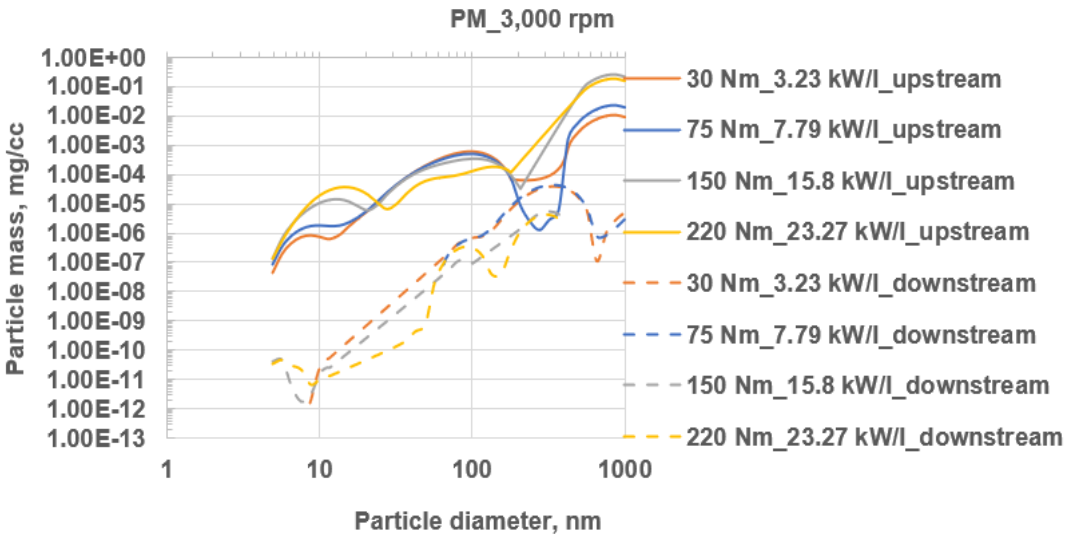

Figure 6.45 Comparison of PM emissions (3,000 rpm modes)

Figures 6.33, 6.39, and 6.45 show that the mass concentrations of the agglomeration mode particles (ultrafine particles) were higher than those of the nucleation mode particles for all the tested engine modes. This was because the mean particle size, Dp as well as the mean mass of the agglomeration mode particles were greater than those of the nucleation mode. The peak PM occurred at Dp=100 nm for all the tested modes. It was also observed in Figures 6.33, 6.39, and 6.45 that the lowest peak PM occurred when the engine was run at the highest load (220 Nm) for all the tested speeds.

The engine-out total PN in this work for the 1,600 rpm intermediate load (150 Nm) engine condition was 3.1×10^8 n/cc. Wu et al. (2017) reported an engine-out total PN of 1.36×10^8 n/cc for the same engine mode and engine (IVECO engine). The total PN that was reported by Wu et al. (2017) for ULSD is of the same order as the result in the current work.

6.3.2.2 Effects of changing the speed of the engine at constant torque on particulate emissions

Figures 6.46 to 6.53 show the effect of changing the speed of the engine at constant load on the engine-out particulate emissions. At the lowest load (30 Nm), the peak PN occurred at the particle diameter, Dp of 56 nm (ultrafine particles) as shown in Figures 6.46 and 6.47 for all the tested engine speeds. However, the observed peak PN was lowest at the highest engine speed (3,000 rpm). The peak PN at 3,000 rpm was relatively low compared to the peaks at the other speeds because the temperature of the flame increased as the speed of the engine was increased at constant load (Table 6.2). Relatively high flame temperatures do not favour the condensation of gas-phase species which is necessary for the agglomeration of particles (particle growth). Therefore, at the highest engine speed, the engine-out exhaust had the lowest agglomeration mode peak PN.

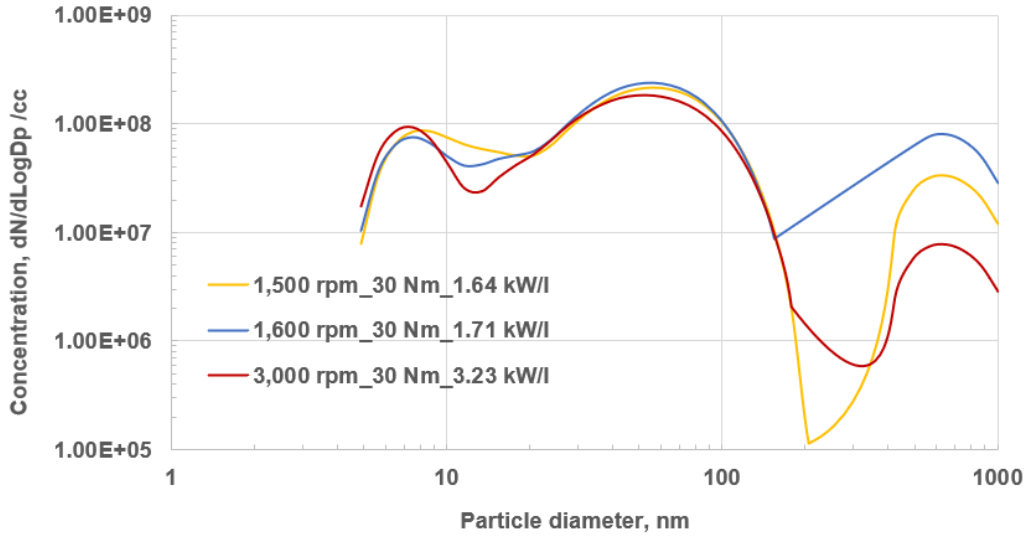

Figure 6.46 Particle Number (PN) profiles at 30 Nm

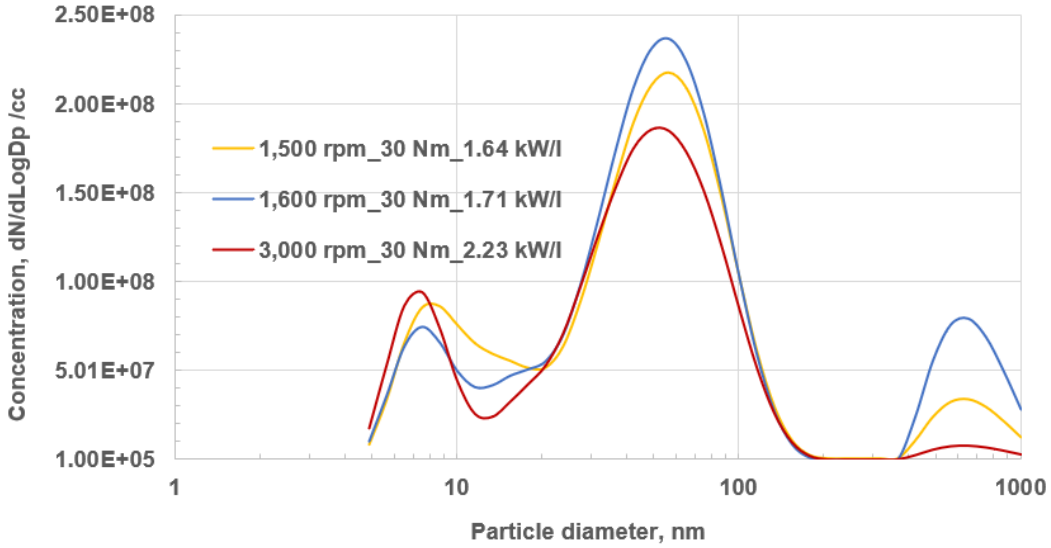

Figure 6.47 Particle Number (PN) profiles at 30 Nm (semi-log plot)

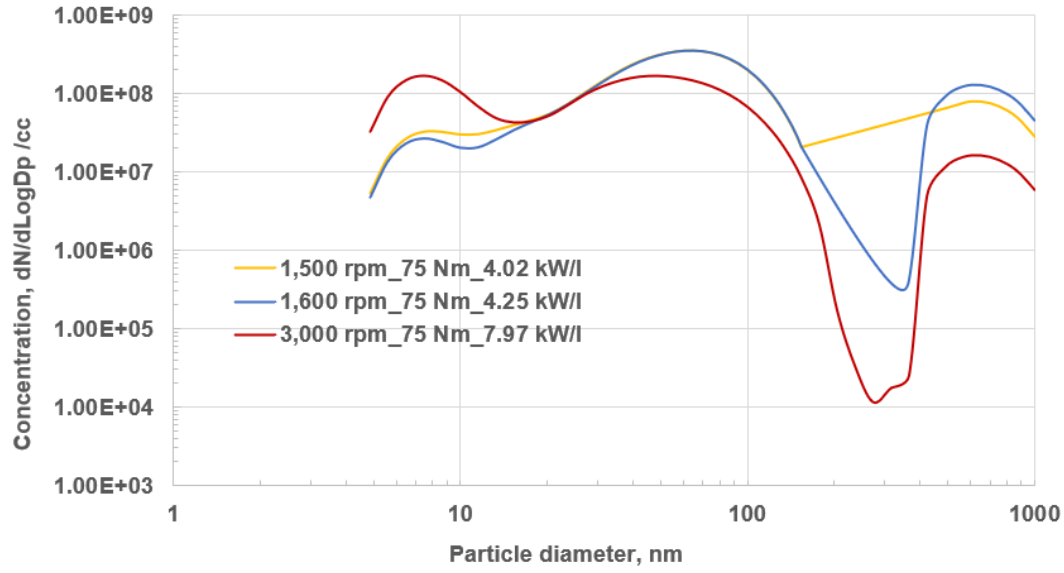

Figure 6.48 Particle Number (PN) profiles at 75 Nm

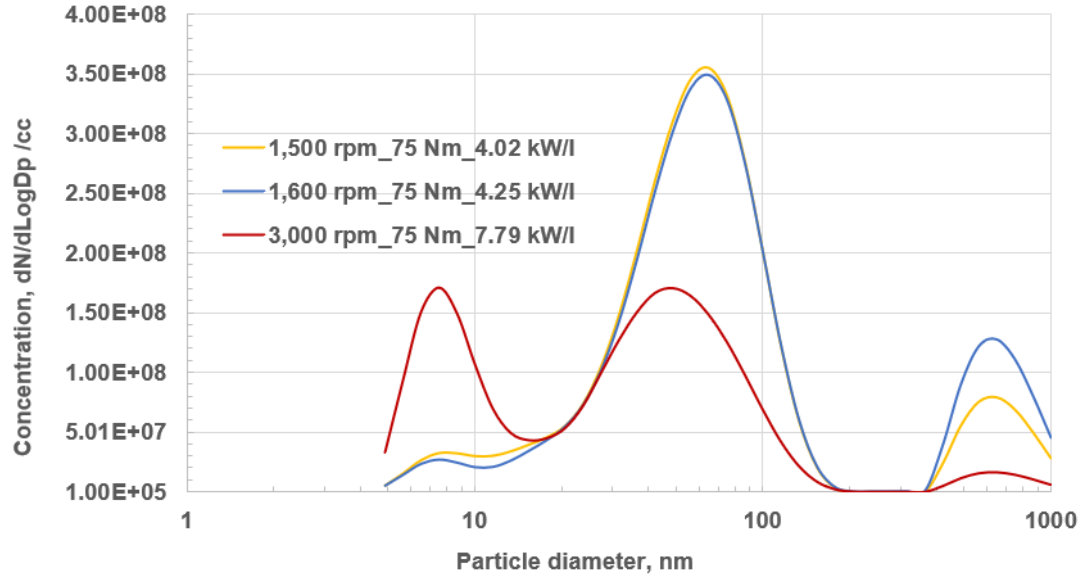

Figure 6.49 Particle Number (PN) profiles at 75 Nm (semi-log plot)

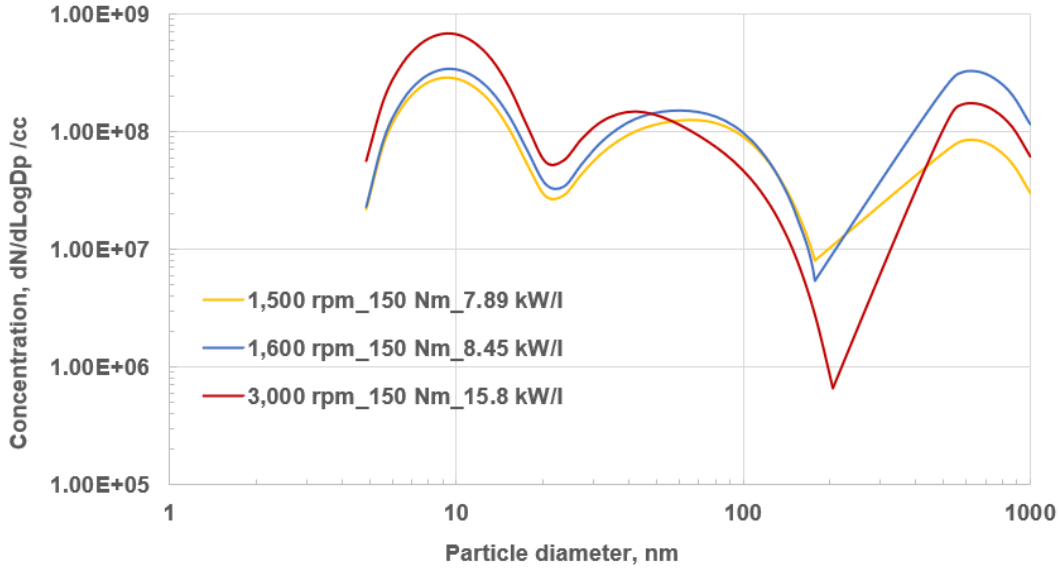

Figure 6.50 Particle Number (PN) profiles at 150 Nm

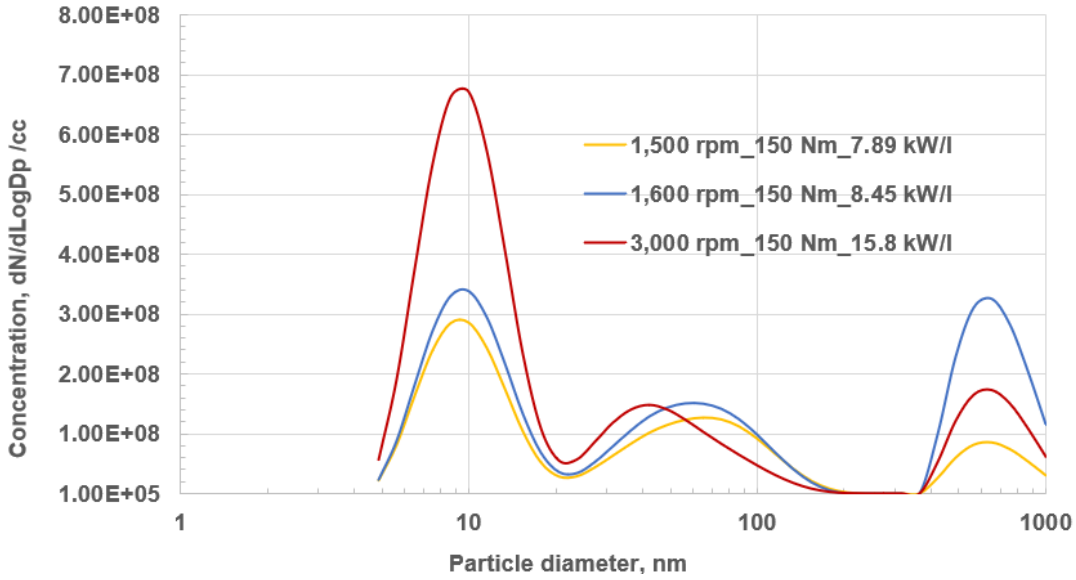

Figure 6.51 Particle Number (PN) profiles at 150 Nm (semi-log plot)

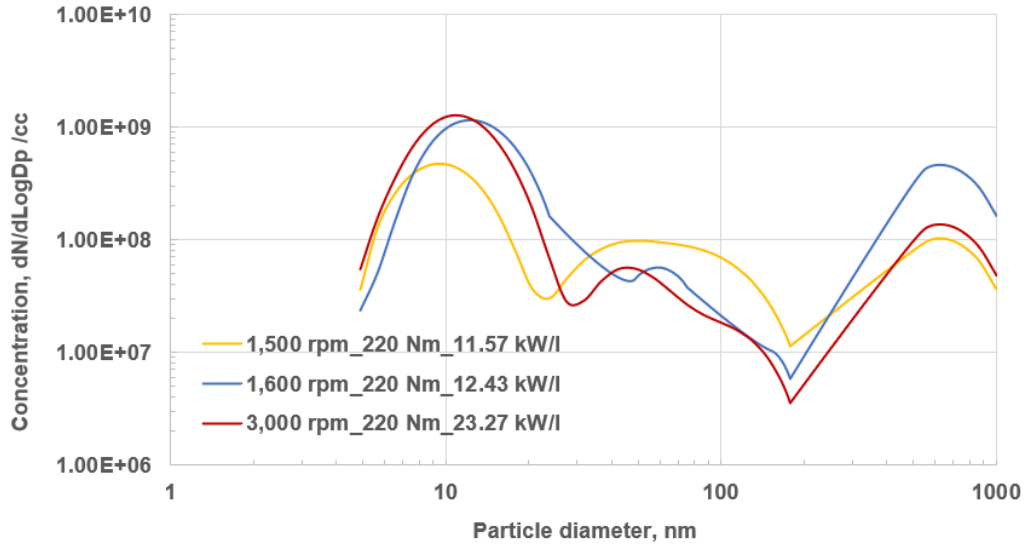

Figure 6.52 Particle Number (PN) profiles at 220 Nm

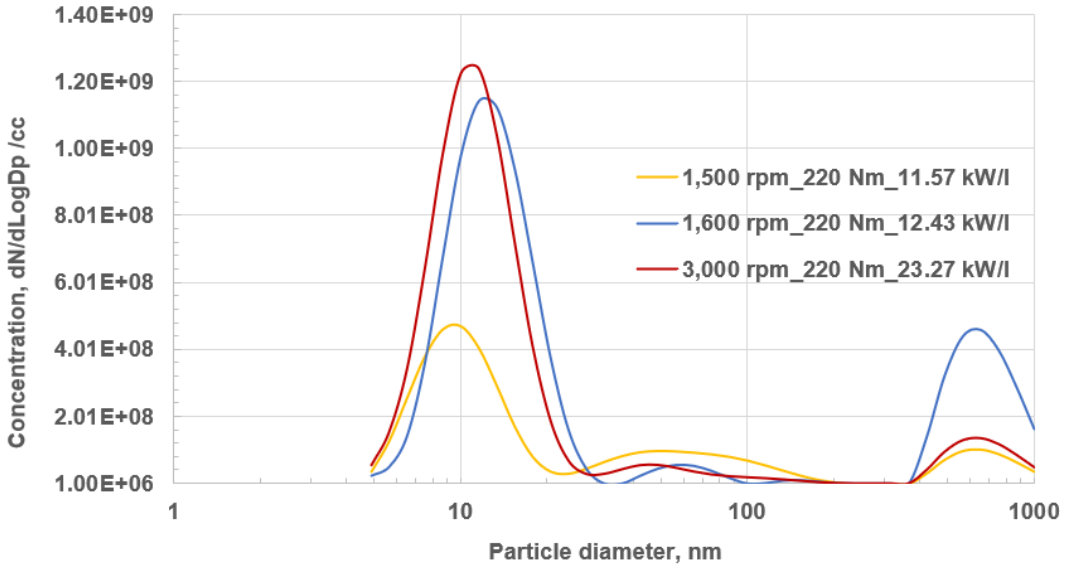

Figure 6.53 Particle Number (PN) profiles at 220 Nm (semi-log plot)

As the load of the engine increased from 30 Nm to 75 Nm at 3,000 rpm, the agglomeration mode peak shifted from the initial Dp of 56 nm to 48.7 nm. The agglomeration mode peak PN was approximately equal to the nucleation mode peak PN at Dp=7.5 nm for the 3,000 rpm; 75 Nm condition (Figure 6.49). This implied that there was a transition from aglomeration mode peak PN to nucleation mode peak PN as the load on the engine was increased from the low load conditions to the high load conditions. Generally, for all the tested conditions of speed, the peak PN switched from the agglomeration mode to the nucleation mode when the load increased to 150 Nm (Figures 6.50 to 6.53). Therefore, at the relatively low loads (30 Nm and 75 Nm), the peak PN occurred in the agglomeration mode while at the medium and high loads (150 Nm and 220 Nm), the peak PN occurred in the nucleation mode (Figures 6.50 to 6.53). By implication, at constant engine speed and low loads, the number concentration of ultrafine particles (agglomeration mode particles) in the engine-out exhaust was more than that of nanoparticles (nucleation mode particles) whereas operation at the relatively high loads and constant speed favoured the production

of nanoparticles. This was due to the drastic increase in flame temperature that occurred as the load on the engine was increased. Condensation of gas-phase species and particle growth occurrs at relatively low flame temperatures. The third column of Table 6.3 shows the observed transition of the peak PN from the agglomeration mode to the nucleation as the load of the engine was increased at constant speed.

Table 6.3 Particle diameter (Dp) at peak Particle Number (PN)

Speed, rpm	**Torque, Nm**	**Dp @ peak PN**	**Mode**
1,500	30	56	Agglomeration
	75	65	Agglomeration
	150	10	Nucleation
	220	10	Nucleation
1,600	30	56	Agglomeration
	75	65	Agglomeration
	150	10	Nucleation
	220	13	Nucleation
3,000	30	56	Agglomeration
	75	7.5, 49	(Mode transition)
	150	10	Nucleation
	220	12	Nucleation

6.3.2.3 Occurrence of second accumulation mode in the 500 to 1,000 nm particle diameter range

The engine that was used for the current work utilised Exhaust Gas Recirculation (EGR). The recirculated exhaust gas passed through the EGR cooler upstream of the engine (Figure 6.54).

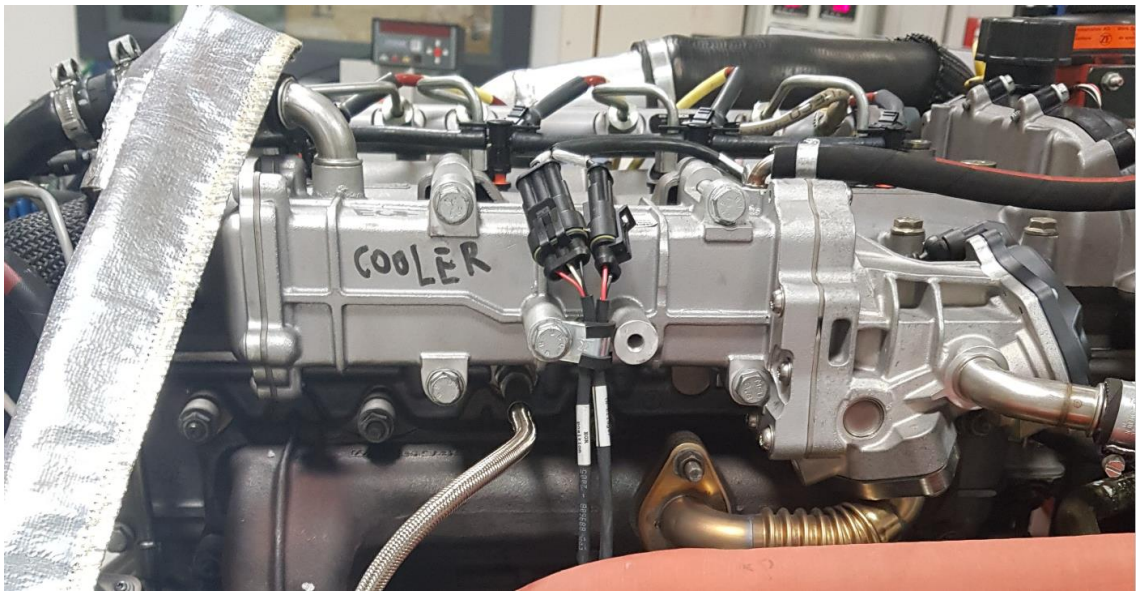

Figure 6.54 IVECO diesel engine EGR cooler

Particles deposit on the EGR system over time in engines that utilise EGR. This results in the fouling of the EGR cooler (Hoard et al., 2008). The EGR system consists of the EGR pipes and the EGR cooler. The observed second accumulation mode particles (Figure 6.25) resulted from the detachment and re-entrainment of the particles that were initially deposited on the EGR system. The agglomeration mode particles that were already in the engine-out exhaust (not previously deposited on the EGR system) also contributed to the second accumulation mode particles observed in Figures 6.25 to 6.53. The recirculated exhaust gas was sourced/tapped upstream of the DPF as shown in Figure 6.54. It is also known that the accumulation mode particles and particle growth result from the deposition of condensed heavy molecular weight organic compounds on

spherules when the exhaust gas is cooled (Heywood, 1988). Therefore, the cooling of the engine-out exhaust by the EGR cooler further enhanced the growth of the agglomerated particles that entered the EGR cooler from the engine. Furthermore, complex geometries in the EGR system such as pipe bends led to eddies (turbulent recirculation of fluid). The eddies enhanced particle agglomeration (coagulation and aggregation) by increasing the frequency of particle collision in the complex geometries. Therefore, the cooling of the exhaust gas in the EGR cooler and the complex geometries in the EGR system inadvertently increased the size of agglomeration/accumulation mode particles that were recirculated to the engine. The detachment and re-entrainment of the deposited particles on the EGR system, the cooling of the recirculated exhaust gas, and the presence of complex geometries in the EGR system led to the occurrence of the second accumulation mode in the 500 to 1,000 nm Dp range in this work.

Mueller et al. (2015) and Nestor (2001) also reported particulate distributions that had accumulation mode peaks between 500 and 1,000 nm Dp. Figure 6.55 compares the second accumulation mode peaks of (Mueller et al., 2015) and Nestor (2001) to the peak of a similar mode in the current work. Nestor (2001) used the Anderson Impactor to measure the particulate emissions while Mueller et al. (2015) utilised the Aerosol Mass Spectrometer (AMS). Figure 6.55 shows that the second accumulation mode peak occurred at a Dp of approximately 866 nm, 850 nm, and 950 nm respectively for the engine modes representing the particulate measurements from the current work (IVECO diesel engine), Mueller et al. (2015), and Nestor (2001).

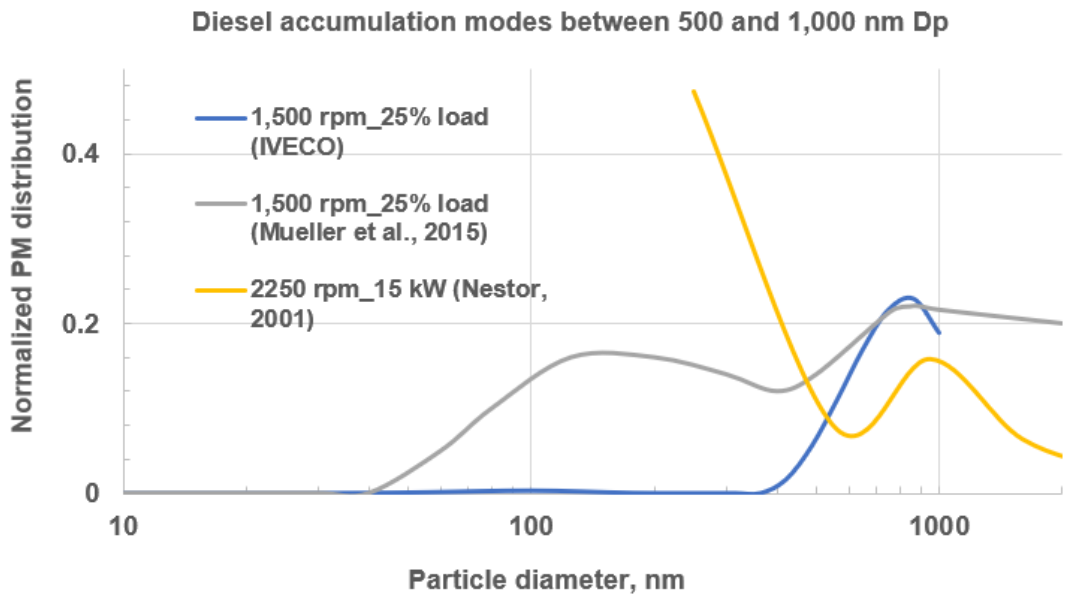

Figure 6.55 Comparison of the second accumulation modes from literature to the current work

6.3.2.4 Particulate yield values for the tested conditions

Figures 6.56 and 6.59 present the computed yields of the emitted particles for the tested engine modes for the exhaust that was sampled upstream and downstream of the DPF respectively. Figure 6.56 shows that the yield of the emitted particles increased as the load on the engine was increased. However, the particulate yields at 3,000 rpm where relatively low compared to the yields for the other speeds. This can be attributed to the relatively high temperatures of the flame at the rated engine speed. The oxidation of soot was enhanced as the flame temperature increased. Soot oxidation occurs at both the soot nuclei/spherule formation stage and the particle growth stage (Heywood, 1988). Therefore, the engine-out particulate emissions were relatively low for the 3,000 rpm engine modes.

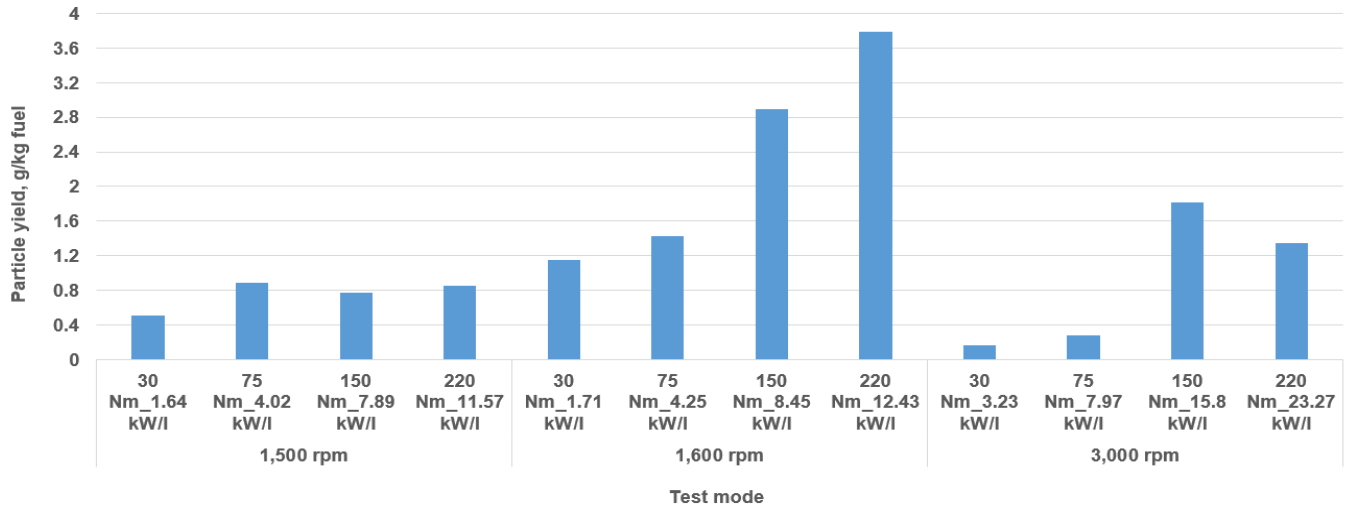

Figure 6.56 Comparison of particulate yields in g/kg for the tested engine modes (upstream of the DPF)

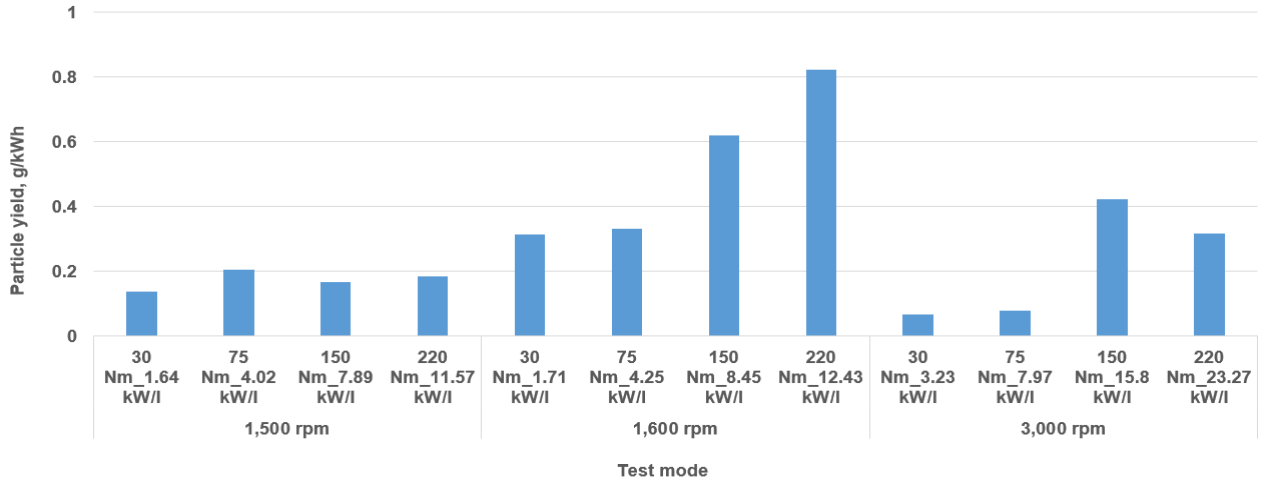

Figure 6.57 Comparison of particulate yields in g/kWh for the tested engine modes (upstream of the DPF)

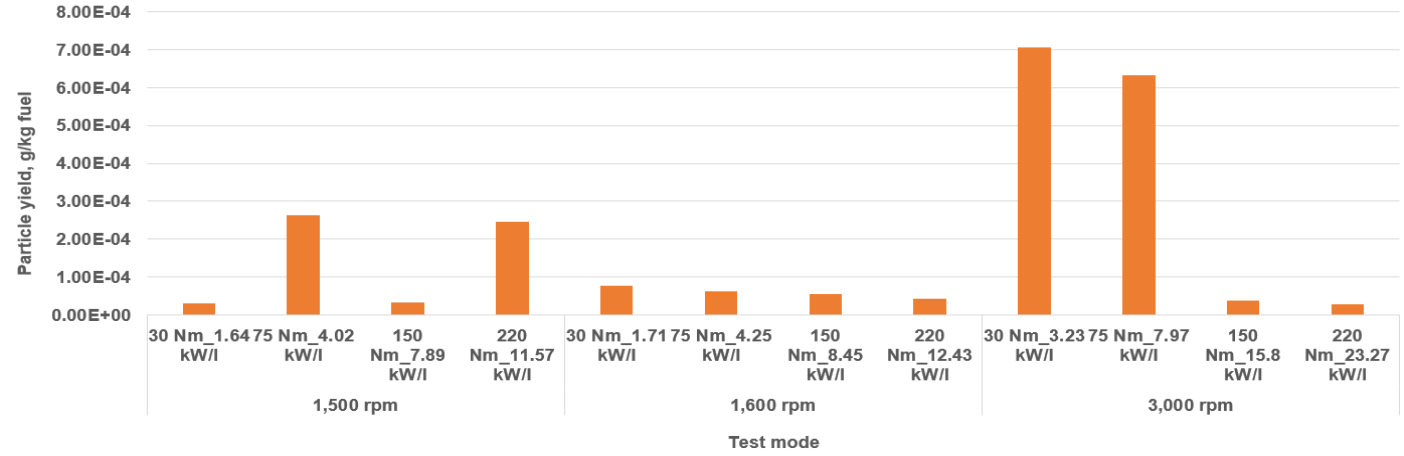

Figure 6.58 Comparison of particulate yields in g/kg for the tested engine modes (downstream of the DPF)

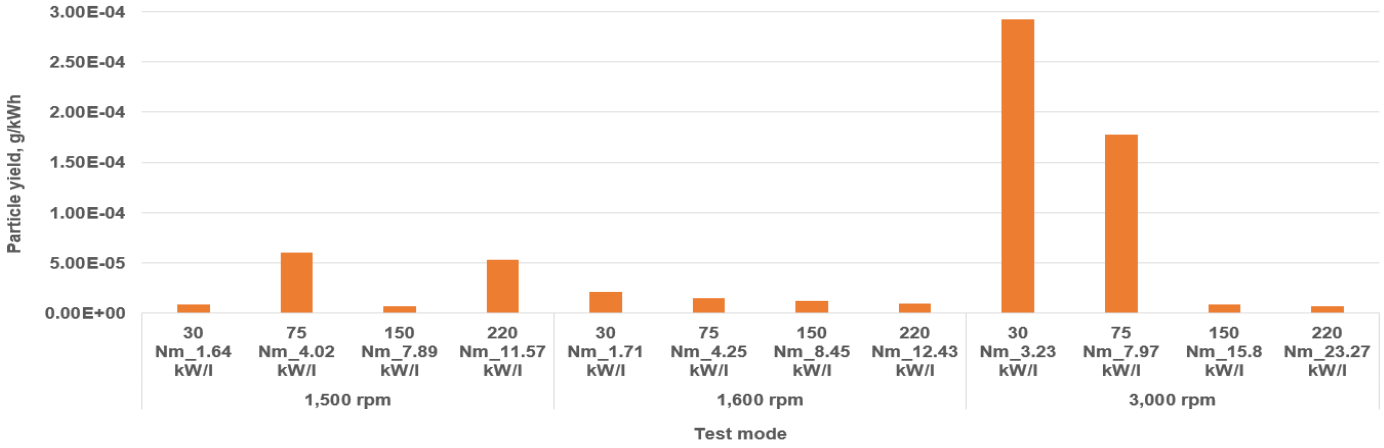

Figure 6.59 Comparison of particulate yields in g/kWh for the tested engine modes (downstream of the DPF)

Figures 6.58 and 6.59 depict the insignificant yield of particles downstream of the DPF. The figures also confirm the 99.9% efficiency of the DPF at trapping the emitted particles in the engine-out exhaust.

6.3.3 Prediction of the emission trends for diesel-ethanol (DE) fuel blends from the emission results for baseline diesel

The emission levels for diesel-ethanol (DE) fuel blends can be predicted for the IVECO diesel engine to some extent based on the results for baseline diesel and the physical properties of ethanol. It is known that ethanol has a relatively high heat of vaporisation (Hv) but low CN and Cv compared to pure diesel. Increase in the concentration of blend ethanol will cause the fuel consumption of the engine to increase above the baseline for all the tested conditions. The fuel consumption will increase above the baseline because of the relatively low Cv of DE fuel blends (more blend fuel mass than the mass of pure diesel will be required to achieve the same power). The relatively high Hv of DE blends will reduce the combustion temperatures below the baseline for the tested modes. The combined effects of reduction in combustion temperature, increase in fuel consumption, and increase in Ignition Delay (due to the relatively low CN of DE blends) will cause the levels of THC and CO to increase quite drastically above the baseline at the lower loads (30 Nm and 75 Nm) for the blend with high concentration of ethanol (DE15). However, at the higher loads (150 Nm and 220 Nm), the levels of THC and CO will decrease below the baseline for the DE blends that have low ethanol concentrations (DE5 and DE10). The temperature of the flame is known to increase as the load on the engine increases. Relatively high temperatures will enhance the vaporisation of unburned hydrocarbons as well as the oxidation of unburned hydrocarbons and CO by the oxygen from air and the oxygen from the -OH group of ethanol. The decrease in the flame temperature that occurs as the

concentration of ethanol increases in the blends will cause NOx emissions (NO and NO_2) to decrease below the baseline.

DE fuel blends reduce the combustion temperature below baseline as the concentration of ethanol increases in the blends. Therefore, at the relatively low loads (30 Nm and 75 Nm), the engine-out particulate emissions will increase above the baseline as the percentage of ethanol increases in the blends. However, at the higher conditions of torque, the particulate emissions from the engine will decrease conspicuously below the baseline for DE5 and DE10 due to the expected drastic increase in the temperature of the flame when the load is increased. As the load of the engine is increased from the low load conditions to the high load conditions (150 Nm and 220 Nm), the increase in combustion temperature will enhance the vaporisation and combustion of the aerosols of the blend fuels. This will lead to a decrease in the particulate emissions below the baseline at the higher loads for DE5 and DE10. It was observed that at temperatures > 448 ^{o}C, corresponding to the higher loads: 150 Nm and 220 Nm (Table 6.2), the peak PN occurred in the nucleation mode for baseline diesel. However, at temperatures < 448 ^{o}C, the peak PN occurred in the agglomeration mode. Also, the transition from agglomeration mode peak PN to nucleation mode peak PN occurred at the intermediate load (150 Nm) for baseline diesel. The transition from agglomeration mode peak PN to nucleation mode peak PN will occur at loads >150 Nm for DE5 and DE10 due to the lowering of the combustion temperature by DE blends. Generally, as the concentration of ethanol increases, at the higher loads, the particle size, Dp will reduce below the baseline due to increase in the combustion temperature. The relatively high flame temperatures that will result at the high loads will enhance the oxidation of the adsorbed soluble organic compounds on the spherules by the -OH group of ethanol as well as the

oxygen from the intake air. This will in turn result in the reduction of the diameter of the emitted particles below the baseline thereby increasing the peak PN for the DE blends above the baseline.

6.4 IVECO engine Heat Release Rate (HRR) model results

The Leeds HRR model (Equation 4.7) was developed from the First Law of thermodynamics. The model was then utilised to investigate the combustion behaviour of the MFIS IVECO engine for the tested engine modes. The basic input data that was used to solve the HRR model were the pressure traces of the engine at the tested modes. The Leeds HRR model was validated for pure diesel (off-road diesel). Thereafter, it was applied to alternative diesels (GTL and HVO diesels).

6.4.1 Pressure traces used as model input data

The pressure-crank angle data which were used as the basic model input data for the HRR analysis are presented graphically in Figures 6.60 to 6.62. The figures show that the pressure in the cylinder increased at each of the investigated speeds as the load on the engine was increased.

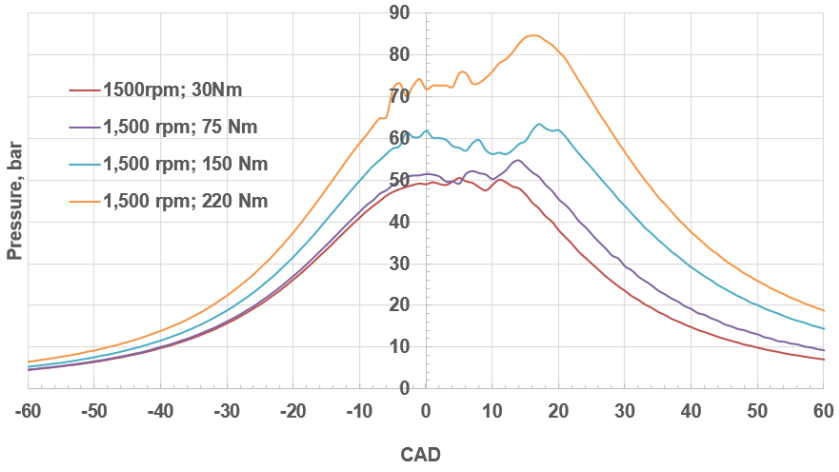

Figure 6.60 Pressure traces (1,500 rpm modes)

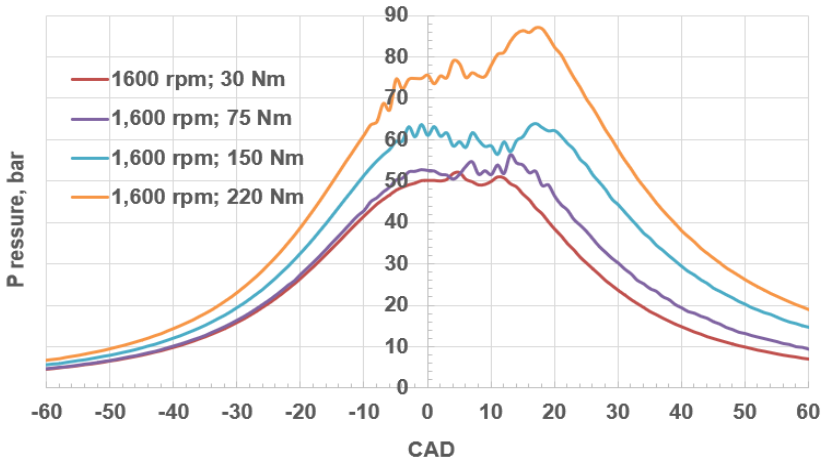

Figure 6.61 Pressure traces (1,600 rpm modes)

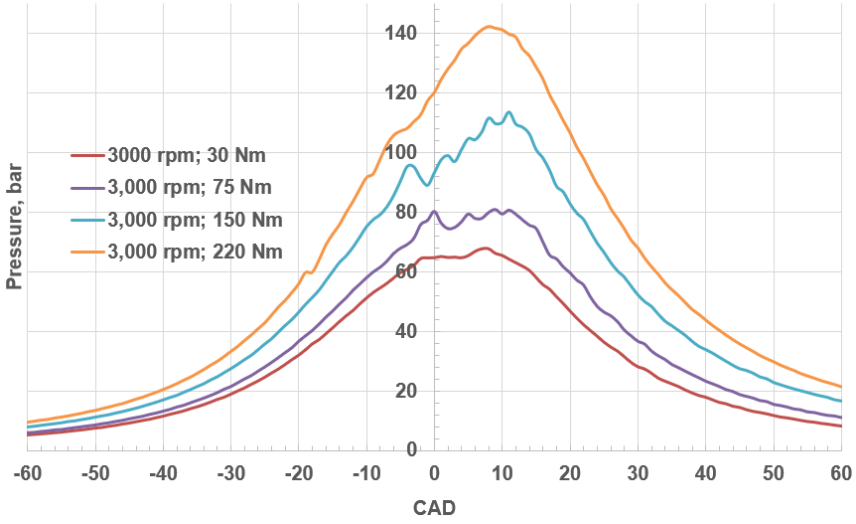

Figure 6.62 Pressure traces (3,000 rpm modes)

6.4.2 Evaluated cylinder temperatures

Figures 6.63 to 6.65 graphically depict the cylinder temperatures that were calculated from the measured cylinder pressures and utilised in the HRR analysis. The figures indicate that, for each of the engine speeds, the temperature of the flame increased as the load on the engine increased. The peak temperatures for the modes at 1,500 rpm and 1,600 rpm occurred at Crank Angle Degree (CAD) of 21, 25, 33, and 31 for 30 Nm, 75 Nm, 150 Nm, and 220 Nm loads respectively. However, the peak temperatures occurred earlier at 21, 22,

22, and 19 CAD respectively for the same loads but at 3,000 rpm. This confirmed that, at the high engine speed and load, the HRR and peak temperature were higher, and the peak temperature occurred earlier than when the engine was operated at the relatively low load conditions.

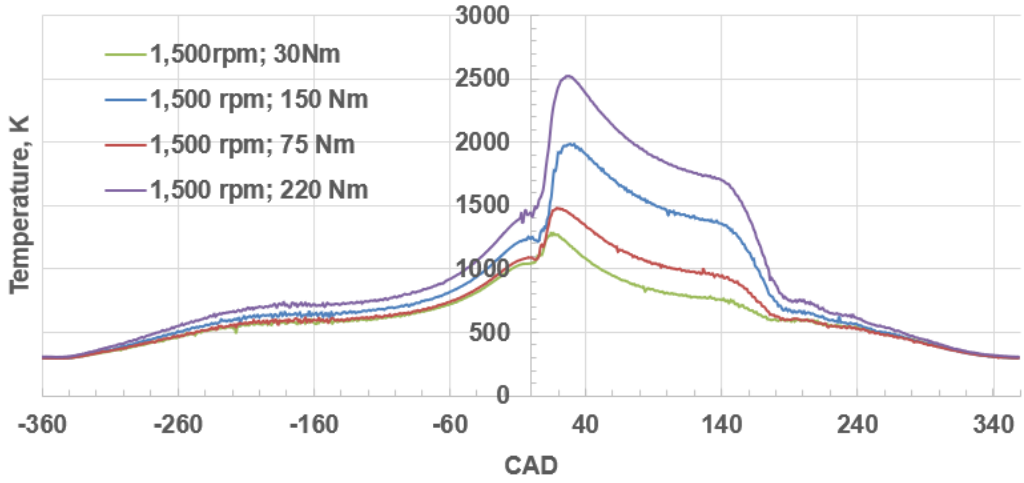

Figure 6.63 Calculated in-cylinder temperatures as a function of crank angle with different loads at 1,500 rm

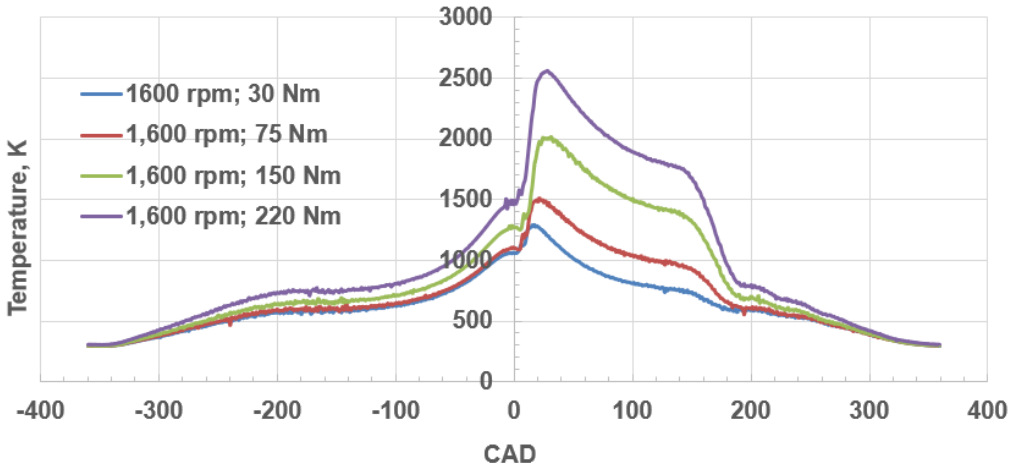

Figure 6.64 Calculated in-cylinder temperatures as a function of crank angle with different loads at 1,600 rpm

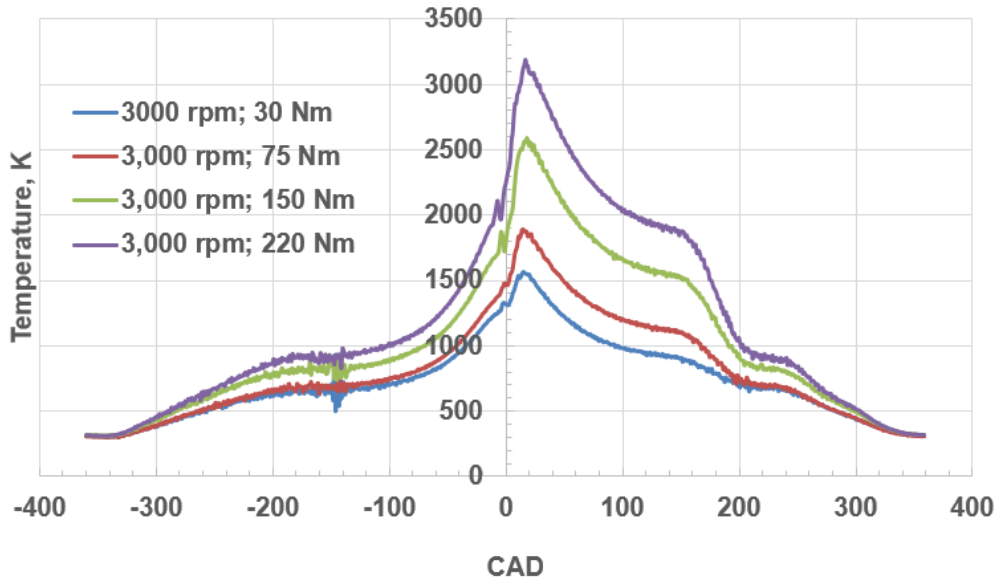

Figure 6.65 Calculated in-cylinder temperatures as a function of crank angle with different loads at 3,000 rpm

The observed fluctuations on the temperature profiles near the Top Dead Centre (TDC) in Figures 6.63 to 6.65 were as a result of the auto–ignition of pilot injection fuel with simultaneous injection of fuel. The engine utilised a Multiple Fuel Injection Strategy (MFIS). Typically, in the EURO V IVECO engine that was used in this work, fuel injection began before the TDC and continued at specific crank angles after the TDC. The maximum number of injections that occurred in the engine per thermodynamic cycle was eight. (The number of fuel injections per cycle as well as the specific crank angle timing of the injections varied as the speed and the torque of the engine was changed.)

6.4.3 Effect of EGR on engine HRR

Figures 6.66 to 6.68 depict the effects of the EGR rate on the HRR model of the engine for near-stoichiometric conditions.

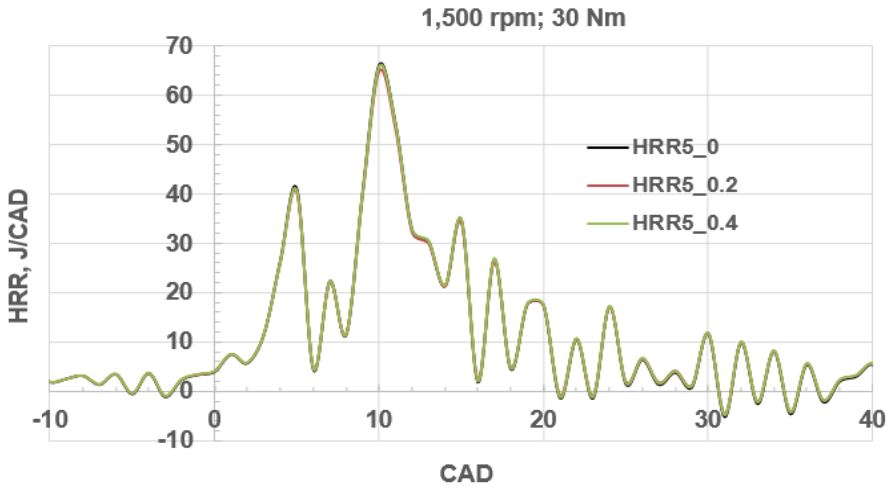

Figure 6.66 HRR as a function of EGR rate at 1,500 rpm; 30 Nm

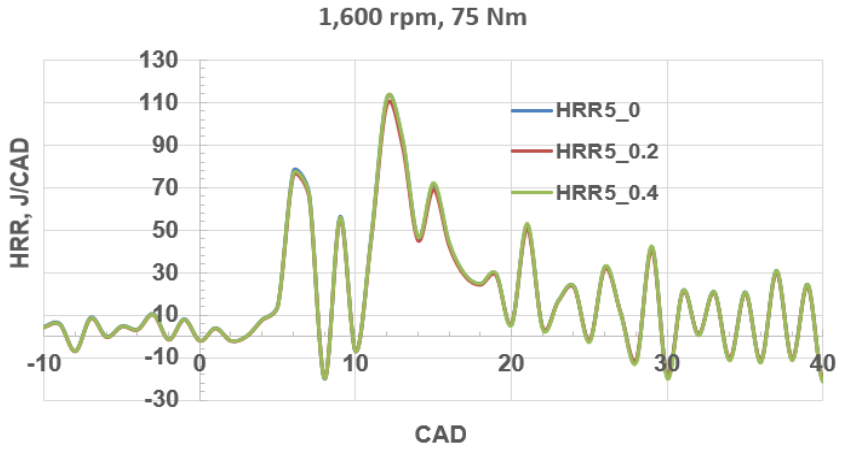

Figure 6.67 HRR as a function of EGR rate at 1,600 rpm; 75 Nm

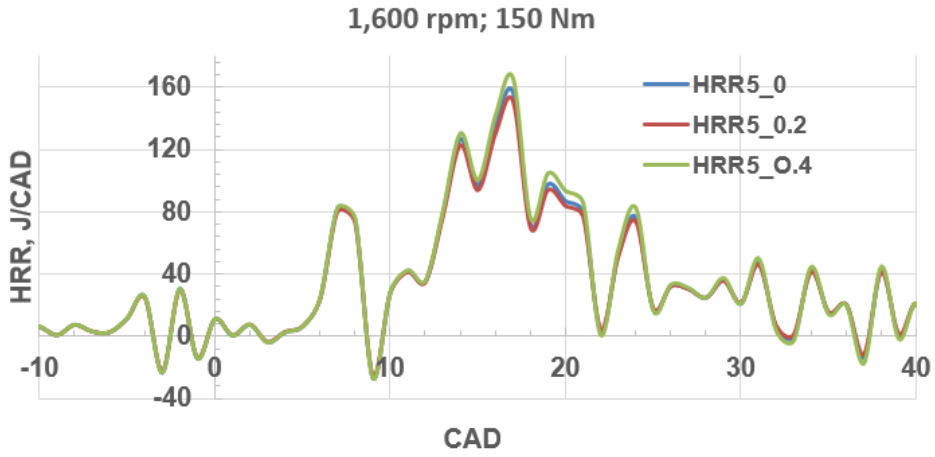

Figure 6.68 HRR as a function of EGR rate at 1,600 rpm; 150 Nm

A near-perfect overlap of the HRR profiles was observed as shown in the figures (except in Figure 6.68) for all the EGR rates that were considered (0, 20% and 40%). This implies that, when ∅=1, for operation at relatively low loads, the effect of EGR rate on the HRR of ICEs is negligible.

Figure 6.69 compares the profiles from the HRR model that was based on the γ function of Blair (1990), HRR4 and the HRR model that was based on the γ model of Heywood (1988), HRR5_0 at zero EGR rate. The model that was based on the γ function of Blair (1990) was chosen for the comparison because the γ function of the author was derived for a stoichiometric engine without EGR. The PHRR predicted by HRR5_0 (66.19 J/CAD) is ~8% higher than the value predicted by HRR4 (60.80) for the engine mode (1,500 rpm; 30 Nm). The observed disparity between the predicted PHRR by HRR4 and HRR5_0 was due to the use of a γ function in HRR5_0 that was derived by fitting and extrapolating experimental data from gasoline–air mixture.

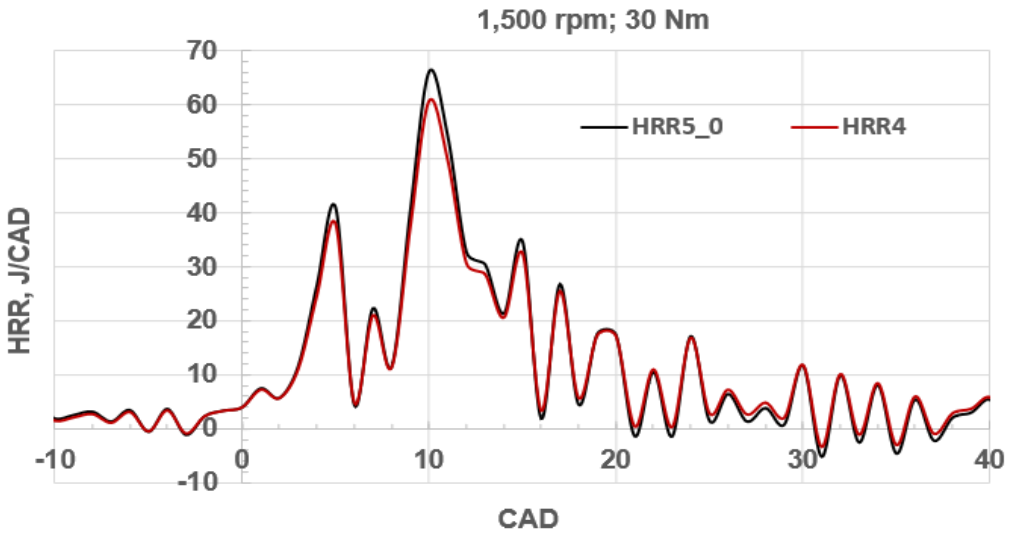

Figure 6.69 HRR profiles based on the γ functions of Heywood and Blair

6.4.4 Comparison of the modified γ function and γ functions from literature

The values of γ estimated from various γ functions were plotted, as depicted in Figure 6.70, against the temperature of the gases in the cylinder for 1,600 rpm; 30 Nm operation mode. The values of γ estimated from Equations 3.29 to 3.32 that expressed γ (T) were graphically compared to the values that were evaluated from the modified gamma function, γ_{mod} as depicted in Figure 6.70. Gamma1 to Gamma4 represent the gamma values predicted by Equations 3.29 to 3.32 respectively. As shown in Figure 6.70, the estimated values of γ from γ_{mod} at all the depicted temperature points were much higher than the estimates from the other functions which expressed γ as a function of temperature only. Therefore, the result depicted in Figure 6.70 confirms that λ has a significant effect on γ.

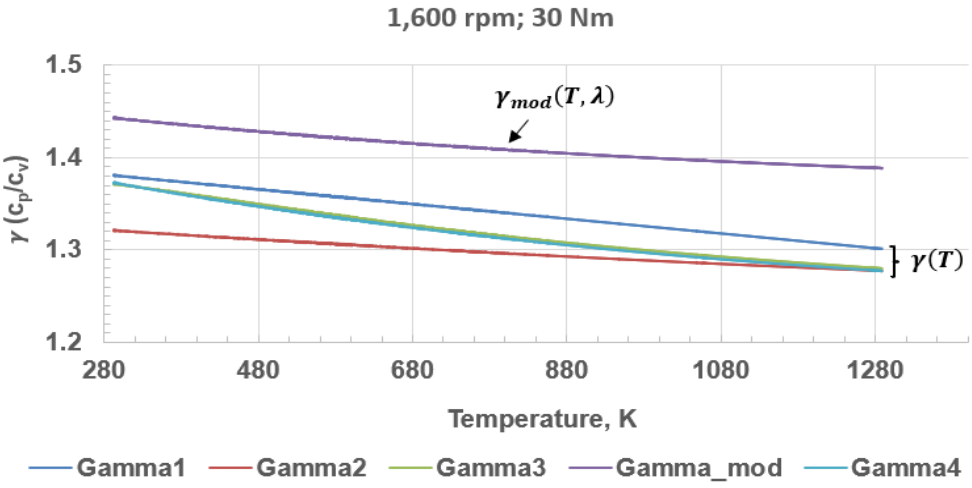

Figure 6.70 Comparison of γ_{mod} and γ functions from literature

6.4.5 Effect of λ on γ using the modified γ function

Figure 6.71 depicts the dependence of γ on temperature and the in-cylinder excess air ratio, λ. The values of γ that were plotted against the temperature of the cylinder in Figure 6.71 were estimated from γ_{mod}. At temperatures below 1,200 K, γ decreased as the temperature increased. However, γ increased as the

excess air ratio of the engine increased due to the decrease in load. Figure 6.71 clearly shows that γ increased as the combustion became leaner (as the in-cylinder λ increased from 2.1 to 8.4).

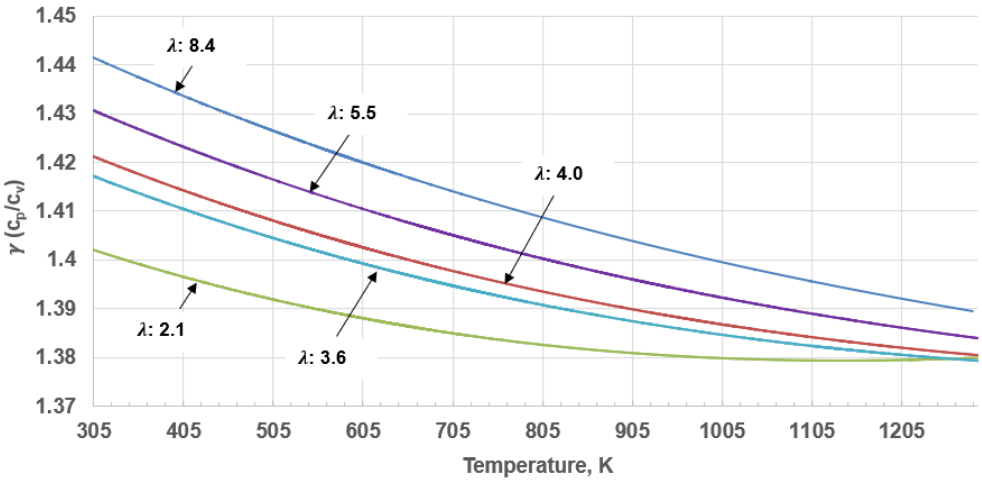

Figure 6.71 Variation of γ with λ and temperature as predicted by γ_{mod}

6.4.6 Sensitivity of engine HRR model to γ functions - comparison of Leeds model to others

Figures 6.72 to 6.83 present the HRR profiles from the investigated HRR models. The figures clearly show the sensitivity of the HRR model of the engine to γ functions as the five HRR models predicted different PHRR values. The Leeds HRR model predicted the lowest PHRR for all the modes that were tested. As observed in Figure 6.70, $\gamma(T,\lambda)$ gave estimates of γ that were higher than the estimates from $\gamma(T)$. However, Figures 6.72 to 6.83 show that the HRR model that utilised $\gamma(T,\lambda)$ predicted lower PHRR values for the CI engine than the HRR models that utilised $\gamma(T)$. The five HRR models exhibited the same trend but predicted different PHRR for the engine modes which were investigated. Therefore, model validation was carried out by comparing the fuel consumption of the engine predicted by the models to the measured fuel consumption (Section 6.4.7).

The timing of the PHRR was determined from the HRR profile. As depicted in Figure 6.72, the PHRR for the 1,500 rpm; 30 Nm mode occurred at 10º aTDC. Multiple peaks were also observed in the HRR profiles due to the Multiple Fuel Injection Strategy (MFIS) of the engine. The 1,500 rpm; 75 Nm engine mode (Figure 6.72) showed two prominent peaks. Peak_1 was as a result of the heat that was released from the combustion of the fuel that was injected during pilot fuel injection. There was a main injection event at 6º aTDC which caused another ignition and heat release that led to Peak_2.

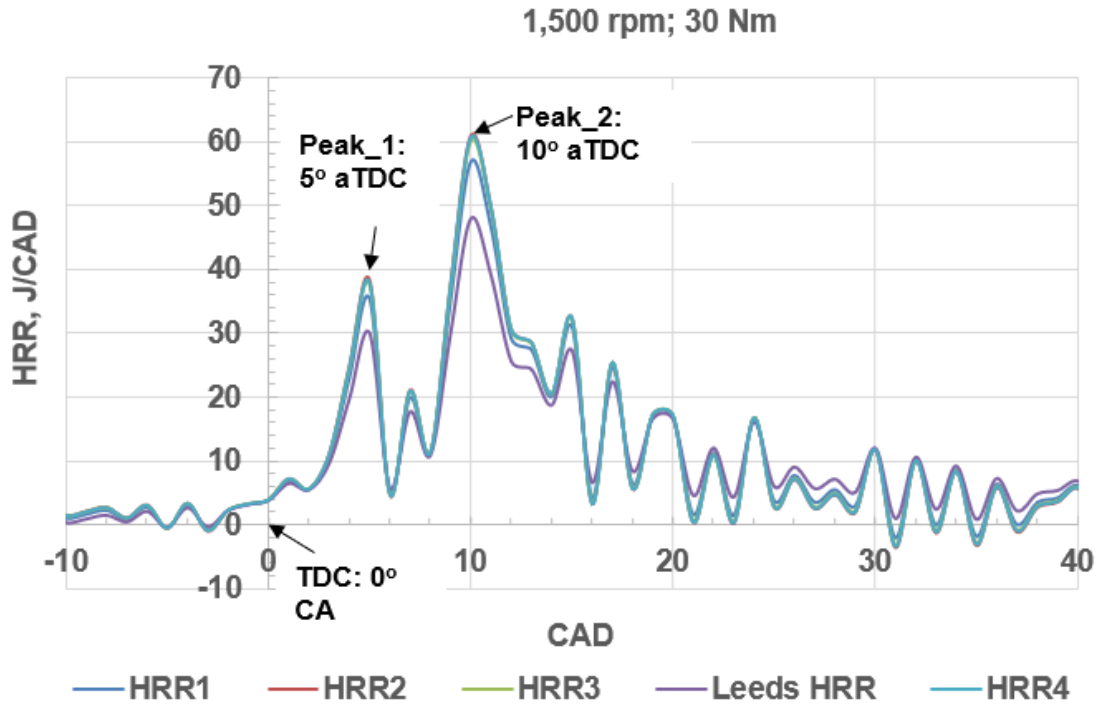

Figure 6.72 HRR profiles from the Leeds model and other models (1,500 rpm; 30 Nm)

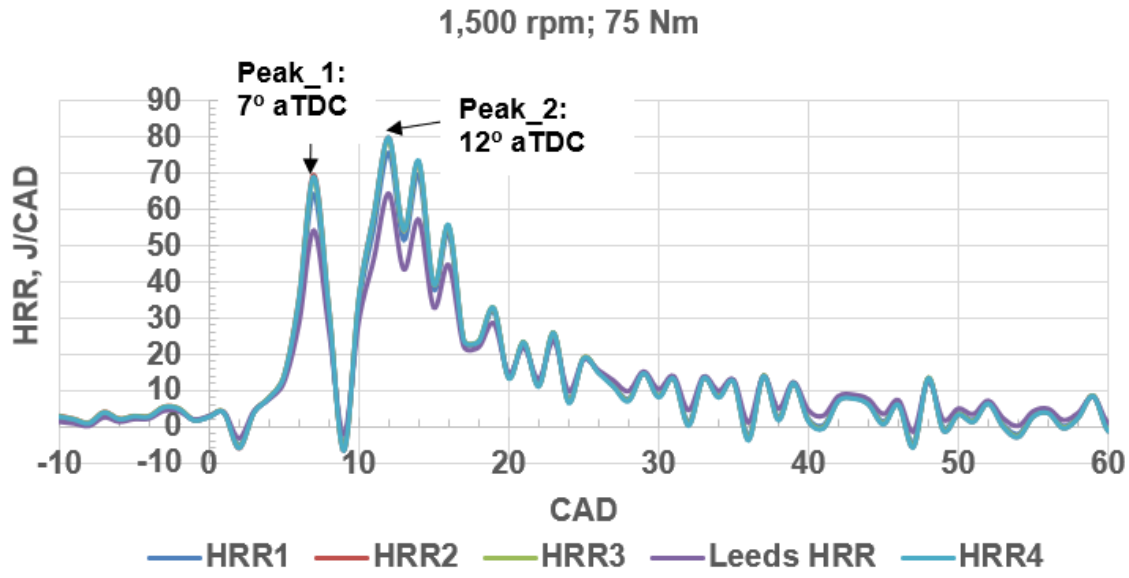

Figure 6.73 HRR profiles from the Leeds model and other models (1,500 rpm; 75 Nm)

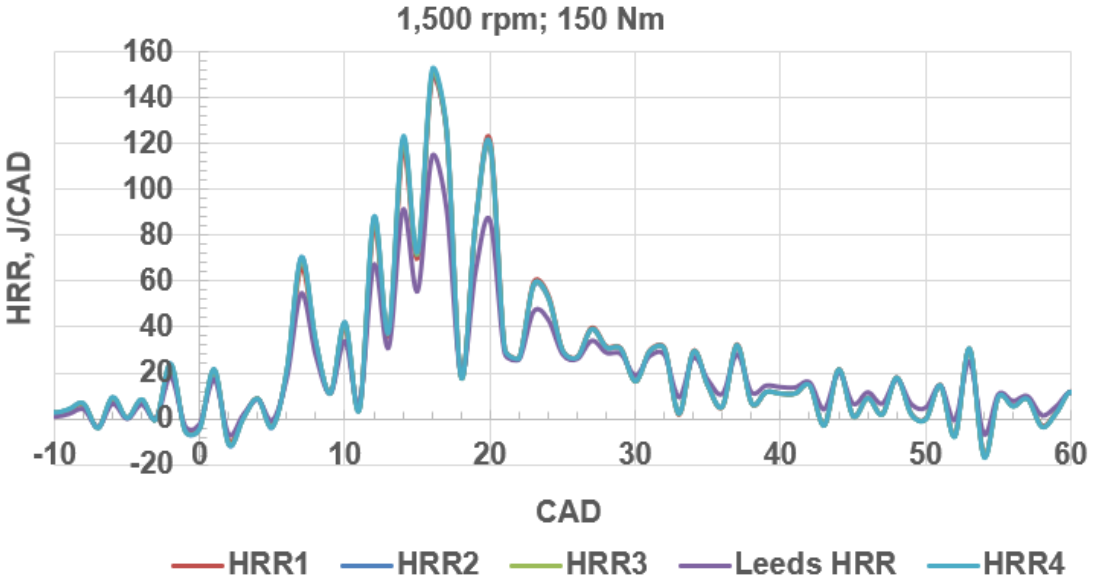

Figure 6.74 HRR profiles from the Leeds model and other models (1,500 rpm; 150 Nm)

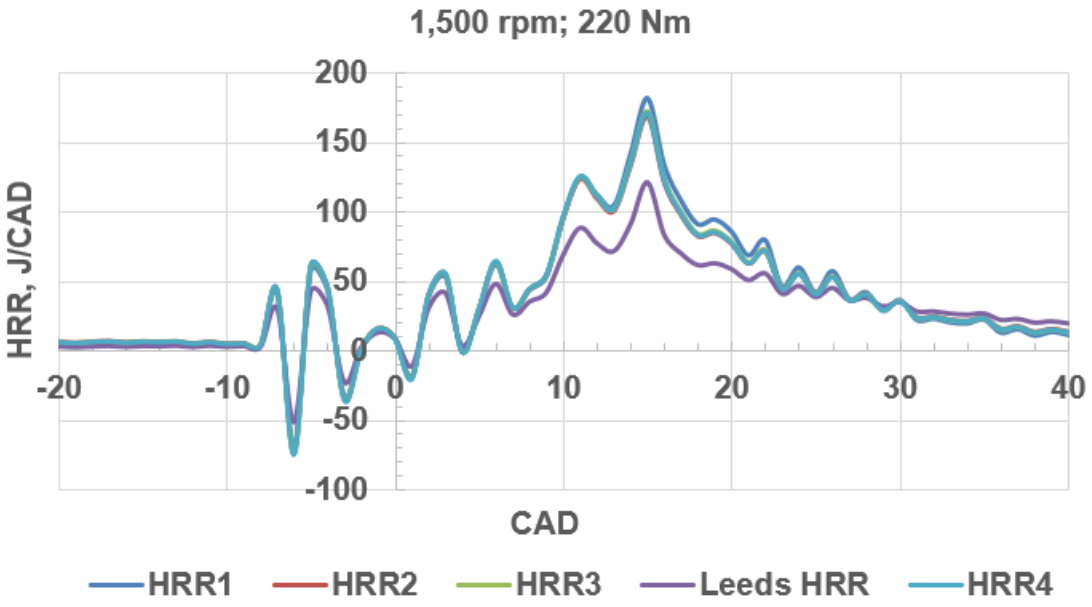

Figure 6.75 HRR profiles from the Leeds model and other models (1,500 rpm; 220 Nm)

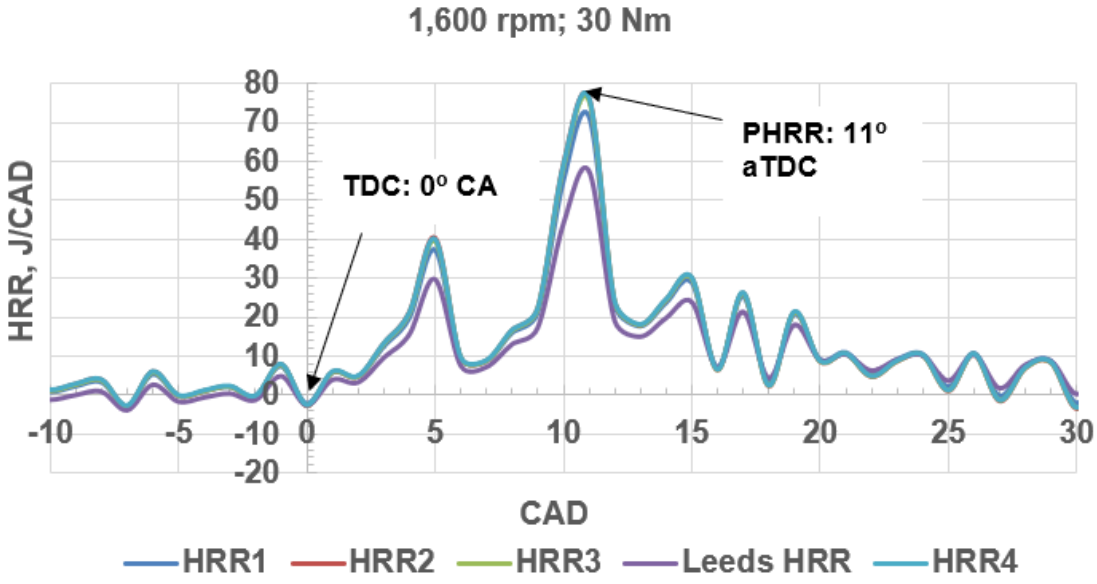

Figure 6.76 HRR profiles from the Leeds model and other models (1,600 rpm; 30 Nm)

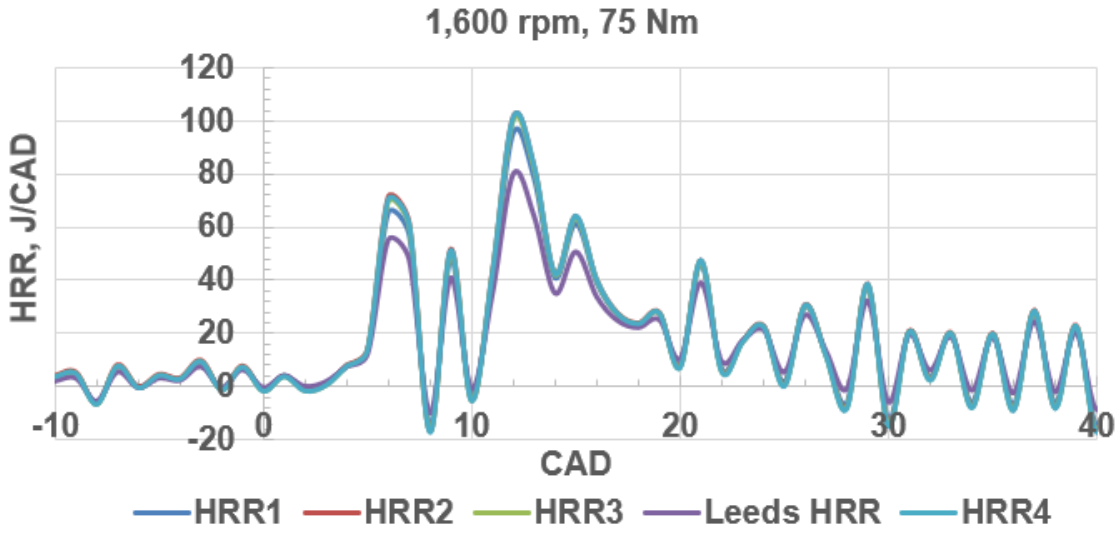

Figure 6.77 HRR profiles from the Leeds model and other models (1,600 rpm; 75 Nm)

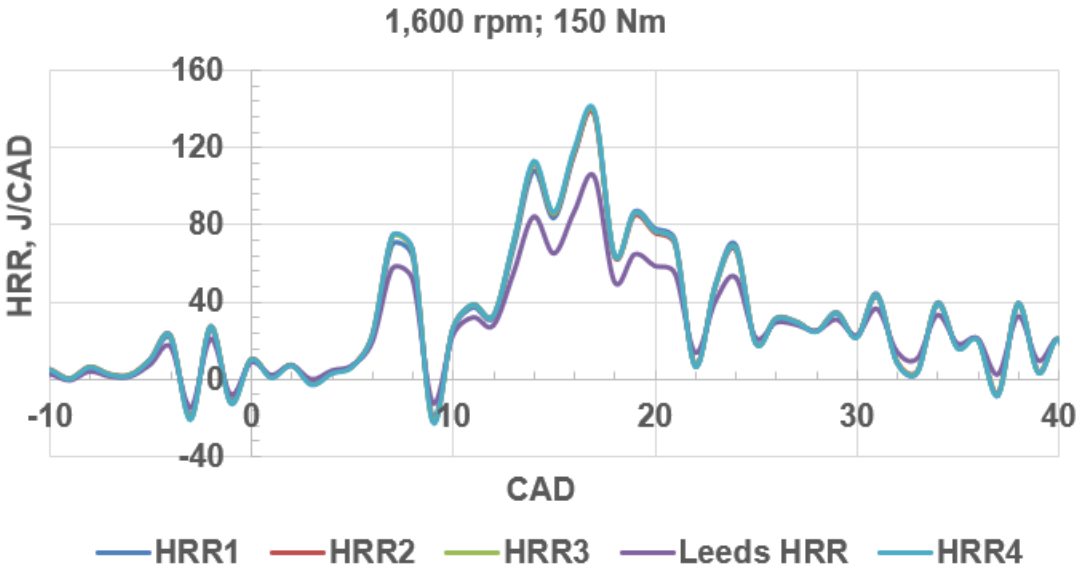

Figure 6.78 HRR profiles from the Leeds model and other models (1,600 rpm; 150 Nm)

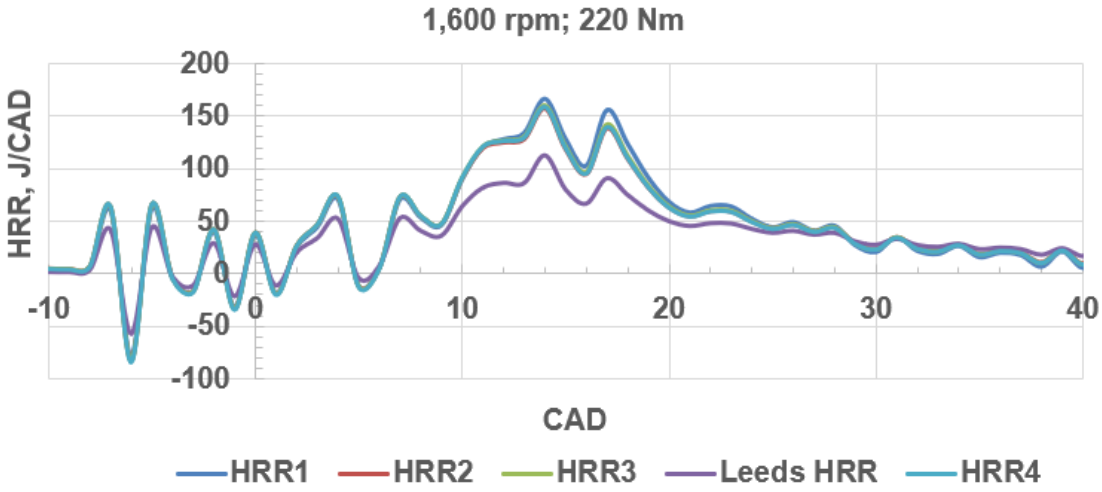

Figure 6.79 HRR profiles from the Leeds model and other models (1,600 rpm; 220 Nm)

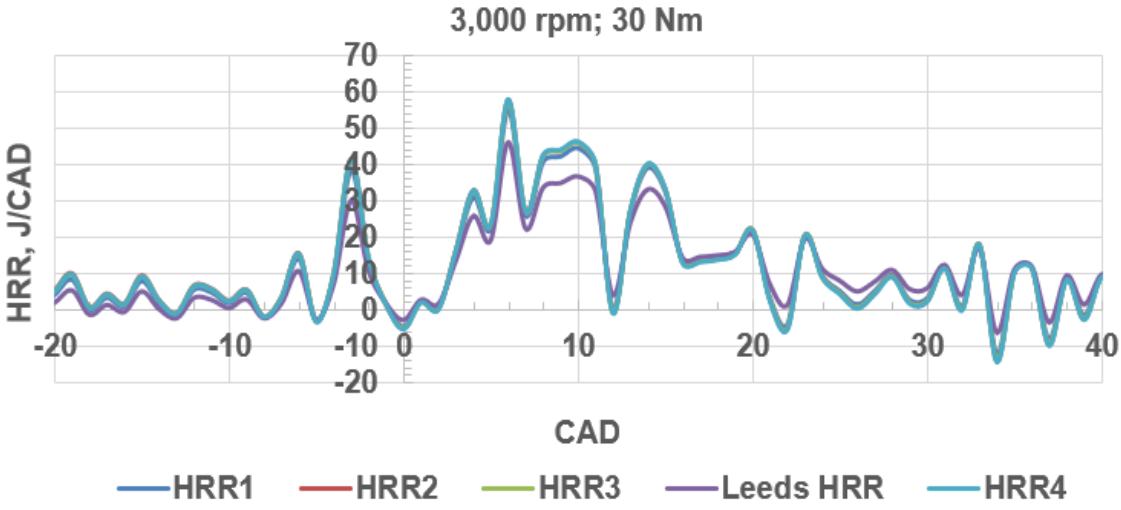

Figure 6.80 HRR profiles from the Leeds model and other models (3,000 rpm; 30 Nm)

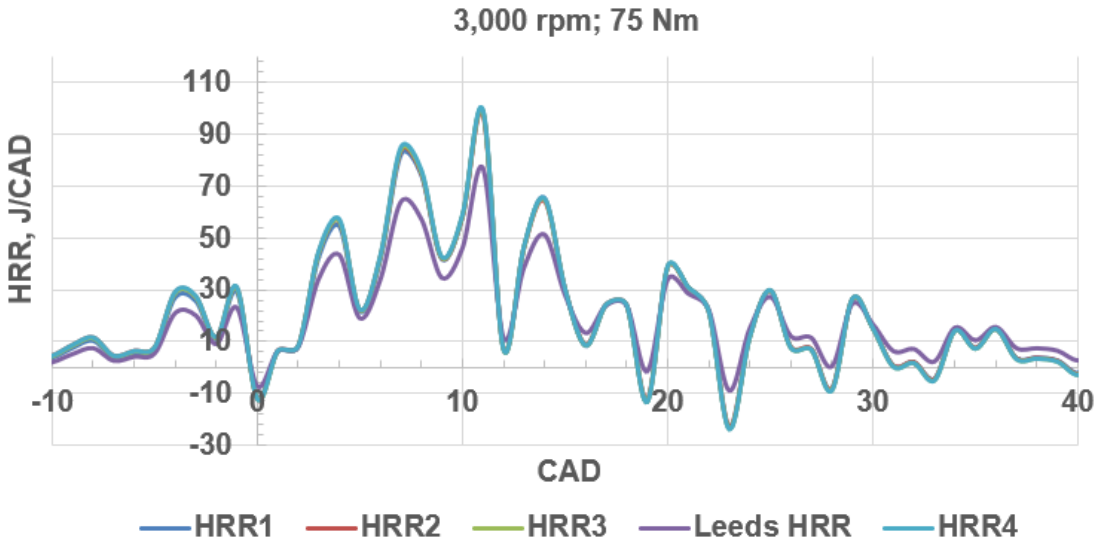

Figure 6.81 HRR profiles from the Leeds model and other models (3,000 rpm; 75 Nm)

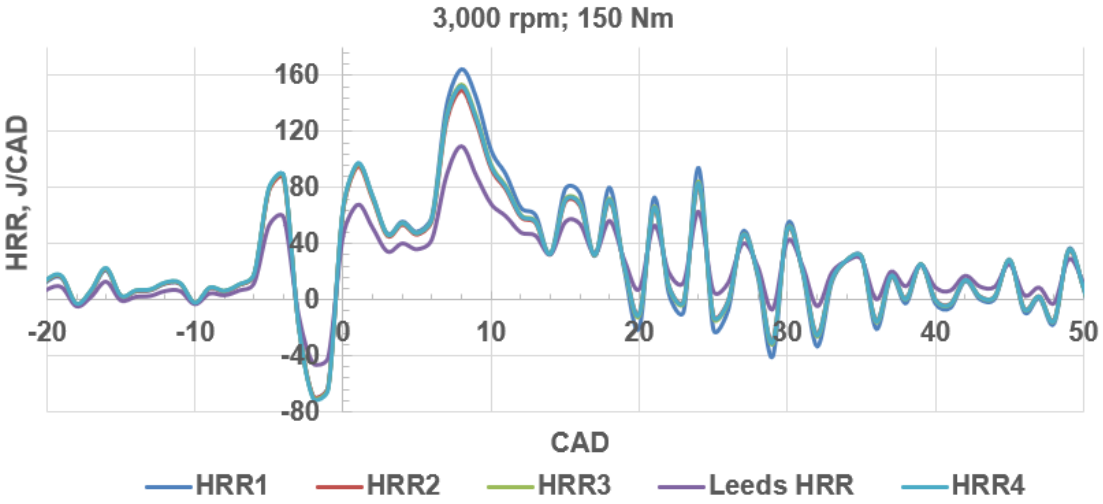

Figure 6.82 HRR profiles from the Leeds model and other models (3,000 rpm; 150 Nm)

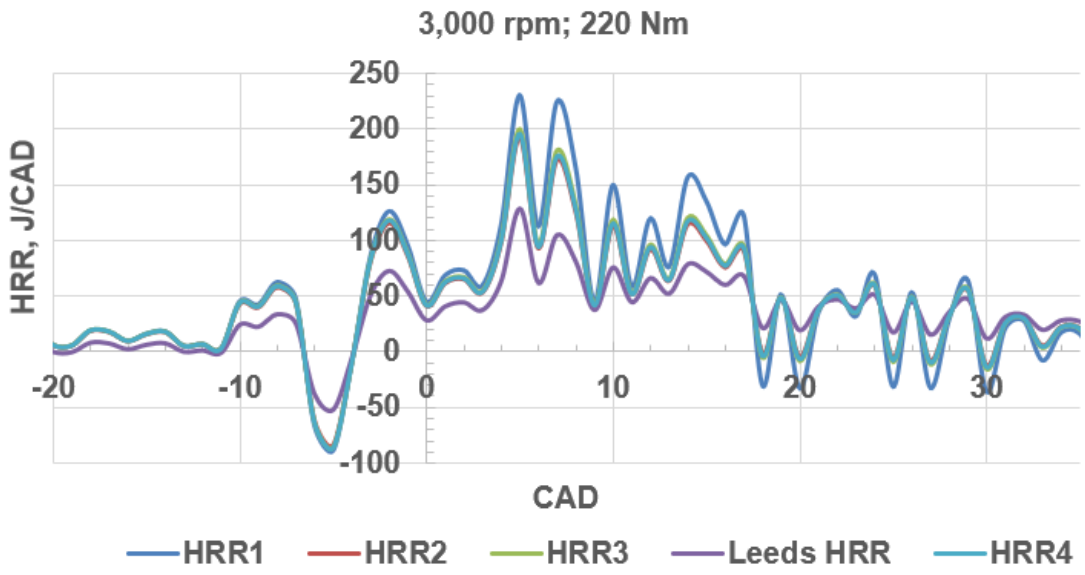

Figure 6.83 HRR profiles from the Leeds model and other models (3,000 rpm; 220 Nm)

6.4.7 Leeds model validation

The fuel consumption of the engine per thermodynamic cycle per cylinder was estimated from the Cumulative Heat Release (CHR) profiles obtained from the five HRR models. Figures 6.84 to 6.86 show the CHR profiles that were derived from the Leeds HRR model, (strictly for the heat that was released as a result of the combustion of the injected fuel). The profiles in Figures 6.84 to 6.86 represent the heat that was released from the combustion of the injected fuel mass in each of the four cylinders per power stroke (in joules) for the tested modes.

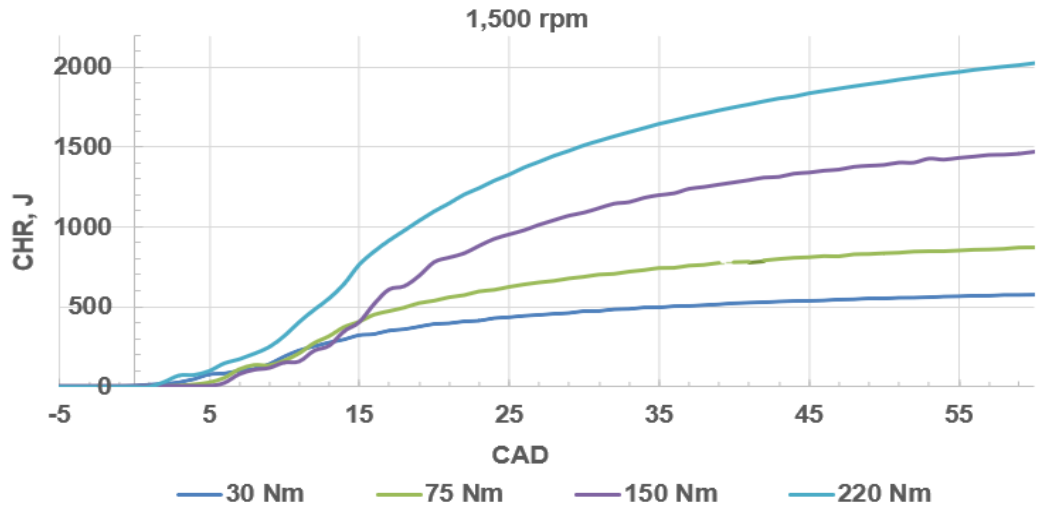

Figure 6.84 Cumulative heat release profiles (1,500 rpm modes)

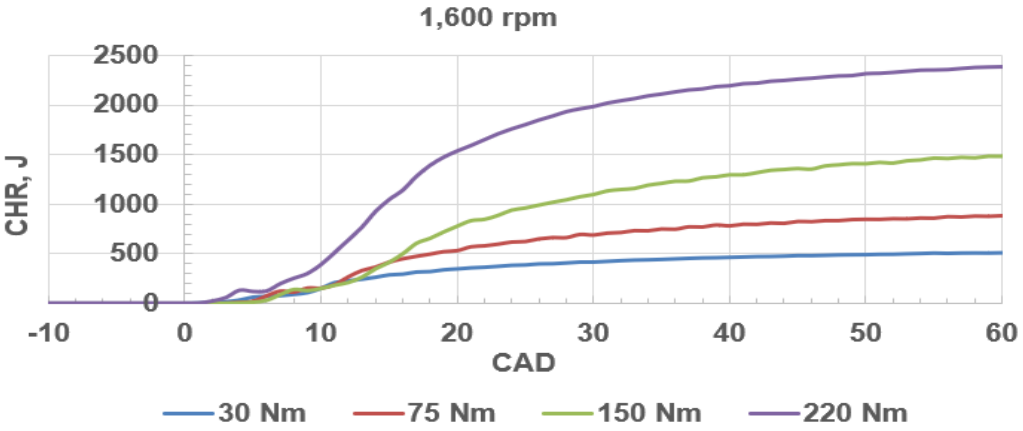

Figure 6.85 Cumulative heat release profiles (1,600 rpm modes)

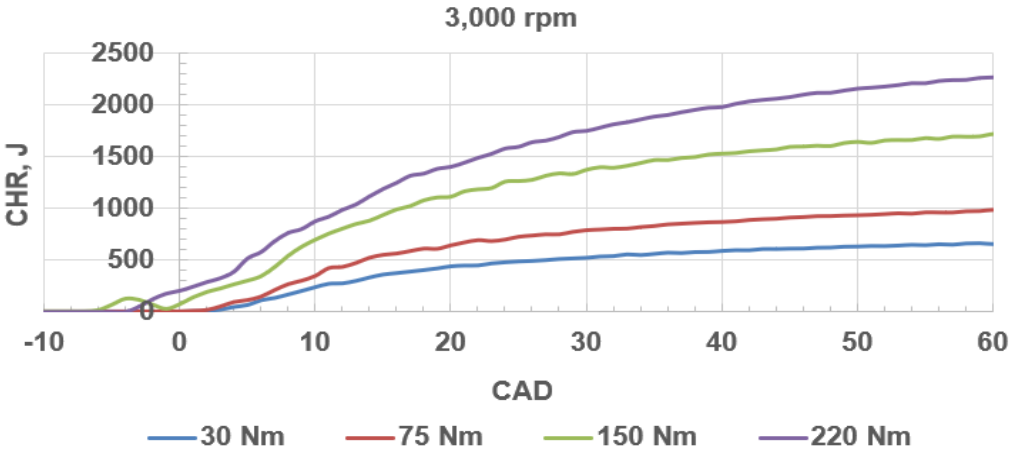

Figure 6.86 Cumulative heat release profiles (3,000 rpm modes)

Figure 6.87 shows the results of the validation of the HRR models. The figure shows that the fuel masses predicted by the Leeds HRR model (the pink bars) were the most accurate for all the tested engine modes. The Leeds HRR model that was based on the modified γ function, $\gamma_{mod}(T, \lambda)$, predicted the fuel consumption of the engine with an average error of 1.41% compared to the measured fuel consumption. The percentage errors of the fuel masses predicted by the Leeds HRR model ranged from -3.68 to +4.08, with a standard deviation of 1.21. The average error in the predicted fuel masses by the other HRR models that were based on γ(T) ranged from 15.85% to 16.36%. The HRR models that were based on γ(T) overpredicted the fuel consumption of the engine because the significant effect of λ on γ was neglected in the models. Figure 6.87 clearly shows that the accuracy of the HRR model of CI engines is enhanced by using γ(T, λ) for both near–stoichiometric and non-stoichiometric operating conditions. Table 6.4 summarises the analysis that was done to compare the predicted fuel masses to the measured fuel masses.

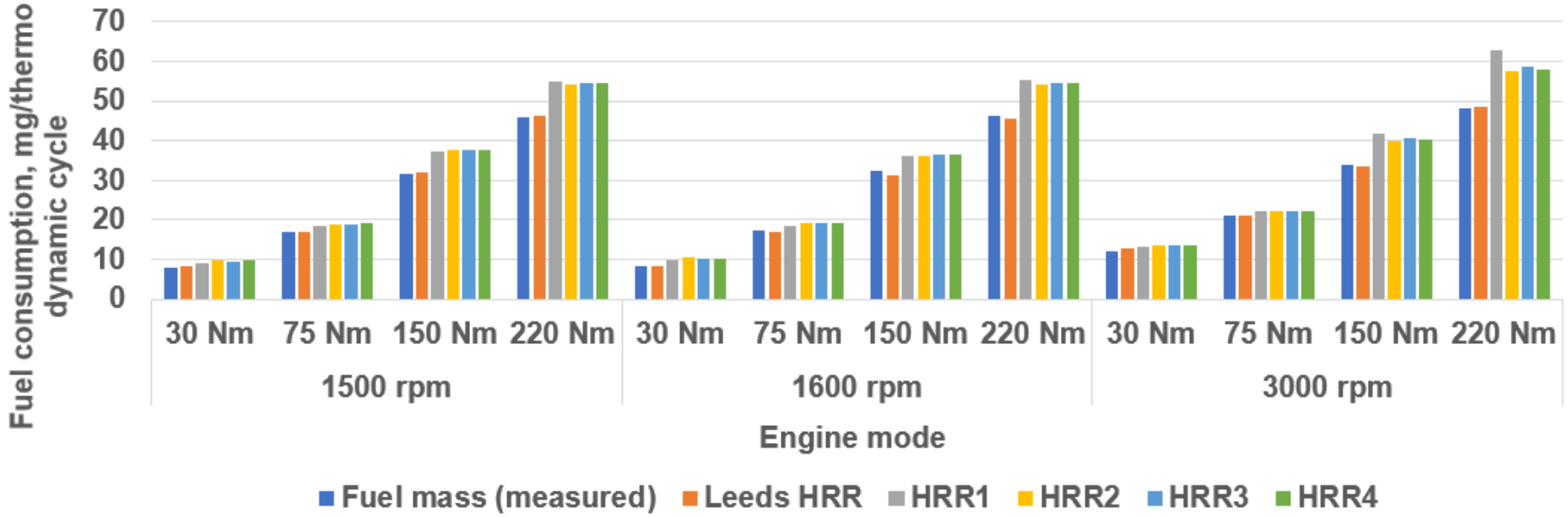

Figure 6.87 Comparison of measured and predicted fuel masses

Table 6.4 Model validation

			Fuel mass, mg/thermodynamic cycle						% Deviation from measured fuel mass				
Engine speed, rpm	**Torque, Nm**	**λ**	**Measured**	**Leeds HRR**	**HRR1**	**HRR2**	**HRR3**	**HRR4**	**Leeds HRR**	**HRR1**	**HRR2**	**HRR3**	**HRR4**
1,500	30	8.40	8.11	8.20	9.23	9.73	9.62	9.69	1.09	13.81	19.98	18.62	19.48
	75	4.04	16.87	16.84	18.41	19.05	18.95	19.06	-0.21	9.11	12.93	12.32	12.97
	150	2.14	31.77	32.08	37.11	37.48	37.57	37.71	0.98	16.82	17.99	18.24	18.69
	220	1.46	46.02	46.18	55.1	54.15	54.52	54.51	0.35	19.73	17.67	18.47	18.45
1,600	30	8.35	8.17	8.15	9.95	10.42	10.32	10.39	-0.20	21.78	27.51	26.30	27.13
	75	3.97	17.18	16.87	18.59	19.22	19.14	19.25	-1.8	8.23	11.87	11.39	12.06
	150	2.10	32.33	31.14	36.02	36.29	36.42	36.56	-3.68	11.41	12.25	12.65	13.08
	220	1.45	46.35	45.63	55.44	54.05	54.50	54.44	-1.55	19.61	16.61	17.58	17.45
3,000	30	5.49	12.23	12.73	13.41	13.57	13.56	13.60	4.08	9.61	10.93	10.88	11.19
	75	3.56	20.97	21.21	22.28	22.28	22.32	22.35	1.16	6.23	6.25	6.45	6.57
	150	2.16	33.96	33.58	41.92	40.01	40.50	40.35	-1.13	23.45	17.81	19.27	18.80
	220	1.53	48.21	48.54	62.88	57.64	58.54	58.08	0.68	30.44	19.56	21.43	20.47
					Average of absolute errors:				1.41	15.85	15.95	16.13	16.36
					Standard deviation:				1.21	7.04	5.26	5.24	5.19
					Error range:				-3.68 - +4.08	6.23-30.44	6.25-27.51	6.45-26.30	6.57-27.13

6.4.8 Determination of combustion phasing

The validated model (Leeds HRR model) was used to determine the SoC, EoC and the crank angle timing at which 50% of the injected fuel mass was burned (MFB50) from the fuel burn profiles of the modes that were tested. The phasing of the combustion (SoC, MFB50, EoC) for the 1,500 rpm; 150 Nm test mode was determined as shown in Figure 6.88. The figure shows that, when the engine was run at 1,500 rpm and 150 Nm, the SoC was at 5^{o} aTDC, 50% of the injected fuel was burned at 19^{o} aTDC while the EoC was at 51^{o} aTDC. The SoC, MFB50, EoC for the other modes were determined in a similar manner and tabulated as shown in Table 6.5.

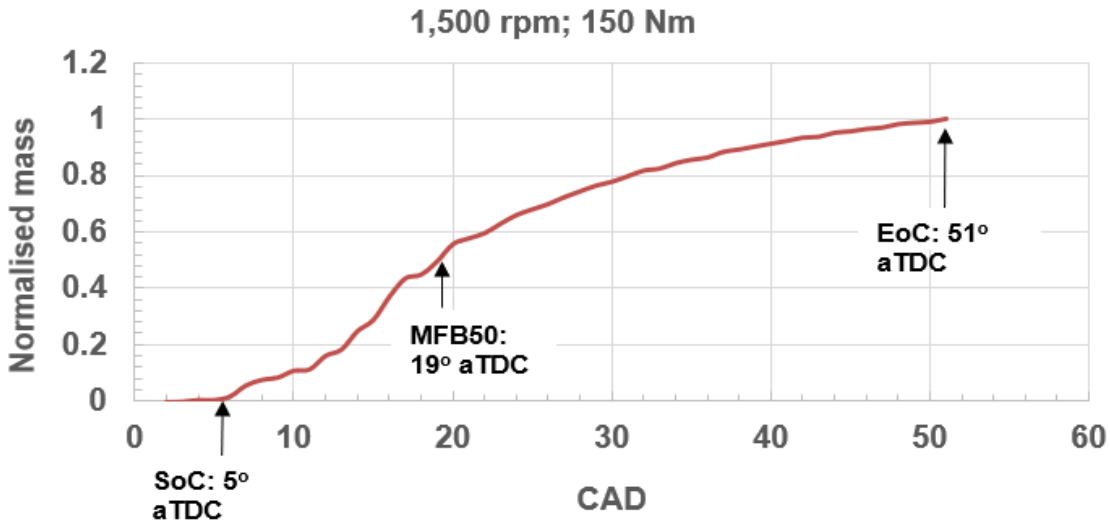

Figure 6.88 Determination of the combustion phasing from the fuel burn profile

Table 6.5 Combustion phasing of the tested engine modes

Engine speed, rpm	Torque, Nm	SoC, CAD	EoC, CAD	MFB50, CAD
1,500	30	0	18	10
	75	3	35	14

	150	5	51	19
	220	2	60	18.5
1,600	30	1	21	10.5
	75	2	33	14
	150	3	45	18.5
	220	2	55	18
3,000	30	0	33	12
	75	1	47	13
	150	-1	35	10.5
	220	-5	47	13

6.5 Heat Release Rate (HRR) results for alternative fuels (GTL and HVO diesels)

The results for the HRR analysis of the tested alternative fuels (GTL and HVO diesels) are presented in this section. The Leeds HRR model was validated for the alternative fuels by comparing the predicted fuel consumption to the measured fuel consumption. The combustion behaviour of the investigated fuels (USLD, GTL, and HVO diesels) were compared graphically. The combustion phasing for the three fuels at the tested conditions were determined from the fuel burn profiles.

6.5.1 Distillation characteristics of USLD, GTL, and HVO diesels

Figure 6.89 shows the distillation characteristics of the tested fuels.

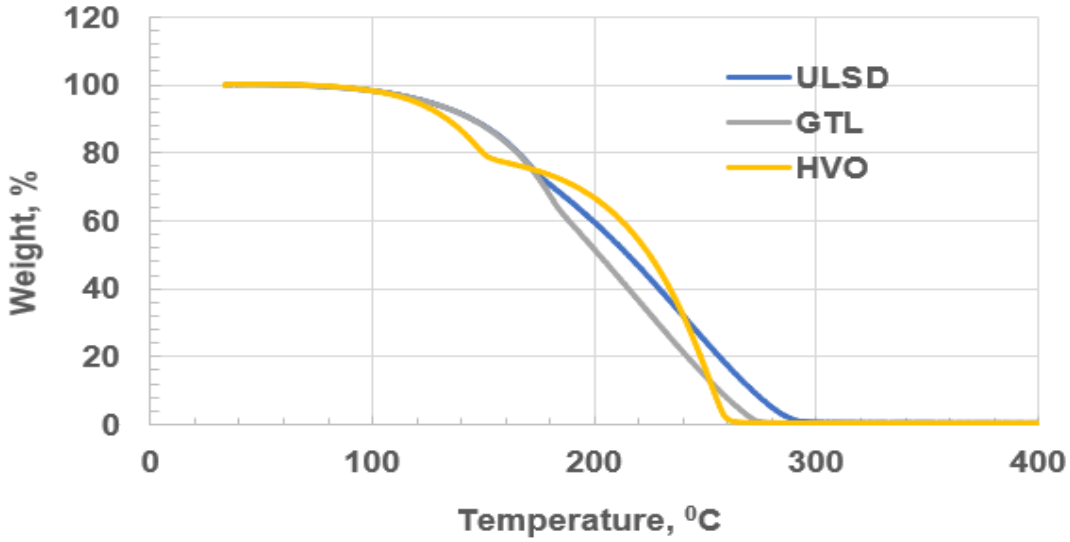

Figure 6.89 Distillation characteristics of ULSD, GTL, and HVO diesels

Figure 6.89 shows that, although GTL and HVO diesels had similar thermo-physical properties (Table 3.12), the alternative fuels had distinctly different distillation characteristics. As stated in Section 3.4.3, HVO diesel and GTL diesel are produced from different starting materials and by different processes. Therefore, due to the difference in the starting raw materials and the processes involved in the production of the alternative fuels, the constituent hydrocarbon fractions that make up HVO and GTL diesels are not identical. Consequently, GTL and HVO diesels have different boiling ranges (distillation characteristics) (Figure 6.89). The observed difference in the distillation characteristics of the two alternative fuels inadvertently implied that the two fuels would have different combustion behaviours notwithstanding the similarities in their fuel properties. Figure 6.89 shows that HVO diesel had the narrowest boiling range of the three fuels.

6.5.2 Pressure-crank angle data as model input

The basic input data that were used to carry out this work were the pressure traces of the engine at the specified test modes (Table 6.6) for each of the three diesel fuels. The values of the power (kW) of the engine at the tested modes are

depicted in Table 6.6. The basic input data (pressure-crank angle data) were plotted and presented as shown in Figures 6.90 to 6.92 respectively for standard diesel, GTL diesel, and HVO diesel.

Table 6.6 Test conditions and the corresponding engine power

Test	Engine test mode	Fuel	Power, kW
1	1,000 rpm; 30% throttle	ULSD	13
2		GTL	13
3		HVO	13
4	1,600 rpm; 50% throttle	ULSD	27
5		GTL	27
6		HVO	27
7	1,900 rpm; 70% throttle	ULSD	47
8		GTL	47
9		HVO	47

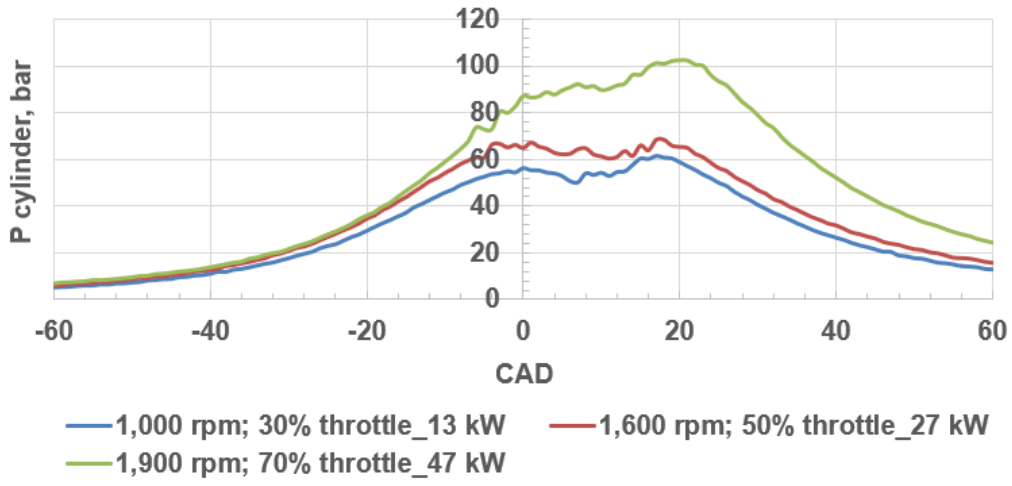

Figure 6.90 Pressure traces (ULSD)

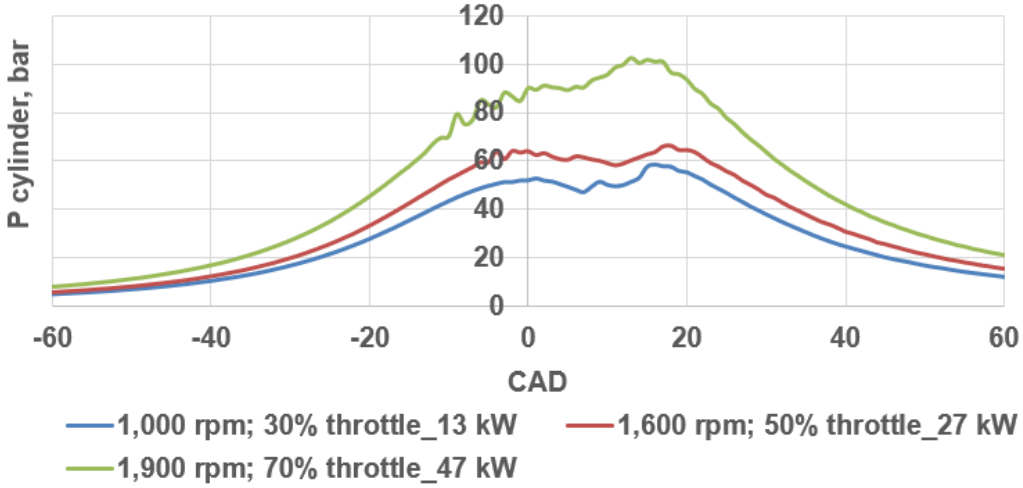

Figure 6.91 Pressure traces (GTL)

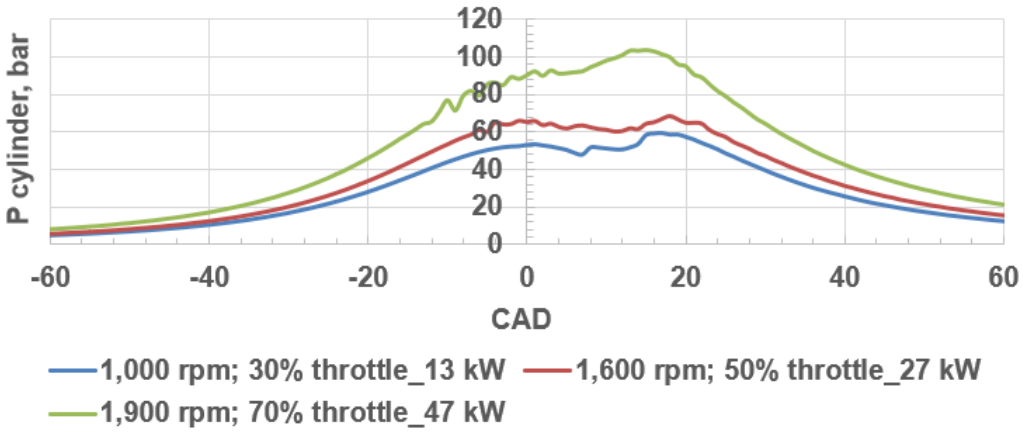

Figure 6.92 Pressure traces (HVO)

6.5.3 Calculated in-cylinder temperatures

Figures 6.93 to 6.95 depict the instantaneous cylinder temperatures that were calculated from the measured in-cylinder pressures and utilised in the HRR analysis.

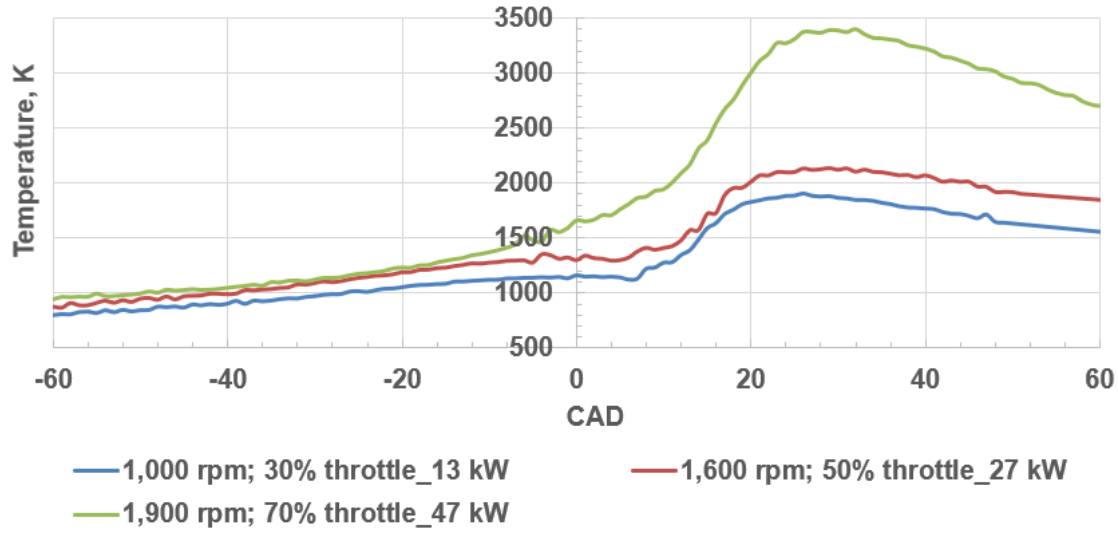

Figure 6.93 Calculated in-cylinder temperatures as a function of crank angle with different loads (ULSD)

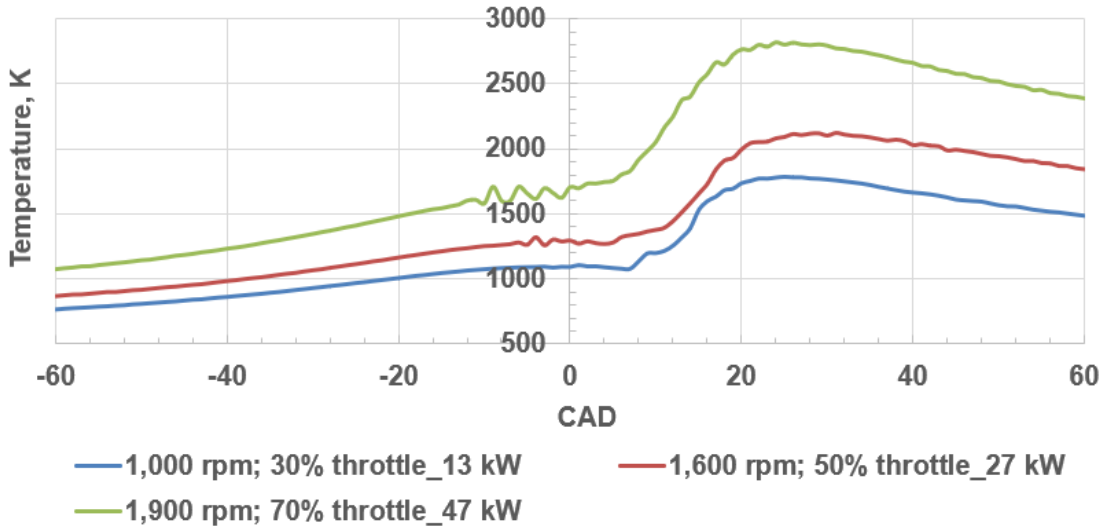

Figure 6.94 Calculated in-cylinder temperatures as a function of crank angle with different loads (GTL)

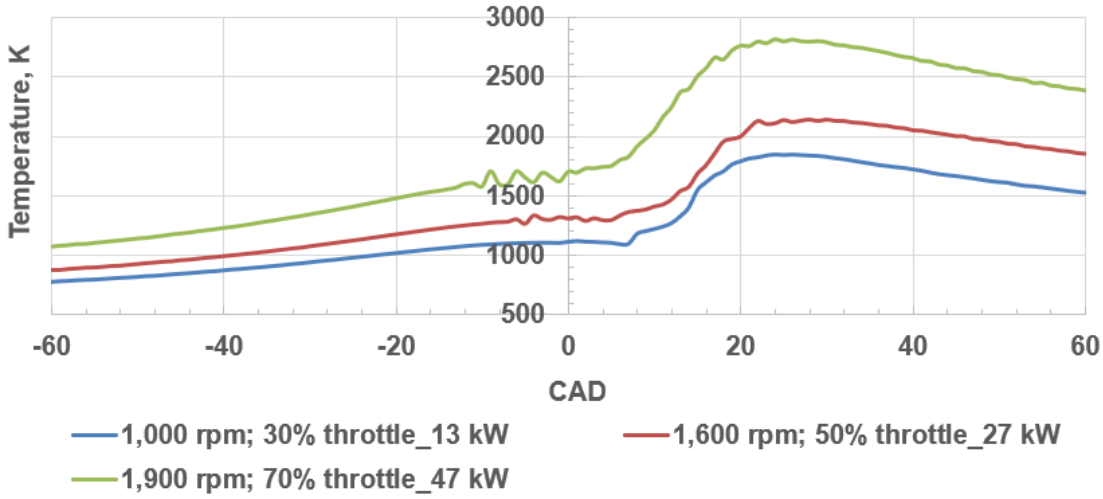

Figure 6.95 Calculated in-cylinder temperatures as a function of crank angle with different loads (HVO)

Figures 6.93 to 6.95 indicate that, for each of the fuels, the instantaneous in-cylinder temperature increased as the power of the engine was increased. The peak temperatures for the low, medium, and high loads occurred at crank angle degrees (CAD) of 26, 29, 32 respectively for standard diesel as shown in Figure 6.93. However, for the alternative fuels (GTL and HVO diesel), the peak temperatures occurred at 25, 31, 24 CAD, and 24, 28, and 25 CAD respectively for the low, medium and high power conditions (Figures 6.94 and 6.95). Therefore, the peak temperature occurred earlier when the engine was run on the alternative fuels than when it was run on fossil diesel. The early occurrence of the peak temperatures that was observed for the alternative fuels was because of the advanced Start of Injection (SoI) and the relatively high Cetane Numbers (CN) of the alternative fuels. The SoI timings can be located on the pressure traces or temperature profiles where fluctuations were observed near the TDC. At the high power condition, much higher compression pressure and temperature were attained as shown in Figures 6.90 to 6.95. Therefore, advanced injection of fuel was triggered by the Engine Control Unit (ECU) of the engine at the high power conditions to prevent undesirable high Peak Pressure Rise Rates (PPRR)

and PHRR, both of which could occur should the SoI and SoC be too close to the TDC. The combined effect of advanced SoI and relatively high CN caused the auto–ignition of the compressed fuel–air mixture to occur earlier when the engine was run on GTL and HVO diesels than when it was run on standard diesel (ULSD).

The pressure traces for the three fuels were quite similar. However, the calculated peak temperatures for the alternative fuels were lower than those of ULSD. The peak temperatures for ULSD were higher than those for GTL and HVO diesels because of the relatively low CN and the late Start of Injection (SoI) of ULSD which meant that most of the fuel energy was released after the TDC in the case of ULSD. Due to the relatively high CN of GTL and HVO diesels as well as the advanced pilot fuel injection of the alternative fuels by the ECU, significant heat was released bTDC during the pilot combustion of the alternative fuels. This led to the observed decrease in the peak temperatures for the alternative fuels below ULSD.

The temperature profiles fluctuated near the Top Dead Centre (TDC) in Figures 6.93 to 6.95. The observed fluctuations were due to the auto–ignition of the pre-injected fuel while pilot injection continued. The CI engine that was used to carry out the tests was a MFIS engine. Fuel injection began before the TDC in the engine and continued at specific crank angles after the TDC.

6.5.4 Comparison of the modified γ functions and γ functions from literature for alternative fuels

The values of γ estimated from various γ functions were plotted, as depicted in Figure 6.96, against the temperature of the gases in the cylinder for the 1,600 rpm; 50% throttle operation mode (medium power) when the engine was run on HVO. Figure 6.96 shows the disparity in the values of γ estimated from the

equations that expressed γ (T) and the values of γ from the modified gamma function, γ_{mod}. Gamma1 to Gamma4 represent the gamma values predicted by the four equations that expressed γ (T) (Equations 3.29 to 3.32). Figure 6.96 shows that the estimated values of γ from γ_{mod} at all the temperature points were much higher than the estimates from the other functions which expressed γ as a function of temperature only. The same trend was observed for standard diesel and GTL diesel. Therefore, it was concluded that λ had a significant effect on γ when alternative fuels were used in the engine. It was shown in Section 6.4.4 that λ had a significant effect on γ when the engine was run on off–road diesel.

The excess air ratio, λ was constant at each of the tested modes. The observed unusual rise in the values of γ predicted by γ_{mod} as the temperature increased above 1,000 K was due to the sensitivity of the polynomial γ model (γ_{mod}) to λ. The predicted γ values were observed to drop in the previous work as the temperature increased. However, for the HRR analysis of the investigated alternative fuels, for values of λ < 2, γ dropped as the temperature increased to 1,000 K for all the fuels. At temperatures above 1,000 K, γ increased as the temperature increased for all the fuels when λ was < 2 (Figure 6.96). The same trends were observed for the alternative fuels for values of λ < 2 and λ > 2. However, the values of γ for pure diesel were observed to drop as the temperature increased for values of λ > 2 in the previous work for which off-road diesel was used. The observed trend of γ for the alternative fuels differed from that for ULSD when λ was > 2.

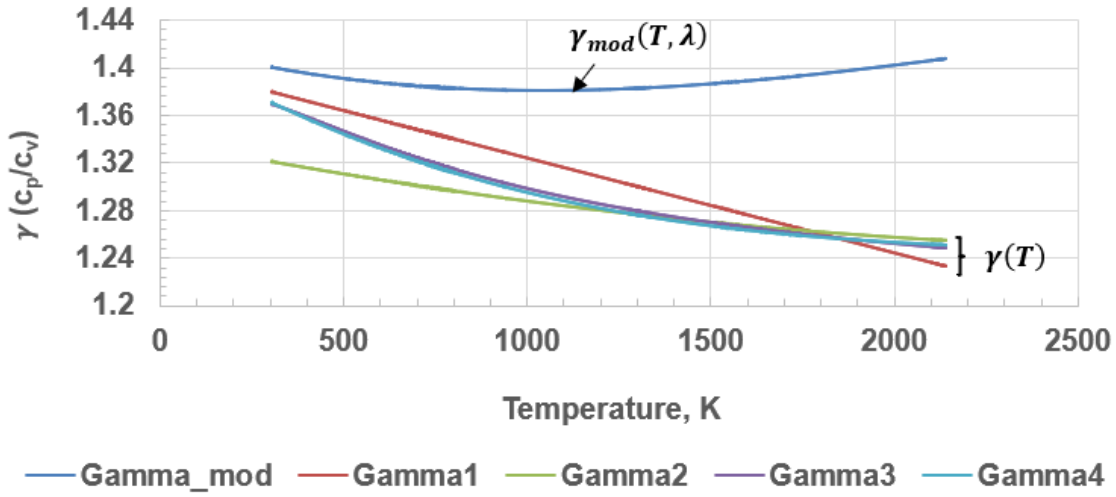

Figure 6.96 Comparison of the modified gamma and gamma functions from literature (HVO: 1,600 rpm; 50% throttle_27 kW)

6.5.5 Sensitivity of diesel engine HRR model to γ functions – comparison of Leeds model to others

Figures 6.97 to 6.105 present the HRR profiles from the investigated HRR models. The profiles for standard diesel are depicted in Figures 6.97 to 6.99, while the HRR profiles for GTL and HVO diesels are depicted in Figures 6.100 to 6.102, and Figures 6.103 to 105 respectively. The figures vividly depict the sensitivity of the HRR model of the engine to γ functions as the five HRR models predicted different PHRR values. The Leeds HRR model predicted the lowest PHRR for all the modes that were tested for the three fuels. Figure 6.96 shows that $\gamma(T,\lambda)$ gave estimates of γ that were higher than the estimates from the functions that expressed $\gamma(T)$. However, Figures 6.97 to 6.105 show that, for both standard diesel and the alternative fuels, the HRR model that utilised $\gamma(T,\lambda)$ predicted lower PHRR values for the CI engine than the HRR models that utilised $\gamma(T)$. Though the five HRR models showed the same trend, they predicted different PHRR for the engine modes which were investigated. This necessitated the validation of the Leeds HRR model by comparing the fuel consumption of the

engine predicted by the models to the measured fuel consumption in the next section (Section 6.5.6).

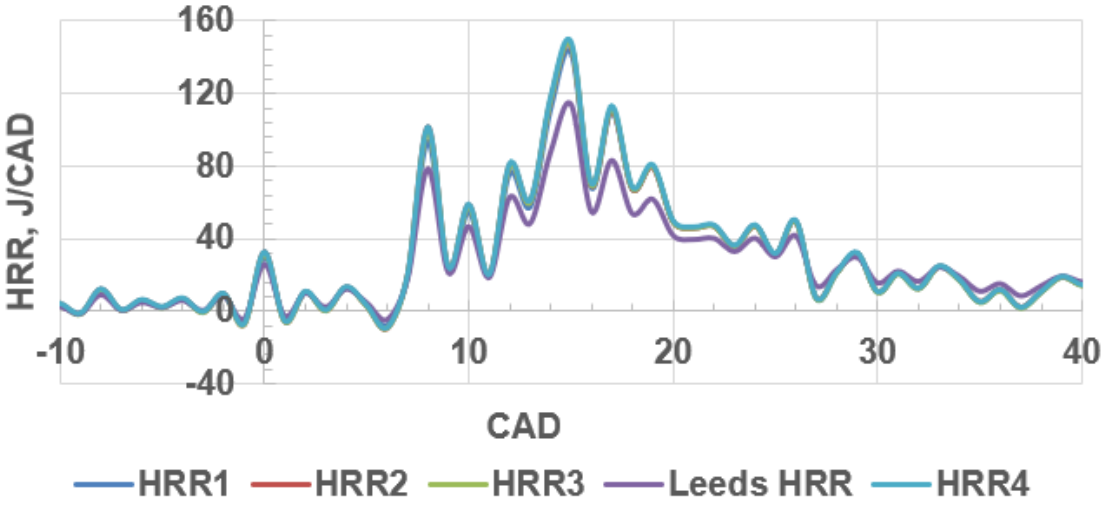

Figure 6.97 HRR profiles from the Leeds model and other model: standard diesel (1,000 rpm; 30% throttle_13 kW)

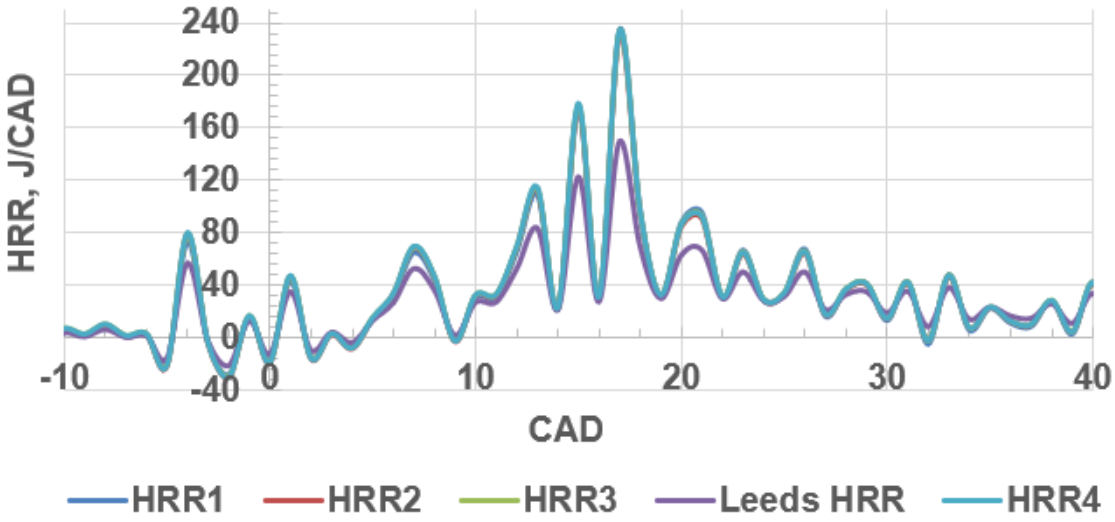

Figure 6.98 HRR profiles from the Leeds model and other models: standard diesel (1,600 rpm; 50% throttle_27 kW)

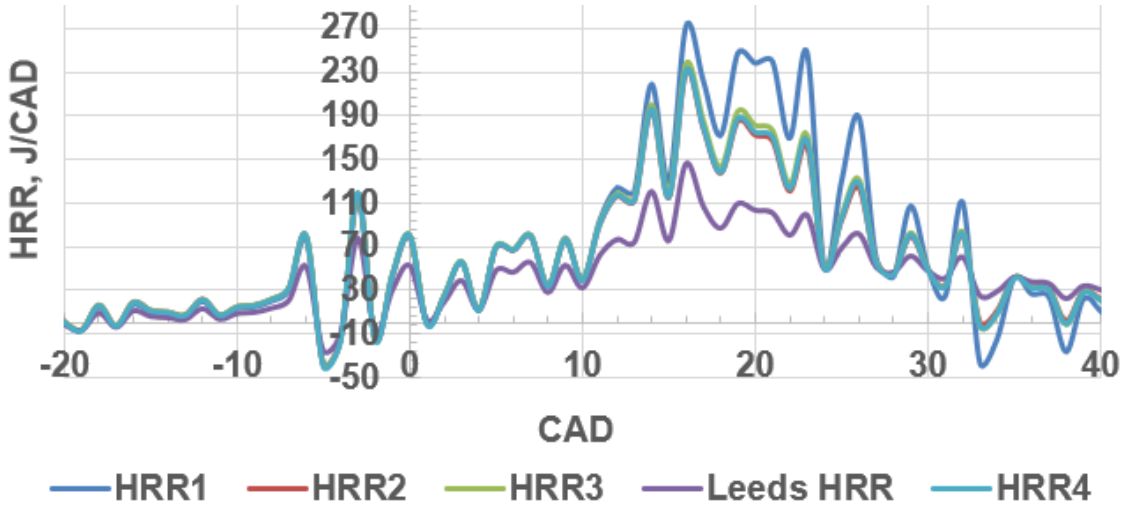

Figure 6.99 HRR profiles from Leeds model and other models: standard diesel (1,900 rpm; 70% throttle_47 kW)

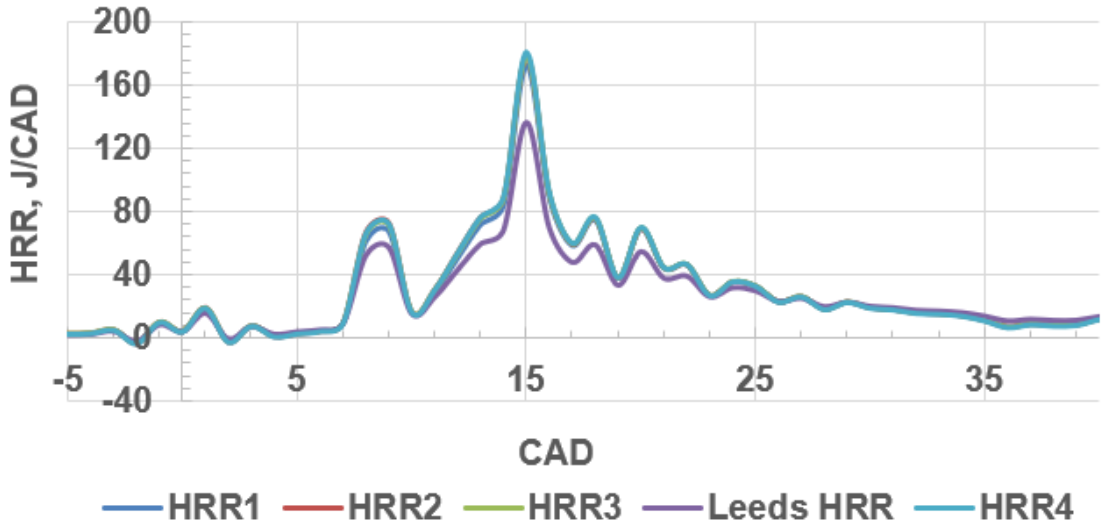

Figure 6.100 HRR profiles from Leeds model and other models: GTL diesel (1,000 rpm; 30% throttle_13 kW)

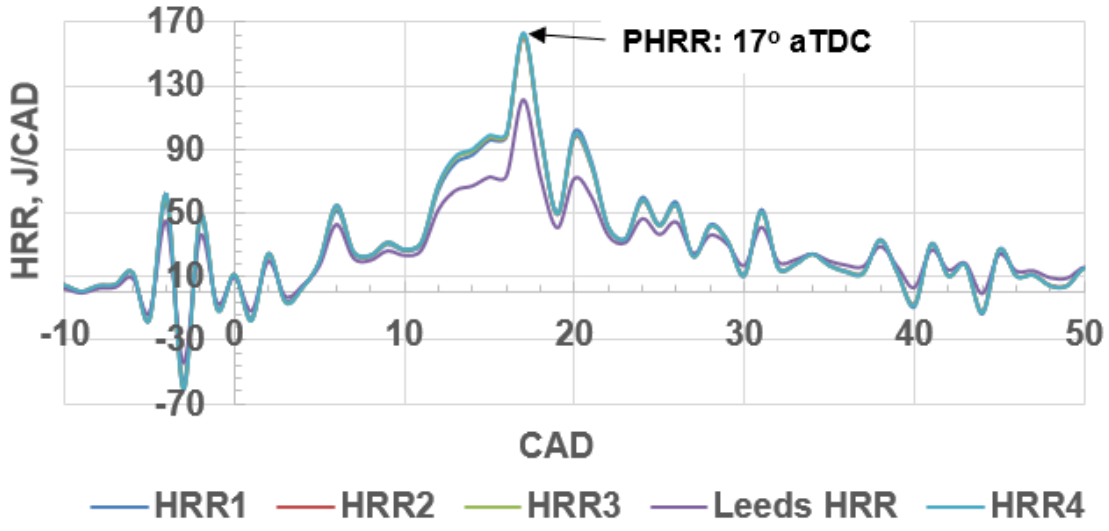

Figure 6.101 HRR profiles from the Leeds model and other models: GTL diesel (1,600 rpm; 50% throttle_27 kW)

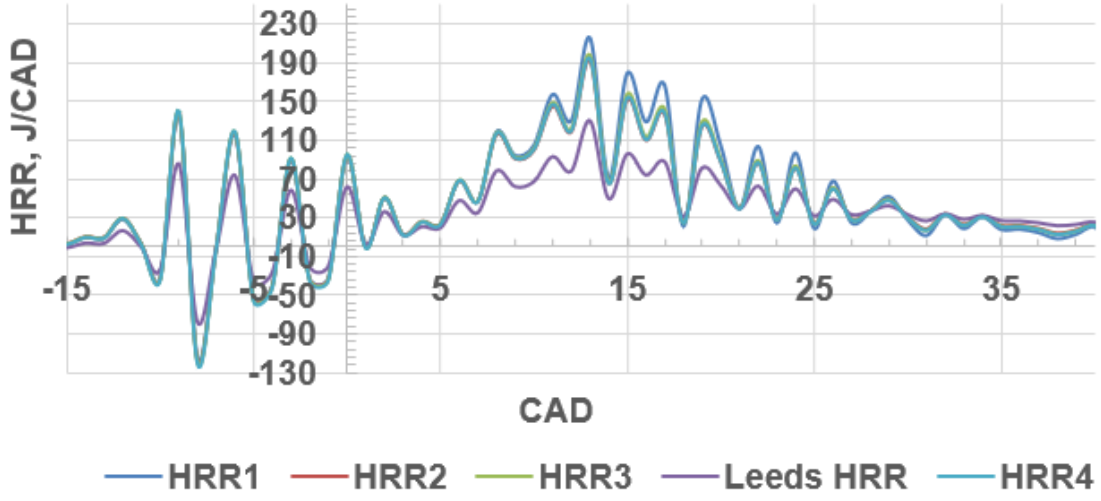

Figure 6.102 HRR profiles from the Leeds model and other models: GTL diesel (1,900 rpm; 70% throttle_47 kW)

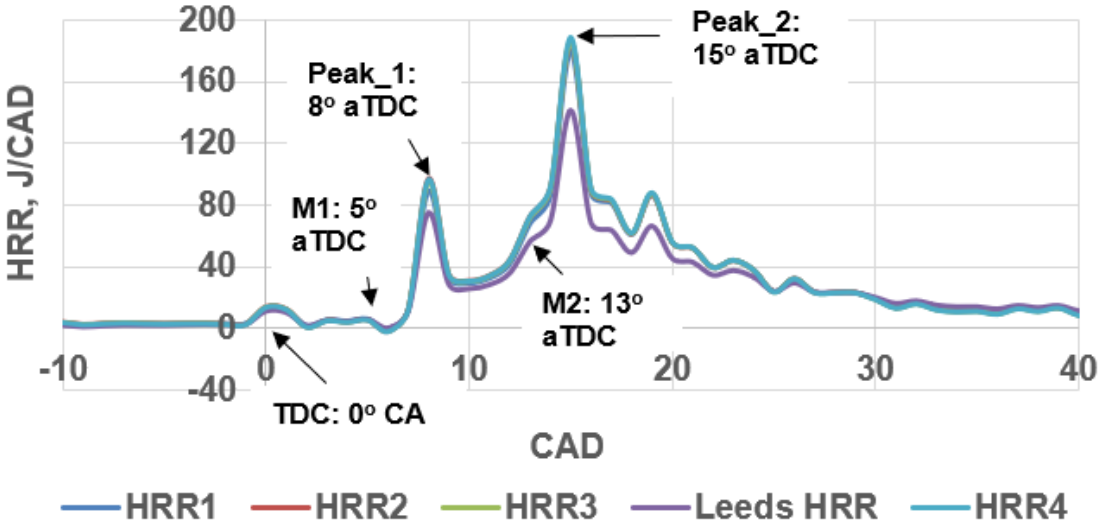

Figure 6.103 HRR profiles from the Leeds model and other models: HVO diesel (1,000 rpm; 30% throttle_13 kW)

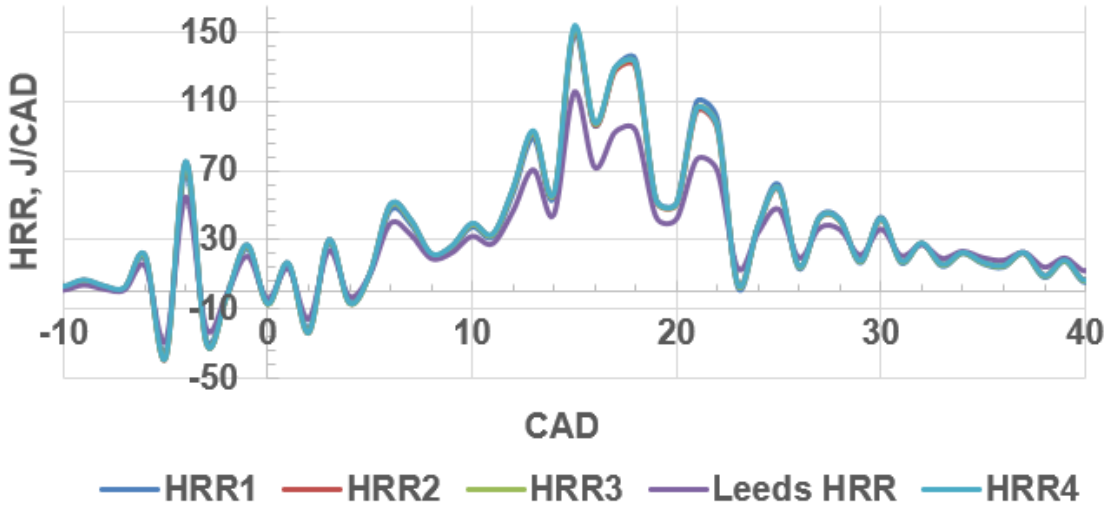

Figure 6.104 HRR profiles from the Leeds model and other models: HVO diesel (1,600 rpm; 50% throttle_27 kW)

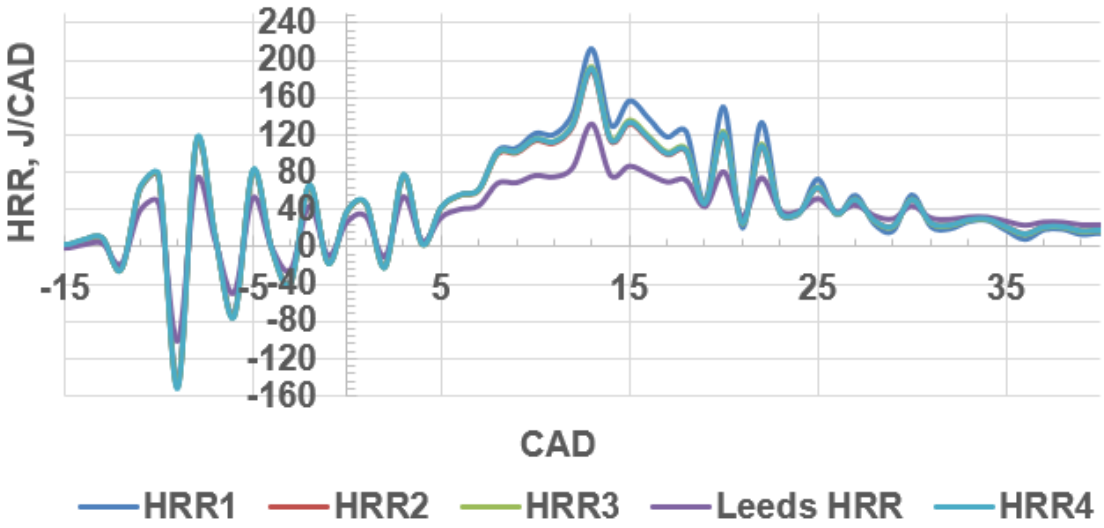

Figure 6.105 HRR profiles from the Leeds model and other models: HVO diesel (1,900 rpm; 70% throttle_47 kW)

The crank angle timing of the PHRR of the engine for each of the tested modes was determined directly from the HRR profile. As depicted in Figure 6.101, the PHRR for the 1,600 rpm; 50% throttle mode occurred at 17^{o} aTDC for GTL diesel. Multiple peaks were also observed in all the HRR profiles as a result of the Multiple Fuel Injection Strategy (MFIS) of the engine. The 1,000 rpm; 30% throttle engine mode (Figure 6.103) showed two prominent peaks for HVO diesel. Peak_1 resulted from the heat that was released from the combustion of the fuel that was injected during the pilot fuel injection and the first main injection, M1 (at 5^{o} aTDC). Thereafter, there was another main injection event, M2 at 13^{o} aTDC which caused another heat release that led to the second prominent peak (Peak_2).

6.5.6 Validation of the Leeds HRR model

The Cumulative Heat Release (CHR) profiles shown in Figures 6.106 to 6.108 (strictly for the heat that was released as a result of the combustion of the injected fuel) were determined from the HRR profiles. The HRR and CHR profiles of the fuels were used to predict the fuel consumption of the engine per thermodynamic

cycle per cylinder. Figures 6.106 to 6.108 graphically depict the heat that was released from the combustion of the injected fuel mass in each of the four cylinders per power stroke (in joules).

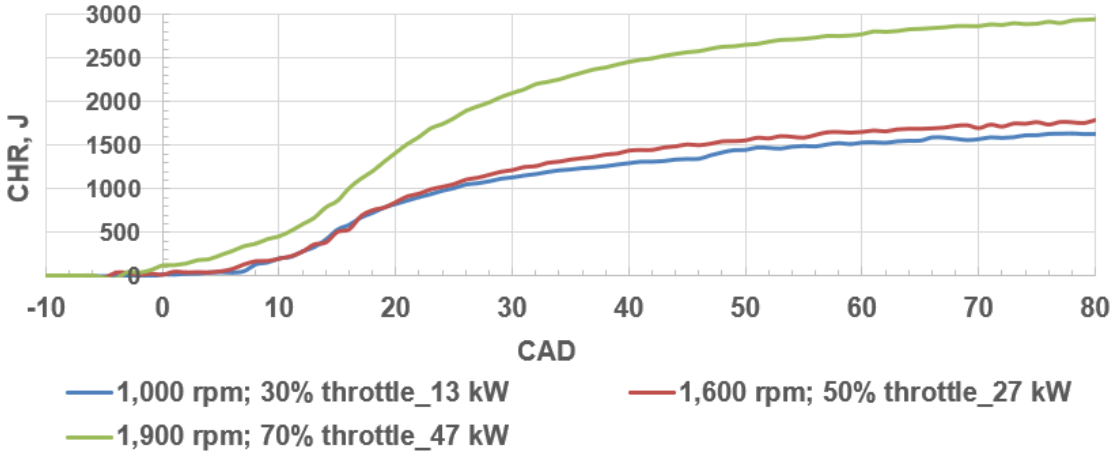

Figure 6.106 Cumulative heat release profiles (standard diesel)

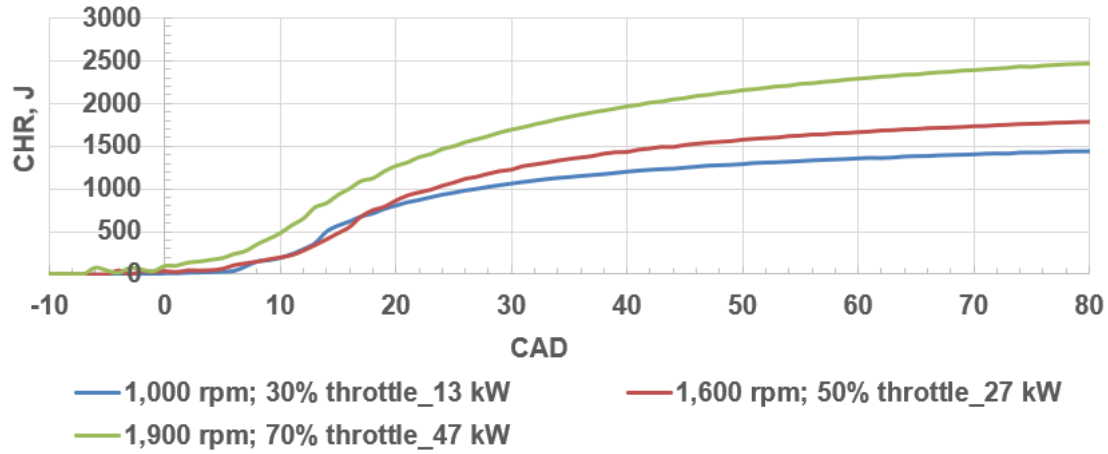

Figure 6.107 Cumulative heat release profiles (GTL)

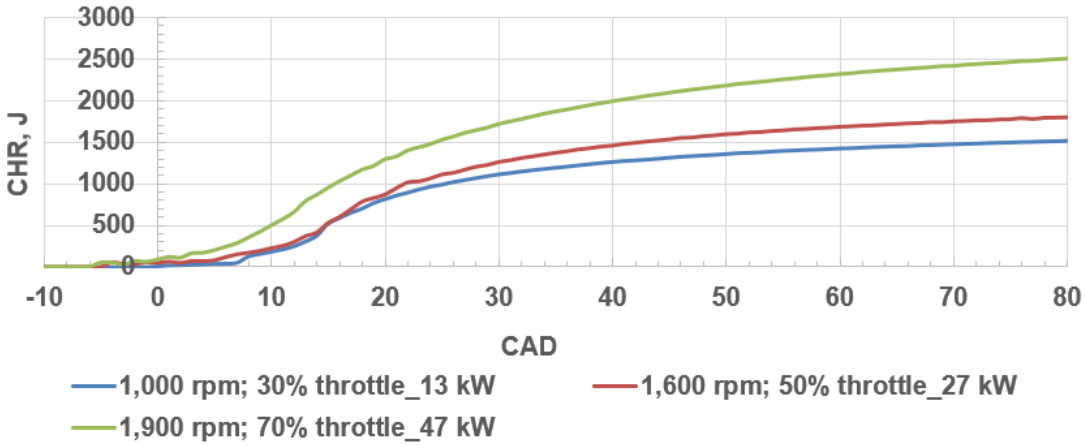

Figure 6.108 Cumulative heat release profiles (HVO)

Figure 6.109 shows the result of the validation of the HRR models. The figure shows that the fuel masses predicted by the Leeds model (the pink bars with black borderline) were the most accurate for all the engine modes and the three fuels that were investigated. The Leeds HRR model predicted the fuel consumption of the engine for ULSD, GTL and HVO diesels with an overall average error of 4.86% compared to the measured fuel consumption (blue bars with black borderline). The percentage errors of the fuel masses predicted by the Leeds HRR model ranged from -8.27 to +8.69, with a standard deviation of 2.39. The overall average error that was obtained for off–road diesel using the Leeds HRR model was 1.41%. The percentage error obtained for the alternative diesel fuels was relatively high compared to that for off-road diesel because in this aspect of the HRR analysis that involved alternative fuels, multiple fuels with quite different HRR behaviours were investigated whereas the previous work predicted the fuel masses for a single fuel (off-road diesel). The overall average errors in the predicted fuel masses by the other HRR models that were based on γ(T) ranged from ~15 to 20%. The HRR models that were based on γ(T) overpredicted the fuel consumption of the engine because the significant effect of λ on γ was not accounted for in the models. Figure 6.109 clearly shows that the accuracy of

the HRR model of CI engines for predicting the combustion behaviour of standard diesel and the alternative fuels was enhanced by using γ(T, λ). The incorporation of the rate of evaporation of the injected fuel into the Leeds HRR model also contributed to the accuracy of the model. Table 6.7 presents the summary of the analysis that was done to compare the predicted fuel masses to the measured fuel masses.

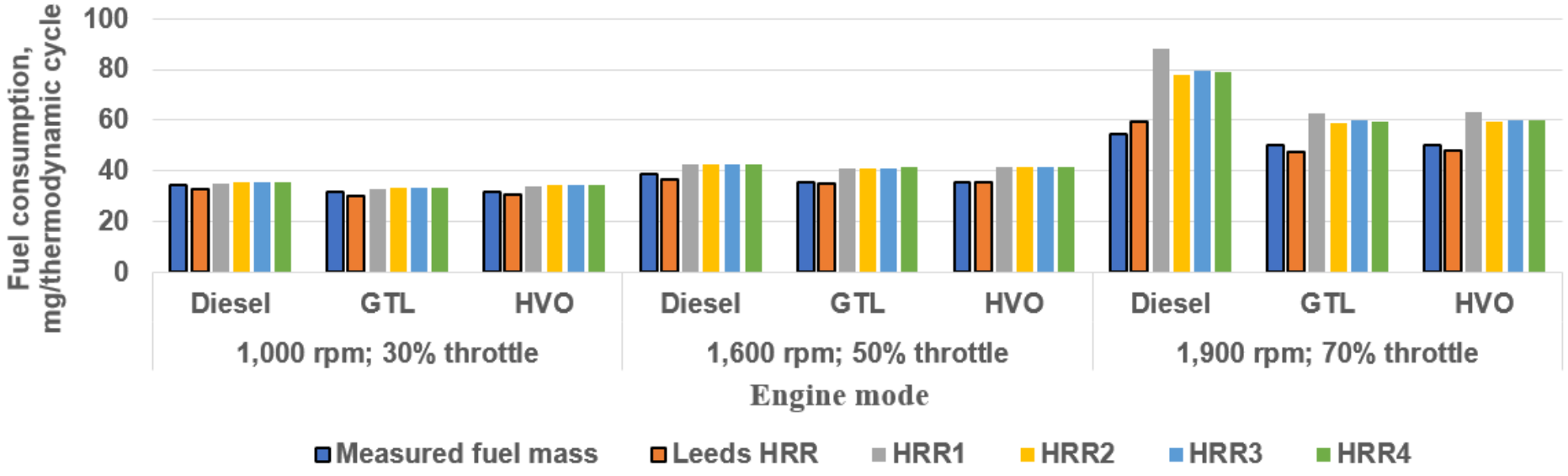

Figure 6.109 Comparison of measured and predicted fuel masses (ULSD, GTL and HVO diesels)

Table 6.7 Validation of the Leeds HRR model for alternative fuels (GTL and HVO diesels)

			Fuel mass, mg/thermodynamic cycle						% Deviation from measured fuel mass				
Engine mode	Fuel	In-cylinder λ	Measured	Leeds HRR	HRR1	HRR2	HRR3	HRR4	Leeds HRR	HRR1	HRR2	HRR3	HRR4
1,000 rpm; 30 % throttle (Low load)	USLD	1.80	34.57	32.82	34.71	35.27	35.27	35.42	-5.06	0.41	2.03	2.04	4.46
	GTL	1.87	31.78	29.15	31.95	32.62	32.57	32.72	-8.27	0.52	2.63	2.49	2.95
	HVO	1.91	31.78	30.59	33.80	34.47	34.44	34.59	-3.74	6.34	8.46	8.36	8.85
1,600 rpm; 50 % throttle (Medium load)	USLD	1.60	38.89	36.78	42.58	42.59	42.75	42.85	-5.43	9.48	9.50	9.93	10.19
	GTL	1.66	35.75	35.10	40.84	40.97	41.14	41.26	-1.81	14.24	14.60	15.06	15.43
	HVO	1.70	35.75	35.34	41.25	41.32	41.50	41.62	-1.14	15.38	15.57	16.07	16.41
1,900 rpm; 70 % throttle (High load)	USLD	1.14	54.58	59.32	88.02	78.05	79.71	79.01	8.69	61.27	43.01	46.05	44.76
	GTL	1.19	50.17	47.52	62.68	59.05	59.86	59.54	-5.28	24.93	17.70	19.31	18.68
	HVO	1.21	50.17	47.99	63.05	59.40	60.21	59.89	-4.35	25.68	18.40	20.01	19.38
					Average of absolute errors:				4.86	19.99	14.66	15.48	15.46
					Standard deviation:				2.39	17.71	11.53	12.48	11.94
					Error range:				-8.27 - +8.69	0.41 – 61.27	2.03 - 43.01	2.04 – 46.05	2.46 - 44.76

6.5.7 Determination of combustion phasing

The validated model (Leeds HRR model) was used to determine the SoC, EoC and the crank angle timing at which 50% of the injected fuel mass was burned (MFB50) from the fuel burn profiles for the fuels and the engine modes that were tested. The determination of the phasing of the combustion (SoC, MFB50, EoC) for a low power condition (1,000 rpm; 30% throttle for HVO diesel) is presented in Figure 6.110. Figure 6.110 shows that, when the engine was run on HVO at the low power condition (1,000 rpm; 30% throttle), the SoC was at 1^{o} bTDC, 50% of the injected fuel was burned at 17^{o} aTDC while the EoC was at 49^{o} aTDC. At the low and medium power conditions, the SoC could easily be determined from the HRR profile as there were no significant heat release and fluctuations from the combustion of pilot injection fuel. However, due to the significant heat release from the combustion of pilot injection fuel mass (pilot combustion) at the high power condition (Figures 6.99, 6.102, and 6.105), two SoC crank angles: SoC1, and SoC2 were identified in the fuel burn profiles for the high power conditions depicted in Figures 6.111 and 6.112. The quantity of fuel that was injected during the pilot fuel injection to achieve optimum charge premix and to minimise peak pressure and peak temperature was relatively high at the high power condition. This led to significant pilot combustion heat release before the TDC as observed in Figures 6.99, 6.102, and 6.105.

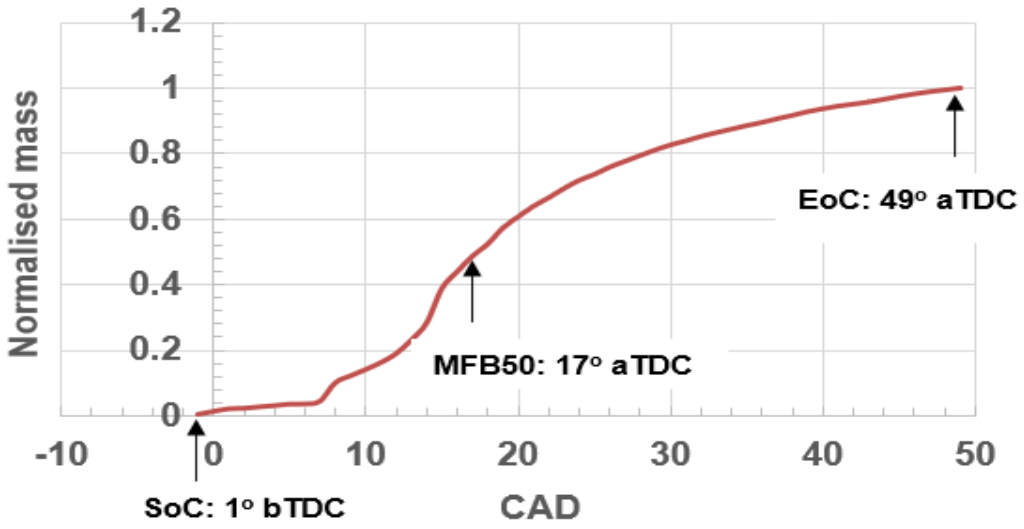

Figure 6.110 Determination of combustion phasing for HVO (1,000 rpm; 30% throttle_13 kW)

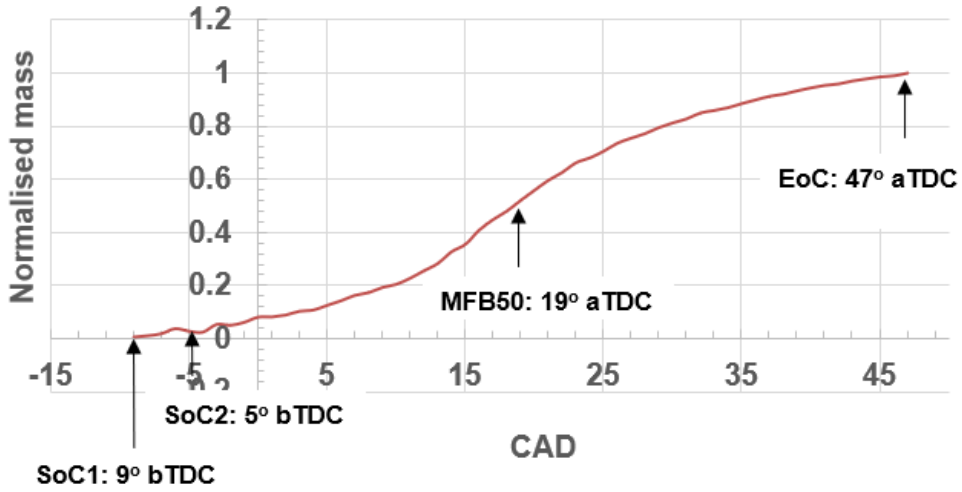

Figure 6.111 Determination of combustion phasing for ULSD (1,900 rpm; 70% throttle_47 kW)

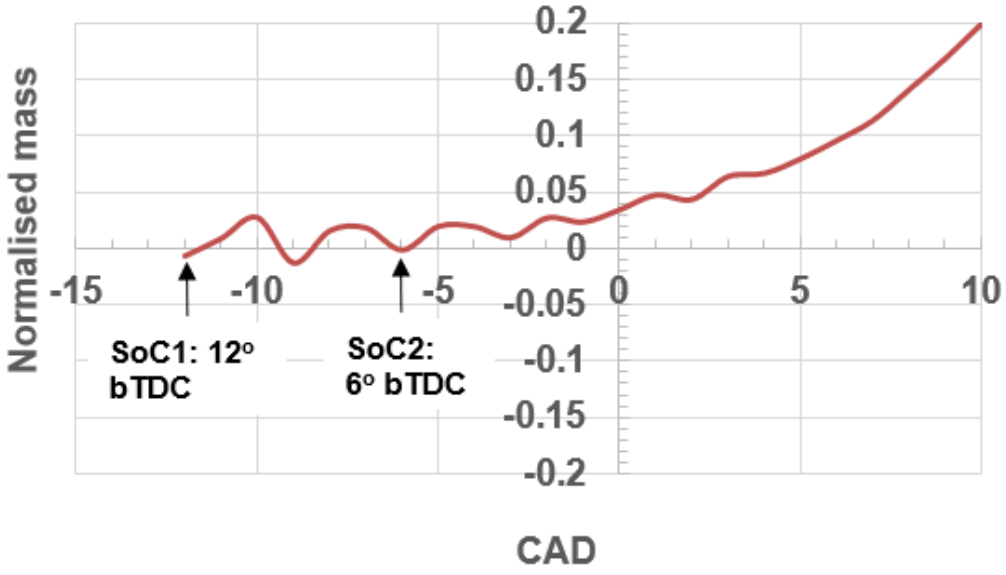

Figure 6.112 Determination of SoC1 and SoC2 for HVO (1,900 rpm; 70% throttle_47 kW)

SoC1 was the start of pilot combustion while SoC2 was the actual (effective) start of combustion for the high power condition. The significant release of heat bTDC (seen as the fluctuation in the HRR profiles for the high power condition) was triggered by the advanced SoI for the high power condition. The fluctuations that were observed near the TDC in the pressure traces and temperature profiles (Figures 6.90 to 6.95) were amplified in the HRR profiles as the power of the engine increased. The crank angle at which the fluctuations began marked the start of fuel injection, SoI. SoC2 was determined so that the significant heat that was released bTDC for the high power condition could be accounted for thereby further increasing the accuracy of the Leeds HRR model. SoC2 could not be determined by direct inspection of the HRR curve alone. As such, it was determined from the fuel burn profile shown in Figures 6.111 and 6.112. The fuel burn profiles that were generated from the HRR profiles resolved the fluctuations that were observed bTDC for the high power conditions such that SoC2 was

clearly distinguished from SoC1. As shown in Figures 6.111 and 6.112, SoC2 was the crank angle timing at which the MFB rose consistently above zero.

SoC2 was clearly identified in Figures 6.111 and 6.112 as the point where the fuel burn profiles for ULSD and HVO diesel rose consistently above zero. As shown in Figure 6.111, SoC1 was 9^{o} bTDC while SoC2 was 5^{o} bTDC for ULSD. It could be seen from the fuel burn profile in Figure 6.112 that the MFB rose consistently above zero at 6^{o} bTDC (SoC2) even though the combustion of the pilot injection HVO fuel commenced at 12^{o} bTDC (SoC1). The MFB cannot be negative. Therefore, for the high load condition, SoC2 was chosen as the actual/effective SoC while SoC1 was designated as the start of pilot fuel combustion. The start of pilot combustion (SoC1) and the actual start of combustion (SoC2) for GTL diesel at the high power condition were 13^{o} bTDC, and 7^{o} bTDC respectively. The combustion phasing for the low and medium power conditions were determined as shown in Figure 6.110, while the combustion phasing of the fuels for the high power condition were determined as shown in Figures 6.111 and 6.112.

Table 6.8 presents the phasing of the combustion for the three fuels. The injection timings for the three fuels were not the same for all the modes (Table 6.8). The injection event was controlled by the ECU of the engine. The estimated injection timings in Table 6.8 were the crank angle timings for the start of pilot injection. The crank angle timing of the Peak Pressures (PP) were determined from the pressure traces. The observed early combustion of GTL and HVO diesels was not only due to their relatively high CN, it was also due to the advanced injection of the alternative fuels by the ECU. Generally, the SoI values at the higher power conditions showed that the injection event occurred much earlier for the alternative fuels than for ULSD. At the high power condition, much higher

compression pressure and temperature were attained as shown in Figures 6.90 to 6.95. Therefore, advanced injection of fuel was triggered by the ECU of the engine at the higher power conditions to prevent undesirable high PPRR and PHRR, both of which could occur should the SoI and SoC be too close to the TDC. The SoI of the alternative fuels was advanced by the ECU because they had a higher CN than ULSD. Generally, as the power of the engine was increased, the SoI was advanced for all the fuels. This was to enhance lean combustion and efficient premixing of fuel and air to prevent high PPRR, PHRR, and the formation of local rich zones which would lead to high THC, CO, and NOx emissions. Apart from the cylinder pressure and temperature, the fuel consumption of the engine also increased as the power of the engine increased. As such, to keep the combustion mixture lean (λ >1), the ECU advanced the injection timing of the fuels as the power was increased so that the multiple injection events occurred over a relatively wide crank angle range at the higher power conditions.

Table 6.8 Combustion phasing of the fuels (ULSD, GTL, and HVO) at the tested engine modes

			CAD					
Speed, rpm	**Throttle, %**	**Fuel**	**PP**	**PHRR**	**SoI**	**SoC**	**EoC**	**MFB50**
1,000	30	ULSD	17	15	-2	-1	50	18
	50	GTL	16	15	-3	-2	49	17
	70	HVO	19	15	-2	-1	49	17
1,600	30	ULSD	18	17	-6	-5	56	19
	50	GTL	18	17	-8	-5	48	19

	70	HVO	18	15	-8	-5	47	18
1,900	30	ULSD	20	16	-10	-5	47	19
	50	GTL	13	13	-14	-7	46	16
	70	HVO	13	13	-13	-6	46	16

Generally, for the three fuels that were investigated, Table 6.8 shows that as the power of the engine was increased, the SoI and SoC of the fuels were advanced (occurred earlier). The auto-ignition of the diesel fuels was enhanced by the relatively high compression pressure and temperature which were attained in the cylinder as the power of the engine was increased.

The Peak Pressures (PP) and the PHRR were determined from the pressure traces and the modelled HRR profiles respectively for the tested modes and fuels. Table 6.9 presents the values of the PP and the PHRR for the tested modes and fuels.

Table 6.9 Model results for Peak Pressure (PP) and Peak Heat Release Rate (PHRR) at the tested engine modes

Speed, rpm	Throttle %	Fuel	PP, bar	PHRR, J/CAD
1,000	30	ULSD	61.24	113.69
	50	GTL	58.23	136.70
	70	HVO	58.49	141.71
1,600	30	ULSD	68.40	150.14
	50	GTL	66.48	121.15
	70	HVO	68.35	114.79

1,900	30	ULSD	102.60	146.25
	50	GTL	102.64	131.01
	70	HVO	103.23	131.08

6.5.8 Smoothness of combustion of fossil diesel and the alternative diesels

The smoothness of the combustion of standard diesel (ULSD) and the alternative fuels was also analysed from the HRR profiles by superimposing the HRR profiles of the three fuels at the tested low, medium and high power conditions as shown in Figures 6.113 to 6.115. The figures show that the combustion of HVO diesel in the engine was smoother than the combustion of standard diesel or GTL diesel. The HRR profiles of HVO diesel (the black curve) in the figures were not as wavy (noisy) as those of the other fuels. This could be attributed to the narrow distillation range of HVO (Figure 6.89). As depicted in Figures 6.113 to 6.115, as the power of the engine increased from the low to the high power condition, the tendency of the compressed charge to combust before the TDC increased. There was more combustion of pilot injection fuel (early SoC before the TDC) when the engine was run on the alternative fuels than when it was run on ULSD. Consequently, to keep the actual SoC near the TDC as much as possible, the Engine Control Unit (ECU) suppressed the combustion of the pilot injection fuel by causing more fuel masses of GTL and HVO diesels to be injected before the TDC compared to the pilot injection fuel mass of ULSD. This MFIS of the ECU was also aimed at preventing the PHRR from occurring before the TDC for the fuels with high CN. This would have a negative impact on the mechanical

efficiency of the engine due to the early release of the chemical energy of the fuel before the actual commencement of the power stroke.

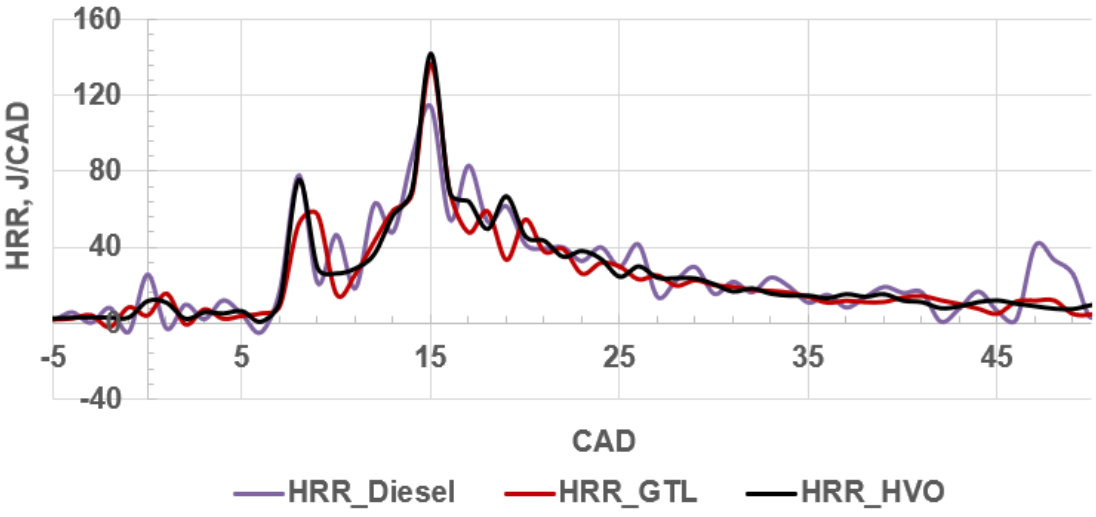

Figure 6.113 Comparison of the smoothness of combustion of ULSD, GTL, and HVO diesels (1,000 rpm; 30% throttle)

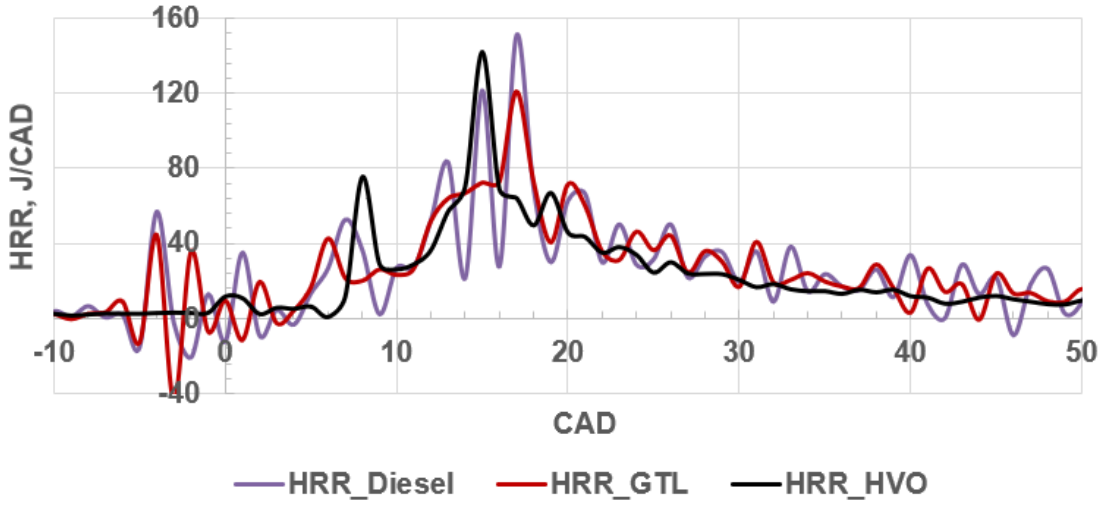

Figure 6.114 Comparison of the smoothness of combustion of ULSD, GTL, and HVO diesels (1,600 rpm; 50% throttle)

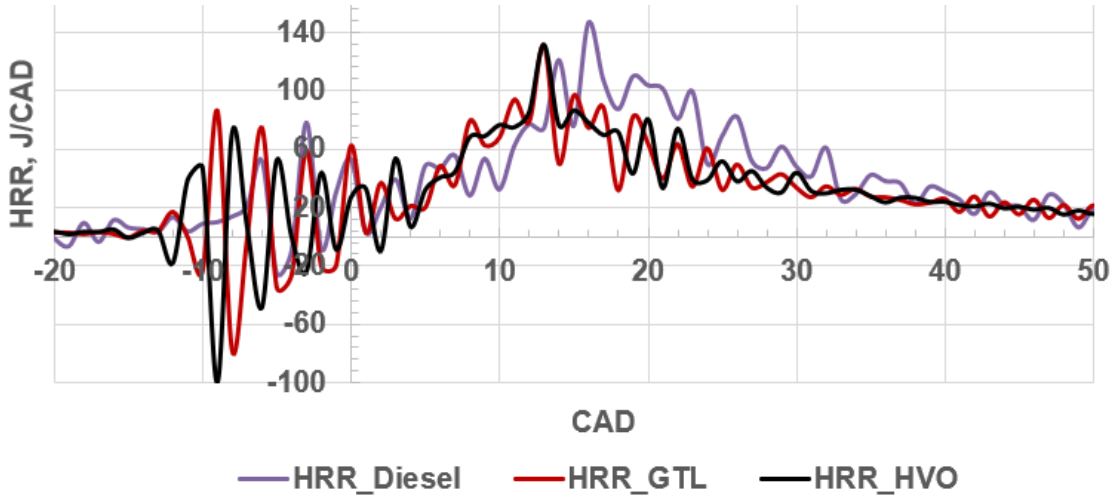

Figure 6.115 Comparison of the smoothness of combustion of ULSD, GTL, and HVO diesels (1,900 rpm; 70% throttle)

The PHRR was highest for ULSD at the higher power conditions (Figures 6.114, and 6.115 and Table 6.9) due to the relatively late SoI and low CN of ULSD that led to relatively late SoC as well as low pilot combustion heat release when the engine was run on ULSD. The start of pilot combustion (SoC1) for ULSD at the high power condition was 9^{o} bTDC while the SoC1 were 13^{o} bTDC and 12^{o} bTDC respectively for GTL and HVO diesel fuels at the high power condition (Figures 6.99, 6.102, and 6.105). This indicated that, at the high power condition for GTL diesel, pilot combustion started 4 CAD earlier than for diesel. Pilot combustion started 3 CAD earlier than it started for ULSD at the same condition (1,900 rpm; 70% throttle) when the engine was run on HVO diesel. The relatively low PHRR values of GTL and HVO diesel fuels compared to ULSD at the high power condition was due to the significant release of heat that occurred during the pilot combustion for the alternative fuels as explained in the previous section.

6.6 Conclusion

This aspect of the work which was conducted on the Engine Test Bed (ETB) involved the investigation of the performance and emissions of the 96 kW, Multiple Fuel Injection Strategy (MFIS), Euro V emission compliant IVECO diesel engine. The engine test matrix consisted of twelve (12) engine modes; three conditions of speed (1,500; 1,600 and 3,000 rpm) and four conditions of torque (30, 75, 150, and 220 Nm). The engine was run at the four conditions of torque for each of the investigated speeds. Engine parameters and emissions data were logged both upstream and downstream of the DPF. An improved HRR model was also developed for the MFIS IVECO diesel engine to analyse the HRR behaviour of the engine for ULSD (standard diesel) as well as alternative diesels (GTL and HVO diesels). No work has been done in the past to develop and validate a mathematical model for the analysis of the HRR of diesel engines within a wide range of non–stoichiometric conditions for ULSD as well as alternative diesels (GTL and HVO diesels). The intended investigation of the effects of diesohol (DE) fuel blends on the performance, emissions, and HRR of the MFIS IVECO engine was not achieved because of the mechanical fault that the engine developed as well as the impact of the pandemic. The DE fuel blends combustion test aspect of the work was completed on the smaller, modern diesel Gen-set engine.

It was confirmed from the baseline results for the performance of the engine that the IVECO diesel engine had a BSFC of 225 g/kWh at the high load condition (3,000 rpm and 220 Nm). The same value was reported for the BSFC of diesel engines at maximum load in literature. The BTE of the engine at the intermediate speed and load (1,500 rpm and 150 Nm) was 37.5% while the engine attained the highest mechanical efficiency of 79% at the 1,600 rpm; 220 Nm engine mode. The values of the BTE and the mechanical efficiency of the engine were lowest

at the maximum (rated) speed (3,000 rpm). This was because of the increase in the frictional losses that was caused by the expansion of the piston rings against the cylinder liner as the speed of the engine increased. The lowest exhaust manifold temperature was 215 ^{o}C at the lowest tested speed and load (1,500 rpm; 30 Nm) while the highest exhaust manifold temperature was ~511 ^{o}C at the highest speed and load (3,000 rpm; 220 Nm).

The baseline emissions results showed that the levels of NO and NOx increased as the load on the engine was increased. This was due to the observed increase in the temperature of the flame as the load on the engine was increased (relatively high temperatures favoured the production of NO and NOx). However, the emissions aftertreatment device reduced the levels of NO and NOx by 47% and 20% respectively. The engine out THC emissions decreased as the load of the engine increased due to the enhanced evaporation and combustion of the unburned hydrocarbons at the relatively high combustion temperatures that occurred as the load of the engine was increased. The lowest concentration of THC downstream of the DPF was ~4 ppm while the highest was ~33 ppm (at 3,000 rpm; 150 Nm). The levels of the engine-out CO decreased as the load of the engine increased. This was also due to the relatively high combustion temperatures at the higher loads that favoured the oxidation of CO. The tailpipe CO emissions were virtually eliminated by the DOC.

The baseline particulate emission results showed that the peak PN occurred in the agglomeration mode (Dp>50 nm) for the low load conditions (30 and 75 nm) for all the tested speeds. The peak PN was observed to occur in the nucleation mode (Dp<15 nm) for all the tested speeds at the high conditions of load (150 Nm and 220 Nm). The 99.9% efficiency of the DPF at eliminating the particulate emissions was ascertained in the current work. The second agglomerated mode

of the emitted particles was observed to occur within the 500-1,000 nm Dp range, contrary to what was (often) reported in literature (Dp<500 nm). The factors that accounted for the occurrence of the second agglomeration mode in the 500-1,000 nm Dp range in the current work were the detachment and entrainment of the particles that were initially deposited on the EGR system, the recirculation of the engine-out agglomeration mode particles in the complex geometries of the EGR system (this enhanced particle collision and growth), and the cooling of the engine-out exhaust gas in the EGR cooler.

The current work has shown that the accuracy of the HRR models of CI engines is strongly depended on the specific heats ratio (γ). Most of the existing HRR models were based on $\gamma(T)$. The effect of the excess air ratio (λ) on γ was investigated in this work. λ was found to have a significant effect on γ. Therefore, in the current work, a modified γ function, $\gamma_{mod}(T,\lambda)$ was used in the Leeds HRR model to model the HRR of the MFIS IVECO diesel engine at the twelve conditions of load. The Leeds HRR model based on $\gamma_{mod}(T,\lambda)$ predicted the fuel consumption of the engine for ULSD with an average error of 1.41%. The errors in the fuel masses predicted by the Leeds HRR model for ULSD ranged from -3.68% to +4.08%, with a standard deviation of 1.21. The average error in the fuel mass predictions of the other models which were based on $\gamma(T)$ ranged from 15.85% to 16.36%. The error in the prediction of the other models was largely because λ was neglected in the models. Therefore, in this work, it was shown that the accuracy of the HRR model of CI engines is enhanced by using $\gamma(T,\lambda)$. The effect of the EGR rate on the HRR model of the engine was also investigated using a γ model that was derived from experimental data. It was found that at stoichiometric condition, the EGR rate had insignificant effect on the accuracy of the HRR model of the engine specifically for operation at low and medium loads.

The second aspect of the modelling of the HRR of the MFIS IVECO engine involved the validation of the Leeds HRR model for alternative diesels (GTL and HVO diesels). The engine was run at low, medium, and high loads (1,000 rpm and 30% throttle; 1,600 rpm and 50% throttle; 1,900 rpm and 70% throttle respectively) for each of the tested fuels (ULSD, GTL, and HVO diesels). The HRR behaviour of the engine was analysed and compared for operations on ULSD, GTL, and HVO diesels. The current work also confirmed that the accuracy of the HRR models of CI engines for both fossil and alternative diesel fuels is strongly depended on the specific heats ratio (γ). λ was also found to have a significant effect on γ for the alternative fuels. The Leeds HRR model predicted the fuel consumption of the engine for ULSD, GTL, and HVO diesels with an overall average (absolute) error of 4.86% compared to the measured fuel consumption. The errors in the fuel masses predicted by the Leeds HRR model ranged from -8.27% to +8.69%, with a standard deviation of 2.39. The average error in the fuel mass predictions of the other models which were based on $\gamma(T)$ ranged from 15% to 20%. The errors in the predictions of the other models were high because λ was neglected in the models. Therefore, in this work, it was also shown that the accuracy of the HRR model of CI engines for the determination of the combustion behaviour of fossil and alternative diesel fuels is enhanced by using $\gamma(T, \lambda)$. The PHRR was highest for ULSD at the high power condition due to the relatively late SoI and low CN of ULSD compared to GTL and HVO diesels. The combustion of HVO diesel was found to be the smoothest of the three fuels due to the narrow distillation range of HVO diesel. The novel techniques that were used to estimate the rate of evaporation of the injected fuels from the HRR profiles and the actual SoC from the HRR and fuel burn profiles (for the case of

significant heat release bTDC) also contributed to the accuracy of the Leeds HRR model.

Chapter 7 Effect of diesel-ethanol (DE) blends on the performance and combustion behaviour of diesel engines

7.1 Introduction

The diesel engine diesel-ethanol (DE) blends combustion test could not be completed on the Euro V IVECO engine for reasons stated in Chapter 6 (Section 6.1). The baseline and DE fuel blends combustion tests were completed on the modern diesel Gen-set. This chapter presents the results of the Gen-set combustion tests. The experimental data were analysed to investigate the effect of ethanol-blended fuels on the fuel consumption and the temperature of the flame. The power that was utilised by the engine to overcome friction and pumping losses was estimated graphically for the tested fuels by plotting the fuel consumption of the engine against the kW electric brake power (kW_e). The Gen-set engine had an alternative power loss of about 25%. Therefore, the 2 and 3 kW_e conditions of load were equivalent to engine-out power conditions of 2.7 and 4 kW respectively. Engine emission results are broadly categorised into two: gaseous emissions and particulate emissions. The results for the Gen-set engine-out gaseous and particulate emissions are presented in Section 7.4 and Section 7.5 respectively. The speciation of the engine-out exhaust gas was done by Fourier Transform Infra-Red spectroscopy (FTIR). Though the FTIR analyser was calibrated for 60 species, the discussion in this chapter focuses on the pollutant gases that were detected by the analyser: NOx (NO and NO_2), CO, THC, ethanol (C_2H_5OH), formaldehyde (CH_2O), acetaldehyde (C_2H_4O), 1,3-butadiene (C_4H_6), and benzene (C_6H_6). The Particulate Matter (PM) distributions were evaluated from the measured Particulate Number (PN) distribution. The Leeds HRR model was also validated and applied to the diesel Gen-set to investigate the combustion behaviour of diesel engines for diesel-ethanol (DE) dual fuel

operation. The tested conditions of load (idle, 2, and 3 kW_e) were also expressed in kW_e per litre of displaced cylinder volume (idle, 4.6, and 7 kW_e/l respectively) for ease of comparison of the combustion behaviour of the single-cylinder diesel Gen-set to those of other diesel engines. It was confirmed from the fuel blends stability test that was carried out (Chapter 5) that the (lower) limit of the solubility of ethanol in diesel at room temperature (20 ^oC) is 20% by volume. However, DE20 was not investigated in the current work because DE20 phase-separated at the temperature of the Engine room (18 ^oC).

7.1.1 Blend Calorific Values and stoichiometric AFRs

Table 7.1 presents the estimated Calorific values (Cv) and stoichiometric AFRs for pure diesel and the tested DE fuel blends. Table 7.1 shows that the Cv of the fuel blends decreased as the concentration of ethanol in the blends increased. The Cv of the DE fuel blends were lower than the Cv of pure diesel because of the relatively low Cv of ethanol (26.9 MJ/kg) compared to the Cv of diesel (44 MJ/kg). The estimated stoichiometric AFR of the fuel blends also decreased below the baseline as the concentration of ethanol increased in the blends. As the concentration of ethanol increased in the oxygenated fuel blends, the percentage of oxygen in the blends increased due to the oxygen atom in ethanol. Consequently, the amount of oxygen (or air) that was required for the complete combustion of a unit mass of the oxygenated fuels was less than the stoichiometric air requirement for pure diesel.

Table 7.1 Calorific values and stoichiometric AFR values of the tested fuel blends

Blend fuel	Cv (MJ/kg)	Stoichiometric AFR
Baseline (DE0)	44	14.40
DE5	42.2	14.11
DE10	41.4	13.75
DE15	40.6	13.61

7.2 Engine fuel consumption

The fuel consumption of the Gen-set in g/s, and the Brake Specific Fuel Consumption (BSFC) in kg/kWh are presented in Figures 7.1 to 7.4. Figure 7.1 shows that the fuel consumption of the Gen-set increased as the load on the engine was increased for each of the tested fuels. However, for each condition of load, the fuel mass increased above the baseline as the percentage of ethanol increased. The observed increase in the fuel consumption above the baseline was more pronounced at 2 kW_e (4.6 kW_e/l) and 3 kW_e (7 kW_e/l) loads than at idle (Figures 7.1 and 7.2).

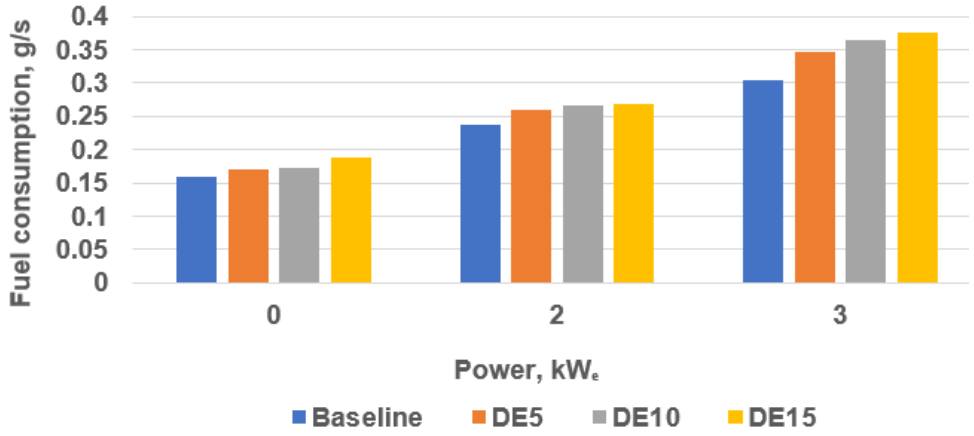

Figure 7.1 Graph of fuel consumption for the tested fuel blends against power (kW_e)

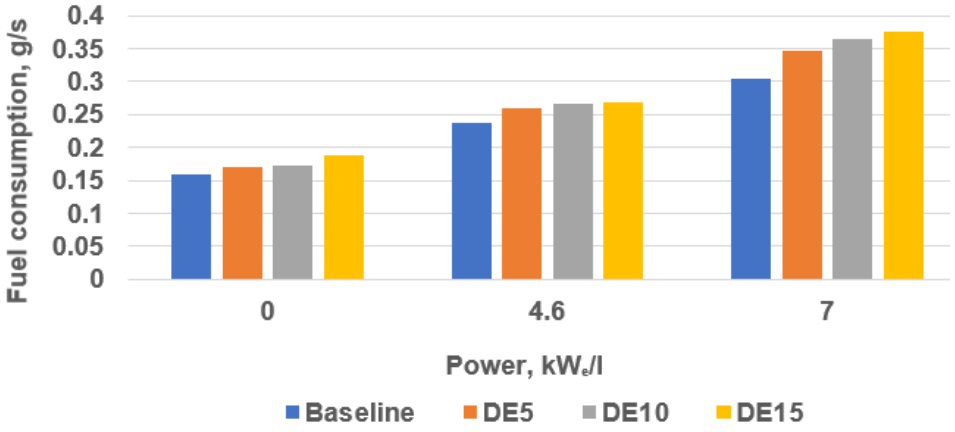

Figure 7.2 Graph of fuel consumption for the tested fuel blends against power (kW_e/l)

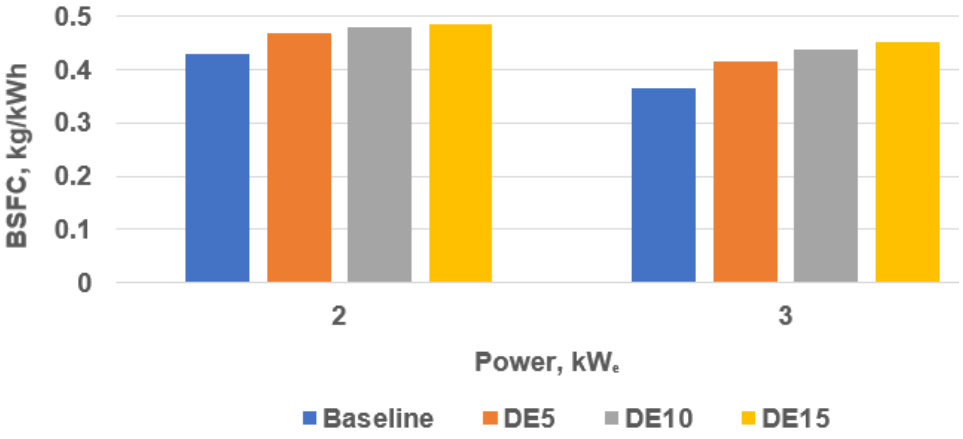

Figure 7.3 Graph of BSFC against power (kW_e)

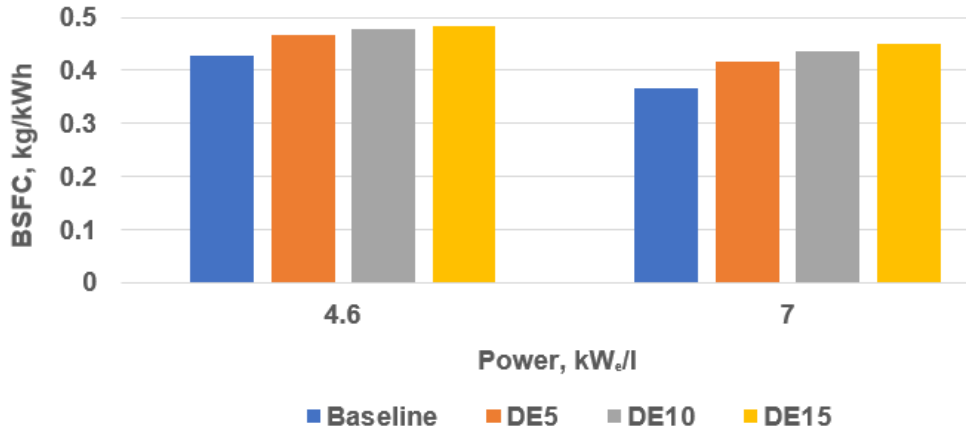

Figure 7.4 Graph of BSFC against power (kW_e/l)

The observed increase in the fuel consumption when the engine was run on the DE fuel blends was due to the relatively low Cv of ethanol compared to pure diesel. The Cv of diesel is 44 MJ/kg while the Cv of ethanol is 26.9 MJ/kg. Therefore, more mass of DE blend fuel was injected than the injected mass of pure diesel at every injection event to attain the same power. The injected fuel mass increased above baseline diesel for all the tested loads as the percentage of ethanol increased in the blends due to the relatively low Cv of ethanol. As the percentage of ethanol increased in the blend fuels, the Cv of the blends decreased. The percentage increases in the fuel masses above baseline diesel at 3 kW_e were 13.44, 19.34, and 23.28 respectively for DE5, DE10, and DE15 (Figure 7.1).

Figures 7.3 and 7.4 show that the BSFC of the engine decreased as the kW_e brake power increased for all the tested fuels. However, the BSFC was observed to increase above the baseline, at each condition of load, as the percentage of ethanol increased in the DE blends. This was due to the drastic increase in the fuel consumption when the engine was run on the ethanol fuel blends. Generally, the BSFC of the engine increased above baseline diesel as the concentration of ethanol increased in the fuel blends. Li et al. (2004), Rakopoulos et al. (2008),

and Lapuerta et al. (2009) reported the same trend for the BSFC for DE blends in their work.

7.2.1 Estimated excess air ratios (λ)

Table 7.2 presents the equivalence ratios (Ø) and the excess air ratios (λ) at the tested conditions. The values of λ in Table 7.2 were estimated using the method of Chan and Zhu (1996).

Table 7.2 Estimated values of λ

Fuel	**Engine-out power, kW**	**Load, kW_e**	**Load, kW_e/l**	**AFR**	**Ø**	**λ**
Baseline	0	0	0	26.40	0.54	1.86
	2.7	2	4.6	18.76	0.76	1.32
	4	3	7	15.43	0.92	1.09
DE5	0	0	0	21.79	0.65	1.54
	2.7	2	4.6	18.28	0.77	1.30
	4	3	7	15.12	0.93	1.07
DE10	0	0	0	17.63	0.78	1.28
	2.7	2	4.6	17.29	0.80	1.26
	4	3	7	15.41	0.89	1.12
DE15	0	0	0	12.99	1.05	0.95
	2.7	2	4.6	15.61	0.87	1.15
	4	3	7	14.52	0.94	1.07

Table 7.2 shows that the estimated values of λ were > 1 (except the value for DE15 at idle). Therefore, the combustion in the Gen-set was lean except at idle for DE15 (which was near-stoichiometric). Generally, the seventh column of Table 7.2 shows that as the load on the engine was increased for each of the tested fuel blends, and as the concentration of ethanol increased in the fuel blends, the combustion became richer due to the increase in the mass of the injected fuel (as explained in Section 7.2). As shown in Figure 7.1, the fuel consumption of the engine increased as the load and the concentration of ethanol in the DE blends increased.

7.2.2 Power to overcome friction and pumping losses

The power that was utilised by the engine to overcome friction and pumping losses for each of the tested blends was determined by plotting the fuel consumption of the engine against the brake power (Figures 7.5). The power that was utilised to overcome friction and pumping losses was estimated by multiplying the intercept on the vertical axis of Figure 7.5 (the fuel consumption at idle) by the Cv of the fuel and the fraction of the input energy that represents the friction and pumping losses. At idle, exhaust thermal and chemical losses were reported to be 31.5% (Andrews, 2018a). Therefore, the friction and pumping losses at idle was 68.5% of the input energy. The energy losses in ICEs range from 10% at full load to 100% at idle (Heywood, 1988). The estimated values of the power to overcome friction and pumping losses, P_{fp} are depicted graphically in Figure 7.6. Figure 7.6 shows that, as the percentage of ethanol increased in the fuel blends, the energy that was utilised by the engine to overcome friction increased above the baseline. This was due to the relatively poor lubricity of DE blends which increased the heat loss due to rubbing/mechanical friction in the

engine, thereby increasing the frictional losses. The DE blends were not as efficient in reducing the friction in the engine as pure diesel.

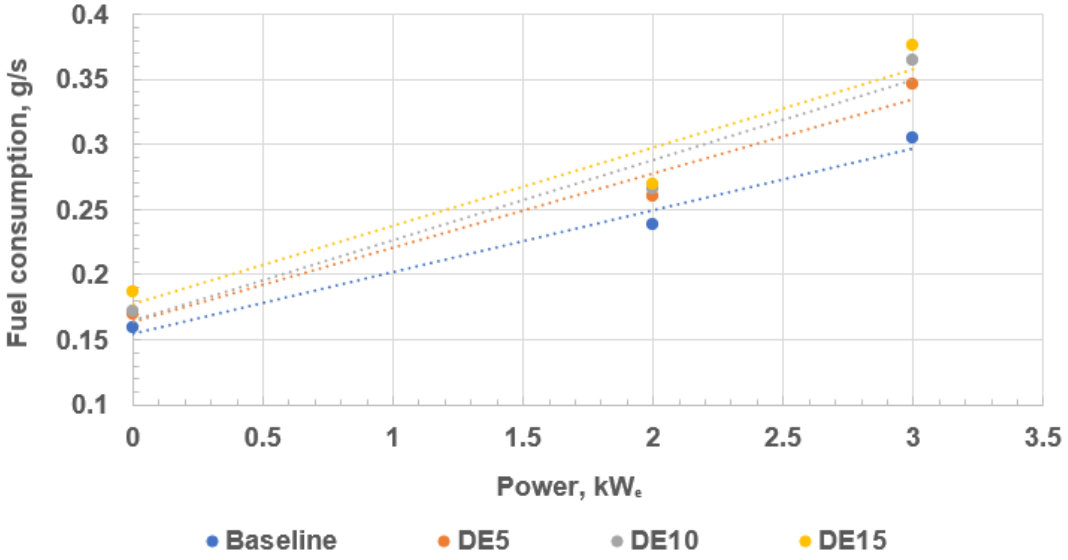

Figure 7.5 Graphical determination of the friction and pumping losses of the Gen-set engine

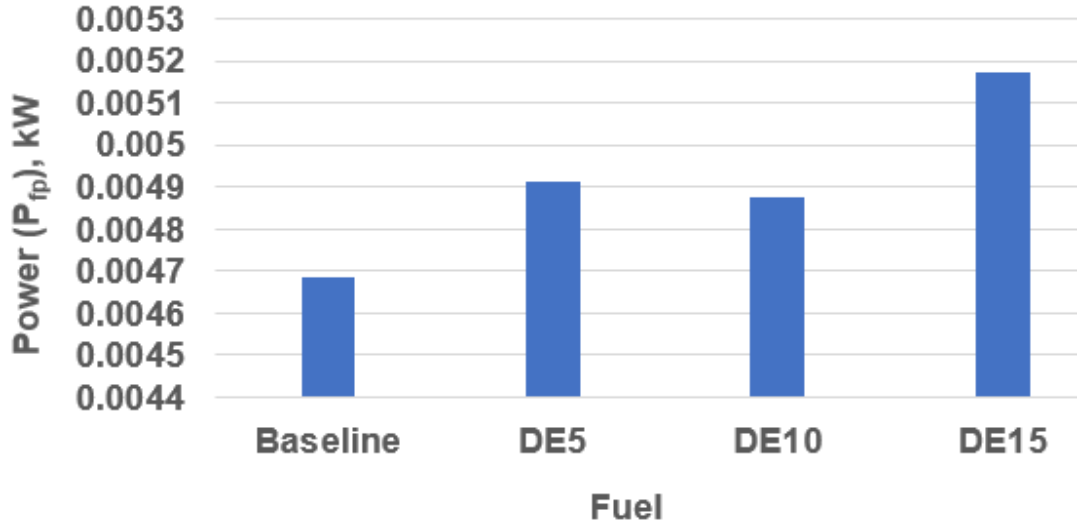

Figure 7.6 Power utilised to overcome friction and pumping losses for the tested fuel blends

7.3 Exhaust manifold temperature

Figures 7.7 and 7.8 depict the exhaust manifold temperatures of the Gen-set engine. Figure 7.7 shows that the temperature of the flame increased as the load on the engine increased (as expected) for all the tested fuel blends. There was

no significant change in temperature when the engine was run at idle. However, at the higher loads (2 kW_e and 3 kW_e), the exhaust manifold temperature decreased below the baseline. At 2 kW_e, the decreases in temperature were 3.67 ^oC, 3.69 ^oC, and 3.92 ^oC respectively for DE5, DE10, and DE15. At 3 kW_e, the decreases in temperature due to the ethanol in the blends were 6.27 ^oC, 6.36 ^oC, and 6.47 ^oC for DE5, DE10, and DE15 respectively. The observed decrease in the temperature of the combustion mixture when the Gen-set was run on the diesel-ethanol blend fuels was due to the relatively high heat of evaporation of ethanol (879 kJ/kg; Table 3.3) compared to the average heat of evaporation of pure diesel (670 kJ/kg; Table 3.2). The heat that was absorbed from the hot gases in the combustion chamber to evaporate a unit mass of ethanol in the injected blend fuel was 1.31 times greater than the specific heat of evaporation of diesel. This inadvertently led to the observed decrease in the exhaust manifold temperature below the baseline when the Gen-set was run on the DE fuel blends.

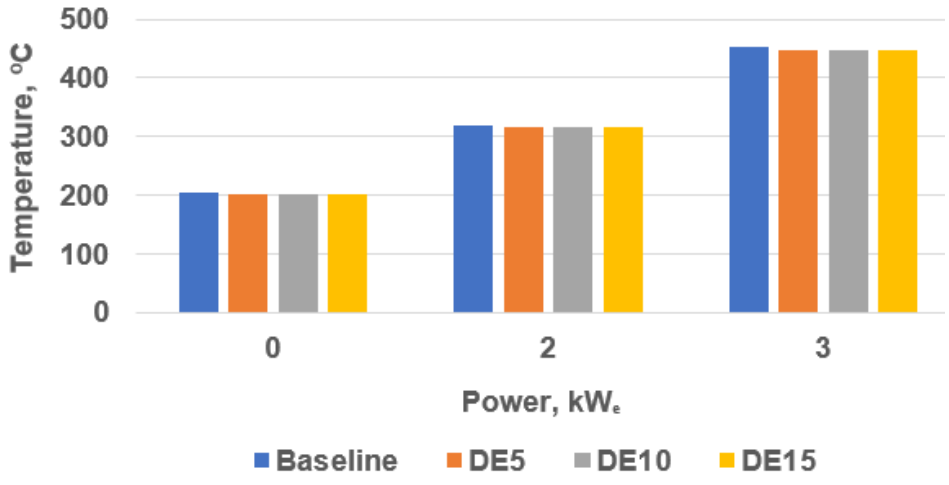

Figure 7.7 Graph of exhaust manifold temperatures against power (kW_e)

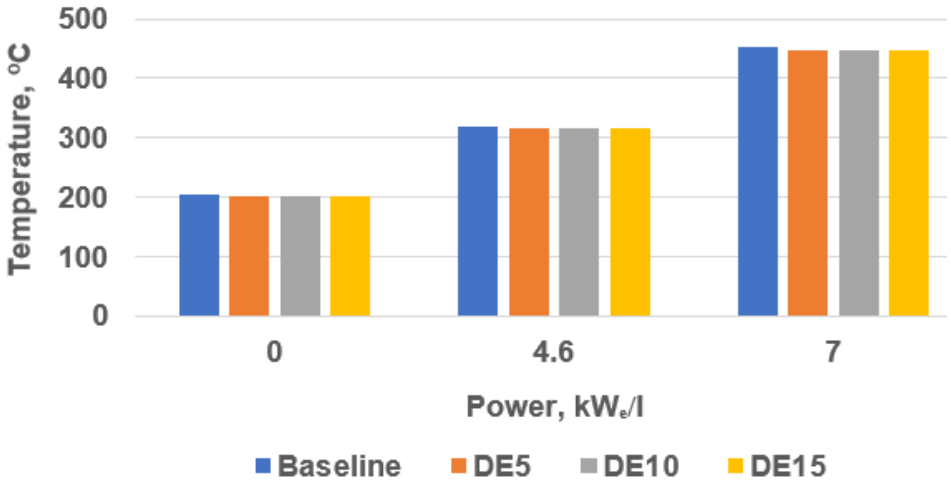

Figure 7.8 Graph of exhaust manifold temperatures against power (kW_e/l)

(The low volatility of ethanol can be attributed to its relatively low boiling point (78.4 °C) compared to water, while the relatively high latent heat of vaporisation of ethanol compared to diesel can be attributed to the presence of inter-molecular hydrogen bond in ethanol due to the -OH group.)

7.4 Gaseous engine-out emissions

This section presents the results for the harmful pollutant gases that were present in significant amounts in the engine-out exhaust gas (NO and NO_2 (nitrogen oxides (NOx)), CO, THC, ethanol (C_2H_5OH), formaldehyde (CH_2O), acetaldehyde (C_2H_4O), 1,3-butadiene (C_4H_6), and benzene (C_6H_6)). The emission levels for the regulated gaseous pollutants (NOx, CO, and THC) were plotted in ppm, g pollutant/kg fuel (Emission Index, EI), and g/kWh against the tested loads to establish the effect of increasing the concentration of ethanol as well as the load of the engine on the levels of the emissions.

7.4.1 NOx emissions

Figures 7.9 to 7.19 present the NOx (NO and NO_2) emissions from the Gen-set engine. The NOx emission from the engine consisted largely of NO. The EI

results in Figures 7.9 to 7.19 depict that the DE fuel blends brought about a reduction in NOx emissions. The level of NOx decreased below the baseline as the percentage of ethanol in the DE blends increased. The emission level for engine-out NOx increases as combustion temperature increases. Therefore, when the engine was run on DE15, the lowest combustion temperature was observed which led to the maximum reduction in the emitted mass of NOx per unit fuel mass at 3 kW_e (a reduction of 40%). Basically, the DE fuel blends eliminated NO_2 from the exhaust of the engine (Figures 7.13 to 7.15). The engine-out NO_2 emission was significant at idle for pure diesel. However, as the engine warmed up at the higher loads, NO_2 was not detected in the exhaust (Figure 7.13). Salih (1990) reported 30% reduction in NOx by ethanol. Andrews and Salih (1990), Li et al. (2004), Rakopoulos et al. (2008), and Lapuerta et al. (2009) also reported that DE blends brought about a reduction in NOx emissions below the baseline. The reduction in NOx that was achieved in this work is 10% higher than the reduction that was reported by Salih (1990). Li et al. (2004) reported a reduction in NOx of about 50% and 32%-35% for both DE10 and DE15 at low and medium loads respectively (when the engine was run at 2,200 rpm). 35% reduction in NOx for DE15 compared well to the 40% reduction that was observed in the current work for DE15 at 3 kW_e (high load).

Figure 7.9 shows that at idle, the emission levels for NO increased above the baseline as the concentration of ethanol increased. This was due to the inefficient vaporisation of the injected DE blends at the relatively low flame temperature of the idle condition. The temperature of the flame decreased as the concentration of ethanol increased leading to inefficient vaporisation of the injected DE blends, poor air-fuel mixing and ultimately, local rich zones. The temperature of the flame was relatively high in the resulting local rich zones within the combustion chamber

at the idle condition (high temperatures lead to increase in NO emissions). Therefore, the presence of local rich zones in the combustion chamber when the engine was run on the DE blends at idle led to the observed increase in the emission levels of NO above the baseline (prompt NOx; Section 3.3.4.3). Generally, as the load on the Gen-set was increased from idle to 3 kW_e, the emission levels for NOx increased for all the tested fuels (Figure 7.16). The observed increase in the levels of NOx at the higher load conditions was due to the increase in the flame temperature when the load on the engine was increased (Figures 7.16 to 7.19).

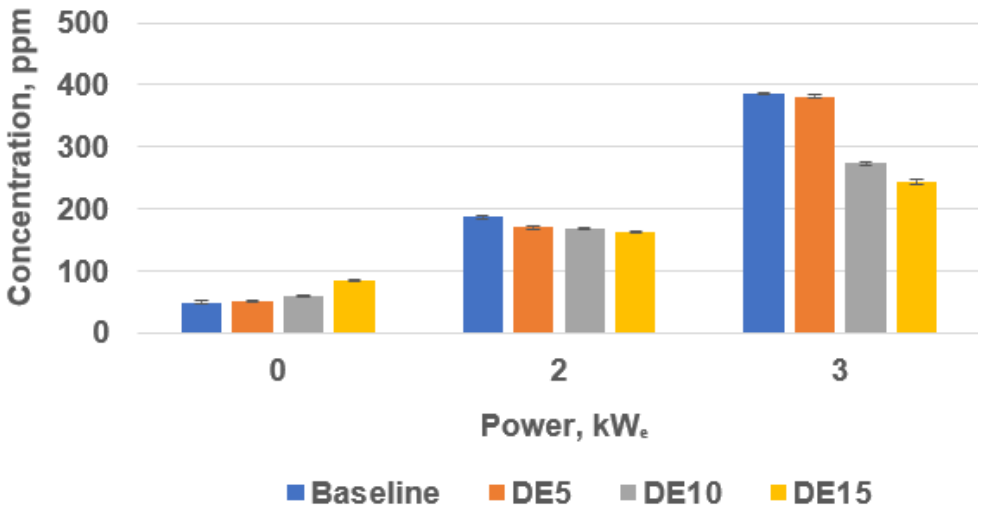

Figure 7.9 Graph of NO (in ppm) versus engine load (kW_e) for the tested blends

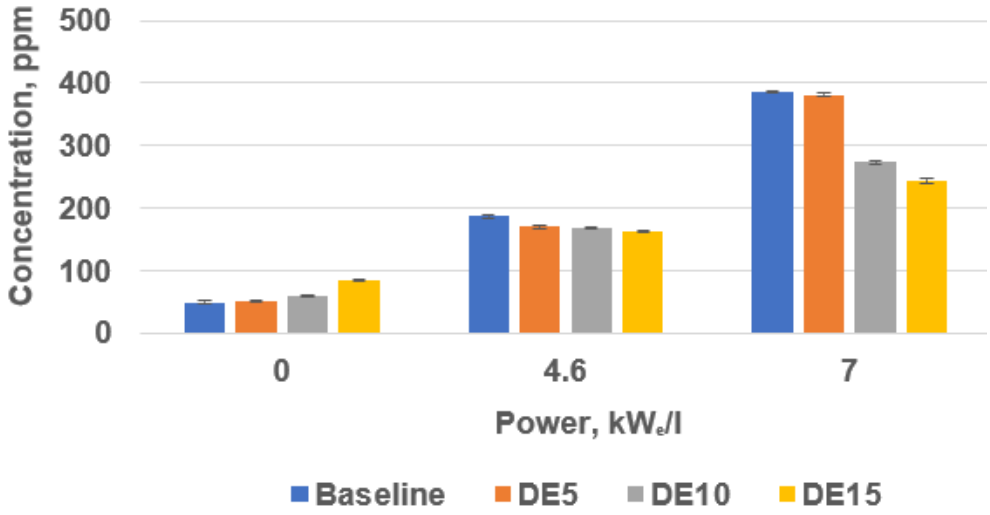

Figure 7.10 Graph of concentration of NO (in ppm) versus engine load (kW_e/l) for the tested blends

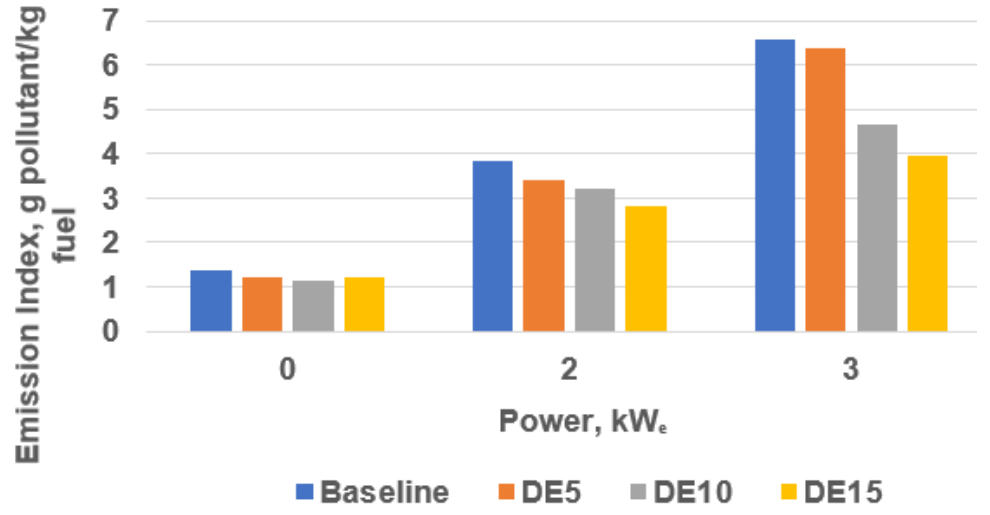

Figure 7.11 Graph of concentration of NO (in g pollutant/kg fuel) versus engine load (kW_e) for the tested blends

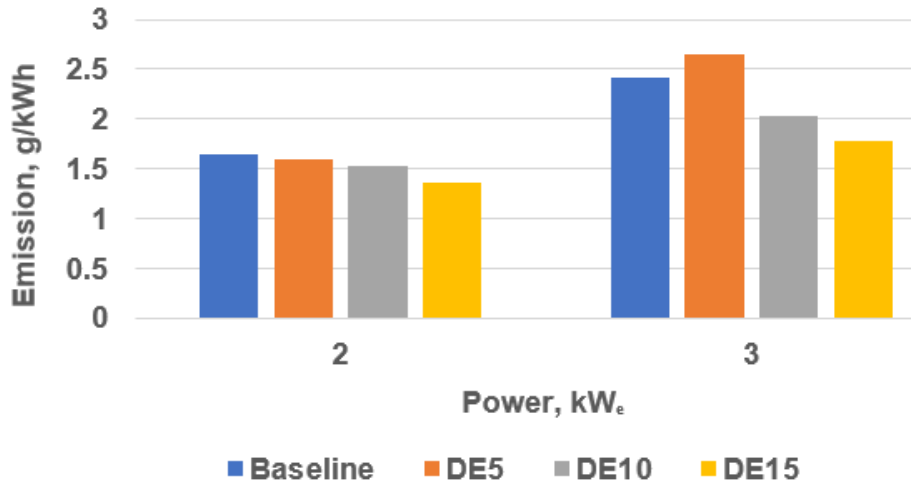

Figure 7.12 Graph of concentration of NO (in g/kWh) versus engine load (kW_e) for the tested blends

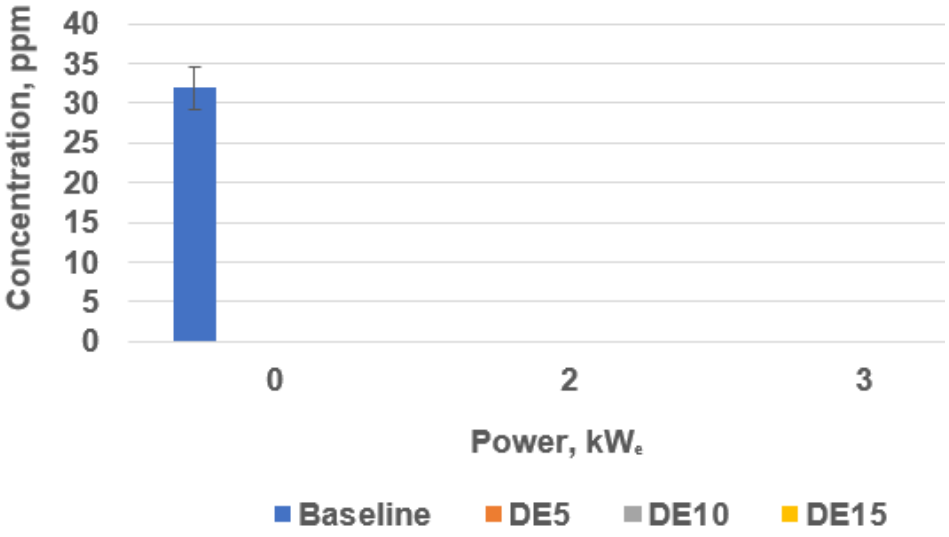

Figure 7.13 Graph of concentration of NO_2 (in ppm) versus engine load (kW_e) for the tested blends

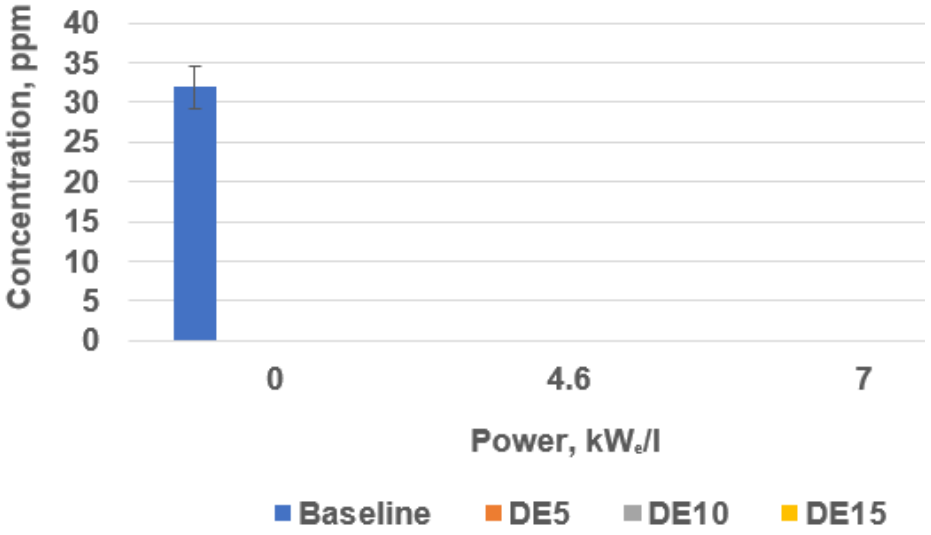

Figure 7.14 Graph of concentration of NO_2 (in ppm) versus engine load (kW_e/l) for the tested blends

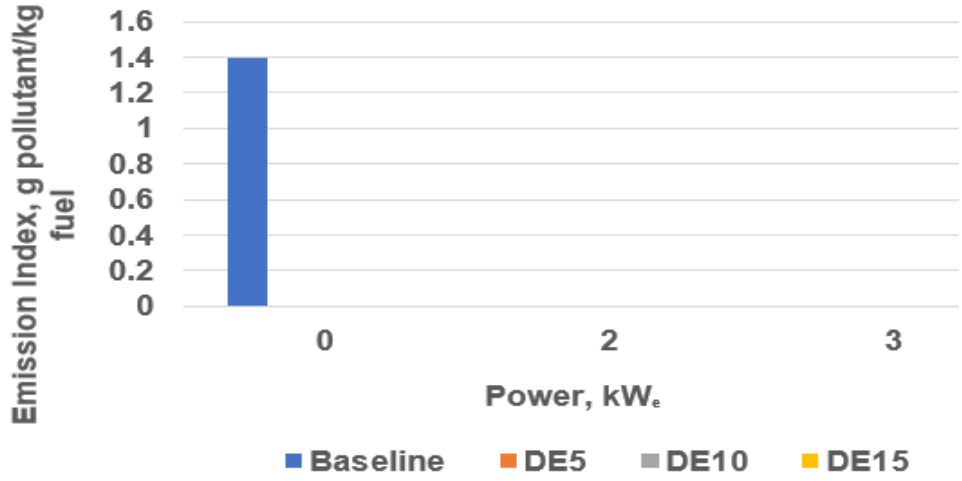

Figure 7.15 Graph of concentration of NO_2 (in g pollutant/kg fuel) versus engine load (kW_e) for the tested blends

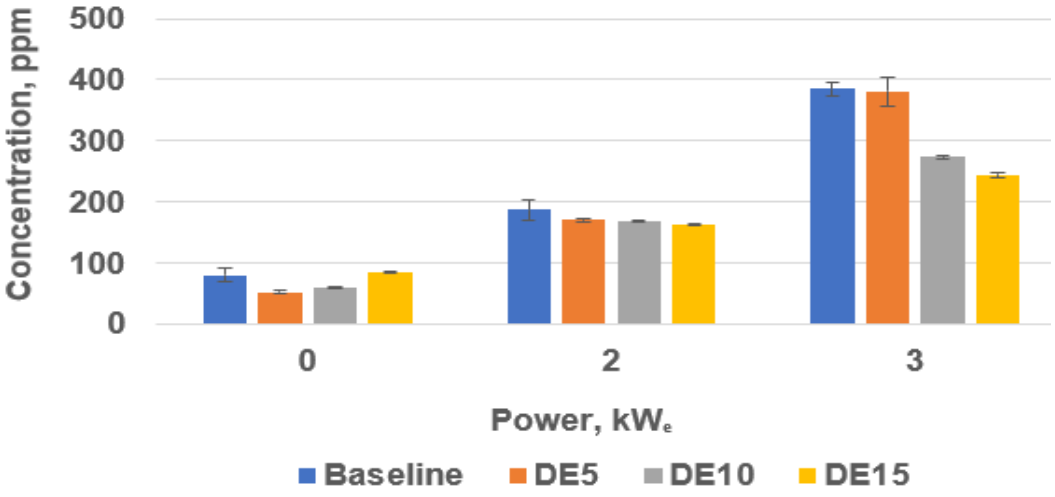

Figure 7.16 Graph of concentration of NOx (in ppm) versus engine load (kW_e) for the tested blends

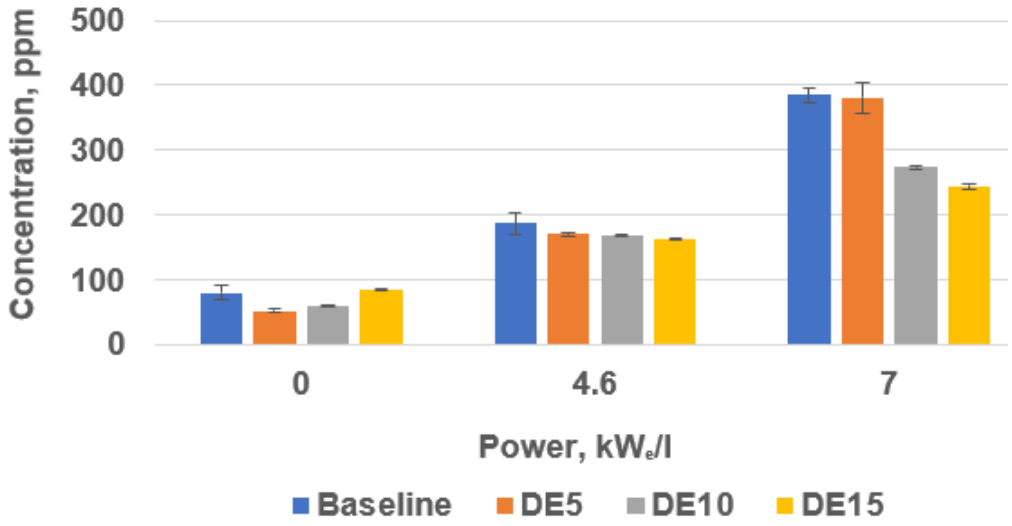

Figure 7.17 Graph of concentration of NOx (in ppm) versus engine load (kW_e/l) for the tested blends

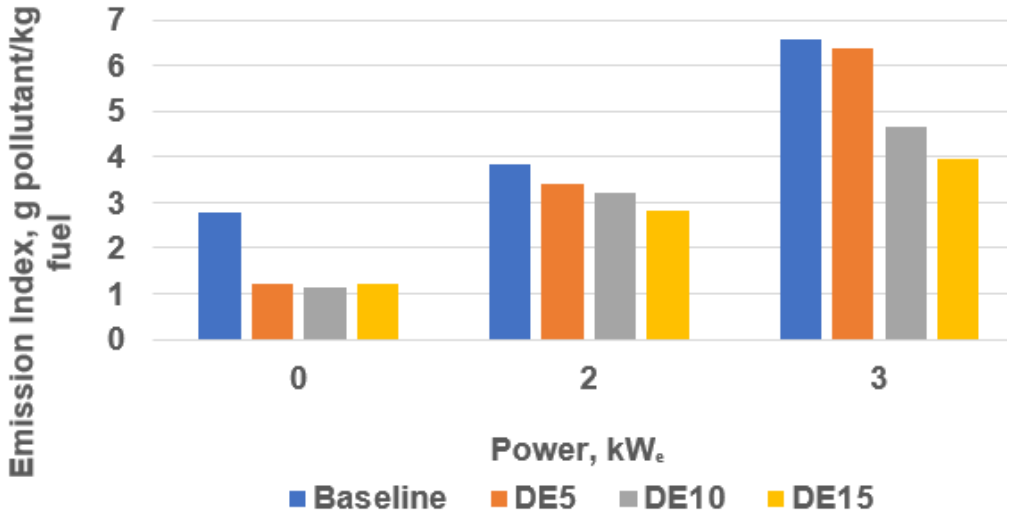

Figure 7.18 Graph of concentration of NOx (in g pollutant/kg fuel) versus engine load (kW_e) for the tested blends

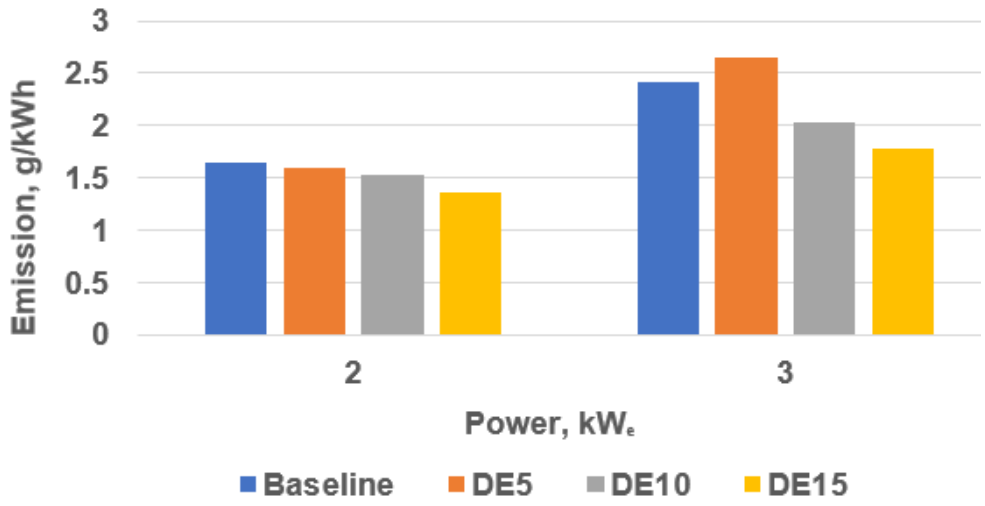

Figure 7.19 Graph of concentration of NOx (in g/kWh) versus engine load (kW_e) for the tested blends

7.4.2 THC emissions

Figures 7.20 to 7.23 depict the THC emission levels of the engine. Generally, the THC Emission Index was higher than the baseline for each of the DE blends. Also, the THC emissions increased as the concentration of ethanol increased in the blends due to the poor vaporisation of the injected fuel at the relatively low flame temperatures that resulted for the DE blends. This led to imperfect air-fuel

mixing, incomplete combustion and consequently, the observed increase in engine-out THC emissions as the blend concentration of ethanol increased. The relatively low fuel injection pressure of the engine (19.6 MPa) led to inefficient atomisation, air-fuel mixing, and the incomplete combustion of the injected fuel mass for all the tested fuels. Figure 7.20 shows that the THC emission from the engine decreased as the load on the engine increased. This was due to relatively high flame temperatures at the higher load conditions. As the temperature of the flame increased with increase in power, the evaporation and combustion of the injected fuel were enhanced thereby leading to the observed decrease in the THC emissions at the relatively high loads.

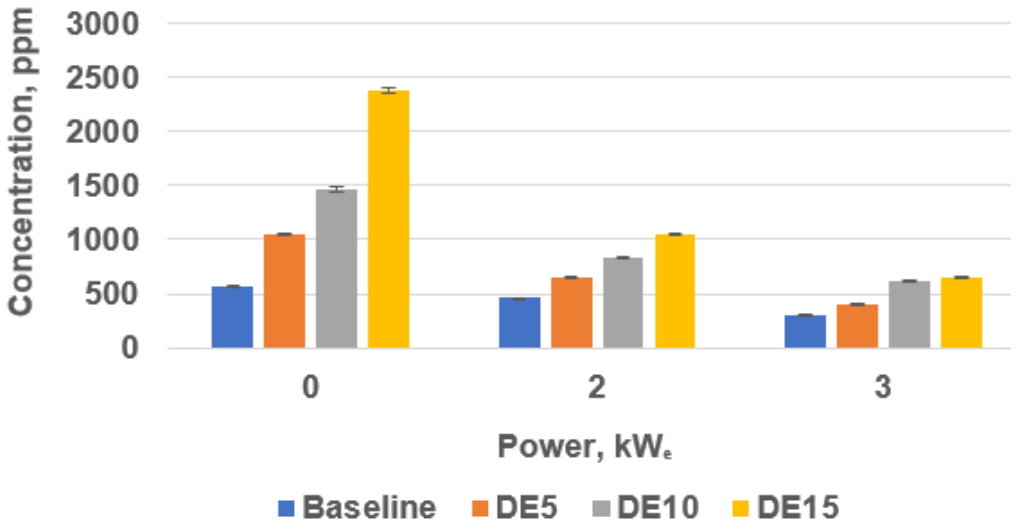

Figure 7.20 Graph of concentration of THC (in ppm) versus engine load (kW_e) for the tested blends

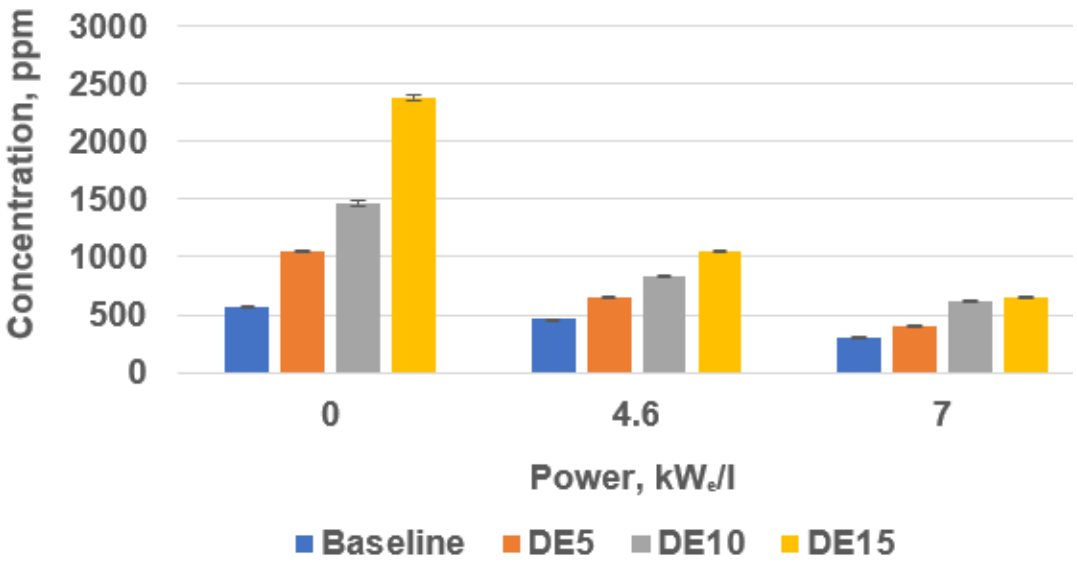

Figure 7.21 Graph of concentration of THC (in ppm) versus engine load (kW_e/l) for the tested blends

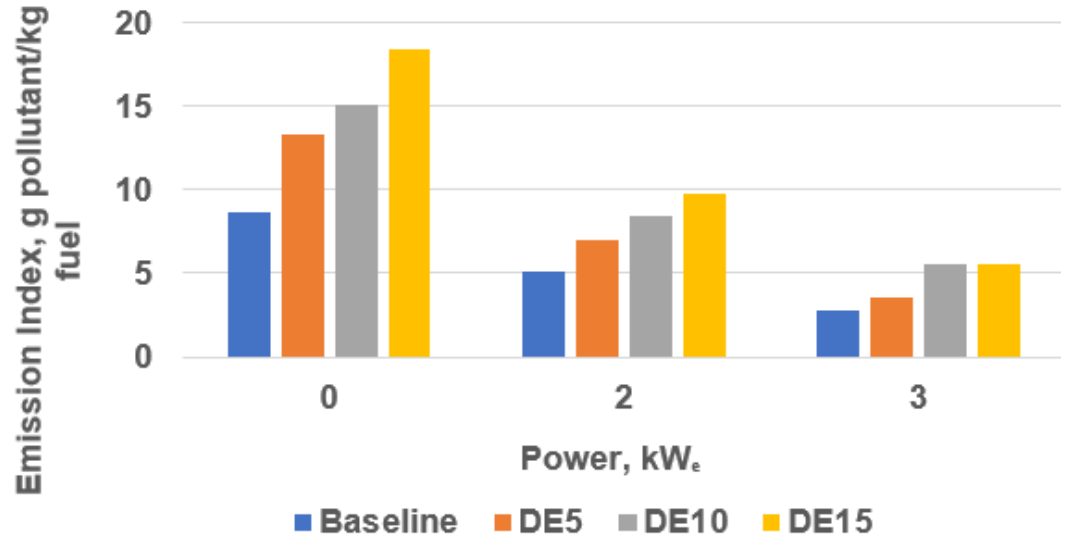

Figure 7.22 Graph of concentration of THC (in g pollutant/kg fuel) versus engine load (kW_e) for the tested blends

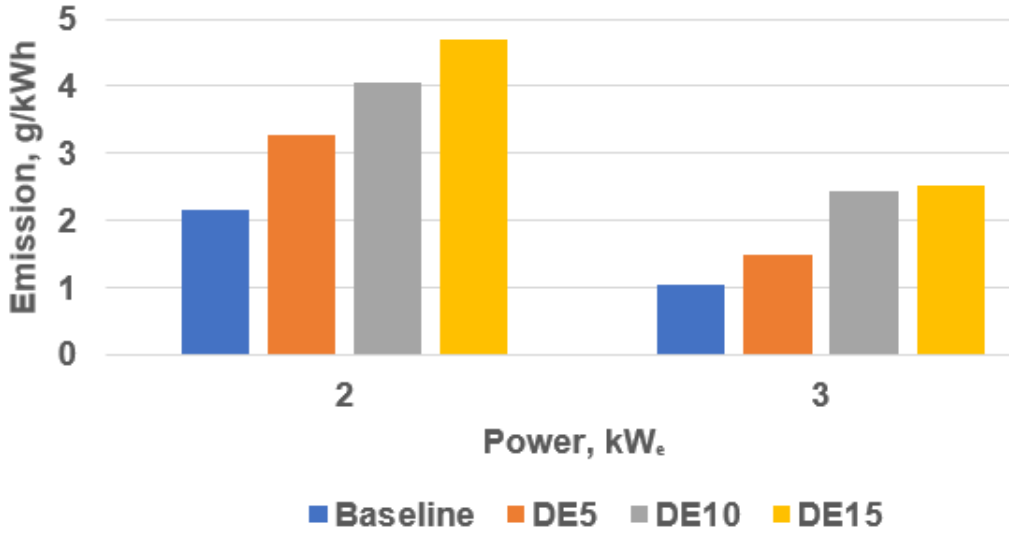

Figure 7.23 Graph of concentration of THC (in g/kWh) versus engine load (kW_e) for the tested blends

The THC level was highest at idle for all the tested fuels because the combustion temperature was lowest at idle. As such, fuel vaporisation and air-fuel mixing were least efficient at idle. The THC level rose by a factor of 2 (approximately) above the baseline for DE15. The THC emissions of the tested fuels at 2 kW_e in g/kg fuel were 5.06, 6.97, 8.48, and 9.71 respectively for pure diesel (DE0), DE5, DE10, and DE15. The engine-out THC emissions from diesel engines for pure diesel was reported to be about 5 g/kg fuel (Heywood, 1988). The observed THC emissions from the engine for the fuel blends were significantly higher than those for pure diesel. The percentage increases in the THC levels above the baseline at 2 kW_e load were 39.4, 69.6, and 94.2 respectively for DE5, DE10, and DE15. The observed drastic rise in THC emissions above the baseline when the engine was run on the DE blends was due to the increase in the Ignition Delay (ID) caused by the ethanol in the blends. DE fuel blends have a much lower CN than pure diesel due to the relatively low CN of ethanol (the CN of ethanol and diesel are 8 and 49 respectively). Consequently, there was a longer delay before the

auto-ignition of the fuel blends occurred than was the case for pure diesel. Furthermore, the Gen-set that was used in this work was a small-capacity (0.435 litre), naturally-aspirated, re-entrant piston bowl, DI, CI engine with an injection pressure and a non-variable injection crank angle of 19.6 MPa and 13^{o} bTDC respectively. Constant injection timing irrespective of the CN of the fuel or blend meant that there was no compensation for the relatively long ID that occurred when the engine was run on the DE blends. Consequently, there was a relatively short duration of combustion for the injected fuel blends prior to the sudden expansion cooling during the power stroke and the associated quenching. Therefore, the degree of completion of the combustion of the injected fuel blends was significantly reduced below the baseline thereby leading to the observed high levels of engine-out THC when the Gen-set was run on the DE blends.

Another major reason for the observed high levels of THC for the DE fuel blends was the poor atomisation of the injected fuel due to the relatively low fuel injection pressure of the engine. The fuel injection pressure of 19.6 MPa was too low to achieve efficient atomisation of the injected fuel compared to the injection pressure in relatively large CI engines such as the 96 kW IVECO engine which had an injection pressure of 160 MPa. Figure 7.24 shows the re-entrant bowl piston of a similar engine. The four regions of impingement of the injected fuel within the bowl of the piston are highlighted in the figure (the injector had four nozzles).

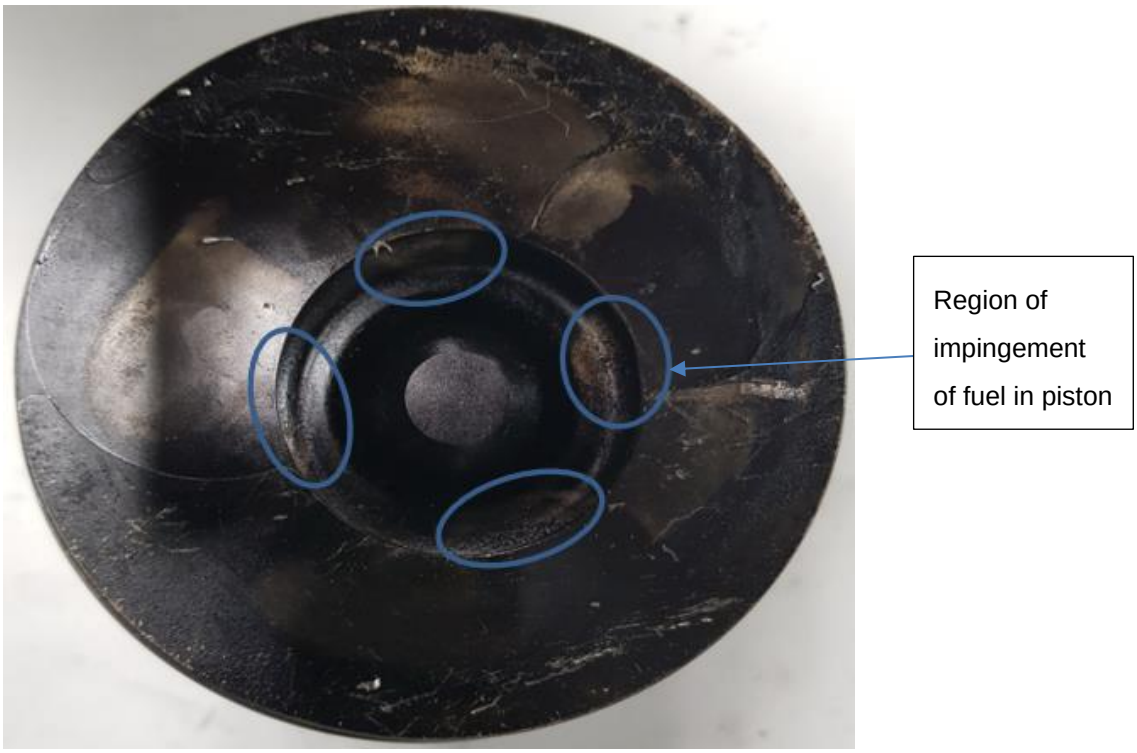

Figure 7.24 Re-entrant bowl piston of a similar Gen-set

The wall of the cylinder of the similar engine was observed, and tarry deposits were seen on it (Figure 7.25). The tarry deposits on the wall of the cylinder confirmed that wall-wetting occurred in the engine due to the impingement of fuel on the wall during fuel injection. The depths of jet penetration in the engine were estimated using Equations 3.1 and 3.2. The average estimated depth of penetration of the injected fuel mass for the tested fuel blends at the high conditions of power (2 kW_e and 3 kW_e) was ~48 mm. The average value of the estimated depth of penetration at the high conditions of power is greater than the radius of the cylinder of the Gen-set engine (43 mm). This further confirmed that the injected fuel impinged on the wall of the cylinder. Table B1 (Appendix B) presents the estimated values of the depth of penetration of the fuel jet at the tested conditions.

The impingement of the injected fuel on the wall of the cylinder of the engine due to the low capacity of the Gen-set (relatively small bore) also contributed to the observed high levels of THC emissions from the engine. The fuel that splashed on the wall of the cylinder ended up in the crevice of the piston. Poor mixing of the crevice fuel mass with air led to locally overrich zones in the crevice. The crevice fuel eventually vaporised off into the cylinder as unburned hydrocarbons towards the end of the power stroke thereby contributing to the THC emissions from the engine.

Salih (1990) and Rakopoulos et al. (2008) also reported that DE blends increased the THC emissions above the baseline. Li et al. (2004) reported that DE blend fuels increased the THC emissions by up to 40%. The same trend that was reported in literature for THC emissions from DE blends was observed in the current work. However, the observed percentage increases above the baseline for the Gen-set were much higher than the values in literature due to the reasons stated above.

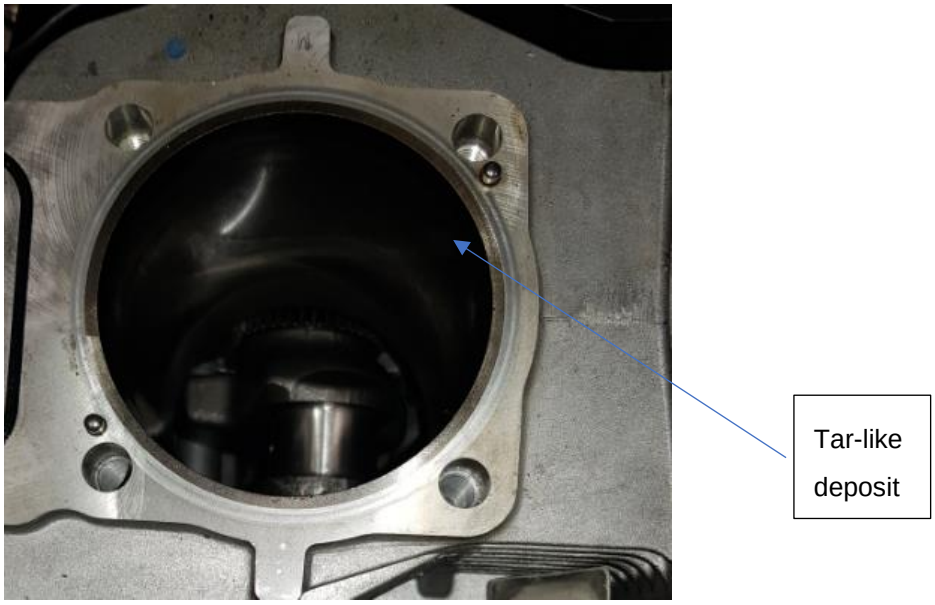

Figure 7.25 Tar-like deposit on the wall of the cylinder of a similar Gen-set

7.4.3 Ethanol emissions

Figures 7.26 and 7.27 show the emission levels for ethanol. As shown in the figures, the concentration of ethanol in the exhaust of the Gen-set increased as the percentage of ethanol in the blends increased for each of the tested loads. The level of the emitted ethanol for DE15 at idle increased by a factor of 16 above the baseline. It was reported that the rate of evaporation of ethanol could be relatively low in naturally aspirated engines at low temperatures (Srivastava et al., 2009). Therefore, at idle, the levels of the emitted ethanol increased as the percentage of ethanol in the fuel blends increased. Basically, due to the relatively low temperature at the idle condition, the relatively low rate of evaporation of ethanol led to the observed increase in the level of unburned ethanol above the baseline (ethanol has a higher heat of vaporisation than ULSD). The level of unburned ethanol increased drastically above the baseline for DE15 (at idle). However, as the load on the engine increased, the levels of the emitted ethanol decreased significantly below the corresponding levels at idle. The observed decrease in the levels of the engine-out ethanol emission as the load on the engine was increased was due to the drastic increase in the temperature of the flame. The relatively high flame temperatures that resulted at the higher loads enhanced the vaporisation and combustion of the ethanol in the injected blends as well as the oxidation of the emitted organic compounds by the oxygen of ethanol and the oxygen from the intake air. This led to the observed decrease in the levels of ethanol in the exhaust when the load on the engine was increased.

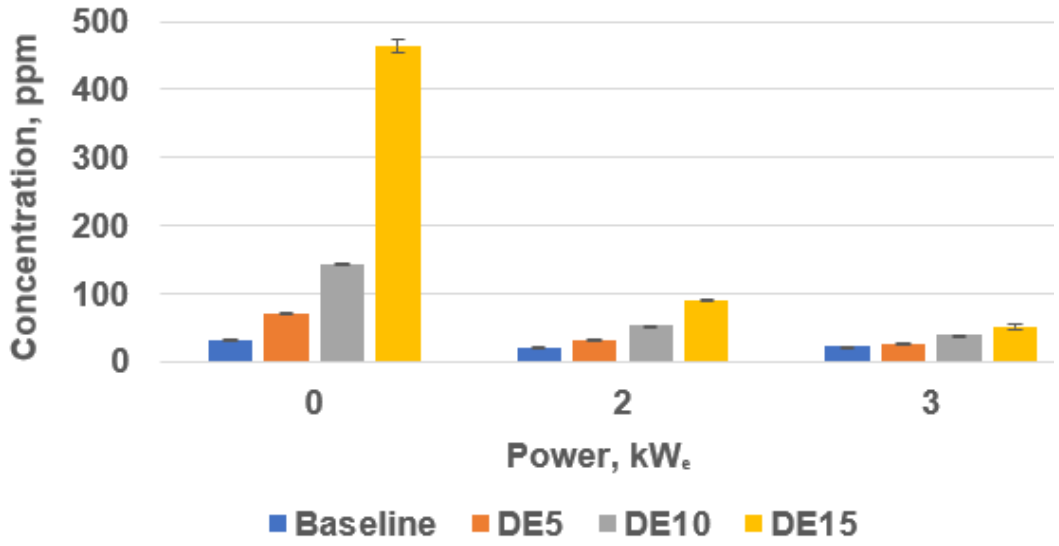

Figure 7.26 Graph of concentration of ethanol (in ppm) versus engine load (kW_e) for the tested blends

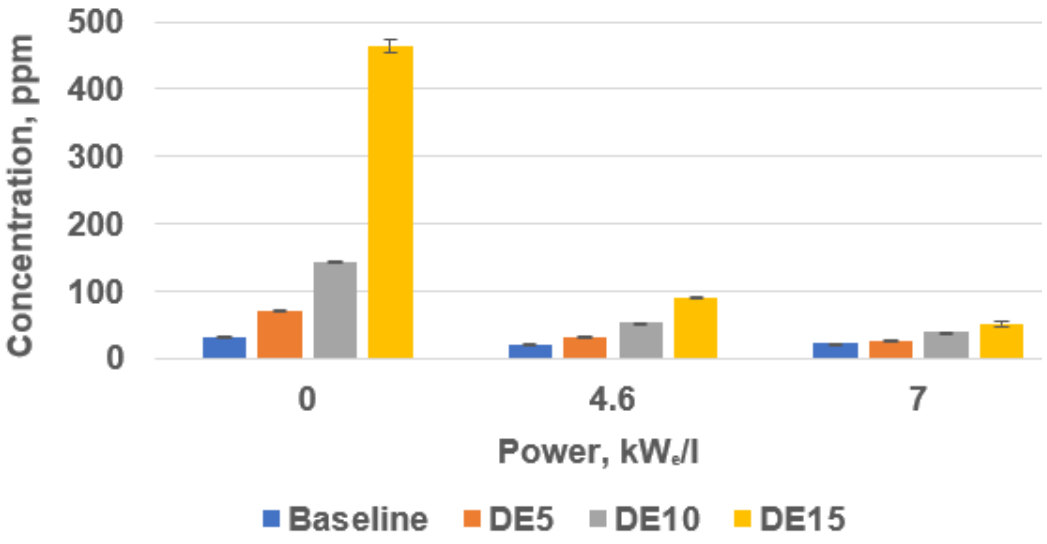

Figure 7.27 Graph of concentration of ethanol (in ppm) versus engine load (kW_e/l) for the tested blends

He et al. (2003) reported that the level of ethanol emission increased with increase in the concentration of ethanol in the fuel blends. The authors also reported that the level of ethanol in the engine-out exhaust decreased as the load on the engine increased. The same trends were observed in the current work. However, the levels of ethanol emission reported in this work were much higher

than the levels reported in literature. This was due to the low fuel injection pressure of the Gen-set that caused inefficient atomisation of the injected fuel as well as the impingement of the fuel jet on the wall of the cylinder (the same conditions explained in the previous section that led to the observed high THC emissions). The emission of ethanol from the engine was further aggravated by the relatively high heat of vaporisation and low CN of ethanol which caused the ethanol to remain unburned in the engine during the power stroke.

7.4.4 CO emissions

Figures 7.28 to 7.30 present the emission levels for CO. The figures clearly show that the tested DE fuel blends led to an increase in the engine-out CO emission. The emitted CO increased above the baseline as the concentration of ethanol increased in the diesohol blends. All the tested blends had CO levels above the baseline at the tested loads. The percentage increases in CO emissions above the baseline were 32.5, 60.3, and 92.9 respectively for DE5, DE10, and DE15. Contrary to the trend that was reported for CO emissions in this work, Rakopoulos et al. (2008), and Li et al. (2004) reported that DE blends led to a decrease in CO emissions. Li et al. (2004) reported that CO levels decreased by 16.7% and 5.8% respectively for DE10 and DE15. The reasons for the observed increase in CO emissions from the Gen-set, contrary to what was reported for diesel engines in literature, were the poor atomisation of the injected fuel, and the impingement of the fuel jets on the wall of the cylinder of the engine, both of which led to the formation of local rich zones. The local rich zones led to incomplete combustion thereby increasing the levels of CO and THC (the products of incomplete combustion) as explained in Section 7.4.2.

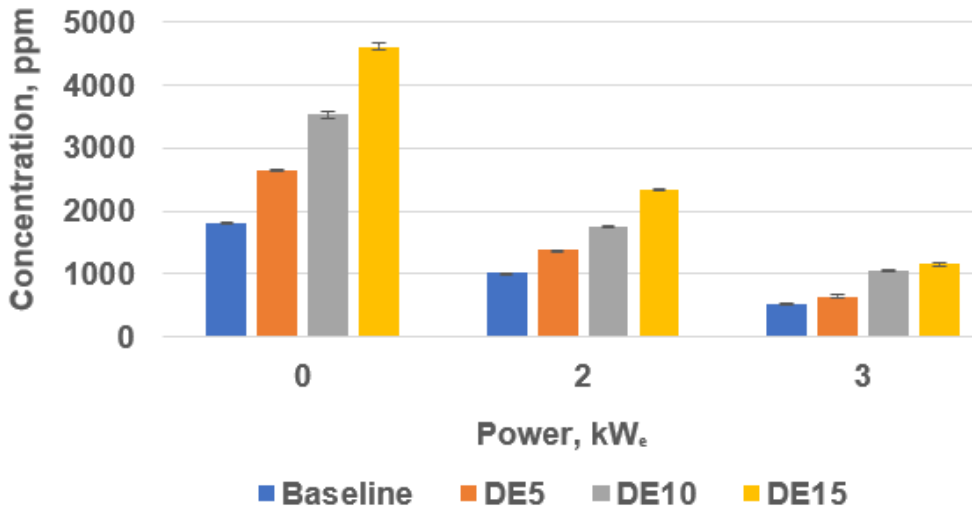

Figure 7.28 Graph of concentration of CO (in ppm) versus engine load (kW_e) for the tested blends

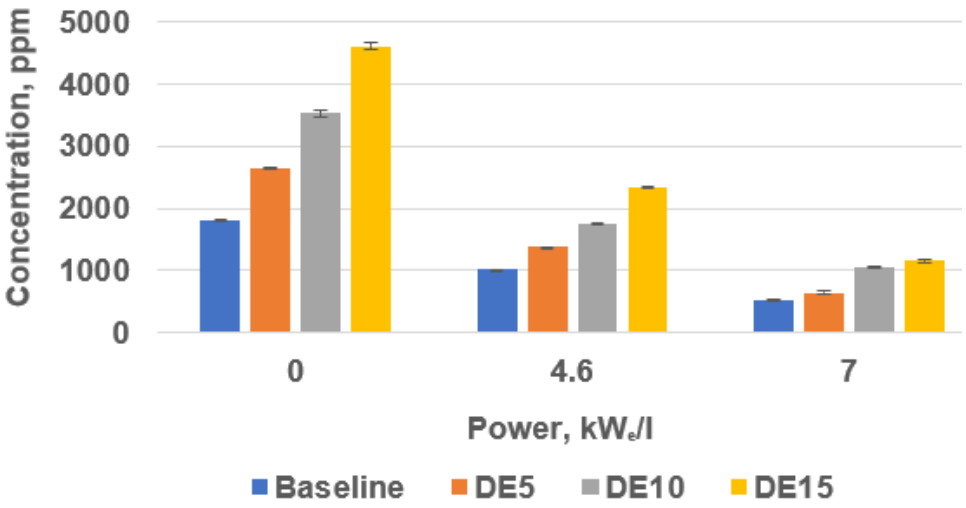

Figure 7.29 Graph of concentration of CO (in ppm) versus engine load (kW_e/l) for the tested blends

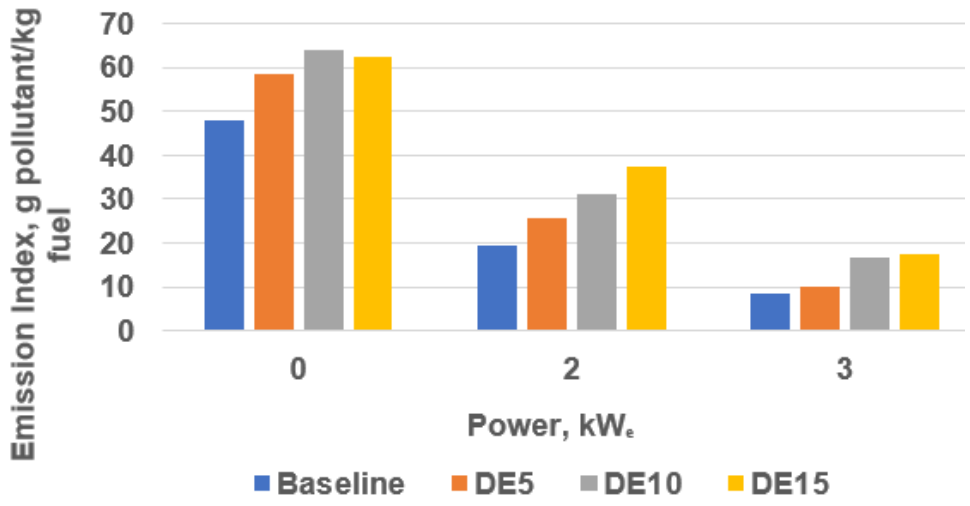

Figure 7.30 Graph of concentration of CO (in g pollutant/kg fuel) versus engine load (kW_e) for the tested blends

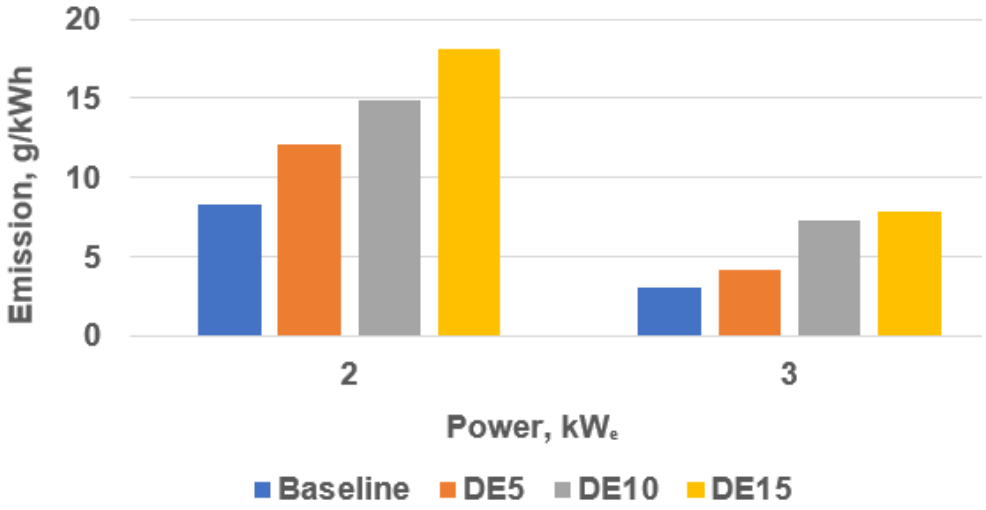

Figure 7.31 Graph of concentration of CO (in g/kWh) versus engine load (kW_e) for the tested blends

As shown in Figure 7.28, DE15 had the highest increase in the engine-out CO above the baseline because at each of the tested conditions, the injected fuel mass and the cooling effect were greater for DE15 than they were for the other fuel blends. Excessive evaporation-induced cooling as a result of the relatively high heat of vaporisation of ethanol led to poor vaporisation of the injected fuel as well as imperfect air-fuel mixing. Consequently, local rich zones were present within the combustion chamber when the Gen-set was run on the fuel blends.

The local rich zones did not have sufficient oxygen for efficient combustion of the fuel therein (Section 3.3.4.2). The formation of the local rich zones led to incomplete combustion and the associated products (CO and unburned hydrocarbons). As the concentration of ethanol in the blends increased, the formation of the products of incomplete combustion also increased thereby leading to the observed rise in the levels of the engine-out CO above the baseline. However, as the load increased for each of the tested fuels, Figures 7.28 to 7.31 show that the CO emissions decreased. As the load on the Gen-set increased, the combustion temperature increased drastically. This increase in temperature enhanced the vaporisation and combustion of the injected fuel thereby reducing the levels of CO. Also, the increase in temperature that occurred as the load on the engine increased enhanced the oxidation of CO to CO_2 thereby reducing the CO levels at the higher loads for all the tested fuels. The oxidation of CO to CO_2 is known to be enhanced at high temperatures.

7.4.5 Aldehyde emissions

Figures 7.32 and 7.35 depict the emission levels for the aldehydes (formaldehyde and acetaldehyde). The use of ethanol blended fuels in diesel engines is known to cause significant emissions of formaldehyde and acetaldehyde (Heywood, 1988). As shown in Figures 7.32 and 7.35, the levels of the aldehydes emitted from the engine increased above the baseline as the concentration of ethanol increased in the blends. The order of the increase in aldehyde emissions above the baseline at idle for DE15 was approximately 3. The increase was more drastic for the operation at idle due to the relatively low combustion temperature which did not favour the oxidation of the aldehydes. The aldehyde emissions decreased for each of the tested fuels as the load on the engine increased due to the increase in the flame temperature that occurred at the high loads. According to

He et al. (2003), the observed high acetaldehyde emissions for DE fuel blends at relatively low loads was caused by the relatively low combustion temperatures of the DE blends.

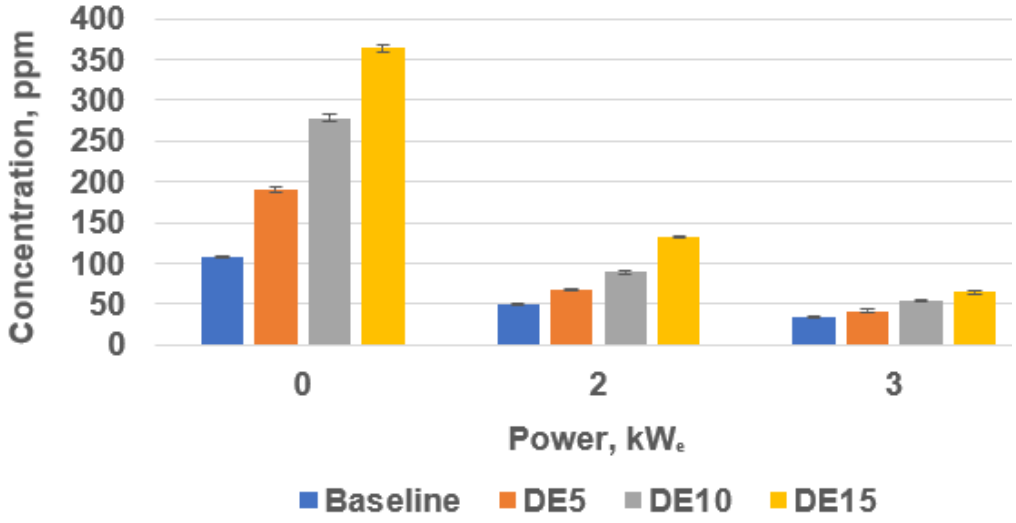

Figure 7.32 Graph of concentration of formaldehyde, CH_2O (in ppm) versus engine load (kW_e) for the tested blends

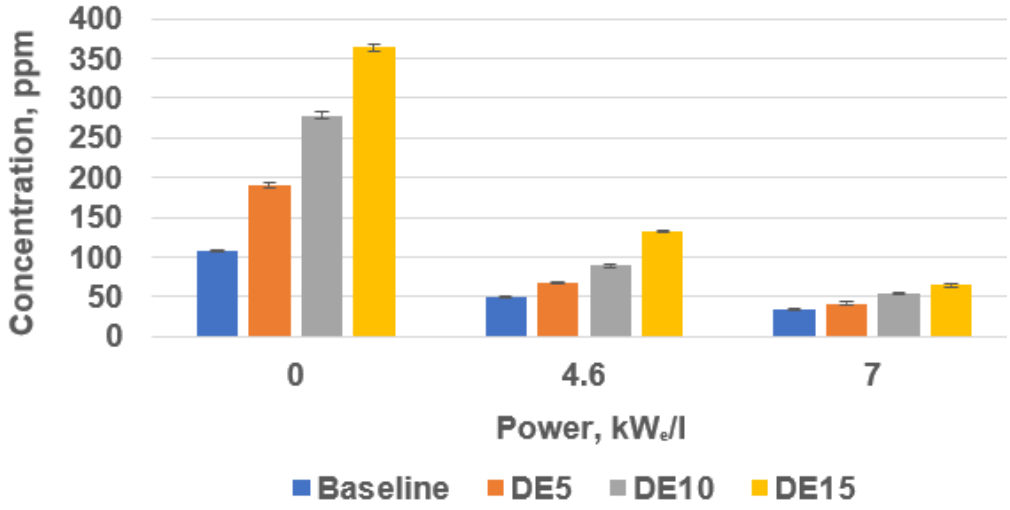

Figure 7.33 Graph of concentration of formaldehyde, CH_2O (in ppm) versus engine load (kW_e/l) for the tested blends

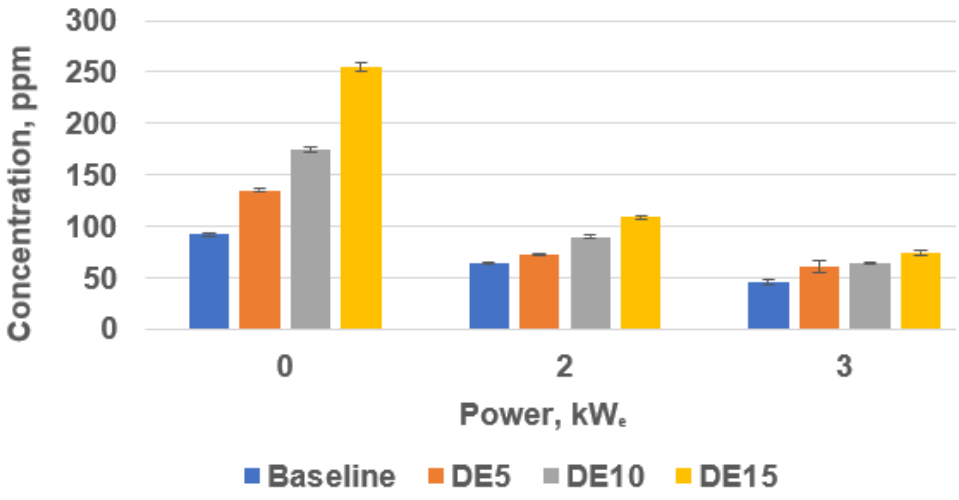

Figure 7.34 Graph of concentration of acetaldehyde, C_2H_4O (in ppm) versus engine load (kW_e) for the tested blends

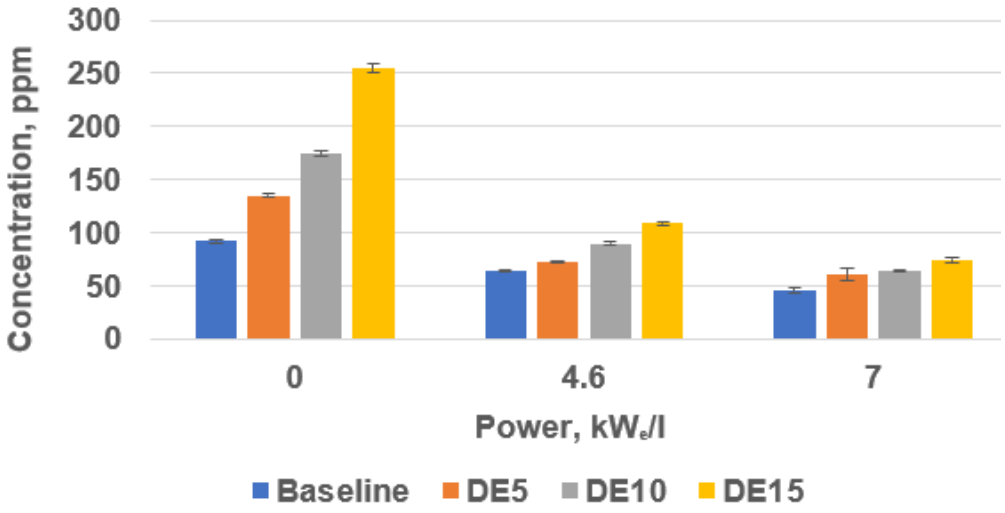

Figure 7.35 Graph of concentration of acetaldehyde, C_2H_4O (in ppm) versus engine load (kW_e/l) for the tested blends

7.4.6 Ethylene emissions

Significant emission of ethylene above the baseline was also observed for the DE fuel blends due to the presence of ethanol in the blends. Figure 7.36 and 7.37 show that the levels of ethylene increased above the baseline as the concentration of ethanol increased in the fuel blends. The emission levels however decreased for each of the tested fuels as the load on the engine was

increased due to the observed increase in the flame temperature which enhanced the oxidation of ethylene.

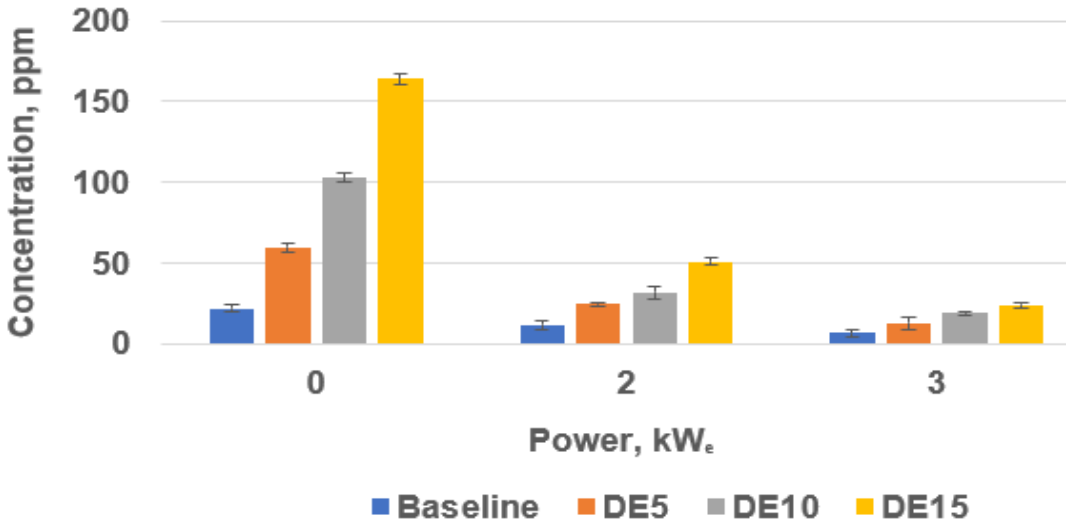

Figure 7.36 Graph of concentration of ethylene (in ppm) versus engine load (kW_e) for the tested blends

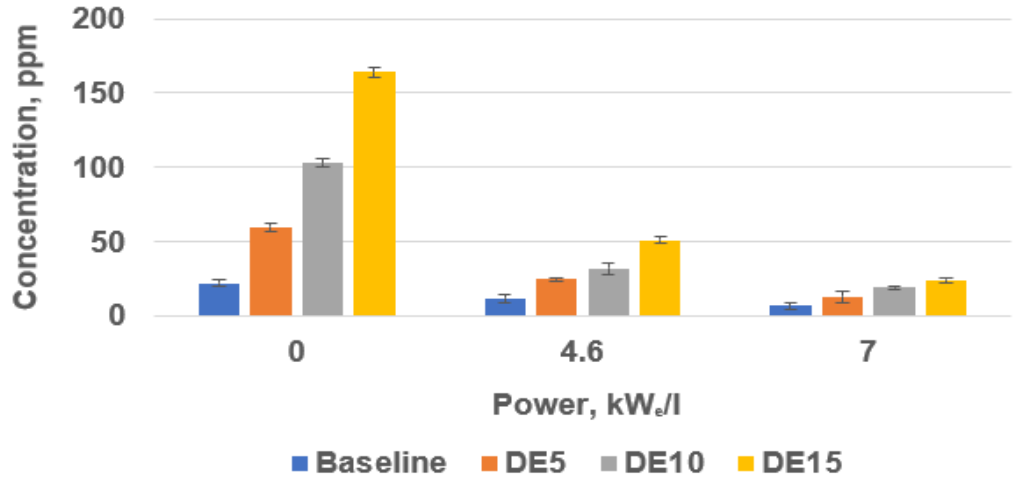

Figure 7.37 Graph of concentration of ethylene (in ppm) versus engine load (kW_e/l) for the tested blends

7.4.7 1,3-butadiene emissions

Figures 7.38 and 7.39 depict the emission levels for 1,3-butadiene. The figures show that the emission of 1,3-butadiene was generally high for both pure diesel and the DE fuel blends. The 1,3-butadiene emission for baseline diesel was

observed to increase as the load on the engine increased while the DE fuel blends did not show any clear trend.

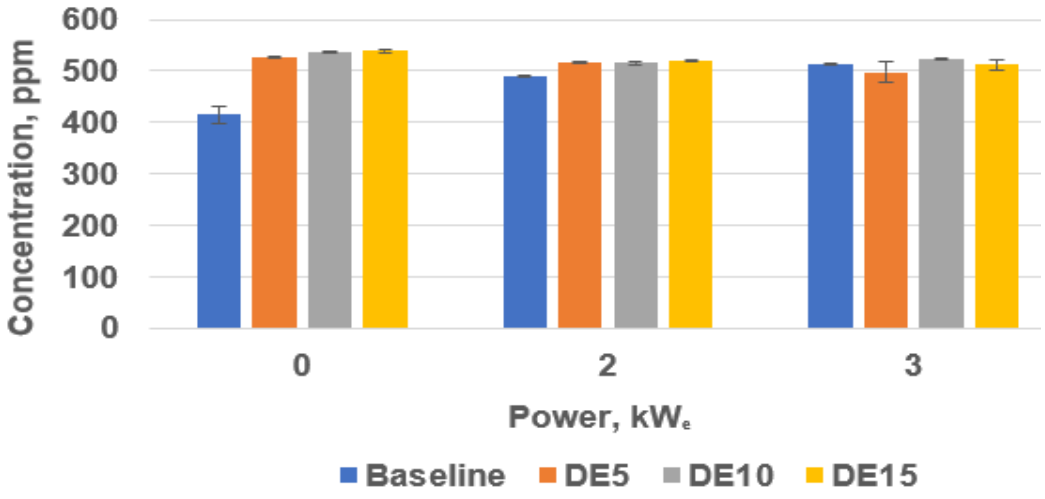

Figure 7.38 Graph of concentration of 1,3-butadiene (in ppm) versus engine load (kW_e) for the tested blends

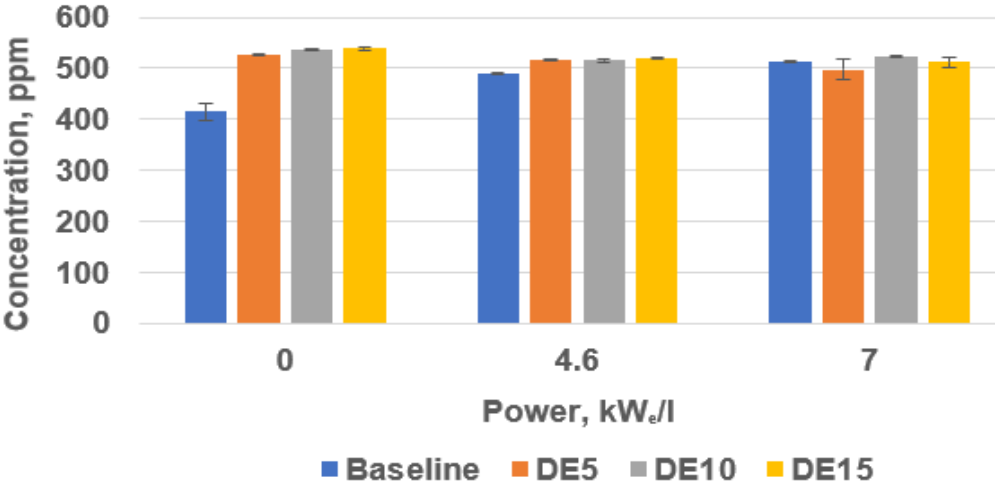

Figure 7.39 Graph of concentration of 1,3-butadiene (in ppm) versus engine load (kW_e/l) for the tested blends

7.4.8 Benzene emissions

Figures 7.40 and 7.41 show the emission levels for benzene (a Polycyclic Aromatic Hydrocarbon, PAH). At the higher loads, no emission of benzene was observed for baseline diesel due to the relatively high combustion temperature which led to the oxidation and thermal decomposition of heavy hydrocarbons.

The benzene emission levels increased above the baseline as the concentration of ethanol increased in the DE fuel blends for engine operation at idle and at 2 kW_e. The emission levels for benzene at 3 kW_e load were, however, insignificant for all the tested fuels. Generally, as the load on the engine increased, the engine-out benzene emission from the tested fuels decreased drastically due to the thermal decomposition of heavy hydrocarbons and the enhanced combustion of unburned hydrocarbons at the relatively high temperatures that characterised the high load conditions.

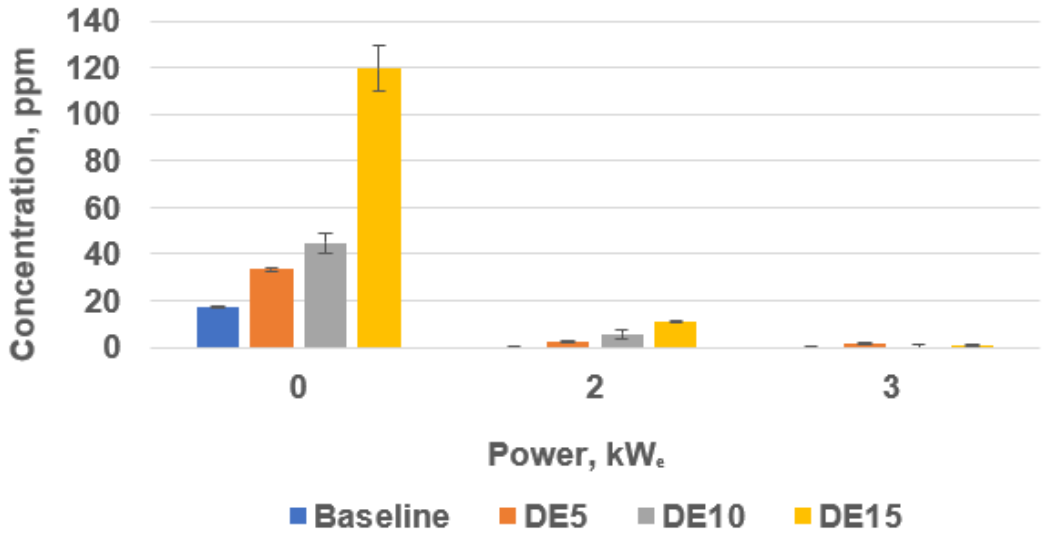

Figure 7.40 Graph of concentration of benzene (in ppm) versus engine load (kW_e) for the tested blends

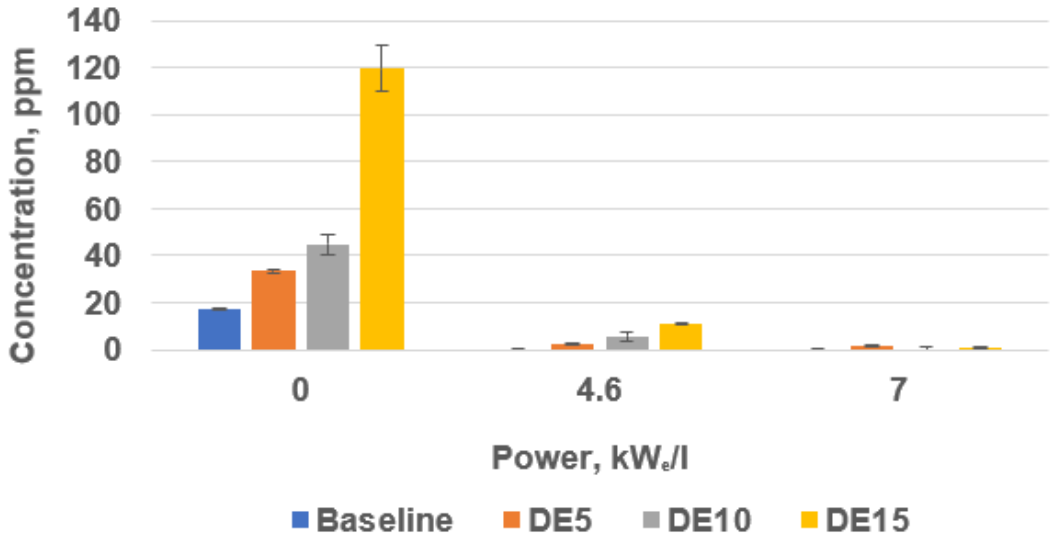

Figure 7.41 Graph of concentration of benzene (in ppm) versus engine load (kW_e/l) for the tested blends

7.5 Particulate emissions

The Particulate Matter (PM) distributions for the tested fuels and loads were estimated from the measured PN distributions. The PN and PM distributions were analysed to determine the effect of ethanol-blended fuels on engine-out particulate emissions.

7.5.1 Comparison of the particulate emission levels for the blends at single loads

The particulate emission levels for the tested blends were compared graphically at each condition of load as shown in Figures 7.42 to 7.47. The diameters of the particles (Dp) at which the peak PN and the peak PM concentrations occurred are given in Table 7.3. Table 7.3 shows that at the idle condition, the diameter of the particles at the peak PN and peak PM concentrations increased as the concentration of ethanol in the fuel blends increased. The diameters of the particles were larger for the fuel blends than for pure diesel at idle due to the inefficient atomisation and vaporisation of the injected DE fuel blends as well as the relatively low flame temperature at idle. The effective heats of vaporisation

for the DE blends were higher than that of pure diesel as noted earlier. However, as the load on the engine was increased, the opposite trend was observed; the diameter of the particles at the peak PN decreased below the baseline as the concentration of ethanol increased in the blends. This was due to the drastic increase in the temperature of the gases in the combustion chamber when the load on the engine was increased.

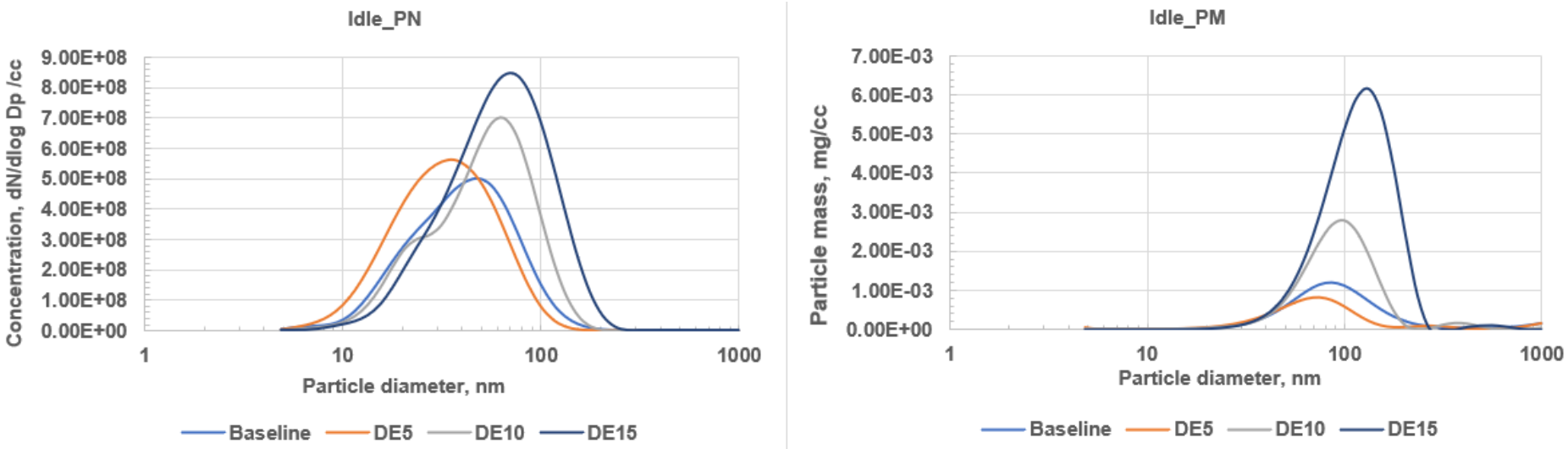

(a) (b)

Figure 7.42 Particulate emissions of the tested fuels at idle (semi-log plots): (a) PN distributions at idle (b) PM distributions at idle

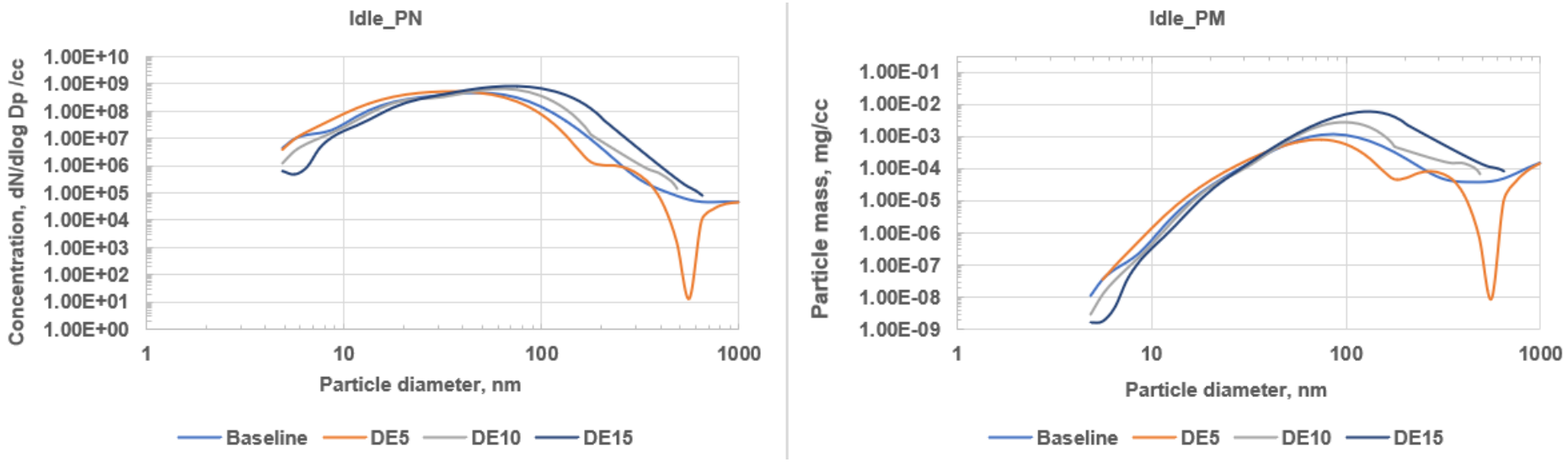

(a) (b)

Figure 7.43 Particulate emissions of the tested fuels at idle: (a) PN distributions at idle (b) PM distributions at idle

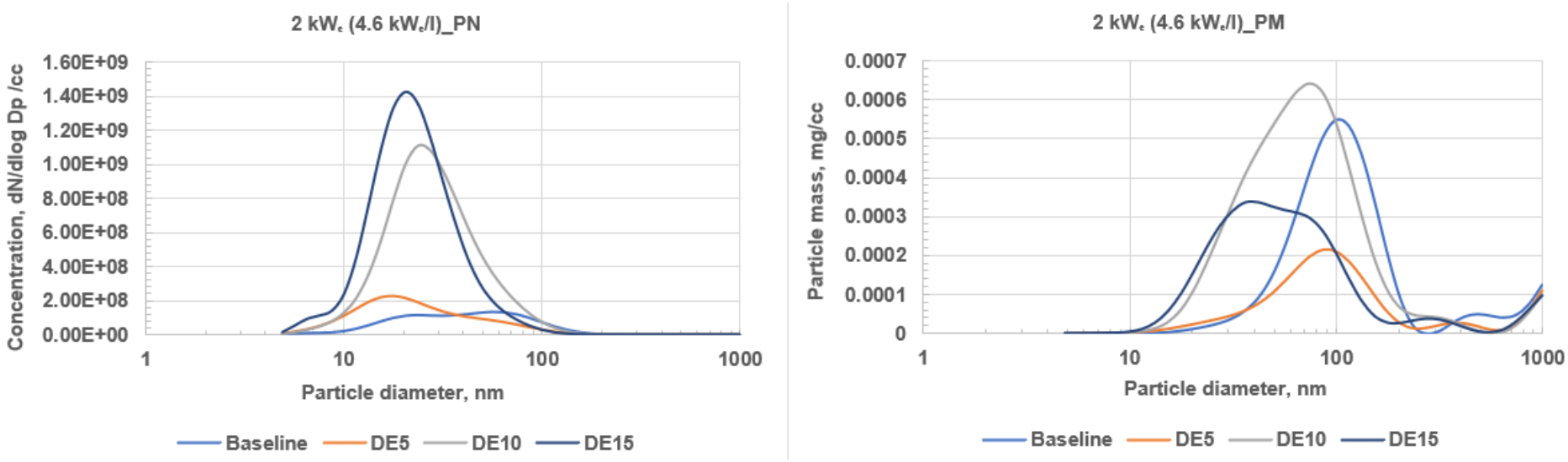

(a) (b)

Figure 7.44 Particulate emissions of the tested fuels at 2 kW_e (semi-log plots): (a) PN distributions at 2 kW_e (b) PM distributions at 2 kW_e

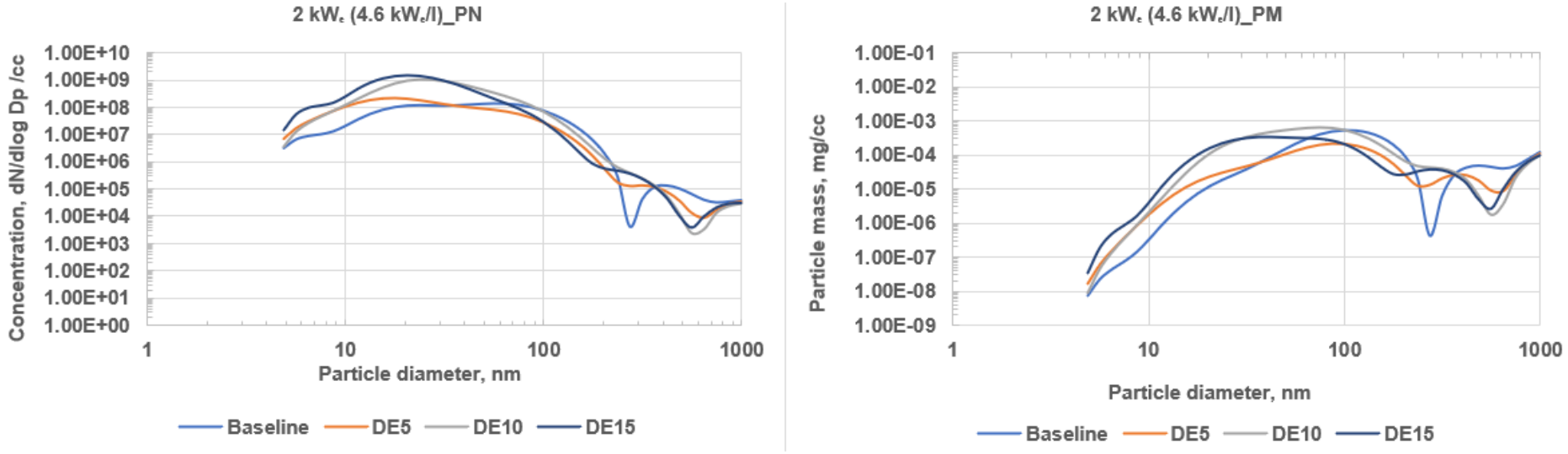

(a) (b)

Figure 7.45 Particulate emissions of the tested fuels at 2 kW_e: (a) PN distributions at 2 kW_e (b) PM distributions at 2 kW_e

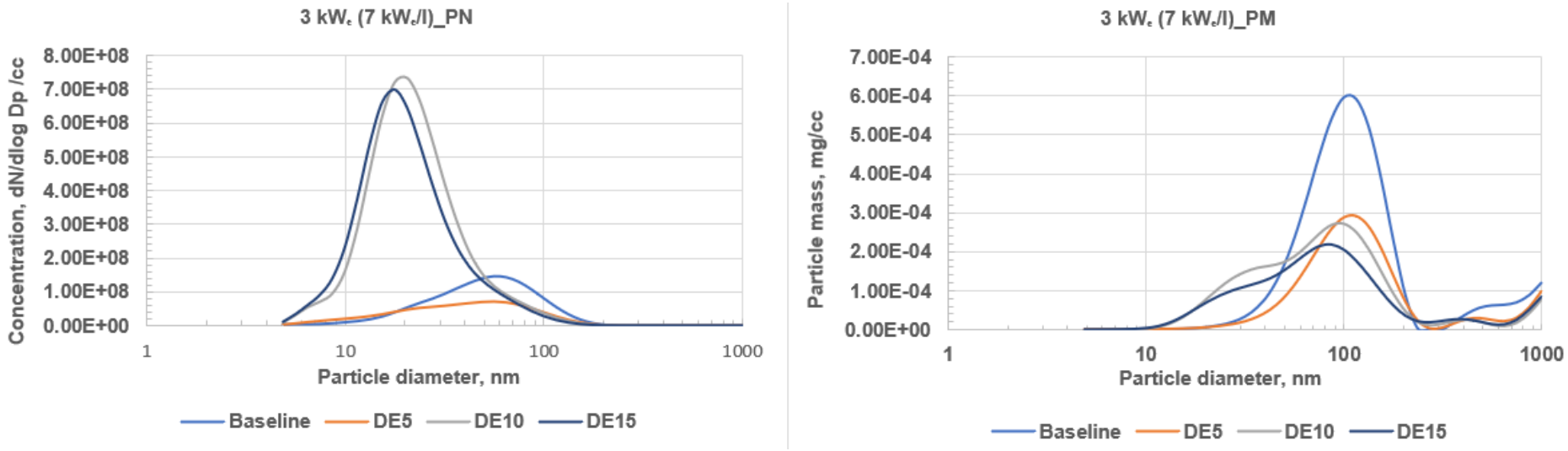

(a) (b)

Figure 7.46 Particulate emissions of the tested fuels at 3 kW_e (semi-log plots): (a) PN distributions at 3 kW_e (b) PM distributions at 3 kW_e

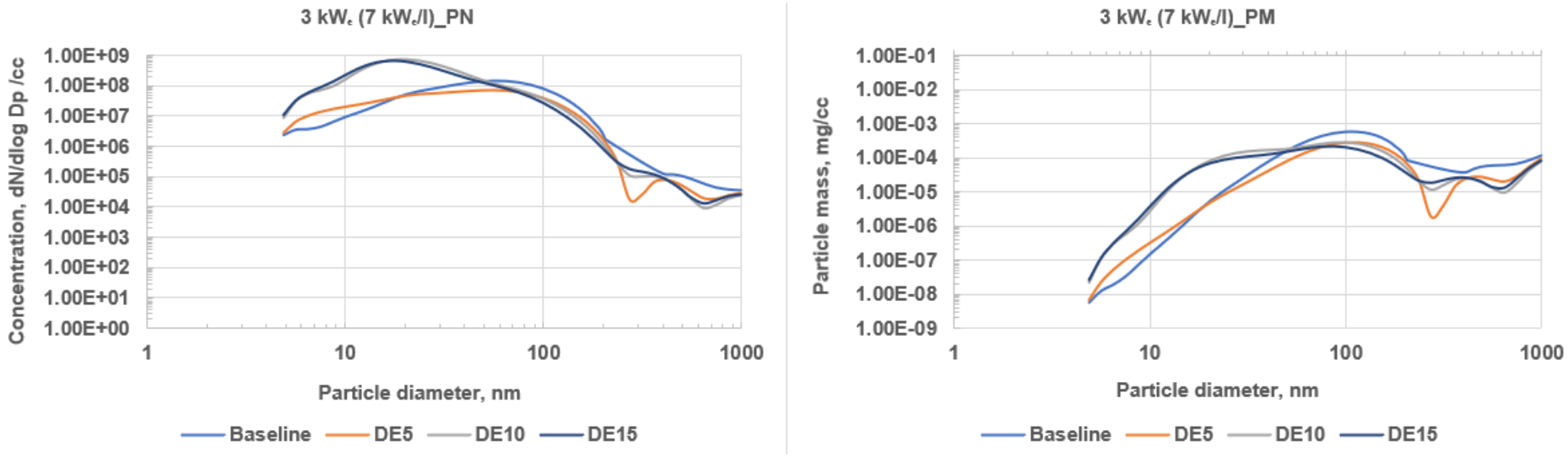

(a) (b)

Figure 7.47 Particulate emissions of the tested fuels at 3 kW_e: (a) PN distributions at 3 kW_e (b) PM distributions at 3 kW_e

Table 7.3 Diameter of particulates at peak PN and PM

	Peak PN diameter, nm			**Peak PM diameter, nm**		
Fuel	**Idle**	**2 kW_e**	**3 kW_e**	**Idle**	**2 kW_e**	**3 kW_e**
Baseline	49	65	56	87	100	115
DE5	37	18	56	75	87	115
DE10	65	24	21	100	75	100
DE15	75	21	18	133	75	87

The temperature of the combustion mixture increased at the higher loads, and oxidation of the soluble organic fraction of the soot particles occurred. This led to the observed reduction in the Dp for the blends with relatively high percentage of ethanol (DE10 and DE15) (Table 7.3). The oxidation of soot at the higher loads was enhanced by the oxygenated blend fuels. The increase in the flame temperature that occurred when the engine was loaded enhanced the oxidation of soot by the -OH group of ethanol in the blend fuels as well as by the oxygen in air. This in turn led to the observed reduction in the Dp at the Peak PN as the load on the engine and the concentration of ethanol in the DE fuel blends increased. At near-stoichiometric conditions, soot oxidation by the -OH group of ethanol is enhanced (Heywood, 1988). The tested conditions in this work were both lean and near-stoichiometric (Table 7.2).

The peak PN in the engine-out exhaust of diesel engines usually occurs in the nucleation mode; the soot nuclei/spherules formation stage. Heywood (1988) reported that the diameter of spherules varied between 10 and 80 nm (but mostly between 15 and 30 nm). The peak PM on the other hand, occurs in the

accumulation mode; the particle growth stage during which 100≤Dp≤150 nm (Heywood, 1988). However, as shown in Table 7.3, the peak PN for the tested conditions and fuels in the current work occurred at Dp>30 nm (except for DE10 and DE15 at 2 kW_e and 3 kW_e loads). The observed high Dp at the peak PN in this work confirmed that the emitted particles were predominantly aerosols of unburned hydrocarbons (HCs) due to the inefficient atomisation of the injected fuels in the engine. This also confirmed the observed high THC emission levels from the Gen-set. Table 7.3 and Figures 7.42 to 7.47 further show that the particle size distribution for DE5 was similar to the distribution for pure diesel. Pure diesel and DE5 both showed PN peaks in the nanoparticles Dp range (Dp<30 nm) as well as at Dp=65 nm (bimodal PN distributions) as shown in Figure 7.48. However, the second peak for DE5, the PN peak at Dp=65 nm, was a weak peak. The particulate emission results in this work are similar to the findings of Lapuerta et al. (2009). The authors reported that the mean diameter of the emitted particles decreased as the concentration of ethanol in the fuel blends increased. The same observation was made in the current work (Table 7.3). Furthermore, Lapuerta et al. (2009) reported that DE7.7 (close in concentration to DE5) had similar particle size distribution to diesel, as was also observed in this work (Table 7.3, Figures 7.45, 7.50, and 7.51).

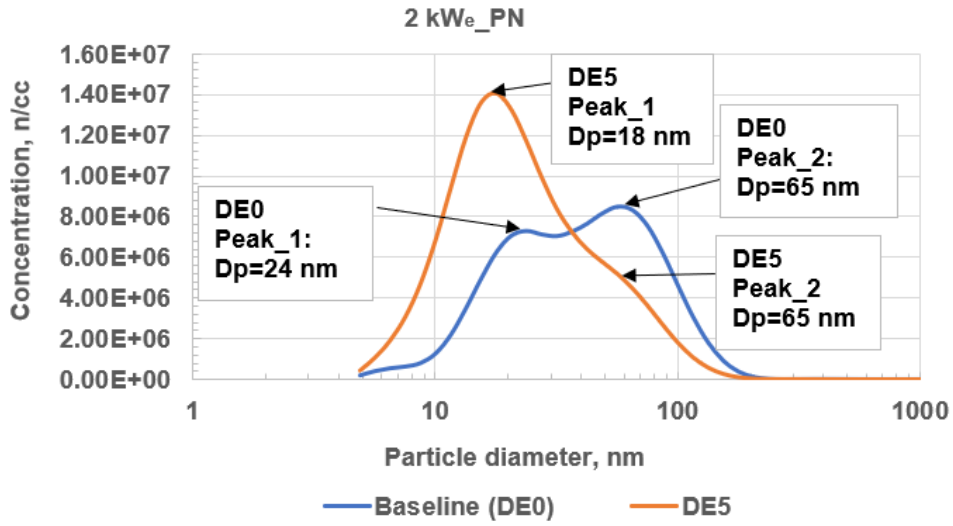

Figure 7.48 Bimodal Particulate Number (PN) distributions of pure diesel (DE0) and DE5 at 2 kW_e

Generally, it was observed in the current work that as the concentration of ethanol increased in the fuel blends at each of the tested engine loads (except at idle), as depicted in Figures 7.44 to 7.47, the emission of nanoparticles (nucleation mode particles: Dp<50 nm) from the Gen-set increased above the baseline. However, as the load on the engine was increased, the particulate emissions from the engine for the blend fuels decreased below the baseline as the concentration of ethanol in the blends increased for particles of diameter > 100 nm (accumulation mode particles). This was because the rise in temperature at the higher loads enhanced the vaporisation and combustion of the injected fuel mass. Consequently, particle growth was impeded. Also, the oxidation of the adsorbed organic compounds on the accumulation mode particles was enhanced by the oxygen in the oxygenated DE blend fuels especially for the blends that had relatively high concentrations of ethanol. This contributed to the reduction of the size of the particles.

7.5.2 Effects of increasing the engine load on particulate emission from each of the tested fuels

The effect of increasing the load on the Gen-set on the particulate emissions from the engine are graphically depicted for each of the tested fuels in Figures 7.49 to 7.58. Figures 7.49 and 7.50 depict the effect of increasing the load on the engine on the peak PN for the tested fuels. The peak PN for DE10 and DE15 occurred in the nanoparticle Dp range (Dp<30 nm) at the tested loads. Generally, for DE10 and DE15, as the load on the engine was increased, the emission levels of nanoparticles (Dp<30 nm) were higher than the emission levels when the engine was run on the same fuel blends at idle. However, for ULSD and DE5, the emission of particulates decreased as the load on the engine was increased (Figures 7.49 to 7.54). Figures 7.49, 7.50, and 7.55 to 7.58 show that the peak PN and the emission of nanoparticles were highest at 2 kW_e for DE10 and DE15. Although the temperature of the flame increased when the load was increased to 2 kW_e, the aerosol vaporisation and combustion enhancing effect of the temperature rise did not offset the effect of increasing the load on the engine on the fuel consumption (increase in the injected blend fuel mass and increase in the number of aerosols of the injected blend). The increase in the flame temperature with increase in the load on the engine paid off for DE10 and DE15 at the 3 kW_e load. At the 3 kW_e load, the rise in the temperature of the flame was sufficiently high to enhance the vaporisation and combustion of the injected blend aerosols such that the peak PN and the emission levels of nanoparticles (nucleation mode particles) for DE10 and DE15 at the 3 kW_e load were lower than the corresponding levels of the nanoparticles at 2 kW_e load (Figures 7.49 and 7.50).

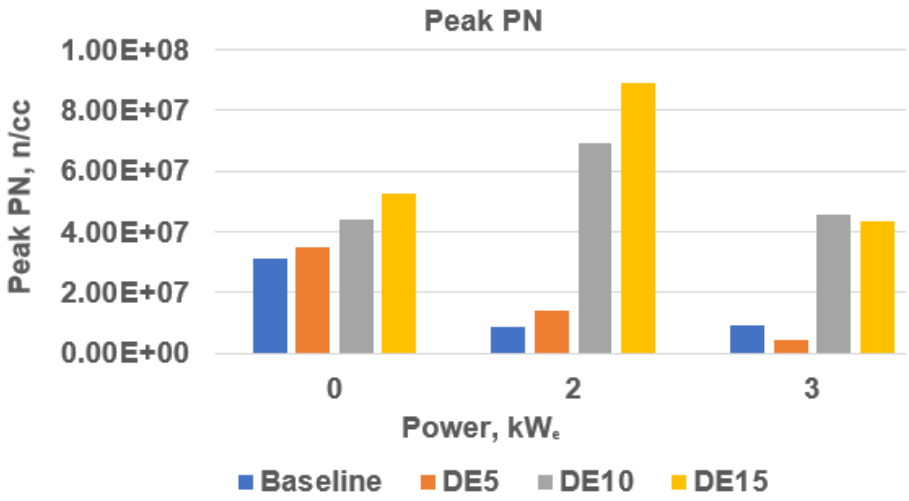

Figure 7.49 Graph of peak Particulate Number (PN) for the tested fuel blends versus engine load (kW_e)

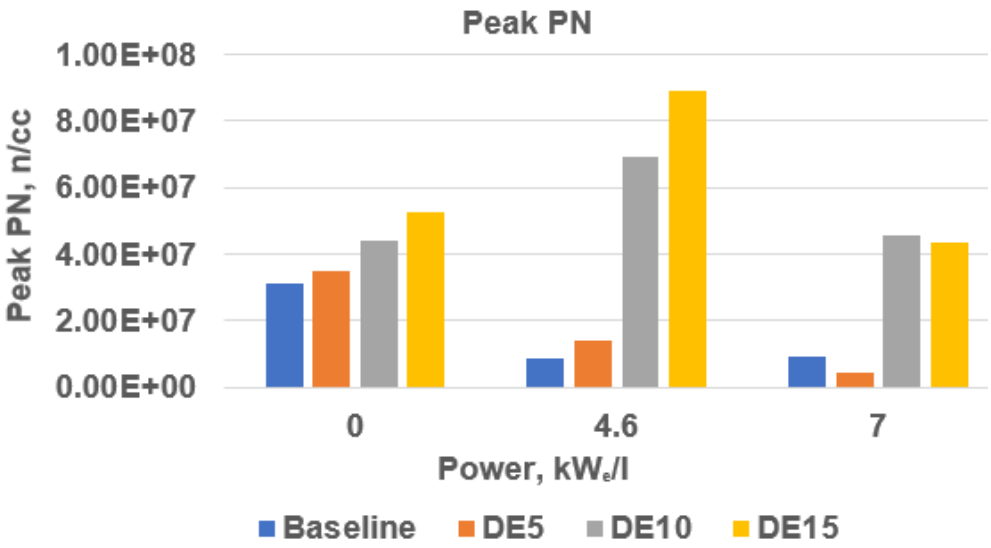

Figure 7.50 Graph of peak Particulate Number (PN) for the tested blends versus engine load (kW_e/l)

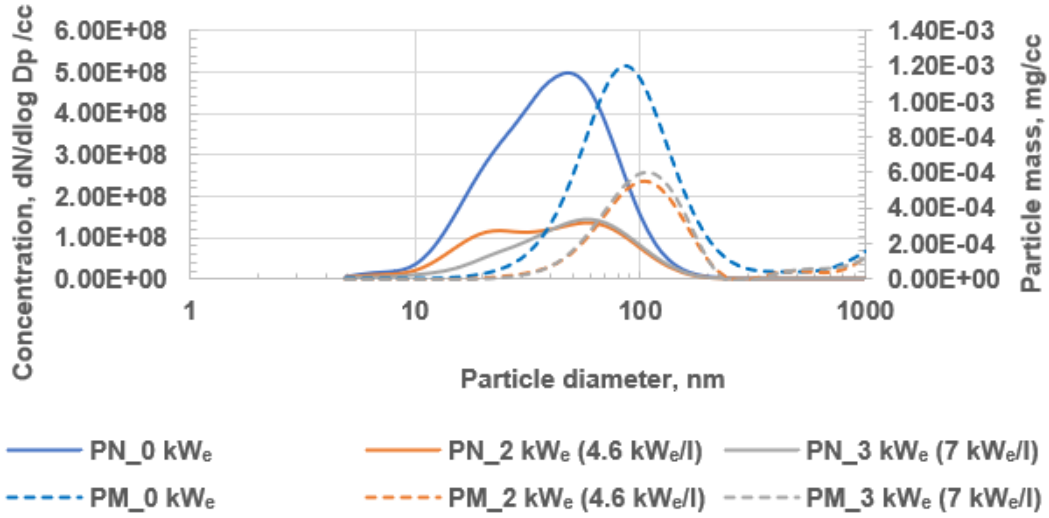

Figure 7.51 Comparison of particulate emissions at the tested loads (baseline diesel)

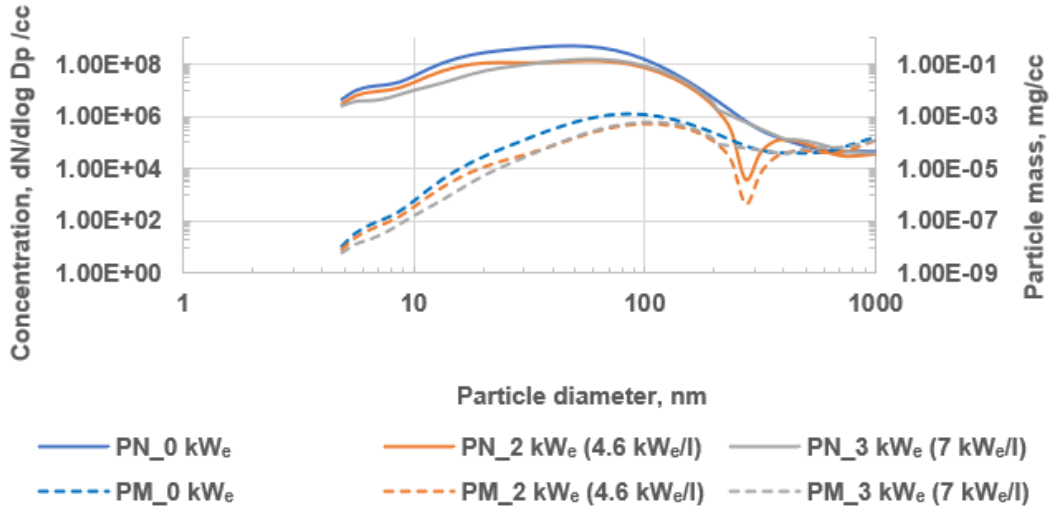

Figure 7.52 Comparison of particulate emissions at the tested loads (baseline diesel; log-log scale)

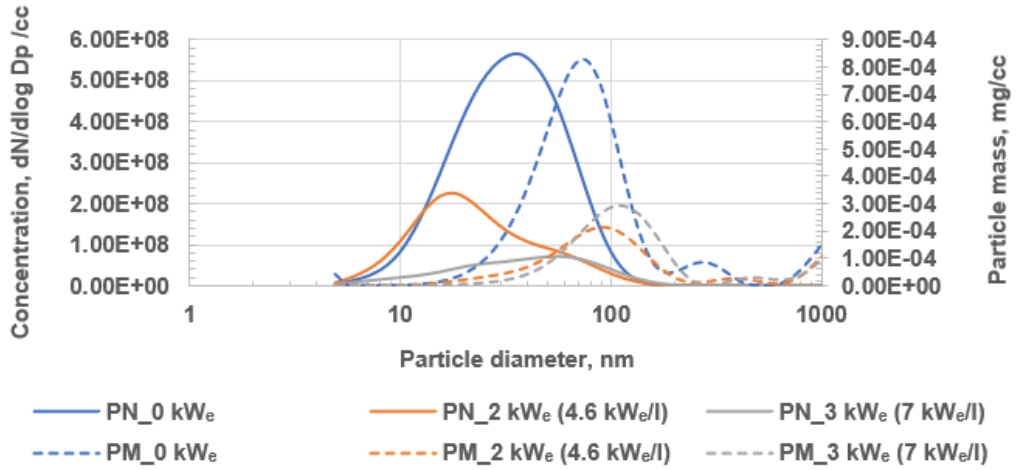

Figure 7.53 Comparison of the particulate emissions at the tested loads (DE5)

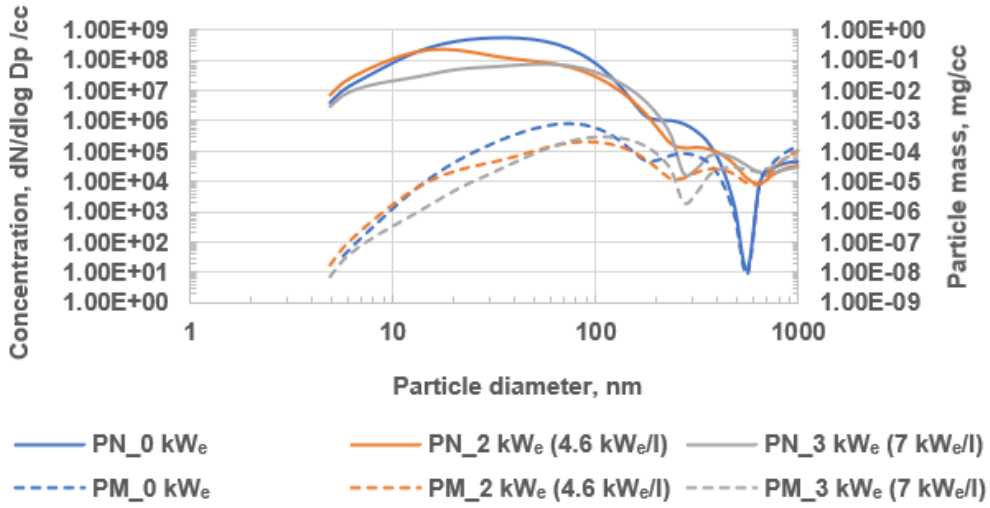

Figure 7.54 Comparison of the particulate emissions at the tested loads (DE5; log-log scale)

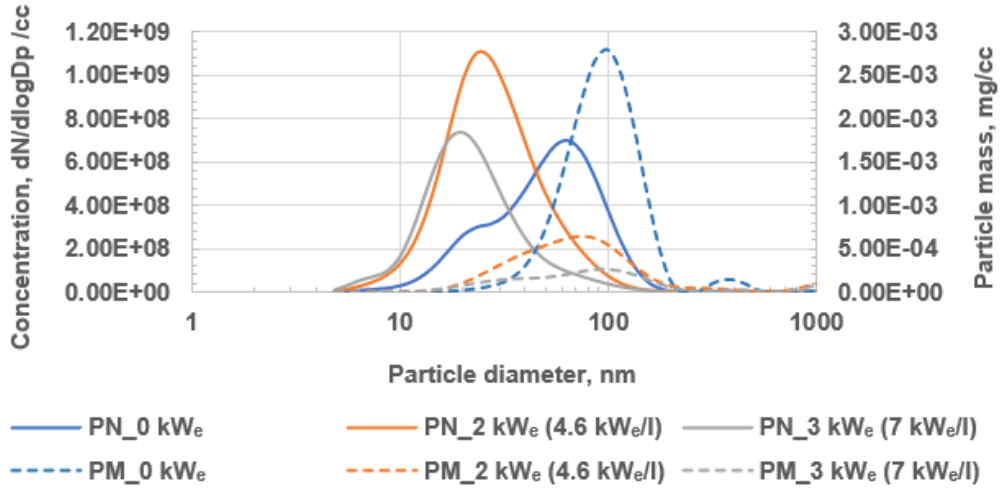

Figure 7.55 Comparison of the particulate emissions at the tested loads (DE10)

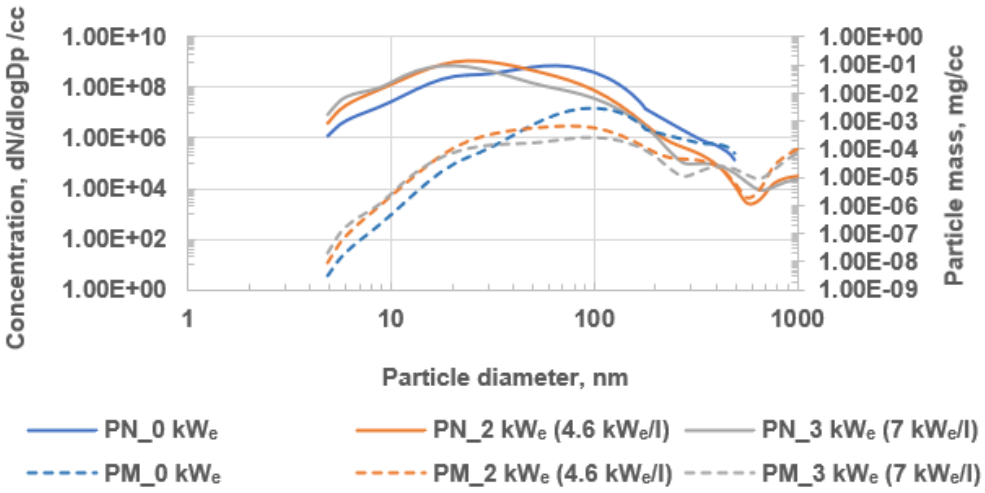

Figure 7.56 Comparison of the particulate emissions at the tested loads (DE10; log-log scale)

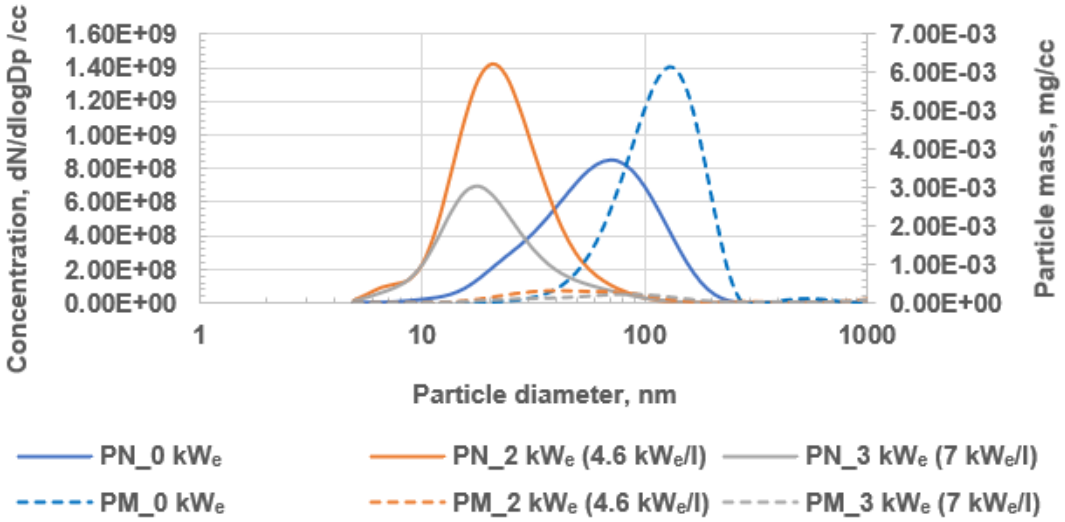

Figure 7.57 Comparison of the particulate emissions of the tested loads (DE15)

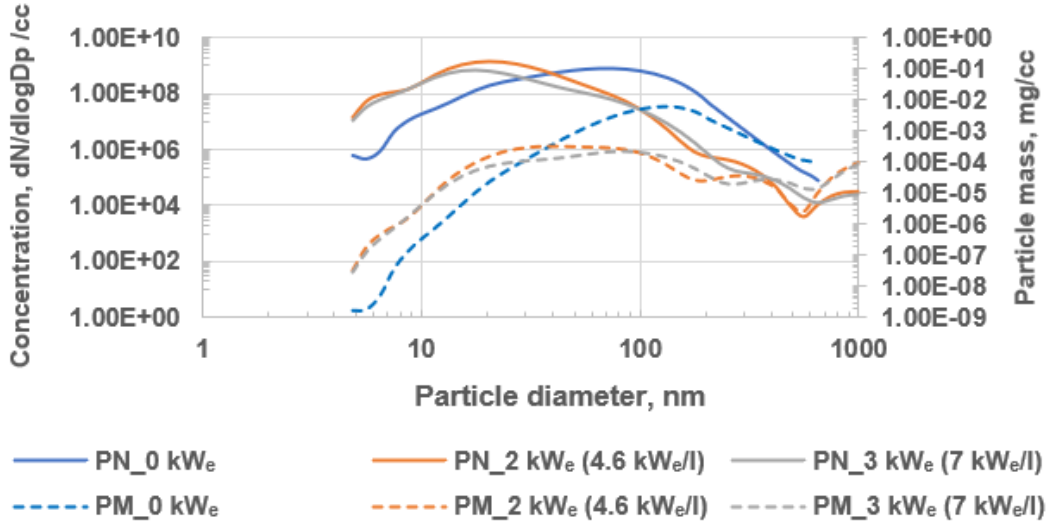

Figure 7.58 Comparison of the particulate emissions of the tested loads (DE15; log-log scale)

Figure 7.59 and 7.60 present the observed trends for the yield of Particulate Matter from the Gen-set. Figure 7.59 shows that the values of the yield of PM for the DE fuel blends were generally lower than those for pure diesel at the high load conditions. Rakopoulos et al. (2008) and Lapuerta et al. (2009) also reported that the PM emissions decreased below baseline diesel as the load on the engine was increased and as the concentration of ethanol increased from 5% to 15%.

(At ethanol concentration of 20%, the authors reported that particulate emissions began to rise above baseline diesel.)

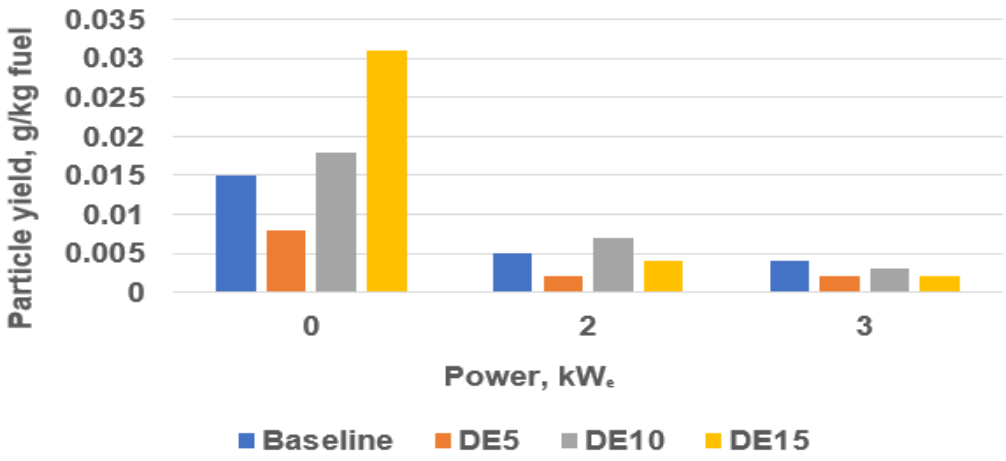

Figure 7.59 Graph of particulate yield for the tested blends (g/kg) against engine load (kW_e)

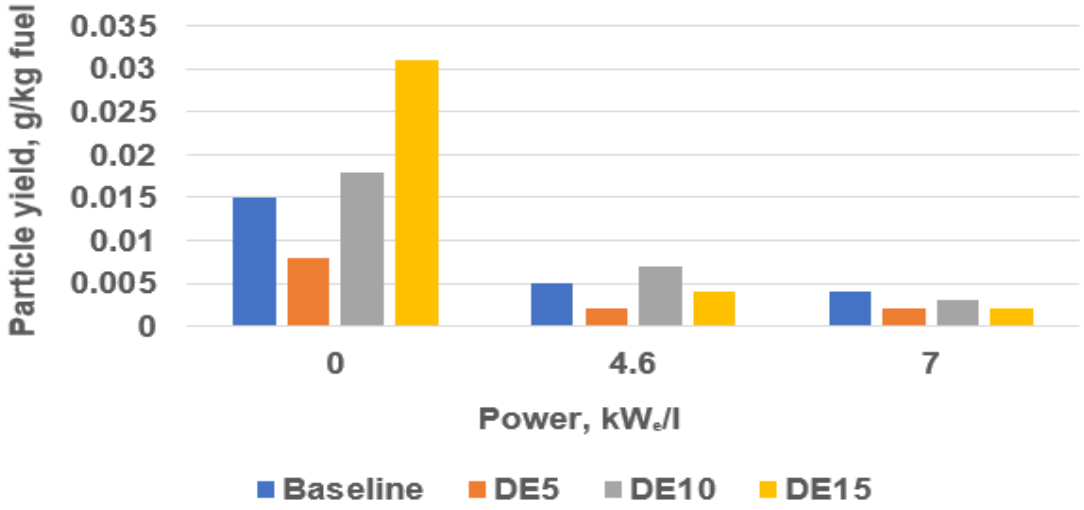

Figure 7.60 Graph of the particulate yield for the tested blends (g/kg) against engine load (kW_e/l)

The results for the PN emissions from the Gen-set (Figure 7.49) showed that the DE blends caused the peak PN to increase above diesel baseline. Therefore, the observed reduction in the levels of PM emissions below diesel baseline as the concentration of ethanol and the power of the engine increased confirms that ethanol-blended fuels reduce the diameter of the emitted particles as the load on

the engine increases. This favours the production of nucleation mode particles (nanoparticles). Nucleation mode particles are lighter than accumulation mode particles.

The PN emissions from the Gen-set ranged from $4.4 \times 10^6 – 8.9 \times 10^7$ /cc for the tested fuels and loads. The maximum PN concentration of 8.9×10^7 /cc occurred at Dp of 21 nm when the engine was run on DE15 at 2 kW_e load. The yield of particulates from the Gen-set for the tested fuels and loads ranged from $2.1 \times 10^{-3} – 3.1 \times 10^{-2}$ g/kg fuel.

7.6 BTE and combustion stability

Figures 7.61 and 7.62 present the BTE and the combustion stability of the Gen-set for the tested fuels. Figure 7.61 shows that the BTE of the engine generally decreased below the baseline as the concentration of ethanol increased in the blends. Rakopoulos et al. (2008) and Lapuerta et al. (2009), however, reported slight increase in the BTE above the baseline for DE fuel blends. The opposite trend to the trend that was reported by the authors was observed in the current work for the BTE when the engine was run on the DE blends. This was due to the increase in the ID as the concentration of ethanol increased in the blends while the fuel injection timing was constant (maintained at 13^o bTDC). There was insufficient time for the complete combustion of the injected fuel blends. Consequently, the levels of the unburned ethanol and THC increased above the baseline when the engine was run on the ethanol blended fuels. The degree of completion of the combustion decreased as the percentage of ethanol in the fuel blends increased. Therefore, the fuel energy was not fully utilised thereby leading to the observed decrease in the BTE below the baseline when the engine was run on the DE blends. Generally, the BTE values of the engine were lower than expected for all the fuels including pure diesel due to the poor atomisation of the

injected fuel, and the impingement of fuel on the wall of the cylinder. These conditions led to the incomplete combustion of the injected fuel mass.

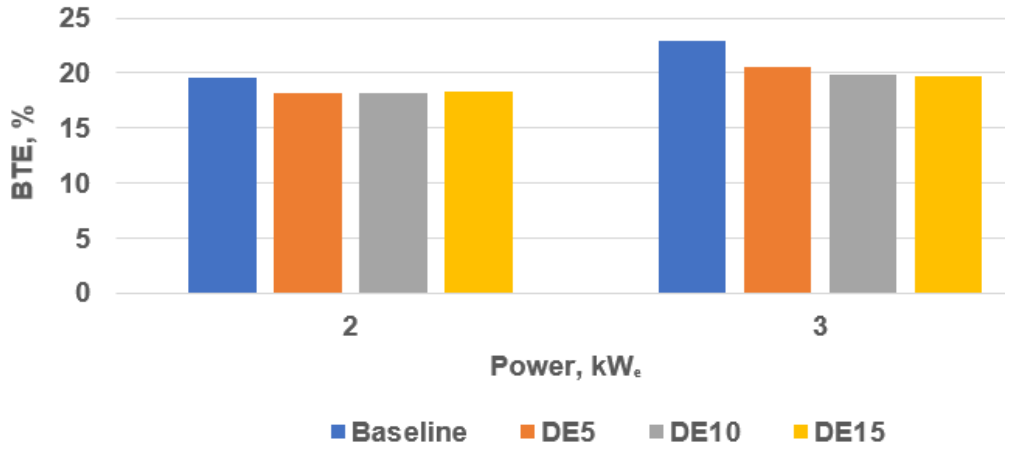

Figure 7.61 Graph of the Brake Thermal Efficiencies (BTE) of the tested fuel blends versus engine load (kW_e)

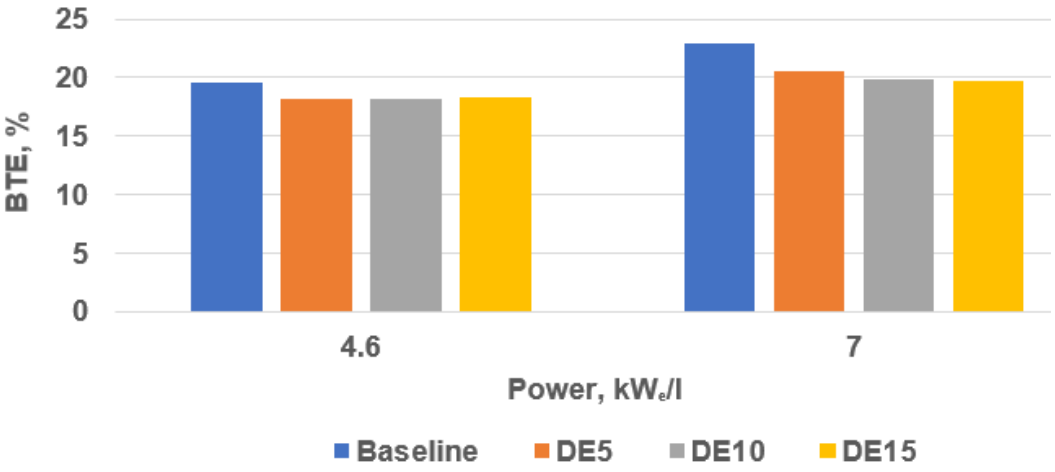

Figure 7.62 Graph of the Brake Thermal Efficiencies (BTE) of the tested fuel blends versus engine load (kW_e/l)

Figure 7.63 shows the stability of the combustion for the tested blends and loads. The figure shows that the engine was most stable on ULSD. However, for all the tested fuels, the stability of the combustion decreased as the load on the engine increased. Generally, the combustion of the fuel blends in the Gen-set was stable at all the tested loads as the combustion stability values were well below the benchmark.

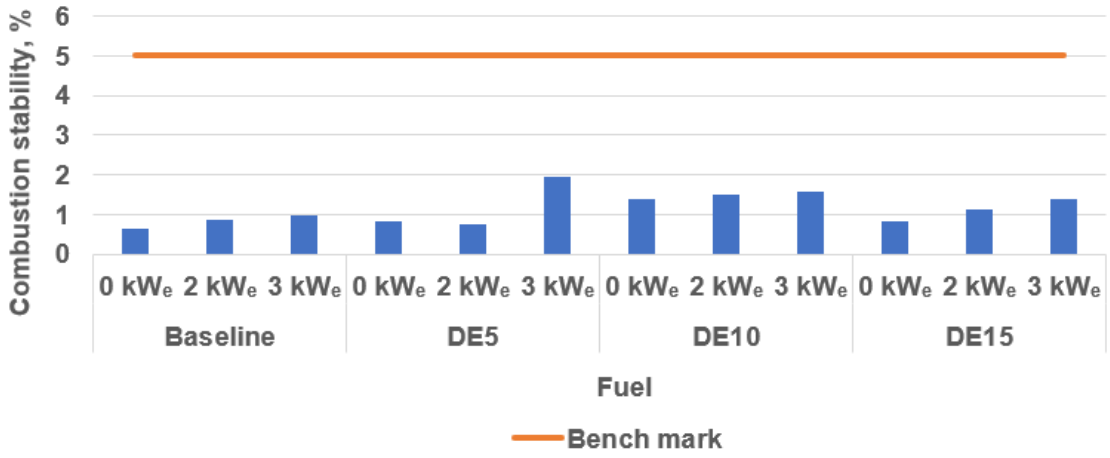

Figure 7.63 Combustion stability of the tested fuel blends by oxygen concentration

7.7 Achievable CO_2 savings from the use of ethanol-blended fuel in diesel engines

Bioethanol (green ethanol) is a renewable fuel. Therefore, splash-blending ethanol with fossil diesel replaces diesel energy to some extent depending on the blend concentration of ethanol. The substitution of fossil diesel with the biofuel (ethanol) in diesel engines leads to savings in CO_2 (reduction in CO_2 emissions). The effect of DE blends on CO_2 emissions from the Gen-set and the possible reduction in CO_2 emissions that is obtainable by substituting 15% by volume of fossil diesel with ethanol are presented in this section.

7.7.1 Effect of ethanol-blended fuels on engine-out CO_2

Figure 7.64 presents the CO_2 emission levels for the tested DE blends in g/kWh. Generally, at each of the tested conditions of load, the CO_2 emissions increased above baseline diesel as the concentration of ethanol increased in the DE blends. The observed increase in the emission of CO_2 above the baseline was because the fuel consumption and the BSFC of the engine increased as the concentration of ethanol increased in the DE blends (Figures 7.1 and 7.3). By implication, more mass of DE fuel blend was burned than the mass of pure diesel to attain the same

power. As such, the engine-out CO_2 increased as the concentration of ethanol increased in the injected fuel. Figure 7.64 also shows that as the load of the engine increased above the medium load (2 kW_e), the CO_2 emission levels decreased for all the tested fuels. This was because the BSFC of the engine improved as the load on the engine was increased (Figures 7.3). The observed improvement in the BSFC at the relatively high loads was due to the drastic increase in the flame temperature that occurred as the load on the engine was increased. The vaporisation and combustion of the injected fuel and the BTE of the engine were enhanced at the relatively high flame temperatures (Figures 7.7 and 7.61).

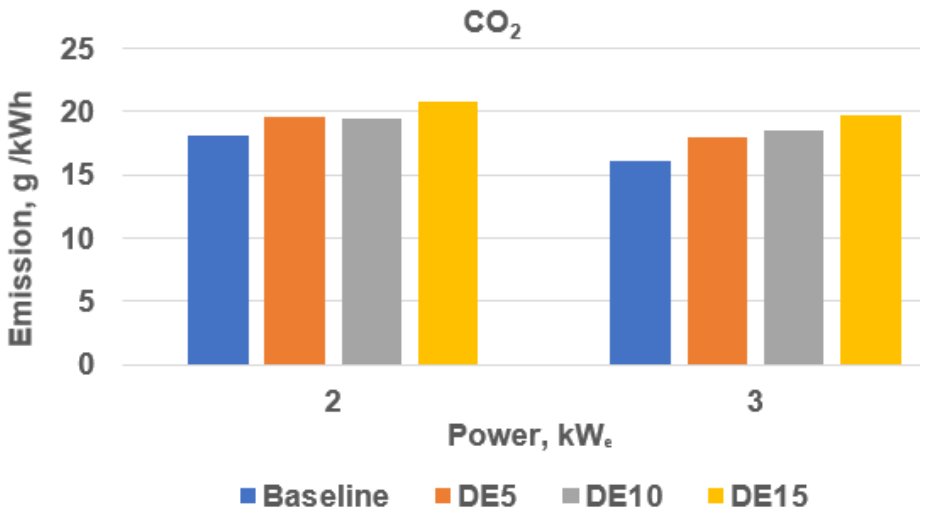

Figure 7.64 Graph of CO_2 emissions (g/kWh) against engine load (kW_e)

7.7.2 Estimation of possible CO_2 savings from the utilisation of diesel-ethanol blend in diesel engines

The current work confirms that diesel-ethanol fuel blends containing up to 15% of (anhydrous) green ethanol can be utilised in diesel engines. 15% by volume of green ethanol in diesel (DE15) is equivalent to an ethanol substitution of diesel of 9% by energy. This implies that, if 15% by volume of diesel is replaced with

green ethanol in diesel engines, CO_2 emissions from the engines will reduce by 9%. Table 7.4 summarises the analysis that was carried out to determine the equivalent potential reduction in CO_2 emissions in million tonnes per year (based on the consumption of diesel for transport in the UK in 2020 and the consumption of diesel in Nigeria in 2019). The efficiency of the combustion of the ethanol fraction of the DE blend was assumed equal to that of pure diesel. Ethanol was also assumed to be a zero-carbon fuel.

Table 7.4 Potential reduction in CO_2 emissions from the substitution of diesel with 15% by volume of green ethanol

S/n	Item	Calculation	Value
1	Energy density of diesel, MJ/litre	-	36
2	Energy density of ethanol, MJ/litre	-	21.4
3	Green ethanol substitution of diesel by volume, %	-	15
4	Green ethanol substitution of diesel by energy, %	15 x 21.4/36	9
5	Consumption of diesel by transport in the UK in 2020 (DUKES, 2021), million tonnes	-	19.69
6	Consumption of diesel in Nigeria in 2019 (NNPC, 2019), million tonnes	-	0.19
7	CO_2 emission per kg of diesel combusted (FR, 2021), kg CO_2/kg diesel	-	3.1
8	Transport CO_2 emissions from diesel in the UK, million tonnes	19.69 x 3.1	61.05
9	CO_2 emissions from the combustion of diesel in Nigeria, million tonnes	0.19 x 3.1	0.58

10	Reduction in transport CO_2 emissions for 9% substitution of diesel by energy (UK), million tonnes	9 x 61.5/100	~5.5
11	Reduction in CO_2 emissions for 9% substitution of diesel by energy (Nigeria), million tonnes	9 x 0.58/100	~0.05

Table 7.4 shows that 15% by volume substitution of diesel with green ethanol in transport vehicles in the UK will reduce transport CO_2 emissions by ~5.5 million tonnes while the same percentage substitution of diesel in Nigeria will reduce CO_2 emissions in the country by ~0.05 million tonnes. The consumption of diesel and the associated CO_2 savings in Nigeria are relatively low compared to the UK because in Nigeria fossil diesel is only utilised in trucks (for transportation) and in diesel Gen-sets (for power generation).

7.8 Heat Release Rate (HRR) results for diesel-ethanol (DE) fuel blends

HRR analysis was carried out on the diesel Gen-set engine to investigate the effect of ethanol-blended fuels on the HRR of the engine. The Leeds HRR model was validated for the Gen-set and the DE fuels blends by comparing the predicted fuel consumption to the measured fuel consumption for each of the tested fuels (pure diesel (DE0), DE5, DE10, and DE15) at the tested conditions of load (idle, 2 kW_e, and 3 kW_e). This section also presents the combustion phasing for the fuel blends at the tested conditions.

7.8.1 Estimated instantaneous cylinder volume

The instantaneous volume of the cylinder of the Gen-set engine was estimated from the standard function for calculating the volume of the cylinder as a function of the crank angle (Rajkumar, 2002). Figure 7.65 presents the estimated

instantaneous volume of the cylinder of the Gen-set. The volumes of the cylinder of the Gen-set at the BDC and the TDC were 459 cm^3 and 22.9 cm^3 respectively as shown in the figure.

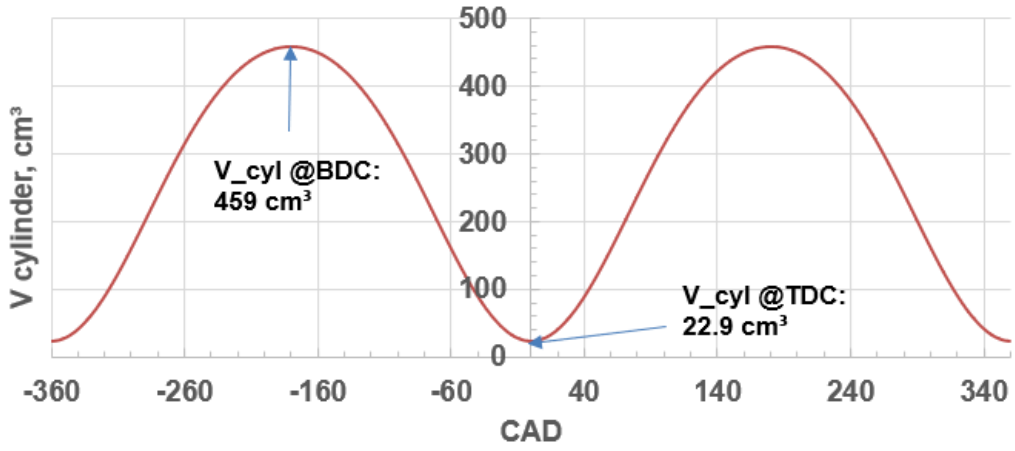

Figure 7.65 Instantaneous volume of the cylinder of the Gen-set

7.8.2 Gen-set pressure-crank angle data as model input

The pressure traces of the Gen-set were utilised to model the Heat Release Rate (HRR) of the engine at the tested loads. The input data were plotted and presented as shown in Figures 7.66 to 7.68 for the tested fuel blends and engine loads. Figures 7.66 to 7.68 show that, at each of the tested conditions of power, the Peak Pressure (PP) decreased below the baseline as the concentration of ethanol increased in the DE blends. This confirmed the potential of ethanol-blended fuels to reduce the Peak Pressure in ICEs. As the load on the engine was increased from idle to 3 kW_e, the PP increased for all the tested fuels.

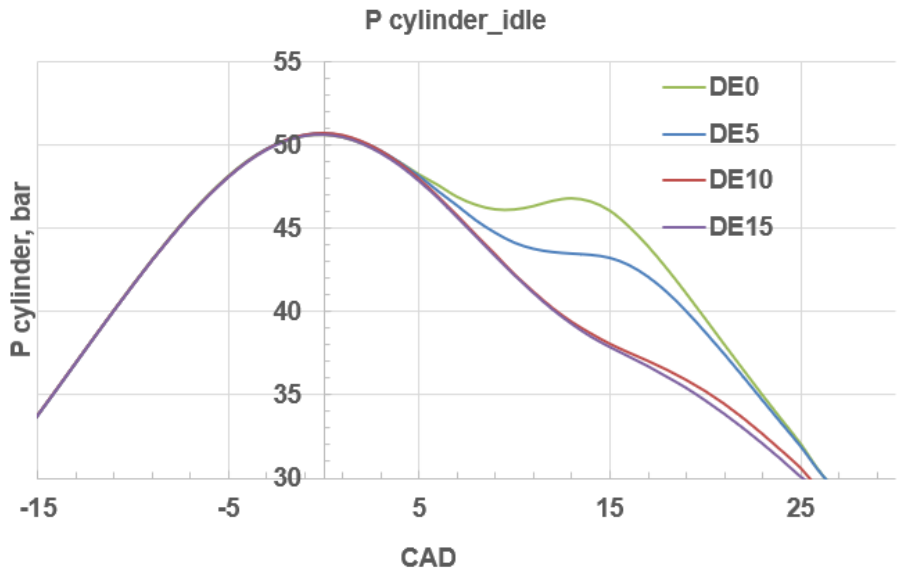

Figure 7.66 Pressure traces for DE0, DE5, DE10, and DE15 at idle

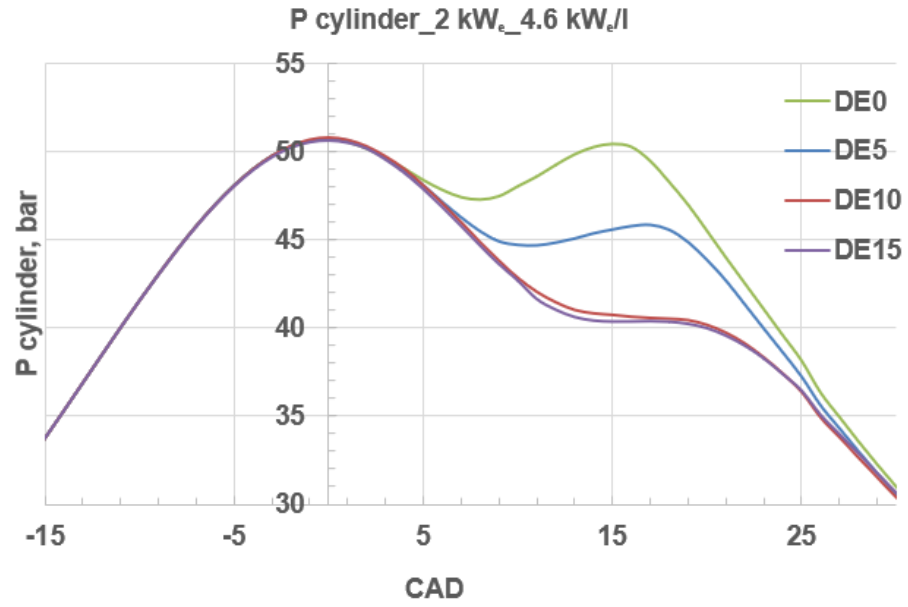

Figure 7.67 Pressure traces for DE0, DE5, DE10, and DE15 at 2 kW_e (4.6 kW_e/l)

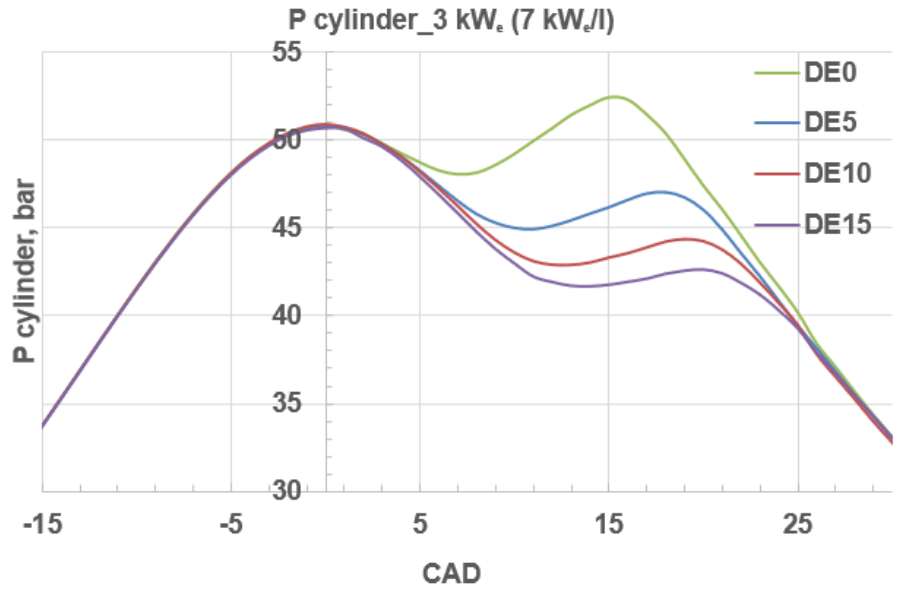

Figure 7.68 Pressure traces for DE0, DE5, DE10, and DE15 at 3 kW_e (7 kW_e/l)

Figures 7.69 and 7.70 present the values of the PP for the tested conditions and fuels.

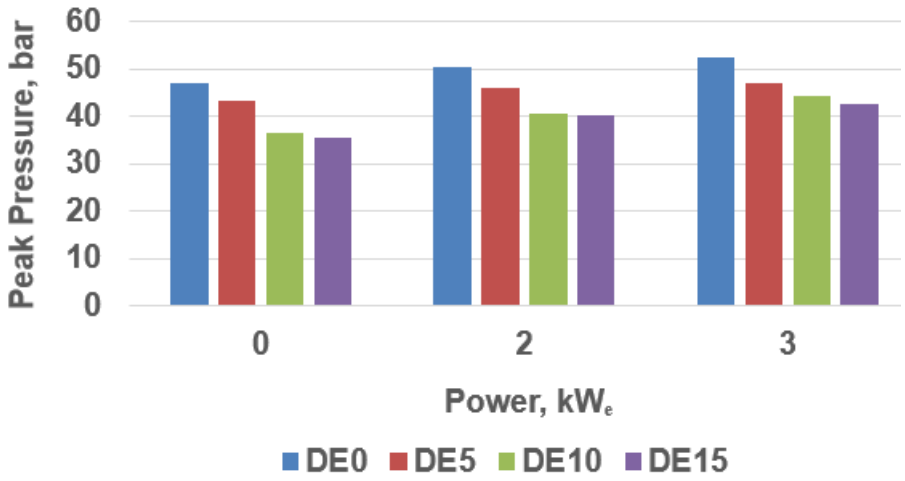

Figure 7.69 Graph of Peak Pressures (PP) versus power (kW_e)

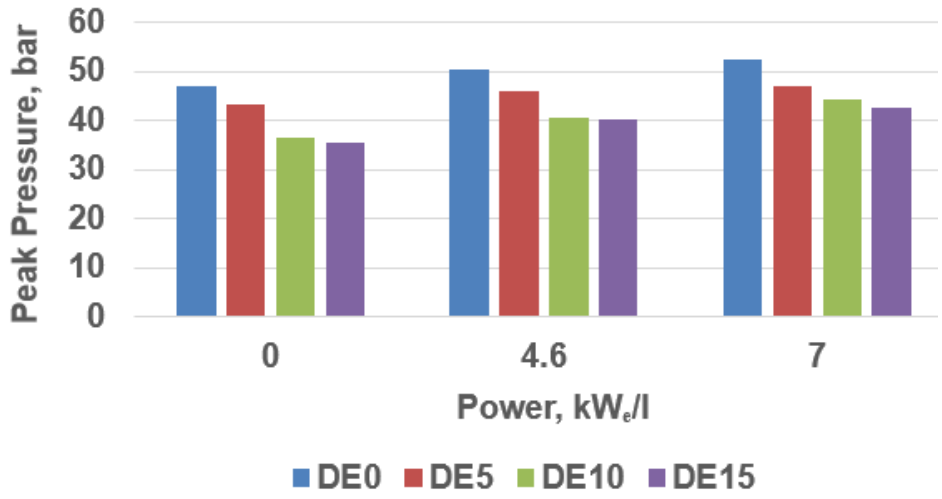

Figure 7.70 Graph of Peak Pressures (PP) versus power (kW$_e$/l)

7.8.3 Calculated in-cylinder temperatures for the Gen-set

Figures 7.71 to 7.73 depict the instantaneous cylinder temperatures that were calculated from the measured in-cylinder pressures and utilised in the HRR analysis.

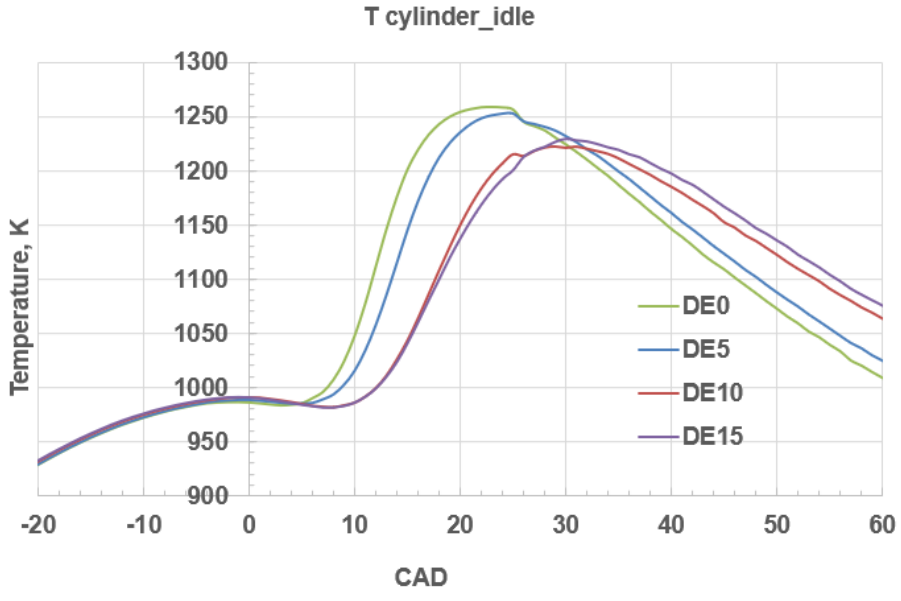

Figure 7.71 Calculated in-cylinder temperatures as a function of crank angle at idle

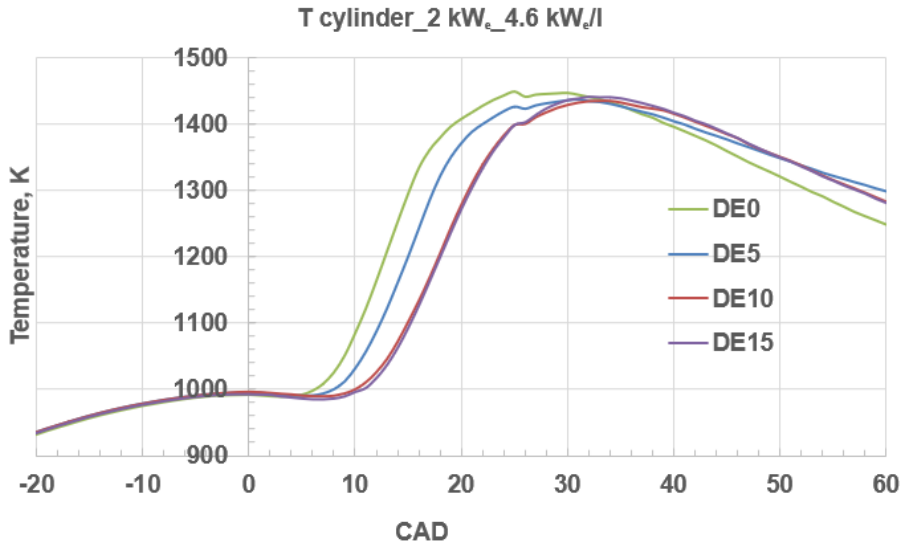

Figure 7.72 Calculated in-cylinder temperatures as a function of crank angle at 2 kW$_e$ (4.6 kW$_e$/l)

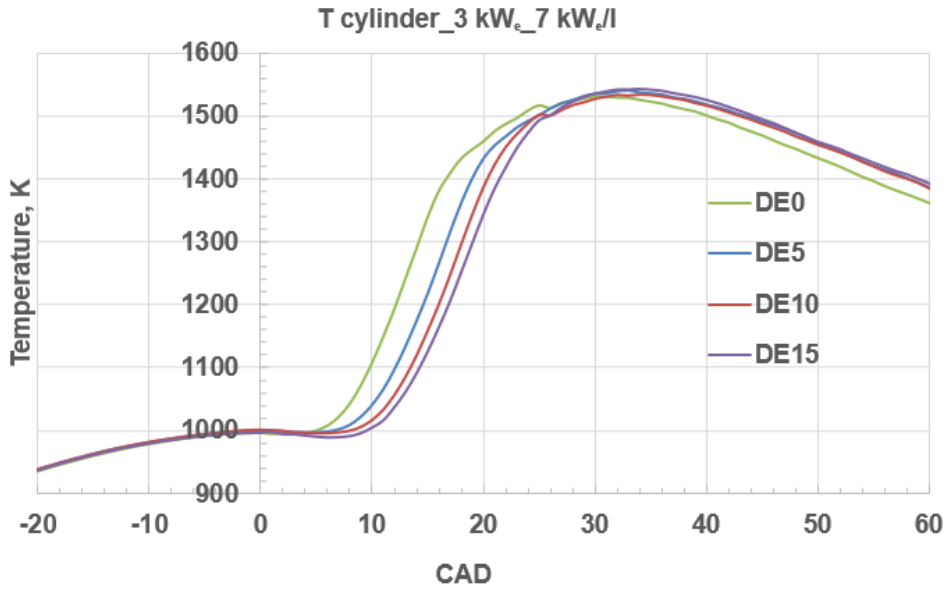

Figure 7.73 Calculated in-cylinder temperatures as a function of crank angle at 3 kW$_e$ (7 kW$_e$/l)

Figures 7.71 to 7.73 show that, for all the tested loads, the temperature gradient after the SoC was greatest for pure diesel. As the concentration of ethanol increased in the blends, the rate of rise in cylinder temperature during the rapid combustion stage decreased (the rate of combustion decreased below the baseline as the concentration of ethanol in the blends increased). This was due

to the increase in the ID of the DE blends above the baseline as the concentration of ethanol increased in the blends (coupled with the relatively low CN of the DE fuel blends).

Figures 7.71 to 7.73 also show that, at idle, the peak temperature decreased drastically below diesel baseline for DE10 and DE15. The observed decrease in the peak temperature below the baseline at the idle condition was due to the relatively low combustion temperature which did not favour the vaporisation and combustion of ethanol in the fuel blends. The low combustion temperature at the idle condition did not enhance the release of heat from the injected DE fuel blends. Therefore, the Peak Temperatures (PT) were relatively low for the DE fuel blends compared to pure diesel. However, as the load on the Gen-set engine was increased, the peak cylinder temperatures for the DE fuel blends approached the baseline (the peak temperatures of the blends became approximately equal to that of pure diesel at the highest power condition). This was due to the observed drastic increase in the combustion temperature when the load on the engine was increased. The increase in the combustion temperature at the higher conditions of power enhanced the vaporisation of ethanol in the DE blends, the release of heat from the injected DE blends, and ultimately the thermal efficiency of the engine. This also confirms the observed decrease in the engine-out ethanol emission (Figure 7.26).

7.8.4 Comparison of the modified γ functions and γ functions from literature for diesel-ethanol (DE) blend fuels

The values of γ estimated from various γ functions were plotted, as depicted in Figures 7.74 and 7.75, against the temperature of the gases in the cylinder for DE10 and DE15 at idle and 3 kW_e conditions respectively. The values of γ estimated from the equations that express γ (T) were compared to the values of

γ that were evaluated from the modified gamma function, γ_{mod} in Figures 7.74 and 7.75. Gamma1 to Gamma4 represent the gamma values predicted by the four equations that express γ (T) (Equations 3.29 to 3.32). Figures 7.74 and 7.75 show that the estimated values of γ from γ_{mod} at all temperature points were much higher than the estimates from the other functions which express γ as a function of temperature only. The same trend was observed for the other DE blends and power conditions. The same trend was also observed for standard diesel and the alternative diesels (Sections 6.4.4 and 6.5.4). Therefore, it was concluded that λ had a significant effect on γ when biofuel blends (DE fuel blends) were used in the diesel Gen-set.

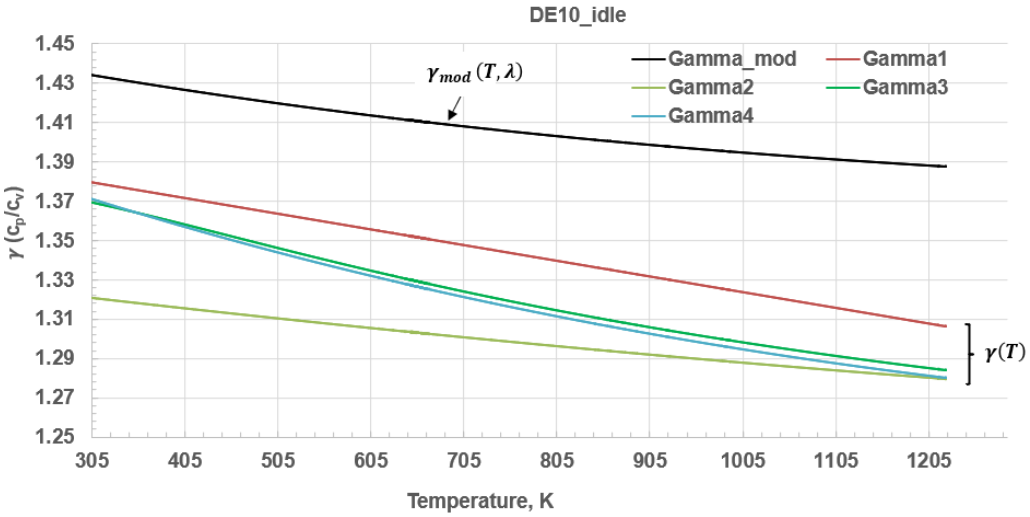

Figure 7.74 Comparison of modified gamma and gamma functions from literature for DE10 at idle

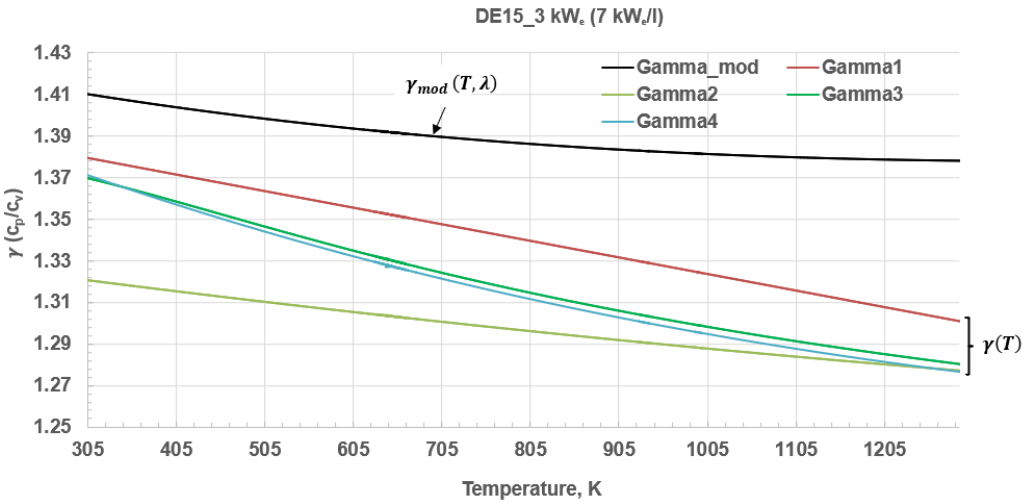

Figure 7.75 Comparison of modified gamma and gamma functions from literature for DE15 at 3 kW_e (7 kW_e/l)

7.8.5 Effect of λ on γ for diesel-ethanol blends

Figure 7.76 depict the dependence of γ on temperature and the excess air ratio, λ for the selected DE blends and power conditions. The values of γ in Figure 7.76 were estimated from γ_{mod}. At temperatures below 1,200 K, γ decreased as the temperature increased as was the case when the 96 kW IVECO diesel engine was run on off-road diesel (Chapter 6, Figure 6.71). Generally, it was observed that γ increased as the excess air ratio of the engine increased for the DE blends depicted in the figure. Figure 7.76 clearly shows that γ increased as the combustion became leaner (as λ increased in the depicted narrow range from 1.26 to 1.86).

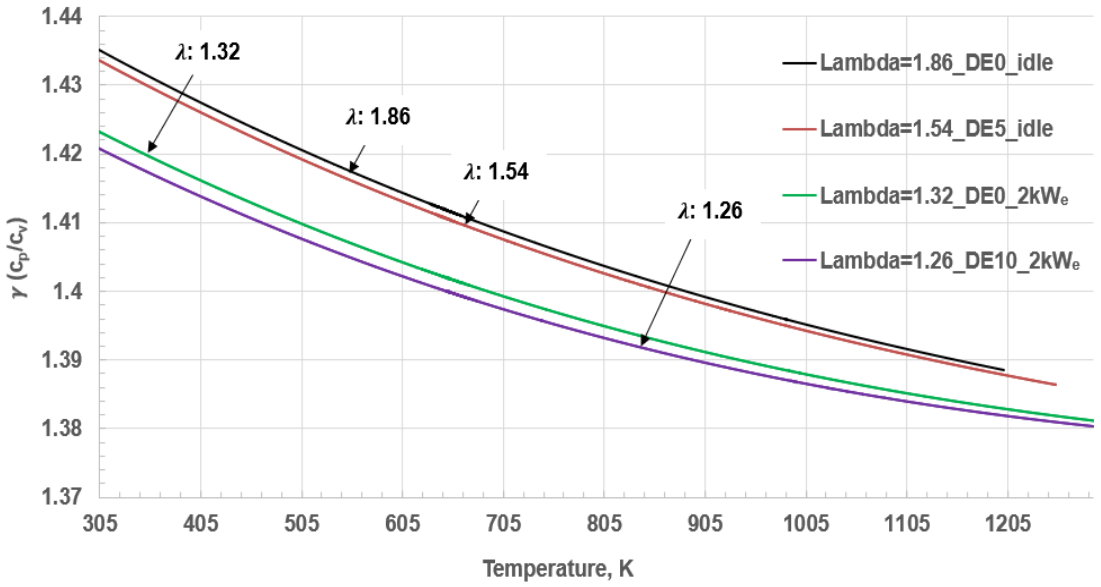

Figure 7.76 Variation of γ with λ and temperature as predicted by γ_{mod} for DE fuel blends

7.8.6 Sensitivity of diesel engine HRR model to γ functions for diesel-ethanol fuel blends – comparison of Leeds model to others

Figures 7.77 to 7.88 present the HRR profiles for the investigated γ and HRR models. Figures 7.77 to 7.79 show the profiles for ULSD (DE0), while Figures 7.80 to 7.82, Figures 7.83 to 7.85, and Figures 7.86 to 7.88 show the HRR profiles for DE5, DE10, and DE15 respectively. The figures vividly depict the sensitivity of the HRR model of the engine to γ functions as the five HRR models predicted different PHRR values. The Leeds HRR model predicted the lowest PHRR for all the fuel blends and power conditions that were tested. Figures 7.74 and 7.75 show that $\gamma(T,\lambda)$ gave estimates of γ that were higher than the estimates from the functions that express $\gamma(T)$. However, Figures 7.77 to 7.88 show that, for both pure diesel and the DE blend fuels, the HRR model that utilised $\gamma(T,\lambda)$ predicted lower PHRR values for the diesel Gen-set engine than the HRR models that utilised $\gamma(T)$. Though the five HRR models showed the same trend, they predicted

different PHRR for the fuel blends and the engine loads which were investigated (just as in the case of the MFIS IVECO engine and the alternative fuels). This necessitated the validation of the Leeds HRR model for the diesel Gen-set and diesel-ethanol (DE) blends by comparing the fuel consumption of the engine predicted by the HRR models to the measured fuel consumption.

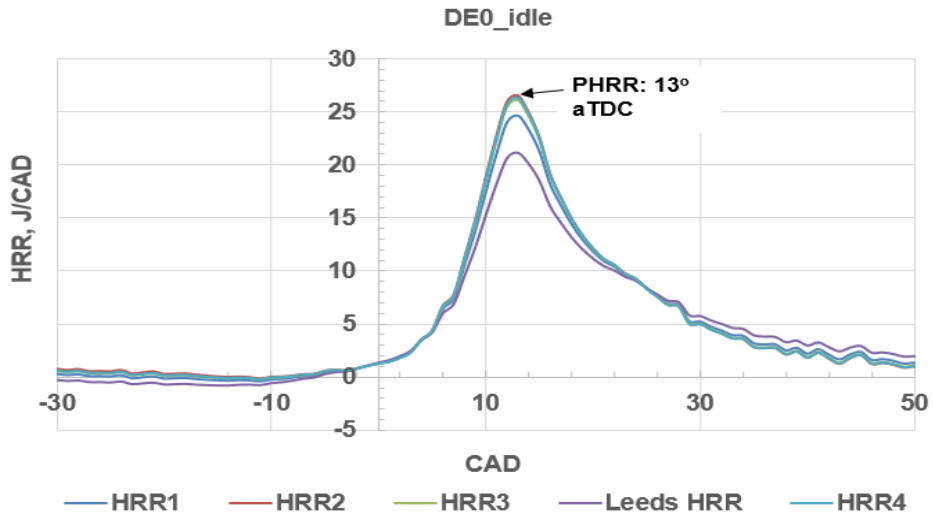

Figure 7.77 Diesel-ethanol fuel blends HRR profiles from the Leeds model and other models: DE0 at idle

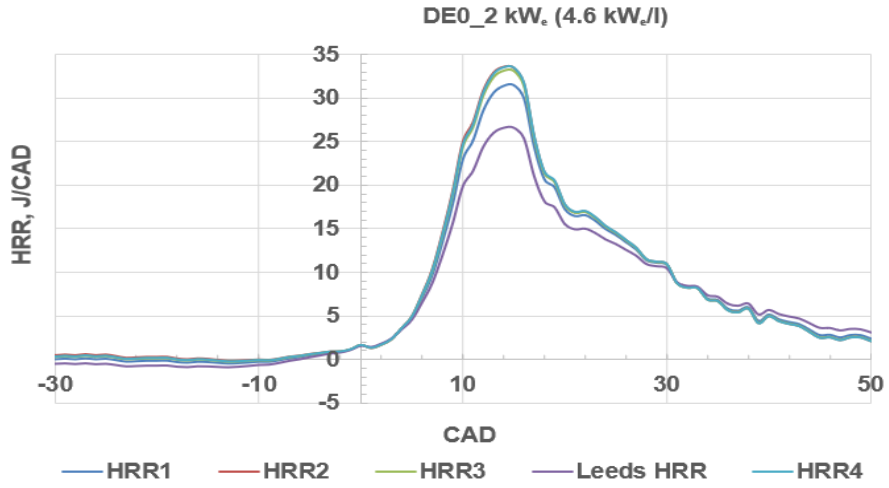

Figure 7.78 Diesel-ethanol fuel blends HRR profiles from the Leeds model and other models: DE0 at 2 kW_e (4.6 kW_e/l)

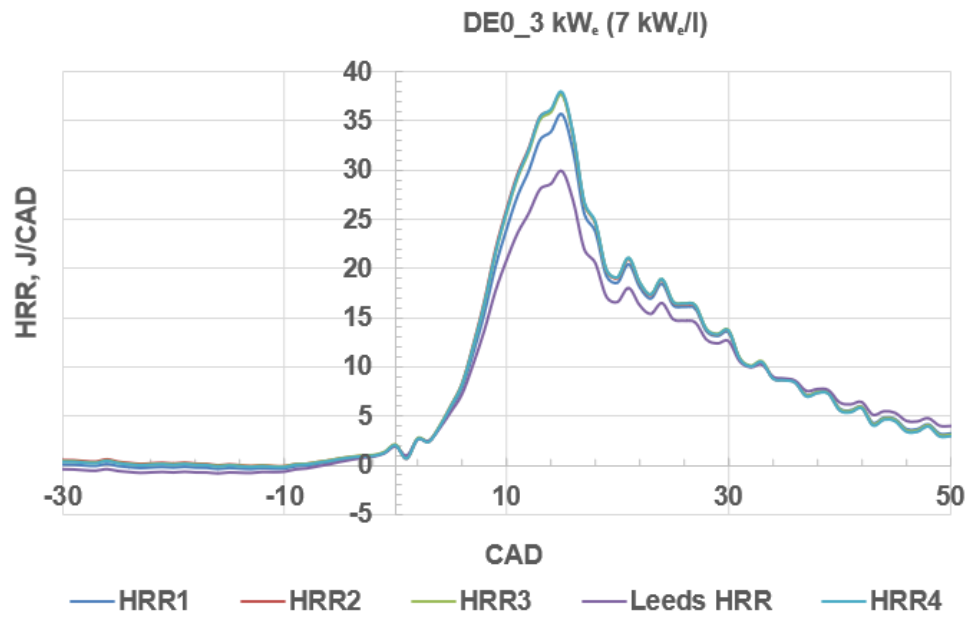

Figure 7.79 Diesel-ethanol fuel blends HRR profiles from the Leeds model and other models: DE0 at 3 kW$_e$ (7 kW$_e$/l)

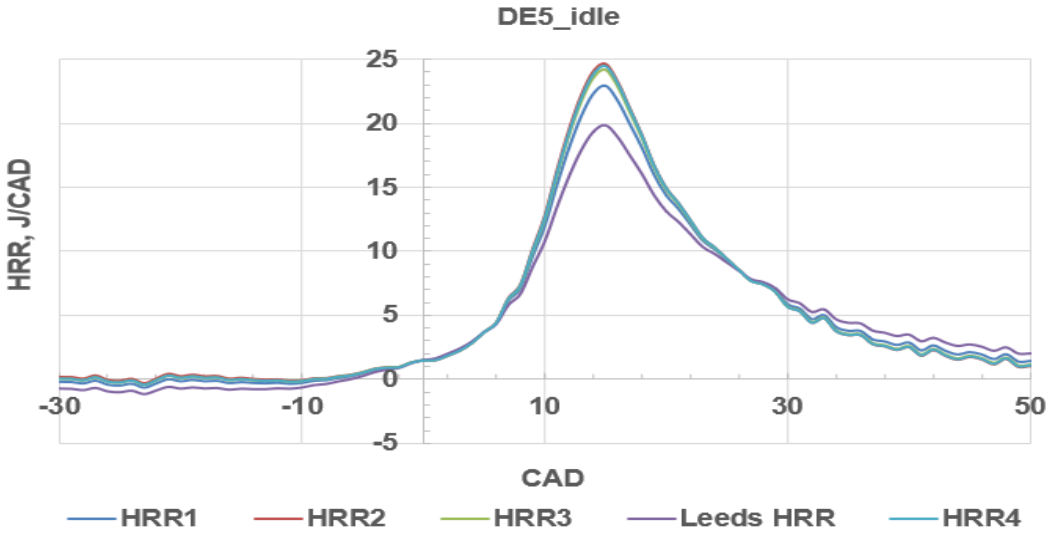

Figure 7.80 Diesel-ethanol fuel blends HRR profiles from the Leeds model and other models: DE5 at idle

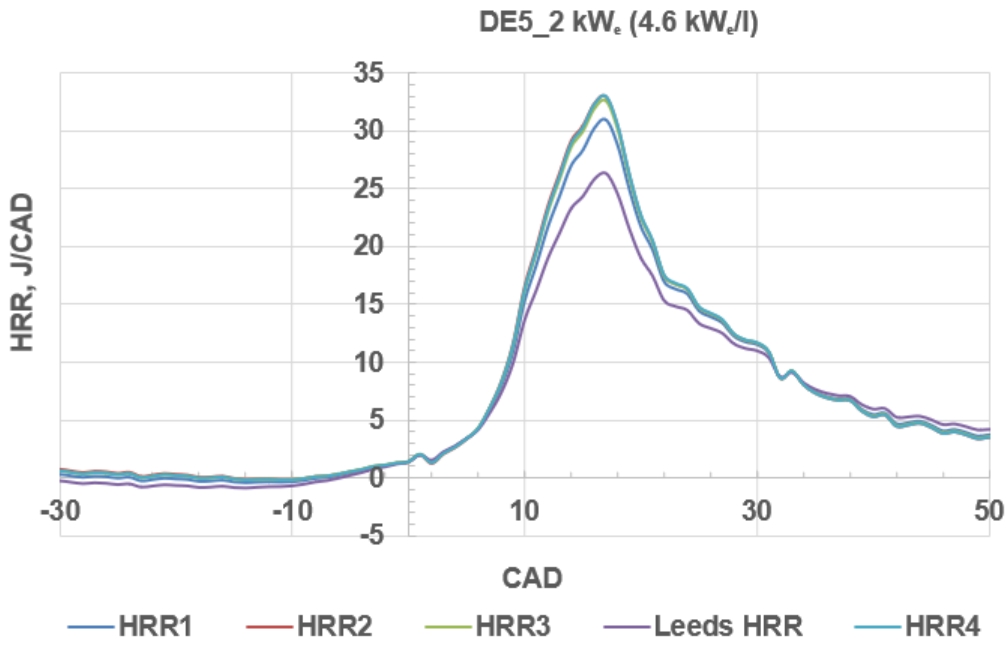

Figure 7.81 Diesel-ethanol fuel blends HRR profiles from the Leeds model and other models: DE5 at 2 kW_e (4.6 kW_e/l)

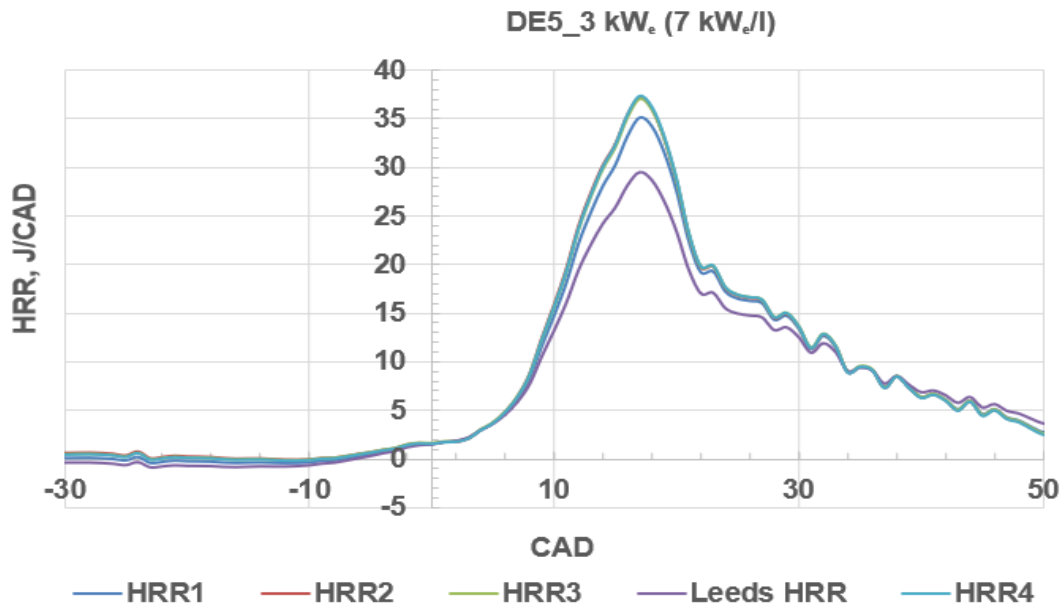

Figure 7.82 Diesel-ethanol fuel blends HRR profiles from the Leeds model and other models: DE5 at 3 kW_e (7 kW_e/l)

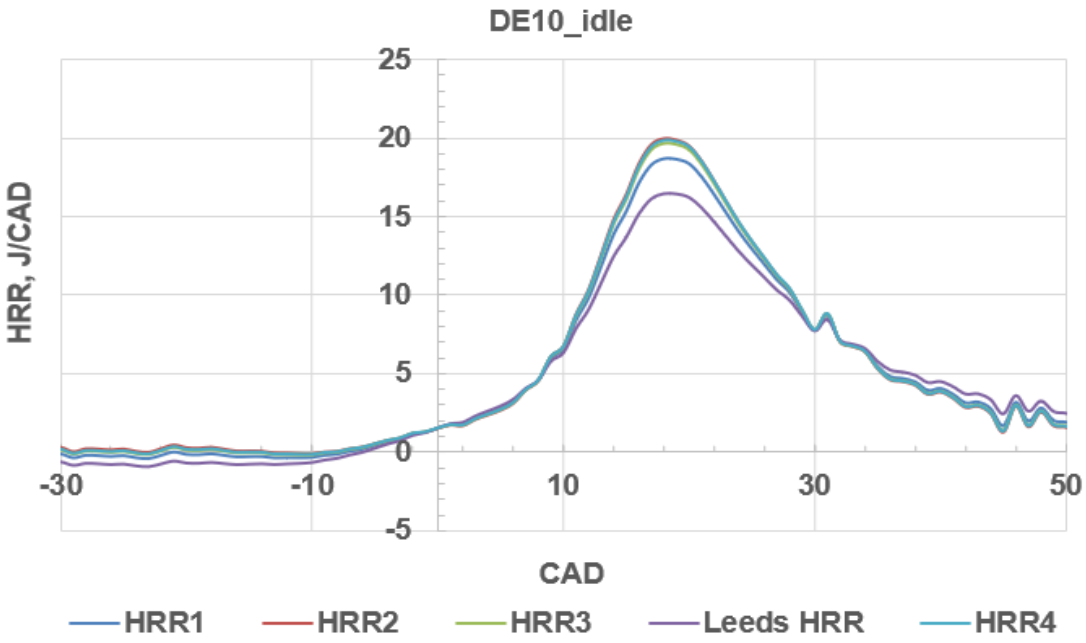

Figure 7.83 Diesel-ethanol fuel blends HRR profiles from Leeds model and other models: DE10 at idle

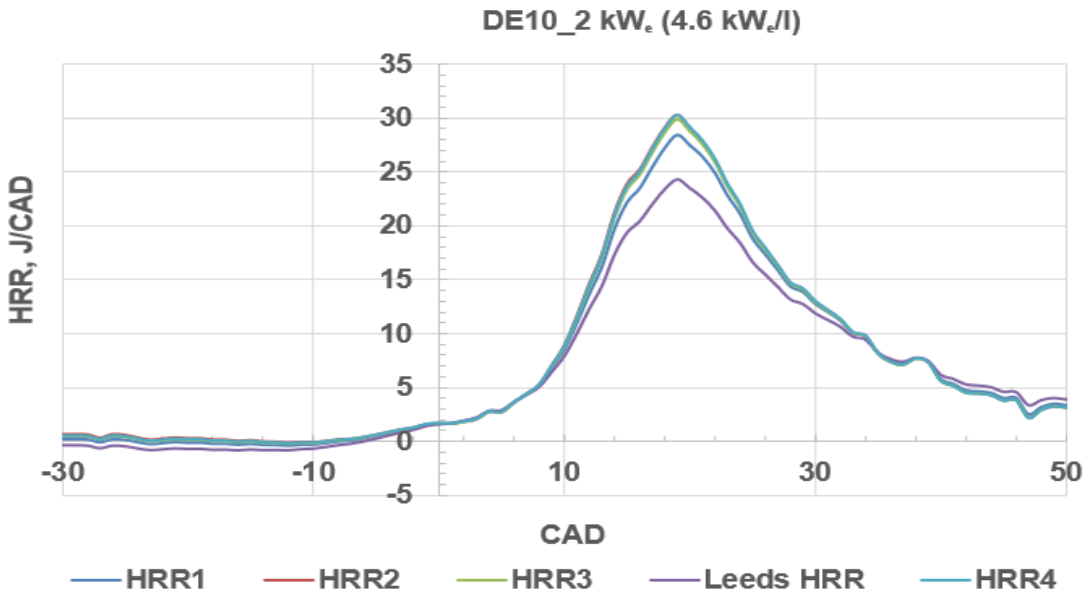

Figure 7.84 Diesel-ethanol fuel blends HRR profiles from Leeds model and other models: DE10 at 2 kW_e (4.6 kW_e/l)

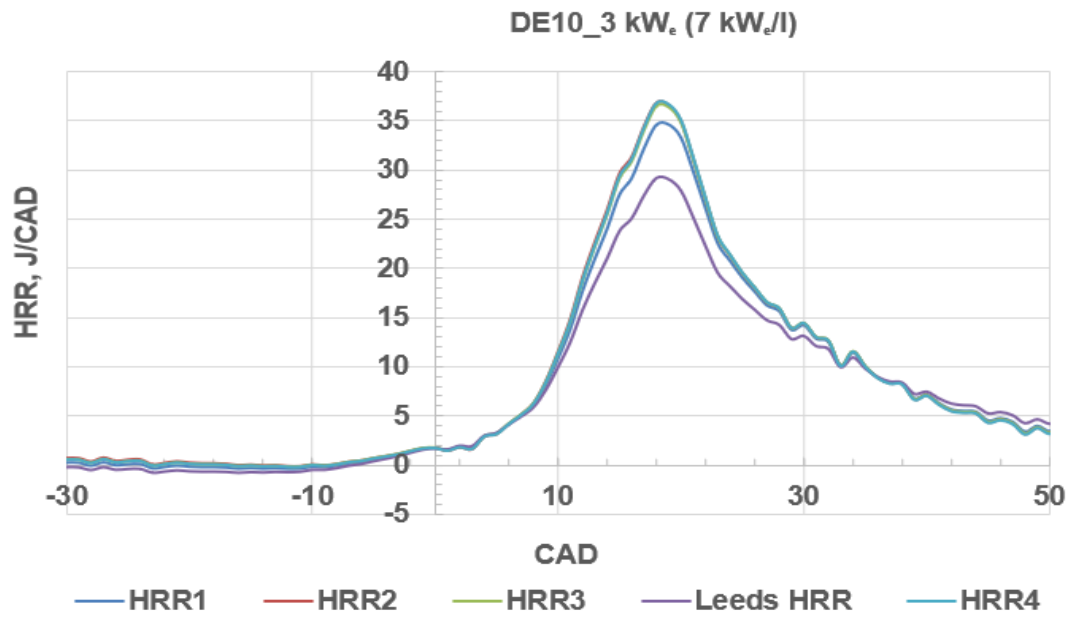

Figure 7.85 Diesel-ethanol fuel blends HRR profiles from the Leeds model and other models: DE10 at 3 kW$_e$ (7 kW$_e$/l)

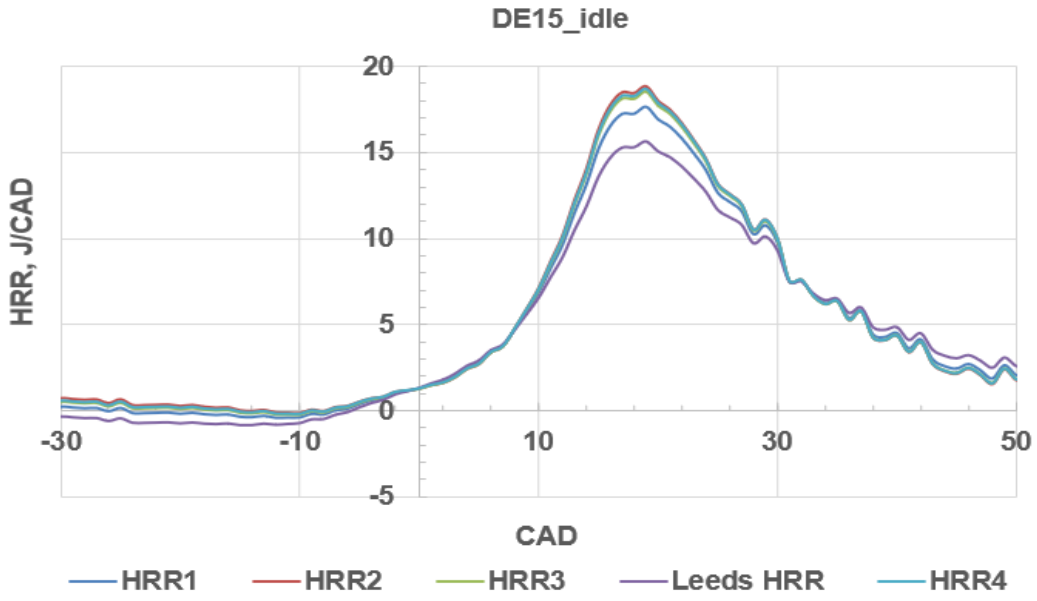

Figure 7.86 Diesel-ethanol fuel blends HRR profiles from the Leeds model and other models: DE15 at idle

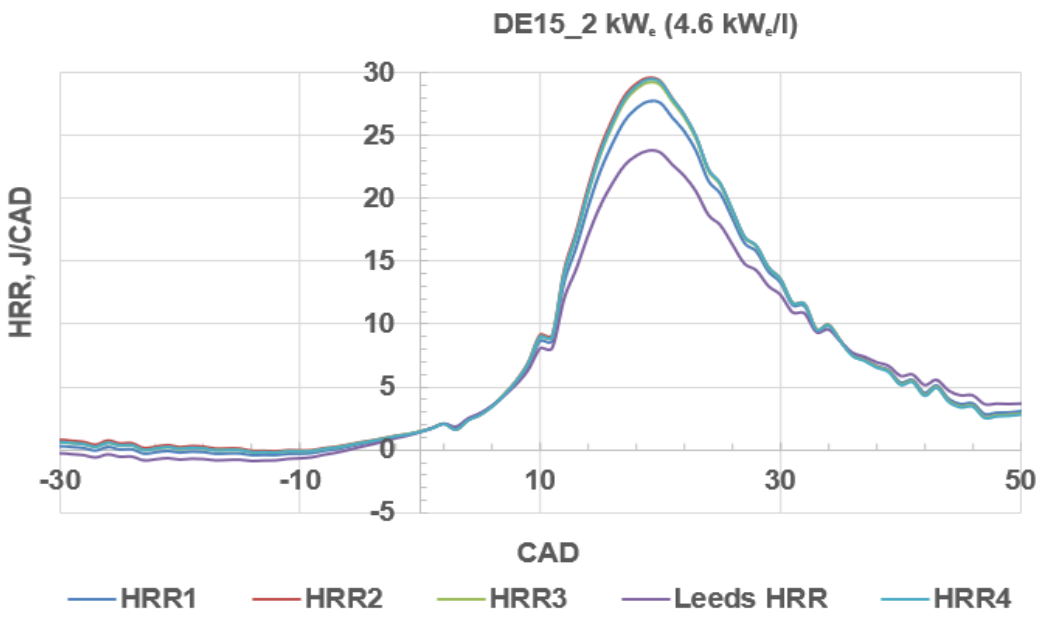

Figure 7.87 Diesel-ethanol fuel blends HRR profiles from the Leeds model and other models: DE15 at 2 kW$_e$ (4.6 kW$_e$/l)

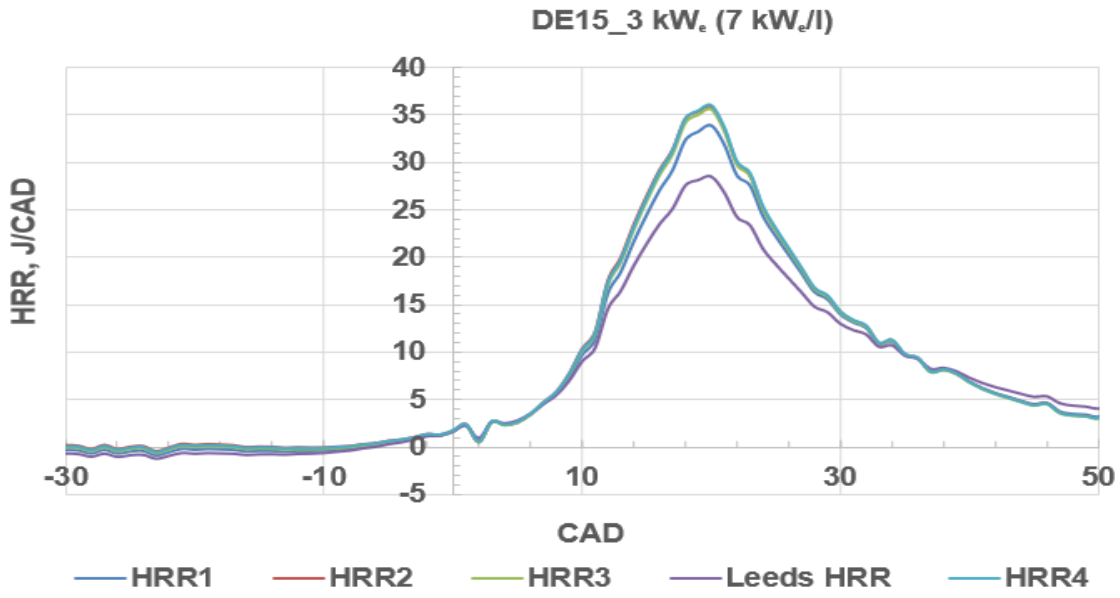

Figure 7.88 Diesel-ethanol fuel blends HRR profiles from Leeds model and other models: DE15 at 3 kW$_e$ (7 kW$_e$/l)

Multiple peaks were observed in the HRR profiles of the IVECO engine due to the Multiple Fuel Injection Strategy (MFIS) of the engine (Chapter 6). However, only single peaks were observed in the HRR profiles of the diesel Gen-set engine because the injection of fuel in the Gen-set engine occurred at a single crank

angle per power stroke (Single Fuel Injection Strategy (SFIS)) as shown in Figures 7.77 to 7.88. The crank angle timing of the PHRR of the engine for each of the tested fuel blends and loads was determined directly from the HRR profile. As depicted in Figure 7.77, the PHRR for DE0 at idle occurred at 13^{o} aTDC.

7.8.7 Validation of the Leeds HRR model

The Cumulative Heat Release (CHR) profiles shown in Figures 7.89 to 7.91 (strictly for the heat that was released as a result of the combustion of the injected fuel mass) were determined from the HRR profiles. The fuel consumption of the single-cylinder diesel Gen-set engine per thermodynamic cycle for each of the tested fuels and load was predicted from the HRR and CHR profiles. Figures 7.89 to 7.91 show the heat that was released from the combustion of the injected fuel mass in the cylinder of the engine per power stroke (in joules) as a function of the crank angle for each of the tested loads and fuels.

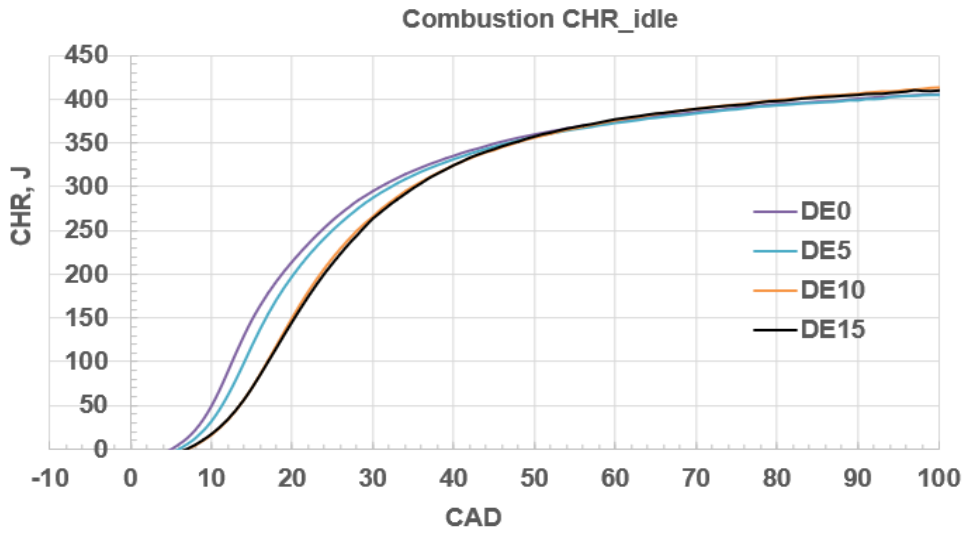

Figure 7.89 Cumulative Heat Release profiles for the tested fuel blends (idle)

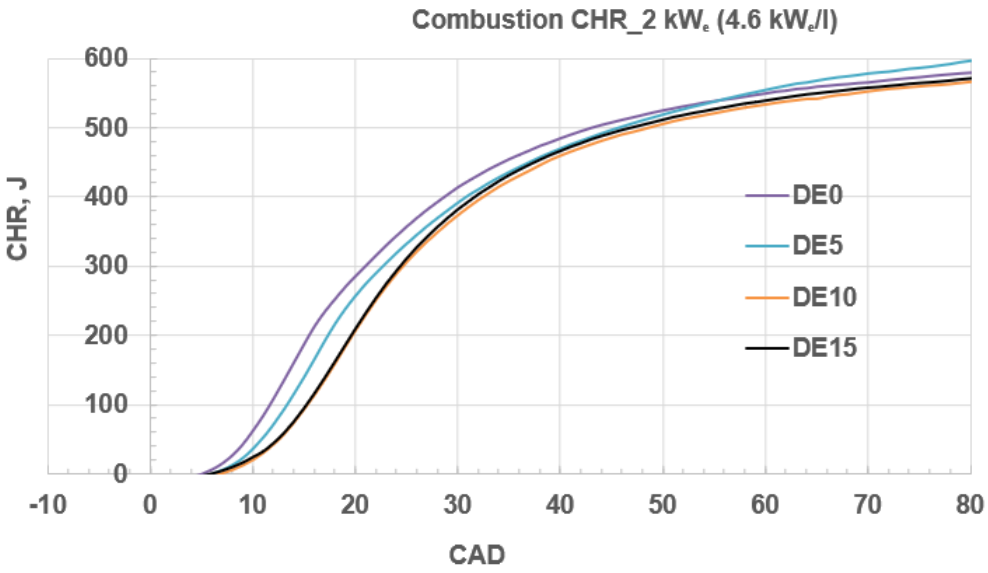

Figure 7.90 Cumulative Heat Release profiles for the tested fuel blends: 2 kW$_e$ (4.6 kW$_e$/l)

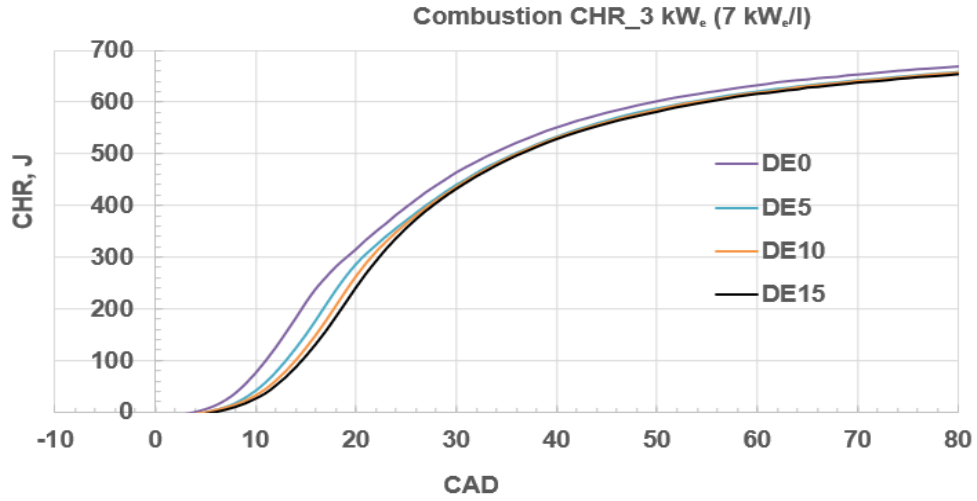

Figure 7.91 Cumulative Heat Release profiles for the tested fuel blends: 3 kW$_e$ (7 kW$_e$/l)

Figures 7.92 and 7.93 show the result of the validation of the Leeds HRR model for the diesel Gen-set and the investigated fuel blends. The predicted fuel energy input values were estimated from the CHR profiles (Figures 7.89 to 7.91). Figure 7.92 depicts the comparison between the fuel energy input (in J/thermodynamic cycle) predicted by the Leeds HRR model and the HRR models that were based

on $\gamma(T)$ and the measured fuel energy input. The predicted fuel masses were estimated from the predicted fuel energy input values by dividing the energy input by the corresponding Cv of the fuel blend. Figure 7.93 compares the injected fuel mass (in mg/thermodynamic cycle) predicted by the Leeds HRR model and the HRR models that were based on $\gamma(T)$ to the measured fuel mass. Figures 7.92 and 7.93 show that the fuel masses and the energy input predicted by the Leeds model (the red bars with black borderline) were the most accurate for all the investigated fuel blends and power conditions. The analyses which were carried out to compare the predicted fuel energy input and fuel masses to the measured fuel energy input and masses are summarised in Tables 7.5 and 7.6.

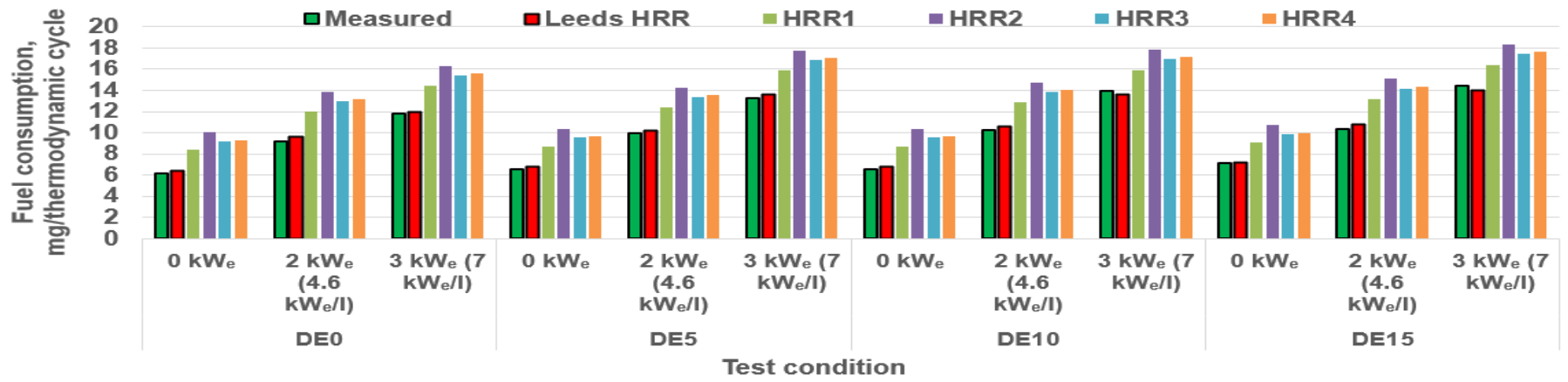

Figure 7.92 Comparison of the measured and predicted fuel energy input for the investigated DE fuel blends

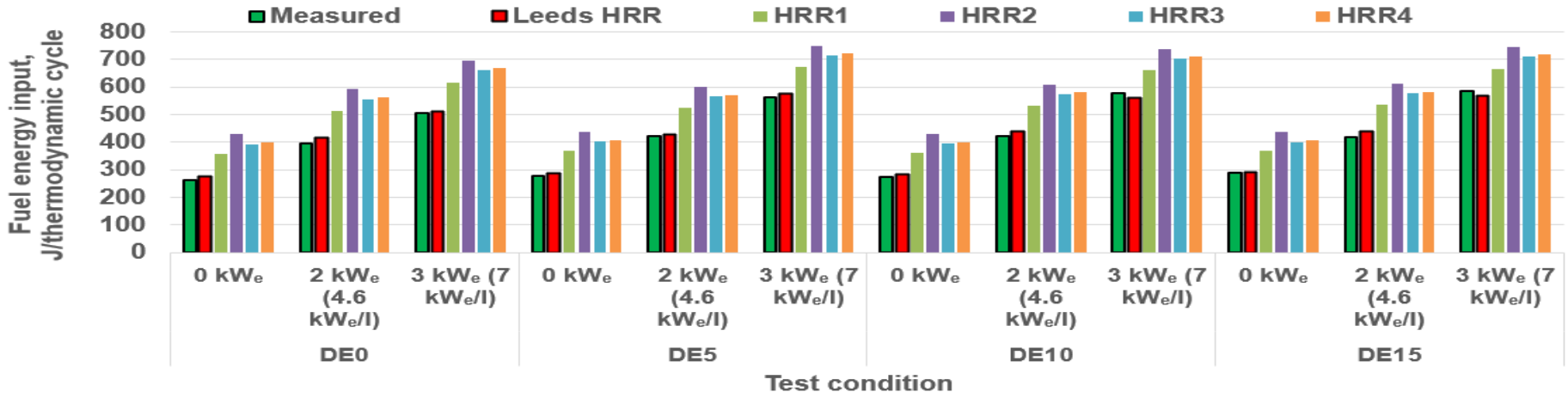

Figure 7.93 Comparison of the measured and predicted fuel masses for the investigated DE fuel blends

Table 7.5 Predicted fuel input energy for the tested diesel-ethanol (DE) fuel blends and engine power conditions

Fuel blend	Power, kW_e (kW_e/l)	In-cylinder, λ	Fuel energy input, J/thermodynamic cycle					
			Measured	Leeds HRR	HRR1	HRR2	HRR3	HRR4
DE0	0	6.47	263.18	276.98	358.49	428.62	392.95	398
	2 (4.6)	4.29	394.79	414.77	513.43	590.98	555.11	561.82
	3 (7)	3.32	507.01	512.01	616.77	696.53	660.55	667.85
DE5	0	6.11	275.99	287.7	368.17	438.86	402.83	407.87
	2 (4.6)	3.97	421.2	429.14	523.51	600.91	564.6	571.14
	3 (7)	2.96	560.71	574.91	671.3	750	713.94	720.92
DE10	0	6.19	273.16	281.8	360.52	430.25	394.5	399.4
	2 (4.6)	3.98	422.57	437.88	532.03	609.43	573.18	579.72
	3 (7)	2.89	578.23	561.66	659.69	738.47	702.63	709.71
DE15	0	5.76	290.61	291.62	367.34	367.34	400.69	405.48
	2 (4.6)	3.99	418.83	439.35	534.61	612.41	576.02	582.62
	3 (7)	2.83	585.53	568.87	666.34	745.85	709.6	716.69

Table 7.6 Validation of the Leeds HRR model for diesel-ethanol (DE) fuel blends

			Fuel mass, mg/thermodynamic cycle						% Deviation from measured fuel mass				
Fuel blend	**Power, kW_e (kW_e /l)**	**In-cylinder λ**	**Measured**	**Leeds HRR**	**HRR1**	**HRR2**	**HRR3**	**HRR4**	**Leeds HRR**	**HRR1**	**HRR2**	**HRR3**	**HRR4**
DE0	0	6.47	6.15	6.44	8.38	10.01	9.18	9.3	4.73	36.22	62.86	49.31	51.23
	2 (4.6)	4.29	9.22	9.65	12	13.81	13	13.13	4.62	30.05	49.7	40.61	42.31
	3 (7)	3.32	11.85	11.91	14.41	16.27	15.43	15.6	0.54	21.65	37.38	30.28	31.72
DE5	0	6.11	6.54	6.82	8.72	10.4	9.55	9.67	4.28	33.4	59.01	45.96	47.79
	2 (4.6)	3.97	9.98	10.17	12.41	14.24	13.38	13.53	1.89	24.29	42.67	34.05	35.6
	3 (7)	2.96	13.29	13.62	15.91	17.77	16.92	17.08	2.51	19.72	33.76	27.33	28.57
DE10	0	6.19	6.6	6.81	8.71	10.39	9.53	9.65	3.21	31.98	57.51	44.42	46.22
	2 (4.6)	3.98	10.21	10.58	12.85	14.72	13.84	14	3.65	25.9	44.22	35.64	37.19
	3 (7)	2.89	13.97	13.57	15.93	17.84	16.97	17.14	-2.84	14.09	27.71	21.51	22.74
DE15	0	5.76	7.16	7.18	9.05	10.75	9.87	9.99	0.31	26.4	50.14	37.88	39.52
	2 (4.6)	3.99	10.32	10.82	13.17	15.08	14.19	14.35	4.89	27.64	46.22	37.53	39.11
	3 (7)	2.83	14.42	14.01	16.41	18.37	17.48	17.65	-2.86	13.8	27.38	21.19	22.4
					Average of absolute error:				3.03	26.26	44.88	35.48	37.03
					Standard deviation:				1.47	6.85	11.26	8.72	8.95
					Error range:				-2.86 - +4.89	13.8 – 36.22	27.38 - 62.86	21.19 – 49.31	22.4 – 51.23

The Leeds HRR model predicted the fuel consumption of the Gen-set engine for pure diesel (DE0), DE5, DE10, and DE15 at the tested conditions of power with an overall average error of 3.03% compared to the measured fuel consumption (green bars with black borderline). The percentage errors of the fuel masses predicted by the Leeds HRR model ranged from -2.86 to +4.89, with a standard deviation of 1.47. The overall average errors which were obtained for off–road diesel and the alternative diesel fuels for the MFIS IVECO diesel engine were 1.41% and 4.86% respectively (Chapter 6, Sections 6.4.7 and 6.5.6). The percentage error obtained for the DE fuel blends was relatively low compared to that for the alternative diesel fuels (GTL and HVO) because it was relatively easy to determine the SoC and EoC crank angle timings from the HRR profiles of the SFIS Gen-set engine compared to the MFIS IVECO engine. MFIS in the IVECO engine as well as the relatively high CN of the alternative diesel fuels compared to ULSD led to significant fluctuations after the start of pilot fuel injection (for the high power conditions). Consequently, the SoC could not be determined directly from the HRR profiles of the alternative fuels by direct eye inspection. Two novel graphical approximation techniques were used in Section 6.5.7 to circumvent this challenge (Olanrewaju et al., 2020b). The overall average errors in the predicted fuel masses for the DE fuel blends by the other HRR models that were based on γ(T) ranged from 26% to 45%. The HRR models that were based on γ(T) overpredicted the fuel consumption of the Gen-set engine because the significant effect of λ on γ was not accounted for in the models.

Figures 7.92 and 7.93 clearly show that the accuracy of the HRR model of CI engines for predicting the combustion behaviour of DE fuel blends in the SFIS diesel Gen-set engine is enhanced by using $\gamma(T, \lambda)$. Therefore, the validity and the accuracy of the Leeds HRR model for different diesel engine configurations

(multiple cylinder, MFIS CI engine and single cylinder, SFIS CI engine) as well as different diesel fuels (ULSD, alternative diesels, and diesel-ethanol, DE biofuel blends) was ascertained in the current work.

7.8.8 Effect of ethanol on the combustion behaviour of CI engines

The effect of ethanol on the combustion behaviour of CI engines was investigated by plotting the HRR profiles for the four blends (DE0, DE5, DE10, and DE15) that were tested on the same graph for each of the tested engine loads. Figure 7.94 shows the three phases of the combustion of the injected fuel mass in the cylinder of the engine, as identified by Heywood (1988). The rate of release of heat during the rapid/premixed combustion phase (phase A) was the highest. The HRR reduced during the mixing-controlled combustion phase (phase B) as the combustion became less spontaneous than it was in the first phase. The late combustion phase (phase C) was characterised by a drastic reduction in the HRR.

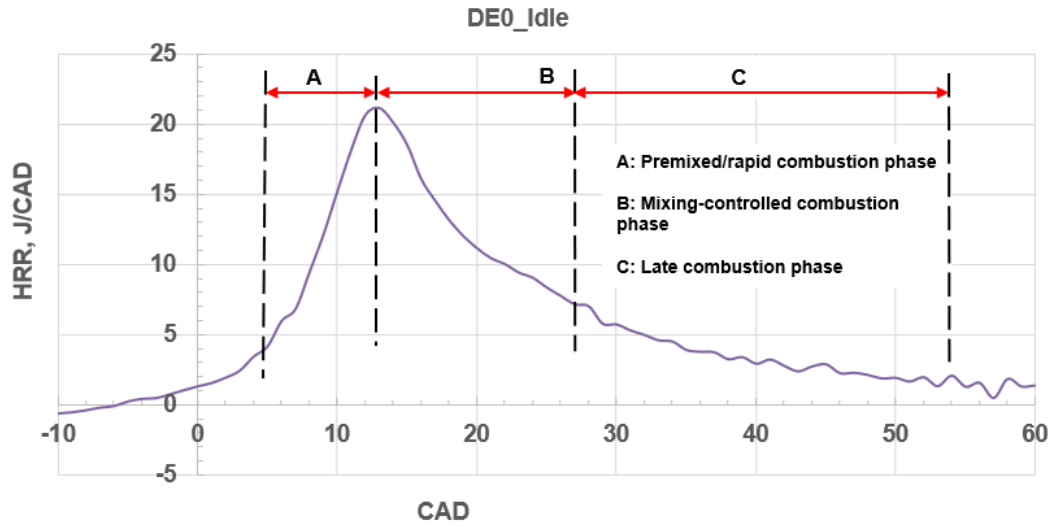

Figure 7.94 Stages in the combustion of the injected fuel during the power stroke

Figures 7.95 to 7.98 depict the effect of increasing the concentration of ethanol in the blends as well as increasing the load on the engine on the combustion behaviour of the diesel Gen-set engine.

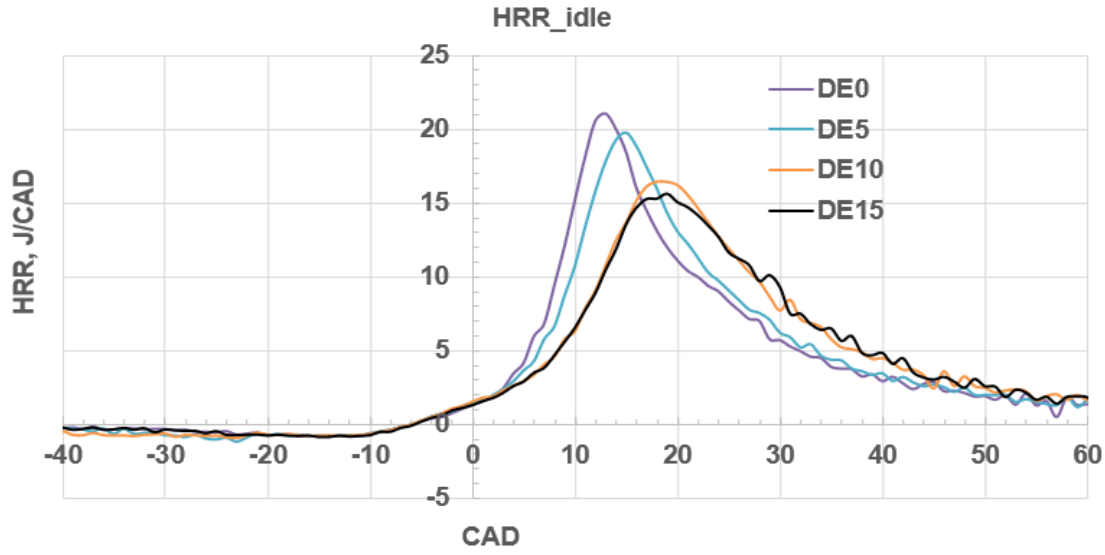

Figure 7.95 Effect of ethanol on the Heat Release Rate (HRR) of the Gen-set at idle

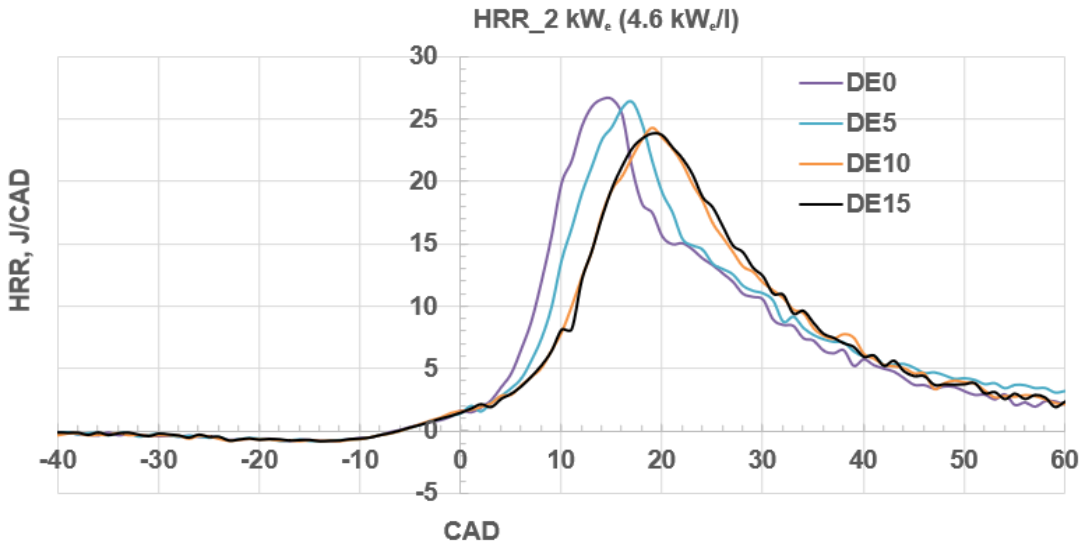

Figure 7.96 Effect of ethanol on the Heat Release Rate (HRR) of the Gen-set at 2 kW_e (4.6 kW_e/l)

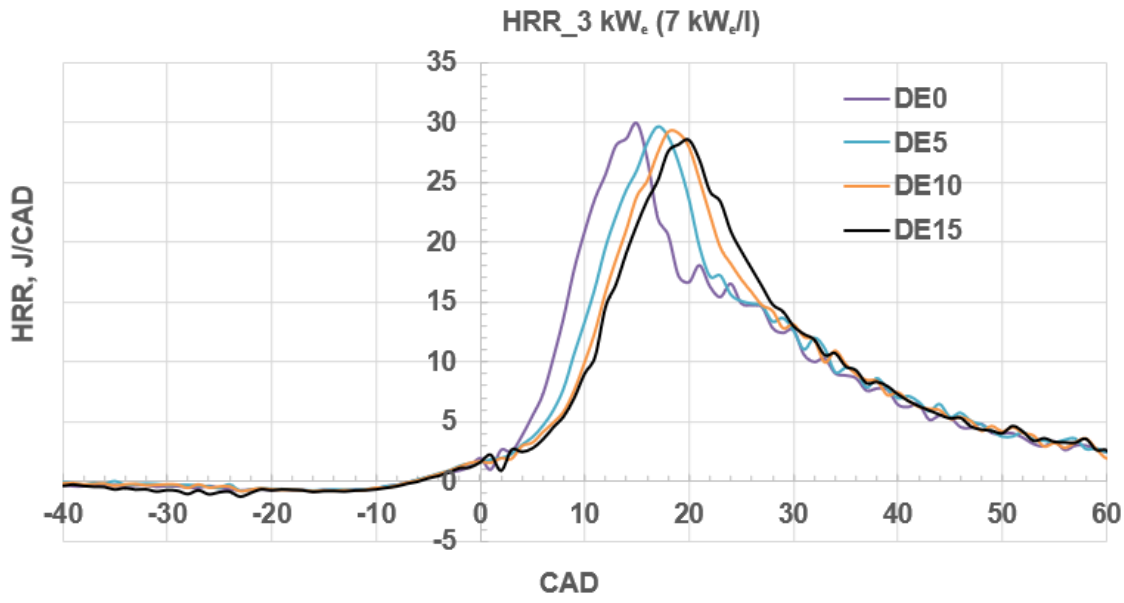

Figure 7.97 Effect of ethanol on the Heat Release Rate (HRR) of the Gen-set at 3 kW_e (7 kW_e/l)

Figure 7.95 for the operation at idle shows that the gradient of the rapid combustion phase was highest for pure diesel (DE0). As the concentration of ethanol increased in the blends, the gradient of the rapid combustion phase decreased below the baseline. By implication, the rate of combustion of the injected fuel (the HRR) decreased below the baseline as the concentration of ethanol increased in the DE blends. DE0 had the highest HRR during the first phase because of the relatively high CN and the low heat of vaporisation of pure diesel compared to the DE blends. The DE blends experienced Ignition Delay due to the relatively low CN of ethanol and the high heat of vaporisation of the ethanol component of the blends. The rate of evaporation of the diesel in the ethanol blended fuels was higher than that of the ethanol such that the diesel in the blends vaporised and ignited earlier than the ethanol component. Basically, the effective fuel mass evaporated and combusted per time reduced below the baseline as the concentration of ethanol in the DE blends increased (this was due to the retarded/delayed evaporation and combustion of the ethanol fraction of the

blends). Therefore, the HRR reduced below the baseline as the concentration of ethanol increased in the fuel blends. The same trend was observed in the rapid combustion phase for the 2 kW_e and 3 kW_e load conditions (Figures 7.96 and 7.97).

The decrease in the HRR of the ethanol-blended fuels in the mixing-controlled combustion phase was more gradual than that of pure diesel. By implication, the decrease in the HRR of the ethanol-blended fuels in phase B of the combustion was less rapid than was the case for pure diesel (DE0). This was because the evaporation (and combustion) of ethanol was delayed in the first phase but enhanced towards the start of the second phase during which time the temperature of the combustion mixture in the cylinder was relatively high. This led to the observed widening of the area under the HRR curves of the DE fuel blends. Furthermore, the end of the mixing-controlled combustion phase was not conspicuous for the DE blends as was the case for pure diesel due to the observed relatively slow decrease in the rate of the mixing-controlled combustion as the concentration of ethanol increased in the DE blends. The increase in the ID for the ethanol-blended fuels and the retarded start of combustion of the ethanol fraction in the blends led to the observed high levels of THC and ethanol emissions from the Gen-set as well as the decrease in the BTE of the engine below the baseline as the concentration of ethanol increased in the blends (Figures 7.20, 7.26 and 7.61).

Generally, Figures 7.95 to 7.97 depict that as the concentration of ethanol in the DE blends increased, the HRR profiles of the ethanol-blended fuels (DE5, DE10, and DE15) shifted to the right of the HRR curve for pure diesel while the PHRR for the DE blends decreased below the baseline. Furthermore, for the ethanol-blended fuels, the PHRR occurred at a later crank angle timing than pure diesel.

However, at the high load condition (3 kW_e), the differences between the values of the PHRR of DE0 and those of the ethanol-blended fuels were relatively small compared to those at idle and at the 2 kW_e load conditions. This was due to the drastic increase in the combustion temperature at the high load condition which enhanced the evaporation, combustion, and release of heat from the ethanol-blended fuels. The observed shift to the right of the HRR curves for the ethanol-blended fuels relative to the position of the curve for pure diesel and the relatively late occurrence of the PHRR for the ethanol-blended fuels compared to pure diesel were due to the relatively long ID (and low CN) of the DE blends. The observed decrease in the PHRR of the ethanol-blended fuels below the baseline was due to the combined effects of the relatively low heating values (energy densities) and the relatively high heats of vaporisation of the ethanol-blended fuels compared to pure diesel.

7.8.9 Determination of combustion phasing for the investigated power conditions and fuel blends

The validated model (Leeds HRR model) was used to determine the SoC, EoC, and the crank angle timing at which 50% of the injected fuel mass was burned (MFB50) from the fuel burn profiles of the investigated fuel blends and engine loads. The SoC, MFB50, and EoC for pure diesel at idle were determined as shown in Figure 7.98. The figure shows that, when the engine was run on pure diesel (DE0) at idle, the SoC was at 5^o aTDC, 50% of the injected fuel was burned at 14.5^o aTDC while the EoC was at 27^o aTDC. The SoC, MFB50, and EoC for the other power conditions and investigated fuels were determined in a similar manner. The crank angle timings for the Peak Pressures (PP) and the Peak Temperatures (PT) were determined from the pressure traces and the temperature profiles (Figures 7.66 to 7.68, and Figures 7.71 to 7.73) by eye

inspection. Table 7.7 presents the phasing of the combustion for the investigated fuel blends and engine loads (SoC, MFB50, EoC, the crank angle timings at the PP, PT, and PHRR). Table 7.7 shows that, as the concentration of ethanol increased in the DE blends, the crank angle timing for the important combustion phasing parameters increased above the baseline. This was due to the increase in the ID that occurred as the concentration of ethanol increased. As the load on the engine was increased for each of the tested fuels, the crank angle timing for the combustion phasing parameters increased except for the SoC. The observed increase in the crank angle timings for the MFB50, EoC, PP, PT, and PHRR for each of the tested fuels was due to the increase in the injected fuel mass as the power of the engine increased.

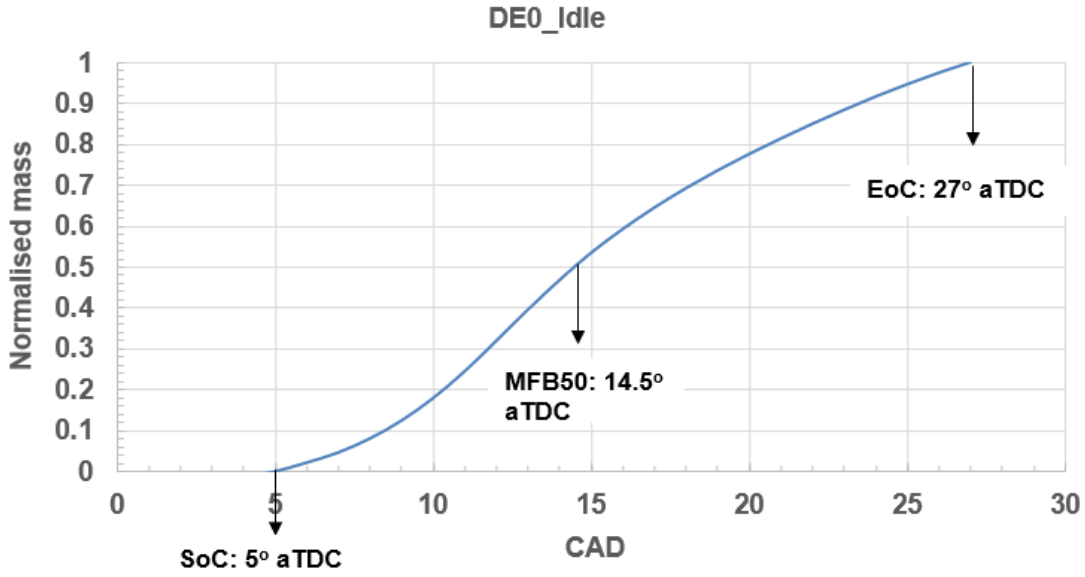

Figure 7.98 Determination of the SoC, MFB50, and EoC from the fuel burn profile (baseline diesel at idle)

Table 7.7 Combustion phasing for the tested fuel blends and engine loads

		CAD					
Fuel blend	**Power, kW_e (kW_e /l)**	**SoC**	**MFB50**	**EoC**	**PP**	**PT**	**PHRR**
DE0	0	5	14.5	27	13	23	13
	2 (4.6)	5	15.5	30	15	25	15
	3 (7)	4	17	35	15	30	15
DE5	0	6	16.5	30	15	25	15
	2 (4.6)	6	18	34	17	31	17
	3 (7)	5	20	47	18	33	17
DE10	0	7	19.5	32	18	29	18
	2 (4.6)	7	20.5	37	19	34	19
	3 (7)	5	21	45	19	34	19
DE15	0	7	20	34	19	30	19
	2 (4.6)	6	20.5	36	19	32	19
	3 (7)	6	21.5	47	20	34	20

The values of the Peak Pressure (PP), the Peak Temperature (PT), and the PHRR for the tested blend fuels and power conditions are presented in Table 7.8. The table shows that the values for the Peak Pressure (PP) decreased below the baseline as the concentration of ethanol increased in the fuel blends. This confirmed the potential of ethanol-blended fuels to reduce the peak pressure in CI engines.

Table 7.8 Model results for the Peak Pressure (PP), Peak Temperature (PT), and Peak Heat Release Rate (PHRR) for the tested fuel blends and engine loads

Fuel blend	Power, kW_e (kW_e/l)	PP, bar	PT, K	PHRR, J/CAD
DE0	0	46.8	1259.51	21.1
	2 (4.6)	50.46	1447.96	26.63
	3 (7)	52.41	1531.57	29.95
DE5	0	43.26	1252.87	19.8
	2 (4.6)	45.82	1436.24	26.3
	3 (7)	47.03	1540.33	29.56
DE10	0	36.5	1222.99	16.43
	2 (4.6)	40.42	1435.25	24.32
	3 (7)	44.37	1534.72	29.09
DE15	0	35.43	1229.43	15.63
	2 (4.6)	40.22	1440.5	23.79
	3 (7)	42.64	1543.85	28.56

7.8.10 Effect of ethanol on the Ignition Delay (ID) of the diesel Gen-set

The ID values for the tested fuel blends and engine loads were estimated by adding the corresponding SoC crank angles (aTDC) to the Start of Injection (SoI) crank angle (13^{o} bTDC). The estimated values for the ID are shown in Table 7.9 and Figure 7.99.

Table 7.9 Estimated Ignition Delay (ID) values for the investigated fuel blends and engine loads

Fuel blend	Power, kW_e (kW_e/l)	ID, CAD	ID, milliseconds
DE0	0	18.5	1.028
	2 (4.6)	18.5	1.028
	3 (7)	17.5	0.972
DE5	0	19.5	1.083
	2 (4.6)	19.5	1.083
	3 (7)	18.5	1.028
DE10	0	20.5	1.139
	2 (4.6)	20.5	1.139
	3 (7)	18.5	1.028
DE15	0	20.5	1.139
	2 (4.6)	19.5	1.083
	3 (7)	19.5	1.083

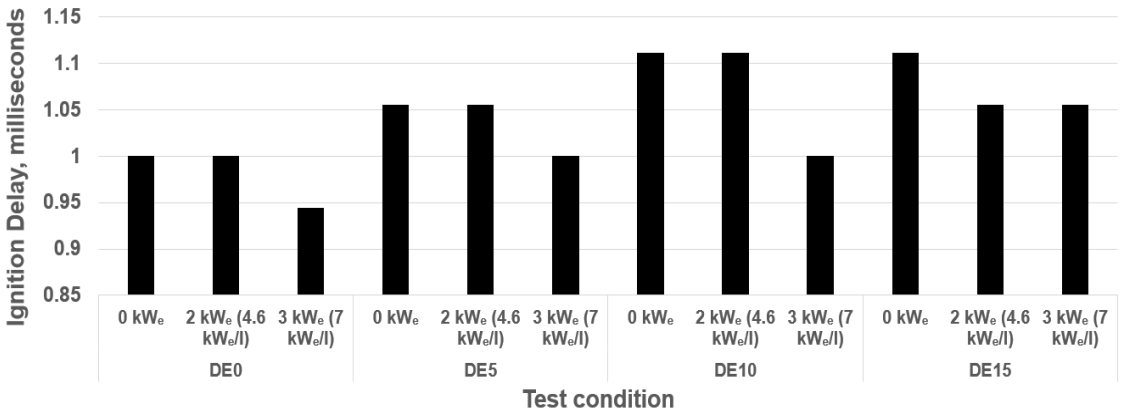

Figure 7.99 Effect of ethanol-blended fuels on the Ignition Delay (ID) of the diesel Gen-set

Figure 7.99 and Table 7.9 show that the ID of the diesel Gen-set engine increased above the baseline as the concentration of ethanol in the fuel blends increased. This was because the CN of the blend fuel (tendency of the fuel to auto-ignite) decreased as the percentage of ethanol increased in the blends. The CN of ethanol is much lower than that of pure diesel. However, for each of the tested fuels, as the power of the engine was increased, the ID decreased (Figure 7.99 and Table 7.9). The temperature and pressure of the charge in the cylinder increased drastically as the load on the engine was increased from idle to 3 kW_e. The auto-ignition property of the tested fuels was enhanced/increased at the relatively high temperatures and pressures that resulted when the load on the engine was increased.

7.8.11 Regression analysis on the estimated PHRR and Ignition Delay data

Regression analysis was carried out to establish the mathematical relationship between the PHRR, the crank angle at the PHRR, the ID, and the blend concentration of ethanol. A linear fit was established between each of the parameters (the PHRR, the crank angle at the PHRR, the ID) and the

concentration of ethanol for each of the tested fuels and engine loads. Figures 7.100 to 7.105 depict the results of the regression analysis together with the R^2 values.

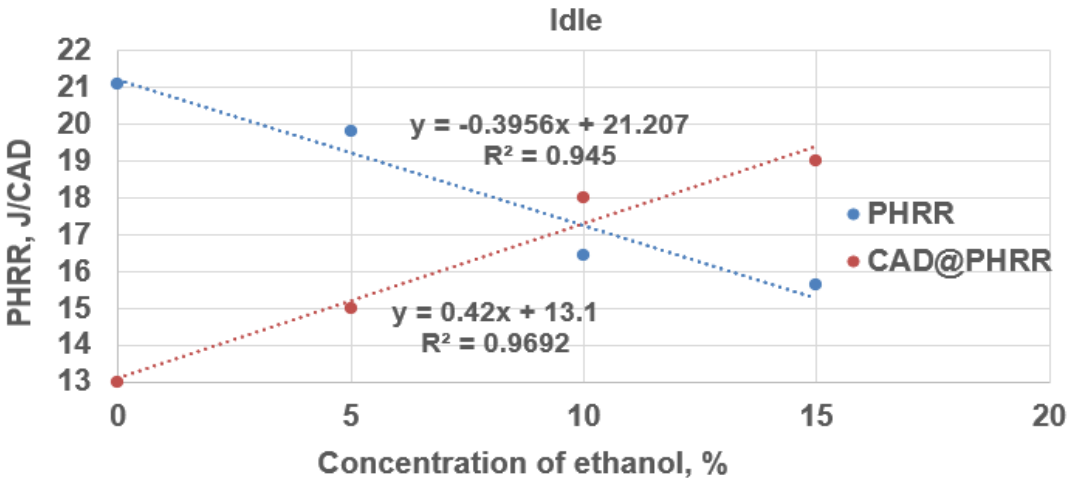

Figure 7.100 Plot of the PHRR against the concentration of ethanol: idle

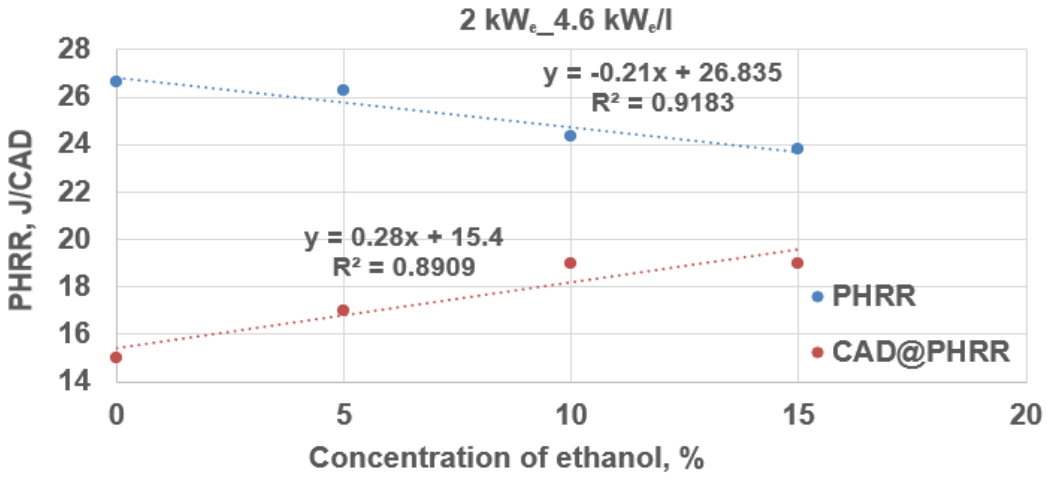

Figure 7.101 Plot of the PHRR against the concentration of ethanol: 2 kWe (4.6 kWe/l)

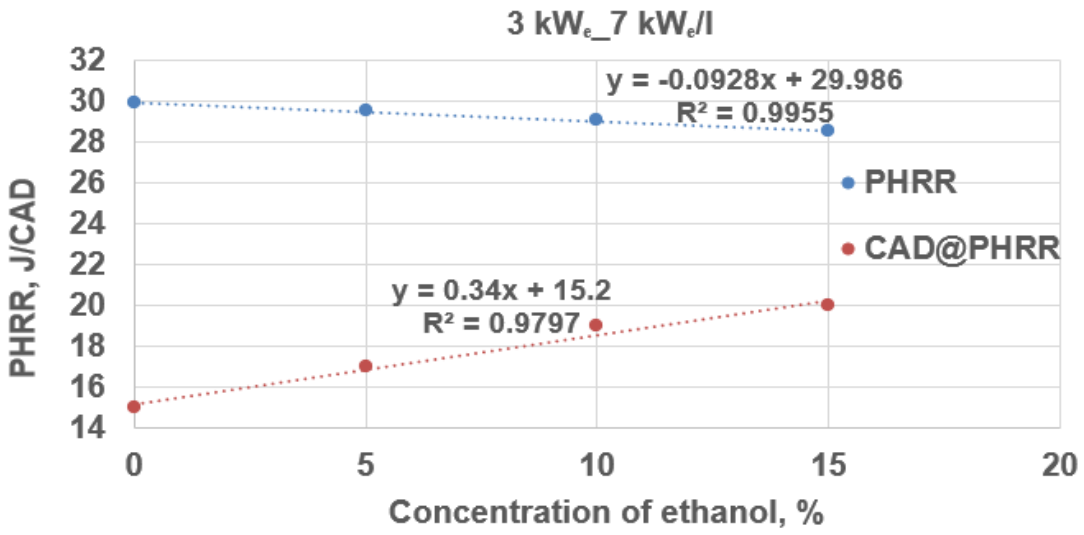

Figure 7.102 Plot of the PHRR against the concentration of ethanol: 3 kWe (7 kWe/l)

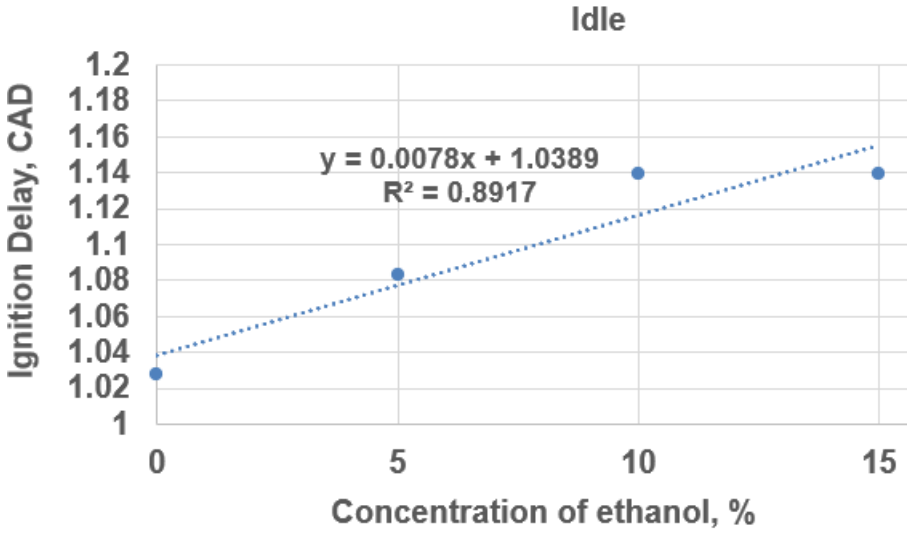

Figure 7.103 Plot of the Ignition Delay (ID) against the concentration of ethanol: idle

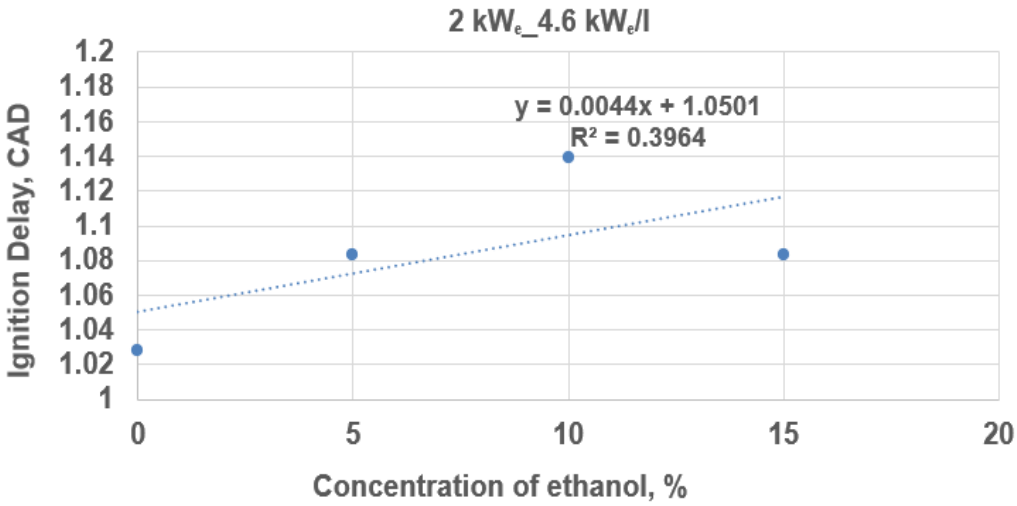

Figure 7.104 Plot of the Ignition Delay (ID) against the concentration of ethanol: 2 kWe (4.6 kWe/l)

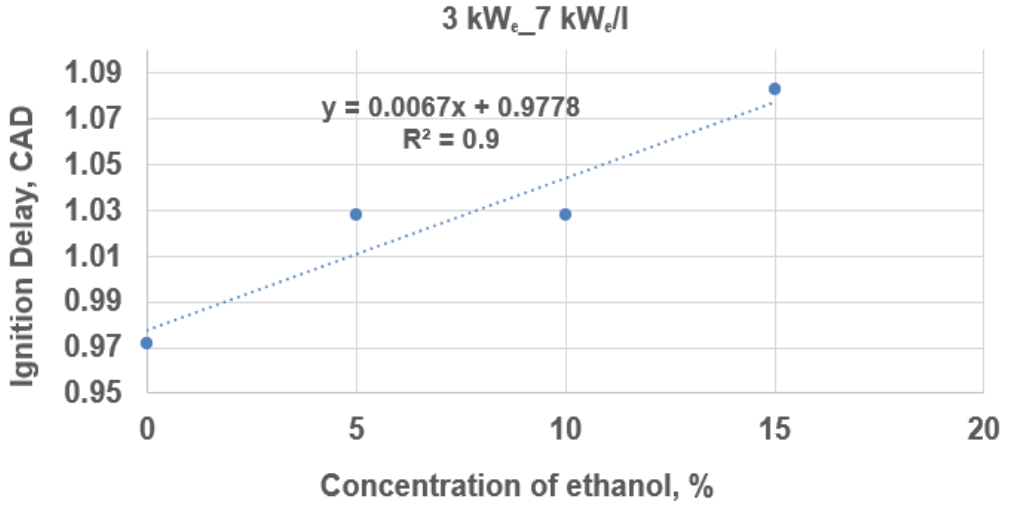

Figure 7.105 Plot of the Ignition Delay (ID) against the concentration of ethanol: 3 KWe (7 kWe/l)

The established linear relationships depicted in Figures 7.100 to 7.105 show that, for each of the tested loads, as the concentration of ethanol increased, the PHRR decreased below the baseline; the crank angle at the PHRR increased above the baseline, while the ID also increased above the baseline. The observed decrease in the PHRR as the concentration of ethanol increased was due to the combined effect of the relatively low Cv and the relatively high heat of vaporisation of ethanol compared to pure diesel. The observed linear increase in the ID and the

crank angle at the PHRR above the baseline as the concentration of ethanol increased in the blends were both due to the relatively low CN of ethanol compared to pure diesel.

7.8.12 Applicability of the results from the current work to 4-cylinder diesel engines

The single-cylinder diesel Gen-set that was used in the current work was compared to other CI engines by dividing the rated power of the engines in kW by their displacements in litres as shown in Table 7.10.

Table 7.10 Comparison of the diesel Gen-set to 4-cylinder diesel engines

Yanmar diesel engine	**Cylinders**	**Bore x Stroke, mm**	**Rated power, kW**	**Swept volume, litre**	**kW per litre**
Gen-set	1	86 x 75	5.7	0.435	13.10
Marine	4	78 x 86	25.7	1.644	15.63
Marine	4	105 x 125	57.4	4.33	13.26

Table 7.10 shows that the single-cylinder Yanmar Gen-set that was used in the current work had a kW rated power to displacement ratio that compared well to those of 4-cylinder Yanmar diesel engines (Yanmar, 2016). Therefore, the results obtained for the Gen-set in the current work can be extended to other diesel engines.

7.9 Conclusion

The effects of DE fuel blends on the performance of a modern, 5.7 kW, DI, 0.435 litre, single cylinder diesel Gen-set in terms of the thermal efficiency, gaseous, and particulate emissions from the engine as well as the HRR of the engine were presented in this Chapter. The test matrix consisted of three (3) conditions of

kilowatt electric (kW_e) loads (idle, 2, and 3 kW_e) for each of the tested fuels (DE0 (pure diesel), DE5, DE10, and DE15). The tested DE fuel blends increased the BSFC of the engine above the baseline due to the relatively low Cv of ethanol. However, the DE blends reduced the BTE of the engine below the baseline, contrary to what was reported in literature. The estimated BTEs for the Gen-set were lower than expected for both pure diesel and the ethanol-blended fuels. This was due to the observed high levels of the THC in the engine-out exhaust. The DE blend fuels increased the THC emissions above the baseline (the same trend was reported by previous authors). However, relatively high levels of THC emissions were reported in this work. The high THC levels from the Gen-set were due to the inefficient atomisation of the injected fuel mass (owing to the relatively low fuel injection pressure of the Gen-set engine) as well as the impingement of fuel on the wall of the cylinder. The DE fuel blends decreased the NOx emission from the engine below the baseline due to the lowering of the flame temperature when the engine was run on the ethanol-blended fuels. The reduction in NOx was 40% at the 3 kW_e load for DE15. CO emissions were also increased above the baseline at the tested loads when the engine was run on the DE blend fuels. The levels of CO from the engine were significantly high for all the fuels due to the incomplete combustion of the injected fuel mass. The emission of aldehydes (formaldehyde and acetaldehyde) and ethylene from the engine increased significantly above the baseline as the concentration of ethanol increased in the blends. However, the levels of the aldehydes and ethylene in the exhaust decreased drastically as the load on the engine was increased. The DE blends led to significantly high levels of benzene emission above the baseline at idle. At the higher loads, the emission of benzene became insignificant. Generally, the DE fuel blends reduced the yield of particulates below the baseline as the power

of the engine increased. The number of emitted nanoparticles from the Gen-set increased above the baseline for the fuel blends as the load on the engine increased. The problem of high THC and CO emissions from the Gen-set as a result of the use of ethanol-blended fuels can be solved by using a larger capacity engine (an engine with a larger cylinder bore). This will check the impingement of fuel on the wall of the cylinder thereby reducing the THC emissions. High-pressure injection of fuel will also enhance the efficiency of fuel atomisation and combustion. This will in turn reduce the THC and CO emissions by minimising the formation of the local rich zones which led to the incomplete combustion of the injected fuel in the Gen-set. The BTE of the of the engine will also be improved for operation on DE fuel blends if a larger capacity engine with a much higher fuel injection pressure is utilised. The emission levels that were reported in this work were all engine-out emissions. Therefore, the incorporation of emission aftertreatment devices (DOC and DPF) in the Gen-sets that will be run on ethanol-blended fuels in the targeted localities in Nigeria will further enhance clean combustion by drastically reducing the levels of the emitted pollutant gases and particles. This will encourage the use of bioethanol for power generation in the rural areas in Nigeria and in sub-saharan African countries in general. The current work also showed that 15% substitution by volume of diesel with green ethanol in transport vehicles in the UK will reduce transport CO_2 emissions by 9% which is equivalent to ~5.5 million tonnes reduction in transport CO_2 emissions. The same percentage substitution of diesel in Nigeria will reduce CO_2 emissions in the country by ~0.05 million tonnes. The HRR analysis that was carried out for the Gen-set in the current work confirmed that the Leeds HRR model could also be applied to the diesel Gen-set engine as well as for binary (diesel-ethanol) fuel blends. The Leeds HRR model predicted the fuel consumption of the Gen-set

engine for the investigated fuel blends with an overall average (absolute) error of 3.03% compared to the measured fuel consumption and a standard deviation of 1.47.

Chapter 8 Investigation of the optimum gasification conditions of sweet sorghum stalk residue

8.1 Introduction

This Chapter presents the results of the gasification tests that were carried out on sweet sorghum stalk residue using the restricted ventilation Cone calorimeter method. The current work is the first investigation of the gasification of sweet sorghum stalks (and the other stalks – grain sorghum and corn stalks). The chapter presents the composition of the tested biomass residues and the results of the analytical tests: elemental (ultimate) analysis, TGA (proximate analysis), and bomb calorimetry. The yields of the combustible gases (CO, H_2, and THC), the Hot Gas Efficiency (HGE – ratio of total energy in the hot gas from the gasifier to the original energy in the biomass), and the optimum equivalence ratio to operate the gasifier for sweet sorghum stalk residue, were estimated and compared to those of grain sorghum stalk, corn stalk, and pine wood. Gasification involves very rich combustion and a possible problem is that rich combustion can form soot which would be undesirable, so the Particle Number (PN), Particulate Mass (PM) emissions, and size where the maximum PN occurred were investigated. A conceptual design of a downdraught biomass gasifier is presented in Section 8.10 based on the experimental results. A manually operated gasifier was proposed for ease of operation/maintenance in the targeted locations – rural areas in Nigeria where the biomass is abundant.

8.1.1 Biomass residue composite structure

The tested biomass stalk residues were roughly cylindrical composites consisting of an outer core and an inner, relatively soft core. The percentages by weight of the inner core and the outer core of the tested crop residues are presented in Table 8.1.

Table 8.1 Weight percentages of inner and outer cores of the tested residues

Biomass residue	Inner core, wt%	Outer core, wt%
Sweet sorghum	30.00	70.00
Grain sorghum	25.00	75.00
Corn	21.88	78.13

Table 8.1 shows that the percentage of the inner core of the tested sweet sorghum stalk residue samples was the largest of the three crop residue samples. (This is because, the glucose-rich juice of sweet sorghum is stored in the inner core of the fresh stalks.)

The inner core and the outer core of the stalk residue are shown in Figure 8.1. The inner cores of the stalk residues of sweet sorghum, grain sorghum, and corn are enclosed within the outer cores of the residues as shown in Figure 8.1.

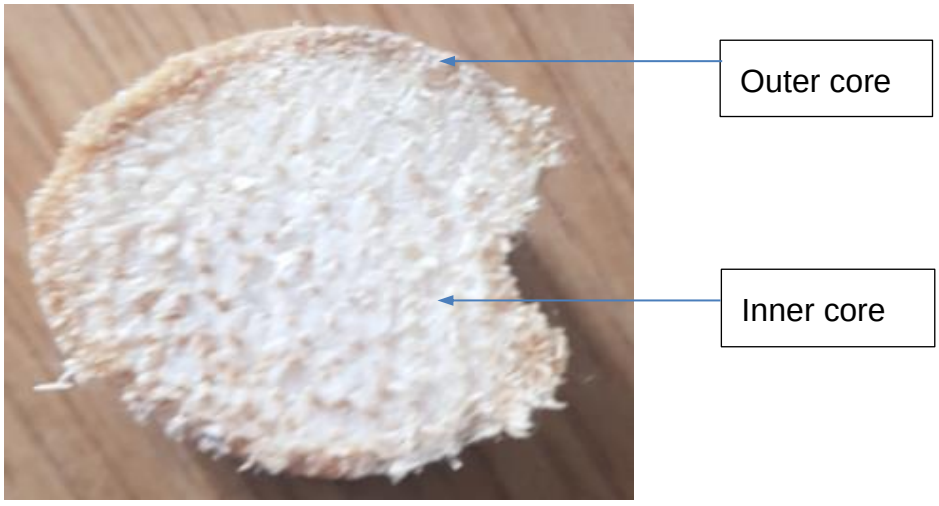

Figure 8.1 Transverse section of sorghum stalk residue (maximum diameter: 20 mm)

Figure 8.2 shows the prepared sweet sorghum stalk samples in the aluminium foil prior to the test.

Figure 8.2 Sweet sorghum stalk samples prepared for the gasification test

8.1.2 Biomass analytical test results

The CHNS-O, TGA, and bomb calorimetry test results of the three biomass residues are presented in Tables 8.2, 8.3, and 8.4 respectively. Table 8.2 shows that the inner and outer cores have a similar composition, in spite of the difference in bulk density. All parts of the stems have a high oxygen content, much higher than for wood and this results in a low stoichiometric AFR, which means less air is required to achieve the rich gasification mixtures compared with wood. The moisture content, Volatile Matter (VM), Fixed Carbon (FC), and ash contents of the crop residues are given in Table 8.3. Table 8.4 presents the stoichiometric AFR and the Gross Calorific Values (GCV) of the crop residues. The method of Chan and Zhu (1996) was utilised to calculate the stoichiometric AFR of the biomass residues. Table 8.4 shows that the estimated GCV of the tested biomass residues compared well to the measured GCV. The GCVs estimated by the

empirical equation of Channiwala and Parikh (2002) (Equation 4.13) for the biomass residues were higher than the measured values. The average percentage deviation of the predicted GCVs from the analytically determined values was 3.49.

Figures 8.3 to 8.10 depict the TGA results of the tested crop residues. Nitrogen gas was blown through the analyser at the beginning of the TGA at 50 ml/min. Towards the end of the TGA (in the last 15 minutes), air was blown through the analyser at 50 ml/min for the oxidation of Fixed Carbon and ash. The CHNS-O test and the TGA results presented in Tables 8.2, 8.3, and Figures 8.5, 8.7, and 8.9 showed that the physical properties of the inner and the outer cores of the tested biomass residues were quite different. The TGA results for the tested biomass samples also showed that the moisture in the samples began to evaporate at temperatures below the boiling point of water (50 ^{o}C to 54 ^{o}C). Liquids are known to evaporate within a wide range of temperatures below their boiling points when the TGA samples are placed in open crucibles (Widmann, 2001).

Table 8.2 Biomass residues CHNS-O test results

Stalk residue	**Component**	**C, wt%**	**H, wt%**	**N, wt%**	**S, wt%**	**O, wt%**
Sweet sorghum	Whole	41.20	6.21	0.52	0	51.57
	Inner core	40.70	5.80	0.8	0	52.70
	Outer core	41.44	5.58	0.4	0	52.58
Grain sorghum	Whole	43.11	5.97	0.27	0	50.58
	Inner core	42.43	5.93	0.28	0	51.36
	Outer core	43.92	6.11	0.27	0	49.70

Corn	Whole	43.65	6.01	0.44	0	49.94
	Inner core	39.75	5.96	0.92	0	53.37
	Outer core	44.08	5.82	0.31	0	49.79

Table 8.3 Biomass residues TGA results

Stalk residue	**Component**	**H_2O, wt%**	**VM, wt%**	**FC, wt%**	**Ash, wt%**
Sweet sorghum	Whole	10.72	70.95	17.91	0.15
	Inner core	7.63	72.78	15.41	2.20
	Outer core	6.17	73.79	17.18	1.03
Grain sorghum	Whole	7.68	72.35	17.00	0.64
	Inner core	8.19	71.31	17.05	1.10
	Outer core	7.33	70.47	18.79	1.19
Corn	Whole	7.51	70.00	18.84	1.31
	Inner core	5.99	68.89	16.05	3.17
	Outer core	6.78	69.53	19.40	2.04

Table 8.4 Biomass stoichiometric AFR and Gross Calorific Values (GCV)

Biomass stalk residue	**Stoichiometric AFR**	**Measured GCV, MJ/kg**	**Estimated GCV, MJ/kg**	**% deviation from measured GCV**
Sweet sorghum	4.57	17.97	18.32	1.95

Grain sorghum	4.79	17.37	18.24	4.99
Corn	4.89	17.51	18.13	3.53

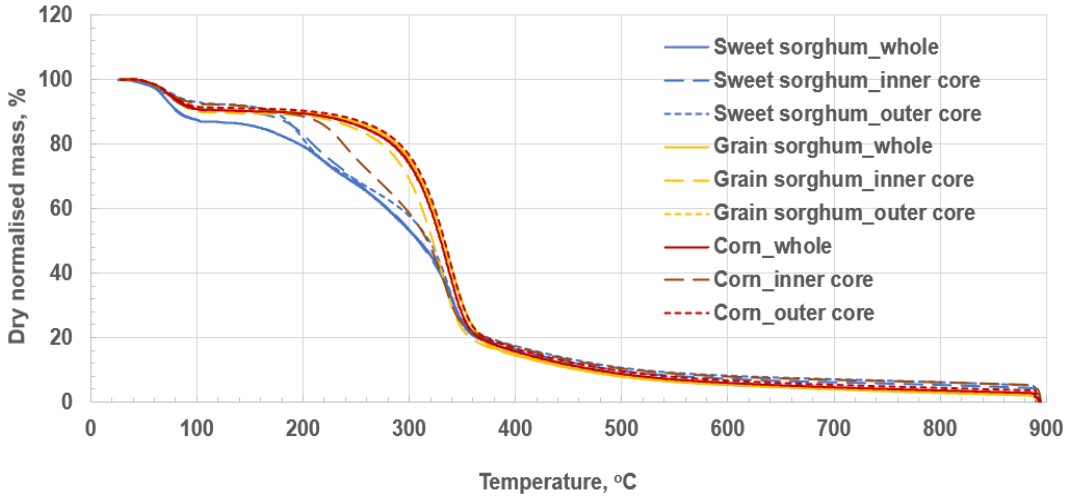

Figure 8.3 TGA profiles for the biomass residues (whole stalks, inner, and outer cores)

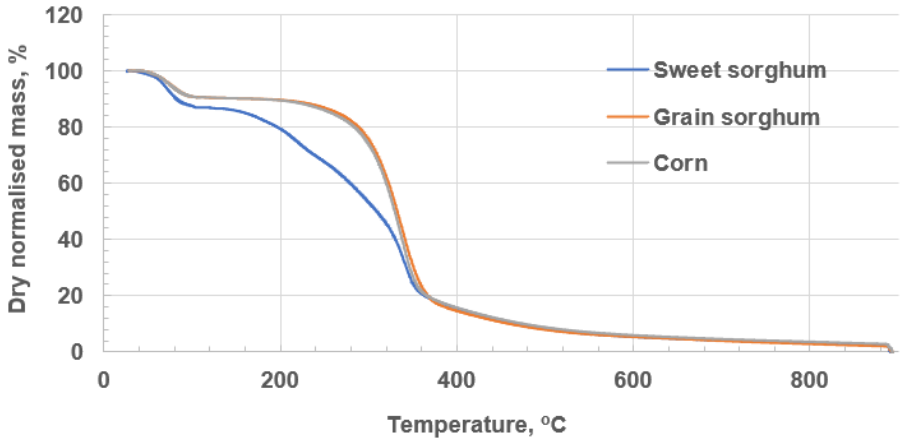

Figure 8.4 TGA profiles for the tested biomass residues (whole stalks)

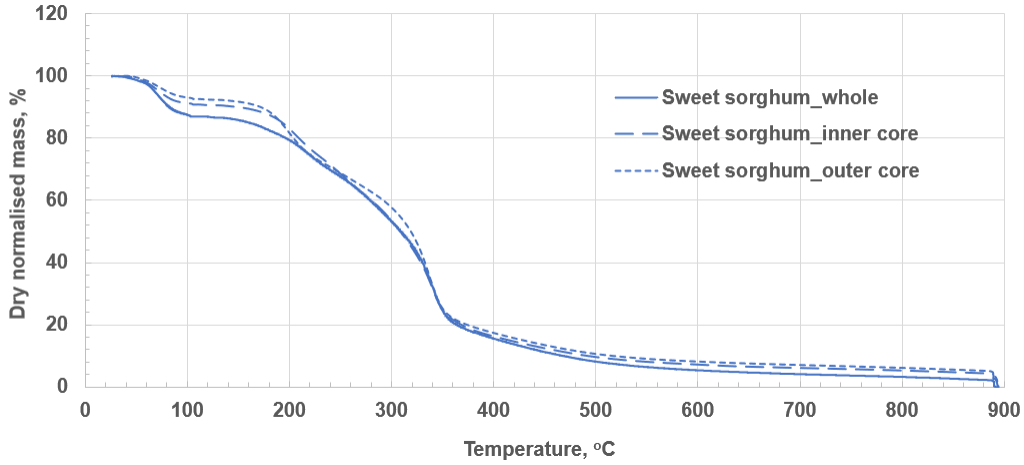

Figure 8.5 TGA profiles for sweet sorghum stalk residue

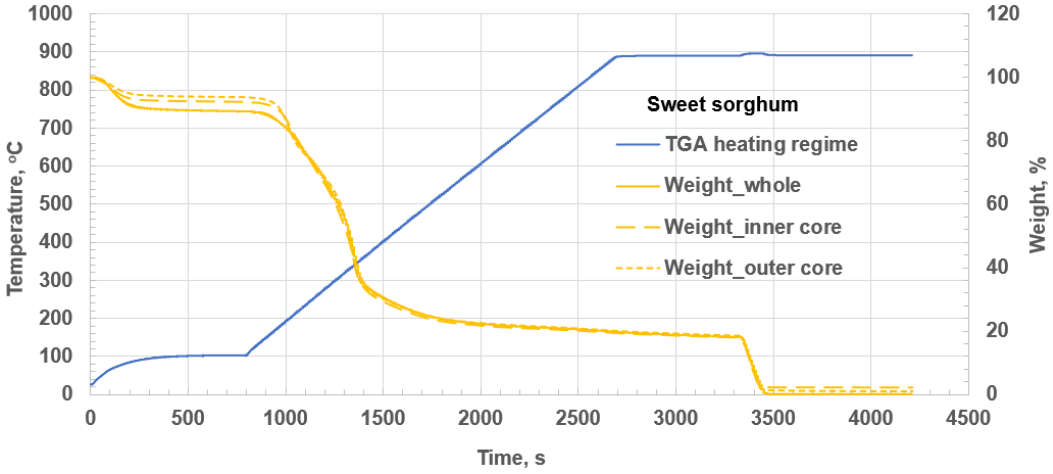

Figure 8.6 Temperature and percentage weight versus time TGA profiles (sweet sorghum stalk residue)

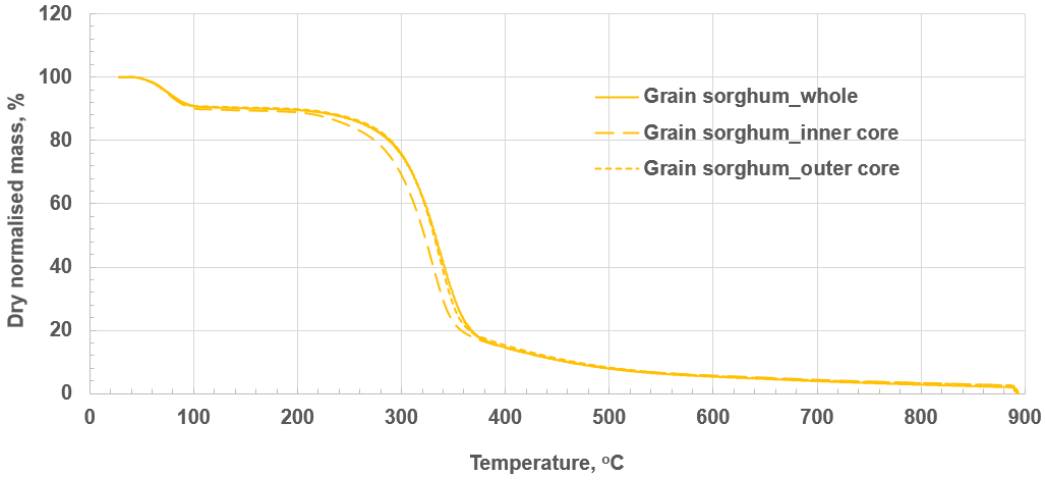

Figure 8.7 TGA profiles for grain sorghum stalk residue

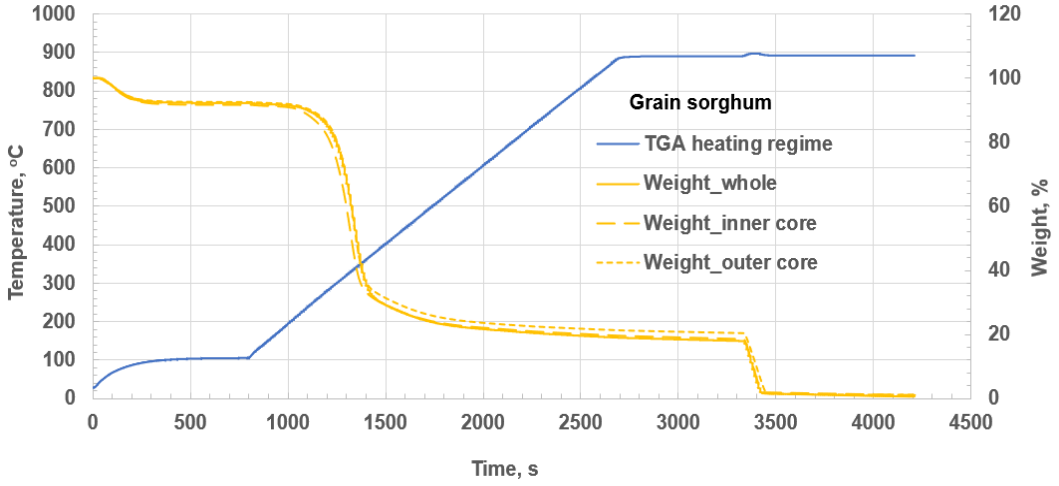

Figure 8.8 Temperature and percentage weight versus time TGA profiles (grain sorghum stalk residue)

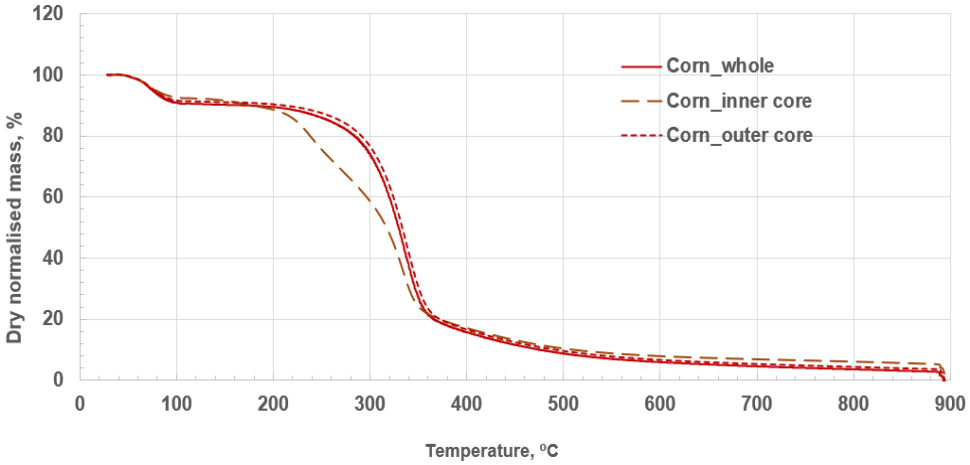

Figure 8.9 TGA profiles for corn stalk residue

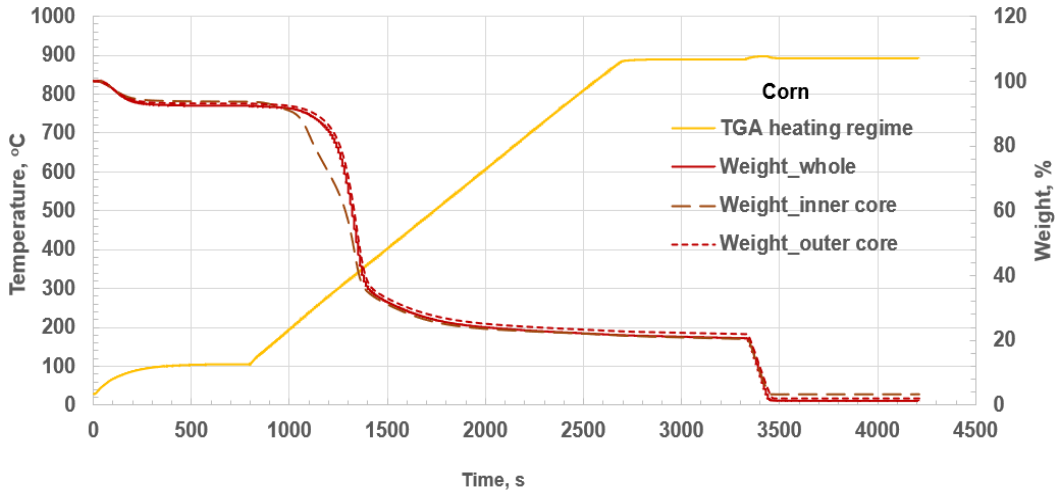

Figure 8.10 Temperature and percentage weight versus time TGA profiles (corn residue)

Figures 8.8 and 8.10 show that the inner cores of grain sorghum and corn stalk residues underwent thermal decomposition sooner than the outer cores of the biomasses (unlike sweet sorghum; Figure 8.6). The outer core of the tested sweet sorghum stalk residue was relatively thin and soft while its inner core was relatively hard compared to those of grain sorghum or corn.

8.2 Mass Loss Rate (MLR) profiles for Sweet sorghum stalk residues

The normalised mass loss and the Mass Loss Rate (MLR) profiles for the gasification of sweet sorghum stalk residues at the tested air flow conditions (9, 11.2, 12.9, 14.3, 15.5, 16.3 and 19.2 g/(m^2.s)) are depicted in Figures 8.11, 8.12, and 8.13. Figure 8.11 shows that at the end of the test when the flame had gone out there was a remaining mass that had not been gasified which varied between 30% of the initial biomass mass for 19.2 kg_{air}/m^2s to 15% at 11.2 kg_{air}/m^2s, which is similar to the fixed carbon of 18% in the TGA analysis. This was undergoing smouldering combustion as the mass was still reducing slowly in Figure 8.11 and the mass loss rate in Figure 8.12 goes to a low value at the end of the test, but not to zero. Smouldering combustion is a very slow char oxidation process. It is shown in the energy analysis of the results that the thermal efficiency of the process is 81.1% at the optimum Ø, but lower for other biomass. It is likely that the inefficiency is due to the char produced not being efficiently gasified.

Four stages (A, B, C and D) were identified during the rich burning of the sweet sorghum biomass residue, as shown in Figure 8.13 for the 16.3 g/(m^2.s) air ventilation condition. The period of negligible mass loss, during which the gradient of the normalised mass loss profile was zero, represents the Ignition Delay (ID) for the test (the duration between the test start time and the auto-ignition of the

biomass sample). The ID of the sweet sorghum stalk samples for the tested conditions ranged from 7 s to 25 s. The auto-ignition of the sample was followed by a period of rapid loss in mass due to the rapid burning of the biomass sample in the air inside the compartment at the start of the test (stage A). Stage A was initial lean combustion using the air in the chamber at the start of the test as well as that supplied to the chamber. Stage A was followed by the steady state flaming rich combustion (gasification) phase (B). This is the steady state gasification period of the test in terms of steady mass loss rate and relatively constant HRR. Stage C is the char combustion stage (C) but with some visible flame, due to CO combustion, and a lower rate of mass loss than the flaming rich burning gasification phase B. The end of stage C was the flameout time (420 s for the 16.3 g/(m^2.s) air flow condition. Stage D was the smouldering combustion phase giving a mass loss but with no flaming combustion.

The AFR and the yield of the products of gasification were determined when the gasification was at steady state. It is shown later that steady state gasification occurs later when CO and THC are roughly constant and this period is about 120 – 220 s. The delay in the establishment of steady state gasification conditions is the delay in heat transfer to the biomass sample, which releases volatiles as the heat is conducted through the biomass fuel.

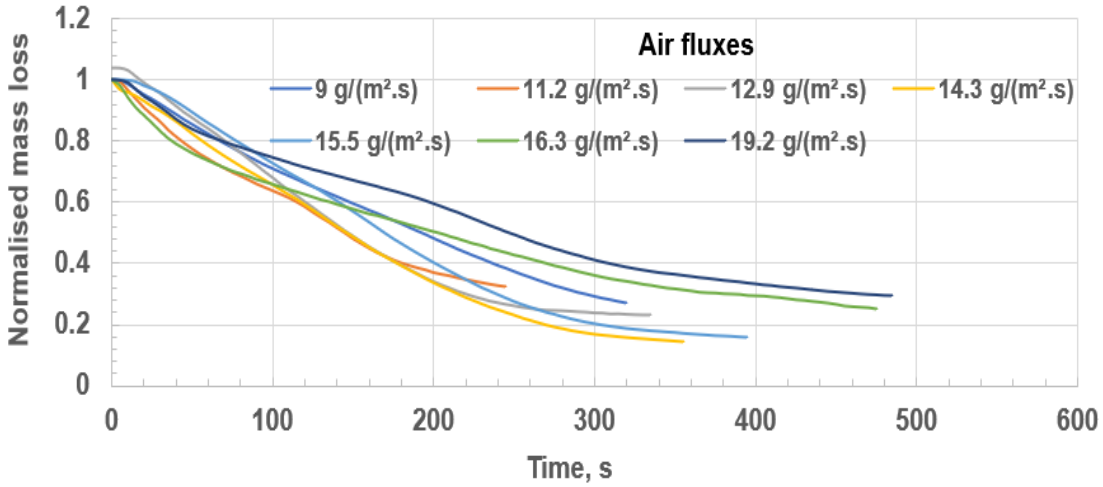

Figure 8.11 Normalised mass loss profiles for the gasification of sweet sorghum stalk

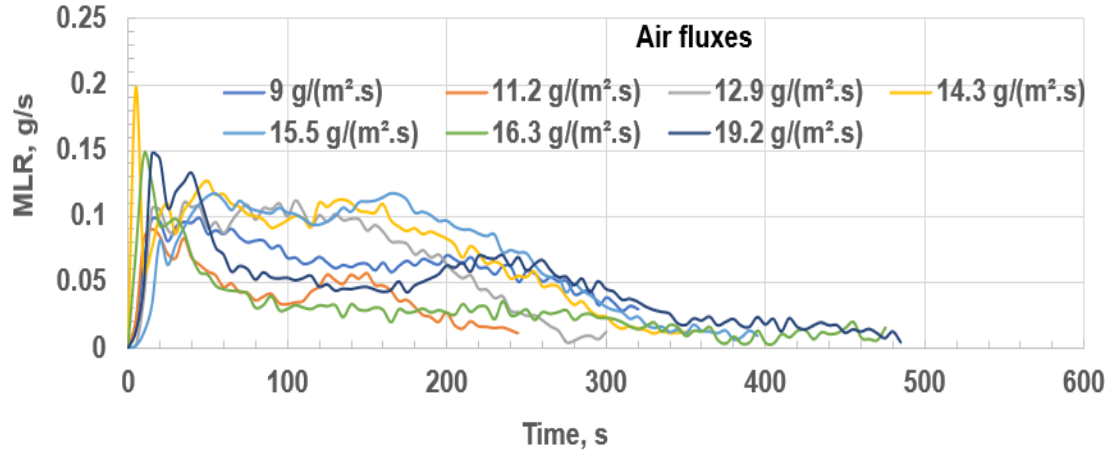

Figure 8.12 Mass Loss Rate (MLR) profiles for the gasification of sweet sorghum stalks for different air fluxes

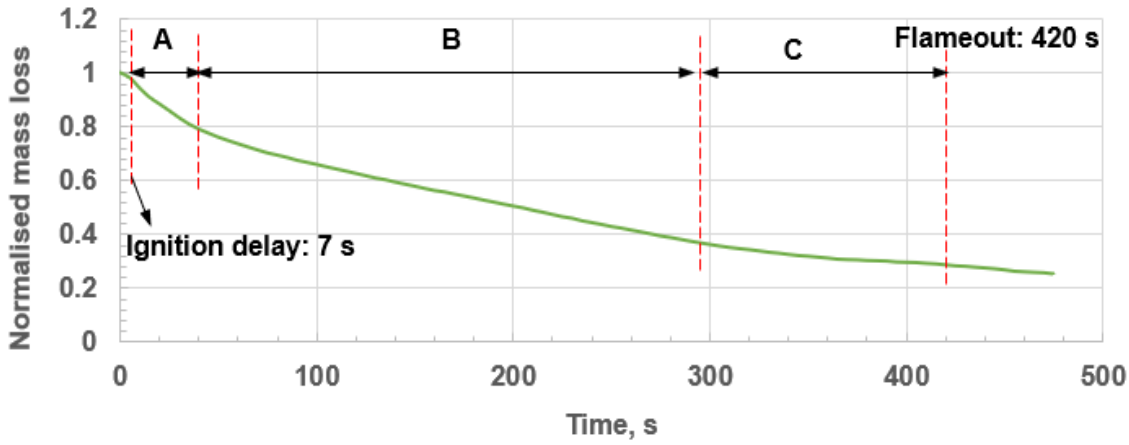

Figure 8.13 Normalised mass loss profile of sweet sorghum stalk residue at 16.3 g/(m^2.s) air flow

The flame photographs for the different stages are shown in Figures 8.14, 8.15, and 8.16 for the gasification of sweet sorghum and grain sorghum stalk residues at 11.2 g/(m^2.s) air flux and 25 kW/m^2 heat flux.

Figure 8.14 Rapid combustion (few seconds after the auto-ignition of the sample)

Figure 8.15 Steady state flame combustion

Figure 8.16 Typical smouldering combustion (grain sorghum stalk residue)

It was observed that the MLR profiles of the gasification tests in this work were relatively noisy compared to the MLR profiles for pine wood (Irshad, 2017). The observed noise in the MLR profiles was due to the composite nature of the stalk residues, the stacking together of quite irregular (fairly cylindrical) stalks leading to an exposed surface that was not perfectly continuous, the relatively short duration of the flaming combustion of the sweet sorghum stalk residue, and the release of volatiles from the bottom of the bed. The release of volatiles from the bottom of the bed led to momentary weight loss whenever there was suspension of the biomass material as a result of the volatiles released from the bottom of the bed.

The intensity of the rapid combustion stage reduced as the oxygen in the enclosure was consumed and the exposed outer core of the samples was burned. The burning of the outer core of the samples exposed the inner core to the flames. The burning of the inner core of the samples was less rapid than the burning of the outer core. This was due to the relatively low concentration of oxygen in the enclosure after the rapid combustion stage as well as the relatively soft nature of the inner core compared to the outer core. Towards the end of the test, as the concentration of oxygen increased in the enclosure, the flame was boosted. The

flame went out completely for the relatively low air flow conditions (9, 11.2, and 12.9 g/(m^2.s)) before the sample was completely burned due to the drastic decrease in the level of oxygen in the box. However, as the flow of air continued, the concentration of oxygen increased in the enclosure and the sample auto-ignited again.

8.2.1 Estimated AFRs and equivalence ratios (Ø)

The estimated AFRs and equivalence ratios (Ø) for the tested conditions (air flows) are shown in Table 8.5. The table shows that the equivalence ratio, Ø decreased as the air flow was increased. This was because the rate of consumption of fuel in the gasifier is a linear function of the air flow as for all fuels the HRR is close to 3 MJ/kg_{air}. Thus, increasing the air flow increases the fuel consumption and this makes the gasification zone leaner. Table 8.5 shows that increasing the air flow changed the equivalence ratio from 3.6 to 1.4, which is the range that normally includes the optimum gasification Ø.

Table 8.5 Estimated AFRs and equivalent ratios (Ø) for the gasification tests

Test conditions		**Estimated gasification parameters**	
Air flow rate, lpm	**Air flux, g/ (m^2.s)**	**AFR**	**Ø**
4.4	9.0	1.3	3.6
5.5	11.2	1.9	2.4
6.3	12.9	2.2	2.1
7.0	14.3	2.4	1.9
7.6	15.5	2.8	1.6
8.0	16.3	3.1	1.5
9.4	19.2	3.3	1.4

8.2.2 Variation of equivalence ratio (Ø) with air flow

The variation of the estimated equivalence ratios with the air flow is depicted in Figure 8.17. Figure 8.17 shows that as the air flow increased, Ø decreased. The inverse relationship that was observed between Ø and the air flow in this work was also reported by Irshad (2017) for pine wood. Figure 8.18 shows the observed similar trend in the variation of Ø with air flow for sweet sorghum stalk residue and pine wood.

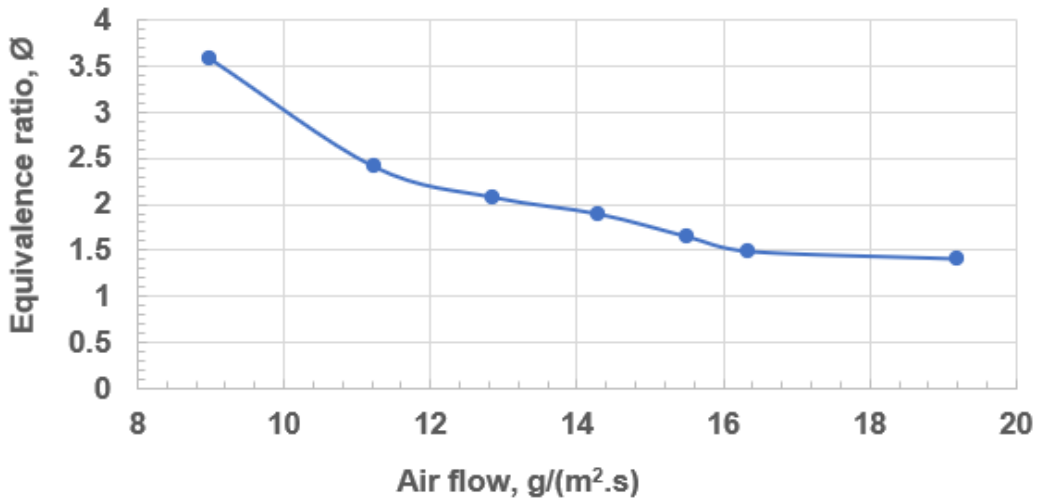

Figure 8.17 Variation of Ø with air flow for sweet sorghum stalk residue

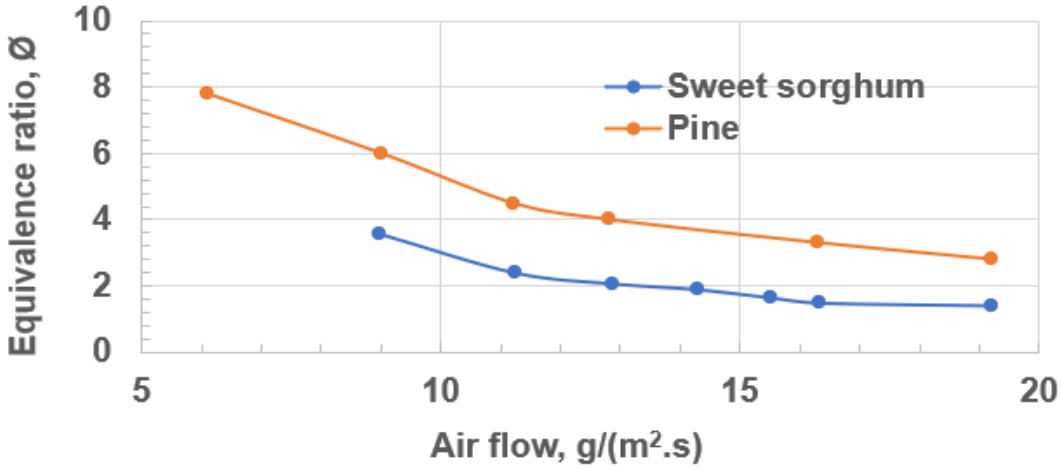

Figure 8.18 Comparison of the variation of Ø with air flow for sweet sorghum stalk residue and pine wood

8.3 Heat Release Rate (HRR) profiles of sweet sorghum stalk residues

The Heat Release Rate (HRR) profiles of the sweet sorghum stalks at the tested conditions are depicted in Figures 8.19 to 8.25. The HRR in the primary stage of the gasification (P'HRR) was estimated by oxygen consumption calorimetry using the equation of Parker (1982) for incomplete combustion. The P'HRR and the SHRR were expressed as percentages of the overall/total HRR based on the mass loss rate (THRR_mlr) as shown in Figures 8.19 to 8.25. The period of steady state heat release for each of the tested conditions is depicted on the HRR profiles (Figures 8.19 to 8.25). Figure 8.19 shows the period of steady state total HRR for the 9 g/(m^2.s) condition was from 65 to 130s. The exposed top surface of the sample (the outer core) combusted first after the auto-ignition of the sample. The burning of the exposed top outer core exposed the inner core of the stalks to the flames. After 200 s, (Figure 8.19) the inner core was burned up thereby exposing the outer core at the base of the sample holder. The combustion of the outer core at the base of the sample holder led to the third P'HHR peak. Therefore, the period of steady state gasification of the composite biomass was carefully delineated as the period between the end of the combustion of the exposed (top) outer core and the beginning of the combustion of the outer core at the bottom (after 200 s for the condition shown in Figure 8.19). In this manner, the true steady-state HRR period for the composite material (both outer and inner cores) was marked out so that the period of combustion of the outer core alone was not erroneously included in the delineation.

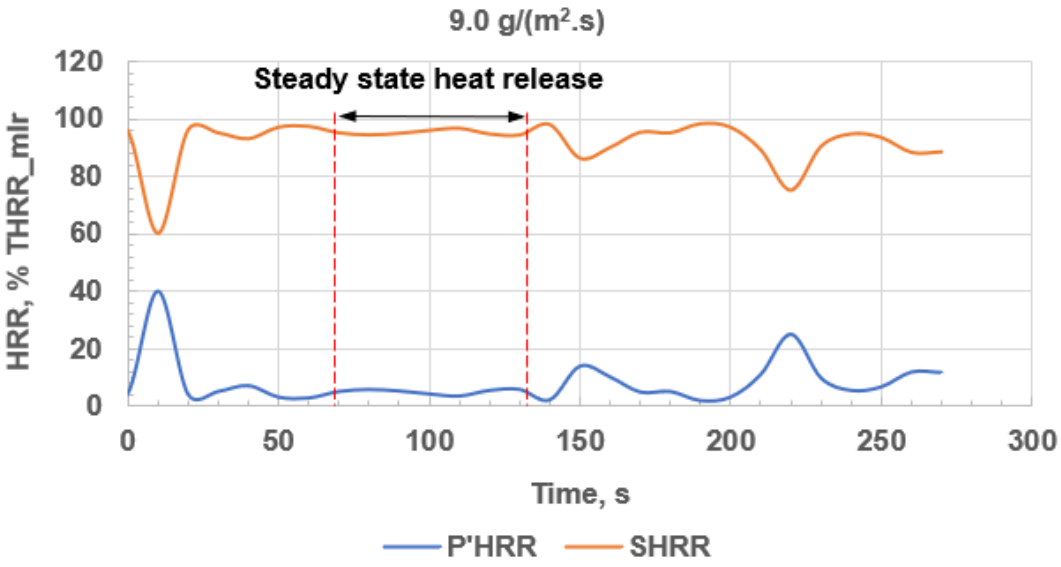

Figure 8.19 P'HRR and SHRR profiles for Ø=3.6

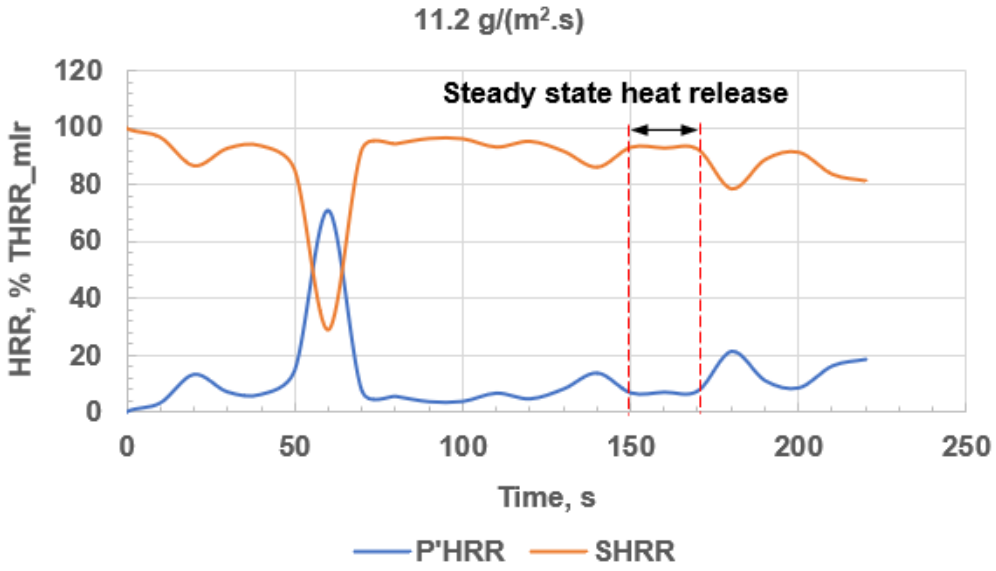

Figure 8.20 P'HRR and SHRR profiles for Ø=2.4

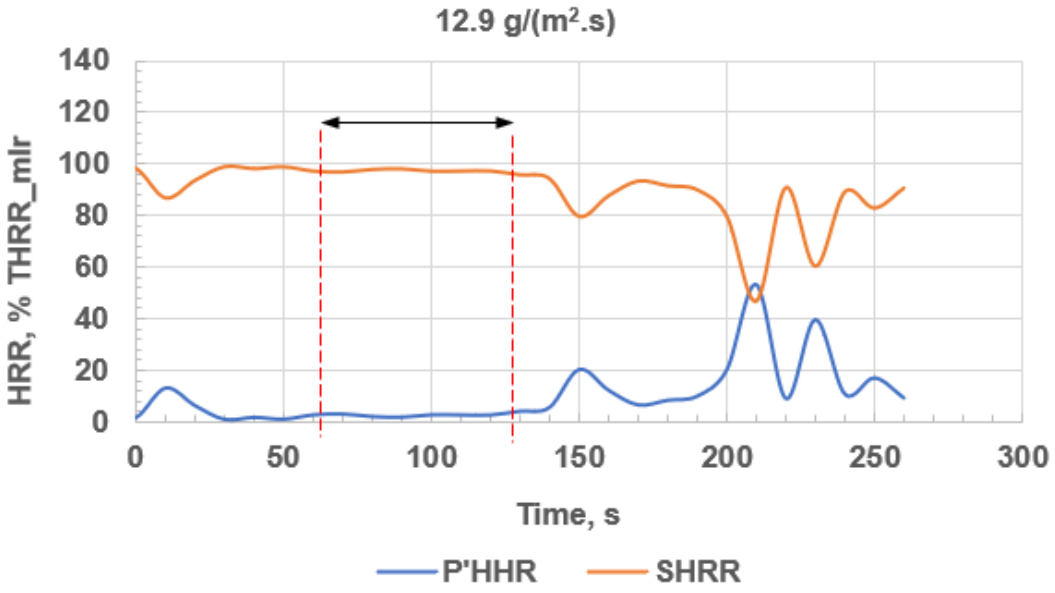

Figure 8.21 P'HRR and SHRR profiles for Ø=2.1

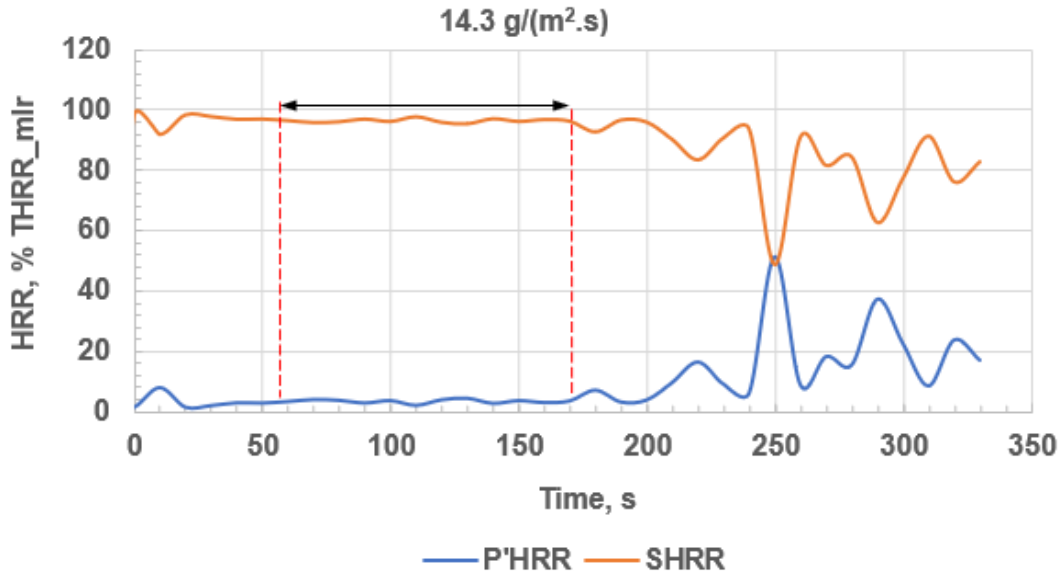

Figure 8.22 P'HRR and SHRR profiles for Ø=1.9

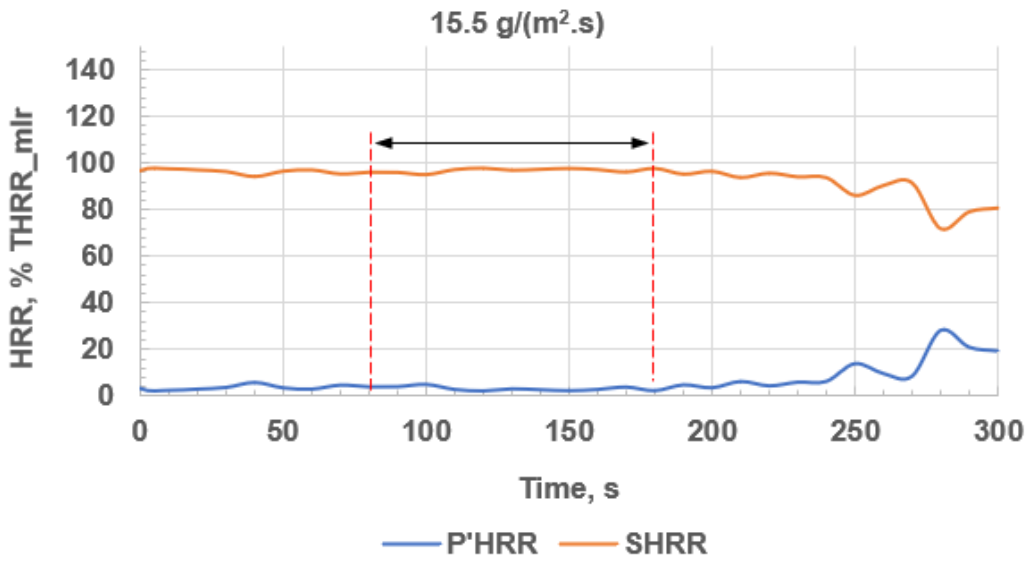

Figure 8.23 P'HRR and SHRR profiles for Ø=1.6

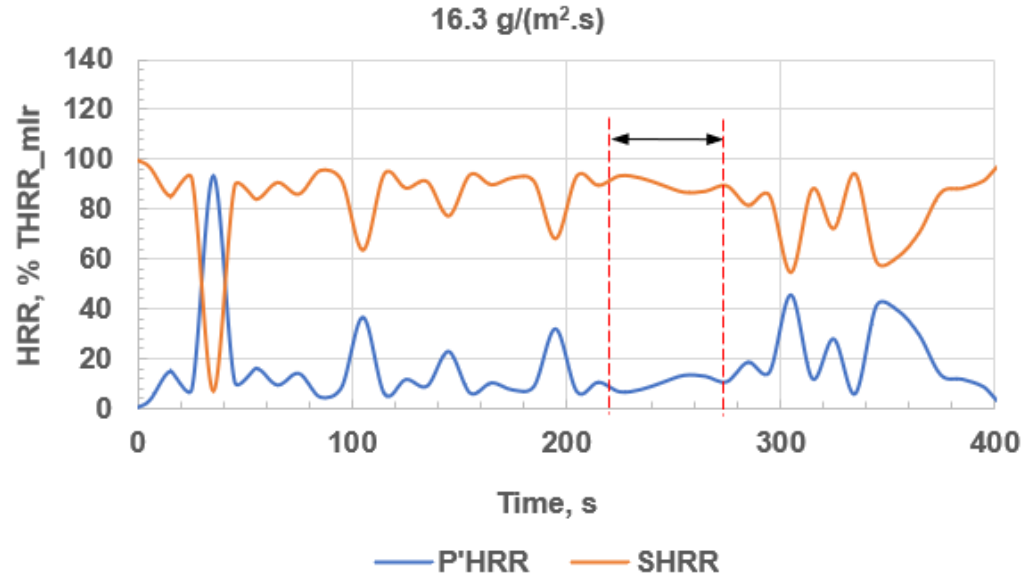

Figure 8.24 P'HRR and SHRR profiles for Ø=1.5

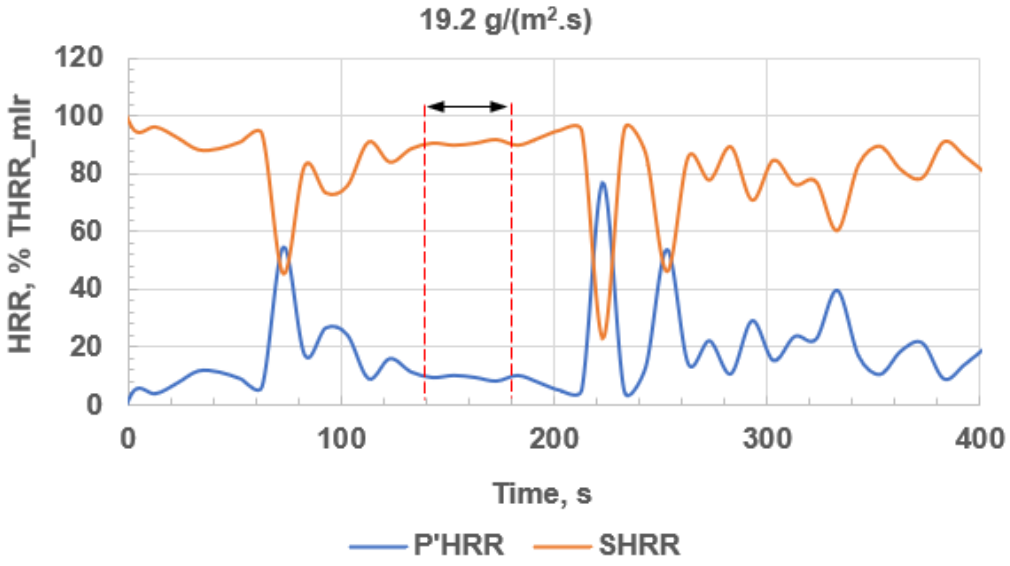

Figure 8.25 P'HRR and SHRR profiles for Ø=1.4

The Total Heat Release (THR) profiles for the sweet sorghum stalk residues at the tested conditions are displayed in Figure 8.26. The figure shows that the THR values for the gasification of the sweet sorghum stalk for equivalence ratios (Ø) between 1.6 and 2.1 were relatively high compared to the values of the THR at the other Ø values. This suggested that the optimum Ø for the gasification of the sweet sorghum stalk residue would be between 1.6 and 2.1.

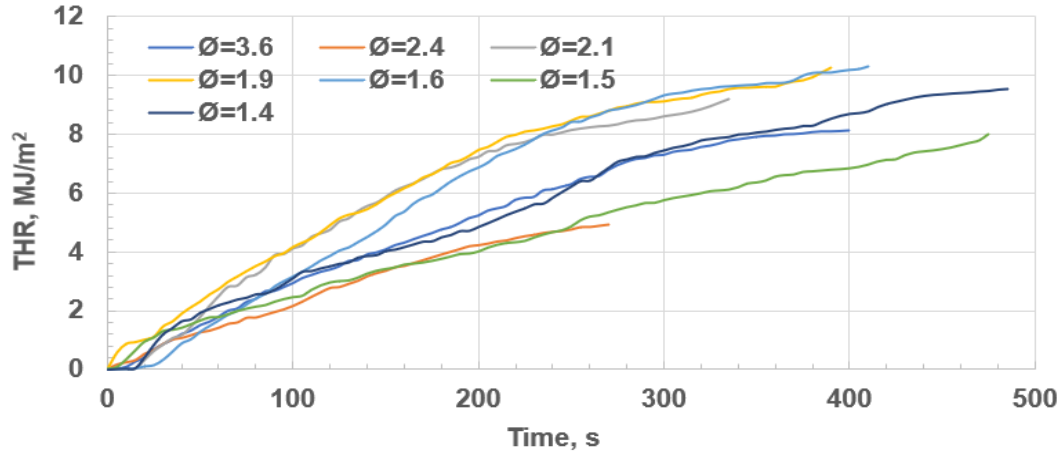

Figure 8.26 Total Heat Release (THR) profiles for sweet sorghum stalks

8.4 Evolution of CO and THC during the rich burning of sweet sorghum stalk

Figures 8.27 and 8.28 show the evolution of CO and THC gases from the gasification of the sweet sorghum stalk residues. The spikes in the concentration profiles that occurred within the first 50 s of the gasification were as a result of the rapid combustion of the test samples immediately after auto-ignition (Figure 8.13; stage A and Figure 8.14). The effect of complete combustion on the evolution of CO and THC gases is depicted in Figures 8.27 and 8.28 for the high air flow condition (Ø=1.4). As shown in the figures, the concentrations of CO and THC gases were lowest at Ø=1.4 during the flaming combustion phase of the gasification (70 s to 350 s). However, there was a transition from complete combustion to incomplete and smouldering combustion after 350 s due to the drastic drop in the level of the oxygen in the enclosure. The increase in the concentration of oxygen in the enclosure that boosted the flame (prior to flame out) led to the observed increase in the concentration of CO and THC gases in the last phase of the gasification at Ø=1.4. The second rise in the concentrations of the combustible gases observed in Figures 8.27 and 8.28 for the Ø=1.6, Ø=1.9, and Ø=2.1 test conditions was due to the increase in the rate of the gasification of the test sample after the initial rapid combustion stage.

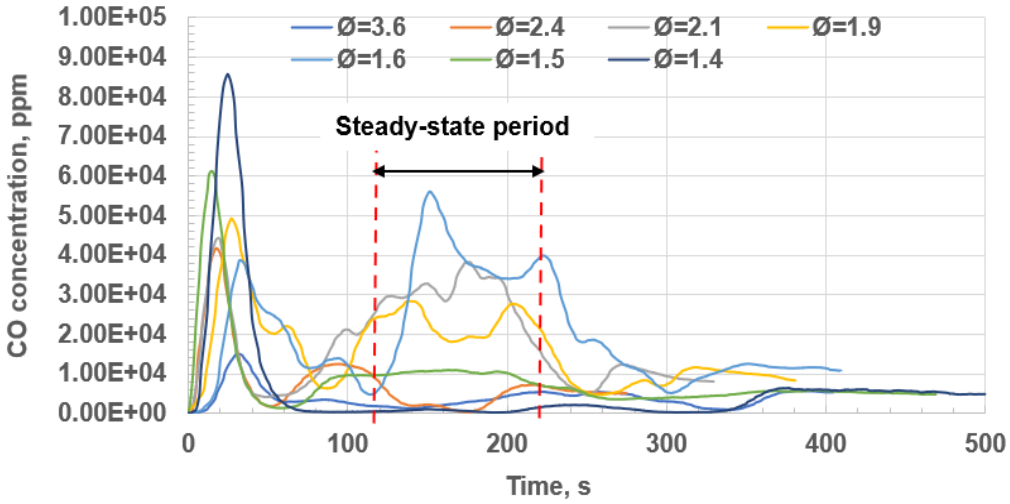

Figure 8.27 Evolution of CO from the primary stage of the gasification

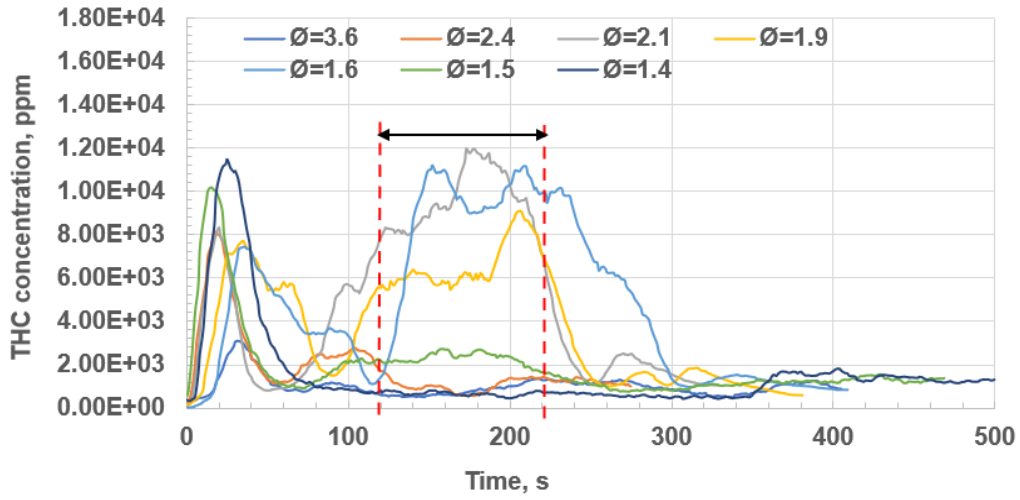

Figure 8.28 Evolution of THC from the primary stage of the gasification

8.5 Estimation of the optimum Ø for the gasification of sweet sorghum stalk residue

The yields of the combustible gases (CO, H_2, and THC) that were evolved during the gasification of the crop residue were averaged at steady state for the air fluxes that were tested. The THC yield was computed in terms of the methane (CH_4) equivalent of the emitted hydrocarbon gases. The estimated yields (in g/kg

biomass residue) as well as the flow rates of the combustible gases were plotted against the equivalence ratios as depicted in Figures 8.29 and 8.30 respectively.

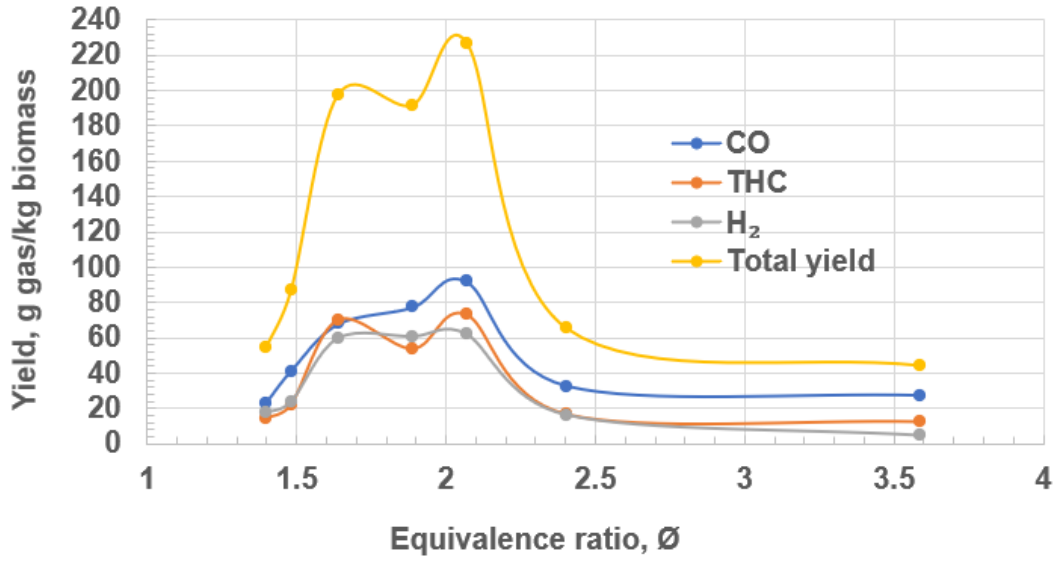

Figure 8.29 Yield of combustible gases from the gasification of sweet sorghum stalk residue

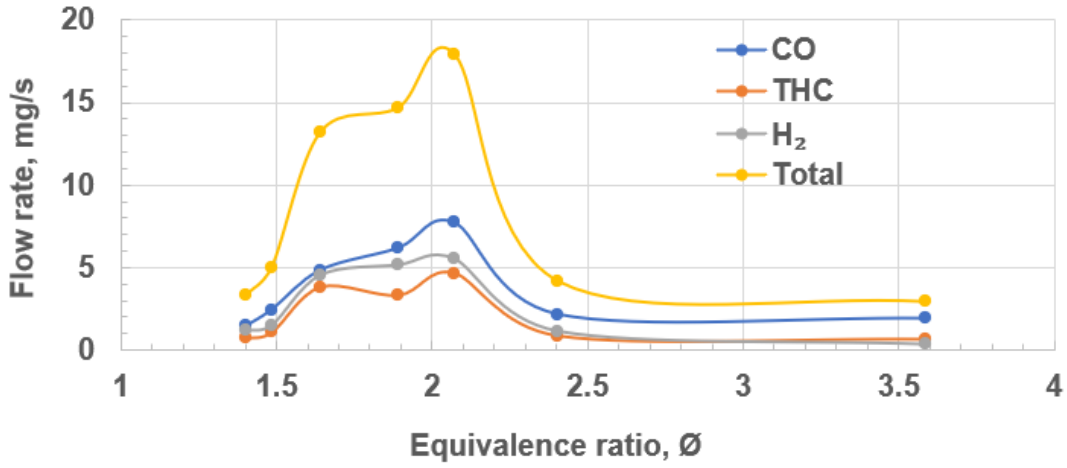

Figure 8.30 Flow rates of combustible gases from the gasification of sweet sorghum stalk residue

Figures 8.29 and 8.30 show that the maximum values for the yield and the flow rate of the combustible gases occurred at Ø=2.07 (≈2.1). The total yield of the combustible gases at the optimum condition was 227 g/kg biomass (Figure 8.29). The total hydrocarbons were an important part of the gas composition and energy

transfer. It is important to keep the outlet gases hot in transfer to an engine or burner so as to avoid condensation of the hydrocarbons and formation of tars. Many more traditional gasification systems have a poor HGE due to the loss of the tars, they see the tars as a problem not as an important part of the energy transfer from the biomass. The estimated optimum value of Ø (2.1) for the gasification of sweet sorghum stalk residue compared well to the value that was estimated for pine wood (2.8) by Irshad (2017) using the same equipment.

8.5.1 Comparison of the optimum gasification equivalence ratios for sweet sorghum, grain sorghum, and corn stalk residues

The optimum equivalence ratios (Ø) for the gasification of the stalk residues of grain sorghum and corn were also determined as shown in Figures 8.31 to 8.34.

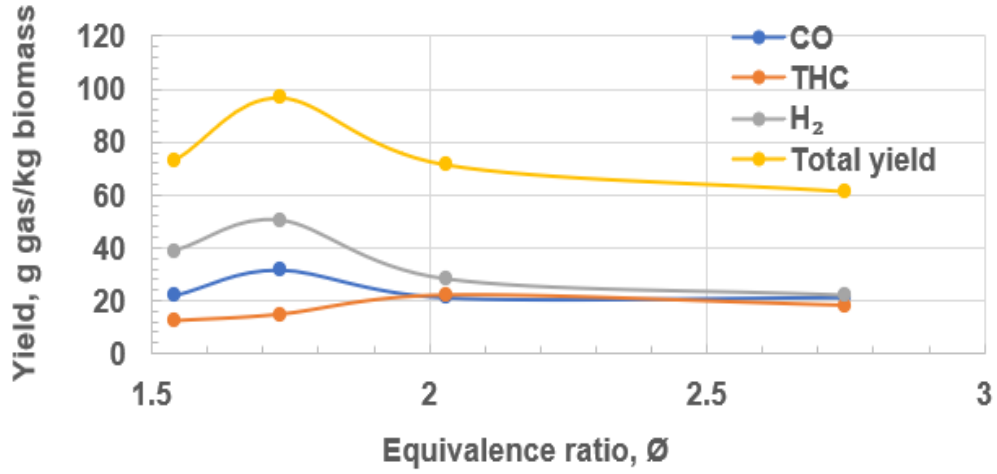

Figure 8.31 Yield of combustible gases (grain sorghum stalk)

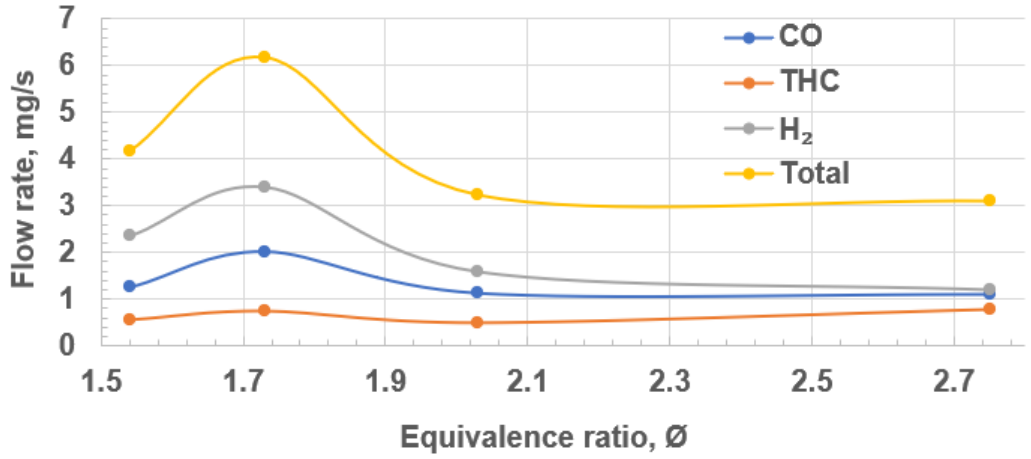

Figure 8.32 Mass flow rate of combustible gases (grain sorghum)

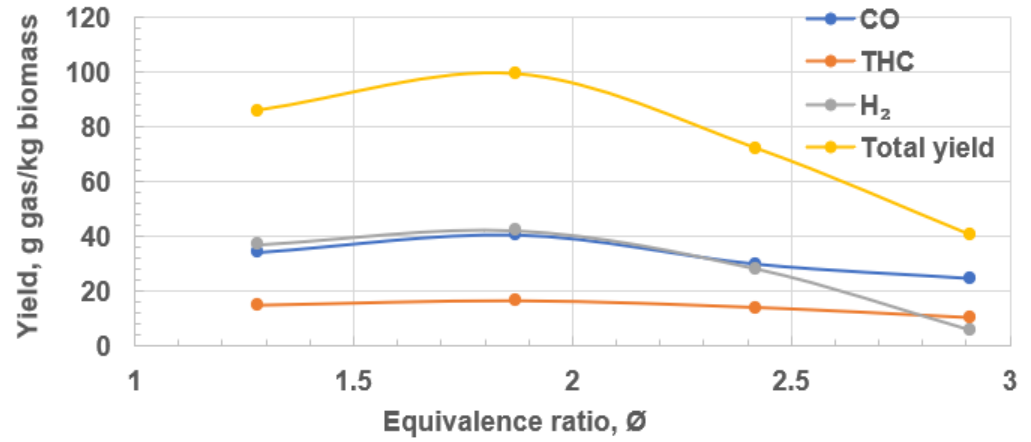

Figure 8.33 Yield of combustible gases (corn)

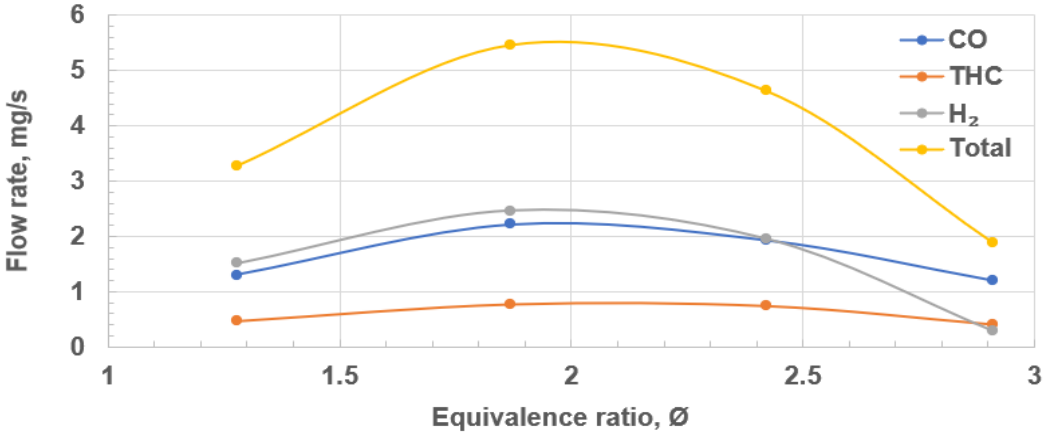

Figure 8.34 Mass flow rates of combustible gases (corn)

As shown in Figures 8.31 and 8.34, the determined optimum gasification Ø for grain sorghum and corn stalk residues were 1.7 and 1.9 respectively. These values also compared well to the estimated optimum gasification Ø for sweet sorghum biomass residue.

8.5.2 Investigation of the relationship between the Maximum Flue Temperature (MFT), Char Gasification Temperature (CGT), and equivalence ratio

The maximum temperature of the flue/chimney (MFT) and the steady state Char Gasification Temperature (CGT) for the tested air flows were determined from the flue (chimney) temperature profiles. The temperature profile of the chimney for the gasification of the sweet sorghum stalk residue for the 14.3 g/(m^2.s) air flow condition is shown in Figure 8.35. The MFT for the condition (401 ^oC) occurred 124 s after the start of the test while the flameout time was 312 s.

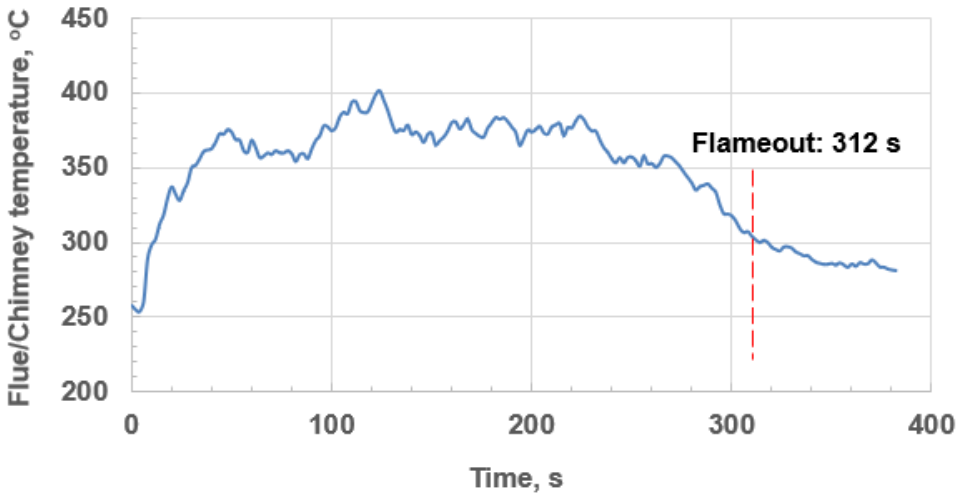

Figure 8.35 Flue (chimney) temperature profile for the gasification of sweet sorghum stalk residue at Ø=1.9

The MFT and the steady state CGT values were plotted against the equivalence ratios as shown in Figures 8.36 and 8.37 for the stalk residues of sweet sorghum, grain sorghum, and corn. Figures 8.36, 8.37, and Table 8.6 show that the MFT

and the maximum steady state CGT for the crop residues occurred at Ø values that were approximately equal to the estimated optimum equivalence ratios for the tested crop residues. Therefore, the optimum equivalence ratio can be achieved in the biomass gasifier (designed for automatic operation) through temperature control by adjusting the air flow to achieve the MFT for the biomass (Figure 8.36). (The gasifier that is intended for use in the rural areas can be designed for manual control of the air inlet.)

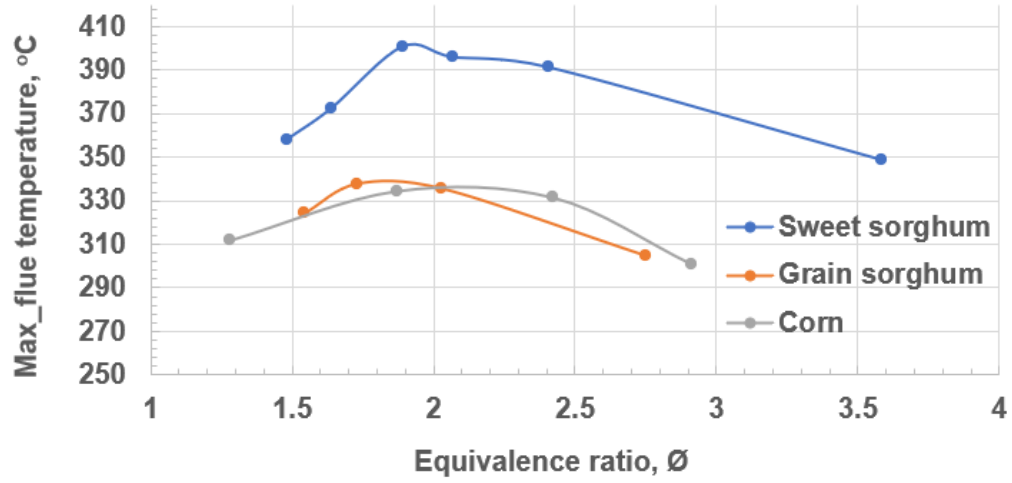

Figure 8.36 Relationship between the Maximum Flue Temperature (MFT) and equivalent ratio (Ø)

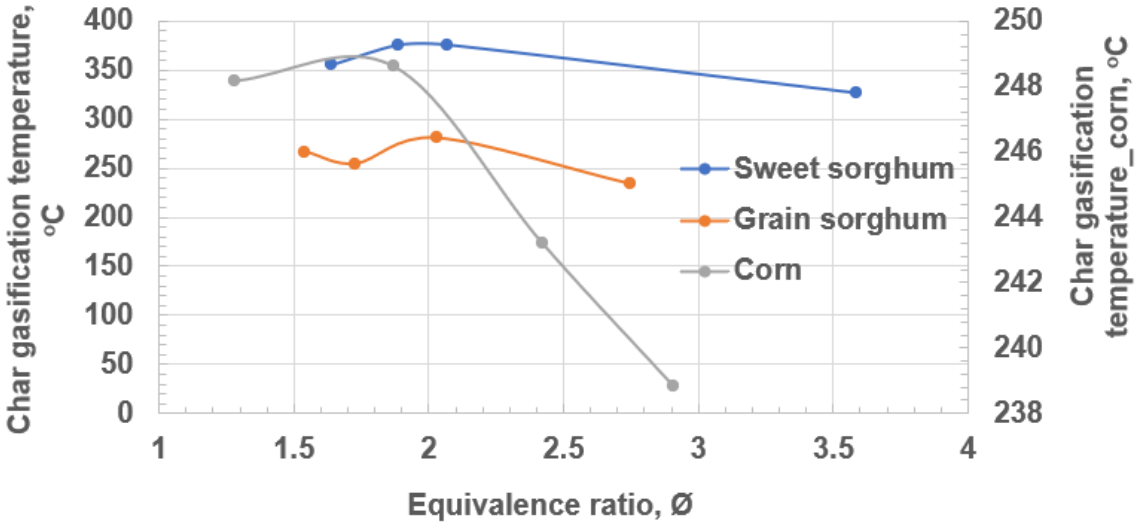

Figure 8.37 Relationship between the Char Gasification Temperature (CGT) and equivalence ratio (Ø)

Table 8.6 Relationship between the Maximum Flue Temperature (MFT), Char Gasification Temperature (CGT), and equivalence ratio

Biomass stalk residue	MFT, ºC	CGT, ºC	Optimum Ø	Ø at peak temperature	
				MFT	CGT
Sweet sorghum	401	375	2.1	1.9	1.9
Grain sorghum	340	280	1.7	1.7	2
Corn	337	249	1.9	2.2	1.8

Figures 8.36 and 8.37 and Table 8.6 show that the stalk residue of corn had the lowest MFT and CGT. The observed relatively low MFT and CGT for the stalk residue of corn compared to the other stalk residues can be attributed to the difference in the porosities of the residues. The porosity of the stalk residue of corn was the greatest of the three stalk residues that were gasified.

8.5.3 Char gasification

Char gasification in real gasifiers is a large contributor to the formation of syngas because of the relatively high carbon content of char compared to the original biomass. The calorific value of char is ~30 MJ/kg (Boley and Landers, 1969). The calorific value of char is about 1.67 times the calorific value of the original sweet sorghum stalk (~18 MJ/kg; Table 8.4). Therefore, if char is not efficiently gasified, the Cv of the syngas and the thermal efficiency of the gasifier will be low. It is therefore not advisable to minimise the gasification of char in practical/real application. Oxygen was depleted in the flue during the gasification as shown in Figure D.1 (Appendix D) for the 9.0 g/(m^2.s) condition. The figure also represents the profile of oxygen in the gasifier during the gasification. Phase C in Figure 8.13,

after 300 s had low CO and THC at all air ventilation rates (Figures 8.27 and 8.28), yet there was a significant but low mass loss rate, as shown in Figure 8.12. This is the char oxidation phase after all the volatiles have been gasified. There was an observable flame in this period, as shown in Figure 8.16. At the end of the char oxidation phase (Phase C), the flame was observed to go out, but smouldering combustion remained, as shown in Figure 8.16, as there was a continuing mass loss. The transition from gasification near zero oxygen rich oxidation to char oxidation was observed to occur after 350 s (Figure D.1). The increase in oxygen in the char oxidation region was because the air flow was kept constant notwithstanding the difference in the stoichiometric AFR of the char and the original biomass. If char is assumed to be pure carbon, then the stoichiometric AFR is 11.5/1 which is much higher than for the sweet sorghum biomass which was 4.6 (Table 8.4). For a constant air flow this means that the char oxidation rate would be lower than for the biomass by a factor of 2.5. Consequently, the char oxidation region became relatively lean as the concentration of oxygen increased under constant air flow. This is the key reason for the inefficient gasification of the char.

This change from biomass gasification to char oxidation had an influence on the gasifier exit temperature as shown in Figure 8.35, for the gasification at Ø=1.9. In the peak gasification phase from 120 to 220s (deduced from the CO and THC results, Figures 8.27 and 8.28), Figure 8.35 shows that the gasifier outlet temperature was constant at the average temperature of 380 ^{o}C or 657 K. This is a much lower temperature than the 800 – 900 ^{o}C used in many gasifiers (Ngo et al., 2011). After 220 s, the mass loss rate decreases due to the start of char oxidation in the surplus oxygen that occurs due to the change of stoichiometric AFR for char compared to the biomass. Char gasification requires relatively high

temperatures for efficient conversions (Moreira et al., 2021). Therefore, to gasify the resulting char efficiently, the temperature in Figure D.1 would be increased by reducing the air flow to produce rich char gasification conditions with near zero oxygen. This could be achieved in a practical application of batch gasification with the increase in oxygen signaling a requirement to reduce the air flow until the temperature increased and oxygen was near zero.

8.6 Cold Gas Efficiency (CGE) and Hot Gas Efficiency (HGE)

The Cold Gas Efficiency (CGE) and the Hot Gases Efficiency (HGE) of the investigated sweet sorghum stalk residue samples were estimated at the tested conditions from Equations 4.16 and 4.17. The CGE and HGE values were also estimated for the stalk residues of grain sorghum and corn. The estimated maximum CGE for sweet sorghum, grain sorghum, and corn stalk residues were 76.6, 46.1, and 40.7% respectively while the estimated maximum HGE for the biomass residues were 81.1, 52.1, and 45.9%. The estimated optimum CGE and HGE for sweet sorghum stalk residue (76.6 and 81.1%) compared well to corresponding values reported by Kirsanovs and Zandeckis (2015) (75.1 and 83.2%).

Figure 8.38 compares the estimated HGEs to the HGE for pine wood that was estimated by Irshad (2017). The estimated (maximum) HGE for sweet sorghum stalk residue in this work (81%) compared well to the HGE that was estimated for pine wood by Irshad (2017) (78%).

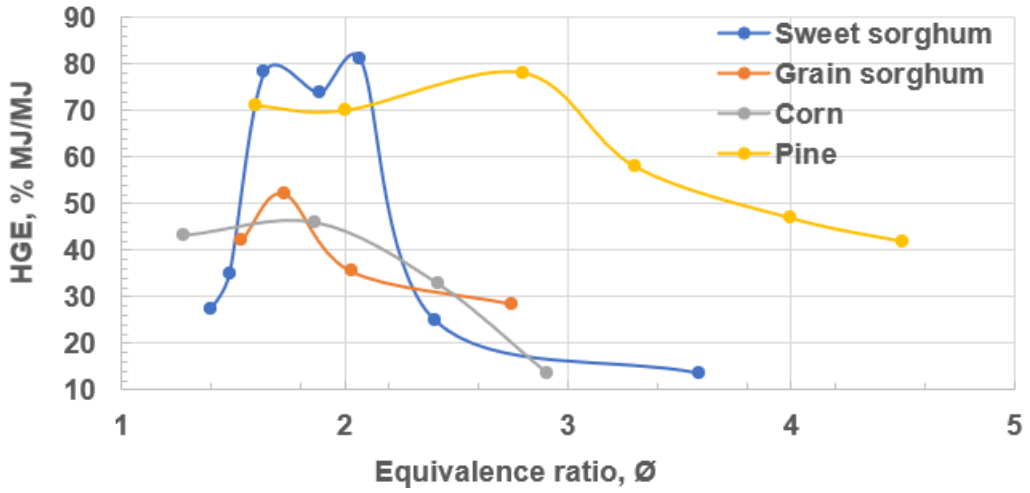

Figure 8.38 Comparison of the Hot Gases Efficiency (HGE) of sweet sorghum stalk residue to other biomasses

The combustible gases (CO, H_2, and THC) from the rich burning of the crop residues can be channeled into a dual-fuel, fuel-flexible, CI Gen-set that is operated in Reactivity Controlled Compression Ignition (RCCI) mode. RCCI operation involves the introduction of the combustible gases (syngas) into the cylinder of the engine through the air inlet port (Port Fuel Injection, PFI) while diesel is injected by Direct Injection (DI). They could also be used for process heat application by the addition of air at a flame stabiliser.

8.7 Particulate emissions from the gasification of sweet sorghum stalk residues

The Particle Matter (PM) distributions for the gasification of sweet sorghum stalk residues at the tested conditions were estimated from the measured Particle Number (PN) distributions. The PM distributions were estimated at steady state after the measured data were corrected for dilution.

8.7.1 Particle Number (PN) and Particle Matter (PM) distributions for the gasification of sweet sorghum stalk residue

Figures 8.39 to 8.45 depict the Particle Number (PN) and Particle Matter (PM) distribution for the tested conditions. The peak PN and peak PM were determined from the figures. Table 8.7 presents the peak PN and peak PM values for the tested conditions. Figures 8.39 to 8.45 and Table 8.7 show that the tested conditions had peaks in the nanoparticles range (Dp < 30 nm). Mustafa et al. (2019) used the restricted ventilation Cone calorimeter method to investigate the fire behaviour of Construction Pine wood at 19.2 g/(m^2.s) air flow and 35 kW/m^2 heat flux. The authors reported a peak PN concentration of 1x10^{10} /cc at particle diameter, Dp of 20 nm. Generally, the observed peak PN concentrations in this work for the gasification of the stalk residue of sweet sorghum were much lower than the concentration that was reported for pine wood. Altaher et al. (2015) reported a peak PN of 5x10^8 /cc at 30 nm for the combustion of biomass pellet. The peak PN that was reported by the authors falls within the reported range of peak PN concentrations for the gasification of sweet sorghum residue (7.2x10^6 - 7.8x10^8 /cc).

The peak PM concentrations and particle diameters (Dp) given in Table 8.7 were also the accumulation mode Dp and PM concentrations for the tested conditions. Multiple peaks were observed in the PM profiles for the 12.9, 14.3, 15.5, and 16.3 g/(m^2.s) conditions between 80 and 1,000 nm Dp. Apart from the peak PM shown in Table 8.7 (the maximum peak PM), the 12.9 and 14.3 g/(m^2.s) conditions exhibited PM peaks at 100 and 86.6 nm Dp respectively. The 15.5 g/(m^2.s) condition had two other peaks at 100 and 316.2 nm Dp while the other PM peaks for the 16.3 g/(m^2.s) condition occurred at 133.4 and 421.7 nm Dp (Figures 8.43 and 8.44). Gaegauf et al. (2001) reported that particles with Dp > 300 nm do not

contribute substantially to total PN emission rate. The authors' report is in agreement with the PN results in the current work as Figures 8.39 to 8.45 show that the prominent PN peaks of the investigated modes occurred when Dp was < 300 nm.

Mustafa et al. (2019) reported accumulation mode peak at 200 nm Dp which compared well to the observed accumulation mode Dp for the gasification of sweet sorghum stalk residue at 9, 11.2, and 19.2 g/(m^2.s) air flux conditions (Table 8.7). Generally, Figures 8.39 to 8.45, Tables 8.7 and 8.8 show that the peak PN resulted mostly from nanoparticles with Dp < 30 nm while the peak PM resulted from the fine particles. The fine particles are particles with Dp between 100 nm and 2.5 μm (Kittelson, 1998).

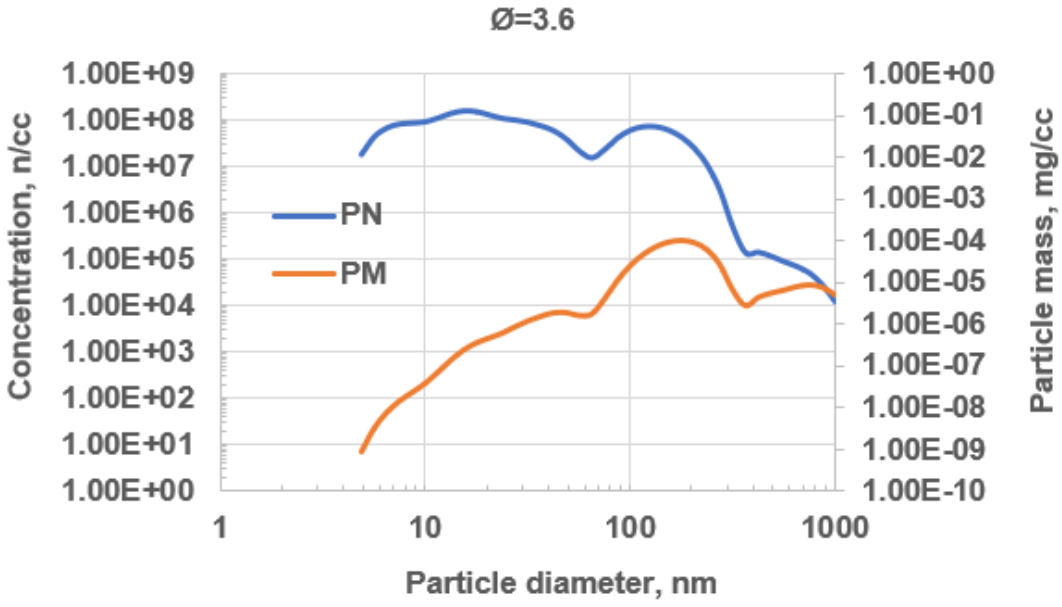

Figure 8.39 PN and PM concentrations for sweet sorghum stalk residue (9 g/(m2.s))

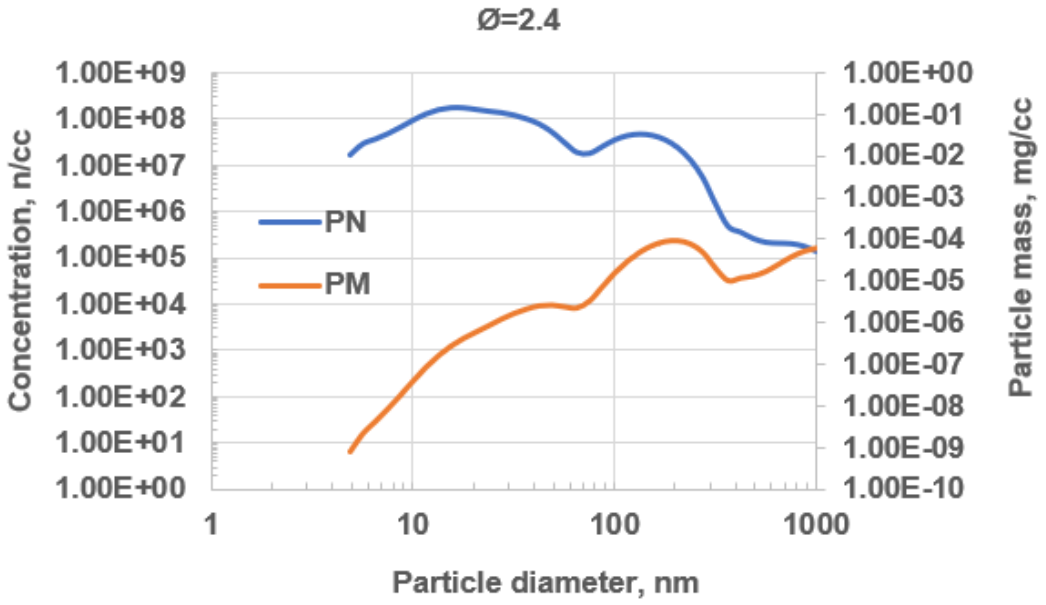

Figure 8.40 PN and PM concentrations for sweet sorghum stalk residue (11.2 g/(m2.s))

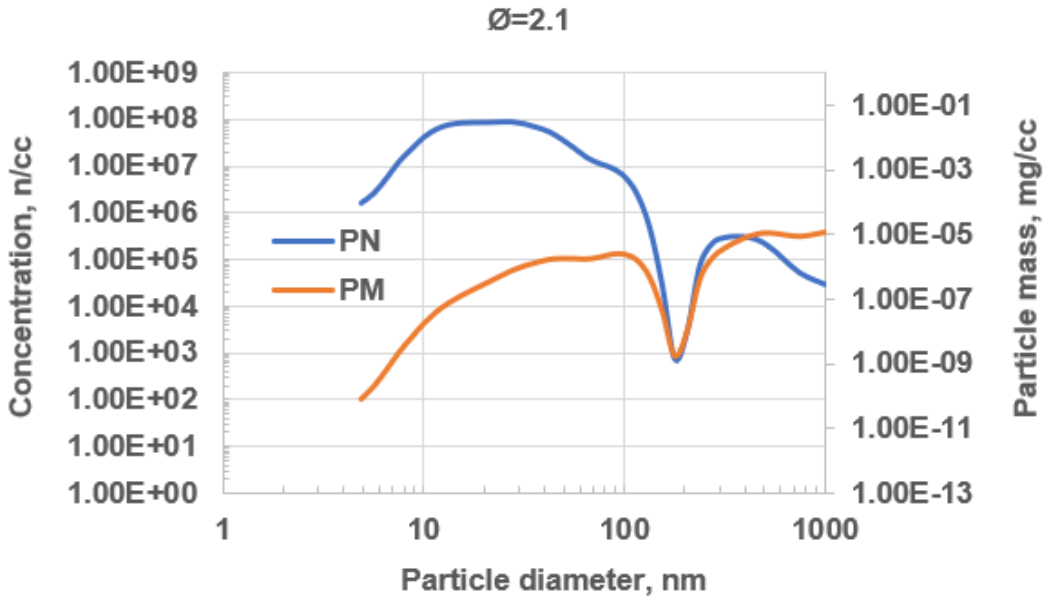

Figure 8.41 PN and PM concentrations for sweet sorghum stalk residue (12.9 g/(m2.s)

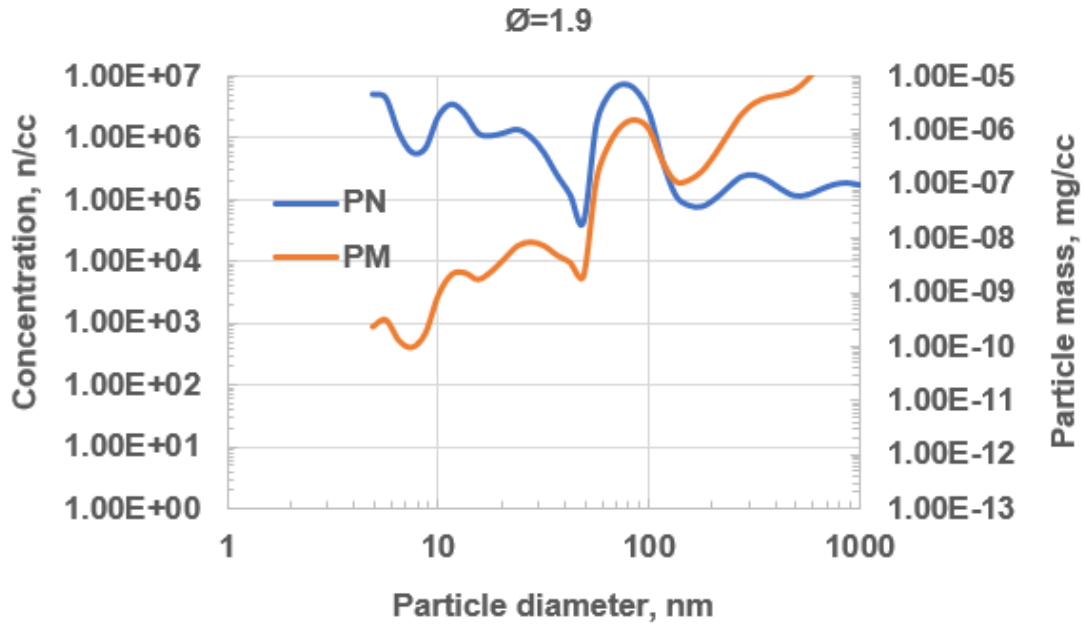

Figure 8.42 PN and PM concentration for sweet sorghum stalk residue (14.3 g/(m2.s))

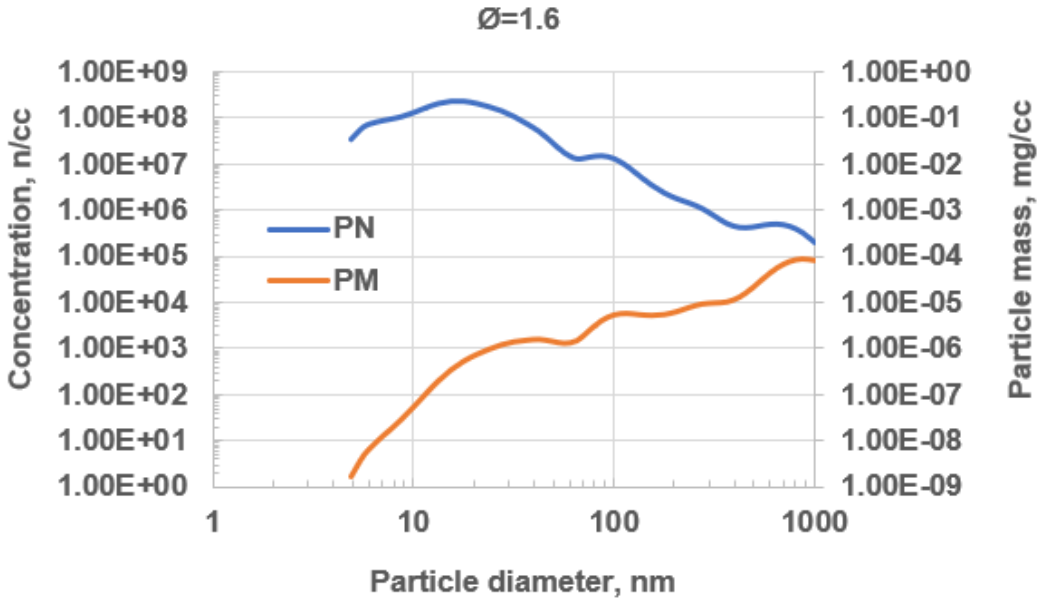

Figure 8.43 PN and PM concentrations for sweet sorghum stalk residue (15.5 g/(m2.s))

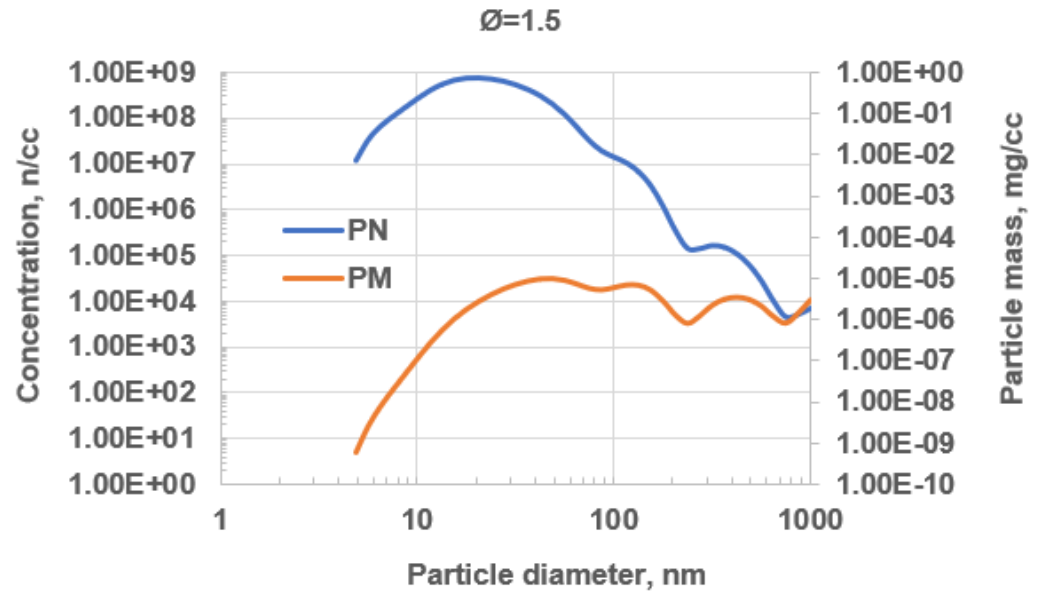

Figure 8.44 PN and PM concentrations for sweet sorghum stalk residue (16.3 g/(m2.s))

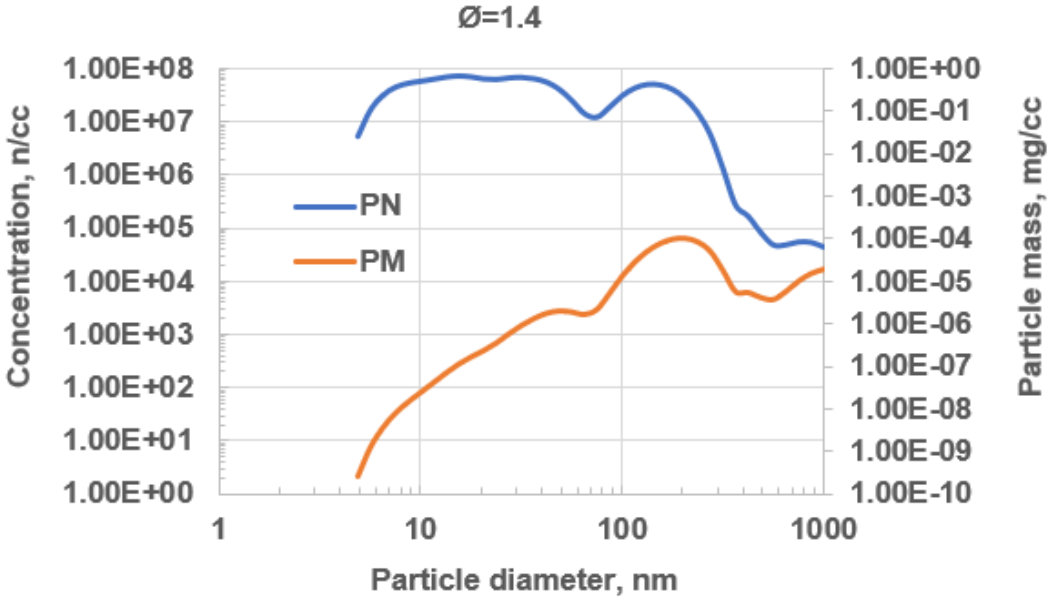

Figure 8.45 PN and PM concentrations for sweet sorghum stalk residue (19.2 g/(m2.s))

Table 8.7 Comparison of peak Particulate Number (PN) and peak Particulate Matter (PM) for the gasification of sweet sorghum stalk residue

Air flow, g/(m^2.s)	Ø	Peak PN		Peak PM	
		Dp, nm	Concentration, n/cc	Dp, nm	Concentration, mg/m^3
9.0	3.6	15.4	1.6x10^8	177.8	100
11.2	2.4	17.8	1.8x10^8	205.4	90
12.9	2.1	27.4	8.9x10^7	487	11
14.3	1.9	75	7.2x10^6	365.2	4.1
15.5	1.6	17.8	2.3x10^8	866	88
16.3	1.5	20.5	7.8x10^8	48.7	10
19.2	1.4	15.4	7.4x10^7	205.4	100

Figures 8.46 and 8.47 present the PN and PM distributions at the tested air flows. The figures show that the PN and PM distributions for the gasification conditions defined by Ø=2.1, Ø=1.9, and Ø=1.6 were relatively lower than the distributions for the other air flow conditions. The estimated optimum equivalence ratio (2.1) falls within the region of relatively low PN and PM emissions (Figures 8.46 and 8.47).

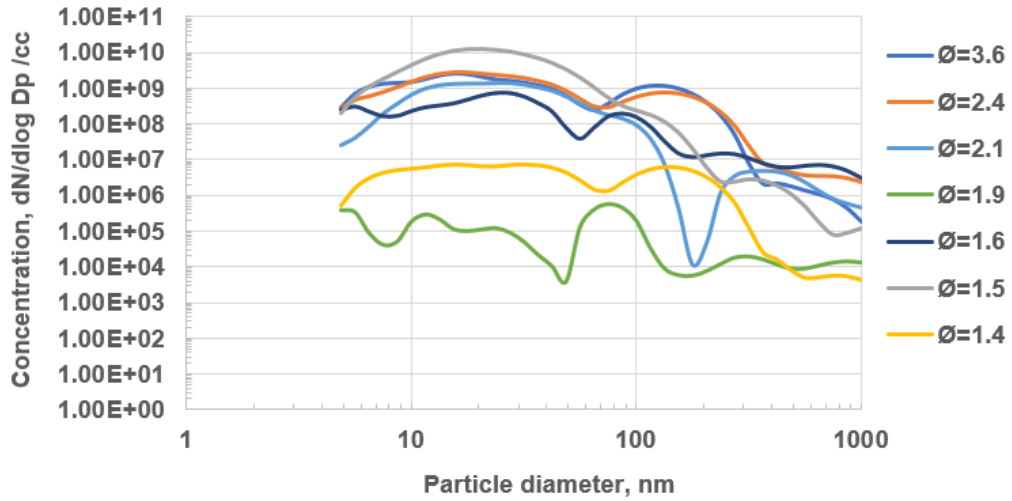

Figure 8.46 Comparison of PN emissions for the tested air flows

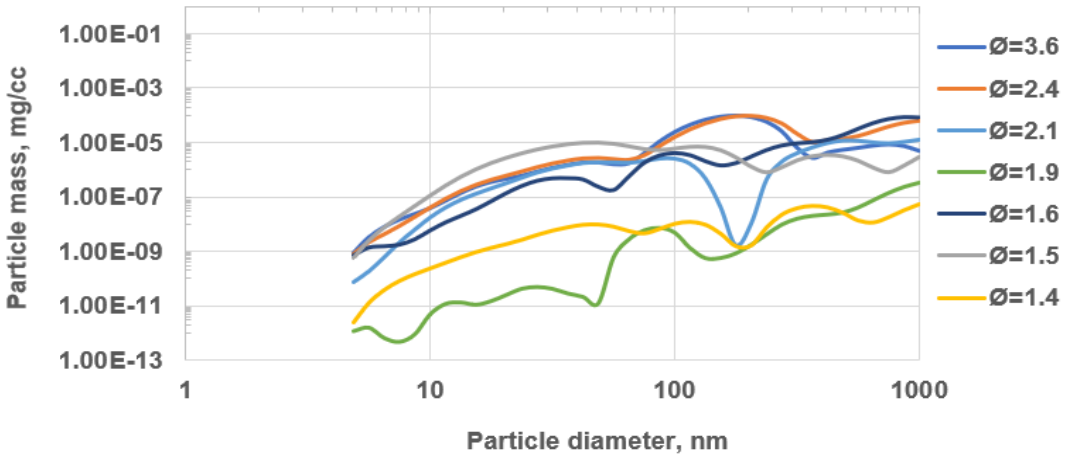

Figure 8.47 Comparison of PM emissions for the tested air flows

8.7.2 Particulate yield

The values for the particulate yield (in g particles/kg biomass residue) at the tested conditions for the gasification of the sweet sorghum stalk residue were estimated from the logged PN distributions. Figure 8.48 shows that the yield of particulates was lowest at the estimated optimum equivalence ratio (2.1).

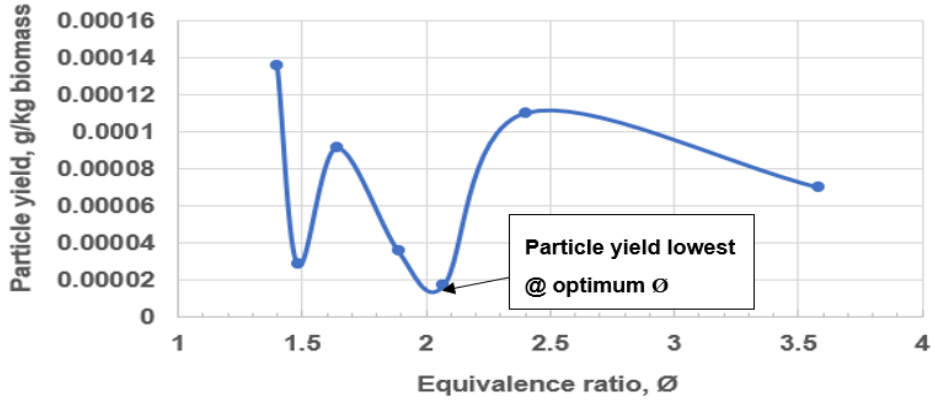

Figure 8.48 Particulate yield as a function of equivalence ratio for the gasification of sweet sorghum stalk residue

Johansson et al. (2004) reported PM emissions of 62 to 180 mg/m^3 for pellet burners. However, in the current work, the range of PM emissions for the rich burning of sweet sorghum stalk residue for the tested conditions was 104 to 730 mg/m^3. The particle emission in ventilation-controlled compartment fires was reported to be about 100 mg/m^3 for wood fires (Andrews et al., 2001). The reported particle emission in ventilation-controlled compartment fires for wood fires compared well to the particle emission of 104 mg/m^3 for the 12.9 g/(m^2.s) air flow condition in this work (the optimum condition). This comparison is a little unfair to the gasifier gases as in a burner application air would be added and a downstream flame achieved that would burn most of the particles from the gasification stage. Similarly for diesel engine applications the engine would consume the particles as apart from ash the particles will all burn.

8.7.3 Comparison of the particulate emission from sweet sorghum stalk residue to the particulate emission from 5.7 kW diesel Gen-set

Table 8.8 compares the particulate emissions from the gasification of the sweet sorghum stalk residues and the particulate emissions from the diesel Gen-set engine. The comparison in Table 8.8 was made because the syngas that aim of

gasifying the biomass residues was to produce syngas for use in diesel-syngas dual-fuel RCCI engines for electricity generation. It was shown in Chapter 7 that the engine-out particulate emissions from the 5.7 kW diesel Gen-set was quite significant. The previous section also shows that significant particulate emissions results from the gasification of biomass. Therefore, it was necessary to compare the particulate emissions from the two processes in order to discern the possible effect that syngas injection could have on the PN and PM emissions from a diesel-syngas dual-fuel RCCI engine.

Table 8.8 Comparison of particulate emissions from the gasification of sweet sorghum stalk and 5.7 kW Gen-set exhaust

Test	**PN concentration range, n/cc**	**Yield range, g/kg fuel**
Gasification of sweet sorghum stalk	$7.2 \times 10^{6} – 7.8 \times 10^{8}$	$1.7 \times 10^{-5} – 1.4 \times 10^{-4}$
Diesel Gen-set combustion	$4.4 \times 10^{6} – 8.9 \times 10^{7}$	$2.1 \times 10^{-3} – 3.1 \times 10^{-2}$

Table 8.8 shows that the maximum PN emission from the gasification of the stalk residue of sweet sorghum was a single order of magnitude greater than the observed maximum PN emission from the exhaust of the 5.7 kW diesel Gen-set. In both cases, the particle diameter at the upper limit of the PN emissions was 20.5 nm. On the other hand, the yield of the particles from the exhaust of the Gen-set was two orders of magnitude greater than the particulate yield from the gasification of the stalk residue of sweet sorghum.

The use of the combustible gases from the gasification of biomass residues in dual fuel, RCCI diesel Gen-sets can potentially increase the particulate emissions from the engines, but this assumes that none of the particles will be burnt in the engine combustion process, which is unlikely. This challenge can be overcome by incorporating Diesel Particulate Filters (DPF) in the engines.

8.8 NOx and NH_3 emissions during the gasification of the stalk residues of sweet sorghum, grain sorghum, and corn

Thermal NOx results from the reaction between the oxygen and the nitrogen in air at combustion temperatures greater than 1,800 K (Section 3.3.4.3). Biomass gasification temperatures are much lower than 1,800 K. Therefore, the gasification of biomass will not lead to thermal NOx. NOx also results from the reaction of Fuel Bound Nitrogen (FBN) with oxygen. If the emission levels for NO and NO_2 are high during the gasification of a biomass, then such NOx is generated from the FBN.

Liu and Gibbs (2003) modelled the emission of NH_3 from biomass in a circulating fluidised bed gasifier. The authors reported that the emission of NH_3 from the gasification of biomass decreased with increase in the gasification temperature, Ø, and biomass moisture content.

Table C.1 (Appendix C) presents the NO, NO_2, and NH_3 emission levels for the tested biomass residues and equivalence ratios. The average emission levels for NOx in ppm in the current work for the tested biomass stalks were 246, 146, and 173 (0.025, 0.015, and 0.017 vol%) respectively for the stalk residues of sweet sorghum, grain sorghum, and corn. The average emission levels for NH_3 for the stalk residues of sweet sorghum, grain sorghum, and corn were 18.12, 14.88, and 75.23 ppm respectively. These emission levels for NOx and NH_3 from the

tested biomass residues are relatively low. The NH_3 emissions in the current work did not show a particular trend with respect to the equivalence ratio, unlike the results of Liu and Gibbs (2003). This could be attributed to the gasification method that was used in the current work (fixed bed gasifier) which is different from the gasifier that was modelled in the work of the authors. The observed low levels of NOx and NH_3 emissions in this work for the tested residues suggests that rich combustion of biomass leads to the conversion of FBN into nitrogen gas rather than NOx or NH_3.

8.9 Implications of the experimental results on the design of the gasifier

The particulate emissions from the tested biomass residues were quite significant. Also, tar deposits were observed on the aluminum foil in the sample holder after the tests. Therefore, a natural, downdraught gasifier design is recommended. A downdraught gasifier will minimise the entrainment of tar in the flue gas thereby preventing the formation of tar deposits on the walls of the pipe and the cylinder of the Gen-set (Chapter 3; Section 3.6.3).

The objective of biomass gasification for electricity generation is to pipe the combustible gases generated during the rich-combustion of the biomass fuel into the Gen-set without the oxidation/secondary combustion of the syngas. Oxidation of syngas will occur within the gasifier if the temperature is sufficiently high. The pipe that links the gasifier to the Gen-set will be insulated to prevent excessive cooling of the syngas. Secondary combustion of syngas in the pipe/gasifier will reduce the combustible gases content and the Cv of the syngas. Excessive cooling on the other hand, will lead to the condensation of heavy hydrocarbon components in the flue gas, both of which are not desirable.

The yield of the syngas during the steady gasification period was observed to be a factor of five (5) higher than the yield during the char gasification stage. However, char gasification is a large contributor to the formation of syngas as explained in Section 8.5.3. For the gasifier to convert char to CO efficiently, it needs to operate richer with reduced air flow. Also, water injection helps the conversion of carbon to CO and hydrogen. For batch gasification of biomass, future work will investigate reducing the air flow in the char gasification stage and increasing the hydrogen yield with water injection into the residual char.

8.10 Preliminary design of the biomass gasifier

This section presents the preliminary design calculations as well as the sketch of the proposed manual, downdraught biomass residue gasifier. A manual gasifier/design has been chosen because the operational and maintenance procedures of an automated design will be too complex for the targeted localities in Nigeria. The capacity of the gasifier was estimated at the determined optimum conditions. The proposed design is based on the implications of the experimental results that were highlighted in Section 8.9.

8.10.1 Estimation of the Cv and viscosity of the syngas

The estimated Cv and viscosity of the syngas at the optimum gasification condition were 6.2 MJ/kg and 0.0000232 Pa.s respectively as shown in Tables 8.9 and 8.10. The estimated average molecular weight of the syngas on the other hand was 19.82 kg/kgmol.

Table 8.9 Estimation of the Cv of the syngas at optimum Ø

Species	**Composition @ Ø=2.1, vol%**	**Molar mass, kg/kmol**	**Mass, kg**	**Mass fraction, w/w**	**Cv, MJ/kg**
CO	3	28	0.84	0.042	10.1
H_2	27.8	2	0.556	0.028	141.97
THC	4	16	0.64	0.032	55.48
CO_2	9.8	44	4.312	0.218	-
H_2O	22.1	18	3.978	0.201	-
O_2	4.3	32	1.376	0.069	-
N_2	29	28	8.12	0.41	-
Total	100		19.822	1	
Cv of syngas = (0.042 x 10.1) + (0.028 x 141.97) + (0.032 x 55.48) = 6.202 MJ/kg					

Table 8.10 Estimation of the viscosity of the syngas at the optimum Ø

Species	**Mole fraction @ Ø=2.1**	**Viscosity @ 1 bar, 600 K, Pa.s**	**Reference**	**Mole fraction x viscosity, Pa.s**
CO	0.03	2.91×10^{-5}	(Liley et al., 1988)	8.73×10^{-7}
H_2	0.278	1.45×10^{-5}	(May et al., 2007)	4.03×10^{-6}
THC (as CH_4)	0.04	1.95×10^{-5}	(May et al., 2007)	7.8×10^{-7}

CO_2	0.098	2.8×10^{-5}	(Fenghour et al., 1998)	2.74×10^{-6}
H_2O	0.221	2.14×10^{-5}	(Huber et al., 2009)	4.73×10^{-6}
O_2	0.043	3.47×10^{-5}	(Lemmon and Jacobsen, 2004)	1.49×10^{-6}
N_2	0.29	2.96×10^{-5}	(Lemmon and Jacobsen, 2004)	8.58×10^{-6}
Total	1			2.32×10^{-5}

The reported compositions of syngas in volume % for CO, H_2, THC, CO_2, H_2O, and N_2 ranged from 11.5-27, 7.7-25, 1-8, 9-26, 4.1-23, and 35-53 respectively (Table 3.13). The composition of the syngas at the optimum condition of Ø in the current work (Table 8.9) falls within the reported range for THC, CO_2, and H_2O. The proportion of hydrogen (at the optimum Ø) for the syngas in the current work, on the other hand, is ~3% above the upper limit that was reported while the proportion of CO is relatively low compared to the reported values. The air-dried sweet sorghum stalk residues that were gasified were quite high in moisture content (Table 8.3). Therefore, the observed relatively high percentage of hydrogen and low percentage CO for the syngas in the current work can be attributed to a forward shift in the equilibrium of the water-gas shift reaction (Equation 4.16) due to the presence of steam in relatively high amount. The steam that is evolved is relatively high when the biomass feed is quite high in moisture. A forward shift in the equilibrium of the water-gas shift reaction favours the production of H_2 at the expense of CO. (The composition of the syngas that

was produced from diary biomass using a fixed bed, updraught gasifier (Table 3.13) confirms that the percentage of hydrogen in syngas is increased when steam is injected into the gasifier.)

8.10.2 Estimation of the capacity of the gasifier

The estimated total flow rate of the combustible species (CO, H_2, and THC) at the optimum gasification condition (Ø=2.1) was 18 mg/s (Figure 8.30). The estimated equivalent product gases flow rate was 180 mg/s (based on the measured concentrations of the inert species at the optimum Ø). The estimated total yield of the combustible gases (227 g/kg biomass; Figure 8.29) is equivalent to product gases yield of 2,270 g/kg biomass (2.27 kg product gases/kg biomass).

Table 8.11 summarises the analysis that was done to estimate the capacity of the proposed biomass (sweet sorghum stalk residue) gasifier. A typical diesel Gen-set in a tropical country like Nigeria will be required to power a deep freezer, a refrigerator, and a split-cooling system among other electronic devices. A 6 kW (6,000 J/s) Gen-set will suffice.

Table 8.11 Design parameters and constraints for the gasifier

Parameter	**Value**
Power of Gen-set, kW	6
Average BTE of the Gen-set, % (Figure 7.42)	~21
Estimated optimum total yield of syngas @ steady state, g/kg biomass	227

Cv of syngas, MJ/kg	6.2
Duration of operation of gasifier, hours/day	12

Table 8.12 Estimation of the capacity of the gasifier

Parameter	**Calculation**
Capacity of the gasifier (Basis: 1 second)	180 mg of syngas generates: 180x6.2=1,116 J 6,000 J requires: 6,000x0.18/1,116=0.97 g of syngas @ optimum syngas yield of 2,270 g/kg biomass, sweet sorghum biomass required per second=0.97/2,270=0.00042 kg=0.42 g biomass Biomass gasification rate per day for 12 hours operation: (0.42x12x3,600)/1,000=18 kg biomass/day The capacity of the gasifier (@ 21% Gen-set BTE): 18x100/21=86 kg biomass/day
Syngas pipe diameter	Diameter of combustion zone of gasifier set at: 0.8 m Cross-sectional area of combustion zone: 0.5 m^2 Atmospheric pressure assumed for the throttle box, p_2=101,325 Pa, p_1 = pressure of syngas at the outlet of the gasifier Experimental flue flow rate: 106 cm^3/s (for 100 cm^2 exposed sample area) Estimated gasifier flue flow rate for 0.5 m^2 heat transfer area, Q: 0.5x106/(0.01x1,000,000)=0.0053 m^3/s

	Viscosity of the syngas, μ corrected to the chimney temperature 362 ^{o}C (635 K) at optimum Ø: 0.0000232x632/600=0.000025 Pa.s Specified length of pipe, L: 3 m Diameter of pipe, D: 0.04 m Poiseuille's equation: $\Delta p = p_1 - p_2 = 128\mu LQ/(\pi D^4)$ $\Delta p = 128 \times 0.000025 \times 3 \times 0.0053/(3.142 \times 0.04^4) = 6.36\ Pa$ (Δp is positive; therefore, the specified syngas pipe diameter of 0.04 m can be used)

8.10.3 Conceptual design of biomass gasifier

Figure 8.49 shows the conceptual design of the gasifier. The proposed design was based on the considerations, objectives, and constraints highlighted in Section 8.9 and Table 8.12.

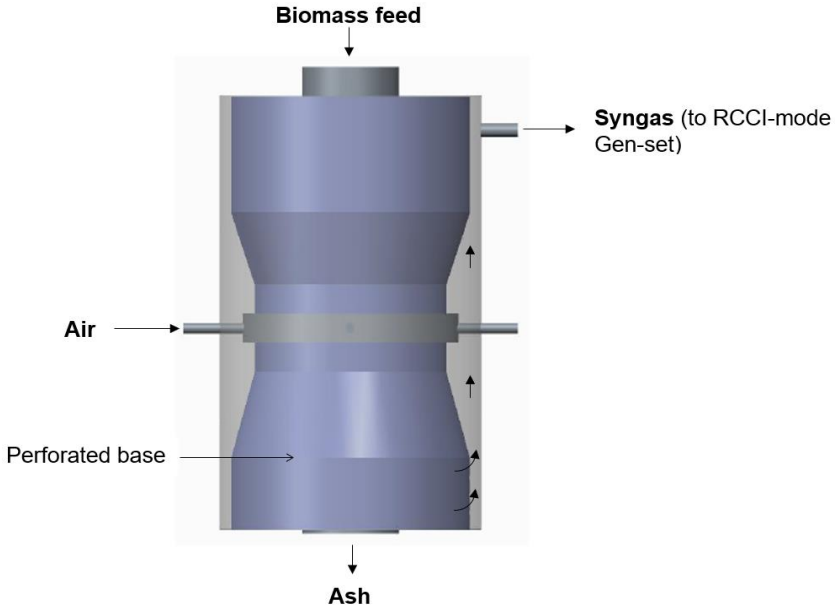

Figure 8.49 Conceptual design of 86 kg biomass/day natural, downdraught biomass gasifier

The major parts of the gasifier are depicted in Figure 8.49. The stalk residues will be fed into the gasifier from the top as shown in the figure. Air will flow into the combustion zone by suction (natural draught) via the four air intake pipes. The syngas rises from the perforations at the base of the gasifier and exits through the top of the gasifier to the RCCI-mode Gen-set. The ash that is formed, on the other hand, will drop by gravity through the perforated base (plate).

The estimated capacity of the gasifier is based on the estimated (average) BTE of the 5.7 kW Gen-set engine (21%) in Chapter 7. As recommended in Chapter 7, the use of a diesel Gen-set with a larger capacity (displacement) than the 5.7 kW engine that was used in the current work will increase the BTE by minimising the impingement of fuel on the walls of the cylinder. The use of a Gen-set with a relatively high BTE will in turn reduce the amount of biomass that is required per day for the gasifier. A cluster of three or four households in the targeted localities in Nigeria can possibly buy a larger capacity Gen-set which will have a higher BTE than the 5.7 kW Gen-set engine that was used in the investigation. The gasifier will be coupled to the Gen-set (in RCCI mode) through a throttle box to generate electricity for the households. The flow of syngas into the engine shall be by engine suction as indicated by the throttle box between the gasifier and the Gen-set (Figure 8.50).

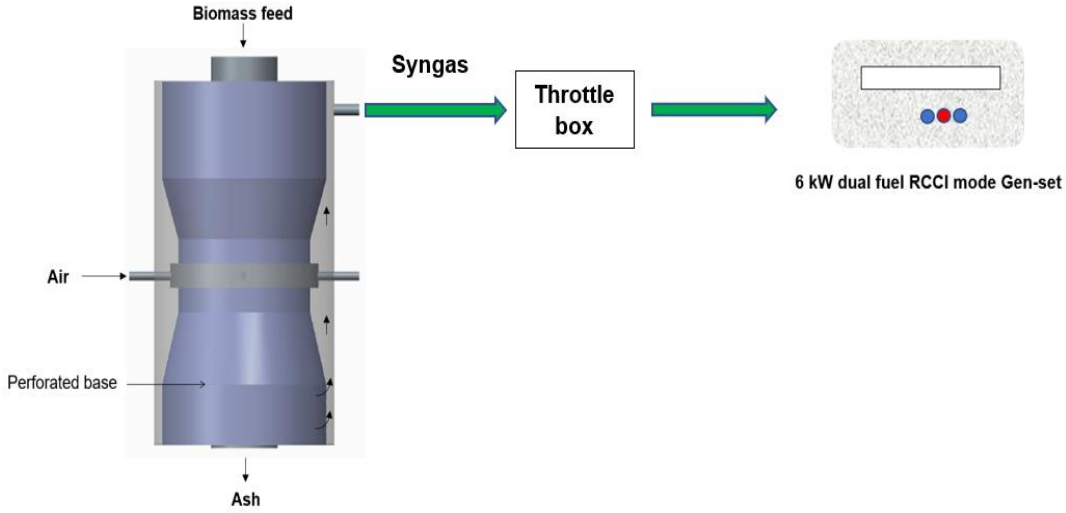

Figure 8.50 Proposed scheme for the generation of electricity from the gasification of sweet sorghum stalk residue

The major dimensions of the gasifier are depicted in the engineering drawing in Figure 8.51. The four (4) air intake pipes have a diameter of 30 mm.

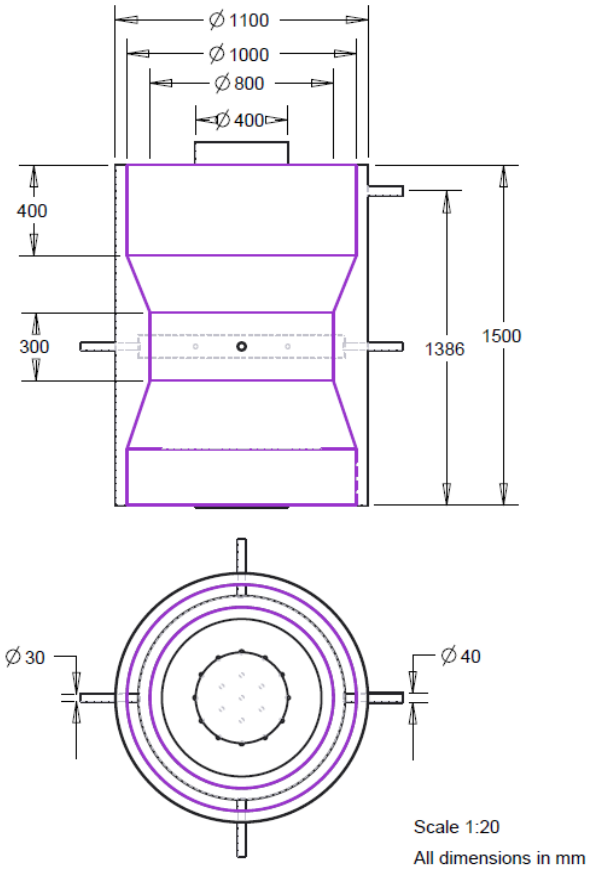

Figure 8.51 Engineering drawing of the proposed biomass gasifier

8.10.4 Estimation of the gasifier intake air area for manual operation

The open area of air intake will differ at the start of the combustion during the first stage of the gasification (relatively lean combustion) and during the gasification stage (rich combustion). The four air intake pipes will be opened at start up. However, after the ignition of the biomass feed, some of the air intake pipes will be closed to achieve the optimum gasification air flux (for the manually operated gasifier). The air intake velocity of the gasifier at the start of the combustion (v_{as}) as well as at the optimum gasification condition (v_{ag}) were estimated from Equation 4.18. v_{as} and v_{ag} were estimated as ~3.94 m/s and ~3.73 m/s respectively. The estimated value of the stoichiometric air flux, Af_s from Equation 4.19 was 26.68 g/m^2.s.

The volumetric intake air flow rates were estimated under near-stoichiometric and optimum gasification conditions from the air fluxes as 0.0111 m^3/s and 0.0054 m^3/s respectively. The initial (pre-gasification) and final (optimum gasification) air intake areas were calculated from the estimated volumetric intake air flow rates and velocities as 0.0028 m^2 and 0.0014 m^2 respectively. The estimated intake air area for optimum gasification can be achieved in the proposed gasifier design by closing two of the four air intake pipes after the biomass ignition stage.

The details of the estimation of the initial and the final air intake areas for the proposed gasifier are summarised in Table 8.13.

Table 8.13 Estimation of the initial and the final air intake areas for the proposed gasifier

Parameter	Value	Comments
Air density @ 0 ^{o}C, kg/m^3	1.293	
Gen-set air intake pressure, bar	1.31	

Sweet sorghum stoichiometric AFR	4.57	
Biomass feed requirement, kg/day	86	
Optimum gasification Ø	2.1	
Optimum gasification AFR_actual	2.21	
Optimum gasification air flux, $g/m^2.s$	12.9	
Acceleration due to gravity, m/s^2	9.81	
Darcy-Weisbach friction coefficient	0.019	
Summation of minor loss coefficients	1	Assumed
d_h (hydraulic diameter of duct), m	0.2	Gasifier treated as an (irregular) annulus; d_h is difference between outside diameter and inside diameter (average)
Duct length, m	~1.4	Distance from base of the gasifier to the syngas outlet
Distance between air inlet and syngas outlet, m	0.69	

T1 (maximum chimney temperature @ optimum Ø), ^{o}C	401	674 K
T2 (average temperature during gasification), ^{o}C	362	635 K
Ambient temperature, ^{o}C	20	293
Density of air @ T1, kg/m^3	0.5237	
Density of air @ T2, kg/m^3	0.5559	
Density of inlet air, kg/m^3	1.205	
Stoichiometric air flux, g/m^2.s	26.68	Equation 4.21
Excess air flux, g/m^2.s	32.01	Assuming 20% excess air
Cross-sectional area of gasifier feed bed, m^2	0.5	Cross-sectional area of combustion zone
Inlet air flow rate at start up, m^3/s	0.0111	
Inlet air flow rate (gasification), m^3/s	0.0054	
Natural draught air velocity_pre-gasification, m/s	~3.94	Equation 4.20
Natural draught air velocity_ gasification, m/s	~3.73	Equation 4.20
Open inlet air area at start up, m^2	0.0028	All inlet pipes (30 mm diameter) will be open

Open inlet air area during gasification, m^2	0.0014	Equivalent to two (preferably opposite) inlet pipes open

8.11 Conclusion

The results for the fire behaviour of sweet sorghum, grain sorghum, and corn stalk residues under restricted ventilation conditions (rich combustion) were presented in this Chapter. The gasification of the biomass residues was carried out on the Cone calorimeter. The restricted ventilation Cone calorimeter method was used to carry out the experiment.

The optimum equivalence ratio (Ø) values for sweet sorghum, grain sorghum, and corn stalk residues were 2.1, 1.7, and 1.9 respectively. The optimum Ø value for sweet sorghum stalk residue compared well to the value that was reported for pine wood (2.8).

The estimated optimum CGEs for sweet sorghum, grain sorghum, and corn stalk residues were 76.6%, 46.1%, and 40.7% respectively while the estimated optimum HGEs for the biomass residues were 81.1%, 52.1%, and 45.9% respectively. The optimum HGE for pine wood, using the same equipment, was 78%. The particulate yield of sweet sorghum stalk residue was found to be a minimum at the optimum gasification air flux condition (12.9 $g/m^2.s$).

The maximum PN emission from the gasification of the stalk residue of sweet sorghum was a single order of magnitude greater than the observed maximum PN emission from the exhaust of the 5.7 kW modern technology Yanmar diesel Gen-set. In both cases, the particle diameter at the upper limit of the PN emissions was 20.5 nm.

The yield of particulates from the exhaust of the Gen-set, on the other hand, was two orders of magnitude greater than the particulate yield from the gasification of the stalk residue of sweet sorghum.

The estimated capacity of the proposed natural, downdraught gasifier that was designed for the gasification of sweet sorghum stalk residues for 12 hours steady-state production of syngas was 86 kg biomass/day. The estimated capacity was based on the estimated average BTE of the 5.7 kW Gen-set (21%).

The use of a Gen-set with a relatively high BTE will reduce the biomass feed requirement of the proposed gasifier. A cluster of three or four households in the targeted localities in Nigeria can possibly buy a larger capacity Gen-set which will have a higher BTE than the 5.7 kW Gen-set engine that was used in the current work. The gasifier can be coupled to the Gen-set (in RCCI operation mode) to generate electricity for the households.

Chapter 9 Conclusions and future work

9.1 Conclusions

The significant findings from the four (4) components of the current work are presented:

i) resources assessment,

ii) alcohol fuel blends stability test,

iii) diesel engine combustion test, and

iv) energy recovery from Sweet sorghum stalk residue/biomass gasification.

9.2 Resources assessment

This work's resources assessment showed that, if properly harnessed, Nigeria's biomass resources (200 billion kg/year) can generate sufficient bioenergy to reduce the pump price of petroleum products in the country as well as stabilise the power sector. Furthermore, the country has the potential to become an exporter of bioethanol, as its estimated potential annual yield of bioethanol from sweet sorghum is 10.1 billion litres. The nation's estimated potential annual yield of bioethanol is 47% of the country's projected total demand for gasoline and diesel (21.6 billion litres) in 2020. The co-production of bioethanol from other agricultural crops such as cassava (which is cultivated in large quantities in Nigeria) will further boost the bioethanol potential of the country and position the country as a major producer and exporter of the biofuel. The combustion of biofuels produce relatively low CO_2 emissions compared to fossil fuels such as diesel. Therefore, the extended use of biofuels in Nigeria, based on its own crops, is its best route to the decarbonisation of transport. There would also be considerable export potential.

9.3 Diesel-ethanol (DE) fuel blends stability

The current work has shown that at room temperature (20 ^{o}C), diesel-ethanol (DE) fuel blends that contain up to 20% of anhydrous ethanol and > 70% of anhydrous ethanol are perfectly stable. The blend wall of pure ethanol in diesel at 20 ^{o}C (25 to 70% pure ethanol by volume) implies that (at equilibrium) the concentration of pure ethanol in the diesel (lower) phase of the unstable DE blends is less than 25% while the concentration of pure ethanol in the ethanol (upper) phase of the unstable blends is >70%. Each of the separated phases in the unstable DE blends was homogeneous at equilibrium (Chapter 5).

The unstable DE fuel blends (those that have ethanol concentration between 20 and 75% can be stabilised (made to become homogeneous) either by the addition of stabilisers/co-solvents or by subjecting them to temperatures above 20 ^{o}C. Temperature-stabilisation of the DE fuel blends that phase-separated at 20 ^{o}C for diesel applications is most feasible in tropical countries like Nigeria, where the average ambient temperature is 28 ^{o}C (such as the tropical rain forest region). Typically, temperature-stabilisation is most feasible for DE70 (which has a stabilisation temperature of 25 ^{o}C). DE25 and DE60 both became a clear, single phase at 33 ^{o}C. Temperature-stabilisation becomes feasible for DE25 and DE60 in the tropics when the temperature is fairly stable at 35 ^{o}C. 30, 40, and 50% anhydrous ethanol in diesel (DE30, DE40, and DE50) have relatively high temperatures of stabilisation (36 ^{o}C, 38 ^{o}C, and 36 ^{o}C respectively). As such, blend stabilisation by the use of additives or co-solvents such as biodiesel will be more feasible for DE30, DE40, and DE50. Thus, very large proportions of ethanol in diesel can be used in Nigeria, which is not the case for countries with low ambient temperatures in winter such as the UK and most of Europe.

9.4 IVECO diesel engine combustion test

The diesel baseline tests on particle size analysis showed that the Diesel Particulate Filter (DPF) trapped the particles that were emitted from the engine with an overall efficiency of 99.9%, which solves the nano-particle emissions problem. Unfortunately, because of a fault on the engine fuel injectors that could not be solved, diesel-ethanol (DE) blends combustion tests were not carried out on the EURO V, Multiple Fuel Injection Strategy (MFIS), IVECO diesel engine This aspect of the work was completed on the modern Yanmar diesel Gen-set engine.

The HRR analysis that was carried out in the current work using the Leeds HRR model, showed that λ has a significant impact on the accuracy of the HRR model of Compression Ignition (CI) engines. The Leeds HRR model predicted the fuel consumption of the MFIS IVECO diesel engine for pure diesel with an average error of 1.41% while the average error in the fuel mass predictions of the other models which were based on $\gamma(T)$ ranged from 15.85% to 16.36%. The Leeds HRR model was also applied to alternative diesels: Gas-to-Liquid (GTL) and Hydrotreated Vegetable Oil (HVO) diesels. The model predicted the fuel consumption of the MFIS IVECO diesel engine for pure diesel, GTL, and HVO diesels with an overall average error of 4.86% compared to the measured fuel consumption. The average error in the fuel mass predictions of the other models which were based on $\gamma(T)$ ranged from 15 to 20%. The errors in the predictions of the other models were high because λ was neglected in the models.

The two novel graphical techniques that were used to estimate the rate of evaporation of the injected fuel masses from the HRR profiles and the actual Start of Combustion (SoC) from the HRR and fuel burn profiles (when there was significant heat release bTDC) also contributed to the accuracy of the Leeds HRR

model. The improved HRR model leads to more accurate prediction of fuel consumption. This in turn, enables the development of and enhances better fuel consumption management strategies for Internal Combustion Engines (ICEs) and fuels.

9.5 Diesel Gen-set engine combustion test

The diesel-ethanol (DE) fuel blends combustion test, carried out on the modern, 5.7 kW, single cylinder, Yanmar diesel Gen-set, showed that DE fuel blends are feasible. The maximum concentration of ethanol that was tested was 15%. DE20 that was stable at 20 ^{o}C phase-separated at the temperature of the engine room (18 ^{o}C). Therefore, DE20 was not investigated. DE15 (15% ethanol in diesel) reduced the engine-out NOx by ~40% at the high condition of power (3 kW_e). This was due to the lower peak flame temperature of ethanol diesel blends

The replacement of fossil diesel with 15% by volume of bioethanol in diesel engines will lead to 9% reduction in transport CO_2 emissions in the UK (which is equivalent to a reduction of 5.5 million tonnes of CO_2 based on the consumption of diesel in the UK by transport in 2020). The estimated percentage reduction in CO_2 emissions is equivalent to a CO_2 savings of 0.05 million tonnes in Nigeria. Therefore, blending fossil diesel with 15% by volume of bioethanol will contribute towards achieving net-zero CO_2 emissions from diesel engines. The DE fuel blends increased the number of the emitted nanoparticles from the diesel Gen-set above the baseline as the load on the engine increased. Also, DE fuel blends increased the engine-out CO and THC emissions above the baseline.

The use of emission aftertreatment devices (Diesel Oxidation Catalyst, DOC and Diesel Particulate Filter, DPF) will eliminate the emission of nanoparticles, CO, and THC from diesel Gen-set engines when ethanol-blended fuels are used in

the engines. This will encourage the use of the ethanol-blended fuels in diesel Gen-sets to enhance clean combustion in sub-saharan African countries. The impingement of fuel on the wall of the cylinder and the relatively low fuel injection pressure of the Gen-set that was used also led to the observed high engine-out THC emissions which diminished the Brake Thermal Efficiency (BTE) of the engine (the relatively low fuel injection pressure of the engine led to the inefficient atomisation of the injected fuel mass). A Gen-set engine with a larger capacity (a larger bore and a much higher injection pressure) will minimise wall-wetting, enhance fuel atomisation and combustion thereby boosting the BTE of the engine.

The Leeds HRR model was validated for the combustion of ethanol-blended fuels in the modern Single Fuel Injection Strategy (SFIS) diesel Gen-set. The improved HRR model predicted the fuel consumption of the Gen-set engine for the investigated DE fuel blends with an overall average error of 3.03% compared to the measured fuel consumption. The overall average errors in the predicted fuel masses for the DE fuel blends by the other HRR models that were based on γ(T) ranged from 13.8% to 62.9%. The current work has shown that the accuracy of the HRR model of CI engines for different engine configurations (MFIS and SFIS) and different fuels (pure diesel, alternative diesels, and ethanol-blended fuels) is enhanced by using $\gamma(T, \lambda)$.

The utilisation of DE fuel blends with relatively high concentrations of ethanol in diesel engines will require major infrastructural changes such as the replacement of rubber seals and rubber tubes in the engines with fluorocarbon rubber (due to the corrosive nature of anhydrous ethanol). Furthermore, cetane improvers will be required to use relatively high concentrations of ethanol is diesel engines. The HRR model results for the DE fuel blends showed that there was a progressive

shift of the HRR profiles of the DE blends to the right of the profile for pure diesel while the PHRR decreased below the baseline as the concentration of ethanol increased. The HRR profiles for the investigated DE fuel blends shifted to the right of the baseline while the PHRR decreased below the baseline because ethanol-blended fuels increase the Ignition Delay (ID) in diesel engines. The relatively low Cetane Number of ethanol compared to pure diesel leads to an increase in the ID when ethanol-blended fuels are used in diesel engines. The implication of the observed trend in the HRR profiles of DE fuel blends is that, the use of DE fuel blends with ethanol concentrations >20% in diesel engines without cetane enhancers will cause the engine to misfire. As such, cetane enhancers will be required to effectively utilise DE blends with ethanol concentration >20% in diesel engines.

9.6 Energy recovery from biomass residue

The estimated optimum equivalence ratio, Ø values for sweet sorghum, grain sorghum, and corn stalk residues were 2.1, 1.7, and 1.9 respectively. The estimated optimum Ø values for the investigated biomass residues compared well to the estimated value of 2.8 for pine wood. The estimated optimum CGEs for sweet sorghum, grain sorghum, and corn stalk residues were 76.6%, 46.1%, and 40.7% respectively while the estimated optimum HGEs for the biomass residues were 81.1%, 52.1%, and 45.9% respectively. The estimated HGE for pine wood, using the same equipment, was 78%. The particulate yield of sweet sorghum stalk residue was found to be minimum at the optimum gasification air flux condition (12.9 g/m^2.s), where the area here is the flat top area of the cone calorimeter sample tray (100 mm x 100 mm). Where applied to a larger scale gasifier would be the top surface area of the gasifier biomass bed.

The estimated capacity of the proposed natural, downdraught gasifier that was designed for the gasification of sweet sorghum stalk residues for 12 hours steady-state production of syngas was 86 kg biomass/day. The estimated capacity was based on the estimated average BTE of the 5.7 kW diesel Gen-set (21%). The current work has shown that bioenergy can be recovered from sweet sorghum stalk residue by the gasification of the residue to produce syngas. The syngas that is produced from a downdraught gasifier can be introduced via Port Fuel Injection (PFI) into a diesel Gen-set operating in Reactivity Controlled Compression Ignition (RCCI) mode to generate electricity. RCCI is known to be a Low Temperature Combustion (LTC) strategy in CI engines. LTC strategies reduce engine-out NOx emissions. Therefore, the use of syngas that is produced from the gasification of sweet sorghum stalk residue will ultimately enhance clean combustion in diesel Gen-set engines by reducing engine-out NOx.

The use of a Gen-set with a relatively high BTE will reduce the biomass feed requirement for the proposed gasifier. A cluster of three or four households in the targeted localities in Nigeria can possibly buy a larger capacity Gen-set which will have a higher BTE than the 5.7 kW Gen-set engine that was used in the current work. The current work has shown that Nigeria can maximise the bioenergy potential of its sweet sorghum resource by producing bioethanol from the glucose-rich juice in the stalk of the crop for use as a transportation fuel while syngas is produced from the stalk residue of the crop. The syngas can be used in RCCI mode diesel Gen-sets for electricity generation.

9.7 Future work

Nigeria’s production of sweet sorghum can be drastically increased by cultivating the crop in the vast uncultivated arable lands in the country. This will boost the country’s sweet sorghum potential and bioenergy potential in general. If 50%

(15,000,000 ha) of the uncultivated land in Nigeria is available for the cultivation of energy crops, the production of the crops will increase by 37%. Life-cycle energy consumption and carbon footprint analyses were not carried out on the ethanol production process in Nigeria because of unavailability of data. In the future, these analyses can be carried out as the ethanol plants in Nigeria that were at various stages of completion during this research will most likely be fully operational.

The effect of the diesel-ethanol (DE) fuel blends that have relatively high concentration of anhydrous ethanol (>20%) on the combustion behaviour (performance, emission, and HRR) of diesel engines is also worth investigating in the future. This will require the use of stabilisers (to keep the unstable blends stable), cetane enhancers (to keep the combustion stable), and lubricity enhancers such as biodiesel to minimise the excessive wear of engine parts that can occur due to the low lubricity of ethanol. Infrastructural changes will also be required (replacing rubber seals in the fuel pump with seals made from fluorocarbon rubber).

The effect of stacking the stalk residues of sweet sorghum (or the other stalk residues) vertically in the sample holder on the optimum gasification equivalence ratio and the yield of syngas is worth investigating in the future. This will allow for the investigation of the effect of varying the depth of the biomass on the yield of syngas. Furthermore, the combined gasification of different stalk residues stacked together in the sample holder could be investigated on the Cone calorimeter. Investigation of the concurrent gasification of multiple biomass residues will provide relevant data for the design and optimisation of robust gasifier systems for the efficient gasification of multi-component biomass feed. A gasifier that efficiently gasifies multi-component biomass feed will be desirable in

countries like Nigeria where biomass wastes from different agricultural crops abound (as shown in Chapter 2). For batch gasification of biomass, future work will also investigate reducing the air flow in the char gasification stage and increasing the hydrogen yield with water injection into the residual char.

An alternative design of the downdraught gasifier is one that has a single air inlet pipe and uses an air blower. Using a blower and a single air inlet pipe will make the control of the inlet air flow rate relatively easy. Also, the alternative design will be much easier to automate than the proposed manual design that was presented in Chapter 8. Also with this design a burner can be fitted to the air inlet flow so that rapid heating of the gasifier is achieved, This would be a lean operating burner with sufficient oxygen to gasify the biomass. This design would be suitable for diesel power application or for process heat by sending the resulting gas to a burner where air was added to burn the hydrogen/CO/hydrocarbon mixture in the product gases. This phase of the work has recently been funded by BEIS and a 350 kW gasifier is to be built on these principles. Once built the gasifier could also be used to demonstrate the diesel engine RCCI operation for power generation.

References

AGARWAL, A. K. 2007. Biofuels (alcohols and biodiesel) applications as fuels for internal combustion engines. *Progress in Energy and Combustion Science,* 33**,** 233-271.

AIC 2012. Fuel flow meter AIC -904/908 veritas. [Online]. [Accessed 16 December 2021]. Available from: http://reicon.us/TIcurrent/900/TI%20900_e_07.08.pdf. Switzerland: Automotive Information and Control (AIC) Systems.

ALAKANGAS, E. 2005. Properties of wood fuels used in Finland-BIOSOUTH-project. [Online]. Finland: VTT Processes. [Accessed 20 November 2017]. Available from: https://ec.europa.eu/energy/intelligent/projects/sites/iee-projects/files/projects/documents/bio-south_wood_fuel_properties.pdf.

ALTAHER, M. A., ANDREWS, G. E., GIBBS, B. M., HADAVI, S. A., LI, H. & JONES, E. E. A. 2015. Comparison of Gaseous and Particulate Emissions from Wood Pellet and Oil Fired Combustion for the same Heat Input. The 10th European Conference on Industrial Furnaces and Boiler (INFUB-10), Porto, Portugal. 2015.

AN. 2012. Sorghum production. [Online]. [Accessed 21 July 2017]. Available from: http://agriculturenigeria.com/farming-production/crop-production/crops/sorghum.

ANDREWS, G., LEDGER, J. & PHYLAKTOU, R. 2001. *The gravimetric determination of soot yields in enclosed pool fires*.

ANDREWS, G. E. 2015. Review of diesel engine emission influences of biofuels. Oxygenated fuels and biofuels. School of Process, Environment and Materials Engineering. University of Leeds, UK.

ANDREWS, G. E. 2018a. SI and diesel engine NOx, CO, HC and PM emissions and their control. CAPE5430M Advanced Engines and Turbines. 12 February, University of Leeds.

ANDREWS, G. E., IRSHAD, A., PHYLAKTOU, H. N. & GIBBS, B. M. 2019. Solid Biomass to Medium CV Gas Conversion With Rich Combustion. *Turbomachinery Technical Conference and Exposition GT2019, 17-21 June, Arizona.* [Online]. [Accessed 22 July 2021]. Available from: http://eprints.whiterose.ac.uk/160335/.

ANDREWS, G. E. & SALIH, F. Diesel particulate and NOx emissions. IMechE Seminar Fuels for Automotive and Industrial Diesel Engines, 1990.

ANYAGAFU, V. S. 2014. Nigeria records over 10, 000 deaths through generator fumes. *Nigerian Vanguard. [Online]*, 8 August 2014.

ASTALS, S. & MATA, J. Anaerobic digestion. [Online]. [Accessed 20 November 2017]. University of Barcelonia: EPROBIO-Foggia. Available from: http://www.iperasmuseprobio.unifg.it/dwn/0.pdf 2011.

AVL 2011. *Flexifem Indi,* Germany, AVL.

AVL 2015. *GCA Gas exchange and combustion analysis,* Germany, AVL.

BALDACCI, A., GRADASSI, A. T., ZEPPI, C., BARDUCCI, G. L., DADDI, P., POLZINETTI, G. & ULIVIERI, P. 1994. Syngas Production from Sorghum at Greve in Chianti Gasification Plant. *8th European Biomass Conference Vol.3, 3-5 October 1994, Vienna.* pp.1807-1813.

BARABÁS, I. & TODORUŢ, A. I. 2009. Key Fuel Properties of Biodiesel-diesel Fuel-ethanol Blends. SAE International.

BEAK 1998. Forest resources study. National report (draft). FORMECU. Federal Department of Forestry. Abuja. Nigeria.

BEN-IWO, J., MANOVIC, V. & LONGHURST, P. 2016. Biomass resources and biofuels potential for the production of transportation fuels in Nigeria. *Renewable and Sustainable Energy Reviews,* 63**,** 172-192.

BLAIR, G. P. 1990. *The basic design of two-stroke engines*, Warrendale, PA (United States); Society of Automotive Engineers; None.

BOLEY, C. C. & LANDERS, W. S. Entrainment drying and carbonization of wood waste. 1969.

BP 2017. BP energy outlook. [Online]. [Accessed 18 November 2017]. Available from: https://www.bp.com/en/global/corporate/energy-economics/energy-outlook.html.

BRAUN, D. E. & STEPHENSON, K. O. Alternative fuel blends and diesel engine tests International conference on plant and vegetable oils as fuels, August 1982 1982 Michigan. American Society of Agricultural Engineers.

BRIDGEWATER, A. V. & EVANS, G. D. 1993. An assessment of thermochemical conversion systems for processing biomass and refuse, Energy Technology Support Unit Report B/T1/00207/REP, Department of Trade and Industry, London.

BRUNT, M. F. J. & EMTAGE, A. L. 1997. Evaluation of Burn Rate Routines and Analysis Errors. SAE International.

CAMBUSTION 2011. *DMS500 user manual*. Cambridge: Cambustion Ltd.

CEVIZ, M. A. & KAYMAZ, İ. 2005. Temperature and air–fuel ratio dependent specific heat ratio functions for lean burned and unburned mixture. *Energy Conversion and Management,* 46**,** 2387-2404.

CHAN, S. H. & ZHU, J. 1996. Exhaust Emission Based Air-Fuel Ratio Model (I): Literature Reviews and Modelling. SAE International.

CHANNIWALA, S. A. & PARIKH, P. P. 2002. A UNIFIED CORRELATION FOR ESTIMATING HHV OF SOLID, LIQUID AND GASEOUS FUELS. *Fuel,* 81**,** 1051-1063.

CHOI, Y. & STENGER, H. G. 2003. Water gas shift reaction kinetics and reactor modeling for fuel cell grade hydrogen. *Journal of Power Sources,* 124**,** 432-439.

CHONG, C. N. & IDRUS, A. Z. 1988. Biomass energy potential in Malaysia. [Online]. *ASEAN J. Sci. Technol. Dev.,* 5**,** 15-27.

COELHO, E. P. D., MOLES, C. W., DOS SANTOS, M. A. C., BARWICK, M. & CHIARELLI, P. M. 1996. Fuel Injection Components Developed for Brazilian Fuels. SAE International.

COHCE, M. K., ROSEN, M. A. & DINCER, I. 2011. Efficiency evaluation of a biomass gasification-based hydrogen production. *International Journal of Hydrogen Energy,* 36**,** 11388-11398.

DESANTES, J. M., PAYRI, R., SALVADOR, F. J. & GIMENO, J. 2003. Measurements of Spray Momentum for the Study of Cavitation in Diesel Injection Nozzles. SAE International.

DOGRU, M., MIDILLI, A. & HOWARTH, C. 2002. Gasification of sewage sludge using a throated downdraft gasifier and uncertainty analysis. *Fuel Processing Technology - FUEL PROCESS TECHNOL,* 75**,** 55-82.

DSG 2014. Dynamometer services group. DSG Ltd.

DUKES 2021. Digest of UK energy statistics [Online]. [Accessed 6 August 2021]. Available from: https://www.gov.uk/government/statistics/digest-of-uk-energy-statistics-dukes-2021.

DUTTA, K., DAVEREY, A. & LIN, J.-G. 2014. Evolution retrospective for alternative fuels: First to fourth generation. *Renewable Energy,* 69**,** 114-122.

EBRAHIMI, R. 2011. Effect of specific heat ratio on heat release analysis in a spark ignition engine. *Scientia Iranica,* 18**,** 1231-1236.

EGNELL, R. 1998. Combustion Diagnostics by Means of Multizone Heat Release Analysis and NO Calculation. SAE International.

EISA, M. & VISVANATHAN, C. 2002. *Municipal solid waste management in Asia and Africa: A comparative analysis,* Vienna: Cleaner Production and Environmental Management Branch, United Nations Industrial Development Organisation.

ET. 2003. Air flow and velocity due to natural draft. [Online]. [Accessed 6 January 2021]. Available from: https://www.engineeringtoolbox.com/natural-draught-ventilation-d_122.html.

FAO 2008. Greenfacts. [Online]. [Accessed 24 October 2017]. Available from: https://www.greenfacts.org/en/biofuels/figtableboxes/biofuel-yields-countries.htm. Greenfacts.

FAO. 2012. Trade data base. [Online]. [Accessed 21 July 2017]. Available from: http://faostat.fao.org.

FAO 2014. FAOSTAT. [Online]. [Accessed 26 October 2017]. Available from: http://www.fao.org/faostat/en/#data/RL

FAO 2015. FAOSTAT. [Online]. [Accessed 26 October 2017]. Available from: http://faostat.fao.org/ FAO.

FAO 2016. Country fact sheet. [Online]. [Accessed 16 October 2017]. Available from: http://www.fao.org/nr/water/aquastat/data/cf/readPdf.html?f=NGA-CF_eng.pdf

FENGHOUR, A., WAKEHAM, W. A. & VESOVIC, V. 1998. The Viscosity of Carbon Dioxide. *Journal of Physical and Chemical Reference Data,* 27**,** 31-44.

FGN 2006. *Renewable Electricity Policy Guidelines,* Nigeria, Federal Ministry of Power and Steel.

FORMICA, M., FRIGO, S. & GABBRIELLI, R. 2016. Development of a new steady state zero-dimensional simulation model for woody biomass gasification in a full scale plant. *Energy conversion and management,* 2016 v.120**,** pp. 358-369.

FR 2021. Carbon emissions of different fuels [Online]. [Accessed 7 August 2021]. Available from: https://www.forestresearch.gov.uk/tools-and-resources/fthr/biomass-energy-resources/reference-biomass/facts-figures/carbon-emissions-of-different-fuels/.

FRN. 2007. Official gazette of the Nigerian biofuel policy and incentives [Online]. [Accessed 23 October 2017]. Available from: https://community.irena.org/rbsvc25562/.../97/.../National%20Biofuels%20policy.pdf.

FUNGTAMMASAN, B. 2010. An Investigation of Diesel-Ethanol-Biodiesel Blends for Diesel Engine: Part 1. Emulsion Stability and Fuel Properties AU - Cheenkachorn, K. *Energy Sources, Part A: Recovery, Utilization, and Environmental Effects,* 32**,** 637-644.

GAEGAUF, C., WIESER, U. & MACQUAT, Y. 2001. Field investigation of nanoparticle emissions from various biomass combustion systems [Online]. *5th Conference on nanoparticle-measurement, Zurich*.

[Accessed 20 December 2021]. Available from: https://www.nanoparticles.ch/archive/2001_Gaegauf_PR.pdf.

GATOWSKI, J. A., BALLES, E. N., CHUN, K. M., NELSON, F. E., EKCHIAN, J. A. & HEYWOOD, J. B. 1984. Heat Release Analysis of Engine Pressure Data. SAE International.

GIDNEY, J. & GORSMANN, C. Introduction to emission control by catalysts [PowerPoint presentation]. NOx and Particulate Real Drive Emissions, 23 May 2018 2018 Leeds, UK.

GORDILLO, G., ANNAMALAI, K. & CARLIN, N. 2009. Adiabatic fixed-bed gasification of coal, dairy biomass, and feedlot biomass using an air–steam mixture as an oxidizing agent. *Renewable Energy,* 34**,** 2789-2797.

GS 2013. Nigeria-vegetation [Online]. [Accessed 12 May 2019]. Available from: https://www.globalsecurity.org/military/world/nigeria/images/map-1979-veg.jpg.

GUARIEIRO, L. L. N., DE SOUZA, A. F., TORRES, E. A. & DE ANDRADE, J. B. 2009. Emission profile of 18 carbonyl compounds, CO, CO2, and NOx emitted by a diesel engine fuelled with diesel and ternary blends containing diesel, ethanol and biodiesel or vegetable oils. *Atmospheric Environment,* 43**,** 2754-2761.

HAMMERTON, J. 10 May 2018 2018. *RE: Calibration of HORIBA.* Type to OLANREWAJU, F. O.

HE, B.-Q., SHUAI, S.-J., WANG, J.-X. & HE, H. 2003. The effect of ethanol blended diesel fuels on emissions from a diesel engine. *Atmospheric Environment,* 37**,** 4965-4971.

HEFT-NEAL, S., BURNEY, J., BENDAVID, E. & BURKE, M. 2018. Robust relationship between air quality and infant mortality in Africa. *Nature,* 559**,** 254-258.

HEYWOOD, J. B. 1988. *Internal combustion engine fundamentals,* New York, McGraw-Hill, Inc.

HOARD, J., ABARHAM, M., STYLES, D., GIULIANO, J. M., SLUDER, C. S. & STOREY, J. M. E. 2008. Diesel EGR Cooler Fouling. SAE International.

HOHENBERG, G. F. 1979. Advanced Approaches for Heat Transfer Calculations. SAE International.

HSIEH, W., CHEN, R.-H., WU, T.-L. & LIN, T.-H. 2002. *Engine performance and pollutant emission of an SI engine using ethanol–gasoline blended fuels*.

HUBER, M. L., PERKINS, R. A., LAESECKE, A., FRIEND, D. G., SENGERS, J. V., ASSAEL, M. J., METAXA, I. N., VOGEL, E., MAREŠ, R. &

MIYAGAWA, K. 2009. New International Formulation for the Viscosity of H2O. *Journal of Physical and Chemical Reference Data,* 38**,** 101-125.

HULWAN, D. B. & JOSHI, S. V. 2011. Performance, emission and combustion characteristic of a multicylinder DI diesel engine running on diesel–ethanol–biodiesel blends of high ethanol content. *Applied Energy,* 88**,** 5042-5055.

IEA 2015. Nigeria balance. [Online]. [Accessed 17 October 2017]. Available from: https://www.iea.org/Sankey/#?c=Nigeria&s=Balance.

IRSHAD, A. 2017. *Gasification burning of biomass.* PhD Thesis, University of Leeds.

JAIN, M. C. 1993. Bioconversion of organic wastes for fuel and manure, Fertilizer News, 38(4), 55-61.

JEKAYINFA, S. O. & SCHOLZ, V. 2009. Potential Availability of Energetically Usable Crop Residues in Nigeria. *Energy Sources, Part A: Recovery, Utilization, and Environmental Effects,* 31**,** 687-697.

JIA, L.-W., SHEN, M.-Q., WANG, J. & LIN, M.-Q. 2005. Influence of ethanol–gasoline blended fuel on emission characteristics from a four-stroke motorcycle engine. *Journal of Hazardous Materials,* 123**,** 29-34.

JOHANSSON, L. S., LECKNER, B., GUSTAVSSON, L., COOPER, D., TULLIN, C. & POTTER, A. 2004. Emission characteristics of modern and old-type residential boilers fired with wood logs and wood pellets. *Atmospheric Environment,* 38**,** 4183-4195.

JOSHI, A., BOGER, T. & TANNER, C. Diesel particulate filters [PowerPoint presentation]. NOx and Particulate Real Drive Emissions, 24 May, 2018 2018 Leeds, UK.

JOSSY, M. T. 1994. *A study of greenhouse gases emission from agricultural residues in Asia.* M. Eng, Asian Institute of Technology.

K. RUTTO, L., XU, Y., BRANDT, M., REN, S. & KERING, M. 2013. *Juice, Ethanol, and Grain Yield Potential of Five Sweet Sorghum (Sorghum bicolor [L.] Moench) Cultivars*.

KASS, M. D., THOMAS, J. F., STOREY, J. M., DOMINGO, N., WADE, J. & KENRECK, G. 2001. Emissions From a 5.9 Liter Diesel Engine Fueled With Ethanol Diesel Blends. SAE International.

KIRSANOVS, V. & ZANDECKIS, A. 2015. Investigation of Biomass Gasification Process with Torrefaction Using Equilibrium Model. *Energy Procedia,* 72**,** 329-336.

KITTELSON, D. B. 1998. Engines and nanoparticles: a review. *Journal of Aerosol Science,* 29**,** 575-588.

KOOPMANS, A. & KOPPEYAN, J. Agricultural and forest residues generation, utilization and availability. Regional consultationon modern applications of biomass energy, 6-10 January 1997 Kuala Lumpur, Malaysia.

KWANCHAREON, P., LUENGNARUEMITCHAI, A. & JAI-IN, S. 2007. Solubility of a diesel–biodiesel–ethanol blend, its fuel properties, and its emission characteristics from diesel engine. *Fuel,* 86**,** 1053-1061.

LAPUERTA, M., ARMAS, O. & GARCÍA-CONTRERAS, R. 2007. Stability of diesel–bioethanol blends for use in diesel engines. *Fuel,* 86**,** 1351-1357.

LAPUERTA, M., ARMAS, O. & GARCÍA-CONTRERAS, R. 2009. Effect of Ethanol on Blending Stability and Diesel Engine Emissions. *Energy & Fuels,* 23**,** 4343-4354.

LEE, B.-S. 2018. Pressure, temperature and concentration effects on hydrogen bonding in poly(ethylene oxide) aqueous solution. *Journal of Molecular Liquids,* 262**,** 527-532.

LEMMON, E. W. & JACOBSEN, R. T. 2004. Viscosity and Thermal Conductivity Equations for Nitrogen, Oxygen, Argon, and Air. *International Journal of Thermophysics,* 25**,** 21-69.

LEPSZY, S. & CHMIELNIAK, T. 2010. Technical and Economic Analysis of Biomass Integrated Gasification Combined Cycle. *ASME Turbo Expo 2010 GT2010 Vol.1, 14-18 June 2010, Glasgow.* [Online]. pp.631-637. [Accessed 22 July 2021]. Available from: https://journals.asmedigitalcollection.asme.org/GT/proceedings-abstract/GT2010/43963/631/347795.

LI, D., ZHEN, H., XINGCAI, L., WU-GAO, Z. & JIAN-GUANG, Y. 2004. Physico-chemical properties of ethanol-diesel blend fuel and its effect on performance and emissions of diesel engines. *Renewable Energy,* 30**,** 967-976.

LI, H., EBNER, J., REN, P., CAMPBELL, L., DIZAYI, B. & HADAVI, S. 2014. *Determination of Carbon Footprint using LCA Method for Straight Used Cooking Oil as a Fuel in HGVs*.

LIKOS, B., CALLAHAN, T. J. & MOSES, C. A. 1982. Performance and Emissions of Ethanol and Ethanol-Diesel Blends in Direct-Injected and Pre-Chamber Diesel Engines. SAE International.

LILEY, P., MAKITA, T. & TANAKA, Y. 1988. *Properties of inorganic and organic fluids. CINDAS data series on material properties. Vol. V-1*. [Online]. New York. Hemisphere Publishing. [Accessed 15 August 2021]. Available from: https://aiche.onlinelibrary.wiley.com/doi/abs/10.1002/aic.690350541.

LIU, H. & GIBBS, B. M. 2003. Modeling NH3 and HCN emissions from biomass circulating fluidized bed gasifiers☆. *Fuel,* 82**,** 1591-1604.

MATHIVANAN, K., MALLIKARJUNA, J. M. & RAMESH, A. 2016. Influence of multiple fuel injection strategies on performance and combustion characteristics of a diesel fuelled HCCI engine – An experimental investigation. *Experimental Thermal and Fluid Science,* 77**,** 337-346.

MATHUR, S., UMAKANTH, A. V., TONAPI, V. A., SHARMA, R. & SHARMA, M. K. 2017. Sweet sorghum as biofuel feedstock: recent advances and available resources. *Biotechnology for Biofuels,* 10**,** 146.

MAY, E. F., BERG, R. F. & MOLDOVER, M. R. 2007. Reference Viscosities of H2, CH4, Ar, and Xe at Low Densities. *International Journal of Thermophysics,* 28**,** 1085-1110.

MCKENDRY, P. 2002. Energy production from biomass (part 2): conversion technologies. *Bioresource Technology,* 83**,** 47-54.

MOREIRA, R., BIMBELA, F., GIL-LALAGUNA, N., SÁNCHEZ, J. L. & PORTUGAL, A. 2021. Clean syngas production by gasification of lignocellulosic char: State of the art and future prospects. *Journal of Industrial and Engineering Chemistry,* 101**,** 1-20.

MUELLER, L., JAKOBI, G., CZECH, H., STENGEL, B., ORASCHE, J., ARTEAGA-SALAS, J. M., KARG, E., ELSASSER, M., SIPPULA, O., STREIBEL, T., SLOWIK, J. G., PREVOT, A. S. H., JOKINIEMI, J., RABE, R., HARNDORF, H., MICHALKE, B., SCHNELLE-KREIS, J. & ZIMMERMANN, R. 2015. Characteristics and temporal evolution of particulate emissions from a ship diesel engine. *Applied Energy,* 155**,** 204-217.

MUSTAFA, B. G., KIAH, M. H. M., IRSHAD, A., ANDREWS, G. E., PHYLAKTOU, H. N., LI, H. & GIBBS, B. M. 2019. Rich biomass combustion: Gaseous and particle number emissions. *Fuel,* 248**,** 221-231.

NAEGELI, D. W., LACEY, P. I., ALGER, M. J. & ENDICOTT, D. L. 1997. Surface Corrosion in Ethanol Fuel Pumps. SAE International.

NAERLS & FDAE 2014. *Annual Agricultural Performance Survey Report of 2014 Wet Season in Nigeria,* Zaria, NAERLSPress.

NASS 2012. *Collaborative survey on national agricultural sample survey 2010/2011* NAtional Bureau on Statistics and Federal Ministry of Agriculture and Rural Development.

NBS. 1987. Literature review of cetane number and its correlations. [Online]. Washington, D.C.: Geo-Centers, Inc. [Accessed 19 September 2018]. Available from: http://www.dtic.mil/dtic/tr/fulltext/u2/a181753.pdf

NEILFA, A., CANO, R. & FDZ-POLANCO, M. 2014. Theoretical methane production generated by the co-digestion of organic fraction municipal solid waste and biological sludge. Biotech. Report, 5, 14-21.

NESTE 2020. Neste renewable diesel handbook [Online]. [Accessed 13 December 2021]. Available from: https://www.neste.com/sites/default/files/attachments/neste_renewable_diesel_handbook.pdf.

NESTOR, Y. R. 2001. *Diesel exhaust system influences on transient particulate emissions and particle size distribution.* PhD Thesis, University of Leeds, UK.

NGO, S. I., NGUYEN, T. D. B., LIM, Y.-I., SONG, B.-H., LEE, U.-D., CHOI, Y.-T. & SONG, J.-H. 2011. Performance evaluation for dual circulating fluidized-bed steam gasifier of biomass using quasi-equilibrium three-stage gasification model. *Applied Energy,* 88**,** 5208-5220.

NNPC 2019. Annual statistical bulletin [Online]. [Accessed 9 August 2021]. Available from: https://nnpcgroup.com/NNPCDocuments/Annual%20Statistics%20Bulletin%E2%80%8B/2019%20ASB.pdf.

OBADA, F. B. 2011. *The sweet sorghum-to-ethanol initiative; the Nigerian experience*. SWAC. 6 December. Cape Verde.

OGUNESAN, T. 2017. Otu, Ilero, local charcoal production gets boost for export. [Online]. *Nigerian Tribune*.

OHIMAIN, E. I. 2010. Emerging bio-ethanol projects in Nigeria: Their opportunities and challenges. *Energy Policy,* 38**,** 7161-7168.

OLANREWAJU, F. O., LI, H., ANDREWS, G. E. & PHYLAKTOU, H. N. 2020a. Improved model for the analysis of the Heat Release Rate (HRR) in Compression Ignition (CI) engines. *Journal of the Energy Institute,* 93**,** 1901-1913.

OLANREWAJU, F. O., WU, Y., LI, H., ANDREWS, G. & PHYLAKTOU, H. 2020b. An Improved Heat Release Rate (HRR) Model for the Analysis of Combustion Behaviour of Diesel, GTL, and HVO Diesel. SAE International.

OSTADFAR, A. 2016. Chapter 1 - Fluid Mechanics and Biofluids Principles. *In:* OSTADFAR, A. (ed.) *Biofluid Mechanics.* Academic Press.

PAISLEY, M. A., FARRIS, M. C., BLACK, J., IRVING, J. M. & OVEREND, R. P. 2000. Commercial demonstration of the Battelle/FERCO biomass gasification process: startup and initial operating experience, in *A Growth Opportunity in Green Energy and Value-Added Products: Proceedings of the Fourth Biomass Conference of the Americas,* Elsevier, London, pp. 1061-1066. 2000.

PARKER, W. J. 1982. Calculations of the heat release rate by oxygen consumption for various applications. Washington, DC: Department of Commerce, National Bureau of Standards, Centre for Fire Research.

PIDOL, L., LECOINTE, B., STARCK, L. & JEULAND, N. 2012. Ethanol–biodiesel–Diesel fuel blends: Performances and emissions in conventional Diesel and advanced Low Temperature Combustions. *Fuel,* 93**,** 329-338.

PIKONAS, A., PUKALSKAS, S. & GRABYS, J. 2003. Influence of composition of gasoline - ethanol blends on parameters of internal combustion engines. *Journal of KONES,* Vol. 10, No. 1-2**,** 205-211.

PINTA, F. & VERGNET, L. 1994. Testing of wood gasification pilot plant for industrial heat generation. *8th European Biomass Conference Vol.3, 3-5 October 1994, Vienna.* pp.1791-1800.

PORTA, M., TRAVERSO, A. & MARIGO, L. 2006. Thermoeconomic Analysis of a Small-Size Biomass Gasification Plant for Combined Heat and Distributed Power Generation. *ASME Turbo Expo Vol.4 GT2006, 8-11 May 2006, Barcelonia.* [Online]. pp.357-365. [Accessed 22 July 2021]. Available from: https://asmedigitalcollection.asme.org/GT/proceedings-abstract/GT2006/42398/357/315375.

RAHIMI, H., GHOBADIAN, B., YUSAF, T. F., NAJAFI, G. & KHATAMIFAR, M. 2009. *Diesterol: An environment-friendly IC engine fuel*.

RAJKUMAR, M. 2002. *Heat release analysis and modeling for a common-rail diesel engine. [Online].* MSc Thesis, University of Tennessee - Knoxville. [Accessed 28 April 2021]. Available from: https://trace.tennessee.edu/cgi/viewcontent.cgi?article=3523&context=utk_gradthes.

RAKOPOULOS, D. C., RAKOPOULOS, C. D., KAKARAS, E. C. & GIAKOUMIS, E. G. 2008. Effects of ethanol–diesel fuel blends on the performance and exhaust emissions of heavy duty DI diesel engine. *Energy Conversion and Management,* 49**,** 3155-3162.

RAKOPOULOS, D. C., RAKOPOULOS, C. D., PAPAGIANNAKIS, R. G. & KYRITSIS, D. C. 2011. Combustion heat release analysis of ethanol or n-butanol diesel fuel blends in heavy-duty DI diesel engine. *Fuel,* 90**,** 1855-1867.

RASLAVICIUS, L. & ŽILVINAS, B. 2010. *The possibility of increasing the quantity of oxygenates in fuel blends with no diesel engine modifications*.

REED, T. B. & SIDDHARTHA, G. 2001. *A survey of biomass gasification, 2nd ed.*, Biomass Energy Foundation, Franktown, CO.

REGULATIONS. 2015. Automotive diesel fuel. [Online]. [Accessed 27 May 2018]. Available from: https://www.dieselnet.com/standards/eu/fuel_automotive.php.

REITZ, R. D. & DURAISAMY, G. 2015. Review of high efficiency and clean reactivity controlled compression ignition (RCCI) combustion in internal

combustion engines. *Progress in Energy and Combustion Science,* 46**,** 12-71.

REKSOWARDOJO, I. K., TRICHANH, P., FERDYAMIN, K. & AKBAR, M. Z. 2017. The Effect of Gasoline-Ethanol Blended on Performance and Emission of a Fuel Injection Motorcycle 115 cc with Automatic Transmission in Indonesia. Society of Automotive Engineers of Japan.

ROSER, M. & ORTIZ-OSPINA, E. 2017. World population growth. [Online]. [Accessed 18 November 2017]. Available from: https://ourworldindata.org/world-population-growth/. OurWorldInData.org.

RYAN, T. W., MAYMAR, M., OTT, D., LAVIOLETTE, R. A. & MACDOWALL, R. D. 1994. Combustion and Emissions Characteristics of Minimally Processed Methanol in a Diesel Engine Without Ignition Assist. SAE International.

SAEED, M., IRSHAD, A., SATTAR, H., ANDREWS, G., PHYLAKTOU, R. & M. GIBBS, B. 2015. *Agricultural Waste Biomass Energy Potential In Pakistan*.

SAJJAD, H., MASJUKI, H. H., VARMAN, M., KHAN, M. M. R., ARBAB, M. I., IMTENAN, S. & SANJID, A. 2014. Comparative Study of Biodiesel, GTL Fuel and Their Blends in Context of Engine Performance and Exhaust Emission. *Procedia Engineering,* 90**,** 466-471.

SALIH, F. M. 1990. *Automotive fuel economy measures and fuel usage in Sudan.* Ph.D Thesis, University of Leeds.

SAMBO, A. S. 2006. Renewable energy electricity in Nigeria: The way forward. *Renewable Electricity Policy.* Shehu Musa Yar'adua Centre, Abuja.

SCHASCHKE, C., FLETCHER, I. & GLEN, N. 2013. Density and Viscosity Measurement of Diesel Fuels at Combined High Pressure and Elevated Temperature. *Processes,* 1**,** 30-48.

SHAHID, E. M. & JAMAL, Y. 2008. A review of biodiesel as vehicular fuel. *Renewable and Sustainable Energy Reviews,* 12**,** 2484-2494.

SHAHIR, S. A., MASJUKI, H. H., KALAM, M. A., IMRAN, A., FATTAH, I. M. R. & SANJID, A. 2014. Feasibility of diesel–biodiesel–ethanol/bioethanol blend as existing CI engine fuel: An assessment of properties, material compatibility, safety and combustion. *Renewable and Sustainable Energy Reviews,* 32**,** 379-395.

SHOEMAKER, C. E. & BRANSBY, D. I. 2010. *The role of sorghum as a bioenergy feedstock,* Auburn, US, Auburn University.

SHRIVASTAVA, K., THIPSE, S. S. & PATIL, I. D. The phase stability and solubility of diesel, biodiesel and ethanol blends-a review. 16th IRF International Conference, 14 December 2014 Pune, India.

SIMONYAN, K. J. & FASINA, O. 2013. Biomass resources and bioenergy potentials in Nigeria. *African Journal of Agricultural Research,* 8**,** 4975-4989.

SINNOTT, R. K. (ed.) 2003. *Coulson and Richardson's Chemical Engineering,* Oxford: Butterworth Heinemann.

SINNOTT, R. K. (ed.) 2005. *Chemical engineering design,* Oxford: Butterworth-Heinemann.

SMITH, M. Unit Injectors and Common Rail Fuel Injection Systems. Delphi Diesel Systems 2012, May 18 2012 2012 UK.

SPEIGHT, J. 2020. The Fischer-Tropsch Process.

SPELLMAN, F. R. 2012. *Forest-based biomass energy concepts and application,* New York, CRC Press.

SRINIVASA RAO, P., REDDY, B., BLÜMMEL, M., SUBBARAO, G., CHANDRARAJ, K., SANJANA REDDY, P. & PARTHASARATHY RAO, P. 2009. Sweet sorghum as a biofuel feedstock: can there be food-feed-fuel trade-offs? ICID.

SRIVASTAVA, S., SCHOCK, H., JABERI, F. & HUNG, D. L. S. 2009. Numerical Simulation of a Direct-Injection Spark-Ignition Engine with Different Fuels. SAE International.

STONE, R. 1992. *IC Engines*, SAE.

STONE, R. 1995. *IC Engines*, SAE.

STULTZ, S. C. & KITTO, J. B. 1993. *Steam: its generation and use*, Babcock & Wilcox, Barberton, OH.

SUBERU, M. Y., BASHIR, N. & MUSTAFA, M. W. 2013. Biogenic waste methane emissions and methane optimization for bioelectricity in Nigeria. *Renewable and Sustainable Energy Reviews,* 25**,** 643-654.

SUKJIT, E., HERREROS, J. M., DEARN, K. & TSOLAKIS, A. 2014. Improving Ethanol-Diesel Blend Through the Use of Hydroxylated Biodiesel. SAE International.

TWILLEY, W. H. & BABRAUSKAS, V. 2001. User's guide for the Cone Calorimeter. UK: Fire Testing Technology Limited.

UN 2017. Energy statistics database [Online]. [Accessed 26 November 2017]. Available from: https://data.un.org/Data.aspx?d=EDATA&f=cmID%3aCH%3btrID%3a1231.

USGS. 2015. *Surface tension and water-US Geological Survey Water Science School. [Online].* [Online]. Available: https://water.usgs.gov/edu/surface-tension.html [Accessed 27 May 2018].

VIPAVANICH, C., CHUEPENG, S. & SKULLONG, S. 2018. Heat release analysis and thermal efficiency of a single cylinder diesel dual fuel engine with gasoline port injection. *Case Studies in Thermal Engineering,* 12**,** 143-148.

WAKELING, D. & PASSANT, N. R., MURRELLS, T.P., PANG, Y., THISTLETHWAITE, G., WALKER, C., BROWN, P., DEL VENTO, S., HUNTER, R., WILTSHIRE, J., PEARSON, B., RUSHTON, K., HOBSON, M., SMITH, H., AND MISSELBROOK, T. 2017. UK information inventry report (1990-2015). [Online]. UK: Richardo Energy and Environment. [Accessed 5 June 2018]. Available from: https://uk-air.defra.gov.uk/assets/documents/reports/cat07/1703161205_GB_IIR_2017_Final_v1.0.pdf.

WALLEN, S. L., PALMER, B. J., GARRETT, B. C. & YONKER, C. R. 1996. Density and Temperature Effects on the Hydrogen Bond Structure of Liquid Methanol. *The Journal of Physical Chemistry,* 100**,** 3959-3964.

WB 2016. Population density. [Online]. [Accessed 18 November 2017]. Available from: https://data.worldbank.org/indicator/EN.POP.DNST?end=2016&start=1961&view=chart.

WE 2006. *Values of wood fuel parameters*. [Online]. [Accessed 20 November 2017]. Available from: woodenergy.ie/woodasafuel/listandvaluesofwoodfuelparameters-part1/

WEC 2017. World Energy Trilema Index. London: World Energy Council.

WIDMANN, G. 2001. Interpreting TGA curves. [Online]. [Accessed 15 January 2021]. Available from: https://www.mt.com.

WPR. 2017. Africa population. [Online]. [Accessed 18 November 2017]. Available from: http://worldpopulationreview.com/continents/africa-population/

WU, C.-W., CHEN, R.-H., PU, J.-Y. & LIN, T.-H. 2004. The influence of air–fuel ratio on engine performance and pollutant emission of an SI engine using ethanol–gasoline-blended fuels. *Atmospheric Environment,* 38**,** 7093-7100.

WU, Y., FERNS, J., LI, H. & ANDREWS, G. 2017. Investigation of Combustion and Emission Performance of Hydrogenated Vegetable Oil (HVO) Diesel. *SAE International Journal of Fuels and Lubricants,* 10.

YANMAR. 2016. Marine diesel engine. [Online]. [Accessed 23 December 2020]. Available from: www.yanmar.com.

YEDITHASATYAM, M. & REDDY, R. 2015. Combustion heat release rate analysis of C.I. engine with secondary co-injection of DEE-H2O solution - A vibrational approach. *Journal of Engineering Science and Technology,* 10**,** 1086-1102.

ZÖLDY, M. 2011. Ethanol-biodiesel-diesel blends as a diesel extender option on compression ignition engines. *Transport,* 26**,** 303-309.

APPENDIX A

Table A.1 Binary diesel-ethanol (DE) fuel blends room temperature stability test records/data

		Blends											
Day	**Blend time**	**DE10**	**DE20**	**DE25**	**DE30**	**DE40**	**DE50**	**DE60**	**DE70**	**DE75**	**DE80**	**DE90**	**DnB90**
12/03/2018	**Preparation time**	**10:56**	**11:06**		**11:16**	**11:30**	**11:52**	**12:07**	**12:21**		**12:30**	**12:44**	**10:06**
	11:57	Stable	Stable		Turbid (41min)	Turbid (27min)	Turbid (5min)	-	-		-	-	Stable (1hr 51min)
	12:00	Stable	Stable		2 turbid phases; interphase @ 18ml (44min)	2 turbid phases; interphase @ 8ml (30min)	2 turbid phases; interphase @ 4ml (8min)	-	-		-	-	Stable
	12:49	Stable	Stable		2 clear phases (1hr 33min)	2 clear phases (1hr 19min)	2 clear phases (57min)	2 turbid phases; interphase @ 1.4ml (42min)	Stable (28min)		Stable (19min)	Stable (5min)	Stable
	13:00	Stable	Stable		2 clear phases (1 hr 44min)	2 clear phases (1 hr 30min)	2 clear phases (1 hr 8min)	2 phases, turbid; interphase @1.4ml(53min)	Stable		Stable	Stable	Stable
	15:09	Stable	Stable		2 clear phases (3hr 53min)	2 clear phases (3hr 39min)	2 clear phases (3 hr 17min)	2 clear phases, interphase @1.4ml (3 hr 2min)	Stable		Stable	Stable	Stable
	16:25	Stable	Stable		2 clear phases; interphase @ 15.9ml (5hr 9min)	2 clear phases; interphase @ 8.4ml (4hr 55min)	2 clear phases; interphase @ 4.6ml (4hr 33min)	2 clear phases, interphase @1.4ml (4 hr 18min)	Stable		Stable	Stable	Stable
13/03/2018	10:00	Stable	Stable		interphase @ 15.2ml (22hr 44min)	interphase @ 8.4ml (22hr 30min)	interphase @ 4.6ml (22hr 8min)	interphase @ 1.4ml (21hr 53min)	Stable		Stable	Stable	Stable
	11:00	Stable	Stable		Interphase at 15.2ml (23 hr 44min)	Interphase at 8.4ml (23 hr 30min)	Interphase at 4.6ml (23 hr 8min)	Interphase at 1.4ml (22 hr 53min)	Stable		Stable	Stable	Stable
	14:40	Stable	Stable		interphase @ 15ml	Interphase at 8.4ml	Interphase at 4.6ml	Interphase at 1.4ml (26 hr 33min)	Stable		Stable	Stable	Stable

					(27hr 24min)	(27 hr 10min)	(26 hr 48min)						
14/03/2018	09:00	Stable	Stable		Interphase at 15ml (45 hr 44min)	Interphase at 8.4ml (45 hr 30min)	interphase @ 4.8ml (45hr 8min)	Interphase at 1.4ml (44 hr 53min)	Stable		Stable	Stable	Stable
15/03/2018	10:15	Stable	Stable		Interphase at 15ml (58 hr 59min)	Interphase at 8.4ml (58 hr 45min)	Interphase at 4.8ml (58 hr 23min)	Interphase @ 1.6ml (58hr 8min)	Stable		Stable	Stable	Stable
16/03/2018		Stable	Stable		Interphase at 15ml (82 hr 59min)	Interphase at 8.4ml (82 hr 45min)	Interphase at 4.8ml (82 hr 23min)	Interphase at 1.6ml (82 hr 8min)	Stable		Stable	Stable	Stable
17/03/2018	11:00	Stable	Stable		interphase @ 14.8ml (107hr 44min)	interphase @ 8.6ml (107hr 30min)	Interphase at 4.8ml (107 hr 8min)	Interphase at 1.6ml (106 hr 53min)	Stable		Stable	Stable	Stable
18/03/2018	11:00	Stable	Stable		Interphase at 14.8ml (131 hr 44min)	Interphase at 8.6ml (131 hr 30min)	Interphase at 4.8ml (131 hr 8min)	Interphase at 1.6ml (130 hr 53min)	Stable		Stable	Stable	Stable
19/03/2018	11:00	Stable	Stable		Interphase at 14.8ml (155 hr 44min)	Interphase at 8.6ml (155 hr 30min)	Interphase at 4.8ml (155 hr 8min)	Interphase at 1.6ml (154 hr 53min)	Tiny gelatinous precipitate along tube wall; 0.25H from bottom (154 hr 39min)		Stable	Stable	Stable
20/03/2018	17:00	Stable	Stable		14.6ml (185 hr 44min)	Interphase at 8.6ml (185 hr 30min)	Interphase at 4.8ml (185 hr 8min)	Interphase at 1.6ml (184 hr 53min)	Suspended gel. ppt* along tube (184 hr 39min)		Stable	Stable	Stable
21/03/2018	12:00	Stable	Stable		14.3ml (204 hr 44min)	Interphase at 8.6ml (204 hr 30min)	5ml (204 hr 8min)	1.8ml (203 hr 53min)	Gel ppt along tube (203 hr 39min)		Stable	Stable	Stable
	16:30	Stable	Stable		14.2ml (209 hr 14min)	8.8ml (209 hr)	5.2ml (208 hr 38min)	2ml (208 hr 23min)	Gel ppt along tube (208 hr 9min)		Stable	Stable	Stable
22/03/2018	10:00	Stable	Stable		14.2ml (226 hr 44min)	8.8ml (226 hr 30min)	5.2ml (226 hr 8min)	2ml (225 hr 53min)	Gel ppt along tube (225 hr 39min)		Stable	Stable	Stable

23/03/2018	17:00	Stable	Stable		14.2ml (257 hr 44min)	8.8ml (257 hr 30min)	5.2ml (257 hr 8min)	2ml (256 hr 53min)	Gel (0.01ml) @ tube bottom (256 hr 39min)		Stable	Stable	Stable
26/03/2018	17:00	Stable	Stable	16:40; Stable	14.1ml (329 hr 44min)	8.8ml (329 hr 30min)	5.2ml (329 hr 8min)	2ml (328 hr 53min)	Gel (0.01ml) @ tube bottom (328 hr 39min)	17:12; Stable	Stable	Stable	Stable
27/03/2018	17:00	Stable	Stable	Stable; 24 hr	14.1ml (353 hr 44min)	8.8ml (353 hr 30min)	5.2ml (353 hr 8min)	2ml (352 hr 53min)	Gel (0.01ml) @ tube bottom (352 hr 39min)	Stable; 24 hr	Stable	Stable	Stable
29/03/2018	17:00	Stable	Stable	Stable; 72 hr	14.1ml (401 hr 44min)	8.8ml (401 hr 30min)	5.2ml (401 hr 8min)	2ml (400 hr 53min)	Gel (0.01ml) @ tube bottom (400 hr 39min)	Stable; 72 hr	Stable	Stable	Stable
31/03/2018	17:00	Stable	Stable	Stable; 120 hr	14.1ml (449 hr 44min)	8.8ml (449 hr 30min)	5.2ml (449 hr 8min)	2ml (448 hr 53min)	Gel (0.01ml) @ tube bottom (448 hr 39min)	Stable; 120 hr	Stable	Stable	Stable
7/04/2018	17:00	Stable	Stable	Stable; 288 hr	14.1ml (617 hr 44min)	8.8ml (617 hr 30min)	5.2ml (617 hr 8min)	2ml (616 hr 53min)	Gel (0.01ml) @ tube bottom (616 hr 39min)	Stable; 288 hr	Stable	Stable	Stable
21/04/2018	17:00	Stable	Stable	Stable	14.1ml (953 hr 44min)	8.8ml (953 hr 30min)	5.2ml (953 hr 8min)	2ml (952 hr 53min)	Gel (0.01ml) @ tube bottom (952 hr 39min)	Stable	Stable	Stable	Stable
5/05/2018	17:00	Stable	Stable	Stable	14.1ml (1,289 hr 44min)	8.8ml (1,289 hr 30min)	5.2ml (1,289 hr 8min)	2ml (1,288 hr 53min)	Gel (0.01ml) @ tube bottom (1,288 hr 39min)	Stable	Stable	Stable	Stable
26/05/2018	17:00	Stable	Stable	Stable	14.1ml (1,793 hr 44min)	8.8ml (1,793 hr 30min)	8.8ml (1,793 hr 30min)	2ml (1,792 hr 53min)	Gel (0.01ml) @ tube	Stable	Stable	Stable	Stable

									bottom (1,792 hr 39min)				
12/06/2018	17:00	Stable	Stable	Stable	14.1ml (2,201 hr 44min)	8.8ml (2,201 hr 30min)	8.8ml (2,201 hr 30min)	2ml (2,200 hr 53min)	Gel (0.01ml) @ tube bottom (2,200 hr 39min)	Stable	Stable	Stable	Stable

*Precipitate

Table A.2 Diesel phase percentage in blends at the end of the room temperature stability test

DE Blend	**D:E**	**Volume of diesel added, x (ml)**	**Actual diesel phase, y (ml)**	**Diesel phase (100*y/20), vol%**
DE10	90:10	18	(Stable blend)	(Stable blend)
DE20	80:20	16	(Stable blend)	(Stable blend)
DE25	75:25	15	16.8	84
DE30	70:30	14	14.10	70.50
DE40	60:40	12	8.80	44
DE50	50:50	10	5.20	26
DE60	40:60	8	2	10
DE70	30:70	6	0.01	0.05
DE75	25:75	5	(Stable blend)	(Stable blend)
DE80	20:80	4	(Stable blend)	(Stable blend)
DE90	10:90	2	(Stable blend)	(Stable blend)

Table A.3 Volume of diesel phase in the unstable blends as a function of time (20 ^{o}C)

	Volume of diesel (lower) phase (y), ml				**% volume of diesel phase (100*y/20)**			
Time, hour	**DE30**	**DE40**	**DE50**	**DE60**	**DE30**	**DE40**	**DE50**	**DE60**
0.13	TP*	TP	4	TP	TP	TP	20	TP
0.75	18	8	4	TP	90	40	20	TP
5	15.90	8.40	4.60	1.40	79.50	42	23	7
23	15.20	8.40	4.60	1.40	76	42	23	7
27.50	15	8.40	4.60	1.40	75	42	23	7
45	15	8.40	4.80	1.40	75	42	24	7
58	15	8.40	4.80	1.60	75	42	24	8
108	14.80	8.60	4.80	1.60	74	43	24	8
155	14.80	8.60	4.80	1.60	74	43	24	8
186	14.60	8.60	4.80	1.60	73	43	24	8
204	14.30	8.60	5	1.80	71.50	43	25	9
209	14.20	8.80	5.20	2	71	44	26	10
329	14.10	8.80	5.20	2	70.50	44	26	10
353	14.10	8.80	5.20	2	70.50	44	26	10

*Turbid Phase

Table A.4 Diesel-ethanol (DE) fuel blends temperature sensitivity test data

Time, h	**Temperature, ºC**		**Volume of diesel phase, ml**						**% Diesel phase**				
	Set point	**Bath**	**DE25**	**DE30**	**DE40**	**DE50**	**DE60**	**DE70**	**DE25**	**DE30**	**DE40**	**DE50**	**DE60**
0	25	26	16.8	14.1	8.8	5.2	2	Gel	84	70.5	44	26	10
69.5	25	25.3	11.6	11.8	7.8	4.5	1.4	CSP	58	59	39	22.5	7
70.5	27	27.3	11.4	11.8	7.8	4.5	1.4	CSP	57	59	39	22.5	7
90	27	27.2	10.3	10.8	7.1	3.8	1	CSP	51.5	54	35.5	19	5
92	27	27.2	10.2	10.8	7.1	3.8	1	CSP	51	54	35.5	19	5
94	28.5	29	10	10.8	7.1	3.8	1	CSP	50	54	35.5	19	5
98	28.5	29	10	10.8	7.1	3.8	1	CSP	50	54	35.5	19	5
117.5	28.5	29	9.6	10.6	7	3.8	0.8	CSP	48	53	35	19	4
123	30	30.2	9.5	10.4	7	3.8	0.8	CSP	47.5	52	35	19	4
140	30	30.5	8.6	10	6.8	3.6	0.6	CSP	43	50	34	18	3
146	31.5	32.5	8	9.8	6.6	3.6	0.5	CSP	40	49	33	18	2.5

162	31.5	32.1	6.3	8.8	6	3.2	0.4	CSP	31.5	44	30	16	2
164	31.5	32.5	6	8.8	6	3.2	0.4	CSP	30	44	30	16	2
168.5	32.5	33	5.2	8.5	6	3	0.2	CSP	26	42.5	30	15	1
170.5	32.5	33	5.2	8.5	6	3	0.1	CSP	26	42.5	30	15	0.5
239	32.5	32.8	CSP*	4.8	4.2	1.4	CSP	CSP	-	24	21	7	-
243	33.5	34	CSP	4.6	4	1.4	CSP	CSP	-	23	20	7	-
259.5	33.5	34.4	CSP	3.3	3.6	1	CSP	CSP	-	16.5	18	5	-
262	34.5	35	CSP	3.3	3.6	1	CSP	CSP	-	16.5	18	5	-
284	34.5	35	CSP	2	3.1	0.6	CSP	CSP	-	10	15.5	3	-
289.5	35.5	36.2	CSP	2	3	0.3	CSP	CSP	-	10	15	1.5	-
309	35.5	36	CSP	CSP	2.6	CSP	CSP	CSP	-	-	13	-	-
312	36.5	37	CSP	CSP	2.4	CSP	CSP	CSP	-	-	12	-	-
314	36.5	37	CSP	CSP	2.2	CSP	CSP	CSP	-	-	11	-	-

333.5	36.5	37	CSP	CSP	2	CSP	CSP	CSP	-	-	10	-	-
335.5	37.5	38	CSP	CSP	2	CSP	CSP	CSP	-	-	10	-	-
406.5	37.5	38	CSP	CSP	CSP	CSP	CSP	CSP	-	-	-	-	-

*Clear Single Phase

APPENDIX B

Table B.1 Estimated depths of penetration of the injected fuel

Fuel blend	**Load, kW_e**	**Fuel mass, mg**	**Nozzle open period, ms**	**Depth of penetration, mm**
DE0	0	6.03	0.68	29.33
	2	6.33	0.72	30.06
	3	6.5	0.74	30.47
DE5	0	6.6	0.75	30.7
	2	11.67	1.33	40.81
	3	12.73	1.45	42.63
DE10	0	13.1	1.49	43.25
	2	15.8	1.8	47.51
	3	15.67	1.78	47.29
DE15	0	17.67	2.01	50.22
	2	19.83	2.25	53.21
	3	26.57	3.02	61.61

APPENDIX C

Table C.1 NOx and NH_3 emission levels for the gasification of the stalk residues of sweet sorghum, grain sorghum, and corn

Stalk residue	Equivalence ratio (Ø)	NO, ppm	NO2, ppm	NOx, ppm	NH_3, ppm
Sweet sorghum	3.60	155.5	1.63	157.13	13.49
	2.40	165.9	0.23	166.13	3.54
	2.10	297	0	297	19.55
	1.90	397.5	6.13	403.63	30.41
	1.60	421.7	10.8	432.50	25.23
	1.50	133.8	0.25	134.05	6
	1.40	134.1	0.41	134.51	28.61
Grain	2.75	225.9	1.10	227	9.52
	2.03	40	0	40	18.30
	1.73	203	0.50	203.50	14.55
	1.54	113	1.10	114.10	17.13
Corn	2.91	166	0	166	26.09
	2.42	165	0	165	90.76
	1.87	274	0	274	144.06
	1.28	88	0	88	40.02

Appendix D

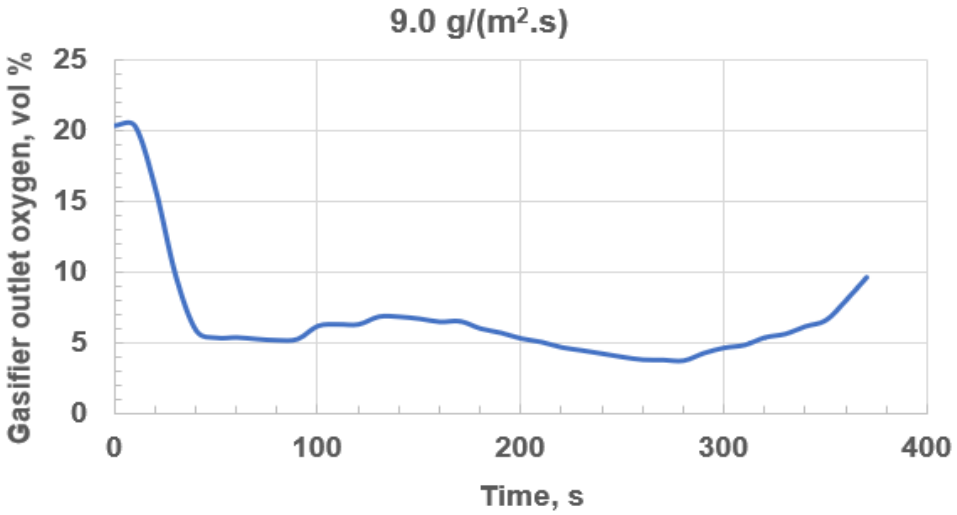

Figure D.1 Gasifier outlet oxygen as a function of time